Modelling Ageing Skeletal Muscle *In Vitro* to Determine the Effect of Aged Skeletal Muscle Secretomes on Macrophage Function and Their Role in Sarcopenia Progression

Volume I

Parbata Chauhan

Doctor of Philosophy

ASTON UNIVERSITY

June 2022

Aston University

Modelling Ageing Skeletal Muscle *In Vitro* to Determine the Effect of Aged Skeletal Muscle Secretomes on Macrophage Function and Their Role in Sarcopenia Progression

Parbata Chauhan

Doctor of Philosophy

2022

Thesis Abstract

Skeletal muscle to immune system crosstalk maintains normal functioning of muscle tissue, however this communication could be altered during age-associated muscle conditions. This body of work aims to better understand this communication and suggests components of an ageing muscle secretome, including extracellular vesicles (EVs) could be responsible for the progression of the age-related muscle wasting disorder, sarcopenia.

Most studies in the muscle field employ serum-based methods to generate differentiated skeletal muscle, however the use of serum can interfere with EV-related research. This study is built on the foundation of a serum-free skeletal muscle model for the uncomplicated study of muscle-derived EVs; an approach many muscle EV researchers avoid. Data here show a serum-free murine skeletal muscle system can be used to model sarcopenia and muscle cellular senescence *in vitro* for the investigation of downstream effects of aged muscle secretomes on both skeletal muscle cells and macrophages, and their involvement in furthering muscle atrophy.

Sarcopenic and senescent myotube secretomes propagate an atrophic muscle phenotype in healthy myotubes and therefore facilitate the progression of sarcopenia via the bystander effect. Regarding immunomodulation, sarcopenic and senescent myotube secretomes and their isolated components are shown to have different and at times contradictory effects on macrophage function. Data presented here highlight the complexity of the aged skeletal muscle secretome role in modulating macrophage function, and suggest they induce an intermediate macrophage phenotype, which is responsible for maintaining age related muscle atrophy. It is proposed that aged muscle secretomes can promote anti-inflammatory features in these hybrid macrophages, such as reducing nitric oxide production and therefore limiting an M1 macrophage phenotype, whilst concomitantly encouraging pro-inflammatory functions, including reactive oxygen species release.

Moreover, proteomic analyses suggest a role for aged skeletal muscle secretome derived EVs in both directly stimulating sarcopenia in healthy muscle cells and indirectly by stimulating an aberrant macrophage response to ageing skeletal muscle.

Key words: Sarcopenia, muscle atrophy, cellular senescence, macrophages, extracellular vesicles

Acknowledgements

I would like to thank my supervisors Professor Andrew Devitt and Dr James Brown for providing me with this opportunity and for putting up with me for so long.

Thank you to my colleagues, Kiran Shabir, James Gavin and Lois Grant for travelling the PhD road with me and without whom the lab would be a much quieter and less fun place to work.

A special thanks to my friends Ivana Milic and Andrea Markou for being with me every step of the way. Ivana, thank you for both your guidance and patience with me in the lab, as well as for teaching me all things mass spec related. A huge thank you to Andrea Markou for always putting a smile on my face and for the many sit-down times we had. Above all, I appreciate the friendship and support you have both provided over the years, I will treasure this always.

Thank you to my parents and sister for their continuous support and for not letting me give up when the going got tough.

To everyone who held my hand on this long journey, thank you.

Table of Contents

Abbreviations

•NO	Nitric oxide
AIMP1	Aminoacyl tRNA synthase complex-interacting multifunctional protein 1
ATIR	Angiotensin type I receptor
CaMK2α	Calcium/calmodulin dependent protein kinase type II alpha
CCL17/TARC	Thymus and activation regulated cytokine
CCL2	CC chemokine ligand 2
CCL22/MDC	Macrophage derived chemokine
CD81	Cluster of differentiation 81
CoA	Cosine of angle
COX-2	Cyclo-oxygenase 2
CRP	C reactive protein
CXCL1	CXC chemokine ligand 1
CXCL1/KC	Keratinocyte derived cytokine
CYLD	Ubiquitin carboxyl-terminal hydrolase CYLD
DAMPs	Damage associated molecular patterns
DEX	Dexamethasone
DNAJA1	DNAJ homolog subfamily A member 1
DXA	Dual energy X-ray absorptiometry
ECM	Extracellular matrix
ENO-β	Beta enolase
ER	Endoplasmic reticulum
ESCRT	Endosomal sorting complexes required for transport
ESCRT III	Endosomal sorting complexes required for transport III
EV(s)	Extracellular vesicles
FBS	Foetal bovine serum
FGF	Fibroblast growth factor
G6PDH	Glucose-6 phosphate dehydrogenase
G-CSF	Granulocyte-colony stimulating factor

GM-CSF	Granulocyte monocyte-colony stimulating factor
GO	Gene ontology
GSH	Glutathione
H_2O_2	Hydrogen peroxide
HGF	Hepatocyte growth factor
HS	Horse serum
IDE	Insulin degrading enzyme
IFGFBP-5	Insulin like growth factor binding protein 5
IFN-γ	Interferon gamma
IGF	Insulin like growth factors
IGF-1	Insulin like growth factor-1
IL-10	Interleukin-10
IL-12	Interleukin-12
IL-12p40	Interleukin-12 subunit 40
IL-12p70	Interleukin-12 subunit 70
IL-13	Interleukin-13
IL-15	Interleukin-15
IL-17	Interleukin-17
IL-18	Interleukin-18
IL-1α	Interleukin-1 alpha
IL-1β	Interleukin-1 beta
IL-23	Interleukin-23
IL-4	Interleukin-4
IL-6	Interleukin-6
IL-8	Interleukin-8
iNOS	Inducible nitric oxide synthase
ITS	Insulin transferrin selenium
LBP	LPS binding protein
LOX	Lysyl oxidase
LPS	Lipopolysaccharide
MCP-1	Monocyte chemotactic protein-1
MFI	Mean fluorescence intensity
mH2A1	Core histone macro-H2A.1
mH2A1.2	Core histone macro-H2A.1 isoform 2

MHC	Major histocompatibility complex
MHC1	Major histocompatibility complex 1
miRNAs	MicroRNAs
MØ	Macrophage(s)
MP	Microparticles
MS	Mass spectrometry
MuRF-1	Muscle RING 1
MYL4	Myosin light chain 4
NADPH	Nicotinamide adenine dinucleotide phosphate (reduced)
NED	N-1-naphthylethylenediamine dihydrochloride
NEV	Normal myotube-derived EVs
NF	Normal myotube-derived filtrate
NF-κB	Nuclear factor-kappa B
NK cells	Natural killer cells
NO_{2^-}	Nitrite
NOX	NADPH oxidase
NOX2	NADPH oxidase 2
NP	Normal myotube-derived soluble proteins
NR	Normal myotube-derived retenate
PDGF	Platelet derived growth factor
PGE2	Prostaglandin E2
Prx-1	Peroxiredoxin 1
ROS	Reactive oxygen species
SASP	Senescence-associated secretory phenotype
SA-β-gal	Senescence-associated beta-galactosidase
SDS-PAGE	Sodium-dodecyl-sulphate polyacrylamide gel electrophoresis
SEC	Size exclusion chromatography
SenEV	Senescent myotube-derived EVs
SenF	Senescent myotube-derived filtrate

SenP	Senescent myotube-derived soluble proteins
SenR	Senescent myotube-derived retentate
SEV	Sarcopenic myotube-derived EVs
SF	Serum free
SF	Sarcopenic myotube-derived filtrate
SOD1	Superoxide dismutase 1
SOD2	Mitochondrial superoxide dismutase
SOD3	Superoxide dismutase 3
SP	Sarcopenic myotube-derived soluble proteins
SR	Sarcopenic myotube-derived retentate
TET2	Methylcytosine dioxygenase TET2
TGF-β1	Transforming growth factor-beta 1
Th1	T helper cell 1
Th2	T helper cell 2
THP-1/VD3	VD3 differentiated THP-1 macrophage-like cells
TLR(s)	Toll-like receptor(s)
TLR-4	Toll-like receptor 4
TNF-α	Tumour necrosis factor alpha
Tregs	Regulatory T cells
TRPS	Tunable resistive pulse sensing
TSAP6	Tumour suppressor activated pathway 6
TSG101	Tumour susceptibility gene 101
UPR	Ubiquitin proteasome system
USP19	Ubiquitin specific protease 19
VD3	1α,25-dihydroxyvitamin D3
VEGF	Vascular endothelial growth factor
yFMI	y-axis forward migration index

List of figures

List of tables

1. Introduction

1.1 Skeletal muscle structure and function

Skeletal muscle is one of the 3 main types of muscle found within the body and constitutes approximately 40% of total bodyweight (Frontera and Ochala, 2015). It has an organised structure and is comprised of groups of multinucleated muscle fibres surrounded by connective tissue. Muscle fibres are comprised of myofibrils which in turn consist of multiple myofilaments. It is the arrangement of myofibrils into contractile units that creates the characteristic striated morphology of skeletal muscle (Sanger et al., 2010). Skeletal muscle also contains a population of muscle stem cells, known as satellite cells. Satellite cells are involved in muscle growth and regeneration as they can be activated to differentiate to produce new muscle fibres (Bareja et al., 2014, Macaluso and Myburgh, 2012).

Skeletal muscle is responsible for numerous functions, with the primary function being mechanical. Skeletal muscle has contractile ability which is used in force generation to induce movement (Lieber and Bodine-Fowler, 1993). In addition to facilitating motility, this tissue also has a role in energy metabolism and is responsible for regulating energy homeostasis. Skeletal muscle has a high metabolic capacity and uses glucose to generate ATP for muscle contraction (Mukund and Subramaniam, 2020). When glucose is not in high demand, skeletal muscle, like the liver functions as an energy store by storing glucose in the form of glycogen (Argilés et al., 2016). By storing excess glucose, skeletal muscle can release it to organs and tissues during periods of fasting. Glucose is not the only energy substrate stored by skeletal muscle. It is also a source of amino acids, which are stored as proteins that can be metabolised to provide energy during extreme malnourishment (Wolfe, 2006).

To maintain tissue structure and undertake the functions it is responsible for, skeletal muscle has processes in place for tissue repair and the generation of new muscle during instances of damage.

1.2 Myogenesis and skeletal muscle regeneration

Due to its vital role in force generation for movement, skeletal muscle is prone to trauma and this tissue frequently incurs damage. Routine wear and tear causes only minor muscle damage and does not impact overall function. However, following injury or strenuous exercise, serious damage sustained by muscle fibres can be repaired intrinsically by skeletal muscle tissue through myogenesis. The restorative myogenic process is a rapid but well-coordinated series of events involving the activation, proliferation and differentiation of skeletal muscle stem cells known as satellite cells (figure 1) (Tidball, 2017). These stem cells, which usually

reside in a quiescent state can be induced to proliferate by various stimuli including inflammatory factors, as well as mechanical and oxidative stresses (Yin et al., 2013). After reentering the cell cycle, a proportion of these proliferating satellite cells will advance to a differentiation stage, whilst any cells not committed to this route undergo self-renewal and are returned to their inactive state, to restore the existing population of satellite cells for future regenerative events (Murphy et al., 2011). Once satellite cells cease proliferating, they will differentiate into myoblasts. Differentiating myoblasts align and fuse to form long, multinucleated myotubes which in turn undergo differentiation to generate mature muscle fibres with contractile potential (Das et al., 2007).

Skeletal muscle regeneration following damage involves numerous cell types to restore tissue homeostasis, however this reparative process can only be facilitated and modulated by cells of the immune system. Innate immune cells initiate a sterile inflammatory response to remove damaged myofibers and subsequently promote healing.

1.2.1 Skeletal muscle regeneration and inflammation

Prior to the regenerative phase of skeletal muscle repair, damaged muscle fibres undergo a degenerative process (CHARGÉ and RUDNICKI, 2004). During degeneration, trauma to muscle fibres disrupts membrane integrity and increases cell permeability, leading to the influx of extracellular calcium (St Pierre and Tidball, 1994), resulting in protein degradation and cell necrosis. Necrotic myofibres leak a range of factors normally contained within the cytosol into the local microenvironment to activate the small number of tissue resident inflammatory cells, however, these factors, which include damage associated molecular patterns (DAMPs) and myokines are also released into the blood and are responsible for the recruitment of circulating immune cells into the muscle, initiating acute inflammation (Sciorati et al., 2016).

Muscle resident immune cells activated by myofibre damage include mast cells which immediately degranulate post-injury, releasing pro-inflammatory mediators including histamine, eicosanoids, tumour necrosis factor alpha (TNF-α) and interleukin 1 (IL-1) to recruit additional mast cells and promote neutrophil infiltration, which in turn further encourages inflammation in the muscle (Côte et al., 2008, Krystel-Whittemore et al., 2016).

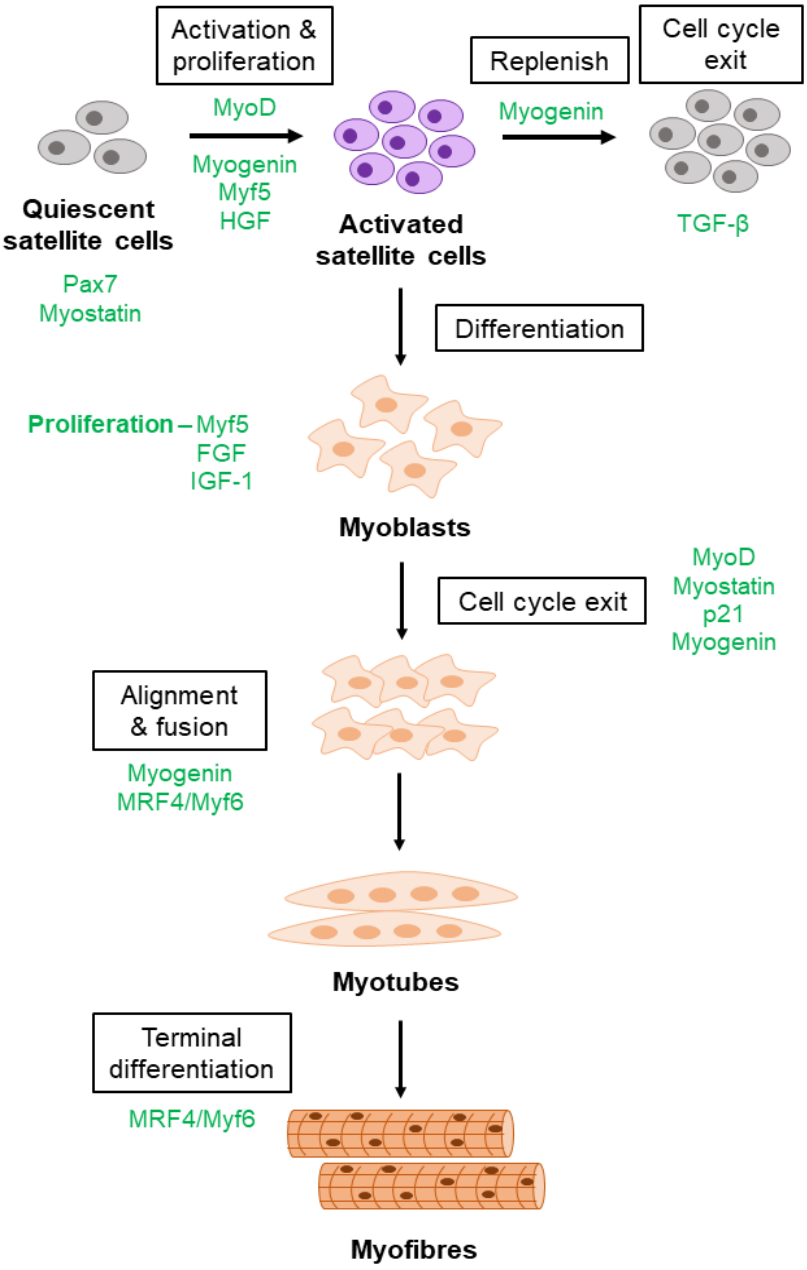

Figure 1. Skeletal muscle regeneration. Myogenesis is a tightly regulated process that can be stimulated by exercise or injury to the muscle tissue and is controlled by numerous myogenic factors that mediate each stage of muscle repair (shown in green). Muscle damage induces quiescent stem cells to re-enter the cell cycle and proliferate, after which they will either commit to differentiation or return to their original resting state to replenish the satellite cell stock. Following a period of proliferation, activated satellite cells differentiate into skeletal muscle precursor cells known as myoblasts. In the absence of local growth factors, myoblasts withdraw from the cell cycle to align and fuse with neighbouring myoblast cells to form multinucleated myotubes. Myotubes undergo a growth phase, terminal differentiation and lastly organise themselves into myofibers, the contractile units of skeletal muscle.

In addition to mast cells, skeletal muscle also comprises a population of resident macrophages that are involved in the early stages of the acute inflammatory response. Like the activated mast cells, these resident macrophages produce the chemoattractants CC-chemokine ligand 2 (CCL2) and CXC-chemokine ligand 1 (CXCL1), as well as expressing DAMPs to induce recruitment and activation of other immune cells (Brigitte et al., 2010).

1.2.1.1 The first wave of immune cells - neutrophils

Chemoattractants secreted by resident immune cells in combination with damage associated myokines released by myofibres cause peripheral neutrophils to rapidly extravasate from the blood and enter the muscle to become the first wave of responding immune cells (Butterfield et al., 2006). Mice with acutely injured skeletal muscle tissue show increased neutrophil numbers as early as 2 hours post injury, with numbers peaking between 6 and 24 hours after damage initiation, and rapidly decline after 72 to 96 hours (Shireman et al., 2007) (Arango Duque and Descoteaux, 2014). Once within the damaged muscle, neutrophils produce proteases and reactive oxygen species (ROS) to aid the removal of necrotic myofibres by phagocytosis. Despite the presence of these factors exacerbating existing muscle damage, the absence of neutrophils from the acute inflammatory phase has been shown to have a detrimental effect on muscle repair. Depletion of these cells in 19-day old mice subsequently diminished myofibre necrosis in mice aged 21 days, however at 28 days these mice exhibited significantly reduced myogenesis (Hodgetts et al., 2006). Later studies have also suggested neutrophils to have a beneficial impact on the subsequent stages of muscle repair due to their supposed inflammation resolving properties, highlighting their contradictory but important role throughout the regenerative process (Sugimoto et al., 2016). These cells are short lived and 72 to 96 hours post muscle injury, infiltrated neutrophil numbers decline, returning to normal levels following the release of interleukin 8 (IL-8) and IL-1, which initiate monocyte and macrophage recruitment to the site of damage. Macrophage recruitment signifies the beginning of the second wave of immune cell infiltration.

1.2.1.2 The second wave of immune cells (part 1) – pro-inflammatory macrophages

Increases in macrophage number coincide with neutrophil decline and are observed in damaged skeletal muscle within 24 to 48 hours to become the predominant immune cell within the tissue (Chazaud et al., 2009). The influx of monocytes and macrophages denotes the beginning of the regenerative stage of muscle repair and these cells play a fundamental role in regulating this process. The local muscle microenvironment influences the activation state and subsequently the effector function of the infiltrating macrophages. Two different macrophage activation states have been identified in regenerating skeletal muscle, giving rise

to two subpopulations: M1 or 'classically' activated macrophages and M2 or 'alternatively' activated macrophages (Mantovani et al., 2004). Despite the presence of both M1 and M2 macrophages in skeletal muscle following injury, the numbers of each subpopulation are skewed depending on the stage of muscle repair, with M1 macrophages emerging during the early stages of the inflammatory response and M2 macrophages developing in the later stages.

Monocytes arrive in a muscle environment enriched with many pro-inflammatory cytokines secreted by both resident and peripheral immune cells, which facilitate monocyte to macrophage differentiation and activate monocyte-derived macrophages to exhibit a proinflammatory M1 phenotype. This category of macrophage is involved in the removal of apoptotic neutrophils and clearance of necrotic cell debris, which triggers ROS release.

In addition to augmented respiratory burst, M1 macrophages are also known to secrete reactive nitrogen species, such as the free radical nitric oxide ($^{\bullet}NO$) produced by the enzyme inducible nitric oxide synthase (iNOS) and is important in aiding muscle regeneration (Villalta et al., 2008). Increasing levels of $^{\bullet}NO$ aid the removal of cell debris by promoting apoptosis of damaged myofibres to be subsequently internalised by M1 macrophages, whilst low $^{\bullet}NO$ levels have a shielding role and protect cells within muscle tissue against oxidative damage (Fujii et al., 2010, Yoshioka et al., 2003).

More importantly, M1 macrophages secrete pro-inflammatory, T helper 1 (Th1) immune response inducing cytokines (TNF-α, interleukin 6 (IL-6) , interferon-γ (IFN-γ) and IL-1β) at the site of damage (Yang and Hu, 2018). These pleiotropic cytokines have dual roles when released in response to muscle damage. They have significant involvement in regulating the progression of acute inflammation but are also implicated in muscle homeostasis and repair.

1.2.1.3 The second wave of immune cells (part 2) – T lymphocyte recruitment

T cells also comprise the second wave of immune cells that infiltrate damaged muscle tissue, following the arrival and activation of the pro-inflammatory macrophages and signifies the onset of the adaptive immune response. Both helper CD4+ and cytotoxic CD8+ T cells are recruited to the site of damage, with the majority being CD8+ cells, by M1 macrophages approximately 3-5 days after injury occurrence and remain as long as 10 days post injury (Cheng et al., 2008). Once within the muscle, T cells contribute to and sustain the inflammatory microenvironment through the secretion of cytokines. Similar to M1 macrophages, T cells also release a range of pro-inflammatory cytokines, including TNF-α, IFN-γ, IL-1β, interleukin 4 (IL4), interleukin 12 (IL-12) and interleukin13 (IL-13) (Yang and Hu, 2018).

Their arrival in injured muscle induces regeneration since they maintain the myocyte population. Treatment of satellite cells with T cell conditioned medium activates them to migrate and re-enter the cell cycle. Furthermore, murine satellite cells cultured directly in T cell conditioned medium for long periods of time maintained both the proliferative and myogenic capacity of muscle stem cells over multiple passages (Fu et al., 2015). These researchers found the conditioned culture medium contained high levels of the aforementioned cytokines which upheld the ability of the muscle stem cells to divide. These findings were also replicated in mice *in vivo,* as cultured satellite cells maintained their "stemness" when transplanted into injured muscle. The transplanted satellite cells migrated to the site of damage and proliferated to both restore the endogenous muscle stem cell population and to undergo differentiation (Fu et al., 2015). However, the conditioned medium used was collected from a general population of CD3+ T cells rather than a specific subset, therefore the individual contributions of certain types of T cell on the myogenic process cannot be determined from this study.

The absence of CD3+ T cells is detrimental in both young and old individuals. Young T cell deficient mice experience delays in growing mature muscle tissue, with adult mice exhibiting similar difficulties following muscle injury. Although, transplanting CD3+ T cells into adult mice restores the ability of skeletal muscle to repair itself (Fu et al., 2015). Similarly, administration of a cytokine cocktail containing TNF-α, IFN-γ, IL-1α and IL-13 to T cell deficient mice completely rescues the regenerative capacity of the muscle, emphasising the importance of T cell secreted factors in the formation of new muscle.

The CD4+ helper T cell population, specifically Th1, Th2 and Th17 cells have been shown to increase myoblast proliferation *in vitro*, whilst inhibiting their differentiation and *in vivo* sustained the initial stages of myogenesis (Kwee et al., 2018). However, the ability of CD4+ T cells to limit myogenic differentiation is dependent on the level of IL-4 and IL-13 in the microenvironment, suggesting a combination of cytokines and/or other secreted factors are needed to stimulate proliferation (Kwee et al., 2018).

Cytotoxic CD8+ T cells influence the behaviour of immune cells in addition to regulating the myogenic process. They induce macrophages to upregulate their expression of monocyte chemotactic protein 1 (MCP-1) to further recruit peripheral inflammatory monocytes to the site of damage (Lu et al., 2011). The contribution of this T cell subtype to myogenesis is highlighted in CD8+ T cell knockout mice, which did not increase MCP-1 secretion resulting in fewer satellite cell numbers, reduced cross-sectional area of myofibres and increased fibrosis (Zhang et al., 2014).

1.2.1.4 The third wave of immune cells (part 1) – pro-inflammatory macrophage to pro-resolving macrophage transition

The pro-inflammatory microenvironment created and sustained by damaged myofibres and ensuing infiltrating neutrophils and M1 macrophages during the acute inflammatory stage, is eventually converted to an anti-inflammatory, pro-resolving microenvironment which initiates the change from myogenic proliferation to differentiation (figure 2). This change is characterised by a shift in macrophage subtypes, with M1 macrophages switching to the alternatively activated M2 phenotype, to become the predominant macrophage population at the site of damage almost 3 days post damage (Arnold et al., 2007). Consequently, M2 macrophages are the principal instigators of the later phases of skeletal muscle regeneration and tissue remodelling.

M1 to M2 phenotype transition is initiated by the internalisation of apoptotic cells and debris by pro-inflammatory macrophages, which reduces the production of pro-inflammatory cytokines whilst enhancing anti-inflammatory cytokine release. Macrophage switching can also be stimulated by lipid mediators, such as the eicosanoid prostaglandin E2 (PGE2) (Luan et al., 2015, Liu et al., 2012). Though PGE2 contributes to skeletal muscle regeneration by activating satellite cell and myoblast proliferation, its role in influencing macrophage phenotype in skeletal muscle is unknown and requires further investigation (Mo et al., 2015, Ho et al., 2017).

In contrast to M1 macrophages, M2 macrophages are involved in Th2 immune responses, which include immunoregulatory functions, reducing inflammation, stimulating tissue remodelling and tumour progression (Sica and Mantovani, 2012). M2 macrophages are associated with increased expression of the mannose receptor CD206, CD163 and arginase1 activity. In addition to cell surface marker expression, M2 macrophages can also be characterised by their cytokine panel, which includes interleukin 10 (IL-10), transforming growth factor beta (TGF-β) and insulin-like growth factor 1 (IGF-1), all of which are associated with moderating the inflammatory response (Viola et al., 2019) (Murray et al., 2014).

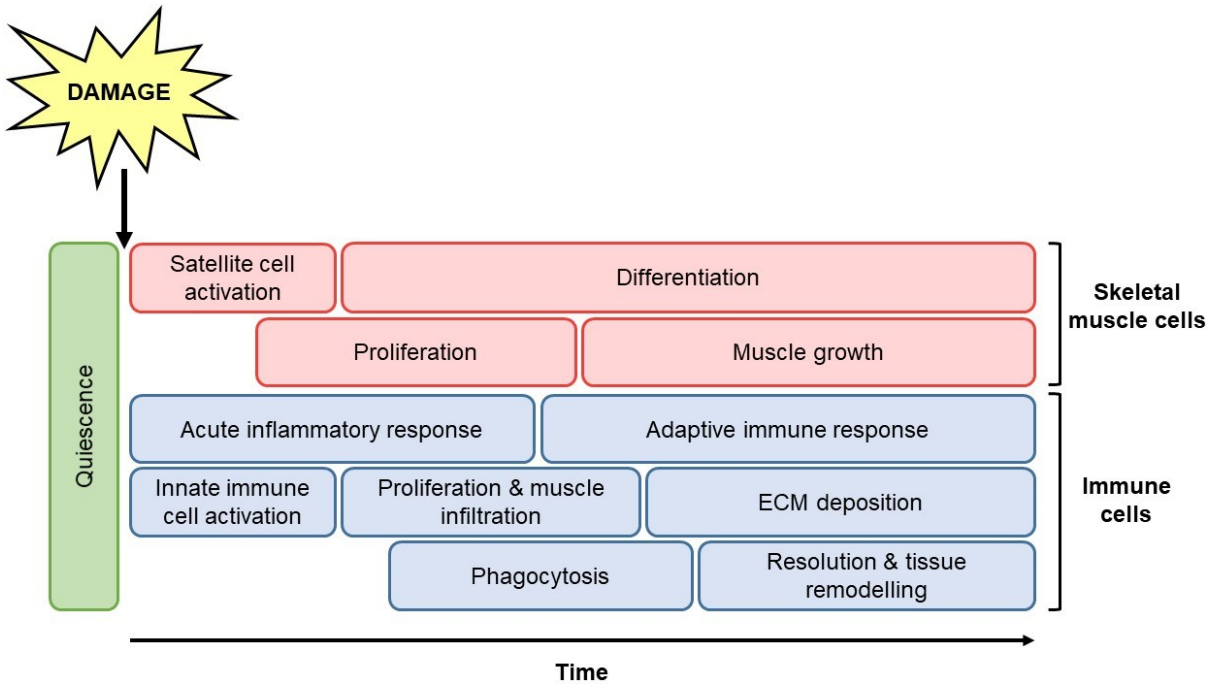

Figure 2. Damage associated muscle regeneration coincides with the immune response. Myogenesis is concurrent with the initial innate and type 2 or adaptive immune responses, with cells in each tissue influencing the activity of the other. The pro-inflammatory response during the initial stages of regeneration is necessary to activate satellite cells and initiate myoblast proliferation. Whilst the proresolving stage promotes myoblast differentiation for the formation of mature myofibres and also initiates remodelling of muscle tissue. Consequently, progression of the immune response is key to maintaining skeletal muscle homeostasis (Adapted from Tidball, 2017).

When discussing alternatively activated macrophages, referring to the M2 phenotype is a simplified view of macrophage switching. In fact, polarisation to the M2 subtype is more complex than observed with M1 polarisation. Following activation, M2 macrophages can be further polarised into three different subsets (M2a, M2b, M2c and M2d), each of which has a distinct role in tissue repair but all exhibit anti-inflammatory and pro-resolving properties (Yao et al., 2019). The M2a population is produced after exposure to the cytokines IL-4 and IL-13 and is associated with angiogenesis and fibrosis; M2b macrophages are generated following interaction with immune complexes, as well as lipopolysaccharide (LPS), IL-1β and toll-like receptors (TLRs) (Wang et al., 2019a). The M2c subset arise from IL-10, TGF-β or glucocorticoid treatment, which enhances phagocytosis of apoptotic cells to promote the resolution of inflammation and tissue repair (Mantovani et al., 2004). Lastly, M2d macrophages are activated by TLR antagonists and this subtype secretes vascular endothelial growth factors to promote angiogenesis (Ferrante et al., 2013). Despite the existence of several subpopulations under the M2 macrophage umbrella, M2a and M2c macrophages are the predominant cells involved in skeletal muscle repair.

In vitro, both M2a and M2c macrophages enhance myoblast fusion and their differentiation into myotubes (Villalta et al., 2008). M2a macrophages also play a protective role during muscle regeneration as they reduce M1 macrophage associated myocyte lysis by competing for arginine, the substrate used by both the urea cycle enzyme arginase in M2a and iNOS in M1 subsets (Villalta et al., 2008). Due to the high expression of arginase and TGF-β, M2a macrophages also encourage collagen production by fibroblasts, consequently the balance of M2 subsets must be regulated to prevent muscle fibrosis following repair. In contrast to other M2 subtypes, M2c macrophages also express receptors for pro-inflammatory cytokines, which might be involved in their sequestration from the microenvironment thereby limiting inflammation (Perrier et al., 2004). Additionally, the removal of pro-inflammatory cytokines and chemokines could facilitate the progression of myogenesis by limiting myogenic proliferation and enhancing myogenic differentiation. However, when discussing macrophage mediated inflammation resolution and skeletal muscle repair, the effects of all M2 subtypes are commonly encompassed by the "M2 macrophages".

The switch from M1 to M2 macrophages is coupled to the progression of myogenesis and has been shown to coincide with the expression of myogenic genes that correspond to myocyte terminal differentiation. During the pro-inflammatory stage, the M1 macrophage secretome is necessary to induce myoblast proliferation whilst limiting cell fusion, conversely following the subtype switch, pro-resolving M2 macrophage cytokines stimulate myotube formation and the development of mature muscle (Arnold et al., 2007). However, some studies in mice have shown IL-10 stimulated M2 macrophages co-cultured with myoblasts specifically promote their proliferation rather than differentiation, suggesting an additional mitogenic role for this macrophage subtype (Villalta et al., 2011, Deng et al., 2012). Overall, this highlights the importance of macrophage activation states on the behaviour of muscle progenitor cells. This transition must be tightly controlled since prevention of macrophage conversion or skewed polarisation, specifically to a M1 phenotype is detrimental to muscle repair and has been shown to attenuate the growth of muscle fibres (Nie et al., 2016). Impeding the natural sequence of macrophage subtype switching can also hinder muscle regeneration. It is crucial for a pro-inflammatory response, spearheaded by M1 macrophages to occur prior to the antiinflammatory, pro-resolving phase for the successful repair of muscle damage. Local injection of IL-10 to a mouse wound site 2-3 days following injury counteracted the mitogenic effects of TNF-α on satellite cells (Perdiguero et al., 2011). Early IL-10 treatment caused reduced presence of mature myotubes within the skeletal muscle tissue, due to the ability of this cytokine to limit myoblast proliferation. The polarisation of macrophages towards the M2 phenotype is promoted by an increase in IL-10 expression. Similarly, the complete removal of macrophages from injured muscle also elicits a negative effect on regeneration. Limiting

macrophages during the transition stage, such as reducing M1 macrophage numbers and increasing M2 macrophages limited the formation of new myotubes *in vivo* (Tidball and Wehling-Henricks, 2007).

1.2.1.5 Macrophage phenotyping obstacles

The common M1/M2 nomenclature often used to classify macrophages is an oversimplification of the subtypes found within damaged muscle tissue, instead macrophages are considered to be more plastic than previously thought. Despite the findings of some *in vitro* studies in which definitive macrophages phenotypes have been found, the complexity of the damaged skeletal muscle microenvironment to which macrophages are exposed can give rise to a range of activation states. *In vivo* studies of muscle damage have identified a population of macrophages that do not express markers that denote M1 or M2 macrophages entirely, despite detecting pro- and anti-inflammatory macrophage subpopulations. Instead, these macrophages express a combination of both M1 and M2 gene signatures during the initial stages of muscle damage, with the majority of markers being downregulated following resolution and repair (Novak et al., 2014). Consequently, macrophages are considered dynamic immune cells, with the same population of macrophages lysing muscle fibres and inducing a pro-inflammatory response to muscle damage and subsequently being involved in resolving inflammation and promoting tissue repair.

Moreover, macrophage classification can be further complicated due to species variations. Murine macrophage phenotyping is considered straightforward than in human due to the discovery of distinct markers for the identification of both M1 and M2 macrophages in mice, whilst in humans macrophage classification is more difficult due to the absence of reliable markers. Often, the expression of markers and the gene signatures of macrophages do not correlate with their observed function. One such disputed marker is nitric oxide (•NO), the production of which is associated with M1 classically activated macrophages. Whilst M1 polarisation by LPS and IFN-γ *in vitro* induces iNOS activation and •NO release in mice, a similar response does not occur in humans (Murray and Wynn, 2011). These inducers can polarise human macrophages to an M1 phenotype, however these cells do not express iNOS or produce •NO (Schneemann and Schoedon, 2002). Controversy also surrounds the proposed M2 marker, arginase, which like iNOS has different expression patterns in humans and mice (Murray and Wynn, 2011). With the dispute concerning macrophage markers, researchers need to be aware that when conducting macrophage polarisation studies in mice, the results might not fully translate to the human system. Therefore, there is a possibility that the development of macrophage targeting therapies for the treatment of myopathies using mouse models could be ineffective against the human equivalent.

1.2.1.6 The third wave of immune cells (part 2) – regulatory T cells

Concurrent with the switch of M1 macrophages to the M2 subtype, there is also an increase in the regulatory T cell (Tregs) population during the later phases of muscle regeneration (Burzyn et al., 2013). This is a unique type of Treg that is found to specifically infiltrate damaged muscle tissue and differs from the subtype that normally resides within the lymphoid organs. At this stage, the number of other T cell subtypes decline with Tregs becoming the predominant T cell at the site of damage. Tregs are responsible for the decrease in other T cell populations, for example CD8+ T cells which has a beneficial effect on muscle repair. The reduction of CD8+ T cells attenuates myoblast proliferation and promotes myoblast differentiation (Castiglioni et al., 2015). Once recruited and activated, Tregs produce IL-10 to facilitate the change in macrophage activation states and encourage new myofibre production (Villalta et al., 2011).

Tregs not only mediate immune cell responses, but also exert their influence directly on the muscle stem cell population. Tregs secrete the protein amphiregulin, which is a member of the epidermal growth factor family that has been shown to stimulate the differentiation of satellite cells both *in vitro* and *in vivo* (Burzyn et al., 2013). Depletion of this T cell population inhibits the expression of myogenic transcription factors and protracts the inflammatory response by limiting M1 to M2 macrophage switching, leading to slow and defective muscle repair. Specifically, removal of Tregs from damaged muscle results in modifications of the entire muscle transcriptome, the production of smaller myofibres and increased fibrotic tissue (Kuswanto et al., 2016, Burzyn et al., 2013). Treatment of Treg deficient mice with amphiregulin restored the normal muscle transcriptome profile and encouraged myoblast to myotube differentiation. However, this conclusion contradicts that of another study, which determined T cell derived amphiregulin to be involved in myogenic proliferation rather than differentiation (Castiglioni et al., 2015).

It is possible that these cells might also provide skeletal muscle with a memory for future regenerative events. Tregs isolated from damaged skeletal muscle tissue from multiple injured mice all showed identical complementary determining regions within their T cell receptors, regions that were not observed in other T cell subsets within muscle tissue or splenic T cells (Burzyn et al., 2013). Memory Tregs will recognise a common antigen specifically released when damage is incurred to regulate the immune response accordingly and to initiate muscle repair.

1.2.2 Tissue remodelling following inflammation resolution

Skeletal muscle is a multifaceted tissue; therefore, the non-muscle cells, ECM and vascular components also incur extensive damage when skeletal muscle is injured. Consequently, successful functional recovery of damaged muscle requires the repair of these architectural constituents in addition to myocyte regeneration. The onset of the inflammatory response has destructive effects on the ECM in particular, with inflammatory cells releasing degradative proteins such as elastase and matrix metalloproteinases (Kim and Lee, 2016).

Following trauma, during the latter stages of the regenerative process, deposition of new ECM components coincides with both myogenic differentiation and the resolution of inflammation. ECM repair is initiated by M2 macrophage-derived TGF-β which activates fibroblasts to produce various collagens (Garg et al., 2015). Collagens form intramuscular connective tissue and are thereby crucial for the provision of structural support within skeletal muscle (Csapo et al., 2020). Moreover, the structure and rigidity provided by collagens facilitate the generation of new muscle, as murine myotubes were found to differentiate more readily on substrates with a stiffness similar to that of skeletal muscle (Engler et al., 2004).

Akin to the other aspects of muscle repair, tissue remodelling must also be tightly regulated to ensure correct healing. Breakdown of the ECM itself can aid muscle recovery, due to it being a growth factor store, which can be released upon ECM degradation to exert their effects on both muscle and immune cells (Goetsch et al., 2003). Fibrosis is a necessary feature of the muscle damage response and is beneficial for efficiently restoring the functionality of this tissue however, excessive production of collagens can cause extensive scarring within the muscle and ultimately lead to a loss of function (Mann et al., 2011).

1.3 Skeletal muscle ageing

Biological ageing is an inevitable yet natural process and involves a functional decline of all major systems of the body including the neuromuscular system. As individuals age, skeletal muscle undergoes a number of physiological changes, some of which are a consequence of the ageing process, i.e. sarcopenia and cellular senescence, whilst others such as cachexia arise due to pre-existing disease. The effects of skeletal muscle ageing on the elderly leads to weakness and fatigue, making it difficult to perform everyday activities and to exercise, which is largely due to a loss of muscle tone and force generation.

1.3.1 Sarcopenia

Sarcopenia is defined as an age-related degenerative loss of skeletal muscle mass and strength, which leads to a decline in function (Santilli et al., 2014). It is associated with poor

quality of life due to the development of physical disabilities, hospitalisation, loss of independence and social exclusion. This condition is one of the main contributors of physical frailty and can eventually lead to premature death (Cruz-Jentoft et al., 2014). Despite it primarily being a disorder of the elderly, sarcopenia can manifest in individuals of a younger age when associated with other conditions, such as inflammatory diseases, malnutrition, prolonged disuse and cachexia (Hwang et al., 2017, Nardone et al., 2021). Whilst cachexia is comparable with sarcopenia, it is imperative to distinguish between the two conditions. Cachexia arises from an underlying disease such as cancer or HIV/AIDS, which results in loss of muscle and fat tissue, anorexia and metabolic changes (Gingrich et al., 2019). Despite having a similar aetiology, the underlying pathological processes contributing to sarcopenia and cachexia differ.

Sarcopenia can be divided into 3 different categories depending on the severity of the condition: presarcopenia, sarcopenia and severe sarcopenia as defined by the European Working Group on Sarcopenia in Older People (Cruz-Jentoft et al., 2010). Presarcopenia is characterised by a reduction in overall muscle mass with no effect on muscle strength or performance. The sarcopenia group is defined by a loss of muscle mass with low muscle strength or low physical performance, whilst severe sarcopenia is identified when all three measures are present in the patient: low muscle mass accompanied by both a decline in muscle strength and physical performance (Cruz-Jentoft et al., 2010). By recognising the existence of different sarcopenia stages, appropriate treatment plans can be formulated based on individual patient states.

1.3.1.1 Epidemiology

Sarcopenia is a progressive disease by nature and loss of muscle mass can begin as early as the third decade of life with 27 years being the age at which decline first begins, however it is only from the fifth decade that substantial changes in muscle mass are observed (Janssen et al., 2000, Silva et al., 2010). It has been estimated there is an 8% decline in skeletal muscle mass for every decade between the ages of 40 and 70, after which a faster loss occurs due to an increase to 15% loss per decade, such that by the age of 80 sarcopenia sufferers will have lost approximately 30% of their total muscle (Grimby and Saltin, 1983).

Due to advances in healthcare and improved socio-economic conditions, the proportion of elderly individuals within a population is increasing globally. The United Nations World Population Ageing Report states the percentage of individuals over the age of 65 worldwide will increase from 9% in 2019 to 16% by 2050 (United Nations Department of Economic and Social Affairs, 2020)(United Nations Department of Economic and Social Affairs, 2020)(United Nations Department of Economic and Social Affairs, 2020)(United Nations Department of

Economic and Social Affairs, 2020) However, despite an increasing ageing population, the prevalence of sarcopenia is difficult to accurately determine. The European, Asian and International Working Groups on Sarcopenia all have a consensus definition of sarcopenia, yet use different parameters and thresholds, particularly when measuring muscle strength to determine its presence in individuals, thus incidence may vary widely between nations (Bischoff-Ferrari et al., 2015, Shafiee et al., 2017).

A 2010 American study investigated the effects of sex and ethnicity on sarcopenia prevalence in individuals over the age of 60 (Silva et al., 2010). This study used dual energy X-ray absorptiometry (DXA) scanning to measure skeletal muscle mass and found African American women to have the greatest decline in mass compared to White, Hispanic and Asian females, whilst Hispanic men showed the greatest rate of decline in the male group. However, it must be noted that this study measured 3 times more female subjects than male and no information was provided regarding the number of subjects measured in each ethnic group.

A later systematic review and meta-analysis of sarcopenia prevalence in the world-wide population found differences based on the method employed to measure skeletal muscle mass (Shafiee et al., 2017). When using bio-electrical impedance analysis to measure muscle mass, men from non-Asian countries had a higher prevalence of sarcopenia than their Asian counterparts however, when DXA scans were used the opposite was observed. In comparison, non-Asian women exhibited a higher prevalence of the disorder compared to Asian women for both methods. More individuals of non-Asian origin were shown to suffer from this condition compared to those from Asian nations. Despite differences in measurement methods and parameters in different regions of the world, both this systematic review and the 2010 study showed most of the healthy elderly population is living with sarcopenia.

Population studies have shown there to be a greater rate of decline for skeletal muscle strength than for muscle mass in both males and females, with men showing a higher loss of strength than their female counterparts, after accounting for the greater initial strength in men (Cheng et al., 2014, Goodpaster et al., 2006, Cooper et al., 2011). Specifically, individuals with the highest muscle strengths experience a faster rate of strength decline than those who are weaker. Globally, the populations of developing nations have lower muscle strengths than individuals in developed nations, therefore it is imperative that reference values specific to region are used when measuring strength (Dodds et al., 2016).

1.3.1.2 A public health burden

Sarcopenia has a substantial impact on public health costs world-wide. Patients are more likely to experience loss of independence, often requiring additional care with many eventually being

admitted to nursing homes (Dos Santos et al., 2017). Alongside age-related bone loss, sarcopenia increases the risk of fractures and falling, resulting in hospitalisation. Studies have shown hospitalised sarcopenia patients, on average had longer stays in hospital compared to non-sarcopenic patients (Gariballa and Alessa, 2013). Frequent hospital admissions in addition to home and ambulatory care all contribute to increasing healthcare expenditure. As well as direct costs, sarcopenia also accrues many indirect costs, such as those associated with depression, other psychological problems and loss of productivity, however as of yet they have not been quantified (Beaudart et al., 2014).

The financial burden of this condition is costly to all health care systems largely due to increased life span without an increase in health span in developed nations (Beaudart et al., 2014). To date no studies have specifically determined the annual healthcare costs of sarcopenia alone in the United Kingdom, however a 2018 UK investigation estimated costs of treating muscle weakness associated conditions, of which sarcopenia was included, at approximately £2707 per person which equated to an annual expenditure of £2.5 billion (Pinedo-Villanueva et al., 2019). These costs are expected to rise each year with the growing ageing population.

It has been projected in the United States that a 10.5% decrease in sarcopenia prevalence could reduce healthcare costs by $1.1 billion each year, by employing physical activity interventions and pharmacological treatment (Janssen et al., 2004). These figures highlight the need for appropriate lifetime interventions to successfully reduce the prevalence of sarcopenia amongst older individuals.

1.3.1.3 Pathophysiology

Sarcopenia is a multifactorial disorder with regards to its development. Numerous mechanisms have been identified in this condition; however, it is thought sarcopenia manifests when several of these causative factors interact and come together to induce reduced muscle mass and strength (figure 3). Despite this, the relative contribution of each cause in the onset of sarcopenia has not been yet been determined.

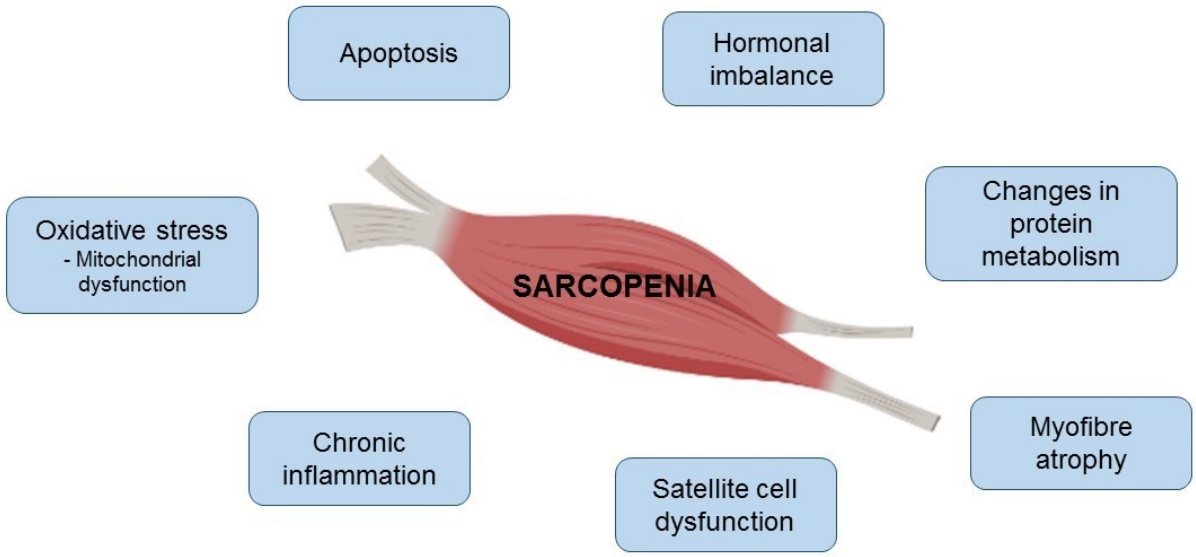

Figure 3. The many causes of sarcopenia. Sarcopenia is a multifactorial disorder that involves both cellular and molecular changes to skeletal muscle. It is likely that the onset of this condition can be attributed to a combination of these factors rather than developing from a single cause. (Figure created using BioRender.com).

Several of the main sarcopenia causative agents are discussed in more detail below, including chronic inflammation, reduced proteostasis due to increased catabolism and oxidative stress.

1.3.1.3.1 Inflammation

The process of ageing is usually accompanied by chronic low-grade inflammation, known as "inflammaging". This age related state is characterised by high levels of circulating inflammatory proteins and an increase in inflammatory cells within certain tissues, and is linked to the development of sarcopenia (Ferrucci and Fabbri, 2018). Macrophages are a primary source of pro-inflammatory cytokines and other pro-inflammatory mediators, such as eicosanoids, which are responsible for regulating acute inflammation in response to pathogen invasion or tissue injury, however as we age these immune mechanisms become impaired (Franceschi and Campisi, 2014). Ageing skeletal muscle is affected by prolonged immune activation which skews the carefully modulated balance of tissue homeostasis towards a damaged phenotype rather than one of repair. Inflammatory damage to muscle tissue promotes increased macrophage infiltration to the site, exacerbating existing damage to create a continuous cycle of damage and non-resolving inflammation. Chronic low-grade inflammation, as seen in sarcopenia causes increased tissue damage due to excessive production of pro-inflammatory cytokines, including TNF-α, IL-6 and C-reactive protein (CRP) (Furman et al., 2019). It is thought this chronic inflammation induces skeletal muscle

degeneration by apoptosis, promoting protein breakdown and modifying intercellular signalling, particularly the NF-κB pathway (García-García et al., 2021).

1.3.1.3.1.1 Cytokine-associated muscle damage

IL-6

During muscle damage, the pleiotropic cytokine IL-6 plays a crucial role in myogenesis by activating the muscle stem cell population to regenerate existing tissue. Frequent TNF-α activation of the NF-κB pathway induces excessive secretion of IL-6 and prolonged exposure to this cytokine, as seen in sarcopenia disrupts the ability of muscle tissue to undertake efficient repair and induces muscle mass loss (Bhatnagar et al., 2010). IL-6 is involved in upregulating the expression of proteins inhibiting muscle growth, as well as muscle atrophy inducing proteins. Tail immobilised mice exhibited elevated serum levels of IL-6 and consequently increased muscle atrophy, due to rapid upregulation of the ubiquitin ligase muscle RING finger 1 (MuRF1) (Yakabe et al., 2018). Administration of an IL-6 receptor blocking antibody inhibited the expression of MuRF1, however this treatment did not show a significant increase in mice body weight, yet it did restore the cross sectional area of the soleus muscles (Yakabe et al., 2018). An earlier study found the opposite and identified no change in MuRF1 and atrogin-1 expression between untreated and IL-6 treated mice (Haddad et al., 2005). However, this study did report direct IL-6 infusion into the muscle induced tissue atrophy by significantly reducing both the total amount of protein and myofibrillar proteins, which can affect muscle functionality. Investigators in this study also determined increased IL6 levels caused aberrant signalling of the JAK/STAT pathway. IL-6 infusion inhibited STAT5 production and simultaneously induced STAT3 phosphorylation (Haddad et al., 2005). Preventing STAT5 activation may interfere with the activity of the growth hormone receptor and therefore blocks anabolic stimuli. Whereas increased STAT3 activation is responsible for the overexpression of ubiquitin E3 ligases, which further promotes protein breakdown in skeletal muscle (Haddad et al., 2005). Using IL-6 neutralising antibodies reverses the effects of STAT3 signalling and attenuates muscle wasting, whilst STAT3 inhibitors were only partially capable of preserving muscle mass, suggesting the necessity for limiting IL-6 production in elderly individuals (Pretto et al., 2015).

Although IL-6 is considered to be the main marker of sarcopenia, it is possible that its action alone is not sufficient to cause extensive muscle wasting and instead relies on the concurrent activity of other pro-inflammatory cytokines, such as TNF-α and IL-1β for the development of sarcopenia.

TNF-α

Typically, TNF-α plays a dual role in the myogenic process, promoting myoblast proliferation whilst inhibiting differentiation during the early stages of muscle repair (Chen et al., 2007). However, with ageing, prolonged exposure to TNF-α can have a detrimental effect on muscle regeneration. A high level of TNF-α promotes a sarcopenic phenotype by impeding myotube formation by limiting satellite cell proliferation and reducing their ability to differentiate (Langen et al., 2004). The negative effects of TNF-α on the myogenic process in elderly individuals might be associated with its ability to stimulate protein catabolism. Previous *in vitro* studies have investigated the direct role of exogenous TNF-α on rodent skeletal muscle proteins, yet none identified a significant increase in protein breakdown with increasing concentrations of the cytokine (García-Martínez et al., 1993) (Goodman, 1991). Nevertheless, later studies found increasing concentration and exposure to TNF-α reduced total protein content in murine muscle tissue with a specific loss of muscle associated proteins, such as the myofibrillar proteins: myosin heavy chain, MyoD and myogenin (Li and Reid, 2000).

Increased protein catabolism is a consequence of TNF-α induced activation of the inflammatory NF-κB signalling pathway (Bhatnagar et al., 2010). Despite the rapid activity of NF-κB, it can alter gene expression which has prolonged downstream effects that result in limiting muscle proteins levels in muscle cells. A study which used genetic ablation to reduce TNF-α expression found the onset of sarcopenia in mice to be limited, with older animals exhibiting increased muscle fibre size compared to age matched wild type mice (Wang et al., 2018). These aged TNF-α null mice also showed a greater number of centrally nucleated myofibres compared to old and young healthy mice, suggesting increased cell fusion and regeneration in the absence of TNF-α. Furthermore, treatment of myocytes with macrophage conditioned medium isolated from aged TNF-α null mice showed increased myogenic fusion compared to wild type mice of the same age. This was further demonstrated with the transplantation of wild type macrophages into TNF-α null mice, which exhibited some reestablishment of sarcopenia due to increased skeletal muscle levels of TNF-α and a reduction in cell fusion (Wang et al., 2018).

IL-1β

IL-1β has also been implicated as one of the many inflammatory causes of sarcopenia. Comparable to IL-6 and TNF-α, excessive release of IL-1β contributes to a loss of muscle mass by facilitating protein catabolism. Repeated exposure to this cytokine stimulated expression of IL-6 mRNA in murine muscle cell lines *in vitro* via increased NF-κB and p38 MAPK signalling which were shown to activate genes responsible for the production of MuRF1

and atrogin-1 (Li et al., 2009). Moreover, IL-1β can also impair insulin signalling in the muscle and impede protein anabolism. Increasing concentrations of IL-1β are able to directly prevent myoblast differentiation into mature myofibres by completely blocking IGF-1 mediated protein synthesis, as well as reducing expression of the pro-myogenic transcription factor myogenin (Broussard et al., 2004).

IL-10

Increased production of pro-inflammatory cytokines is associated with sarcopenia development but a reduction in anti-inflammatory cytokine levels could also be implicated in this age associated condition. IL-10 knockout mice provide a model of sarcopenia and these animals display increased muscle weakness and strength with increasing age, as well as poor muscle repair following injury (Walston et al., 2008). Aged IL-10 null mice also presented with damaged myocyte mitochondria, suggesting absence of this anti-inflammatory cytokine is involved in modifying mitochondrial integrity (Cruz-Jentoft et al., 2014).

Despite the consensus that IL-10 secretion declines in aged individuals, a 2018 study comparing sarcopenia and non-sarcopenia patients found this cytokine, in conjunction with IL6 to be raised in the sarcopenia subjects (Rong et al., 2018). These findings were confirmed in a 2020 investigation which sought to identify how aged muscle responds to resistance exercise. Researchers established that resting elderly skeletal muscle displayed a higher level of IL-10 gene expression than resting muscle in young subjects (Jensen et al., 2020). These results suggest raised IL-10 levels alone are not sufficient to counteract the damaging effects of pro-inflammatory cytokines in aged muscle.

1.3.1.3.1.2 Macrophage populations

It is commonly thought that the chronic inflammation associated with sarcopenia causes increased macrophage infiltration into skeletal muscle, however experimental data contradict this theory. It has been reported in both humans and mice that macrophage polarisation is skewed in sarcopenia, with M2 pro-resolving macrophages, specifically M2a being the most abundant subpopulation in aged muscle and their numbers rise with age (Cui et al., 2019). These M2 macrophages were found to specifically localise to the intermuscular adipose tissue, which also had a higher presence in aged muscle. In older muscle, an increase in the M2 subpopulation correlated with myofibre dystrophy, fewer cytoplasmic nuclei per muscle fibre, as well as increased muscle fibrosis (Collins and Sedivy, 2003). Conversely, M1 macrophages comprised a smaller percentage of the total macrophage population, which declined with age. Despite changes to the M1/M2 ratio with ageing, the total number of macrophages in sarcopenic muscle did not alter compared to younger muscle tissue, denoting a lack of

macrophage infiltration (Cui et al., 2019). A 2012 human study investigating macrophage populations in young and elderly individuals found no significant changes in the total number of macrophages between the two subject groups, yet a higher level of CD206+ gene expression was identified in the elderly group, which corresponds to the M2 macrophage subpopulation (Tam et al., 2012). In contrast, American researchers showed a reduction in both M1 and M2 macrophage populations in older individuals compared to their younger counterparts (Przybyla et al., 2006).

The ageing process is also likely to alter macrophage function, therefore an aged immune system is expected to impair muscle regeneration in sarcopenia. Murine myoblasts treated with conditioned medium collected from old macrophages showed reduced proliferation, implying aged macrophages are less able to release pro-proliferative factors to facilitate myogenesis (Wang et al., 2019b). Moreover, the transplantation of bone marrow cells from young mice into older mice inhibited the increase in M2a macrophages in skeletal muscle. In young individuals, an increase in both pro-inflammatory and pro-resolving macrophages is observed following muscle damage due to acute exercise, an increase that is not witnessed in older individuals which suggests aged macrophages are incapable of mounting an appropriate inflammatory response to muscle damage (Wang et al., 2019b).

The theory of macrophage infiltration into sarcopenic muscle is most likely related to sarcopenic obesity. As mentioned previously, the size of the skeletal muscle macrophage population remains unchanged in sarcopenia, however macrophage numbers are modified in individuals who have developed sarcopenia as a consequence of obesity (Sachs et al., 2019).

Aged muscle is prone to accumulating fatty deposits, creating a pro-inflammatory environment which promotes the recruitment of macrophages to the muscle tissue (Sachs et al., 2019).

These studies indicate the variability of both macrophage numbers and activation status in ageing skeletal muscle and is dependent on the markers used to phenotype these cells and the ageing conditions used.

1.3.1.3.2 Enhanced ubiquitin proteasome activity

An imbalance in protein metabolism is a known characteristic of sarcopenia, arising from a decline in protein synthesis and an increase in the rate of protein degradation. Protein degradation is facilitated by the ubiquitin proteasome system (UPS), which functions to remove misfolded proteins from cells (Rock et al., 1994), however it is thought increased activity of the UPS is responsible for the excessive loss of protein seen in sarcopenia. A positive correlation has been observed between muscle atrophy and the muscle specific ubiquitin ligases, atrogin-1 and MuRF1 (Bodine et al., 2001) (Bodine and Baehr, 2014). Their

expression is upregulated in response to elevated myostatin and or TGF-β levels in both rodents and humans (Bodine and Baehr, 2014). Atrogin-1 ubiquitinates MyoD and myogenin, labelling them for degradation, therefore preventing myoblast differentiation and the synthesis of myofibrillar proteins. Additionally, expression of atrogin-1 induces breakdown of eukaryotic initiation factor 3 subunit 5, which is involved in initiating translation of muscle proteins (Bilodeau et al., 2016). Like atrogin-1, raised MuRF1 expression is also associated with protein catabolism, and specifically targets myofibrillar proteins including actin, myosin light chain, troponin I and myosin binding proteins. Regardless of their involvement in muscle atrophy, inhibition of atrogin-1 and MuRF1 expression does not rescue muscle mass entirely, suggesting other factors are responsible for protein breakdown (Sandri et al., 2013). Furthermore, increased proteasomal activity, especially of the ubiquitin specific protease 19 (USP19) is linked to muscle atrophy. USP19 expression in rat myotubes inhibits the transcription of myofibrillar proteins *in vitro*, due to decreased activity of myogenin (Sundaram et al., 2009).

Despite these aforementioned findings, there is little consensus within the muscle ageing field regarding UPS activity in ageing. Several studies have reported no change in ubiquitin ligase expression or activity between young and old subjects (human and rat) and suggested alternative causes for the decline in muscle protein content during ageing, whilst others have found ubiquitin ligase protein expression to be upregulated under aged conditions (Hepple et al., 2008, Whitman et al., 2005, Ferrington et al., 2005). The particular ubiquitin proteasome complex subunits measured might account for the differences observed in these studies; those investigating the activity of the 20S component showed reduced activity whereas those using the 26S identified heightened proteasomal activity.

1.3.1.3.3 Oxidative stress

Due to its high metabolic activity, skeletal muscle consumes large quantities of oxygen and can generate large amounts of ROS. Additionally, this tissue has a large immune presence and inflammatory immune cells are another source of oxygen derived free radicals. Consequently, skeletal muscle employs antioxidant systems to neutralise the damaging effects of released ROS (Powers et al., 2011). Under aged conditions, ROS production is elevated and antioxidant levels decline, both of which have been implicated in protein degradation and muscle atrophy (Gomes et al., 2017).

Increased ROS synthesis is largely attributed to mitochondrial dysfunction, which arises from age related damage to mitochondrial DNA and proteins (Bua et al., 2006). Damaged mitochondria persist within aged muscle tissue as muscle cells are unable to efficiently remove these dysfunctional organelles, leading to excessive ROS release that further destroy

mitochondria, creating a vicious cycle of damage (Marzetti et al., 2013). Due to impaired repair mechanisms, aged muscle cells are unable to efficiently repair ROS mediated damage and cells no longer express pro-survival signals. Increased •NO levels in old mice are responsible for the phosphorylation of Bcl-2 and activation of caspase 9 and caspase 2, proteins involved in initiating the apoptotic programme (Braga et al., 2008).

Elevated ROS levels can also be attributed to age associated chronic low-grade inflammation. An increase in NF-κB activity due to increased TNF-α secretion can induce the expression of •NO producing enzyme, iNOS. Blocking iNOS enzymatic activity in mice not only reduced •NO release but also prevented the loss of MyoD mRNA, therefore promoting myoblast differentiation and maintenance of the myofibre population (Di Marco et al., 2005). Coinciding with the reduction in MyoD was the loss of myosin heavy chain protein from myofibres, which impairs muscle filament integrity and thus limits muscle strength.

Older mice have been shown to upregulate the expression of iNOS compared to younger animals (Braga et al., 2008). Consequently, the aged mice group exhibited increased oxidative stress which induced myocyte apoptosis. Concomitant with elevated iNOS expression was a decline in glucose-6-phosphate dehydrogenase (G6PDH), which is responsible for regulating levels of the co-factor nicotinamide adenine dinucleotide phosphate (NADPH) (Braga et al., 2008). NADPH in turn maintains cellular levels of the antioxidant glutathione in myocytes. One theory to explain the impact of raised ROS levels is that aged skeletal muscle is unable to respond to redox signalling molecules to facilitate the expression of antioxidant proteins such as G6PDH and glutathione.

Upregulation of the ROS producing enzyme NADPH oxidase (NOX), particularly NOX2 has also been observed in sarcopenia. Sullivan-Gunn and Lewandowski have shown ageing mice exhibit increased NOX2 activity that elevated both hydrogen peroxide and superoxide anion levels. Raised ROS release also corresponded with low levels of the antioxidants superoxide dismutase and catalase, signifying that aged muscle is unable to maintain redox balance (Sullivan-Gunn and Lewandowski, 2013). Heightened ROS production activates both muscle proteases and the UPS, upsetting the proteostatic balance. Hydrogen peroxide in particular has been shown to trigger protein catabolism by increasing expression of MuRF1 and atrogin1 in myotubes, as well as promoting ubiquitin conjugating activity of myotubes, leading to muscle atrophy (Li et al., 2003).

This section has highlighted the various causes of sarcopenia, yet many of the causative agents stem from the development of another (figure 4). For instance, the onset of chronic low-grade inflammation with an aged phenotype is accompanied by increased proinflammatory cytokine production, which in turn induces excessive ROS release that can

activate protein degradation pathways. Despite the multifactorial nature of sarcopenia, all avenues lead to muscle atrophy and a loss of muscle mass and function. This emphasises the challenges of treating sarcopenia, as one therapy might not be sufficient to manage this condition, and most often requires a multi-therapeutic strategy.

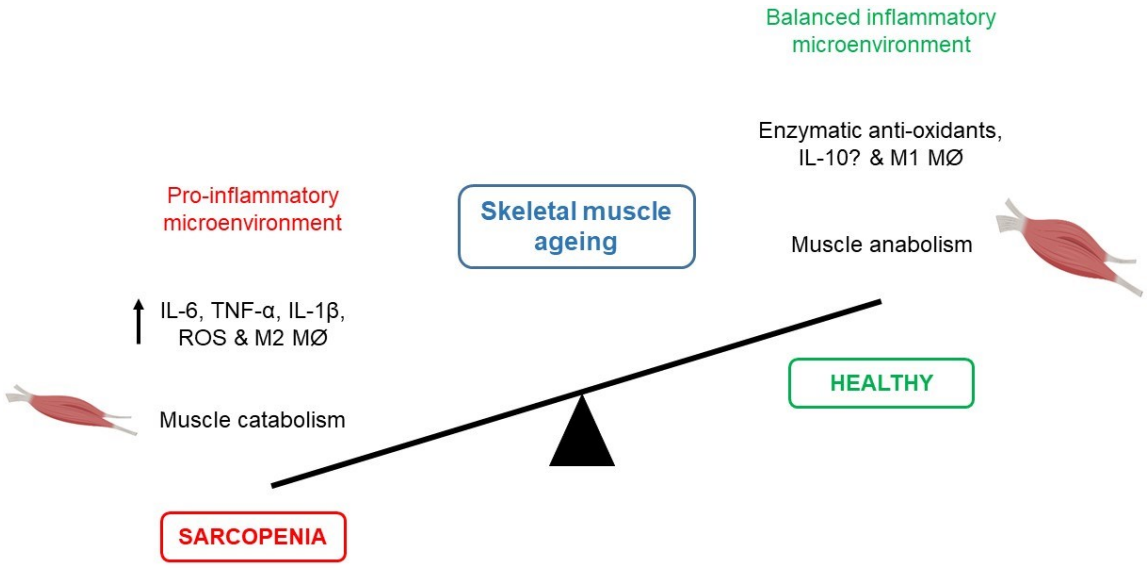

Figure 4. Skeletal muscle ageing – tipping the balance. Skeletal muscle homeostasis is finely balanced and under aged conditions the scales can be tipped in favour of muscle atrophy and disease pathologies. An ageing chronic inflammatory state elevates pro-inflammatory mediator release, including cytokines, eicosanoids and ROS, whilst concomitantly downregulating antioxidant function and possibly anti-inflammatory cytokine production. This highlights the interconnectedness of the many causes of sarcopenia, with one factor often leading to the development of another causative agent. (Figure created using BioRender.com).

1.3.2 Cellular senescence

Over the past decade cellular senescence has become increasingly associated with tissue dysfunction and ageing. Cellular senescence is a phenomenon during which cells undergo cell cycle arrest and present an altered phenotype, yet remain metabolically active (van Deursen, 2014). It is a stress response and is considered to protect organisms from the unwanted growth of damaged cells and therefore provides protection against tumourigenesis but can often lead to a loss of function (Collado and Serrano, 2010). Cellular senescence can arise from cells reaching the end of their replicative lifespan (telomere shortening) or by being exposed to a number of stress inducing factors, such as oxidative and inflammatory stresses, DNA damage and mitochondrial dysfunction (McHugh and Gil, 2018). These stresses are encountered throughout an individual's lifetime and are thought to accumulate with age. At a molecular level, the development of maintenance of cellular senescence is due to two main tumour suppressor pathways controlled by p53/p21 and $p16^{INK4a}$/retinoblastoma (Herranz and

Gil, 2018) (Rayess et al., 2012). The $p16^{INK4a}$ protein in particular is upregulated during cellular senescence and is often used as a biomarker to identify senescent cells.

As well as cell cycle arrest, senescent cells can also be characterised by morphological and metabolic changes. Senescent cells most often present as enlarged flattened cells, with reduced laminin B1 expression resulting in a loss of nuclear envelope integrity (Campisi and d'Adda di Fagagna, 2007). β-galactosidase activity is also upregulated in senescent cells and is considered to be a hallmark of senescence, it is also a phenotype that has been seen to increase with age alongside increased $p16^{INK4a}$ expression (Collins and Sedivy, 2003).

Senescent cells are a normal physiological response to tissue injury and exert beneficial effects before being efficiently eliminated by immune cells. In younger individuals, senescent cell abundance is low, but their numbers rise with age and have been found to accumulate in ageing tissues including skeletal muscle and adipose tissue (Tchkonia et al., 2010). Senescent cells in ageing lose their favourable effects and most often their presence is detrimental to healthy cells, leading to disease pathologies. For instance, increases in senescent cell populations are associated with atherosclerosis and diabetes (Minamino and Komuro, 2007, Minamino et al., 2009).

1.3.2.1 Senescence associated secretory phenotype (SASP)

Despite cessation of cellular proliferation, senescent cells remain metabolically active and produce modified secretory proteins, termed as the SASP, which is another characteristic of senescent cells. The SASP consists of soluble factors that are primarily cytokines, including IL-6 and interleukin- 8 (IL-8), as well as proteases such as MMP-1 and non-protein based soluble factors such as $^{\bullet}NO$ and other ROS (Coppé et al., 2010). The secretome is also comprised of non-soluble factors, for example fibrinogen and numerous collagens (Coppé et al., 2010). Due to the diverse composition of the SASP, it can act locally in an autocrine and paracrine manner or exert effects over long distances (Kumari and Jat, 2021). It has not yet been fully elucidated how the SASP specifically differs between cell types, however SASP composition can vary depending on the stimulus that induces senescence, as cells that are induced to senesce through the overexpression of cell cycle inhibitors, such as p16 and p21 experience cell cycle arrest but do not produce a SASP (Regulski, 2017).

The SASP can be produced by a small population of cells but can have long ranging systemic effects. Due to the complexity of the SASP, it is most likely that it is has a broad range of functions. One of the primary functions associated with SASP is to sustain cell cycle arrest through IL-6 release, which is a major SASP component (Gorgoulis et al., 2019). However, the SASP can at times have contradictory roles, as the presence of growth and angiogenic

factors, such as vascular endothelial growth factor can stimulate cell proliferation and blood vessel growth (Coppé et al., 2006). Furthermore, prolonged exposure to SASP, as is the case in ageing, can act in a paracrine manner and induce cellular senescence in healthy cells (Acosta et al., 2013, Nelson et al., 2012). SASP can contain biphasic WNT modulator secreted frizzled protein 1, which can chronically activate WNT signalling to induce stem cells and differentiated cells to adopt a senescent phenotype, ultimately modifying essential cell populations within tissues (Liu et al., 2007). Consequently, whether the SASP has a beneficial or a detrimental effect on cells is highly dependent on the physiological conditions under which it was secreted.

Despite potential differences in SASP composition from different cell types, the main conserved elements are the pro-inflammatory proteins, which include IL-6, IL-8, IL-1β, monocyte chemotactic proteins and granulocyte/macrophage colony stimulating factor (Coppé et al., 2010). The secretion of these molecules by senescent cells often induces chronic inflammation and in the case of skeletal muscle, can cause muscle atrophy.

1.3.2.2 The immune response to cellular senescence

An important role of the SASP is to stimulate immune cells infiltration to the site of injury to remove senescent cells and allow stem cells to repopulate damaged tissue and initiate tissue repair and remodelling. Senescent cells can be phagocytosed by neutrophils and can be directly destroyed by natural killer cells (NK cells), which release macrophage activating cytokines to recruit macrophages to facilitate clearance of apoptotic senescent cells (Ovadya et al., 2018).

Under aged conditions, senescent cells accumulate in tissues and their removal is impaired due to poor recruitment of macrophages, senescent cells evading immune cell mediated clearance or the rate at which senescent cells are generated is faster than the rate of their removal (Freund et al., 2010). In ageing, senescent cells demonstrate immunosuppressive effects by expressing surface molecules such as the MHC I class E antigen, HLA-E which inhibits receptors on NK and T cells to prevent an appropriate immune response from being mounted (Pereira et al., 2019). IL-6, a known SASP cytokine can also upregulate expression of HLA-E and the SASP sustained pro-inflammatory state encourages the persistence of senescent cells (Pereira et al., 2019). The SASP also contains elevated levels of various MMPs which can cleave cell surface receptors and ligands on NK cells to prevent immune cell-senescent cell binding and inhibit killing (Freund et al., 2010). Moreover, the SASP can facilitate fibroblast activation to increase ECM deposition but SASP components can also directly regulate ECM remodelling, specifically promoting matrix stiffening, which can disrupt macrophage and other immune cell infiltration into the tissue (Fane and Weeraratna, 2020). It

is possible these SASP factors could also act directly on macrophages and indirectly via the ECM to avert senescent cell removal from tissues.

1.4 The skeletal muscle secretome

Due to its many dynamic functions and extensive communication with other organs and tissues of the body, skeletal muscle produces a complex secretome to facilitate these roles. Skeletal muscle is comprised of various cell types that release many soluble mediators, known as myokines which are cytokines and small peptides that can exert autocrine, paracrine and endocrine effects such as TNF-α, IL-6, irisin and myogenin (Pedersen and Febbraio, 2012). In addition to myokines, the muscle secretome is also comprised of other molecules including proteins, amino acids, small RNAs, lipids, metabolites, all of which can be secreted in a free form but could potentially be contained within EVs and are involved in modulating cell to cell communication (Florin et al., 2020). Both myokines and other secreted molecules are known to mediate physiological processes, for example myogenesis, inflammation and metabolic processes (Lee and Jun, 2019). Under diseased conditions, the secretory profile of this tissue is modified and therefore the muscle secretome is also responsible for the development and progression of many disorders. Elevated skeletal muscle IL-6 levels, as seen in ageing are associated with disturbed insulin signalling, increased insulin resistance in both skeletal muscle and the liver, as well as increased fat deposition (Kim et al., 2004). Despite its association with various pathologies, the skeletal muscle secretome, especially the EV component has been nominated as a potential therapeutic agent, as an alternative to cellbased therapies. Severe muscle injuries resulting in impaired mobility could be treated with exercise regulated muscle secretomes from healthy individuals, as they are capable of promoting myogenesis, angiogenesis, repairing nerve connections to regenerate existing tissue and restore tissue functionality (Weigert et al., 2014).

1.4.1 Extracellular vesicles

As with many tissues of the body, skeletal muscle has also been shown to actively release EVs as part of its secretome. EVs are an essential secreted component and are involved in driving many physiological functions but have also been implicated in skeletal muscle pathologies.

Extracellular vesicles are nano-sized lipid membrane enclosed particles released by all cell types via a process that has been highly conserved across different species (Yáñez-Mó et al., 2015). These particles have the capacity to mediate intercellular communication through the transfer of bioactive molecules derived from their parent cell, such as nucleic acids, lipids and proteins between cells, with the purpose of modifying recipient cell behaviour (figure 5) (Doyle

and Wang, 2019). EVs vary in their size and their mode of production; they can either be synthesised by direct budding from the plasma membrane to form microparticles (MPs), which have a size range of ~100 – 1000 nm, or they can be generated via the endosomal pathway in multivesicular bodies to produce exosomes that are ~30 – 150 nm in size (Raposo and Stoorvogel, 2013). Cells can also release a larger EV (> 1000 nm), known as apoptotic bodies, which are produced during apoptosis when the cytoskeleton disassembles and these EVs are released through plasma membrane evagination (Borges et al., 2013). Due to the differences in their biogenesis, the contained cargo can differ between vesicle type and is dependent on the cells from which they are produced, as well as the physiological conditions at the time of release.

1.4.2 Extracellular vesicles produced by skeletal muscle

Skeletal muscle has been shown to release small EVs and MPs, with murine myoblasts and myotubes and primary human myocytes being producers of vesicles (Guescini et al., 2010, Le Bihan et al., 2012). It has been suggested small EV biogenesis differs between myoblasts and myotubes, as myotube-derived EVs were more enriched in the tetraspanin cluster of differentiation protein 81 (CD81), which is a general EV marker and the ESCRT protein Alix than myoblast-derived EVs (Forterre et al., 2014, Romancino et al., 2013). Moreover, these researchers have shown the involvement of Alix in the generation of skeletal muscle proteins. The loss of Alix modified vesicle budding from the plasma membrane and reduced small EV release by myotubes (Romancino et al., 2013). Reduced expression of this protein does not affect EV production in other cell types, as Alix knockdown did not change EV release by human liver stem cells, which suggests Alix might only be required for skeletal muscle EV biogenesis (Iavello et al., 2016). However, the findings of Bydak and colleagues are contradictory to those of Romancino *et al.* This group reported small EVs produced by myotubes exhibited reduced expression of CD81 and Alix compared to vesicles released by myoblasts (Bydak et al., 2022).

Proteomic analysis also highlights differences in the protein content of the vesicle populations and provides insight into the various functions they might be associated with. Gene ontology of human myotube EVs shows MPs were enriched in proteins associated with “amino acid metabolism”, “translational modifications” and “protein synthesis, folding and trafficking”, whilst smaller exosome-like EVs contained proteins involved in “cell to cell interactions and signalling” and “free radical scavenging” (Le Bihan et al., 2012). Small EVs also contribute to the energy metabolism function of skeletal muscle, as these particles are packaged with proteins that regulate insulin signalling and gluconeogenesis (Jethwa et al., 2015, Balbis et al., 2000). Moreover, murine myoblasts, myotubes and human myotubes EVs all express

proteins that are mapped to the biological function of “muscle contraction”, which taken together with the findings of other studies indicate these vesicles are enriched in skeletal muscle specific proteins that reflect the functions of this tissue (Watanabe et al., 2021). This is not limited to proteins linked to muscle contraction, in fact most proteins identified in murine myoblast-derived EVs were also found in the myotube equivalent, which suggests that whilst internal cellular organisation and morphology change during differentiation, the protein cargo of skeletal muscle EVs is not dramatically altered irrespective of muscle cell type (Forterre et al., 2014, Rome et al., 2019).

In addition to carrying proteins, skeletal muscle EVs can also contain a lipid component, which largely comprises the vesicle membrane. Aswad *et al.* have shown EVs produced by murine myotubes can be enriched in palmitic acid, lauric acid, stearic acid and oleic acid, which are fatty acids that are normally used for energy metabolism and to generate the lipid bilayer of cells (Aswad et al., 2014). Lipids carried by skeletal muscle EVs can also have a role in obesity and might be involved in the formation of intramuscular adipose tissue. Palmitate treated C2C12 myotubes release more EVs than untreated cells and these vesicles are packaged with palmitate (Aswad et al., 2014). It is possible that lipid enrichment of the EVs is a mechanism by which muscle cells can protect themselves from lipid accumulation, yet this could result in the development of insulin resistance and influence muscle homeostasis (Roden et al., 1996). Whilst muscle cells are expelling fatty acids, the lipid laden skeletal muscle EVs could be taken up by other muscle cells and upregulate inflammatory genes, for example IL-6, which is elevated in type 2 diabetic individuals, or downregulate protein markers associated with muscle development and differentiation (Aswad et al., 2014).

Skeletal muscle EVs also play an important role in the regulation of myogenesis, which demonstrate the processes governing crosstalk between different muscle cell populations (Wang and Wang, 2016, Choi et al., 2016). Myogenic factors have been identified in human myoblast derived EVs, including fibroblast growth factor 2 and IGFs, which stimulated the differentiation of skeletal muscle stem cells (Choi et al., 2016). Muscle vesicles can modulate muscle mass since myotube-derived EVs can transfer miRNAs and proteins to recipient myoblasts to promote the switch from cell proliferation to differentiation, whilst collagen biosynthesis by fibrogenic cells can be regulated by activated satellite cell EVs via miRNA uptake during damage induced muscle repair (Forterre et al., 2014) (Fry et al., 2017).

Conversely, EVs originating from muscle cells are also involved in disease progression, as the messages they carry under abnormal conditions are often altered, leading to a dysregulation in intercellular communication. For example, myoblasts treated with EVs isolated from either

oxidatively or inflammatory cytokine stressed myotubes struggled to proliferate following treatment and resulted in reduced myotube diameter (Guescini et al., 2017, Kim et al., 2018).

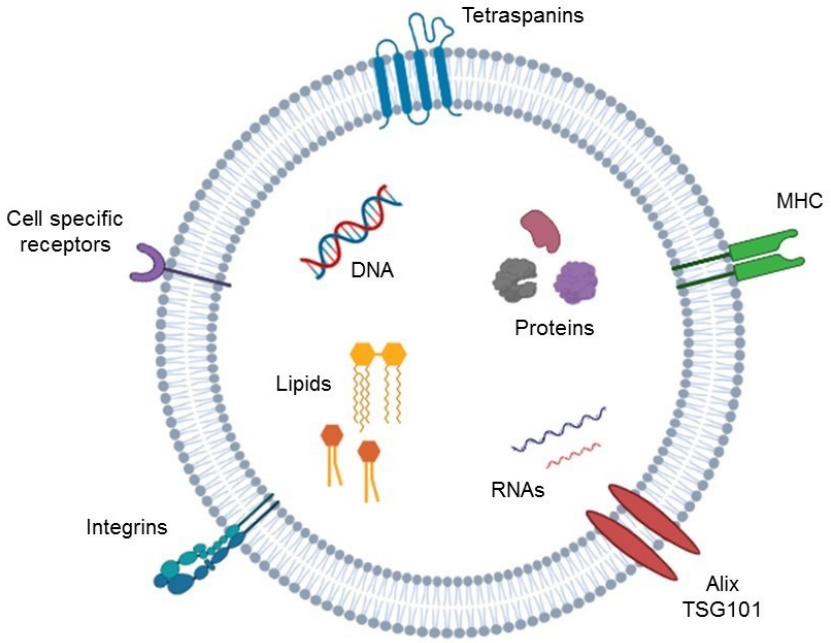

Figure 5. A representation of EV structure. Despite differences in their biogenesis all EV types are comprised of a lipid bilayer. These particles are capable of carrying a range of cargo, including proteins, genetic material and lipids, encapsulated in the vesicle lumen and often have many protein and lipid ligands embedded within the membrane, some of which facilitate docking and internalisation by recipient cells. (Figure created using BioRender.com).

1.4.2.1 Extracellular vesicles and ageing skeletal muscle

EV production is also associated with age related conditions such as sarcopenia and may provide a link between cause and effect to allow for a better understanding of this muscle disorder. Elderly individuals with frailty and sarcopenia show increased production of small circulating EVs isolated from serum, specifically exosomes containing mitochondrial components, compared to healthy age matched individuals (Picca et al., 2020). Elevated exosome release might correspond to muscle cells' attempts to remove damaged and dysfunctional mitochondria from the cell. These mitochondrial DNA containing vesicles can stimulate inflammation by activating the inflammasome and binding receptors such as TLRs to promote pro-inflammatory cytokine secretion and apoptosis, thereby contributing to the muscle wasting process (Picca et al., 2018). It is possible, that these circulating EVs could be used as biomarkers of sarcopenia and frailty in elderly individuals, as they could help identify individuals that require intervention to prevent the onset or progression of sarcopenia (Marzetti

et al., 2020). Muscle atrophy, as seen in sarcopenia also triggers modifications to the nucleic acid content of skeletal muscle EVs, such that the miRNAs specifically packaged into vesicles for release are associated with modifying protein synthesis and degradation pathways (Pelt et al., 2020).

The presence of senescent cells in skeletal muscle causes an increase in the release of EVs, which can also have detrimental effects (Hettinger et al., 2021). These senescent EVs are capable of modulating immune function by increasing arginase-1 and TGF-β1 expression, whilst concomitantly reducing iNOS and IL-6 expression, to promote a pro-resolving M2 phenotype (Alibhai et al., 2020). EVs have also been known to induce skeletal muscle cell senescence and have been shown to target signalling pathways responsible for the progression of myogenesis, resulting in inhibited myoblast proliferation and the development of muscle atrophy (Wang and Wang, 2016).

With an increasingly ageing population, the underlying mechanisms of age-related myopathies, such as sarcopenia require further investigation for the development of appropriate therapies. As the secretome components of cells can facilitate cell-cell communication, i.e., between muscle cells and immune cells, skeletal muscle secretomes are ideal for studying the cause of sarcopenia, specifically how they are modified during ageing and how this contributes to the development of this muscle disorder.

1.5 Aims and objectives

The current study aims to better understand the crosstalk between skeletal muscle and the innate immune system, with a particular emphasis on the ability of aged muscle secretomes to modulate macrophage function in age related muscle wasting conditions. This project aims to fill gaps in existing knowledge in the skeletal muscle/immune cell field by addressing the following research objectives:

1. **To develop an appropriate SF skeletal muscle model of ageing for the simplification of EV studies:**

   To date, there are many *in vitro* models of skeletal muscle ageing, yet most if not all use EV containing animal sera to develop these models. With the onset of EV based studies, the use of animal sera in such models can interfere with the assessment of EVs from the cells/tissues investigated. This objective concerns the development of a serum free skeletal muscle model, which seeks to balance healthy myotube generation with sufficient EV production but can also be used for the development of models of muscle ageing, including sarcopenia and cellular senescence.

2. **To characterise the cellular and EV fractions of aged skeletal muscle:**

   Several studies have conducted proteomic profiling of skeletal muscle cells and their secretomes and this objective intends to contribute to current works. Specifically, this section identifies changes in cell morphology, EV production and protein expression during the myogenic process, which has not been fully investigated in a serum free model of skeletal muscle differentiation.

3. **To assess the ability of aged muscle secretomes to modify muscle phenotype and macrophage function:**

   It has long been established that skeletal muscle communicates with the immune system and therefore influences immune cell behaviour and vice versa. Despite the many studies regarding this cross communication, there are even fewer studies on the topic of the effects exerted by aged skeletal muscle secretomes locally and further afield on macrophage function. This objective intends to test the hypothesis that muscle ageing detrimentally alters the muscle secretome and is thereby capable of exerting paracrine effects on myocytes, but also has a long ranging influence on macrophage behaviour, both of which are responsible for the onset and progression of age associated muscle disorders.

2. Materials and Methods

2.1 Cell culture

2.1.1 Cell lines

C2C12: An adherent murine myoblast cell line subcloned from a normal adult CH3 mouse leg muscle. Cells were maintained according to the manufacturer's instructions and cultured at P<16 to generate normal myotubes.

J774A.1: An adherent murine monocyte macrophage cell line derived from a tumour in a female BALB/c mouse.

THP-1: A semi-adherent human monocytic leukaemia cell line which can be differentiated into macrophage-like cells using various chemical compounds.

2.1.2 Cell culture

C2C12 cell line was cultured in complete DMEM growth medium (cDMEM), consisting of DMEM high glucose (4.5 g/L) supplemented with 10% (v/v) foetal bovine serum, 100 RU/ml penicillin, 100 μg/ml streptomycin and 2 mM L-glutamine, all sourced from Sigma Aldrich (Dorset, UK).

J774A.1 and THP-1 cell lines were cultured in RPMI 1640 supplemented with 10% (v/v) foetal bovine serum, 100 RU/ml penicillin, 100 μg/ml streptomycin and 2 mM L-glutamine, all sourced from Sigma Aldrich (Dorset, UK).

All cell lines were incubated at 37°C in a 5% CO_2 humidified incubator and were passaged every 2–3 days when a high level of confluence was reached. C2C12 myoblasts were maintained at 50-60% confluence prior to subculturing to prevent myoblast differentiation.

2.1.3 Optimisation of C2C12 myoblast differentiation

Differentiation media

Serum-free: DMEM high glucose (4.5 g/L) supplemented with 100 RU/ml penicillin, 100 μg/ml streptomycin and 2 mM L-glutamine.

Horse serum: DMEM high glucose (4.5 g/L) supplemented with 2% (v/v) horse serum (Sigma Aldrich, Dorset, UK) 100 RU/ml penicillin, 100 μg/ml streptomycin and 2 mM L-glutamine.

Insulin-Transferrin-Selenium: DMEM high glucose (4.5 g/L) supplemented with 100 RU/ml penicillin, 100 μg/ml streptomycin, 2 mM L-glutamine, 10 mg/L insulin, 5.5 mg/L transferrin and 0.0067 mg/L sodium selenite (Fisher Scientific, Loughborough, UK).

C2C12 myoblasts were seeded at a density of $1x10^4$ cells/cm^2 in 6 well plates and allowed to proliferate for 48 hours to reach 90% confluence in growth medium. 48 hours post seeding, designated day 0, growth medium was replaced with the following differentiation media: serum-free (SF), 2% horse serum (2% HS) or insulin-transferrin-selenium (ITS).

Cells were incubated for 5 days to induce myotube formation. Phase contrast images (10x) were taken for morphological determination of myotube formation using an EVOS FL microscope (Invitrogen, California, USA).

Following optimisation, ITS induced differentiation was used to induce myoblast formation for all subsequent experiments.

2.1.4 C2C12 myotube sarcopenia model

2.1.4.1 Optimisation of dexamethasone concentration

C2C12 myoblasts were differentiated for 5 days using ITS differentiation medium. On day 5, differentiation medium was replaced with either SF DMEM alone or supplemented with 1 μM, 10 μM or 100 μM of dexamethasone (DEX) and the myotubes incubated for a further 24 hours. Phase contrast images (10x) were taken using an EVOS FL microscope to confirm sarcopenic myotube morphology.

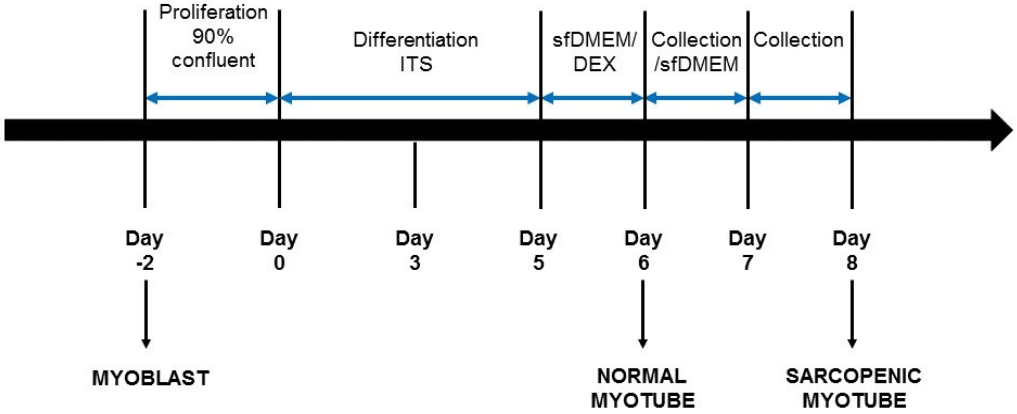

Figure 6. Timeline of myogenic differentiation and sarcopenia induction *in vitro*. C2C12 myoblasts were proliferated for 2 days, after which ITS treatment was used to stimulate differentiation into myotubes for 5 days (days 0–5). Following differentiation, normal or sarcopenic myotubes were created with the addition of sfDMEM or DEX respectively for 24 hours (day 6). Normal myotube-derived secretome was collected on day 7, whilst sarcopenic-derived myotube secretome was collected on day 8, after a 24-hour incubation with sfDMEM.

Following optimisation and assessment of sarcopenia, sarcopenic myotubes were generated by incubating the cells with 10 μM DEX for 24 hours for subsequent experiments. Figure 6 shows the sarcopenia induction timeline, from proliferation, differentiation and DEX treatment.

2.1.4.2 Assessment of sarcopenia

To identify the optimum concentration of DEX, the extent of sarcopenia was monitored in DEX treated myotubes over a 3-day period using light microscopy. Myotubes were imaged daily with 10 images captured per condition per day. 5 myotubes were selected at random and 3 diameter measurements were taken per cell using Image J drawing tool to assess myotube thinning, a morphological feature of sarcopenia. This method was also used to assess myotube thinning in etoposide treated senescent myotubes.

2.1.5 C2C12 myotube senescence model

2.1.5.1 Optimisation of etoposide concentration

ITS differentiated myotubes were induced to senesce using etoposide (Tocris, Bristol, UK). Briefly, differentiation medium was replaced with SF DMEM containing etoposide at the following concentrations, 0 μM, 5 μM, 10 μM, 20 μM, 40 μM and 80 μM. Myotubes were incubated with the etoposide treatment for 24 hours at 37°C, after which cellular senescence was confirmed by senescence-associated β-galactosidase activity. Optimisation experiments identified 10 μM etoposide as the optimal concentration, which was used hereafter for all cellular senescence induction.

Day 5 myotubes were treated with etoposide for 24 hours, after which cells were washed with PBS and SF DMEM was added for a further 24 hours. Senescent myotube-derived secretome was harvested on day 8. Senescence induction in myotubes and secretome collection followed the same timeline as sarcopenic myotube generation shown in figure 6.

2.1.5.2 Senescence-associated β-galactosidase activity

Induction of cellular senescence was confirmed by performing senescence-associated βgalactosidase staining, using a senescence detection kit (Abcam, Cambridge, UK) and following the manufacturer's instructions. Briefly, etoposide treatment media were removed, the cells washed with PBS and fixed with 1X fixative solution (2% formaldehyde and 0.2% glutaraldehyde) for 10 minutes at room temperature. After fixing, the fixative solution was removed, the cells washed with PBS and incubated with a staining solution mix (0.01% potassium hexacyanoferrate and 1 mg/ml X-gal in dimethyl sulfoxide) in the dark for 24 hours at 37°C. Myotubes were imaged using bright field microscopy at 40x magnification with an

EVOS XL microscope (Invitrogen, California, USA) and observed for blue colour staining, the presence of which is indicative of senescent cells.

2.2 Measurement of cell viability

MTT assay was used to measure metabolic activity in DEX and etoposide treated myotubes, to determine the effect of these compounds on cell viability. 1 x 10^4 C2C12 myoblasts were seeded into a 96 well plate and differentiated into myotubes using ITS, as described in section 2.1.3. Myotubes were treated with increasing concentrations of DEX and etoposide for 24 hours, after which the treatment media were removed and the cells washed 3x with PBS. 25 mg/ml MTT (Sigma Aldrich, Dorset, UK) solution was added to the treated cells and the plate incubated at 37°C for 1.5 hours. Following incubation, MTT was solubilised with the addition of acidified isopropanol (0.04 N HCl) (Sigma Aldrich, Dorset, UK) and the plate incubated for 15 minutes at room temperature. The absorbance was read at 570 nm using a Multiskan™ GO microplate spectrophotometer (Thermo Scientific, Loughborough, UK).

2.3 Isolation of myotube secretomes

Conditioned media were collected from normal myotubes on day 6 and from sarcopenic or senescent myotubes on day 8. The conditioned media were centrifuged at 300*xg* for 5 minutes to remove cell bodies to generate cell-free supernatants. Cell-free supernatants were further centrifuged at 2000*xg* for 20 minutes to remove large cell debris, providing a supernatant containing EVs and soluble factors, which were used in downstream functional studies.

2.3.1 Concentrating myotube secretomes

Normal, sarcopenic and senescent myotube supernatants generated from a 2000*xg* spin, were concentrated using Amicon® regenerated cellulose 30 kDa spin filters (Merck Millipore, Watford, UK) to a final retention volume of 1 ml. This generated a concentrated retentate consisting of EVs and high weight soluble factors and a filtrate comprised of low weight soluble factors.

2.3.2 Isolating myotube-derived EVs using size exclusion chromatography (SEC)

Cell-free supernatants isolated from the 2000*xg* centrifugation were ultracentrifuged at 120,000*xg* for 70 minutes to generate an EV pellet for use in mass spectrometric analysis.

For use in functional studies, EVs were isolated using SEC. Filter column concentrated retentates were loaded onto a 70 nm+ qEV column (Izon Science, Oxford, UK) and used according to manufacturer's instructions. Briefly, the qEV column was equilibrated at room temperature, after which it was washed 3 times with PBS. Concentrated myotube retentates

were added and allowed to enter the column bed. Additional PBS was used to flush the column and the first 3 ml eluted was discarded as the void volume. The subsequent 3.5 ml were collected as 500 µl fractions (fractions 7 – 13 following void volume fractions). These EV containing fractions were combined and retained for re-concentration and use in future functional experiments.

The final 8 ml elution volume collected as fractions 14 – 29 (500 µl per fraction) corresponds to the protein fraction. All protein fractions were also pooled and retained for re-concentration and further studies.

2.3.2.1 Concentration of SEC isolated EVs and soluble proteins

The 3 ml EV collected volume from all myotube samples was further concentrated using an Amicon® regenerated cellulose 10 kDa spin filter (Merck Millipore, Watford, UK) to a final retention volume of 1 ml. The 8 ml soluble proteins collected volume from all myotube samples was further concentrated using an Amicon® regenerated cellulose 3 kDa spin filter (Merck Millipore, Watford, UK) to a final retention volume of 1 ml.

2.4 Measurement of EV size and concentration – qNano

The qNano (Izon Science, Oxford, UK) uses tunable resistive pulse sensing to perform single particle analysis of nanoparticles and was used to characterise skeletal muscle derived EVs. EVs were measured using a 150 nm polyurethane membrane nanopore, which was subjected to a maximum stretch of 47 mm with a total pressure of 0.7 kPa. EV containing samples were diluted in PBS and the current recorded. During each measurement, a single EV passes through the nanopore at a time, causing a blockade in current which can be used to determine the size and particle concentration of the EVs within the sample. All measurements were calibrated against 100 nm diameter calibration beads under identical experimental conditions.

2.5 EV uptake by macrophages

Normal, sarcopenic and senescent myotube derived EVs were stained with BODIPY (1:1000) (Fisher Scientific, Loughborough, UK) in the dark at 4°C for 24 hours. BODIPY stained EVs were incubated with 1 x 10^6 J774 macrophages and internal cell fluorescence measured 0, 20, 40, 60, 120, 180, 240 minutes and 24 hours after treatment using a CytoFLEX flow cytometer (Beckman Coulter, High Wycombe, UK). Intracellular macrophage fluorescence was measured by the addition of 0.4% trypan blue (Fisher Scientific, Loughborough, UK) to quench extracellular fluorescence, which was reported as median fluorescence intensity.

2.6 Measurement of myotube atrophy via the bystander effect

2000*xg* sarcopenic or senescent myotube derived secretomes were added to normal myotubes for 24 hours. Phase contrast images of normal myotubes were taken on the day of treatment and 24 hours post treatment at 10x magnification using an EVOS FL microscope (Invitrogen, California, USA).

The phase contrast images were used to assess myotube diameter and surface area in ImageJ software (LOCI, Wisconsin, USA). Briefly, 5 myotubes were selected per field of view and using the drawing tool, 3 lines were drawn along the width of each myotube: 1 in the middle and 2 equidistant from the middle and the tips of the myotube, which provided the diameter measurement. For the measurement of surface area, an outline of the myotube was drawn.

2.7 Macrophage migration towards myotube-derived secretomes

2.7.1 Vertical macrophage migration

A commonly used vertical transwell migration system was initially employed to study the effects of myotube secretomes on macrophage migration.

Normal, sarcopenic and senescent myotube-derived EVs and soluble proteins were added to a 24 well plate, followed by the addition of 8 µm transwell inserts (Corning Life Sciences, New York, USA) to the plate wells. $1x10^5$ J774 macrophages were added to the upper chamber of the transwell and the plate incubated at 37° for 24 hours.

After the incubation period, the wells of the 24 well plate were imaged to determine the presence of cells that had detached from the underside of the transwell membrane and migrated to the bottom of the plate. Phase contrast images were taken at 10x magnification using an EVOS XL microscope (Invitrogen, California, USA). All cells in 4 fields of view were manually counted.

2.7.1.1 Jenner-Giemsa staining

Following the 24-hour migration period, transwell inserts were removed and any remaining cells attached to the internal surface of the permeable membrane were removed using a cotton bud. The transwell inserts were then washed with PBS, fixed in methanol for 10 minutes and left to air-dry. After fixation, the transwell inserts were stained in Jenner stain for 4 minutes, washed in PBS and stained in Giemsa stain for 9 minutes (stains from Sigma Aldrich, Dorset, UK). Transwells were washed in PBS and distilled water and allowed to air dry prior to mounting. The permeable membranes of the transwells were mounted onto glass slides using

DPX mountant (Sigma Aldrich, Dorset, UK) and imaged in colour at 40x magnification using an EVOS XL microscope (Invitrogen, California, USA). All cells in 4 fields of view were manually counted.

2.7.2 Horizontal macrophage migration

A horizontal migration system, using the Dunn chamber (Hawksley, Sussex, UK) was used to establish a true chemotactic gradient, without the effects of gravity.

THP-1 cells were seeded at $4x10^5$ cells/well with vitamin D3 (Enzo Life Sciences, Exeter, UK) in cRPMI on poly-D-lysine hydrobromide (Sigma Aldrich, Dorset, UK) coated glass coverslips (24 mm x 24 mm) in 6 well plates for 48 hours, to allow differentiation into macrophage-like cells and adherence to the coverslips.

Chemically defined macrophage medium (Sigma Aldrich, Dorset, UK) was added to both inner and outer wells of the Dunn chamber. Coverslips with the cultured macrophage-like cells were placed face down onto the glass Dunn chamber using sterile forceps, leaving a loading slit for chemoattractant addition to the outer well. The top and edges of the coverslip were carefully dried of excess medium using filter paper. Using a small paintbrush, 3 sides of the coverslip were sealed with paraffin wax, leaving the loading slit side of the coverslip open. Using more filter paper, the outer well was drained of the macrophage medium via the loading slit, ensuring no contact was made with the cell coated underside of the coverslip. Either 100 ng/ml of monocyte chemoattractant protein-1 (MCP-1) (Sigma Aldrich, Dorset, UK) or normal/sarcopenic muscle secretome was added to the drained outer well and the loading slit edge was sealed with paraffin wax. All 4 edges of the sealed coverslip were further sealed with petroleum jelly to prevent drying. The sealed Dunn chamber was placed inside a 37°C humidified heating chamber and phase contrast time lapse microscopy (10x magnification) was used to observe migrating cells via the viewing bridge of the Dunn chamber. Cells were imaged every 10 minutes for a 2-hour imaging period using a Zeiss Axiovert 200 M fluorescence microscope (Carl Zeiss Ltd, Staffordshire, UK) and Hamamatsu Orca camera driven by Volocity software (Perkin-Elmer, Cambridge, UK).

2.7.2.1 Cell tracking

For each chemotaxis assay, a total of 40 cells were tracked using ImageJ software.

Cell migration was quantitatively assessed using measures provided by Chemotaxis and Migration Tool (Ibidi, Munich, Germany), these include distance (Euclidean and accumulated), velocity and y-axis forward migration index. An additional measure, cosine of angle was

generated using the provided angle measurements to assess the directionality of cell migration towards the putative chemoattractants.

2.8 Measurement of macrophage respiratory burst

J774 murine macrophage ROS release was measured using a GloMax 20/20 single tube luminometer (Promega, Wisconsin, USA). Macrophages were added to a 1.5 ml tube at a density of 5 x 10^5 per tube in the presence or absence of normal, sarcopenic and senescent myotube samples. *Saccharomyces cerevisiae* derived zymosan A (Sigma Aldrich, Dorset, UK) was used as the positive control to stimulate ROS production and was used at a working concentration of 2 mg/ml. All experimental tubes also included 1x10^{-5} M of the chemiluminescent agent *N,N'*-Dimethyl-9,9'-biacridinium dinitrate, more commonly known as lucigenin (Sigma Aldrich, Dorset, UK). ROS release in each experimental tube was measured immediately every 5 minutes for 1 hour.

Additional experiments included a pre-incubation step in which J774 macrophages were incubated with the various myotube secretomes at 37°C for 4 hours. Following incubation, zymosan A was added to all tubes except the negative control tubes and ROS production was measured as described in the previous paragraph.

2.9 Identification of macrophage phenotype

To identify specific macrophage subtypes within an entire macrophage population following treatment with normal, sarcopenic and senescent myotube secretomes.

2.9.1 Griess assay

To determine the presence of M1 macrophages, the level of inducible nitric oxide synthase (iNOS) activity was indirectly measured by calculating the concentration of nitrite (NO_2^-) produced by murine macrophages. J774 murine macrophages were seeded into 24 well plates at a density of 1 x 10^6/ml in phenol-red free cRPMI and allowed to adhere for 24 hours. Phenolred free cRPMI contained FBS due to the presence of LPS-binding protein, without which LPS cannot be delivered to the macrophages. Attached J774 cells were treated with either 0.1 μg/ml or 1 μg/ml lipopolysaccharide (Sigma Aldrich, Dorset, UK), normal, sarcopenic or senescent myotube secretome components for 48 hours. After incubation, supernatants from each treatment well were transferred to a 96 well plate, in addition to sodium nitrite standards. 1% sulphanilamide (Fisher Scientific, Loughborough, UK) in 1 M hydrochloric acid was added to all wells and the plate incubated in the dark at room temperature for 10 minutes. Then 0.1% *N*-1-naphthylethylenediamine dihydrochloride (Sigma Aldrich, Dorset, UK) was added and the plate incubated in the dark at room temperature for a further 10 minutes. NO_2^-

production was measured at an absorbance of 450 nm using a Multiskan™ GO microplate spectrophotometer (Thermo Scientific, Loughborough, UK).

2.9.2 Macrophage cytokine profiling

Alternatively, cytokine production was measured to identify macrophage subtypes within the macrophage population using flow cytometry. 1 x 10^6 J774 murine macrophages were treated with EVs and soluble proteins isolated from normal, sarcopenic or senescent myotubes for 48 hours at 37°C. Following incubation, macrophage secretomes were collected and assayed using a LEGENDplex™ fluorescent multi-analyte flow assay kit (Mouse macrophage/microglia panel – 13 plex, BioLegend, London, UK). Briefly, EVs and soluble proteins, assay buffer and mixed fluorescent beads were added to a V-bottomed 96 well plate and the plate incubated protected from light on a thermoshaker (800 rpm at room temperature) for 2 hours. After 2 hours, the plate was centrifuged (250*xg*, 5 minutes), the supernatant discarded and the plate washed using wash buffer. This process was repeated twice to reduce background fluorescence. Following the washing step, biotinylated detection antibody was added to all samples and incubated protected from light on a thermoshaker (800 rpm at room temperature) for 1 hour, followed by the addition of streptavidin-phycoerythrin to the plate which was then incubated protected from light on a thermoshaker (800 rpm at room temperature) for 30 minutes. After the last incubation period, the plate was washed and beads were resuspended in wash buffer prior to being analysed on a CytoFLEX flow cytometer (Beckman Coulter, High Wycombe, UK).

Acquired FCS files were analysed using the LEGENDplex™ data analysis software (Beckman Coulter, High Wycombe, UK).

2.10 Mass spectrometry

2.10.1 Lysis of myotubes and EVs for Sodium-Dodecyl-Sulphate-Polyacrylamide Gel Electrophoresis (SDS-PAGE)

EVs derived from days 3 and 5 ITS differentiated myotubes were lysed using 1.5 mM Tris-HCl pH 7.4 with 2% CHAPS, 8 M urea and 2 mM thiourea. EV samples in lysis buffer were sonicated on ice for two 30 second sonication cycles followed by a resting period. Sonicated samples were centrifuged at 14,000*xg* for 10 minutes and supernatants retained. Sample protein concentration was determined using a Bradford assay with a BSA standard.

30 μg samples were combined with 1x reducing Laemmli buffer (Sigma Aldrich, Dorset, UK) and heated at 65°C for 15 minutes. Sample proteins were resolved on a 10% SDS polyacrylamide gel and stained using Coomassie brilliant blue G-250 stain (VWR,

Leicestershire, UK) in aqueous 40% methanol (VWR, Leicestershire, UK) with 10% glacial acetic acid (Fisher Scientific, Loughborough, UK). Gels were de-stained using aqueous 10% ethanol with 7.5% glacial acetic acid.

2.10.2 In-gel digestion

Each gel sample lane was cut into five equally sized sections, diced and transferred to 1.5 ml polypropylene tubes. Gel pieces were further de-stained on a thermoshaker (37°C at 550 rpm) with 50% acetonitrile (Fisher Scientific, Loughborough, UK) in 50 mM aqueous ammonium bicarbonate (Sigma Aldrich, Dorset, UK). Following de-staining, gel pieces were completely dehydrated using 100% acetonitrile and vacuum dried for 30 minutes. Dried gel pieces were rehydrated with 6.25 ng/µl trypsin gold sequencing grade (Promega, Southampton, UK) in 3 mM aqueous ammonium bicarbonate. Once fully hydrated, gel pieces were covered in 3 mM of aqueous ammonium bicarbonate and in-gel digestion carried out overnight using a thermoshaker (37°C at 550 rpm).

2.10.3 Extraction of peptides

100% acetonitrile was added to gel pieces following overnight in-gel digestion and sonicated in an ultrasonic water bath for 15 minutes. The peptide containing fraction was collected for each sample. This process was repeated a further 2 times with 50% acetonitrile in 50 mM aqueous ammonium bicarbonate, with the peptide containing fraction collected after each sonication step. Finally, gel pieces were fully dehydrated using 100% acetonitrile and the peptide containing fraction collected and combined with all previously collected fractions. Peptide fractions were vacuum-dried and samples stored at -20°C prior to mass spectrometric analysis.

2.10.4 Data acquisition

Peptide extracts were dissolved in 30 µl of 3% aqueous acetonitrile with 0.1% formic acid (Fisher Scientific, Loughborough, UK). Dissolved samples were transferred to borosilicate vials and placed into a Dionex 3000 autosampler at 10°C (Thermo Scientific, Loughborough, UK). 15 µl of sample were injected into a PepMap™ C18 trap column (5 µm, 100 Å, 300 µm x 1 mm Thermo Scientific, Loughborough, UK). Peptides were trapped and washed at a flow rate of 30 µl/min for 3 minutes with B, which consists of eluent A: 2% acetonitrile in aqueous 0.1% formic acid, and eluent B98% acetonitrile in aqueous 0.1% formic acid. Peptides were separated on an analytical column (AcclaimTM, PepMapTM C18, 3 µm, 100 Å, 75 µm x 150 mm, Thermo Scientific, Loughborough, UK) using a gradient of: 0-3 minutes 2% B; 3-48 minutes 2-45% B; 48-52 min 45-90% B; 52-55 min 90% B and 55-70 min 2% B. A PicoTip™

emitter (New Objective, Germany) was used to spray the nLC eluate at 2500 V to generate the electrospray. A 5600 TripleTof mass spectrometer (AB Sciex, Macclesfield, UK) was used for data acquisition, which was operated in information dependent mode (IDA). 1 IDA cycle involved an MS survey scan of m/z range from 300 to 2000, followed by CID fragmentations of the top 6 most abundant ions. Calibration of the mass spectrometer was performed before data acquisition for the highest mass accuracy (<10 ppm) on MS and tandem MS (MS/MS) levels.

2.10.5 Data analysis

Using PeakView software all runs were calibrated against the measured *m*/*z* range to reach mass accuracy lower than 0.03 Da and accurate relative quantification. MS data were further analysed using Progenesis version 4 software (Waters, Wilmslow, UK). Acquired runs were merged to the corresponding samples and into treatment groups to create a .mgf file, which was exported to allow for the confident protein identification using Mascot Daemon search engine. Data were compared against the SwissProt database for the proteins assigned to the human proteome, allowing for up to 2 cysteine mis-cleavages, peptide confidence of up to 0.5 Da and cysteine carbamidomethylation and methionine oxidation as variable modifications. Only peptides with Mascot Scores indicating confident identifications were exported back into Progenesis software. Relative quantitation was allowed for all proteins identified with at least 1 unique peptide and was calculated for at least 3 peptides per protein (where possible). Progenesis applied an ANOVA statistical test to determine significance between treatment groups (significance >95%).

The SwissProt decoy database was generated, and Mascot Daemon searches were performed to reveal FDR values filtered for the taxonomy of *Mus musculus*. Peptide matches above the identity threshold ranged between 2.60% - 5.26%.

2.10.5.1 Functional enrichment analysis

Proteins identified using Progenesis software were filtered to exclude those with 0 unique peptides, as well as those that were non-quantifiable or non-significant. After applying these exclusion criteria, proteins to be compared between samples (i.e., normal myotube EVs versus sarcopenic myotube EVs) were further filtered using student's t-test and all proteins within 95% confidence interval were selected for functional enrichment analyses.

Functional enrichment analyses of proteomic data were performed using FunRich 3.1.3 with the UniProt database. Gene enrichment analyses were conducted to identify enriched/depleted biological processes in EV samples.

2.11 Western blot

Western blot analysis was used to identify the presence of exosomes within a heterogeneous EV population, by probing for the exosome marker Tumour Susceptibility Gene 101 protein (TSG101).

This technique was also used to determine $p16^{INK4a}$ expression in etoposide induced senescent myotubes.

2.11.1 Sample lysis and SDS-PAGE

Normal, sarcopenic or senescent myotubes or derived EVs were lysed and proteins within samples separated using SDS-PAGE, as detailed previously in section 2.9.1.

2.11.2 Protein transfer

Following protein separation by SDS-PAGE, proteins were transferred from the gel to a nitrocellulose membrane via electroblotting. Briefly, gels were placed into western blot sandwich cassettes in the following order: sponge, filter paper, gel, nitrocellulose membrane, filter paper and finally sponge. Western blot sandwich cassettes were immersed in blotting buffer when placed into blotting tanks (Bio-Rad, Watford, UK) and the transfer completed at 100 V for 1 hour. After the transfer, nitrocellulose membranes were blocked overnight at 4°C. The nitrocellulose membranes were incubated with primary monoclonal antibodies on a shaker at room temperature for 2 hours, followed by two 5-minute wash steps. Secondary detection antibody was incubated with the nitrocellulose membrane on a shaker at room temperature for 1 hour. Detection antibody was removed by 5 wash steps, 5 minutes each on a shaker and ECL blotting reagent added to the nitrocellulose membrane for 2 minutes before being viewed in a G:Box imager to detect the protein of interest (Syngene, Cambridge UK).

3. Results Chapter 1 – Development and characterisation of a murine skeletal muscle model

3.1 Introduction

The generation of mature muscle fibres is essential for the functionality of skeletal muscle tissue *in* vivo, yet this myogenic process can also be mimicked via various methods *in vitro*. Many researchers opt to use animal sera to induce differentiation of myoblast cells into long multinucleated myotubes, however this can be problematic when investigating skeletal muscle derived EVs.

Serum products commonly used in cell culture, either as components of growth or differentiation media contain endogenous populations of EVs (Eitan et al., 2015). It is possible that sera derived EVs may interfere with the analyses of EVs originating from the cells or tissue of interest. For instance, characterisation studies may conclude high cell derived EV concentrations due to the presence of residual sera EVs within experimental samples, which may have an additive effect. Furthermore, sera EVs may influence the ability of parent cells to produce EVs, as well as the functional effects these EVs induce in target cells via the presence of exogenous DNA (Langecker et al., 2014).

Several methods are currently used to remove sera derived EVs to circumvent the aforementioned issues, including ultracentrifugation and commercially available chemical precipitation kits. Despite these methods reducing the number of EVs compared to unprocessed sera, reports show residual EVs still remain in the depleted sera. Eitan and colleagues have reported vesicle number in FBS reduces the longer it has been subjected to ultracentrifugation protocols but EVs still persist in the resultant serum (Eitan et al., 2015). Furthermore, vesicle removal was particle size dependent with larger EVs having a higher efficacy of isolation compared to those with a smaller diameter (Eitan et al., 2015). The Eitan *et al.* study opted to produce their own EV depleted sera, therefore it could be suggested that in house protocols might not be as efficient at removing vesicles from serum as companies specialising in this. However, commercially available EV depleted sera products do not guarantee 100% vesicle removal and nor do they specify the depletion protocols used. Whilst analysis of a commercial exosome depleted FBS (Exo-FBS™) has shown it to contain fewer vesicles than ultracentrifuged FBS, small EVs and EV like particles were still detected in the commercially available product (Kornilov et al., 2018, Lehrich et al., 2018).

Coupled with incomplete vesicle removal, depletion protocols are also time consuming, leading many researchers to purchase ready to use EV depleted sera. Many popular animal sera products are marketed as ultrapure vesicle depleted with a high level of exosome depletion; however, these items are often highly expensive and for some might be considered an unfeasible cost.

To ensure vesicle characterisation and functional studies are not affected by the presence of sera derived EVs, this chapter seeks to identify an appropriate serum-free (SF) method for the induction of skeletal muscle differentiation. This will ensure the study of only endogenously produced EVs, as vesicles are an important constituent of the skeletal muscle secretome.

Skeletal muscle as an endocrine organ produces a secretome consisting of various components and it is now acknowledged this also includes EVs; this vesicle containing secretome could facilitate communication both within skeletal muscle and other tissues (Frühbeis et al., 2015, Rome et al., 2019). Myoblasts and myotubes are both documented as being active producers of EVs, especially during the myogenic process (Guescini et al., 2017, Choi et al., 2016). Human myoblast derived vesicles can carry different growth factors, including HGF, IGFs and FGF, which were conducive for satellite cell differentiation (Choi et al., 2016). Additionally, myotube EVs are likely candidates for the transfer of miRNAs and proteins that are responsible for myoblast exit from the cell cycle and the induction of differentiation. Equally, EVs produced by skeletal muscle can also inhibit myogenesis. During instances of skeletal muscle damage and inflammation, pro-inflammatory immune cells can influence skeletal muscle tissue to release vesicles that preferentially package less decorin and more myostatin, which limits muscle differentiation (Kim et al., 2018, Tidball, 2017). The locomotion function of skeletal muscle can also stimulate vesicle release, as exercise has been documented to increase systemic EV concentration, with the number of EVs produced most likely correlating to exercise intensity (Frühbeis et al., 2015). Damage incurred following intense physical activity requires regeneration of the ECM, as well as the repair of myofibres. Skeletal muscle progenitor cell derived EVs also transport miRNA cargo, specifically miR-206, which is involved in inducing collagen production to support the growth of muscle fibres following injury (Fry et al., 2017). Muscle derived EVs not only affect the function of skeletal muscle cells but also have effects further afield. For instance, muscle EVs are involved in facilitating the remodelling of bone tissue. Xu *et al.* have shown skeletal muscle exosomes deliver miRNAs that stimulate pre-osteoblasts to undergo osteogenic differentiation (Xu et al., 2018).

Whilst skeletal muscle EVs play varied roles within and outside the tissue, this chapter is focused on characterising the process of myogenesis. The numerous stages of muscle

differentiation are accompanied by changes to the cell and EV proteome, both of which have been characterised (Forterre et al., 2014a, Romancino et al., 2013). However, to date most proteomic analyses have solely been performed on serum differentiated muscle cells and the contribution of contaminating serum derived proteins is unclear. This chapter aims to characterise the chosen SF differentiation protocol with regards to its ability to stimulate EV production and furthermore to determine the protein profile of differentiating muscle EVs to enable the appraisal of the proposed SF protocol which would be beneficial for downstream EV analyses.

3.2 Results

3.2.1 Assessing the ability of differentiation media to induce myotube formation

Numerous methods can be employed to stimulate myoblast to myotube differentiation *in vitro*, including supplementing medium with a low percentage of either horse serum (HS) or FBS, the addition of a chemical cocktail containing insulin, transferrin and selenium (ITS) or the use of SF medium alone. ITS is frequently used to reduce the amount of serum used in basal media for cell culture. All three components of this supplement support and maintain cell growth, with insulin eliciting mitogenic effects as it is responsible for the uptake of glucose and amino acids, as well as promoting protein and nucleic acid synthesis. Transferrin is an iron carrier and can reduce the toxicity of oxygen radicals in culture, whilst selenium is a co-factor for glutathione and functions as an antioxidant.

In order to compare and contrast these different conditions for the induction of myotube differentiation, proliferating C2C12 mouse myoblast cells were treated with all 3 differentiation media for a period of 5 days and myotube formation was visually assessed daily, focusing on changes to cell morphology using phase contrast microscopy. The presence of long spindle like cells was used to confirm myotube formation for each method of differentiation.

Analysis of cell morphology across a 5-day period following treatment revealed all 3 differentiation media were capable of inducing myotube formation though to varying degrees (figure 7). Differentiation using SF medium exhibited minimal differences between days 1-2, with the cell population largely comprising of myoblasts and an absence of myotubes, which could be a consequence of the myoblasts not having yet exited the cell cycle. 3 days post treatment showed a minor change, a small number of myoblasts had aligned and apparently fused together to form thin short myotubes, however the majority of cells observed at this time point still comprised of myoblasts. As the period of differentiation progressed to days 4-5, longer and wider myotubes were observed (arrow A), however this was also coupled with an increase in the presence of apoptotic cells (arrow B) in culture due to the absence of serum

growth factors. For all differentiation media tested, apoptotic cells were visually confirmed by observing changes in cell morphology. Myoblasts that were shrunken, shrivelled cells which appeared to be denser were considered to be apoptotic. No additional methods were employed to determine apoptosis in these cultures.

Combining ITS with SF medium appeared a more effective method of stimulating myogenesis. Like the SF medium only approach, 24-48 hours post treatment showed myoblasts to be the predominant cell type. Despite this, the myoblasts exhibited behavioural changes, as the precursor cells had a more ordered appearance, which is indicative of myoblast migration and alignment with the purpose of multiple cell fusion. After 3 days of differentiation induction, myotubes were first visualised. At this stage, ITS myotubes visually appeared longer and thicker than their SF counterparts and the phase density of the myotubes appeared to increase, a likely reflection of increasing cell substance. Furthermore, ITS increased myotube formation, as more myotubes were visualised at day 3 compared to the SF method. Similar to SF differentiation, the use of ITS also gave rise to increasing numbers of apoptotic cells (arrow C) which were seen as dark, small shrunken cells clustered around both myoblasts and myotubes, yet the extent of cell death was not the same as the SF method. Day 4 showed an increase in myotube number and these cells were also seen to increase in size, with changes in both thickness and length. Myotubes at this point of differentiation also exhibited branching (arrow D). This was often observed as a myotube with one or more additional myotubes branching from the main stem, leading to the development of many connections across the entirety of the well. The final day of differentiation mimicked the fourth day in that myotubes were still developing, however differentiation had not reached completion as myoblasts remained in culture alongside the myotubes. Myotubes produced using ITS supplemented SF medium demonstrate minimal directionality with cells aligning and fusing in all directions.

Reducing the serum percentage was the final differentiation method tested and the changes elicited by this medium were visible 24 hours following treatment. The addition of 2% HS appears to maintain myoblast proliferation on day 1, which is apparent from the differences in cell confluency between all three media. 24 hours following myoblast treatment with either SF or ITS, cells had adopted a more spread morphology with a confluency between 90-100%. However, myoblasts exposed to 2% HS for 24 hours had 100% confluency, with some cells aligning in anticipation of cell fusion. The day 2 cell population was largely comprised of myoblasts, although these cells appeared to be entering the early stages of myoblast fusion with the beginnings of small myotubes being observed. 72 hours post differentiation stimulation, small thin myotubes were visible, yet most cells remained in the fusion stages of myogenesis. In contrast to day 3 ITS myotubes, the 2% HS myotubes were thinner and shorter in size, and the overall appearance of the myotubes was more subtle compared to the

aforementioned differentiation method. As with both SF and ITS supplemented media, apoptotic cells (arrow E) were also found in the presence of 2% HS, which is a possible consequence of having a high cell density. Myotube formation progressed on the fourth day of differentiation as cells were longer and thicker (arrow F), and there was an absence of branching often seen with the use of ITS. Unlike the day 4 ITS myotubes, the 2% HS equivalents were smaller in size. Myoblast fusion continued into the fifth day of differentiation leading to an increase in myotube number and size. Accompanied by the growth of myotubes was a reduction in apoptotic cells. As the differentiation period progressed, the muscle culture appeared healthier compared to previous days.

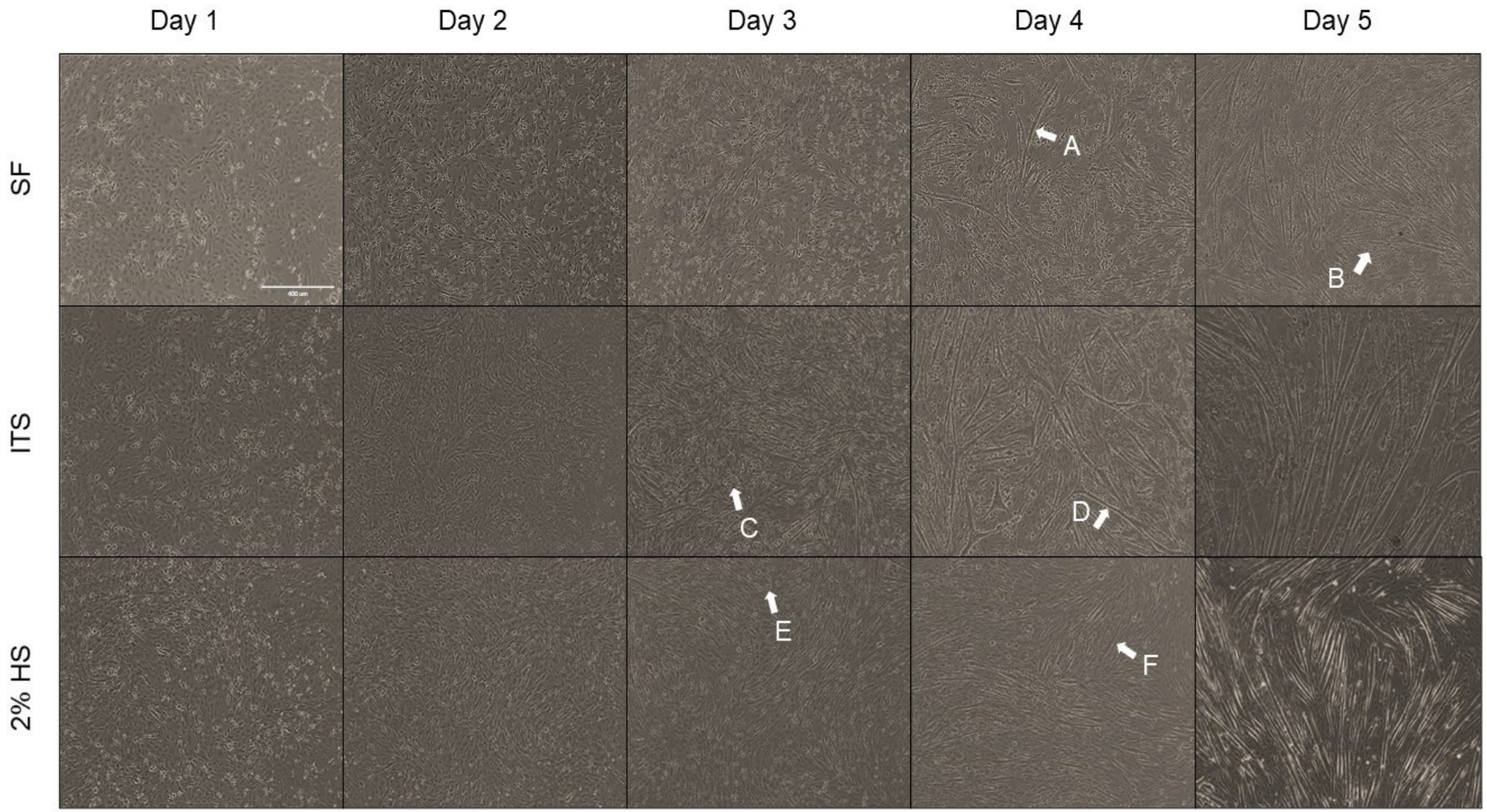

Figure 7. Morphological changes of differentiating C2C12 myoblasts in the presence of multiple differentiation agents. Representative phase contrast images (10x magnification, scale bar = 400 μm) of myoblasts treated with SF medium, SF medium with added insulin, transferrin and selenium (ITS) and medium supplemented with 2% horse serum (HS). Differentiating cells were imaged daily for a period of 5 days. White arrows indicate areas of note.

3.2.2 Concentration and size profile of differentiating C2C12 myoblasts-derived EVs

In addition to identifying a SF yet efficient method of inducing myogenesis in C2C12 myoblasts, it was also necessary to determine the ability of these differentiation media to produce sufficient EVs for use in downstream functional experiments. Myoblasts were treated with either SF, ITS or 2% HS media, as mentioned in section 3.1.1 and EV release was assessed daily for 5 days using tuneable resistive pulse sensing analysis (TRPS).

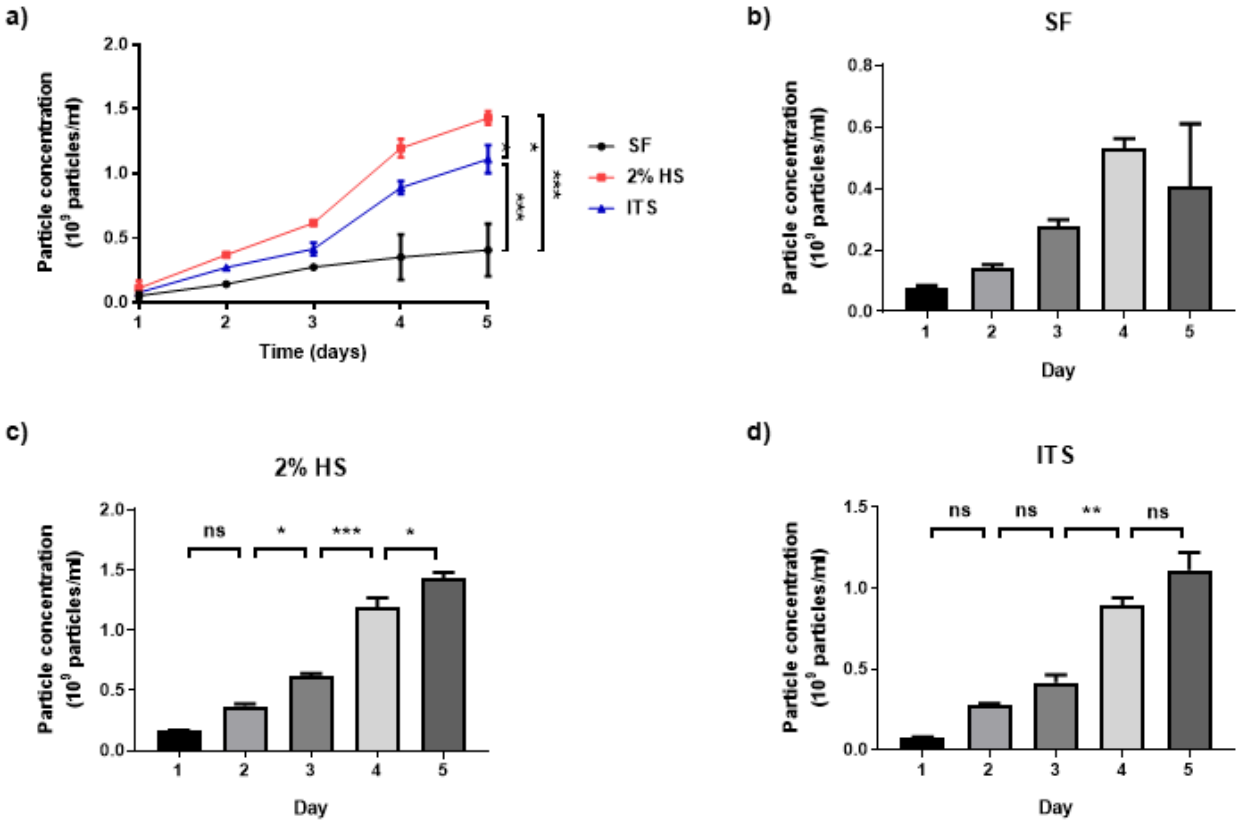

Figure 8. Characterisation of particle concentration in culture off differentiating C2C12 myoblasts. C2C12 myoblasts were differentiated using either SF, ITS or 2% HS and conditioned media collected daily during the 5-day differentiation period. Particles were isolated using differential centrifugation and (a-d) particle concentration was determined using TRPS based qNano analysis. Data shown are mean ± SEM of 3 independent experiments, one-way ANOVA with Tukey's *post-hoc* test, **P<0.05, **P<0.005, ***P<0.0001*.

Measurement of EV concentration was commenced 24 hours after addition of differentiation media to allow cells to initiate vesicle production in response to a change in culture conditions. qNano analysis highlights the disparity between the tested media in their ability to induce EV production. When comparing the day 5 concentration, SF medium generated the fewest vesicles, whilst the addition of 2% HS returned the most EVs, with the ITS method producing an intermediate value (figure 8a).

Differences in EV release were also observed on a day-to-day basis for each differentiation medium. The data indicate that during the 5-day measurement period, SF medium was unable to induce differentiating cells to upregulate EV generation following treatment, therefore particle concentration did not change between days 1-5 despite a possible trend towards increased numbers (figure 8b).

The use of 2% HS showed no significant differences in particle concentration until the transition from day 2 - 3 (figure 8c). During this time point, there was a small increase in vesicle concentration, followed by a greater increase on the fourth day. Despite the increase in EV number continuing into the fifth and final day of differentiation, the rate of release had declined at this point. It is unlikely that elevated EV production may have continued after the fifth day time point, due to the rate slowing down.

Unlike the 2% HS, the addition of ITS did not induce changes in EV concentration during days 1-3 of differentiation (figure 8d). A faster rate of particle generation ensued with the onset of day 4, as an increase in concentration was observed at this time point. However, this surge in EV production was not maintained into day 5 of the differentiation period since particle number did not alter between days 4-5, suggesting the peak of vesicle release had been reached. However, it should be noted that the pattern of change in EV concentration between ITS and 2% HS is similar, which might be indicative of similarities in EV production.

In addition to EV concentration, the modal particle diameter was also determined during the entirety of the differentiation period, allowing for the identification of size and therefore vesicle classification. Irrespective of differences in vesicle concentration between the various media, the diameter of EVs produced by each differentiation inducer was similar, with no changes in particle size detected across this 5 day period (figure 9a). Based on the TRPS analysis, EVs released by each method during the entire differentiation period can all be classified as small EVs with a diameter <200 nm as defined by the minimal information for studies of EVs 2018 (MISEV 2018) (Théry et al., 2018).

Reviewing the results of the 3 differentiation media tested, with regards to their ability to induce myotube formation (changes in cell morphology) and to produce a sufficient amount of EVs (concentration) for future studies, it was decided that ITS supplementation was the optimum differentiation method to establish a skeletal muscle model.

Given the small size of vesicles identified here, it was reasonable to hypothesise that these were of exosomal origin, at least in part. To test this hypothesis, vesicles produced by the ITS method were analysed further using western blotting to seek the presence of markers of small, exosomal EVs as predicted by the TRPS result. ITS produced EVs were isolated at day 3 and 5 and probed for the exosomal marker protein, tumour susceptibility gene 101 (TSG101) to

determine the presence of exosomes within the overall small vesicle population. These time points were specifically chosen for sampling and analysis to obtain an overview of potential changes in EV subtype across the differentiation period. Ideally, day 1 EVs would also have been analysed for TSG101 expression to provide an early time point for comparison, however the addition of differentiation media 24 hours prior to vesicle isolation resulted in insufficient EV harvesting for downstream western blotting analysis. Figure 9b shows both day 3 and 5 vesicles expressed TSG101, suggesting these EVs are likely to be an exosome population. Despite, both sets of EVs being TSG101 positive, the level of expression varied between the two EV populations. Visual analysis indicates day 5 EVs had a higher level of TSG101 expression than day 3 vesicles, providing insight into vesicle composition during myogenesis.

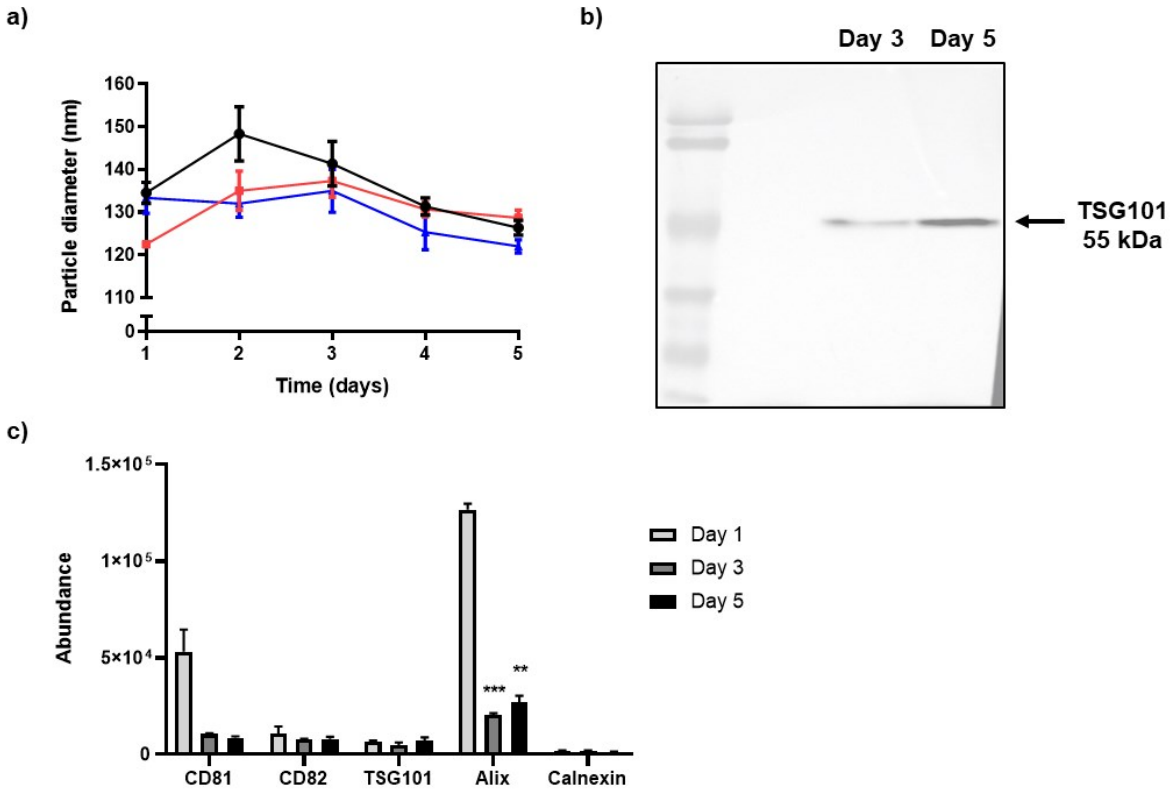

Figure 9. Characterisation of EV size and composition from differentiating C2C12 myoblasts. C2C12 myoblasts were differentiated using either SF, ITS or 2% HS and conditioned media collected daily during the 5-day differentiation period. EVs were isolated using differential centrifugation and (a) particle diameter was determined using TRPS based qNano analysis. Data shown are mean ± SEM of 3 independent experiments, one-way ANOVA with Tukey's *post-hoc* test, all samples *ns*. Day 3 and 5 EV pellets produced via the chosen ITS differentiation method were also analysed for the presence of the exosome marker protein (b) TSG101 by Western blot. (c) Protein abundance of EV markers for day 1, 3 and 5 C2C12-derived EVs. Data shown are mean ± SEM of 3 independent experiments, two-way ANOVA with Tukey's *post-hoc* test, ***P<0.005* and ****P<0.0005*.

The expression of protein markers associated with small EVs (CD81, CD82, TSG101 and Alix) was also assessed for vesicles isolated from day 1, 3 and 5 differentiating C2C12 cells via MS

based proteomic analysis (figure 9c). EVs from all days expressed CD81, CD82, TSG101 and Alix, with day 1 EVs having a greater abundance of Alix than day 3 and 5 EVs. Calnexin (ER marker) expression was minimal for all three EV populations.

3.2.3 Identifying the proteome of ITS differentiated myoblasts and their associated EVs

Having characterised ITS-stimulated cell-derived EVs with regards to their concentration and size, the subsequent stage was to identify changes to the protein profile of vesicles during differentiation and whether changes in protein expression facilitate the myogenic process. Additionally, the proteome of differentiating cells was also ascertained to provide a cellular comparison for the determination of differences between parent cells and their derived EVs. Peptide fractions from both differentiating C2C12 myoblast cells and their released EVs were analysed using mass spectrometry (MS) via the bottom-up approach. MS expertise was provided by Dr Ivana Milic for this purpose.

In total, 1783 cell proteins with at least one unique peptide sequence were identified across the differentiation period (days 0, 1, 3, and 5). Having decided on ITS as the chosen method of differentiation, it was necessary to confirm myoblast to myotube differentiation using methods in addition to visual morphological changes, such as the myogenic proteome. From the exhaustive list of proteins, the expression of 5 skeletal muscle specific proteins indicative of differentiation was determined (figure 10). Protein expression has been reported as a normalised abundance that has been determined by Progenesis Qi for proteomics software. Normalisation is performed to correct for experimental variation during sample acquisition, which can arise when preparing the sample for measurement. The correction of this variation is executed by applying a scalar factor to all measurements (Välikangas et al., 2016). This scalar factor is calculated by Progenesis Qi for proteomics software by using ratiometric data in log space, in addition to a filtering process that employs mean and median deviation outliers.

The abundance of α-actin, a contractile protein was shown to be very low in myoblasts from days 0 and 1 (figure 10a). However, 3 days post differentiation induction, the expression of this protein rapidly increased and this continued into day 5. A similar trend was observed with myosin light chain 4 (MYL4), another mediator of muscle contraction, as abundance did not increase between day 0 and 1 but exhibited an increase in expression on day 3, with the highest abundance on the last day of differentiation (figure 10b). Troponin C, a third contractile protein, was not significantly upregulated during the first 3 days of differentiation (figure 10c), after which a dramatic increase in troponin-C abundance was seen on day 5. The abundance of β-enolase, which is involved in skeletal muscle development, increased with each day of myogenesis, with cells on days 1 to 5 all having a significantly higher expression than in day 0 myoblasts (figure 10d). Lastly, the abundance of the antioxidant enzyme superoxide

dismutase-1 (SOD1) was analysed (figure 10e). Expression of this protein was only more elevated on days 3 and 5 compared to day 0, with day 5 exhibiting the highest expression level.

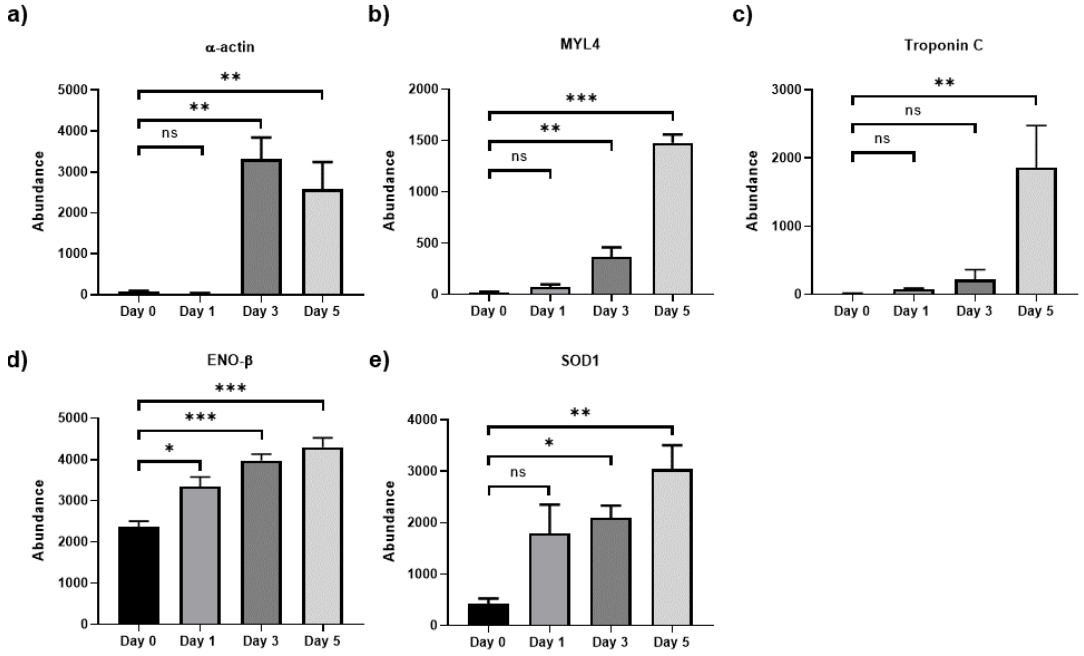

Figure 10. Abundance of skeletal muscle differentiation protein markers in C2C12 cells undergoing myogenesis. The expression of myogenic proteins in ITS differentiated C2C12 myoblasts was analysed using MS. Expression levels of α-actin (a), myosin light chain 4, MYL4 (b), troponin C (c), β-enolase, ENO-β (d) and superoxide dismutase-1, SOD1 (e) were measured at 4 time points during the differentiation process: days 0, 1, 3 and 5 post ITS treatment. Data shown are mean ± SEM of 3 independent experiments, one-way ANOVA with Dunnett's *post-hoc* test. (a) ***P<0.01* (b) ****P<0.0001*, ***P<0.01* (c) ***P<0.01* (d) ****P<0.001*, **P<0.05* (e) ***P<0.005, *P<0.05*.

Characterisation of the differentiating cell proteome was followed by characterisation of EVs released during this process. In total, 1196 proteins with unique peptide sequences were identified in day 1, 3 and 5 EVs harvested during myogenesis. Day 0 EVs were not included in MS analysis due to the presence of serum-derived EVs, which could skew the results. The 5 protein markers of skeletal muscle differentiation assessed in C2C12 cells were also measured in their corresponding EVs. Of the 5 proteins, only 4 were detected in the EV fractions, with MYL4 being the undetected marker (figure 11a). Like the differentiating cells, α-actin expression was upregulated across the entire period of measurement, whilst troponin C exhibited the opposite, with abundance significantly decreasing between day 1 and day 5. This trend was also observed with ENO-β expression, which was elevated in day 1 EVs but declined to a similar level on both days 3 and 5. Lastly, SOD1 antioxidant enzyme had no

abundance in day 1 vesicles, after which expression levels reached their peak on day 3 and dropped again on the final day of differentiation.

Abundance of these 4 proteins was also compared between differentiating C2C12 myoblasts and their isolated EVs across days 1, 3 and 5 (figure 11b). α-actin expression remained the same between cells and EVs, until day 5 when EV abundance exceeded that of myotubes. Regarding troponin C, the expression of this protein did not change across the differentiation period. ENO-β was more abundant in day 1 EVs than cells, after which expression levels were the same between the two samples. The abundance of SOD1 did not change until the last day of differentiation when as expected, the expression of this protein rose to a level greater than that of day 5 EVs.

Skeletal muscle processes were also assessed to determine how their associated proteins change during myogenesis (figure 12). A selection of proteins was compared between myoblasts (day 0) and myotubes (day 5), which are presented in the coloured boxes. The abundance of proteins was also compared between myotubes and myotube EVs, which are shown outside of the coloured boxes. Differentiated skeletal muscle has contractile potential and therefore requires proteins to facilitate this process. As expected, contractile proteins, such as troponin C, α-actin, calsequestrin-2, MYL4 or myosin regulatory light chain 4 were more abundant in myotubes, which mirrors some of the results presented in figure 10. Troponin C and α-actin were the only contraction associated proteins detected in myotube EVs and comparison between myotube cells demonstrated that troponin C was less abundant whilst α-actin was more abundant in the day 5 vesicle sample.

Increased contractile ability requires proteins involved in energy metabolism to provide energy for this process. The proteins glycogen phosphorylase, creatine kinase M-type and carnitine o-acetyltransferase were more expressed in day 5 myotubes than in myoblasts. Glycogen phosphorylase was the only energy associated protein quantifiable in day 5 EVs, however its expression was downregulated in EVs compared to parent day 5 myotubes.

Due to skeletal muscle undertaking contraction for motility, this tissue is a great consumer of oxygen, which is used to provide the energy needed for contraction. Myoglobin is the oxygen carrier in skeletal muscle and its abundance was higher in myotubes than in myoblasts (figure 12) but was not detected in day 5 EVs.

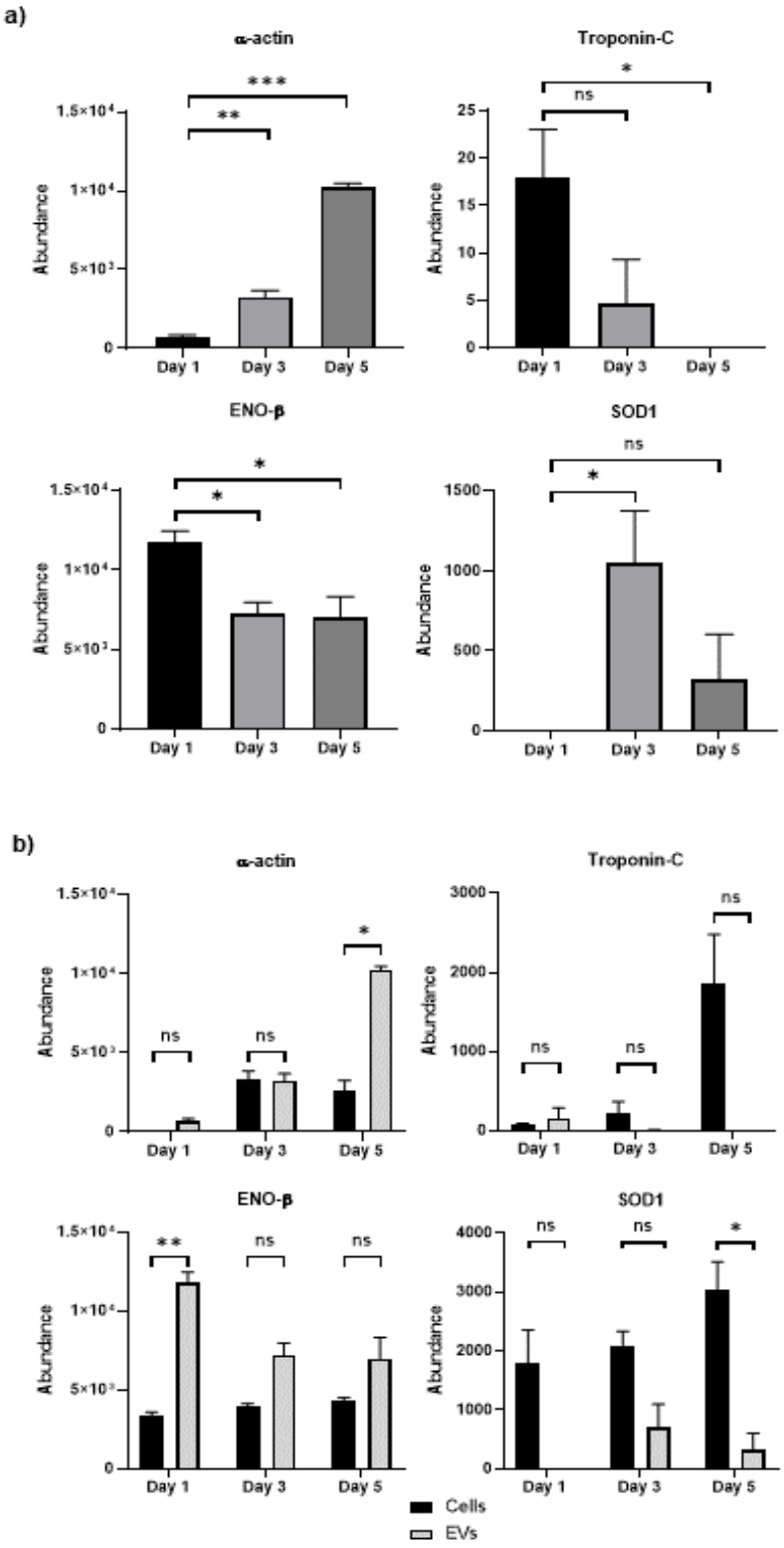

Figure 11. Comparing abundance of proteins associated with skeletal muscle differentiation in myogenic C2C12 cells and their EVs. The expression of (a) α-actin, troponin C, ENO-β and SOD1 in differentiating C2C12-derived EVs on days 1, 3 and 5 following ITS induced myogenesis. (b) These 4 proteins were also compared across the same days for differentiating myotubes and their associated EVs. Data shown are mean ± SEM of 3 independent experiments, one-way ANOVA with Dunnett's *post-hoc* test. (a) ****P<0.0001*, ***P<0.005* and **P<0.05*. (b) ***P<0.001* and **P<0.05.*

Increased contractile ability requires proteins involved in energy metabolism to provide energy for this process. The proteins glycogen phosphorylase, creatine kinase M-type and carnitine o-acetyltransferase were more expressed in day 5 myotubes than in myoblasts. Glycogen phosphorylase was the only energy associated protein quantifiable in day 5 EVs, however its expression was downregulated in EVs compared to parent day 5 myotubes.

Due to skeletal muscle undertaking contraction for motility, this tissue is a great consumer of oxygen, which is used to provide the energy needed for contraction. Myoglobin is the oxygen carrier in skeletal muscle and its abundance was higher in myotubes than in myoblasts (figure 12) but was not detected in day 5 EVs.

With increased oxygen consumption, redox proteins are required to protect skeletal muscle cells from oxidative stress mediated damage. Antioxidant enzymes, such as glutathione (GSH) reductase and SOD1 were upregulated in myotubes compared to undifferentiated myoblasts, however the opposite was true for GSH S-transferase A4, which was more abundant in myoblasts (figure 12). Comparison of SOD1 expression in myotubes and their secreted EVs showed this enzyme was heavily downregulated in vesicles than in cells.

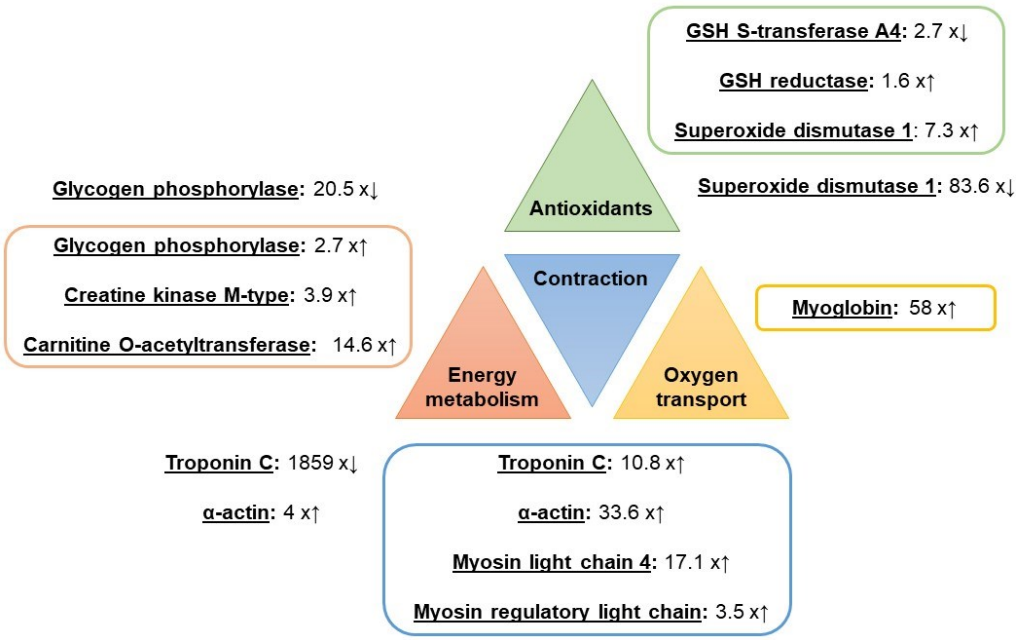

Figure 12. Up- or downregulation of proteins associated with various skeletal muscle processes. The abundances of proteins involved in energy metabolism, antioxidant responses, contraction and oxygen transport were compared in day 0 myoblasts vs. day 5 myotubes (coloured boxes) and day 5 myotubes vs. day 5 myotube-derived EVs (outside boxes). Up arrows indicate upregulation whilst down arrows denote downregulation. Not all proteins detected in myotubes were detected in myotube EVs, hence their absence. (All proteins presented are significantly up- or downregulated as determined by student's t-test, with proteins of a significance >95% selected).

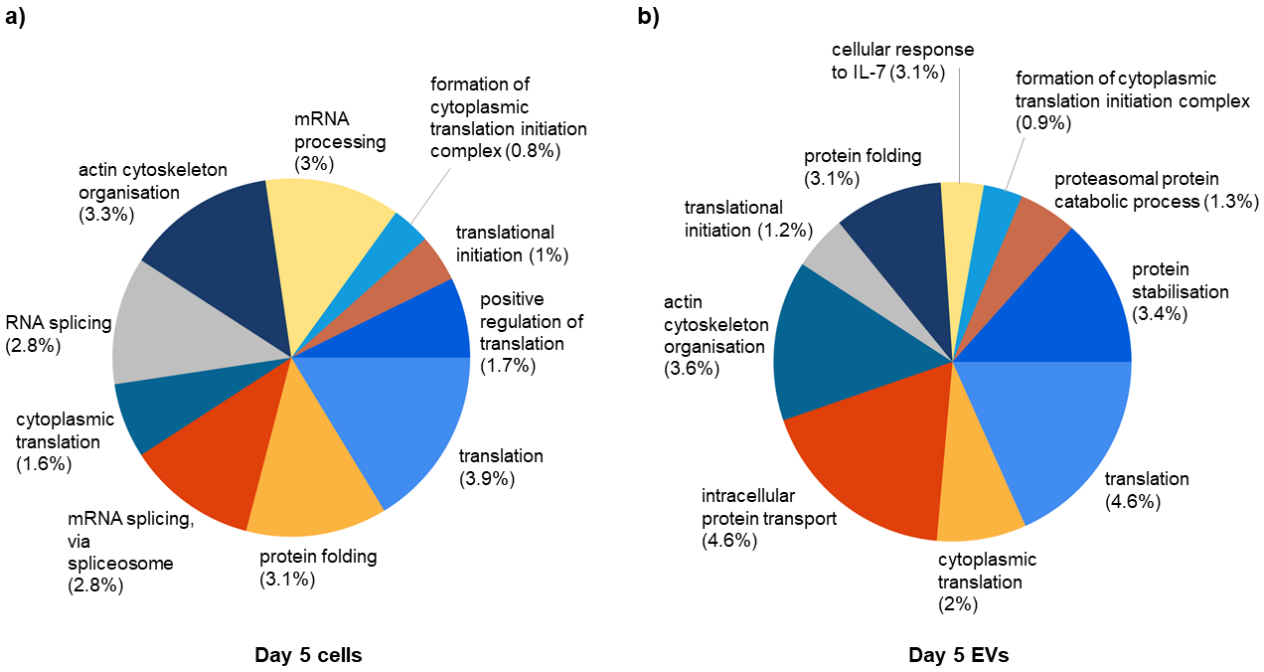

Figure 13. GO for biological processes of differentially expressed proteins. The top 10 GO terms associated with day 5 myotubes (a) and day 5 myotube-derived EVs (b).

GO was conducted on day 5 myotubes and their derived EVs, with figure 13 showing the biological processes for the top 10 terms. Both cells (figure 13a) and EVs (figure 13b) showed increased expression proteins related to translation, actin cytoskeleton organisation and protein processing. As expected, myotubes were enriched in mRNA splicing and transcription due to elevated protein synthesis in differentiating cells.

3.3 Discussion

3.3.1 Methods of inducing myogenesis *in vitro*

The C2C12 murine skeletal muscle cell line is a vital tool in furthering our understanding regarding muscle disorders, largely due to its easy *in vitro* culturability and capacity to be differentiated into mature muscle cells by various methods. The advantage of using numerous differentiation formats allows for the study of skeletal muscle derived EVs, which ideally requires the absence of exogenous vesicles that can often interfere with characterisation and functional studies.

Despite the common use of animal sera to induce C2C12 myoblast differentiation, this is a sub-optimal method for EV researchers due to the presence of EVs in the sera. SF conditions are beneficial for EV research, yet they are rarely used to promote the myogenic process, as shown in this chapter, however the ability of this format to stimulate myotube formation has been previously documented (Fujita et al., 2010, Lawson and Purslow, 2000). These studies have found various compositions of SF media to be conducive for myotube formation and in some respects were better differentiators than serum containing formulations. This contrasts with the findings presented in the current chapter and can be attributed to differences in the types of SF media used. Despite employing SF conditions, Fujita *et al.* ensured optimal growth and differentiation of C2C12 myoblasts through the supplementation of medium with sera substitutes such as sericin, ultroser-G and AIM-V (Fujita et al., 2010). Consequently, the use of SF media alone is not sufficient to promote differentiation and requires the addition of compounds that can mimic the effects of animal sera to create a complex yet adequate differentiator. Nevertheless, it must be stated that the pro-myogenic properties of SF media are likely to be cell specific, as the rat myoblast cell line L6, another skeletal muscle model system, does not differentiate in the presence of sera substitutes and requires animal sera for myotube formation (Lawson and Purslow, 2000).

Vesicle depleted serum products are also commercially available, yet these products can be costly. Some researchers may consider avoiding these costs by employing ultracentrifugation to deplete serum EVs in house for myoblast differentiation, however there is uncertainty regarding the efficacy of EV depleted serum differentiation methods. The growth and differentiation of human and murine C2C12 myoblasts in EV free but serum containing medium is not conducive for myotube formation, since most growth factors are removed during the high-speed ultracentrifugation step (Aswad et al., 2016). The absence of serum EVs produced fewer myotubes and the reduced differentiation could not be rescued by switching to an EV containing medium. The removal of vesicles from serum has been shown to be

detrimental for cells, as it can affect cell proliferation, phenotype, and behaviour (Eitan et al., 2015).

Using EV depleted serum has similar pitfalls to SF medium and the necessity of employing animal sera or sera substitutes for myotube formation has been indicated. Despite this, other differentiation stimulating compounds can also be used to induce myogenesis, including a mix of insulin, transferrin, and selenium (Uozumi et al., 2006, Shiozuka and Kimura, 2000). This chemical cocktail is often used in conjunction with either HS or FBS, to reduce the overall amount of serum required for myoblast differentiation and to increase the rate of differentiation, but it can also be used in isolation (Ferruzza et al., 2013, Shiozuka and Kimura, 2000). The use of ITS is a more feasible SF approach to differentiation, as the individual components facilitate cell survival, which SF medium alone cannot do.

Although the use of ITS as a SF differentiator is not novel as it has been previously used to induce myogenesis in C2C12 myoblasts, it is not commonly used in isolation (Uozumi et al., 2006). It is often used to supplement existing serum-based differentiation methods, i.e. “2% HS or FBS. Despite this, ITS alone is an ideal differentiator due to its ability to induce the early formation of myotubes and could be considered cheaper than other SF options, such as AIM-V and Ultroser-G, when used in conjunction with DMEM. In comparison, it took longer for recognisable myotubes to appear with 2% HS treatment. By reducing the differentiation time, ITS can reduce the volume of differentiation media required to produce myotubes, which ultimately limits culturing costs. Despite ITS inducing myogenesis *in vitro*, it is evident that the appearance and quality of myotubes differs to those produced using 2% HS. In hindsight, a more pragmatic approach would have been to use 2% HS to differentiate the myoblasts into myotubes and prior to harvesting of the conditioned secretome, to sufficiently wash the cells and replace the serum containing differentiation medium with SF medium, thus preventing contamination with serum EVs. However, it is difficult to comment on the complete removal of all EVs originating from serum using this method.

3.3.1.1 Modelling skeletal muscle *in vitro*

Modelling myogenesis and mature skeletal muscle *in vitro* is limited using a 2D platform. Converting the existing model into a 3D system could bridge the gap between *in vitro* 2D cultures and animal models, as it facilitates the production of mature myotubes that are more physiologically representative, as well as the culture of different cell types present in skeletal muscle, which would provide a better understanding of the interaction of these cells during normal and pathological muscle conditions. However, the development of 3D systems also presents challenges when modelling skeletal muscle tissue. Scaffold free approaches, for

example the generation of cell sheets or myospheres is both a time-consuming process and difficult to scale up, whilst for scaffold-based models to be fully representative of native skeletal muscle, they require stable vascularisation for the sufficient delivery of both oxygen and nutrients to the muscle tissue, which has not yet been fully demonstrated and requires further investigation (Romagnoli et al., 2021, Khodabukus et al., 2018).

Converting the 2D model muscle model presented here to an *in vitro* 3D version will present various challenges. It is possible that results obtained with the current 2D model might not correspond to those in a 3D model. The use of ITS alone might not support myotube formation on 3D scaffolds and could require an alternative method of differentiation. Furthermore, to mimic *in vivo* conditions, co-culture would be required with the incorporation of other cell types. Most if not all co-culture models utilise serum and use of SF conditions to maintain the co-culture might not support the viability of all cell types used (Koffler et al., 2011, Afshar Bakooshli et al., 2019, Wragg et al., 2020, Laternser et al., 2018). Whilst many existing 3D skeletal muscle models use serum to induce differentiation, SF 3D models have also been developed, one of which has found SF media were better differentiators than the typically used HS (Gawlitta et al., 2008).

Irrespective of the platform used, *in vitro* skeletal muscle models employ reduced serum levels to stimulate myoblast to myotube differentiation. The model presented in this thesis uses the removal of serum to induce myogenesis and to bypass the effects of serum derived EVs. Whilst this approach simplifies the system by ensuring vesicles from serum are neither included in the endogenous particle count nor influencing cell behaviour, the absence of serum is not physiologically relevant. Serum is a natural component of *in vivo* systems, delivering factors, such as albumins, growth factors, hormones and adhesion molecules, and facilitating communication between tissues (Lee et al., 2022). Removing serum could affect the myogenic potential of the cultured skeletal muscle cells. Sera contain a variety of important protein components that facilitate and support the myogenic process. These proteins include the growth factors fibroblast growth factor (FGF), hepatocyte growth factor (HGF), insulin-like growth factors (IGFs) and platelet derived growth factor (PDGF), all of which are involved in the activation and proliferation of satellite cells, whilst IGFs are also associated with stimulating myoblast differentiation and PDGF is also responsible for promoting vascularisation of the muscle tissue (Syverud et al., 2016, Ahmad et al., 2020, Contreras et al., 2021). In addition to growth factors, serum also contains hormones such as insulin, which can also influence skeletal muscle generation. As an anabolic hormone, insulin promotes muscle growth by increasing the expression of both myogenin and MyoD to initiate satellite cell activation, as well as stimulating protein synthesis and limiting protein degradation (Dhindsa et al., 2019).

In addition to essential proteins, serum is also comprised of EVs and with serum being naturally produced *in vivo* will contain vesicles from various tissues, which could influence skeletal muscle growth and homeostasis (Théry et al., 2006, Tapparo et al., 2021). Therefore, the removal of serum to eliminate the presence of exogenous EVs for the study of endogenous EVs does not recreate the *in vivo* environment. Furthermore, EVs can transport some of the proteins mentioned above, including growth factors and adhesion proteins, therefore it is possible serum derived vesicles could be carrying proteins abundant in serum (Hoang et al., 2020, Jimenez et al., 2019). Since serum products contain essential proteins and EVs, the exclusion of serum could result in inefficient skeletal muscle synthesis and it is possible that data obtained from *in vitro* models might not be replicated *in vivo*, therefore serum-free media must be fully considered before use.

3.3.1.2 Differentiation media affect EV production

C2C12 cells have been shown to release EVs, however the impact of different differentiation media on skeletal muscle EV production is not well defined. Notable differences were observed in EV production, which were dependent on the differentiation media used to induce myotube formation. 2% HS treatment secreted the most EVs by cells undergoing myogenesis and despite serum-based differentiation being the most employed and ideal method of stimulating myotube formation, it can influence EV measurement data. 2% HS could have caused the highest particle concentration as serum will contain additional EVs and nanoparticle protein aggregates, which could have provided an additive effect, thereby increasing the existing vesicle count (Lehrich et al., 2021). In addition to introducing contaminating exogenous particles, EVs present in serum may be biologically active and elicit effects on the production of EVs by recipient cells or affect cell function (Shelke et al., 2014).

Unfortunately, the present study does not determine whether 2% HS derived EVs induced C2C12 cells to produce more EVs or whether particles present within the HS were responsible for creating a true additive effect. To confirm this, the particle count of 2% HS should have been measured in the absence of C2C12 cells, and this number subtracted from the particle count obtained from treated C2C12 cells. Since the percentage of serum used in the differentiation medium was reduced to 2%, it is possible that the number of particles in this HS containing formulation could be negligible and at too low a concentration to be detected by TRPS and therefore would exert minimal influence over endogenous EV production. Thèry *et al.* have recommended solutions to avoid the effects of serum derived EVs on endogenous EV investigations, one of which is to reduce the amount of serum in media preparations, which is the method used to stimulate myogenic differentiation and complies with this advice (Théry et al., 2006).

As expected, SF medium produced the lowest EV concentration of all 3 differentiation media tested. It was hypothesised that SF conditions would limit EV biogenesis due to the absence of serum provided growth factors (Lopatina et al., 2014). Yet specific formulations of SF medium can have the opposite effect and enhance EV synthesis (Li et al., 2015). Opti-MEM is a commercially available SF medium, similar in composition to ITS medium that is supplemented with insulin, transferrin, growth factors as well as other important components, which has been shown to increase EV production to a greater extent than serum containing equivalents (Bost et al., 2022). Opti-MEM medium also facilitated preferential packaging of reporter proteins into EVs, whilst serum containing medium showed a weaker vesicle associated reporter protein signal, indicative of an inhibitory serum factor limiting EV biogenesis (Bost et al., 2022). Whilst media such as Opti-MEM are good SF options for optimal EV generation, they too can be expensive. Supplementing SF medium with ITS has been shown to be a better stimulator of vesicle release than SF medium alone.

Though it is crucial to employ conditions that are favourable for myotube formation, it is equally imperative that these growth and differentiation conditions do not impair vesicle formation and release. EV researchers working with skeletal muscle must consider each aspect equally for both optimal growth and adequate vesicle biogenesis.

Irrespective of the differences in final EV concentration between the various differentiation methods, both 2% HS and ITS show an increase in vesicle production during myogenesis, specifically between day 3 and day 4. Romancino *et al*. have also shown C2C12 myoblasts elevate EV secretion during their differentiation into myotubes, however this group reported an average vesicle diameter of 80 nm, which is of a smaller size than stated in this chapter (Romancino et al., 2013).

Despite differences in the number of EVs produced by treatment with the different differentiation media, all 3 methods induced the release of small EVs, which were <200 nm. It should be noted that a diameter <200 nm was expected as the preparation method used is designed for smaller EVs. Further sizing of EVs secreted during myogenesis was also conducted, however this was undertaken on ITS-derived vesicles only, as this was the preferred differentiation method for the creation of a SF skeletal muscle model. The expression of TSG101, an exosomal marker, was measured in day 3 and day 5 EVs by Western blot. EVs from day 0 and 1 of myogenesis were not used due day 1 EVs not having sufficient protein concentration for use in the Western blot and day 0 EVs would have been isolated from myoblast cells, which would have been contaminated with vesicles from FBS in the growth medium. TSG101 was detected in EVs from both day 3 and 5, with visual observation suggesting expression was elevated in day 5 vesicles. This would suggest TSG101 comprises

more of the EV associated proteins on day 5 than on day 3. This could be a consequence of differentiating C2C12 increasing EV production, therefore requiring more ESCRT machinery to facilitate EV biogenesis, which could result in increased incorporation of TSG101 into vesicles during myogenesis. GO analyses conducted by Rome *et al.* have shown proteins involved in exosome biogenesis and intracellular trafficking were upregulated in myotube derived exosome-like vesicles, which supports findings in the present study (Rome et al., 2019).

Furthermore, it has been reported that whilst myoblasts and myotubes both release exosome-like vesicles, the pathways responsible for their release could be different. Exosome-like EVs produced by myotubes were found to be more enriched in CD81 and Alix compared to the myoblast equivalent (Forterre et al., 2014, Romancino et al., 2013). When comparing to the present study it is difficult to draw parallels as only day 5 myotube EVs were analysed and myoblast EVs were not included due to the presence of FBS. EVs released during the first day of differentiation were analysed and were produced by cells that could be considered as more aligned to myoblasts than myotubes. Therefore, when comparing day 1 EVs to day 5, the opposite was observed, as Alix expression was significantly higher in day 1 vesicles than day 5. Differences between these data and those of previous studies could be due to differentiation protocols. Both studies used 2% HS whilst the model presented in this chapter used SF medium supplemented with ITS. However, it is impossible to comment on these differences due to variations in the EV samples analysed. Additionally, these researchers used slightly different EV isolation methods. Despite these studies also using differential centrifugation to isolate EVs for immunoblotting analyses, they differed by including a 10,000*xg* centrifugation step, with the Forterre *et al.* study filtering the resultant supernatant following this step. It is possible that the absence of this centrifugation step in the current study resulted in the inclusion of microparticles in the EV fraction, which may account for differences between these data and other studies. In contrast, Bydak *et al.* used precipitation to isolated vesicles from cell supernatants, however their findings support the data presented here, as myoblast EVs had significantly higher expression levels of Alix compared to myotube EVs (Bydak et al., 2022). Whilst they also showed that myoblast EVs expressed more CD81, this was not corroborated by the present study despite day 1 EVs appearing to have more CD81 than day 3 and 5 EVs.

Whilst treatment with the differentiation media induced C2C12 cells to produce different particle concentrations, the makeup of the EV populations was not elucidated. All differentiation media produced particles that can be classified as small EVs based on sizing analysis, however these data do not provide full information on whether they were

homogeneous or heterogeneous populations of vesicles. The small EV populations could be comprised of exosomes due to the detection of TSG101 in ITS treated cells, but they could also contain apoptotic cell derived EVs of diameters <200 nm. Apoptotic cells release apoptotic bodies but have also been shown to produce apoptotic microparticles and apoptotic exosomes, suggesting these cells also secrete particles of different sizes (Li et al., 2020b). Apoptotic exosomes are a newly discovered apoptotic derived vesicle and have similar physical characteristics to viable cell derived exosomes, such as size and density which can make the two types of exosome difficult to distinguish (Kakarla et al., 2020). Apoptotic exosomes also share similar protein markers with other exosomes, including CD63; this combined with few unique markers make this EV population challenging to define and isolate with high purity (Park et al., 2018). Though apoptotic EVs were not searched for, it does not imply these vesicles were absent from secretome and EV preparations and may have contributed to the overall vesicle population. Therefore, it cannot be absolutely stated that effects observed in this chapter were a result of viable cell derived EVs or those produced by apoptotic cells and requires further investigation.

It is acknowledged further work is required to fully determine the presence of EVs in the secretomes produced during skeletal muscle differentiation. However, this information is not indicative of the purity of the vesicle preparations, which is an aspect of EV characterisation that is also lacking in this chapter. Contaminating non-vesicle particles of a similar size, such as aggregates can also be co-isolated with vesicles of interest. Usually, detection of lipoproteins such as apolipoproteins A1/A2, B or E would be suggestive of reduced purity, however none were found to be co-isolated with day 1, day 3 or day 5 vesicles based on proteomic analysis (see Appendix, Table 6) (Théry et al., 2018). This could be attributed to lipoproteins being abundant in serum, however serum was not used during C2C12 differentiation or the generation of secretomes, so is unlikely to be present in these samples (Busatto et al., 2022). Despite the absence of apolipoproteins, calnexin, an ER marker and an indicator of reduced purity was also detected in days 1, 3 and 5 of differentiation, however expression levels were very low in comparison to other markers.

Whilst ultracentrifugation was used for EV proteomic analyses, SEC isolation was used for all functional experiments, which are covered in subsequent results chapters. During SEC isolation, elution fractions 7 – 13 were collected as EV containing fractions and fractions 14 – 29 as the soluble protein fractions based on existing vesicle isolation protocols used in the Devitt research group. The EV fractions should have been further analysed to determine the presence of vesicles and to identify contaminants present in each fraction. The overall vesicle purity and the amount of protein contamination could be ascertained by calculating a purity

ratio, which is defined as the number of EVs per µg of measured protein in the sample (Webber and Clayton, 2013). A high ratio implies high purity of EVs whilst a low ratio suggests the presence of protein contaminants. Despite this ratio evaluating the level of purity, caution should be applied when using this method as it can be influenced by the EV source and the isolation protocols used (Van Deun et al., 2014). Ideally, to maintain consistency, SEC isolated EVs would also have been used for MS proteomic analyses rather than those isolated by ultracentrifugation. SEC was chosen for functional studies as this method reduces aggregation of vesicles and retains their biological activity (Ramirez et al., 2018). Furthermore, ultracentrifugation facilitated the isolation of sufficient EV amounts from large volumes of culture supernatants for MS analyses, which would have been more time-consuming and costly with SEC.

3.3.1.3 EVs or other particles?

This chapter presents particle concentrations induced by the differentiation media as measured by TRPS. This technique can characterise all types of particles yet is unable to differentiate between them (Cimorelli et al., 2021). EVs are described as lipid bilayer membrane enclosed nanoparticles but TRPS cannot use this characteristic to specifically identify vesicles (Mathieu et al., 2019). Furthermore, the TRPS data cannot be used in isolation to confirm all detected particles were conclusively EVs, as it is possible the qNano instrument could also have been sensing protein aggregates or non-membranous particles alongside vesicles (Akers et al., 2016). Consequently, TRPS data should be strengthened with alternative techniques to verify EVs in the secretome. TSG101 expression was assessed via Western blot and this in conjunction with the identification of other EV markers including Alix, CD81, CD82 and low levels of calnexin in the MS proteomic data of all measured days would suggest isolated particles are indeed EVs (Théry et al., 2018). However, it would be beneficial to support all presented data with visual confirmation via cryo-EM images.

3.3.1.4 Choosing an optimal skeletal muscle model

This chapter has presented data which was used to choose an optimal skeletal muscle model for the development of pathological muscle states for later use in functional studies. The ITS method of differentiation was selected due to its lack of serum, which would make the study of muscle derived EVs easier and for its ability to induce myotube formation and vesicle production. Overall, these selection criteria were minimally assessed and on reflection additional measures (discussed in the future work section) should have been assessed, which may have ultimately suggested an alternative model to ITS. Consequently, it is evident that the data used to select a model of skeletal muscle were insufficient and further work was

required to validate the chose differentiation system and aid in making an informed decision. Preferably, the additional experiments would have been completed to support the existing analyses, however this was not achieved due to time constraints placed on this project due to both prior teaching responsibilities and the Covid-19 pandemic.

3.3.2 Skeletal muscle markers of differentiating skeletal muscle

Identifying the protein profile of C2C12 cells induced to differentiate using ITS demonstrated whether myogenesis successfully occurred in SF conditions. Markers of skeletal muscle differentiation expressed by C2C12 cells undergoing myogenesis were compared on days 0, 1, 3 and 5 post ITS treatment. 5 upregulated proteins were presented in this section and were chosen based on their previous identification in skeletal muscle, as well as their role in important tissue functions, i.e. contraction. All 5 proteins assessed were shown to be upregulated in cells during the 6 days of differentiation, suggesting their changes in expression were linked to the progression of myogenesis. This is supported by temporal proteomic profiling of myoblasts during differentiation, which revealed 4 major protein clusters with changing expression (Goswami et al., 2021). Cluster 3 proteins associated with muscle contraction exhibited low expression in myoblasts but were upregulated with the development of myotubes. Cluster 4 proteins were mapped to ECM remodelling and gluconeogenesis, which like cluster 3 were initially downregulated during the early stages of myogenesis, after which expression levels rose towards the final stages of differentiation (Goswami et al., 2021). Similar proteomic profiling of human myoblasts was also shown by Le Bihan *et al.* who reported increased expression of ECM components and muscle specific proteins, such as those associated with contraction, whilst cell cycle progression proteins were downregulated during myogenesis (Le Bihan et al., 2015). The latter study also induced differentiation using SF conditions, which in conjunction with the present investigation demonstrate myogenesis can successfully occur in the absence of serum.

Expression of these skeletal muscle associated proteins was mostly similar between differentiating myotubes and their derived EVs across days 1, 3 and 5. There were some day specific exceptions, such as α-actin which was more abundant in day 5 EVs than the cell equivalent. This protein is a member of the actin superfamily and is involved in facilitating the contractile function of skeletal muscle. In adult skeletal muscle, actin filaments interact with myosin filaments to generate movement. It is possible α-actin was intentionally released via EVs, as it has been shown to induce the expression of other myogenic proteins, such as MyoD and contractile related proteins, such as tropomyosin (Gunning et al., 2001). Thus, the active incorporation of α-actin into EVs could serve to maintain myogenesis for the formation of new skeletal muscle and to ensure proteins essential for muscle function are produced. In

comparison, ENO-β was more abundant in EVs at the beginning of differentiation. ENO-β is primarily expressed in skeletal muscle and so would be expected to be found in EVs release by cells of this tissue. This enzyme is involved in muscle differentiation and regeneration processes, and has been found contained in C2C12 myotube-derived EVs (Watanabe et al., 2022). As expected, the contractile protein troponin C was not detected in later myogenic EVs. Despite not being found in day 5 myotube-derived EVs, troponin C has been detected in the secretome of human skeletal muscle, however it is not known whether this protein was associated with vesicles or in soluble form (Florin et al., 2020). Due to its role in muscle contraction, it is likely troponin C would not be deliberately secreted via EVs as it might not serve a purpose outside of the myotubes. Regarding myotube cells, as expected SOD1 expression increased during differentiation compared to EVs, suggesting increased packaging of this protein as vesicle cargo was not required. Whilst SOD1 has been identified in exercise induced rat skeletal muscle-derived EVs, this does not suggest it would be found in EVs during myogenesis or other resting conditions (Bertoldi et al., 2018).

Since EVs are considered to reflect the intracellular conditions of the cells from which they are derived, skeletal muscle proteins were compared between day 5 myotubes and day 5 myotube EVs. This would determine whether the abundance of these proteins in EVs mirrored protein abundance in the parent cells. It was shown that proteins associated with various skeletal muscle functions differed between day 5 C2C12-derived EVs differed to and their parent cells. It is likely that the expression levels of crucial skeletal muscle proteins, such as glycogen phosphorylase were reduced in myotube EVs compared to myotube cells, as it would not be beneficial for differentiated myotubes to expel proteins that are essential for the normal functioning of this tissue.

MYL4 was also used myogenic marker and was detected in differentiating C2C12 lysates but was absent from corresponding EVs. This protein is associated with skeletal muscle growth and was selected as a potential marker of skeletal muscle, however MYL4 is a developmental myosin expressed during embryogenesis and is mostly lost during adulthood (Schiaffino et al., 2015). Developmental myosins like MYL4 are retained into adulthood in some specialist muscles, such as intrafusal muscle and can be reactivated during regeneration (Schiaffino et al., 2015). Despite its role in skeletal muscle formation in the foetus, MYL4 has been detected in adult differentiating myoblasts. MS analysis of differentiating C2C12 cell lysate identified MYL4, and microarray data showed *Myl4* gene expression was upregulated (AlSudais and Wiper-Bergeron, 2019). Codato *et. al* also confirmed these findings and demonstrated an increase in *MYL4* gene expression during C2C12 differentiation (Codato et al., 2019). In addition to its involvement in muscle differentiation, MYL4 could also be associated with

vesicle budding and release from cells. Phosphorylation of myosin light chains at the neck of budding EVs stimulates actin cytoskeleton contraction and the excision of these particles from the membrane (Muralidharan-Chari et al., 2009). It is unknown which myosin light chain isoform is involved in this release process, making it difficult to conclude whether MYL4 would be packaged into EVs. Many of the studies correlating myogenesis with upregulated MYL4 expression have been conducted in myocytes instead of EVs, therefore it is difficult to determine whether this protein would be vesicle cargo under physiological conditions. Due to its role in muscle contraction, it is possible this marker was not secreted into EVs as it is required for normal tissue, though further research is required to confirm this theory.

Basing skeletal muscle formation on the presence of 5 proteins is not sufficiently conclusive or fully informative. Additional skeletal muscle proteins could also have been assessed, which might have been better marker protein candidates, for instance α-sarcoglycan which has previously been used to positively identify skeletal muscle-derived EVs (Guescini et al., 2015). However, the proteomic data show no sarcoglycan proteins were detected in any of the differentiating EV or cell samples, which could be interpreted as the C2C12 cells have not fully differentiated into skeletal muscle cells or are expressing other skeletal muscle markers. Differences between the two studies could have arisen from Guescini *et al.* isolating EVs from human volunteers not from a murine *in vitro* model rather than the isolation method used. Ismaeel *et. al* whilst detecting α-sarcoglycan in C2C12 myotube-derived EVs, only did so at a very low percentage, therefore it is possible that this protein was at too low a level to be detected in the present study (Ismaeel et al., 2023). In addition to α-sarcoglycan, desmin can also be used to identify muscle-derived EVs and this marker was detected in both EV samples and the cell lysates (Table 6) (Watanabe et al., 2022).

Besides these proteins, inducers of myogenesis, such as transcription myogenin and MyoD would confirm the differentiation of C2C12 cells into myotubes. Unfortunately, proteomic analysis did not detect myogenin or MyoD in any of the cell lysate or EV or samples. Despite this finding, Baci *et.al* detected MyoD in the EVs of C2C12 myotubes via Western blot, however expression appeared to be much lower compared to cell lysates (Baci et al., 2020). Whilst EV isolation methods were the same, Baci *et.al* used HS differentiation whilst the present study employed ITS and this could account for differences in MyoD expression.

Furthermore, growth factor levels also change during the myogenic process and the expression of these proteins could be indicators of the stage of muscle development. HGF, IGFs, FGF and PDGF are all involved in myogenesis, however only PDGF was found to be expressed in EVs secreted by days 1, 3 and 5 cells, whilst no growth factors were detected in the corresponding cell lysates (see Appendix, Table 6). This is an unexpected finding as it is

assumed that a protein identified in the EV proteome would also be present in the cells. In comparison, EVs produced by differentiating human skeletal muscle have been reported to contain numerous growth factors, including HGF, FGF, PDGF, VEGF and IGF binding proteins, despite also using ultracentrifugation to isolate vesicles for MS (Choi et al., 2016).

Many of the proteins discussed above were not identified by proteomic analysis, which suggests there are limitation associated with this method. Consequently, alternative methods should also be employed to detect proteins missed by MS, by Western blot or immunohistochemistry, however the latter would be ideal for cell samples rather than EVs. For proteins identified by MS, it would be beneficial to validate the proteomic data by conducting Western blot analysis.

Aside from protein markers, miRNAs such can be used to distinguish EVs of skeletal muscle origin. The myomiRs miR-206, miR-133a and miR-133b are highly expressed in skeletal muscle and are found within skeletal muscle-derived EVs (Mytidou et al., 2021). This study did not investigate miRNAs, however these myomiRs could be used in future to confirm skeletal muscle formation in conjunction with protein markers to improve the rigorousness of the data presented.

Proteomic analysis has previously shown that myotube-derived EVs can be taken up by myoblasts and their internalisation can regulate myoblast differentiation. Myotube EV cargo prevented myoblast proliferation and stimulated differentiation by stimulating withdrawal from the cell cycle and increasing expression of myogenin (Forterre et al., 2014a). Unfortunately, in the present study, regulators of myogenesis, such as myogenin and MyoD were not detected in day 5 myotubes EVs. Therefore, it is difficult to determine whether EVs from a SF skeletal muscle model were aiding the differentiation process. It is possible that EVs mediated differentiation, but via the secretion of lesser-known proteins which were not detected by MS, however it is difficult to confirm this based on these data. To fully investigate the role of EV in myogenesis differentiating C2C12 cells should be exposed to isolated EVs alone. EV associated proteins could also be responsible for the progression of differentiation, for instance those comprising the EV protein corona. The EV protein corona could be present in the secretome but is removed during processing of the secretome for EV isolation, for example via ultracentrifugation or SEC (Wolf et al., 2022a). It would require methods that ensure EVs are isolated with the protein corona intact. There is also the possibility that the differentiation promoting proteins were also present in the soluble factor component of the secretome, which requires further investigation. To understand the role of the soluble factors on myogenesis, C2C12 myoblasts should also be incubated with this fraction in isolation. Western blot analysis

should be conducted on all components of the secretome, both EVs and soluble proteins to identify proteins that were not detected by MS.

Furthermore, other non-vesicle associated components were released in the secretome of differentiating C2C12 cells in addition to EVs, which may have also contributed to the progression of myoblast to myotube differentiation. Ideally, EVs isolated from differentiating myotubes at each measured time point should be incubated with C2C12 cells to investigate the role of EVs during myogenesis in isolation from the remainder of the secretome components.

Proteins are not the only molecules to have different expression levels in EVs derived from myotubes and myoblasts. Forterre *et al.* have shown the miRNA repertoires of myoblast EVs differed to those of myotube EVs (Forterre et al., 2014b). Furthermore, myotube EV miRNAs induced the downregulation of sirtuin-1 in myoblasts to stimulate their differentiation, highlighting the importance of the varied EV cargo in the regulation of skeletal muscle myogenesis (Forterre et al., 2014b).

3.3.3 Biological processes associated with myotubes and their derived EVs

Differentially expressed proteins between day 5 myotubes and day 5 EVs were used to identify gene ontology (GO) based biological processes to determine whether these functions varied between parent cell and their derived vesicles. The findings of Deshmukh *et al.* support the functional enrichment data presented for day 5 myotubes. Their data indicate functions such as “translation” and “RNA splicing” were significantly enriched in C2C12 myotubes (Deshmukh et al., 2015). The upregulation of RNA processing and translation functions would be expected due to increased skeletal muscle mass being regulated by protein synthesis during myotube formation (Goodman, 2019). Furthermore, human skeletal muscle cell proteomics assessed during myotube formation show upregulation of proteins involved in “mRNA splicing” and “control of translation”, which aligns with the proteomic data presented in this chapter (Le Bihan et al., 2015). This group also identified “proteolysis” and “muscle organ and sarcomere development” as enriched functional GO annotations in these cells, however these terms were not included in the top 10 biological processes for day 5 myotubes. It is possible that muscle contraction related functions were not identified as the Le Bihan study used primary muscle cells culture, whilst the present investigation used a murine cell line which required further maturing of cells. Another study assessing the proteome dynamics of differentiating C2C12 cells identified the up- and down-regulation of various protein clusters. Proteins associated with “transcription regulation”; mRNA processing and “cytoskeletal organisation” were enriched in differentiated myotubes, which supports the day 5 myotube biological processes

(Kislinger et al., 2005). In addition to the aforementioned functions, myotubes were also upregulated in “fatty acid oxidation” and “muscle contraction”, however this was primarily in day 10 myotubes. Myotubes of all ages were also accompanied by downregulation of “DNA replication” and “cell cycle” proteins which are concomitant with cell cycle withdrawal and termination of proliferation (Kislinger et al., 2005).

With regards to day 5 myotube-derived EVs, these particles exhibited many of the biological processes identified in day 5 myotubes. Pathway analysis of human skeletal muscle-derived EVs isolated by ultracentrifugation has shown these particles to be enriched in proteins related to “protein synthesis”; “cellular assembly/organisation”; “protein degradation” and “RNA trafficking”, which were similar to the processes presented for day 5 EVs (Le Bihan et al., 2012). Like the day 5 EV functions presented in this chapter, Forterre *et al.* also found C2C12 myotube-derived vesicles also isolated by differential ultracentrifugation were highly upregulated in proteins associated with “intracellular protein transport”, “actin filament based process” and “protein localisation” (Forterre et al., 2014). This group also showed “vesicle-mediated transport” was significantly enriched: which was also identified in day 5 EVs though this was not a significant result (Forterre et al., 2014). Another study conducting GO analysis of C2C12 myotube-derived EV associated proteins, like the day 5 myotube-derived EV proteomics found these particles to be similarly enriched in the following biological processes: “translation”; “intracellular protein transport”; “protein folding” (Watanabe et al., 2022). However, unlike the data presented in this chapter, the Watanabe *et al.* study identified upregulation of “muscle contraction” and “vesicle-mediated transport”.

Taken together, these data suggest an overlap in proteins expressed by both myotubes and their derived EVs, such as those involved in organisation of the cytoskeleton, translation and protein folding. These proteins were enriched in day 5 myotubes and were consequently packaged into vesicles for subsequent release, which is expected as EVs are a reflection of their parent cells to an extent (Chen and Yu, 2022). Certain biological processes identified in other studies were missing from the functional enrichment data presented for day 5 myotubes and EVs, which can be attributed to solely showing the top 10 most significantly overrepresented biological processes for these samples. Many other proteins involved in different biological functions were also expressed which were not included here and this would explain why some GO annotations were observed in other studies but not in the current study. Moreover, certain biological processes whilst identified in the analysis, were not significantly upregulated ($P>0.05$).

3.3.4 Proteomics approach

The approach used to identify the proteome of particles produced by differentiating myoblasts was MS, which has certain limitations when used in isolation. This process is reliant on trypsin digestion of peptides, which has cleavage sites at lysine and arginine residues (Manea et al., 2007). If a protein does not have a high distribution of these residues, the cleavage of this protein can produce peptides that are too large to be analysed and can prevent identification. There is also the possibility that proteins of low abundance may be masked by those of a greater abundance (Steinsträßer et al., 2010). This limitation can be resolved by using modern analysers with a greater dynamic range, such as the Orbitrap, which can increase protein identification 5 – 10-fold, however access to such an instrument was not possible during this project (Zubarev and Makarov, 2013).

Despite these pitfalls, MS is a high throughput analysis technique and the untargeted proteomic approach used in this study generated many hits and identified thousands of proteins, unlike the targeted approach used by Western blot, ELISA or other antibody-based detection methods. These antibody-based techniques are dependent on the presence of the correct epitope being accessible to the primary antibody. Post-translational modifications to the protein of interest can mask epitopes from the antibody and prevent detection, which is not a limitation associated with MS (Dunphy et al., 2021).

RNA detection is another approach that could have been used to characterise particles produced by differentiating cells, which are known to EV cargo (O'Brien et al., 2020). However, the presence of vesicle associated RNAs is not a definitive indicator that the proteins encoded by this genetic material will be expressed and post genomic analysis is required to confirm this. Ultimately, a multi-omics approach should be employed, consisting of both genomic and proteomic analyses.

3.3.5 Future work

The present investigation was initially focused on identifying an appropriate SF skeletal muscle model, with ITS being the chosen method of differentiation. However, existing optimisation methods should have been supported with additional confirmation experiments to help determine the optimal method of inducing myogenesis, as the SF ITS method might not have been the most appropriate system in this study. Rigorous testing of the various differentiation media should have been conducted to supplement existing analyses. These include fusion index measurements, the expression of skeletal muscle markers, in addition to

those identified by proteomic analyses, such as myosin heavy chain and myosin by immunohistochemistry.

The use of HS was rejected as a potential differentiator due to the presence of exogenous EVs, however in future this should be verified by quantitively assessing vesicle associated protein markers using MS analysis or Western blot to determine the amount of EVs contained within the 2% HS medium, as this method was also capable of inducing myotube formation. Furthermore, additional serum controls should be tested for comparison, including EV depleted serum. The depletion of HS derived EVs should be completed using ultracentrifugation or ultrafiltration protocols and the resultant supernatant also analysed for EVs, as this could present a feasible differentiation option as a better alternative to ITS.

Further validation of the differentiation media should be performed with regards to their ability to produce EVs and their specific characterisation. Vesicle characterisation studies, i.e., the expression of TSG101 and other markers, should have been conducted on all differentiation media instead of solely on ITS. To supplement this, negative markers (calnexin and cytochrome C) should also be identified to confirm the exosomal component of the secretome. The levels of these non-exosomal markers will determine the amount of non exosomal based material that are being co-isolated with EVs, therefore indicating the purity of the EV preparations, since cytoplasmic or components of cell compartments are more likely to be spontaneously incorporated into larger vesicles (Théry et al., 2018). In addition to negative exosome markers, the absence or presence of other vesicle types, including microparticles and apoptotic derived EVs should also be analysed to provide further information concerning the different vesicle populations. Visual confirmation of EVs should also be conducted to support the analyses mentioned above, specifically the use of cryogenic electron microscopy to discern the lipid bilayer for the confirmation of vesicles, but also to give insight into the morphology and structure of these particles.

Furthermore, this chapter also attempted to assess the efficacy of the chosen ITS method by analysing myotube cell and EV proteins during the differentiation process. However, the myogenic secretome is comprised of other components including non-EV associated soluble proteins and other mediators, including lipid mediators. It would be advantageous to characterise the other secretome components using MS analyses and determine their role in differentiation. In relation to this, treatment of C2C12 myoblasts with isolated myotube secretome components will confirm which molecules are mediators of myogenesis.

4. Results Chapter 2 – The effect of sarcopenic skeletal muscle on macrophage function

4.1 Introduction

Due to its involvement in numerous processes, skeletal muscle undertakes regular communication with other tissues of the body, including the immune system. Specifically, its contractile ability can often result in tissue damage which requires assistance from both innate and adaptive immune cells to repair and regenerate the muscle to maintain functionality. For efficient and correct repair, interaction between the two systems is bidirectional such that each tissue can influence the behaviour of the other.

Under physiological conditions a small population of immune cells reside within skeletal muscle, yet the overall presence of immune cells is minimal (Pillon et al., 2013). Conversely, pathophysiological conditions, such as muscle damage, result in the infiltration of immune cells from the peripheral circulation and for this to be initiated, injured myocytes must release chemoattractants and polarising factors as components of their secretome (Chazaud et al., 2003, Brunelli and Rovere-Querini, 2008). Immune cells can modify their behaviour and function depending on the environment to which they have been recruited, firstly to perpetuate an inflammatory response and subsequently to facilitate repair. This highlights the importance of crosstalk between the immune system and skeletal muscle to ensure good muscle function in young and healthy individuals, however this communication can be altered during the ageing process, for instance in sarcopenia, and induce detrimental effects in skeletal muscle tissue.

Sarcopenia is an age-related skeletal muscle wasting disorder and is a prime example of a breakdown in communication between muscle cells and cells of the immune system, specifically macrophages (Zhang et al., 2022). Macrophages play a crucial role in the maintenance of skeletal muscle homeostasis, but they are also considered to be drivers of muscle atrophy in sarcopenia (Reidy et al., 2019). There is conflicting evidence regarding the number of macrophages in sarcopenic muscle, with some studies suggesting an increase in the macrophage population with age, whilst others propose no changes in number but rather a switch in macrophage phenotype, altering subpopulation ratios (Reidy et al., 2019, Cui et al., 2019, Wang et al., 2015). The increase in recruited macrophages is most likely associated with the infiltration of sarcopenic muscle with adipose tissue (Neels and Olefsky, 2006). Consequently, the current body of work intends to contribute to existing findings by elucidating the migratory and inflammatory properties of the sarcopenic muscle secretome and its ability to polarise macrophages, which to date have not been fully investigated.

Sarcopenia is multifaceted in its onset, with many factors being interlinked and the development of one causative agent often gives rise to others. One such contributing cause is persistent inflammation, however the role of chronic inflammation in rendering healthy muscle susceptible to atrophy can itself be further subdivided into different factors. For instance, a prolonged inflammatory environment, as seen in sarcopenic muscle, can surface from increases in oxidative stress (Damiano et al., 2019). This is a consequence of ROS accumulation over time and excessive ROS release by muscle cells, but there is a possibility that resident or infiltrating immune cells, such as macrophages may also be a source of ROS that maintain muscle damage.

Furthermore, the inflammatory nature of sarcopenia may be partially dependent on factors released by the macrophages themselves. Polarisation of macrophages towards either proinflammatory M1 or pro-resolving M2 subtypes will result in the production of either inflammatory or inflammation dampening and reparative cytokines, which influence the outcome of damaged ageing muscle.

This chapter details the use of the SF murine skeletal muscle model described in Chapter 3, to develop a SF murine model of sarcopenia, to enable the study of EVs as a component of the sarcopenic muscle secretome. The muscle wasting model was subsequently used firstly to elucidate the paracrine effects of sarcopenic muscle on surrounding healthy muscle and secondly to better understand the feedback mechanism between sarcopenic muscle and innate immune macrophages. Specifically, to investigate the hypothesis that sarcopenic muscle detrimentally influences macrophage behaviour to the extent that macrophages facilitate healthy muscle atrophy.

4.2. Results

4.2.1 Developing a murine skeletal muscle model of sarcopenia

The establishment of an optimal SF model of skeletal muscle, detailed in Chapter 3, provided a foundation for the development of a muscle model of sarcopenia. Numerous reagents can be applied to both myoblasts and myotubes to produce sarcopenic cells *in vitro*, including hydrogen peroxide, inflammatory cytokines such as TNF-α, sphingolipids such as ceramide and palmitate, as well as glucocorticoids (Mankhong et al., 2020). This study employed the glucocorticoid dexamethasone (DEX) to mimic the pathophysiological conditions of sarcopenia, however prior to collecting sarcopenic muscle secretomes for use in functional experiments it was necessary to determine the optimal DEX concentration to induce sarcopenia.

A drug titration was performed on 5 day ITS differentiated myotubes, which were treated with either 0, 1, 10 or 100 μM DEX for 24 hours. Following treatment, muscle wasting, and the extent of sarcopenia development was quantified through the measurement of myotube diameter. The myotube diameter for each DEX concentration after 24 hours was compared to the diameter on the day treatment was initially added, designated day 0 (figure 14).

Figure 14 visually demonstrates the extent of myotube thinning with increasing concentrations of DEX. Myotube diameter was maintained in the presence of 1 μM DEX after 24 hours with limited cell loss. The addition of 10 μM DEX promoted the sectional thinning of the myotubes (white arrows), whilst 100 μM DEX resulted in substantial thinning and cell death (black arrows).

As expected, in the absence of DEX, myotube diameter did not change 24 hours following the addition of treatment. A similar result was also found with the use of 1 μM DEX, which showed an insignificant reduction in myotube diameter. However, once the concentration of DEX increased differences in myotube diameter were observed. Exposing myotubes to 10 μM DEX caused a significant reduction in diameter 24 hours post treatment. This reduction in myotube diameter was also observed in the highest DEX concentration of 100 μM, suggesting the higher glucocorticoid concentrations were the most proficient at inducing skeletal muscle atrophy.

The visual observations made using the phase contrast images were confirmed by undertaking quantitative analysis of the DEX treated myotubes. The images were used to measure the myotube diameter for each concentration of DEX (figure 15). As expected, the

diameter of untreated myotubes and those exposed to 1 μM DEX remained unchanged after 24 hours. However, increasing the DEX concentration to 10 μM exhibited a decrease in myotube diameter, which was further reduced by treatment with the highest DEX concentration of 100 μM.

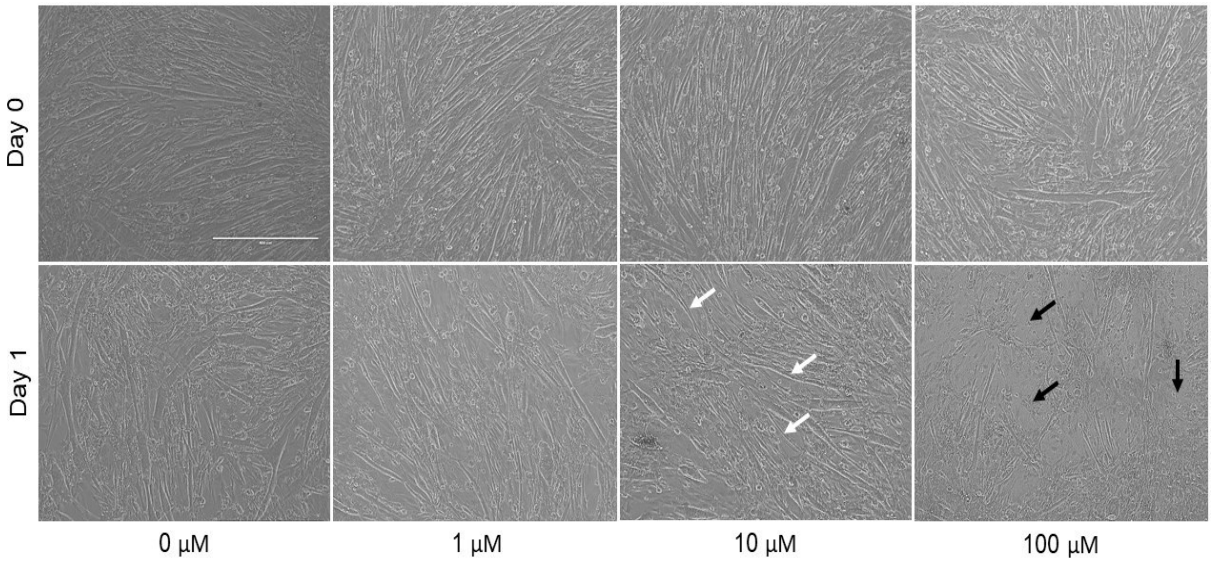

Figure 14. Identification of the optimal DEX concentration to induce muscle wasting in myotube cells. Myotubes were exposed to increasing concentrations of DEX for 24 hours, after which treated cells were imaged at 10x magnification (scale bar = 400 μm). White arrows indicate myotube thinning and black arrows show areas of cell death. Images are representative of the DEX concentrations used to treat cells.

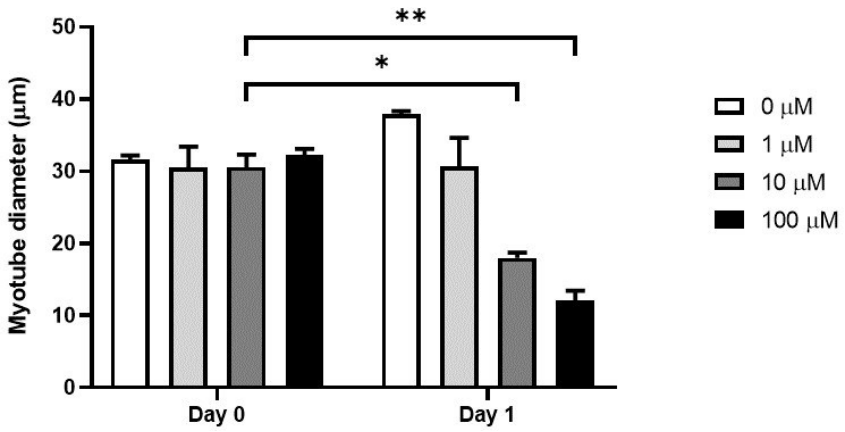

Figure 15. Myotube diameter of DEX treated myotubes. The diameters of myotubes treated with increasing concentrations of DEX were measured using Image J analysis software, both at the time of treatment and 24 hours post treatment. Data shown are mean ± SEM of 3 independent experiments, two-way ANOVA with Sidak's *post hoc* test, ***P<0.005 and *P<0.05.* Day 0 to Day 1 comparisons of 0 μM and 1 μM were found to be *ns*.

Having determined the effect of different DEX concentrations on myotube diameter, it was also necessary to investigate the cytotoxicity of this drug prior to an optimum concentration being decided upon. An MTT assay was employed to measure cell metabolic activity as an indicator of cell viability (figure 16). Figure 16 shows myotube cell viability expressed as a percentage of 0 μM DEX, with all concentrations compared to this condition. Treatment of myotubes with either 1 or 10 μM DEX maintained cell viability compared to the 0 μM DEX control, consequently these concentrations were not toxic to the myotubes. Conversely, the highest DEX concentration of 100 μM exhibited a significant reduction in cell viability 24 hours post treatment. The myotube diameter measurements and the cell viability assay indicated the optimum DEX concentration to induce a sarcopenic phenotype in myotubes was 10 μM. This concentration was taken forward and used to produce sarcopenic myotubes for use in functional experiments discussed in subsequent sections of this chapter.

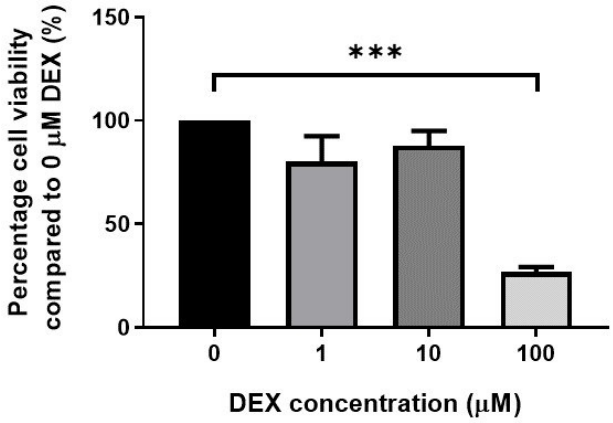

Figure 16. The toxicity of increasing DEX concentration on myotube cells. The viability of myotube cells treated with increasing concentrations of DEX was assessed 24 hours following treatment by MTT assay. Data shown are mean ± SEM of 3 independent experiments, one-way ANOVA with Dunnett's *post hoc* test, ****P<0.0005.*

4.2.1.1 Characterising the vesicle population of the sarcopenic muscle model

Having developed an appropriate *in vitro* model of sarcopenia, it was necessary to characterise the vesicle component of the sarcopenic myotube secretome. Once again, this entailed the measurement of both EV size and concentration using TRPS analysis.

The whole 2000*xg* myotube secretomes were the first to be tested in the functional assays and were consequently the first to have their EVs characterised. The vesicles contained within the whole 2000*xg* secretomes of both normal and sarcopenic myotubes displayed similar features (figure 17). The particle concentrations of the two did not differ, which could be attributed to the high degree of error between repeat measurements for each condition (figure 17a). Instead, it was hypothesised that the normal 2000*xg* secretome would have more EVs

than its sarcopenic counterpart. Like the EV concentration, the size of the vesicles for both types of secretome was also similar. EV diameters for normal and sarcopenic secretomes were less than 200 nm and therefore corresponded to the small EV class, which was expected (figure 17b).

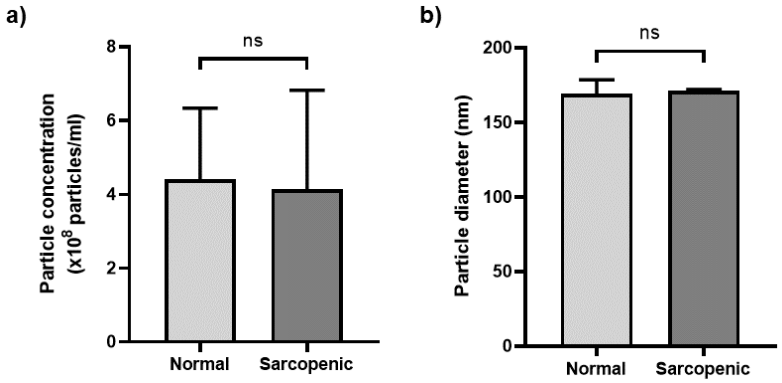

Figure 17. Characterisation of EVs contained within whole sarcopenic myotube secretome. Normal and sarcopenic myotube derived 2000*xg* secretomes were measured using TRPS analysis to determine EV concentration (a) and size (b). Data shown are mean ± SEM of 3 independent experiments with Welch's t-test.

As will be discussed in later sections, the 2000*xg* myotube secretomes were concentrated using 30 kDa spin filters for use in subsequent functional studies. Secretome concentration generated two components: a retentate and a filtrate. The retentate component of the concentrated secretome is the EV-containing fraction and was measured to determine particle concentration and diameter. Measurement of EV concentration indicates that the concentrated normal myotube secretome contained more EVs than its sarcopenic counterpart (figure 18a). Despite the difference in EV concentration between the two myotube samples, EV diameter was unchanged (figure 18b), with both sets of particles corresponding to the small EV class (diameter <200 nm).

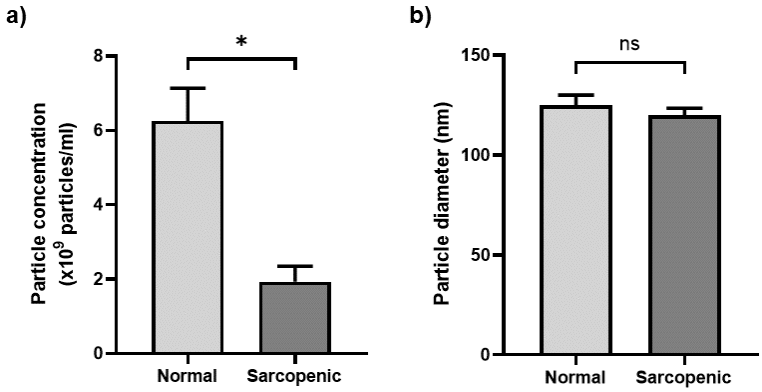

Figure 18. Characterisation of EVs contained within concentrated whole sarcopenic myotube secretome. 2000*xg* secretomes from normal and sarcopenic myotubes were concentrated using 30 kDa spin filters and the particle concentration (a) and size (b) of the EV containing retentate was measured using TRPS analysis. Data shown are mean ± SEM of 3 independent experiments with Welch's t-test, **P<0.05*.

The 2000*xg* normal and sarcopenic secretomes were used in functional assays to determine the impact of the whole secretomes on macrophage function and phenotype. However, subsequent work aimed to identify the specific components contained within the secretomes that caused any later described effects. To do this, 2000*xg* secretomes were concentrated using the 30 kDa spin filters and EVs and <30 kDa soluble proteins were separated using size exclusion chromatography (SEC). The SEC isolated EVs were also characterised using TRPS analysis to ascertain particle concentration and size (figure 19). TRPS analysis was performed on the Izon qNano machine, which experienced difficulties in maintaining a stable current for the measurement of samples during the last period of this study. Due to this setback and the limited time available to source alternative equipment, only a single repeat of the SEC isolated EV samples was conducted.

Taking the data at face value indicates that normal myotubes might produce fewer EVs than sarcopenic myotubes (figure 19a), whilst both types of muscle are likely to generate particles of a similar size (figure 19b). This contradicts the data displayed in figure 18, which shows higher EV concentrations in 30 kDa concentrated secretomes of both normal and sarcopenic myotubes. It is possible that loss of particles during the SEC process might account for this disparity in number. It is likely that there is no difference in particle number following SEC isolation and further replicates are required to confirm this.

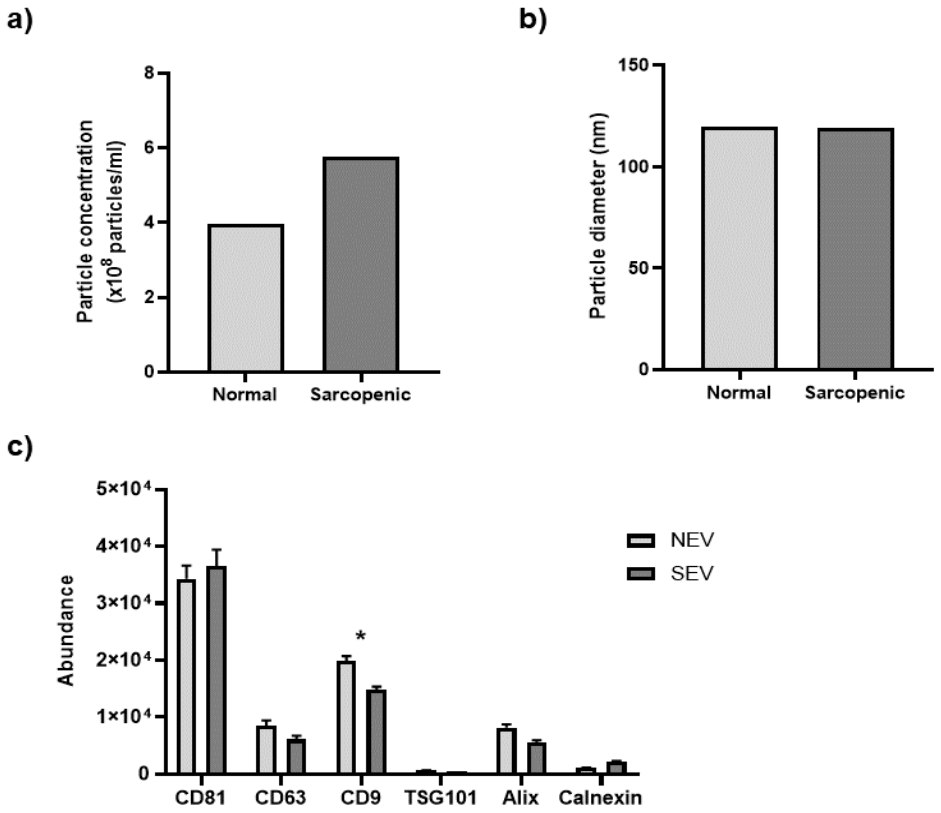

Figure 19. Characterisation of EVs isolated from sarcopenic myotubes. Normal and sarcopenic myotube derived 2000*xg* secretomes were concentrated and EVs were separated using SEC. The EV fraction was measured using TRPS analysis to determine particle concentration (a) and size (b). Data shown are of 1 independent experiment. For MS based proteomic analysis of EV associated proteins, vesicles were isolated via ultracentrifugation (c), data shown are mean ± SEM of 3 independent experiments, two-way ANOVA with Sidak's *post hoc* test, **P<0.05*.

To support the TRPS data, proteomic analysis was conducted on NEV and SEV to identify EV markers for size characterisation (figure 19c). Both EV populations expressed the tetraspanins CD81, CD63 and CD9, with NEV have greater abundance of CD9. The marker Alix was also expressed, whilst TSG101 abundance was low. Calnexin was also measured to determine purity of the EV preps, which was found to be minimally expressed.

In addition to characterising EV concentration and size, it was also imperative to determine the ability of macrophages as recipient cells to incorporate sarcopenic myotube-derived EVs. Putative effects on macrophage function induced by either normal and sarcopenic EVs could be attributed to positive or negative vesicle uptake, therefore it was necessary to confirm whether these phagocytic cells were binding and internalising EVs. To assess EV uptake, both sets of EVs were labelled with the fluorescent dye BODIPY and subsequently incubated with J774 macrophages. At various time points, extracellular BODIPY fluorescence from

noninternalised EVs was quenched to ensure only vesicles incorporated into macrophages were measured by flow cytometry (figure 20).

Median fluorescence intensity (MFI) data show both normal and sarcopenic EVs were internalised by macrophages at each time point. Uptake of normal EVs steadily increased between 0 to 40 minutes, after which the rate of vesicle incorporation plateaued and remained steady up to 240 minutes. Following an incubation period of 24 hours, normal EV internalisation by macrophages was at its highest. In contrast, the rate of sarcopenic EV incorporation appeared to be slower, with a marked increase in particle internalisation occurring after 24 hours. Figure 20 shows macrophages internalised more normal myotube-derived EVs than sarcopenic EVs and this was the case for every time point. Unfortunately, due to difficulties with the qNano, EV concentrations were not measured for either sample. Therefore, it is difficult to comment on the number of EVs the macrophages were exposed to from each sample.

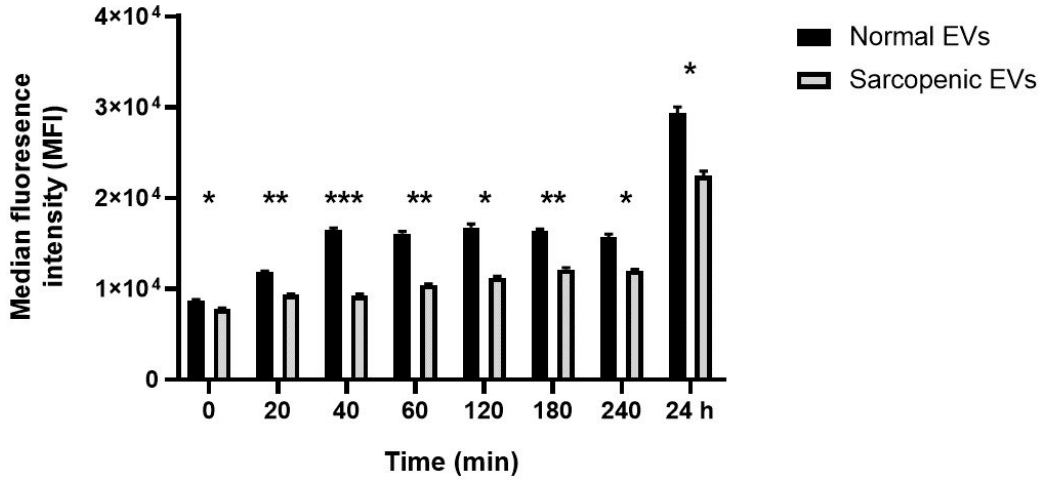

Figure 20. Macrophage uptake of sarcopenic EVs. BODIPY stained EVs derived from normal and sarcopenic myotubes were incubated with J774 macrophages for 0, 20, 40, 60, 120, 180, 240 minutes and 24 hours. At each time point, internal cell fluorescence was measured via flow cytometry following external fluorescence quenching using trypan blue and reported as median fluorescence intensity (MFI). Data shown are mean ± SEM of 3 independent experiments, two-way ANOVA with Sidak's *post hoc* test, **P<0.05, **P<0.01, ***P<0.0005.*

.

4.2.2 The ability of sarcopenic skeletal muscle to induce sarcopenia in healthy skeletal muscle

Sarcopenia is often described as a progressive skeletal muscle disorder and in the absence of medical intervention is thought to worsen with time. The presence of sarcopenic muscle cells within skeletal muscle tissue may contribute to the progressive nature of this condition by transferring the existing sarcopenic phenotype to surrounding healthy cells. The

disseminating ability of sarcopenic myotubes was determined through the treatment of normal myotubes with sarcopenic muscle-derived secretome. The collected sarcopenic myotube secretome was subjected to a 2000*xg* centrifugation to obtain a secretome comprised of EVs and soluble factors but devoid of all cellular debris and apoptotic bodies. Following treatment with the 2000*xg* secretomes, myotube diameter was measured to assess the degree of muscle atrophy, a characteristic of the sarcopenic condition.

Visual observation showed long and thick myotubes on the day of treatment, designated day 0 for all three conditions (figure 21). 24 hours following treatment with SF medium alone exhibited a small degree of myotube thinning and some evidence of apoptotic cells in culture. The addition of the 2000*xg* sarcopenic secretome to healthy myotubes appeared to induce shrinkage and thinning of the myotubes, with the culture demonstrating extensive muscle atrophy due to a reduction in cells.

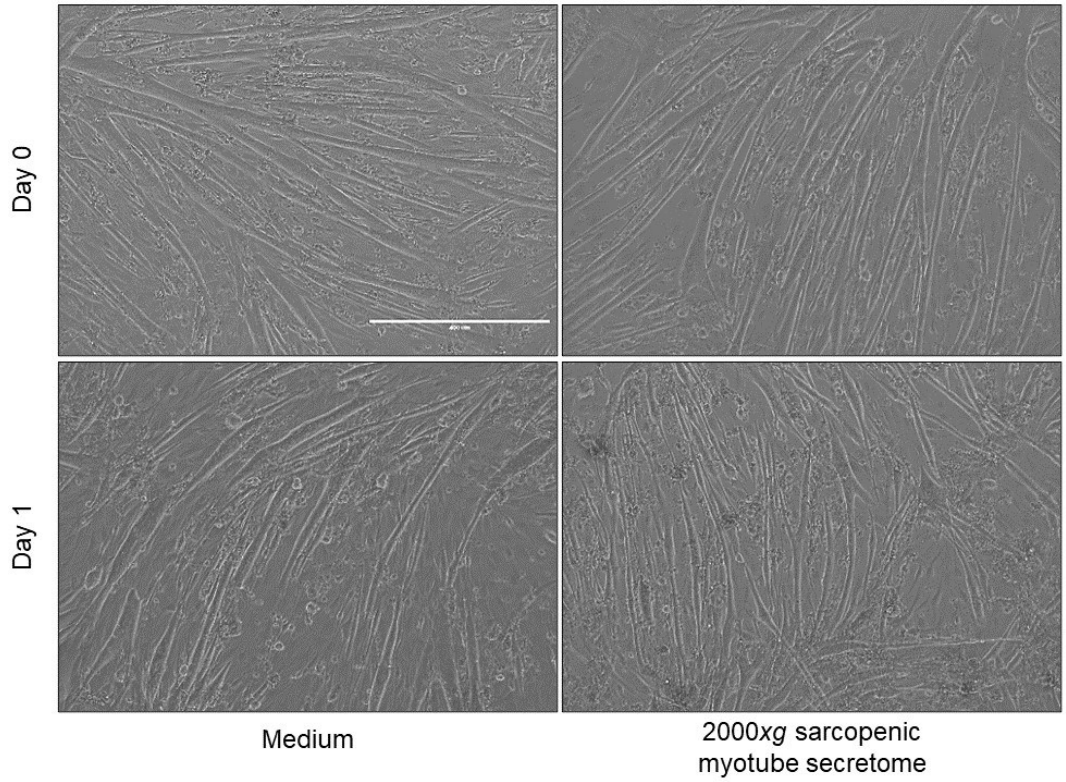

Figure 21. The paracrine effects of sarcopenic muscle derived secretomes. Representative phase contrast microscopy images (10x magnification, scale bar = 400 µm) of healthy myotubes treated with 2000*xg* sarcopenic myotube derived secretome for 24 hours. Treated myotubes were imaged on the day of treatment (Day 0) and 24 hours (Day 1) post treatment.

The observation that the 2000*xg* sarcopenic secretome induced thinning of healthy myotubes was confirmed through diameter measurements (figure 22). The control treatment of SF medium did not reduce myotube diameter 24 hours post addition, however this was not

echoed by the sarcopenic secretome treatment. As expected, there was no difference in myotube diameter between the 2 treatments on Day 0. However, Day 1 showed a significant decrease in myotube diameter (**P=0.0321*) in the presence of the sarcopenic secretome, which was not observed with the medium only control.

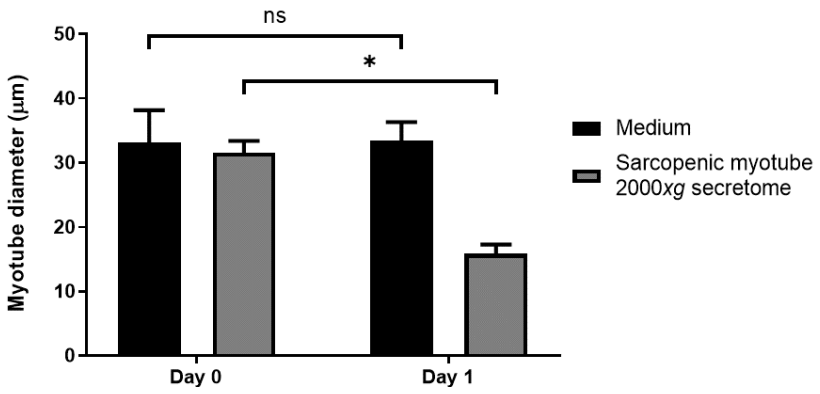

Figure 22. Quantification of bystander effect induced skeletal muscle atrophy. Normal myotubes treated with sarcopenic 2000*xg* myotube secretome were measured for their diameters on the day of treatment and 24 hours post treatment. Data shown are mean ± SEM of 3 independent experiments, two-way ANOVA with Sidak *post hoc* test, **P<0.05*.

4.2.3 The migratory potential of the sarcopenic myotube secretome

4.2.3.1 Vertical migration – transwell assay

There is conflicting evidence regarding an increased immune cell presence in sarcopenic muscle. Therefore, to determine the ability of sarcopenic muscle to recruit monocytes to damaged muscle tissue, the commonly used vertical migration system was employed. This *in vitro* system places macrophage-like cells into the upper chamber of a transwell insert and a putative chemoattractant is added to the lower chamber, which consists of a well in a transwell companion plate (figure 23a). Cell migration between the upper and lower chambers is permitted via a permeable membrane at the bottom of the transwell insert. The kinetics of cell migration can be monitored at regular intervals via time-lapse microscopy, however due to restrictions in the availability of time-lapse microscopy equipment during the current Covid-19 pandemic, an end point measurement was used in this instance.

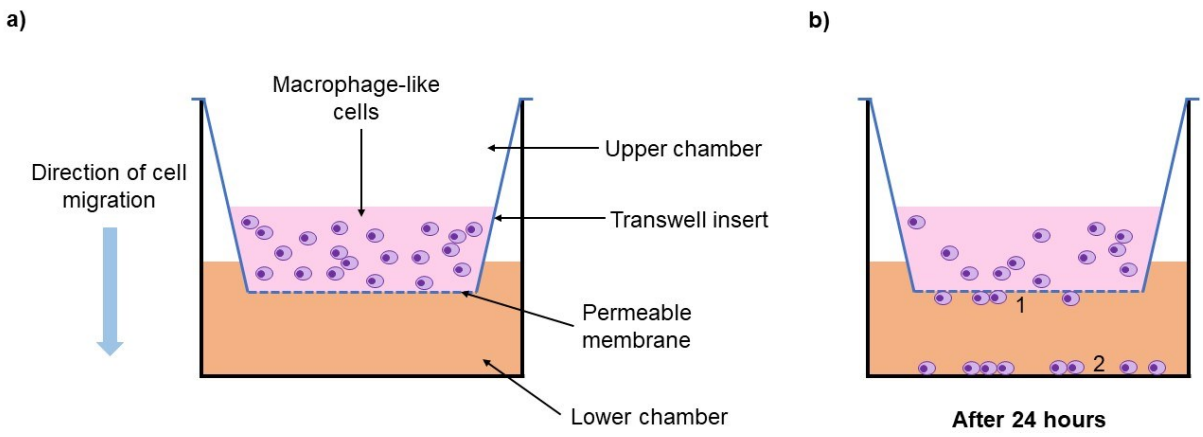

Figure 23. Schematic of cell migration using a vertical transwell migration system. Cross section of the experimental setup of the transwell migration system. This system measures vertical migration of macrophages from the upper chamber of a transwell insert through a permeable membrane and into a lower chamber containing a putative chemoattractant (a). Migrating cells will either move through the permeable membrane and remain adhered to the underside or detach and settle at the bottom of the lower chamber in the plate. Both the underside of the transwell membrane and the bottom of the well, labelled as positions 1 and 2 respectively were imaged to determine the number of migrating cells (b).

J774 macrophages were placed in the upper chamber of the transwell insert and cells were incubated with normal and sarcopenic myotube secretomes for 24 hours. Following the 24hour incubation period, cells adhered to the underside of the transwell permeable membrane were stained with Jenner-Giemsa stains and imaged, whilst phase contrast images were taken of the companion plate well or lower chamber to capture the macrophages that had detached from the underside of the permeable membrane (figure 23b).

J774 macrophages are an adherent cell line and will firmly attach to plastic surfaces. Due to this feature, it was hypothesised that migrating cells would move through the transwell pores and adhere to the underside of the permeable membrane rather than detaching to settle on the bottom of the well in the lower chamber. Consequently, the underside of the transwell membrane was chosen as an imaging position to ensure cells were captured for analysis.

Figure 24 exhibits the migration of J774 macrophages from the upper chamber of the transwell insert, through the pores to the underside of the permeable membrane. The addition of normal myotube 2000*xg* secretome to the lower chamber shows an increase in the number of cells attached to the underside of the transwell membrane (figure 24b). Exchanging the normal secretome for sarcopenic myotube 2000*xg* secretome as the attractant also induces J774 macrophages to adhere to the underside of the membrane, however visual analysis of the images indicates fewer cells were migrating towards the lower chamber (figure 24c).

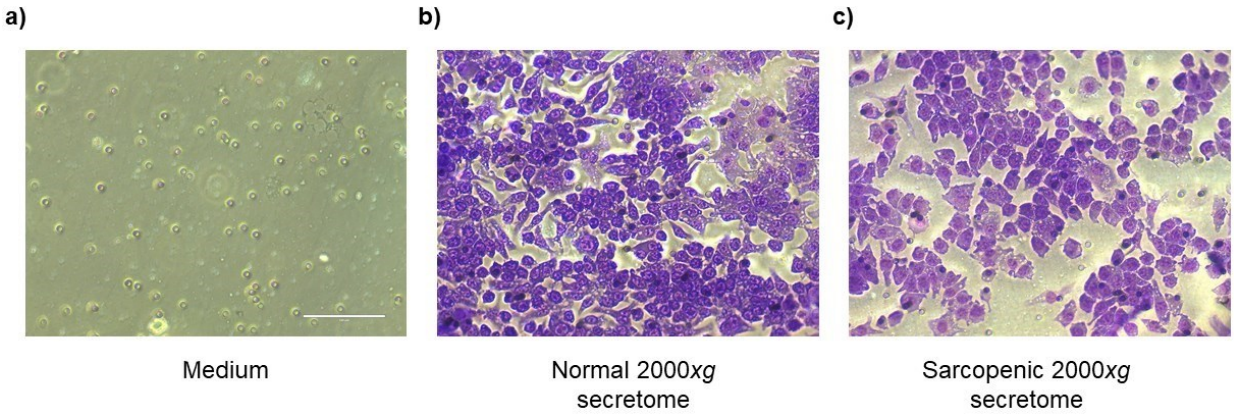

Figure 24. J774 macrophage transwell migration through a permeable membrane towards potential myotube-derived secretomes. J774 cells were placed in the upper chamber of a transwell insert and incubated with either medium (a), normal (b) or sarcopenic myotube secretomes (c) isolated from a 2000*xg* centrifugation, for 24 hours. Following incubation, the transwell inserts were stained with Jenner-Giemsa stains and end point images taken using 40x magnification (scale bar = 100 µm). All images are representative of the conditions shown.

To numerically determine the migratory potential of the normal and sarcopenic myotube secretomes, all cells adhered to the transwell membrane were manually counted for each condition (figure 25). Figure 25 is consistent with the visual observations shown in figure 24, with J774 macrophages migrating towards both the normal and sarcopenic 2000*xg* myotube-derived secretomes. There was no significant difference (*P=0.*1995) between the number of macrophages migrating to either normal or sarcopenic secretome.

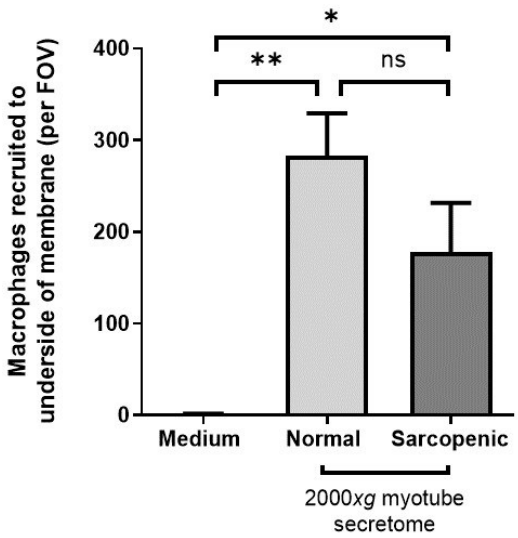

Figure 25. J774 macrophage vertical migration towards normal and sarcopenic myotube secretomes. J774 murine macrophages were exposed to either normal or sarcopenic 2000*xg* secretomes for 24 hours. Post incubation, all cells adhered to the underside of the transwell permeable membrane were manually counted. Data shown are mean ± SEM of 3 independent experiments, one-way ANOVA with Dunnett's *post-hoc* test, **P<0.05* and ***P<0.005.*

In addition to capturing cells on the underside of the transwell membrane, the bottom of the well, situated in the lower chamber was also selected as an imaging position. This allowed for the acquisition of any macrophages that had detached from the membrane and migrated through the lower chamber and reattached to the bottom of the well.

Similar to the results presented in figure 24, exposure to the 2000*xg* myotube secretomes promoted J774 macrophage migration, specifically towards the normal 2000*xg* secretome (figure 26b). Despite inducing cell migration, based on visual assessment of the images, the sarcopenic 2000*xg* secretome recruited fewer cells to the lower chamber compared to its normal counterpart (figure 26c).

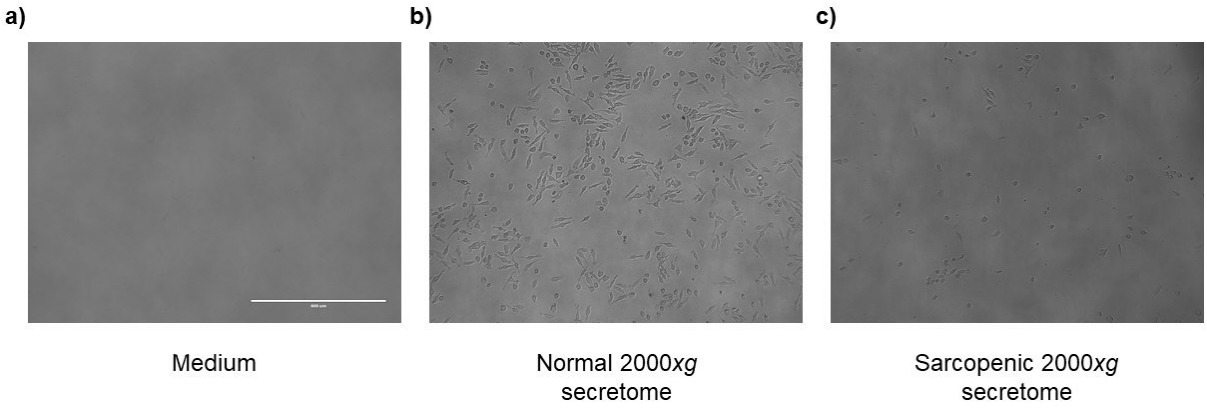

Figure 26. J774 macrophage transwell migration through a permeable membrane towards putative myotube derived secretomes. J774 macrophages 24 hours post incubation with either medium (a), normal 2000*xg* myotube secretome (b) or sarcopenic 2000*xg* myotube secretome (c) situated in the lower chamber of the transwell setup. Phase contrast images were taken of the bottom of the well at 10x magnification (scale bar = 400 µm) following the incubation period. All images are representative of the experimental conditions shown.

To fully determine the chemotactic potential of the 2000*xg* secretomes, further analyses were conducted with the number of macrophages migrating to the bottom of the well also counted. Despite initial observations of the bottom of the well images suggesting more macrophages migrated towards the normal 2000*xg* myotube secretome compared to the sarcopenic equivalent, statistical analyses show the number of macrophages recruited to all three experimental conditions did not differ, which contrasts with the results relating to the underside of the transwell membrane (figure 27).

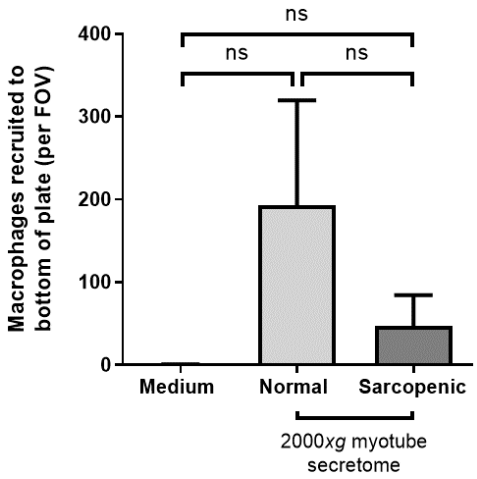

Figure 27. The number of macrophages migrating vertically towards myotube 2000*xg* secretomes. Following a 24-hour incubation with either normal or sarcopenic 2000*xg* myotube secretomes, the number of J774 macrophages at the bottom of the well in the transwell assay were manually counted. Data shown are mean ± SEM of 3 independent experiments, one-way ANOVA with Dunnett's *post-hoc* test.

Combining the macrophage counts for both the underside of the transwell membrane and the bottom of the well provided the total number of cells migrating towards the proposed chemoattractant. As expected, the total number of macrophages reflects the data shown in figures 25 and 27, in addition to the microscopy images of both positions. Figure 28 indicates that the normal myotube secretome stimulated macrophage recruitment, whilst the sarcopenic equivalent was unable to do this to the same extent. Although these data suggest the normal 2000*xg* secretome attracted approximately double the number of macrophages compared to the sarcopenic 2000*xg* secretome, comparison analyses showed no difference in the total number of macrophages recruited by either of these myotube secretomes.

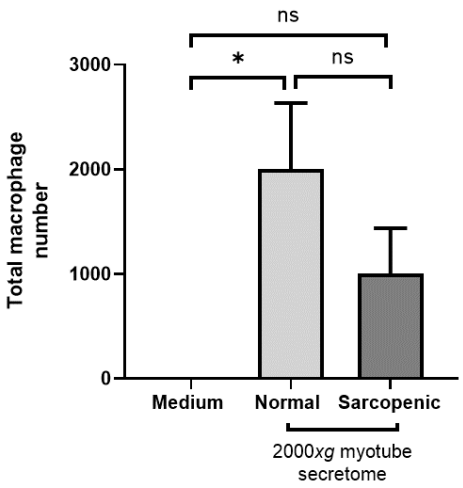

Figure 28. Total number of J774 macrophages migrating toward complete normal and sarcopenic myotube secretomes. The macrophage count for the transwell underside and bottom of the well were combined to generate the total number of macrophages migrating towards either the normal or sarcopenic 2000*xg* secretome 24 hours following exposure. Data shown are mean ± SEM of 3 independent experiments, one-way ANOVA with Dunnett's *post-hoc* test, **P<0.05* and *ns P=0.2184* (normal vs. sarcopenic).

4.2.3.1.1 Vertical migration potential of fractionated sarcopenic secretome

The above experiments exhibit the ability of complete myotube secretomes to recruit macrophages, however these data do not provide an indication as to the specific component (s) within the secretomes that may be responsible for stimulating this migratory behaviour. To further investigate this, both the normal and sarcopenic 2000*xg* myotube secretomes were fractionated using SEC to produce two separate components: the EV fraction and the soluble protein fraction. Both EV and soluble protein fractions from normal (NEV and NP) and sarcopenic myotubes (SEV and SP) were tested in the transwell assay previously described.

Figure 29 exhibits images of Jenner-Giemsa stained J774 macrophages that had migrated to the underside of the permeable membrane of the transwell insert. Visual analyses of these images indicated the EV and soluble protein components of both normal and sarcopenic myotube secretomes were able to induce macrophage migration, however the extent to which these putative chemoattractants recruited these immune cells differed between the normal and sarcopenic samples. Both NEV and NP (figure 29b and 29c) appeared to attract more macrophages to the bottom of the membrane compared to the sarcopenic fractions, which seemed to recruit fewer. Disparities between fractions isolated from the same myotube source were also observed. SEV appeared to attract fewer J774 macrophages than SP (figure 29d

and 29e). This difference was not observed when comparing EV and soluble protein components from the normal myotube secretome.

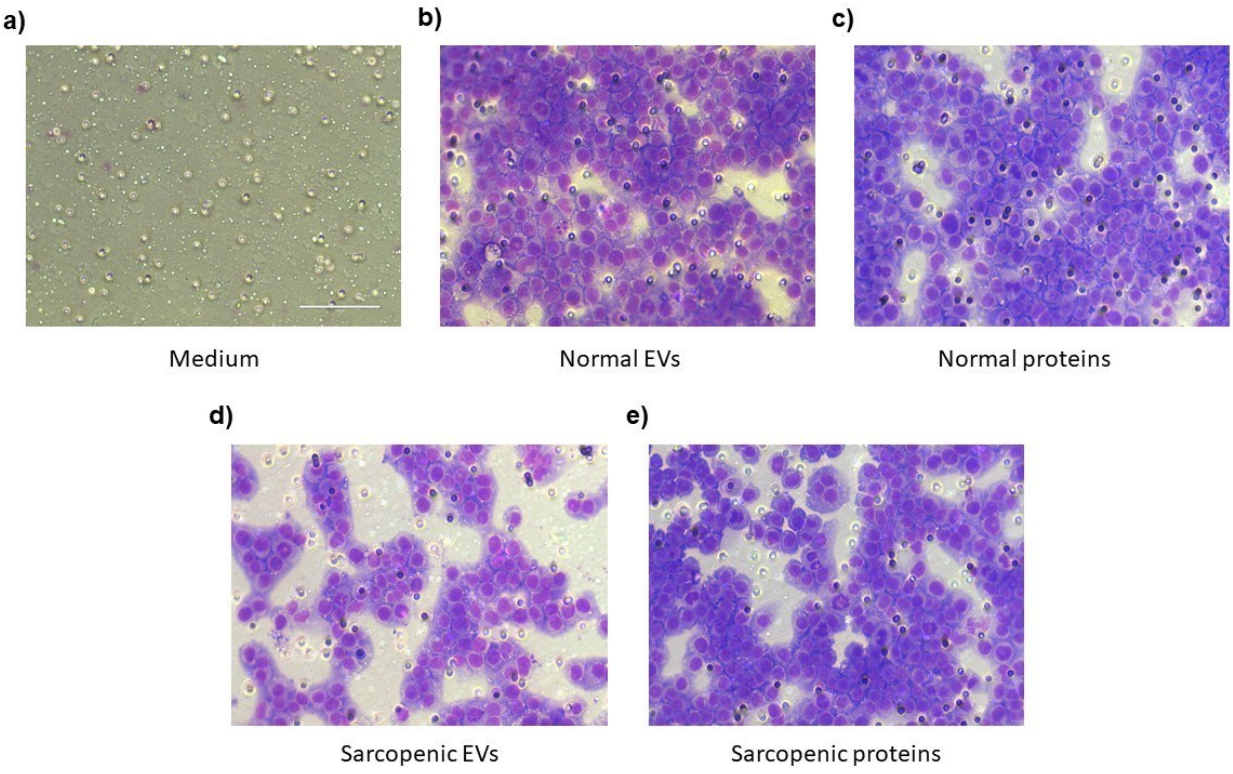

Figure 29. J774 macrophages on a transwell membrane migrating towards normal and sarcopenic myotube secretome fractions. EV and soluble protein components were isolated from normal and sarcopenic 2000*xg* myotube secretomes using SEC. J774 cells were separately incubated with the EV and soluble protein fractions from normal (b and c) or sarcopenic myotubes (d and e) for 24 hours. Following incubation, transwell inserts were stained with Jenner-Giemsa stains and the underside of membranes imaged at 40x magnification (scale bar = 100 µm). Images shown are representative of the experimental conditions tested.

As previously described with the 2000*xg* myotube secretomes, macrophage counts were conducted using the images of the Jenner-Giemsa stained cells. All fractions were capable of stimulating macrophage migration above that of the medium only control (figure 30a). Despite SEV stimulating the migration of approximately 150 macrophages, this was not considered to be a significant increase after statistical analysis. When comparing all fractions to either NEV or NP, no significant differences in the number of recruited macrophages were observed, with SEV being the only exception (figure 30b). SEV were found to encourage fewer J774 cells to migrate than the NP fraction, suggesting a difference in chemotactic potential between normal and sarcopenic conditions.

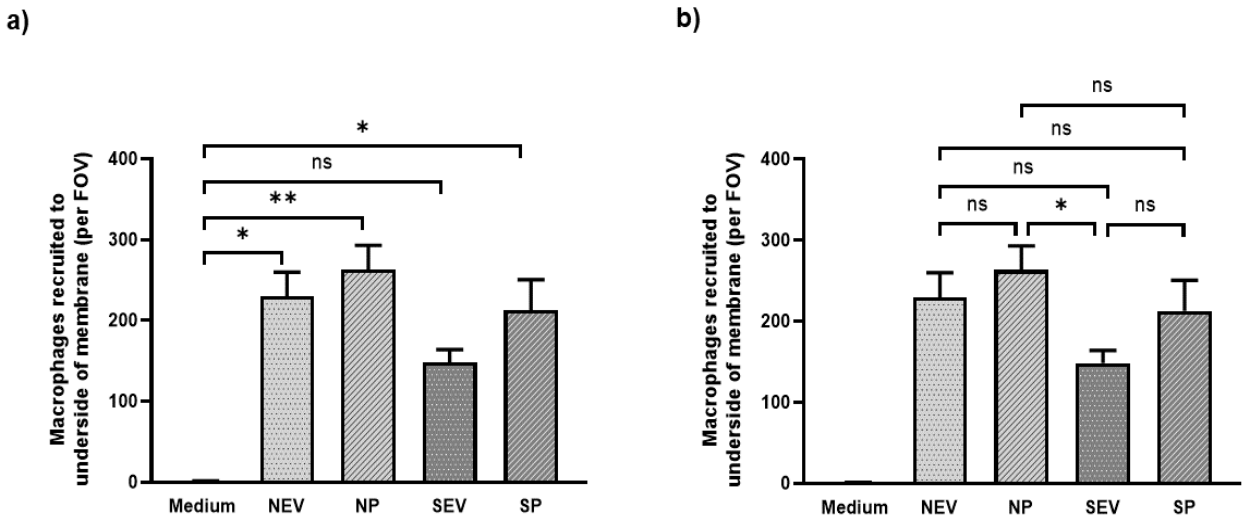

Figure 30. The J774 macrophage count of SEC fractions isolated from normal and sarcopenic myotube secretomes. The number of Jenner-Giemsa stained murine macrophages attached to the underside of the transwell membrane were manually counted after a 24 hour incubation period with normal EVs (NEV), normal soluble proteins (NP), sarcopenic EVs (SEV) and sarcopenic soluble proteins (SP). Data shown are mean ± SEM of 3 independent experiments, one-way ANOVA with Dunnett's *post-hoc* test, **P<0.05* and ***P<0.005* vs. medium (a). One-way ANOVA with Tukey's *post hoc* test was also conducted (b), **P<0.05*.

As with the 2000*xg* myotube secretomes, images of the bottom of the well were also taken in addition to those of the underside of the membrane. Images of this position show both components of the normal and sarcopenic secretomes induced macrophages to migrate from the upper chamber, through the permeable membrane into the lower chamber and attach to the bottom of the well (figure 31). These data proposed the separated fractions derived from the normal myotube secretome (figure 31b and 31c) recruited more cells than their sarcopenic counterparts (figure 31d and 31e). Variance was also observed between the EV and soluble protein fractions from the same origin, for instance from normal myotubes. NP appeared to increase macrophage migration to a greater extent than NEV, whilst there seemed to be a degree of parity between the two sarcopenic components.

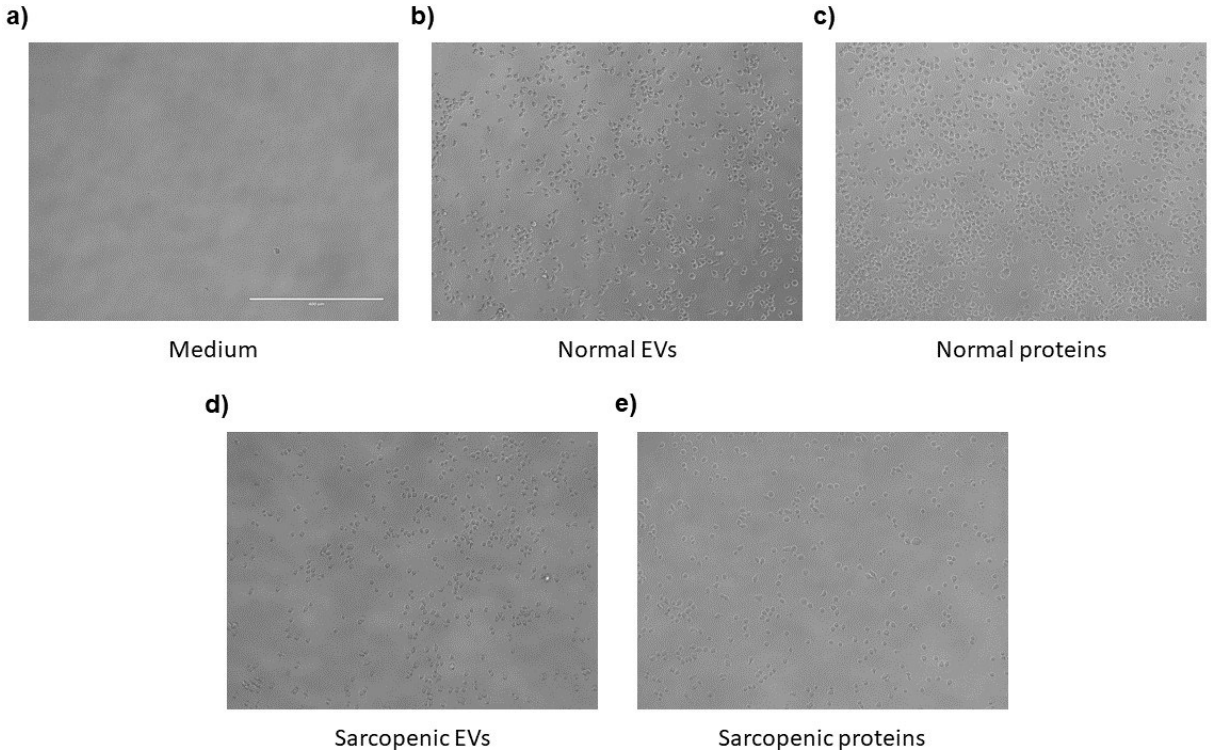

Figure 31. Macrophage migration towards EV and soluble protein fractions isolated from normal and sarcopenic myotube secretomes. Phase contrast images (10x magnification, scale bar = 400 µm) were taken 24 hours following the incubation of J774 macrophages with normal (b and c) or sarcopenic (d and e) myotube-derived EVs and soluble proteins. Images shown are representative of the experimental conditions tested.

Cell counts were conducted using images from figure 31 to numerically determine the chemotactic ability of each secretome component for both normal and sarcopenic myotubes. As initially observed from the microscopy images, all four secretome components induced more macrophages to migrate to the bottom of the well than medium alone, with both NEV and NP recruiting the highest number of cells (figure 32a). Comparison of macrophage numbers for each fraction indicated NP stimulated more macrophage migration than either SEV or SP (figure 32b). In contrast to SEV in figure 30a, SEV in figure 32a exhibits a significant increase in macrophage migration. This can be explained by the difference in number of macrophages recruited, with approximately 150 macrophages migrating in figure 30a and approximately more than 500 macrophages in figure 32a.

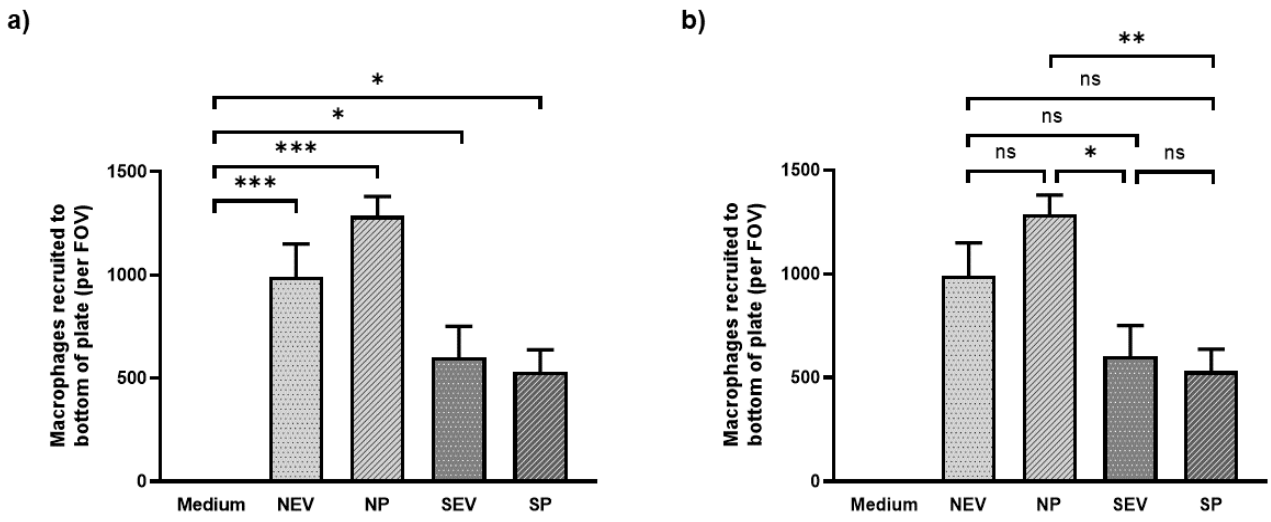

Figure 32. The macrophage count for different secretome fractions isolated from normal and sarcopenic myotubes. Macrophages migrated to the bottom of the well were manually counted following incubation with EVs from normal (NEV) and sarcopenic (SEV) secretomes and soluble proteins derived from normal (NP) and sarcopenic (SP) secretomes. Data shown are mean ± SEM of 3 independent experiments, one-way ANOVA with Dunnett's *post-hoc* test, **P<0.05* and ****P<0.0005* vs. medium (a). One-way ANOVA with Tukey's *post hoc* test was also conducted, **P<0.05* and ***P<0.01* (b).

To identify the most potent chemoattractive preparations, cell counts for the membrane underside and the bottom of the well were combined to provide the total number of migrating macrophages. Mirroring the previous results, NEV and NP both recruited the most macrophages, whilst the EV and soluble fractions from the sarcopenic secretome attracted half the number of cells (figure 33a). No differences were found in the number of macrophages migrating towards the SEV and SP. However, differences were observed between normal and sarcopenic secretome fractions. Both sarcopenic secretome components induced the migration of significantly fewer J774 macrophages than the NP, whilst the NEV showed no variance (figure 33b).

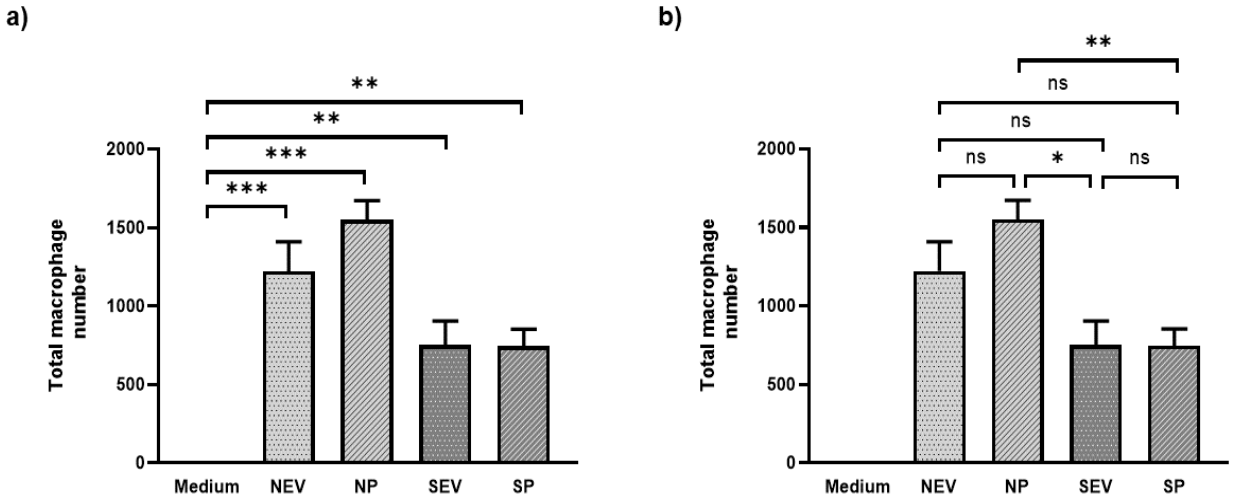

Figure 33. Total number of macrophages recruited by EV and soluble components of normal and sarcopenic myotube secretomes. Cell counts for the underside of the transwell membrane, and the bottom of the well were combined to give the total number of J774 macrophages migrating towards the proposed chemoattractants. Normal EVs (NEV), normal proteins (NP), sarcopenic EVs (SEV) and sarcopenic proteins (SP). Data shown are mean ± SEM of 3 independent experiments, one-way ANOVA with Dunnett's *post-hoc* test, ***P<0.05* and ****P<0.0005* vs. medium (a). One-way ANOVA with Tukey's *post hoc* test was also conducted, **P<0.05* and ***P=0.01* (b).

4.2.3.2 Horizontal migration – Dunn chamber

Vertical migration assays using transwell inserts are commonly used to assess the migratory potential of putative attractants. However, cells tested within these systems are subject to gravity. Additionally, this is an endpoint assay in which cell migration can only be quantified by the number of cells in the upper or lower chambers of the transwell setup, with no additional information relating to the velocity or distance migrated provided. Furthermore, the transwell system uses a temporary step gradient which is subject to dissipation due to the presence of microscopic holes in the permeable membrane, allowing mixing of chemoattractant with non-chemoattractant preparations (Zhang et al., 2016). To overcome these issues, a horizontal migration system was employed to further understand the migratory behaviour of J774 macrophages when exposed to normal and sarcopenic myotube derived secretomes. This horizontal system uses a slide-based Dunn chamber in which macrophage migration along a true linear chemotactic gradient can be observed via time-lapse microscopy (figure 34).

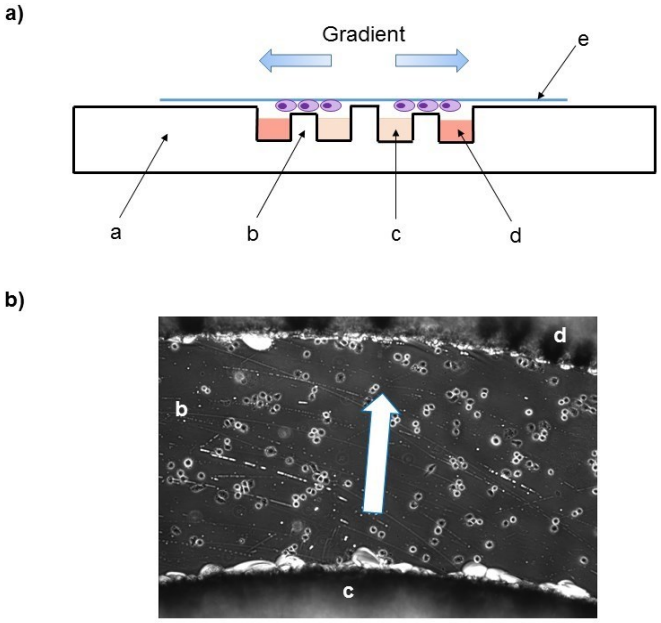

Figure 34. Schematic of horizontal migration using the Dunn chamber. Cross section of the experimental set up of the Dunn chamber slide (a) with a viewing bridge to observe macrophage migration (b), inner well containing chemically defined macrophage medium (c), outer well containing either normal or sarcopenic myotube-derived secretomes (d) and a THP-1/VD3 macrophage coated cover slip inverted onto the chamber (e) (panel a). Microscopy image shows the direction of macrophage migration across the viewing bridge (b), in response to an established chemotactic gradient from the inner well (c) to the outer well (d), as depicted by the arrow (panel b).

J774 mouse macrophage coated cover slips were mounted onto Dunn chambers containing chemically defined macrophage medium in the inner well and either 2000*xg* normal or sarcopenic myotube-derived secretomes in the outer well (figure 35). Results show that despite J774 cells adhering to the cover slips, chemotaxis towards the attractants was not observed. The cells of interest circled in white did not change position at the imaging start point at 0 hours to the end point 2 hours later. It is difficult to conclude whether the macrophages were attempting to move but could not due to their adhesiveness to the cover slip or whether there was no migration due to a lack of chemotactic potential in the samples.

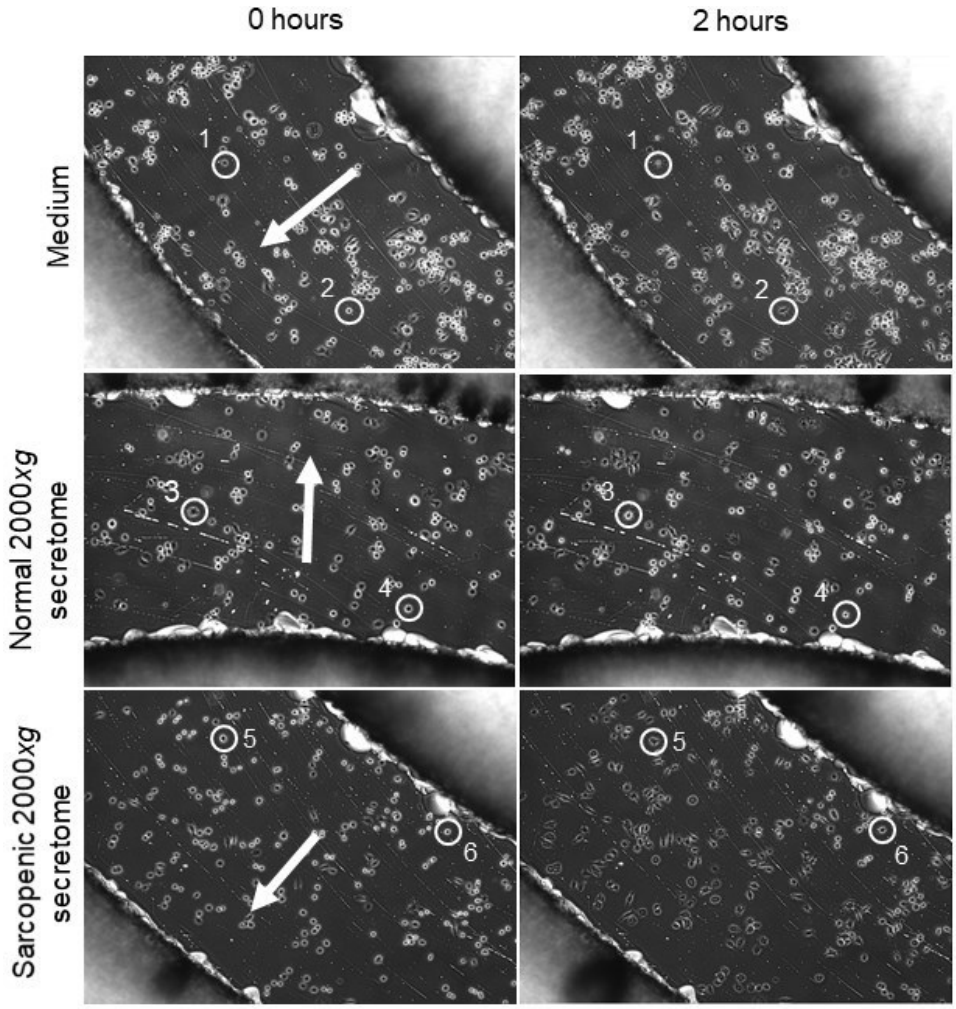

Figure 35. J774 mouse macrophage migration towards putative attractants on horizontal migration chamber. J774 mouse macrophage coated cover slips were inverted onto Dunn chambers containing SF medium in the inner well and either SF medium, normal or sarcopenic myotube 2000*xg* secretomes in the outer well. Macrophage migration was observed using time-lapse microscopy for 2 hours. White arrows denote predicted direction of macrophage migration towards a gradient of putative attractants (low to high). Cells of interest are circled for comparison at 0 hours and 2 hours.

To fully confirm the lack of chemotaxis, J774 cell migration was tracked using ImageJ and Ibidi Chemotaxis and Migration Tool software to generate migration plots. The migration plots verify the visual observations made from the time-lapse microscopy images. No chemotaxis or nondirectional movement, such as chemokinesis occurred since all cells remained at the starting point located at the crosshairs on the migration plots for each chemoattractant tested (figure 36). It was apparent that the J774 cells were too firmly attached to enable sufficient migration, thus this system was not adequate to assess the ability of the sarcopenic muscle secretome to act as a chemoattractant.

The use of a positive control would have confirmed J774 ability to migrate. FBS and apoptotic

Jurkat T cells were used as a positive control (data not shown), however neither were capable of substantial J774 recruitment. It is possible that this murine macrophage cell line does not respond to FBS in the same manner as other cell types and due to Jurkat cells being of human origin, J774 macrophages might not recognise them. Despite the cross-species interaction, human apoptotic B cells can be recognised and bound by murine J774 cells (Torr et al., 2012). Other compounds have been tested as positive controls and have shown to induce J774 migration, including MCP-1, PMA and C5a (Green et al., 2012). In future, it would be beneficial to test these chemoattractants as they could verify J774 migration.

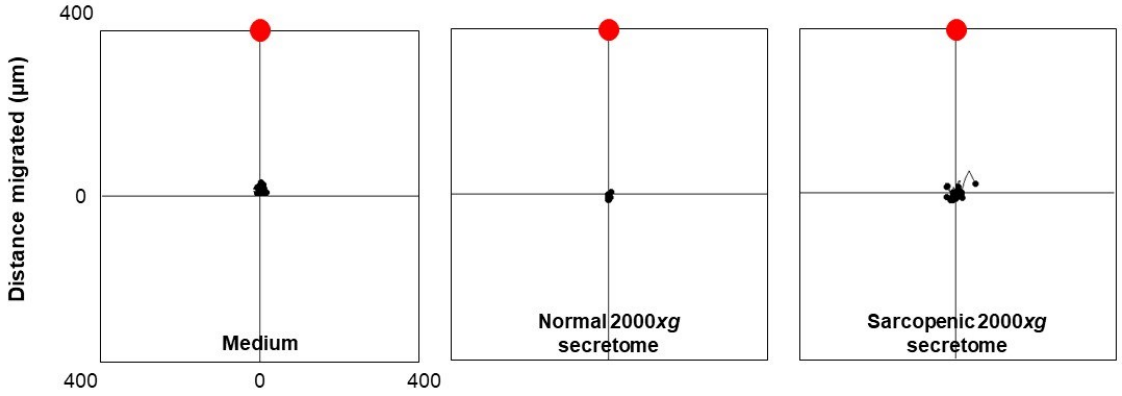

Figure 36. Migratory potential of sarcopenic myotube-derived secretome. Representative migration plots depicting the distance and the direction migrated by J774 macrophages towards 2000*xg* normal or sarcopenic myotube-derived secretomes. Cell migration was tracked using ImageJ and Chemotaxis and Migration Tool software to produce plots displaying the migration paths of 40 cells. Each black dot corresponds to one cell migrating towards the chemoattractant, shown as a red circle at the top of each plot.

To evaluate migration via the horizontal chemotaxis system, the existing assay was modified by exchanging the murine J774 cells with vitamin D3 differentiated human THP-1 macrophage-like cells (THP-1/VD3), which was previously optimised in the Devitt group. Migration plots using the THP-1/VD3 cells show the migration tracks of cells exposed to the 2000*xg* normal secretome almost mirror the MCP-1 cells, with most cells migrating towards the position of the attractant (figure 37). Conversely, migration towards the 2000*xg* sarcopenic secretome was markedly reduced with the cells undertaking non-directional movement when compared to both MCP-1 and the normal secretome.

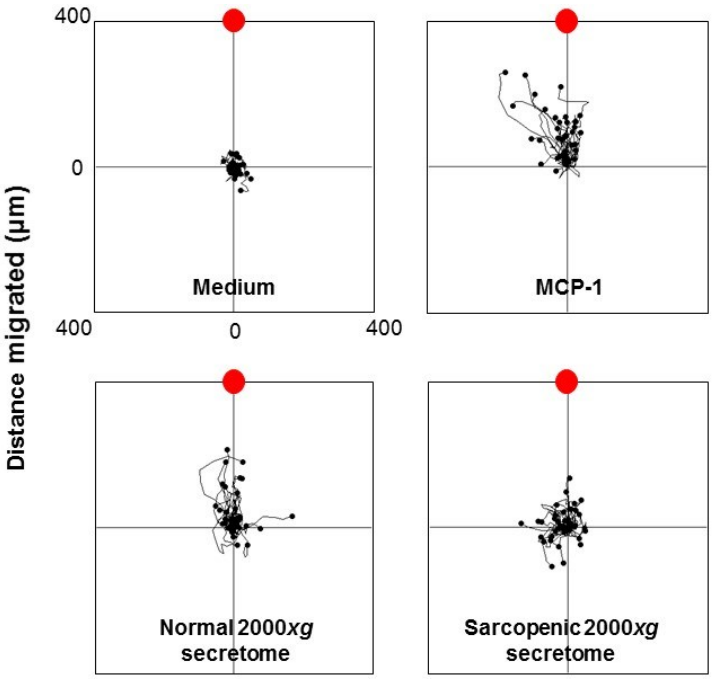

Figure 37. Migration of human macrophage-like cells towards sarcopenic myotube-derived secretomes. VD3 differentiated THP-1 cell coated coverslips were mounted onto Dunn chambers containing macrophage medium in the inner well and either 2000*xg* normal or sarcopenic myotube secretomes in the outer well and imaged for 2 hours. THP-1/VD3 macrophage-like cell migration was tracked and migration plots generated. Each black spot corresponds to one cell with its start point at the crosshairs, migrating towards the attractant designated by the red spot.

The migration plots only qualitatively assessed the ability of sarcopenic muscle to function as a chemoattractant. Chemotaxis and Migration Tool software was employed to quantify macrophage-like cell migration through a series of measures. The first measure to be assessed was the distance of migration, which can be evaluated via two different measurements, Euclidean and accumulated distances. Euclidean distance is the distance migrated from the start point to the end point in a straight line, whilst accumulated distance is the total distance migrated by cells from the start point to the end point (figure 38).

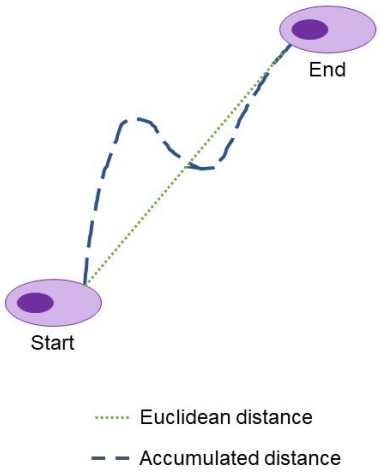

Figure 38. Defining the distance migrated by macrophage-like cells towards putative chemoattractants. Two separate distance measures were generated by Chemotaxis and Migration Tool software, designated Euclidean and accumulated distance. The total distance migrated by cells is termed the accumulated distance, shown by the navy dashed line. The Euclidean distance is the distance travelled from the cell's start point to its end point in a straight line, shown by the green dotted line.

The Euclidean distance migrated by macrophage-like cells was not different to that migrated towards medium only (figure 39a). Furthermore, there were no significant differences in the Euclidean distance migrated between the normal and sarcopenic 2000*xg* secretomes. This trend was mirrored by the accumulated distance when normal 2000*xg* was used as the putative chemoattractant (figure 39b). However, in the presence of the sarcopenic secretome, THP-1/VD3 cells migrated further. Despite this response, no discernible difference was observed between the healthy and sarcopenic samples, with both secretomes inducing macrophage-like cells to travel a similar distance.

The provision of a distance measure also allows for the velocity of migration to be measured. Figure 40 reflects the accumulated distance data, as THP-1/VD3 cells migrated faster towards the sarcopenic 2000*xg* myotube secretome, whilst migration velocity towards the normal secretome did not change above that of the medium only control. Irrespective of this difference, the two secretomes did not differ from each other when compared.

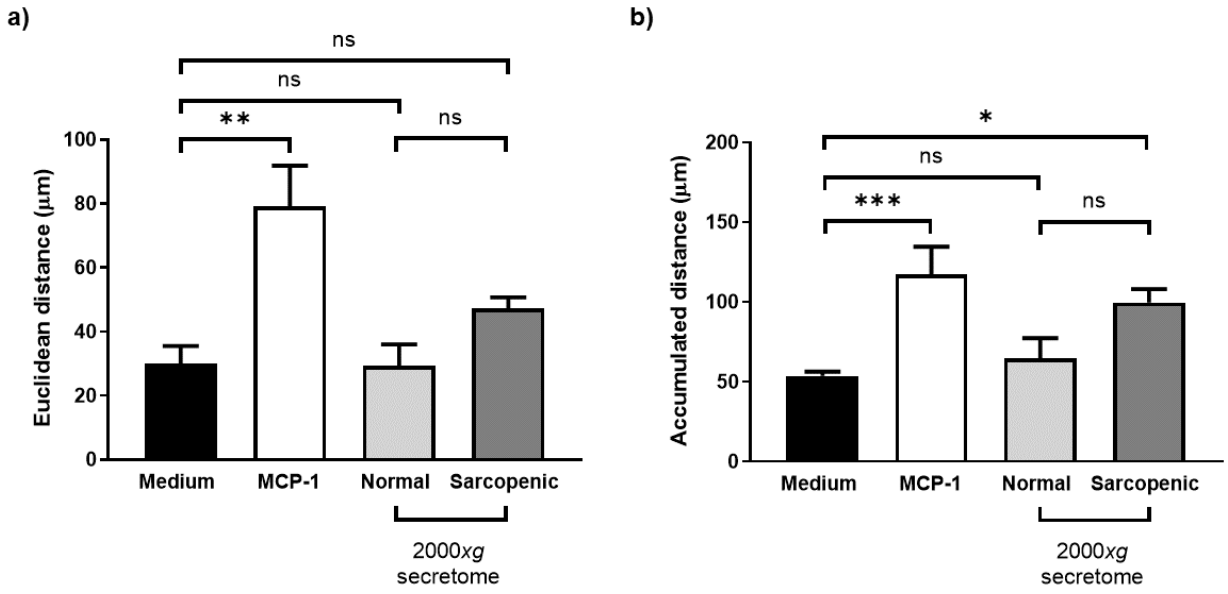

Figure 39. Distance migrated by THP-1/VD3 macrophage-like cells towards normal and sarcopenic secretomes. Following a 2-hour imaging period, THP-1/VD3 cells were tracked, and distance measures provided as either Euclidean distance migrated (a) or accumulated distance migrated (b). Data shown are mean ± SEM of 3 or more independent experiments, one-way ANOVA with Dunnett's *post-hoc* test, ****P<0.001, **P=0.001, *P<0.05* vs. medium or normal 2000*xg* secretome.

.

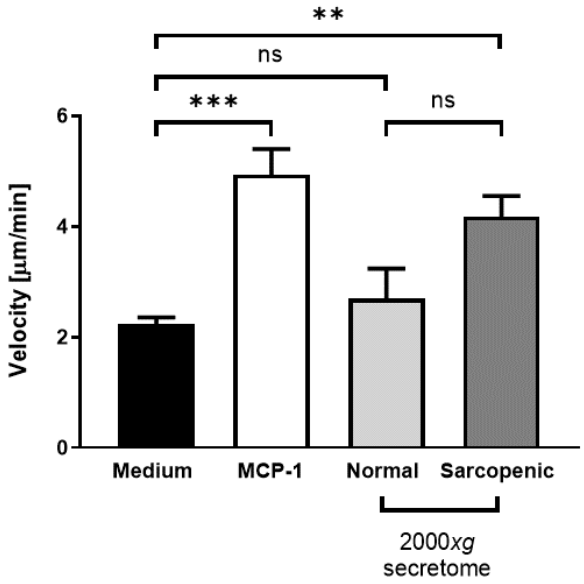

Figure 40. Velocity of macrophage-like cell migration towards normal and sarcopenic putative chemoattractants. THP-1/VD3 macrophage-like cells were tracked and velocity of migration towards 2000*xg* normal and sarcopenic myotube secretomes measured. Data shown are mean ± SEM of 3 or more independent experiments, one-way ANOVA with Dunnett's *post-hoc* test, ****P=0.005, **P=0.01, *P<0.05* vs. medium or normal 2000*xg* secretome.

The horizontal migration platform also allows the directionality of migration to be assessed. Chemotaxis and Migration Tool software provides directionality as a y-axis forward migration index (yFMI) measure. yFMI is defined as the forward migration of cells parallel to the direction

of the chemoattractant gradient. The software generates this measure as a comparative scale between -1 and +1, with high values corresponding to cell migration directly towards the attractant and low values implying cells are moving away from the attractant (figure 41a).

In addition to the yFMI measure, another directionality measure was also employed, which uses the angle of cell migration to comment on the directness of movement. This is the cosine of angle (CoA) measure which calculates the cosine of the angle between the cell's direction of migration and the position of the chemoattractant gradient (figure 41b). As with yFMI, CoA is given as values between -1 and +1. Putative chemoattractants measuring closer to -1 are considered to have weak or no chemotactic effect, whereas those placing towards +1 have a strong chemotactic effect on migrating cells.

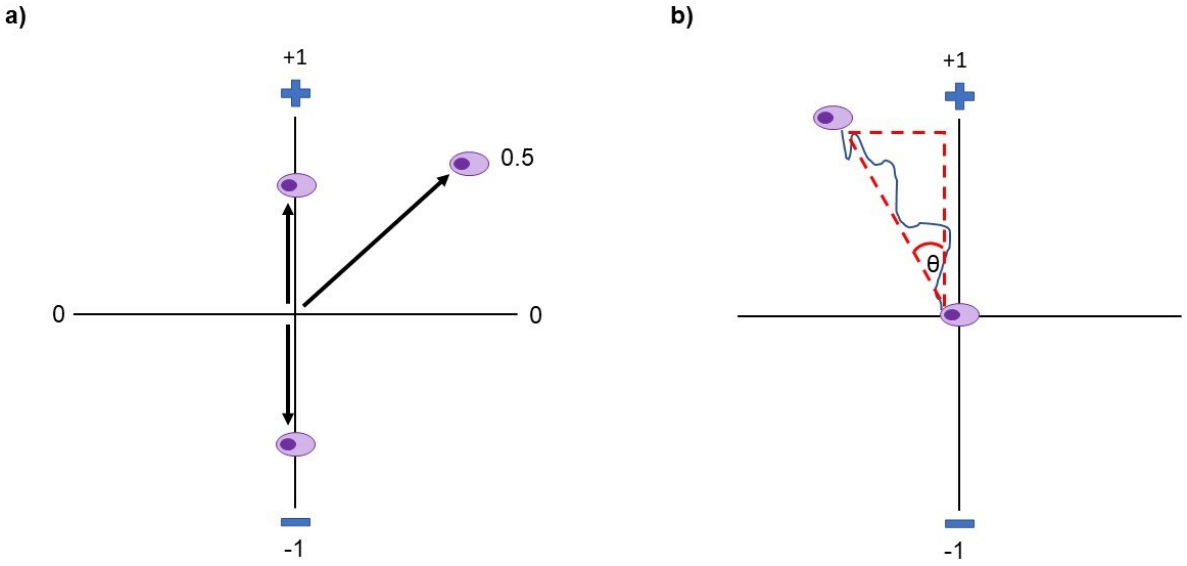

Figure 41. yFMI and cosine of angle measures of directionality. Directionality was measured as yFMI, which is the migration of a cell towards a chemoattractant positioned along the y-axis stated as a value between -1 and +1 (a). Directionality was also determined by the cosine of angle measure, which calculates the cosine of the angle between the direction of cell migration and the position of the chemoattractant on the y-axis, also stated as a value between -1 and +1 (b).

Initial observations suggest macrophage-like cells migrate in a more direct manner towards the normal 2000*xg* myotube-derived secretome with regards to the yFMI measure (figure 42a) However, due to high variability between repeat values, neither the normal nor sarcopenic 2000*xg* secretomes induced direct migration of THP-1/VD3 cells, as shown by each directionality measure. Comparing the normal secretome against its sarcopenic equivalent showed no significant difference in their ability to induce directional migration. This was also observed with the CoA measure (figure 42b).

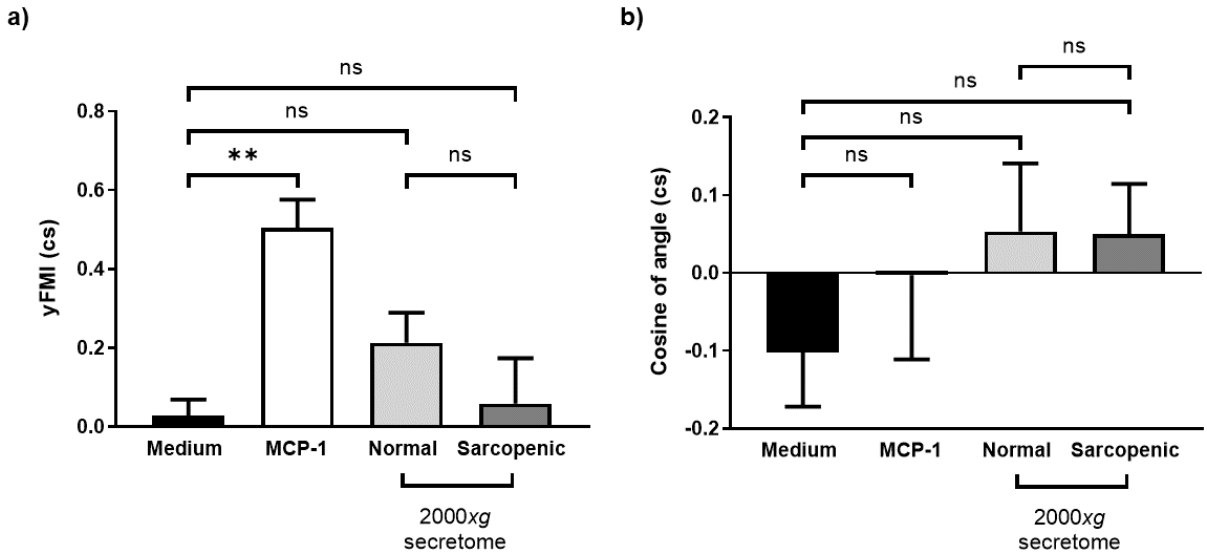

Figure 42. Directionality of macrophage-like cell migration towards the normal and sarcopenic secretomes. THP-1/VD3 macrophage-like cells were tracked and directness of movement towards 2000*xg* normal and sarcopenic myotube secretomes measured. Two directionality measures were used to assess directness, yFMI (a) provided by Chemotaxis and Migration Tool software, and CoA which is calculated using the angle measure (b). Both yFMI and CoA are measured on a comparative scale. Data shown are mean ± SEM of 3 or more independent experiments, one-way ANOVA with Dunnett's *post-hoc* test, ***P<0.005, *P<0.05* vs. medium or normal 2000*xg* secretome.

The 2000*xg* whole secretomes might have been too dilute to generate a sufficient chemotactic gradient. To overcome this potential impediment, the 2000*xg* secretomes were concentrated using 30 kDa centrifugal filters prior to testing on the horizontal migration system.

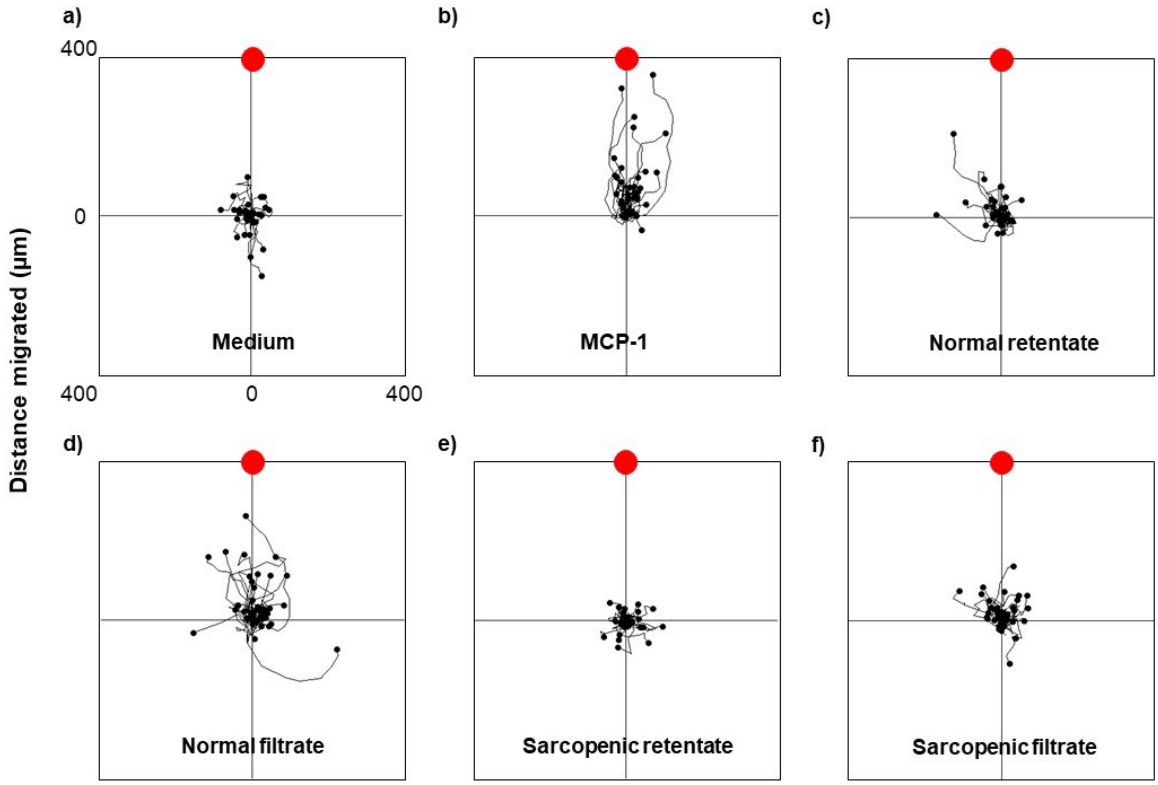

Figure 43. Migration plots of THP-1/VD3 macrophage-like cells towards concentrated 2000*xg* myotube secretomes. THP-1/VD3 cells were measured migrating towards concentrated 2000*xg* normal and sarcopenic secretomes on a horizontal Dunn chamber for 2 hours. The outer well of the Dunn chamber held the EV containing retentates (c and e) and small soluble factor filtrates (d and f). Black dots denote the cells, which were tracked and the course of migration towards the putative attractants, signified by the red dot was plotted. Migration plots are representative of the retentate and filtrates shown.

The 30 kDa concentrated normal retentate induced macrophage-like cell migration to some extent, however it appeared most cells did not travel far from their starting point (figure 43c). In contrast, the macrophage-like cells migrating towards the normal filtrate (NF) seemed to travel further with most movement orientated in the direction of the chemotactic gradient (figure 43d). Cells exposed to the sarcopenic retentate (SR) exhibited limited migration as they did not traverse a large distance and those that did failed to show directional movement (figure 43e). Migration induced by the sarcopenic filtrate (SF) was observed to be different to that of the SR, as despite displaying a wider range of movement, the macrophage-like cells travelled further in the presence of the SF than the SR (figure 43f).

Concentrating the 2000*xg* myotube secretomes did not affect the Euclidean distance migrated by the macrophage-like cells (figure 44a). Retentates and filtrates from normal and sarcopenic secretomes showed no difference in the Euclidean distance migrated when compared to each other (figure 44b). When assessing the accumulated distance migrated, macrophage-like cells travelled significantly further towards the normal myotube filtrate (figure 44c). All concentrated

sarcopenic secretome samples, as well as the NR did not promote cell migration. When comparing all the concentrated secretome samples, only the SR reduced the accumulated distance migrated compared to the NF (figure 44d). The macrophage-like cells were able to cover a greater accumulated distance towards the NF because they moved at a faster rate (figure 44e). In comparison, all other normal and sarcopenic concentrated secretome components did not alter the velocity of migration. Furthermore, these samples showed no difference in the migration velocity amongst each other (figure 44f). yFMI and CoA measures indicate almost all the concentrated secretome samples derived from both normal and sarcopenic myotubes did not promote directional migration in THP-1/VD3 cells (figures 45a and 45c). The exception to this was the migratory response to the SR. Irrespective of the SR limiting the distance migrated, this EV containing component stimulated cells to move in the direction of the attractant, as shown by the CoA results (figure 45c). When secretome fractions were compared against each other, no difference in directionality was observed (figures 45b and 45d).

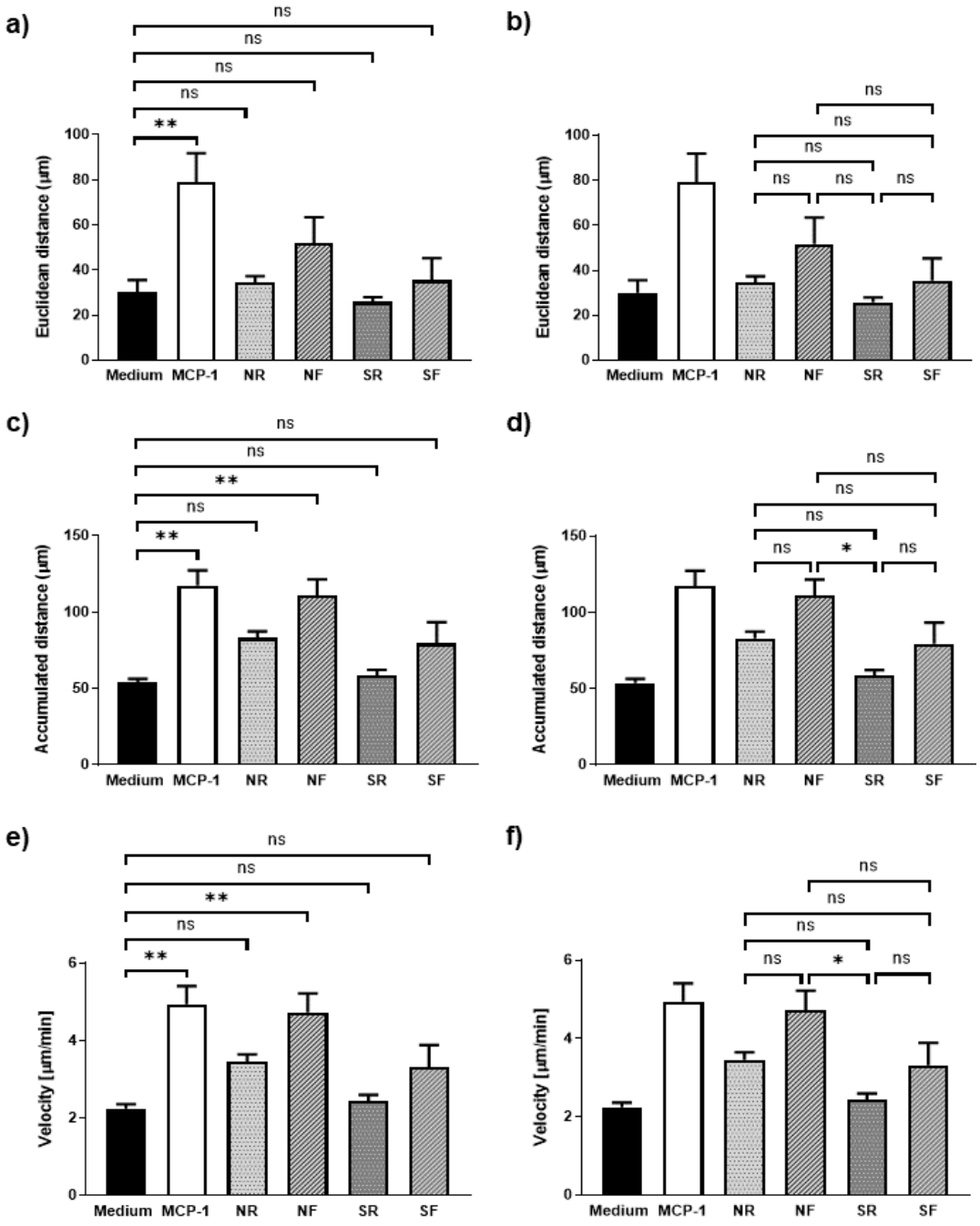

Figure 44. Migratory measures to assess the impact of normal and sarcopenic concentrated secretomes on macrophage-like migration. THP-1/VD3 macrophage-like cells exposed to 30 kDa concentrated normal and sarcopenic retentates (NR and SR respectively) and normal and sarcopenic filtrates (NF and SF respectively) derived from normal and myotube secretomes for 2 hours. The movement of cells was tracked and the distance (a - d) and velocity (e and f) of migration measured. Data shown are mean ± SEM of 3 or more independent experiments, one-way ANOVA with Dunnett's *post-hoc* test, ****P<0.0005* vs. medium. One-way ANOVA with Tukey's *post hoc* test was also conducted (panels b, d and f), **P<0.05*.

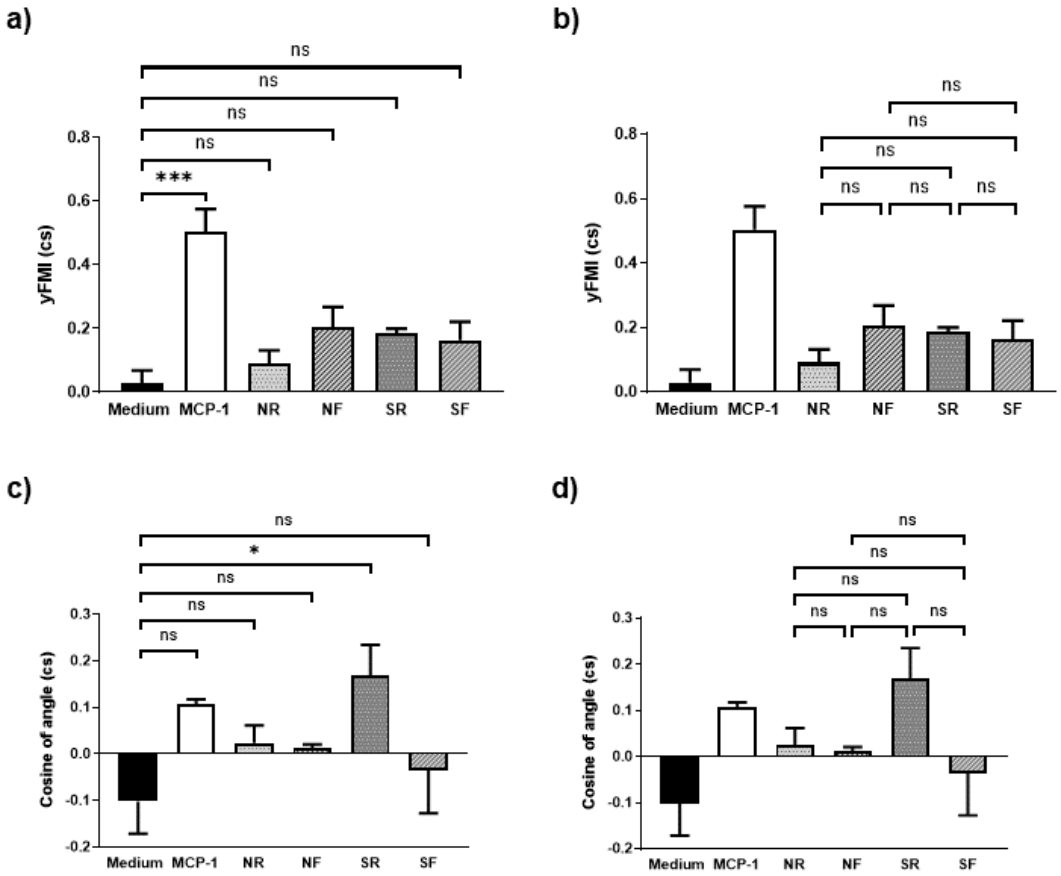

Figure 45. Directionality measures to assess the impact of normal and sarcopenic concentrated secretomes on macrophage-like migration. THP-1/VD3 macrophage-like cells exposed to 30 kDa concentrated normal and sarcopenic retentates (NR and SR respectively) and normal and sarcopenic filtrates (NF and SF respectively) derived from normal and myotube secretomes for 2 hours. The movement of cells was tracked and measures of the directionality of migration, i.e., yFMI (a and b) and CoA (c and d) were determined in addition to the measures in figure 43. Data shown are mean ± SEM of 3 or more independent experiments, one-way ANOVA with Dunnett's *post-hoc* test, ****P<0.0005* vs. medium. One-way ANOVA with Tukey's *post hoc* test was also conducted (panels b and d).

Unfortunately, due to the current Covid-19 pandemic resulting in the shutdown of research laboratories, certain experimental investigations could not be completed. With regards to assessing macrophage migration, the final step would have been the testing of SEC isolated EV and soluble protein fractions from normal and sarcopenic myotubes secretomes on the horizontal migration platform. These data would have supported the vertical transwell migration data and shown whether specific components of the myotube secretomes were important for promoting or limiting macrophage recruitment to the skeletal muscle microenvironment.

4.2.4 Determining the ability of sarcopenic muscle to promote an oxidatively stressed environment

One of the many contributing factors for the onset of sarcopenia is oxidative stress, which is often associated with mitochondrial dysfunction, resulting in increased ROS production (Meng and Yu, 2010). In addition to mitochondrial induced muscle atrophy, it is possible that sarcopenic cells may further contribute to the existing oxidatively stressed environment by promoting a pro-inflammatory phenotype in macrophages. Communication between the two cells may encourage macrophages within the tissue to respond to the aged muscle environment by generating excessive amounts of ROS, exacerbating tissue damage.

The putative ability of sarcopenic muscle to stimulate ROS release in macrophages was tested by treating J774 mouse macrophages with either normal or sarcopenic myotube secretomes and measuring the amount of superoxide anion produced over time using a chemiluminescent probe. The principle of this assay is that high luminescence is indicative of excess superoxide anion production by the macrophages.

Kinetic data show macrophage exposure to either normal or sarcopenic myotube 2000*xg* secretomes did not stimulate superoxide anion production above that of the medium only negative control (figure 46a). In addition to analysing the kinetic data of the respiratory burst, the total amount of luminescence, which correlates to the total amount of superoxide anion produced by macrophages was also determined by calculating the area under the curve. The total luminescence reflects the kinetic data, as the total amount of superoxide anion generated by macrophages did not change when exposed to either normal or sarcopenic 2000*xg* supernatants (figure 46b). Evaluating the difference between the two secretomes showed they did not vary in their ability to induce a respiratory burst.

These data suggest immediate measurement of superoxide anion did not provide sufficient time for the secretomes to exert their influence on the macrophages. Furthermore, the effect of these secretomes on macrophage ROS production could be subtle and the initial format of the chemiluminescent assay employed was not capable of detecting small changes elicited by the myotube secretomes.

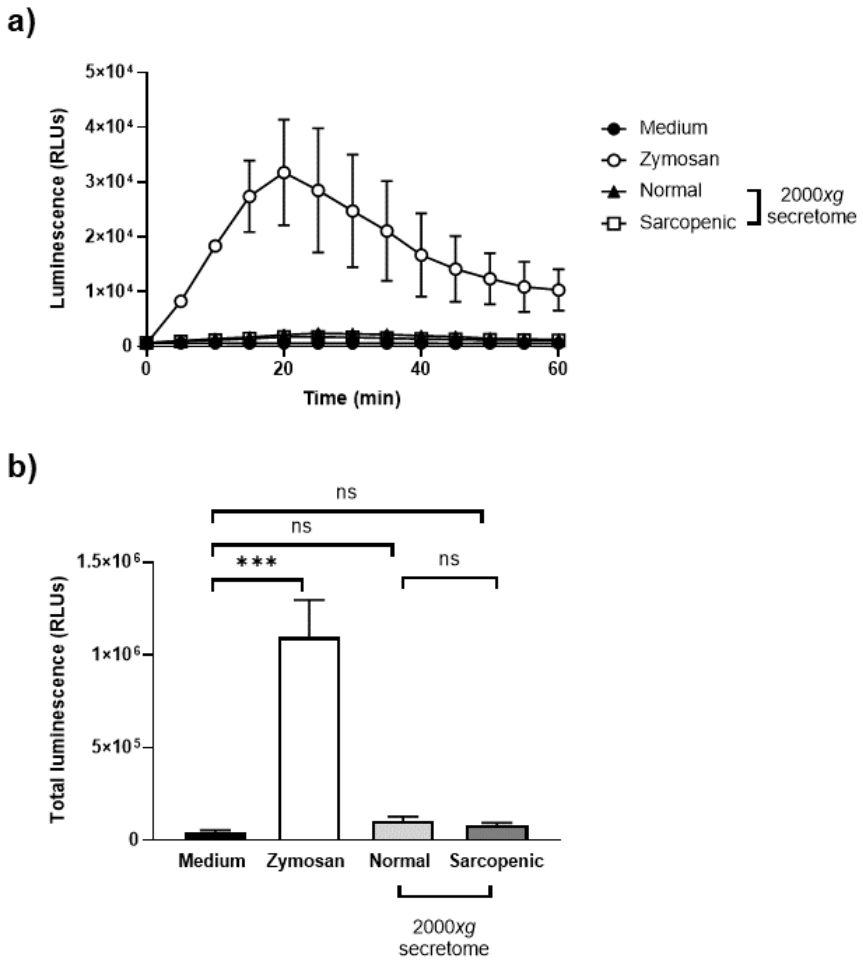

Figure 46. The ability of normal and sarcopenic whole secretomes to modify the oxidative skeletal muscle environment. J774 macrophages were treated with normal or sarcopenic 2000*xg* myotube secretomes. Positive control macrophages were treated with 2 mg/ml zymosan. Macrophage superoxide anion release was measured immediately after addition of secretomes using a chemiluminescent probe (lucigenin) every 5 minutes for 1 hour (a). The total luminescence was calculated by measuring the under the curve (b). Luminescence equates to the amount of superoxide anion produced. Data shown are mean ± SEM of 3 independent experiments, one-way ANOVA with Dunnett's *post-hoc* test, ****P<0.0005* vs. medium. One-way ANOVA with Dunnett's *post hoc* test vs. normal 2000*xg* secretome was also conducted.

To address these issues, the existing assay was modified by pre-treating the mouse macrophages with either normal or sarcopenic whole 2000*xg* secretomes for a period of 4 hours. Following the 4-hour incubation, pre-treated macrophages were exposed to *Saccharomyces cerevisiae* derived zymosan after which superoxide anion production was immediately measured. The addition of zymosan to the pre-treated macrophages allowed for the identification of any obscure effects elicited by the experimental samples, to observe either an increase or decrease in luminescence compared to the zymosan positive control, therefore indicating whether these samples heighten or dampen oxidative stress.

Figure 47a exhibits the changes in superoxide anion production over a 60-minute measurement period by macrophages pre-incubated with either normal or sarcopenic

secretomes. The kinetic data show superoxide anion release is initiated at a faster rate when macrophages were treated with zymosan alone, whilst macrophages pre-treated with normal or sarcopenic secretomes took longer to reach maximal superoxide anion production when in the presence of zymosan. Analysis of total luminescence showed neither the normal nor sarcopenic 2000*xg* secretomes were able to reduce the level of superoxide anion released by macrophages below that induced by zymosan (figure 47b). Comparison of the each secretome against the other exhibited no difference in total superoxide anion produced.

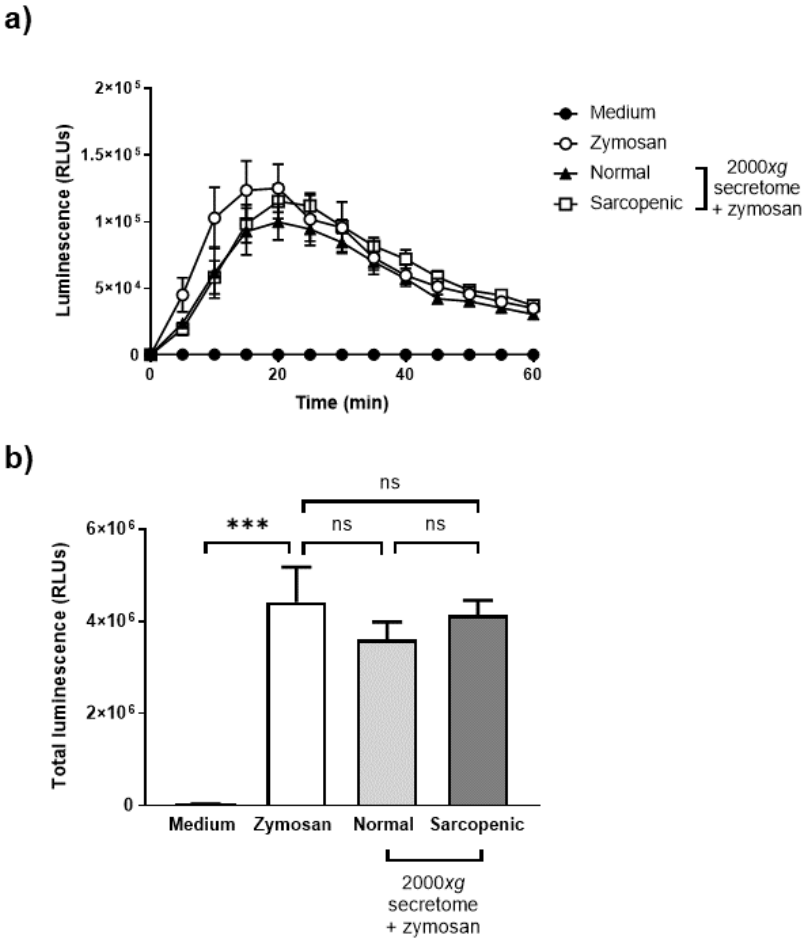

Figure 47. The effect of pre-incubation of macrophages with normal and sarcopenic myotube secretomes on superoxide anion production. J774 macrophages were pre-incubated with normal or sarcopenic 2000*xg* secretomes for 4 hours. Following incubation, macrophages were treated with zymosan and superoxide anion release measured for 1 hour (a). Using the kinetic data in panel a, the total luminescence was calculated to determine total amount of superoxide anion. Data shown are mean ± SEM of 3 independent experiments, one-way ANOVA with Dunnett's *post-hoc* test, ****P<0.0005* vs. zymosan. One-way ANOVA with Dunnett's *post hoc* test vs. normal 2000*xg* secretome was also conducted.

As the immediate treatment of J774 macrophages with normal and sarcopenic 2000*xg* myotube secretomes did not stimulate substantial superoxide anion production, and

preincubation induced subtle changes, pre-treatment of macrophages for 4 hours was conducted on all subsequent experiments.

With the Covid-19 pandemic limiting laboratory access, certain experiments were prioritised above others to ensure completion of the project. Consequently, testing of the 30 kDa concentrated myotube secretomes for their effect on macrophage superoxide production was not undertaken. Alternatively, the concentrated secretomes were used to isolate the EV and soluble protein fractions to be tested in the chemiluminescent assay. Once more, J774 macrophages were pre-treated with the normal and sarcopenic secretome fractions for 4 hours prior to zymosan exposure.

Figure 48a shows the progression of J774 macrophage superoxide anion production after incubation with myotube secretome fractions. Pre-treating macrophages with NEV and NP reduced superoxide anion production across the entire 60-minute measurement period. Furthermore, the rate of release during the first 10 minutes was slower than that of zymosan. Although, the production of superoxide anion by SEV and SP treated macrophages followed that of zymosan; it appeared these secretome fractions altered the rate of release. Cells exposed to the sarcopenic fractions took twice as long to generate a similar amount of superoxide anion produced by zymosan only treated macrophages after 5 minutes. Consequently, these macrophages achieved maximum production 5 minutes later than the positive control. After reaching the maximum, NP seemed to reduce macrophage superoxide anion release faster than SP.

Calculating the total amount of superoxide anion generated highlights the effect that normal and sarcopenic EVs and soluble proteins have on the macrophage respiratory burst response (figure 48b). Both NEV and NP managed to overcome the influence of zymosan to significantly reduce total superoxide anion production. Despite altering the kinetics of superoxide anion release, SEV did not change the total amount produced, whilst SP did reduce production in the presence of zymosan. Differences were also observed between the normal and sarcopenic fractions, as both NEV and NP were better at minimising oxidative stress than either of the two sarcopenic secretome components, but no variance between the normal secretome fractions was seen (figure 48c).

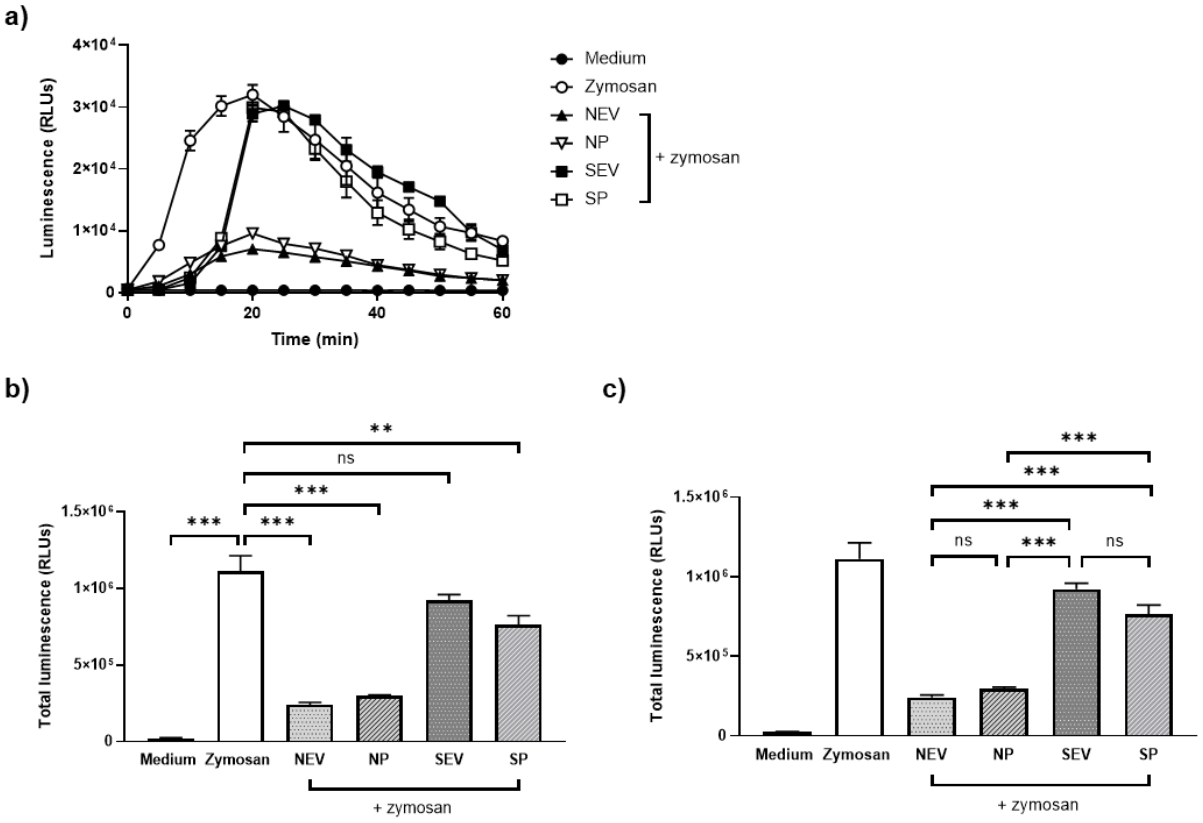

Figure 48. The impact of normal and sarcopenic secretome fractions on macrophage superoxide anion production. J774 macrophages were incubated with normal or sarcopenic myotube secretome derived EVs or soluble proteins for 4 hours. Cells were subsequently treated with 2 mg/ml zymosan and superoxide anion release measured for 1 hour (a). The total amount of superoxide anion produced during the 1-hour measurement period (b). Data shown are mean ± SEM of 3 independent experiments, one-way ANOVA with Dunnett's *post-hoc* test, ****P<0.0001* versus zymosan. One-way ANOVA with Tukey's *post hoc* test was also conducted (c), NEV vs. SEV ****P<0.0001*, NEV vs. SP ****P=0.0001*, NP vs. SEV ****P<0.0001*, NP vs. SP ****P<0.005*.

4.2.5 Identifying macrophage phenotypes in the sarcopenic skeletal muscle environment

The experiments in section 4.2.2 and 4.2.3 demonstrated the effects normal and sarcopenic myotube-derived secretomes have on macrophage function. The secretomes may modify macrophage function in a specific manner due to their potential ability to influence macrophage phenotype. By changing macrophage polarisation to either an M1 or an M2 phenotype, the secretomes can influence the skeletal muscle microenvironment.

Macrophage polarisation to the pro-inflammatory M1 phenotype can be assessed in mice using the Griess assay which indirectly measures $^{\bullet}NO$ production, a RNS commonly released by macrophages during an inflammatory response. Specifically, this assay measures NO_2^- release which corresponds to the amount of nitric oxide produced by stimulated macrophages.

Due to the small sample volume used in the Griess assay, the normal and sarcopenic 2000*xg* secretomes were concentrated using 30 kDa centrifugal filters to ensure sufficient secretome products were assayed. Both retentates and filtrates from normal and sarcopenic whole secretomes were tested for their ability to polarise J774 murine macrophages into proinflammatory M1 macrophages.

Neither normal nor sarcopenic filtrates and retentates stimulated NO_2^- production by J774 macrophages after 48 hours (figure 49). It was hypothesised that these myotube secretomes did not induce an obvious inflammatory response, but instead had a subtle effect on macrophage function, which the current Griess assay was not sensitive enough to detect. To investigate this hypothesis, murine macrophages were treated with LPS in addition to the normal or sarcopenic myotube secretome retentates and filtrates and nitrite release was measured. This would determine whether the retentates or filtrates promoted inflammatory or anti-inflammatory environments.

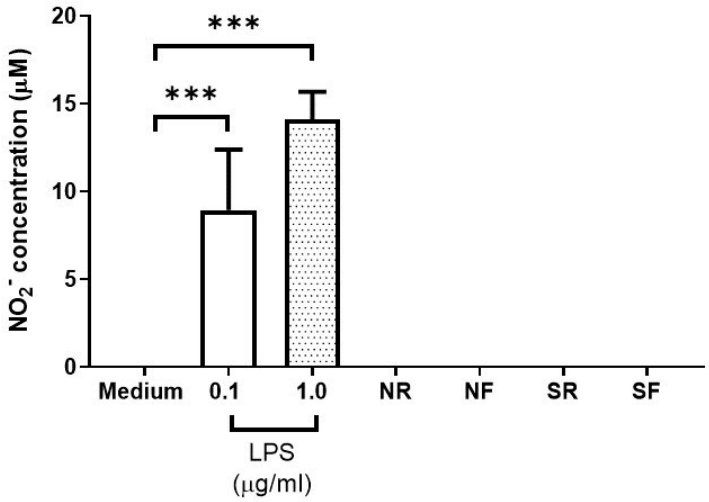

Figure 49. The effect of concentrated normal and sarcopenic myotube secretomes on macrophage phenotype. Normal and sarcopenic 2000*xg* myotube secretomes were concentrated using a 30 kDa centrifugal filter to generate retentate and filtrate fractions. Retentates (NR and SR) and filtrates (NF and SF) derived from normal and sarcopenic myotubes were incubated with J774 macrophages for 48 hours. 0.1 μg/ml and 1.0 μg/ml LPS were also used as positive controls. After 48 hours, macrophage NO_2^- production was measured by Griess assay. Data shown are mean ± SEM of 3 or more independent experiments, one-way ANOVA with Dunnett's *post-hoc* test, ****P<0.0005* vs. medium.

Figure 50a indicates that NR sustained the M1 phenotype as it did not stimulate a change in macrophage NO_2^- production. In contrast, in the presence of LPS, the small soluble factor containing NF significantly reduced the concentration of NO_2^-. This effect was also observed with SR and SF treatment. On comparing each concentrated secretome with the others, it was found that the NF, SR and SF all induced macrophages to produce a lower NO_2^- concentration

than the NR (figure 50b). The NR and SR and SF all stimulated a similar release of NO_2^- by the macrophages.

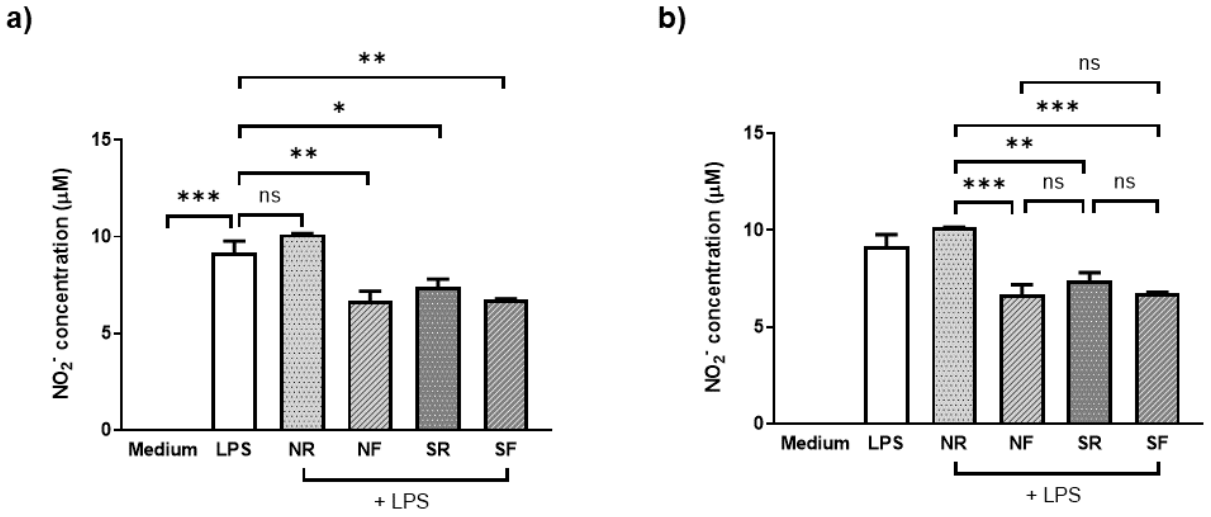

Figure 50. The ability of concentrated normal and sarcopenic secretomes to modify M1 macrophage phenotype. J774 macrophages were treated with 0.1 µg/ml LPS in addition to the normal or sarcopenic concentrated secretome fractions (retentate and filtrate) for 48 hours. Following the incubation period, NO_2^- concentration was measured via Griess assay (a). Data shown are mean ± SEM of 3 or more independent experiments, one-way ANOVA with Dunnett's *post-hoc* test, ****P<0.0001, **P<0.01, *P<0.05* vs. 0.1 µg/ml LPS. One-way ANOVA with Tukey's *post hoc* test was also conducted (b), NR vs. NF ****P<0.0005*, NR vs. SR ***P<0.005*, NR vs. SR ****P<0.001*.

As with the functional assays detailed previously, the EV and soluble protein fractions of the concentrated secretomes were also tested for NO_2^- production to identify any macrophage polarising effects they may possess. In a similar fashion to the 30 kDa concentrated secretomes, it was investigated whether the EV and soluble protein fractions isolated from normal and sarcopenic myotubes alone polarised M0 macrophages to M1 pro-inflammatory cells.

As expected, treatment of macrophages with normal or sarcopenic EV and soluble protein fractions did not stimulate NO_2^- production and so did not induce an M1 phenotype (figure 51). Due to this result, it was once again hypothesised that these separated secretome fractions may elicit an understated effect, which would be better observed by polarising the macrophages to M1 prior to NO_2^- production being measured, to identify any subtle pro- or anti-inflammatory features.

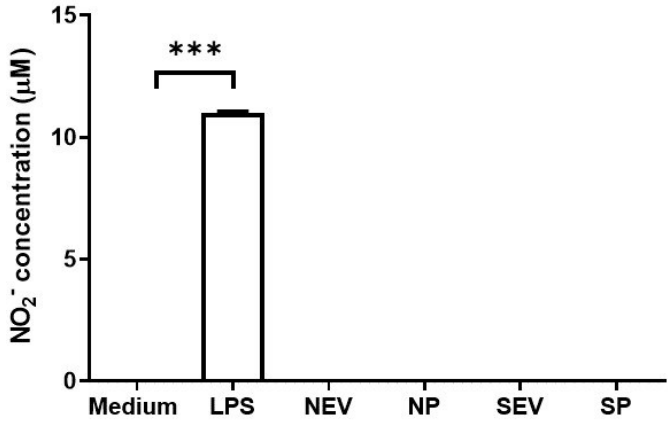

Figure 51. The impact of SEC isolated myotube secretome fractions on macrophage polarisation. Concentrated 2000*xg* normal and sarcopenic myotube secretomes were subjected to SEC to generate EV and soluble protein fractions. J774 macrophages were treated with each fraction or 0.1 μg/ml LPS for 48 hours. 48 hours post incubation, Griess assay was used to measure NO_2production by the macrophages. Data shown are mean ± SEM of 3 or more independent experiments, one-way ANOVA with Dunnett's *post-hoc* test, ****P<0.0001* vs. medium.

Treating M1 polarised J774 macrophages with SEC isolated secretome fractions secreted different amounts of NO_2^- based on the specific component they were incubated with (figure 52a). Both the NEV and SEV significantly reduced NO_2^- production, whilst the NP and SP were unable to do so. Comparisons between the EV and soluble proteins showed none were better at increasing or limiting NO_2^- production than the others, be they from normal or sarcopenic myotubes (figure 52b).

.

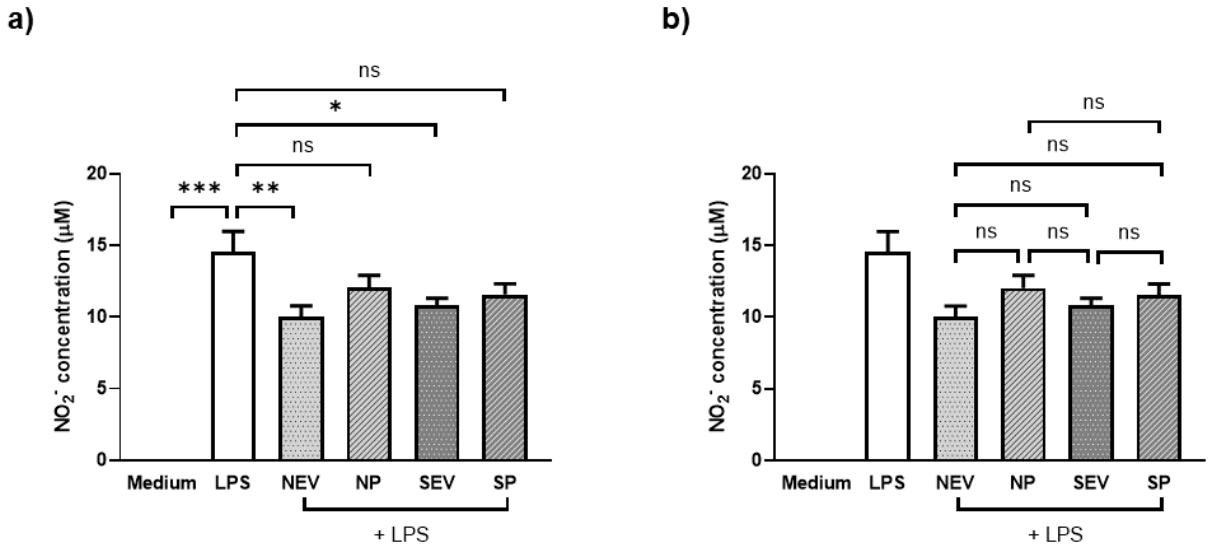

Figure 52. The ability of SEC isolated myotube secretome components to limit the proinflammatory M1 macrophage phenotype. EVs and soluble proteins isolated by SEC from normal and sarcopenic myotube secretomes were incubated with 0.1 µg/ml LPS induced M1 J774 macrophages for 48 hours. Following incubation, the concentration of NO_2^- produced by M1 macrophages was measured by Griess assay. Data shown are mean ± SEM of 3 independent experiments, one-way ANOVA with Dunnett's *post-hoc* test, ****P<0.0001, **P<0.01, *P<0.05* vs. 0.1 µg/ml LPS. One-way ANOVA with Tukey's *post hoc* test was also conducted (b).

4.2.5.1 Macrophage cytokine profiling

The Griess assay aimed to identify the presence of M1 pro-inflammatory macrophages based on their ability to produce NO_2^- in response to exposure to SEV and SP. To further determine the polarisation state of J774 macrophages treated with these sarcopenic myotube secretome components, the levels of certain cytokines released by these macrophages was assessed.

M1 and M2 macrophages are commonly identified by the cytokines they produce upon activation by specific stimuli. For example, macrophages stimulated with LPS will be polarised to the M1 subtype, which will secrete pro-inflammatory cytokines including TNF-α and IL-6 (Wang et al., 2014). In comparison, M2 macrophages can be generated by IL-4, IL-10 or IL13 stimulation and will produce anti-inflammatory or pro-resolving cytokines, such as IL-10 and TGF-β (Wang et al., 2014). Consequently, J774 macrophages were exposed to either NEV, NP, SEV or SP for 48 hours, prior to the level of cytokines generated being measured. A panel of 13 pro- and anti-inflammatory cytokines were simultaneously assessed using a fluorescent bead-based multiplex assay, which employed flow cytometric analysis to identify macrophage phenotypes. This panel consisted of beads that bound 8 different proinflammatory cytokines: TNF-α, IL-6, IL-23, IL-18, IL-1β, CXCL1, IL-12p70 and IL-12p40, which correspond to an M1 macrophage phenotype.

Figure 53 exhibits the predicted concentrations of the 8 pro-inflammatory cytokines measured, with TNF-α being the first. TNF-α is a pleiotropic cytokine that is heavily involved in the maintenance of an inflammatory response. Low concentrations of this cytokine were detected in all normal and sarcopenic myotube fractions, with SEV appearing to induce the most release (figure 53a). However, comparison of the four fractions indicates that they all induce macrophages to produce a similar amount of TNF-α. This result was also observed with IL-6, another cytokine with wide ranging inflammatory effects (figure 53b). The cytokine IL-23 is involved in regulating both innate and adaptive immune response, with its main function being the expansion of the Th17 cell population (Teng et al., 2015). Similar in function to IL-23, IL18 is also associated with regulating Type 1 T cell responses, in addition to stimulating IFN-γ production (Dinarello et al., 2013). Both IL-23 and IL-18 were below the limit of detection for both normal and sarcopenic myotube fractions (figures 53c and 53d). This was also observed with IL-1β, which was undetectable in all experimental samples bar the M1 positive control (figure 53e). The main difference was observed with the release of CXCL1, also known as keratinocyte derived cytokine (KC), which functions as a chemokine and is associated with neutrophil recruitment to sites of inflammation (Sawant et al., 2016). The release of this cytokine was only induced in the presence of NP and SP, with NP producing a higher concentration of CXCL1/KC than their sarcopenic equivalent (figure 53f). The final two proinflammatory cytokines, IL-12p70 and IL-12p40 are members of the IL-12 superfamily. The active heterodimer IL-12p70 is responsible for increased IFN-γ production, which in turn promotes NK cell, Th1 cell and cytotoxic CD8+ T cell responses, whilst IL-12p40 is a subunit which combines with another subunit to form IL-12p70 (Verma et al., 2014). IL-12p40 is also a component of the pro-inflammatory cytokine IL-23. Despite being widely recognised as a constituent of other pro-inflammatory cytokines, an independent function for IL-12p40 has also been proposed as a macrophage chemoattractant (Shimozato et al., 2006). The active form IL-12p70 was not detected, whereas IL-12p40 was produced in minimal quantities by the normal and sarcopenic SEC isolated fractions, the concentrations of which were not significantly different to medium alone (figure 53g and 53h).

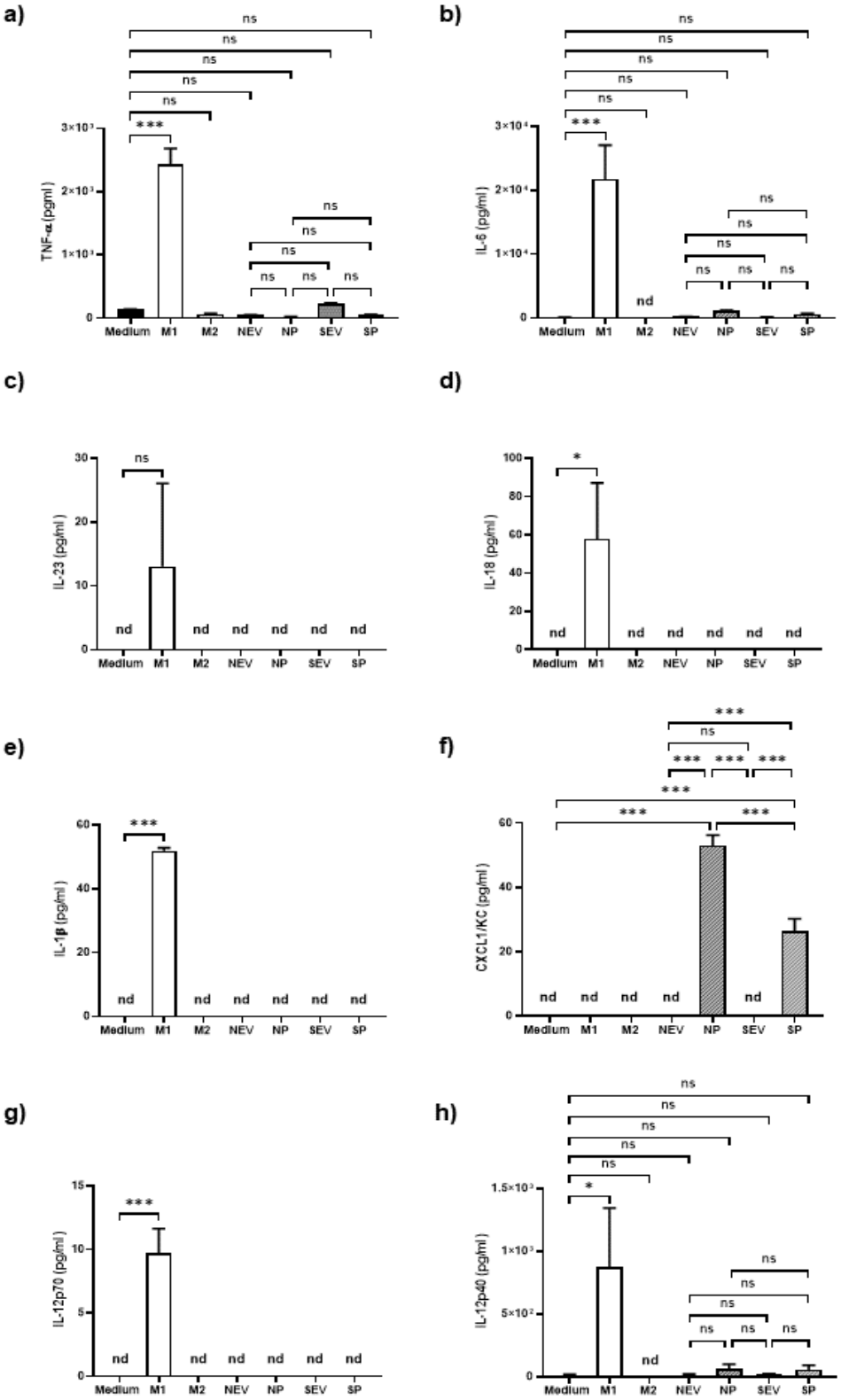

Figure 53. Pro-inflammatory cytokine profile of sarcopenic myotube-derived EV and soluble protein treated murine macrophages. J774 macrophages were incubated with EVs and soluble proteins isolated from normal and sarcopenic myotube secretomes for 48 hours. Following incubation, flow cytometry was used to determine the concentration of TNF-α (a), IL-6 (b), IL-23 (c), IL-18 (d), IL1β (e), CXCL1/KC (f), IL-12p70 (g) and IL-12p40 (h) produced by treated macrophages. Data shown are ± SEM of 3 independent experiments, one-way ANOVA with Dunnett's *post-hoc* test, ****P<0.0001*, **P<0.05*. A one-way ANOVA with Tukey's *post hoc* test was also conducted for all measured cytokines, all combinations tested were *ns* except CXCL1/KC, ****P<0.0001*.

The macrophage cytokine profile was completed by measuring five different anti-inflammatory and pro-resolving cytokines, high concentrations of which would suggest the presence of an M2 macrophage population. Unfortunately, unlike the M1 control for the measurement of pro-inflammatory cytokines, the M2 control did not work as no anti-inflammatory cytokines were detected and if they were the concentrations were very low.

Free active TGF-β1 is an immunomodulatory cytokine and is involved in regulating T cell activity, as well as suppressing cells of the innate immune system. Unfortunately, concentrations of this cytokine were below the range of detection (figure 54a) and was also observed with sarcopenic myotube SEC fractions. IL-10, similarly to free active TGF-β1 has extensive effects, as it can reduce the production of pro-inflammatory cytokines and therefore can limit the activity of macrophages, Th1 and NK cells (Couper et al., 2008). This cytokine was also produced at too low a concentration to be detected by the multiplex bead assay (figure 54b). The next cytokine to be assessed was CCL17, also referred to as thymus and activation regulated cytokine (TARC), facilitates wound healing by attracting fibroblasts to the site of damage was only detected in the secretome of M1 control macrophages and not in any myotube samples (figure 54c) (Kato et al., 2011). CCL22 or macrophage-derived chemokine (MDC) is the partner cytokine to CCL17/TARC and was the only M2 macrophage associated cytokine to be detected. CCL22 is a chemoattractant and recruits immunosuppressive cells, including regulatory T cells (Ruytinx et al., 2018). All EVs and soluble proteins isolated from both normal and sarcopenic myotubes produced similar amounts of this chemokine, however these concentrations were not significantly different to that induced by medium alone (figure 54d). The final cytokine measured was granulocyte colony stimulating factor (G-CSF), which can influence the polarisation of macrophages to induce an anti-inflammatory phenotype. Like CCL22/TARC, G-CSF was detected in all experimental samples and distinct differences were observed in the amount released by each myotube fraction (figure 54e). Treating J774 macrophages with NEV or SEV did not affect G-CSF release, whereas in the presence of NP or SP, cytokine production increased. Furthermore, NP stimulated more G-CSF production than SP.

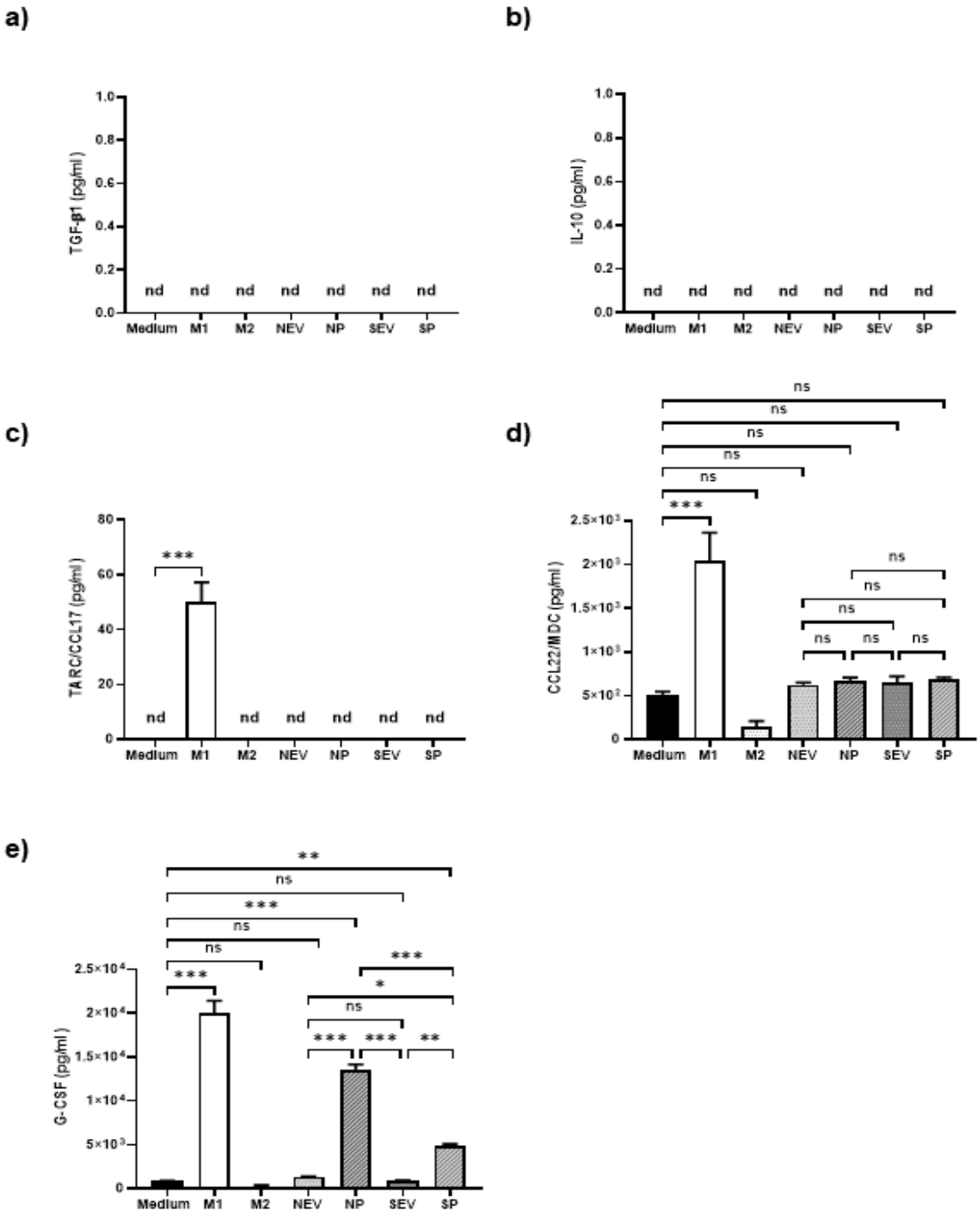

Figure 54. Anti-inflammatory and pro-resolving cytokine production by sarcopenic EV and soluble protein treated macrophages. Normal and sarcopenic myotube-derived EVs and soluble proteins were incubated with J774 macrophages for 48 hours, after which a fluorescent multiplex bead assay in conjunction with flow cytometric analysis was used to measure the concentration of free active TGF-β1 (a), IL-10 (b), TARC/CCL17 (c), CCL22/MDC (d) and G-CSF (e). Data shown are mean ± SEM of 3 independent experiments, one-way ANOVA with Dunnett's *post-hoc* test, ****P<0.0001, **P<0.005*. A one-way ANOVA with Tukey's *post hoc* test was also conducted for all normal and sarcopenic myotube fractions, all combinations tested were *ns* except for G-CSF, ****P<0.0001, **P<0.005* and **P<0.05*.

4.2.6 The protein profile of sarcopenic myotube-derived EVs

As prolific trafficking particles, EVs carry a variety of cargo either encapsulated within the vesicle itself or bound to the surface. One such example of this cargo is proteins that have been selectively packaged into the EVs by the parent cell. It is possible that during the age-related muscle wasting disorder, sarcopenia, the profile of proteins released by sarcopenic muscle into vesicles is modified to reflect the pathophysiological changes of the tissue. This section aims to identify SEV associated proteins using MS analyses and to determine the biological functions they may positively or detrimentally influence using bioinformatic tools.

Both SEV and NEV were quantified using MS to determine relative protein abundances for each sample. Preparation of samples and MS analyses were undertaken by Dr Ivana Milic. In total, 1152 proteins with unique peptide sequences were identified for both NEV and SEV, with all proteins with no unique peptides excluded from each dataset. Due to the MS analyses generating large datasets, only proteins with significantly different abundances between SEV and NEV i.e., significantly up- or downregulated, were included in the final list. To do this, proteins were filtered using student's t-test to identify all proteins with a significance greater than 95%, which reduced the list from 1152 proteins to 513 proteins.

These 513 proteins were further analysed using bioinformatics software FunRich 3.1.3; a functional enrichment analysis tool. FunRich analysis assigned biological functions to each uploaded protein in the datasets and quantified whether these proteins were enriched (positive value) or depleted (negative value), which was stated as a fold change value. Fold change here is defined as the measure of protein expression in SEV in relation to the expression of the same proteins in NEV. Assessing fold change will show which proteins and therefore biological functions were upregulated or enriched and which were downregulated or depleted in the SEV sample.

Overall, 1441 gene ontology (GO) biological processes were more depleted in SEV compared to NEV. Due to the high number of processes identified, only 7 relevant functions were selected that were specifically related to this study (figure 55). Of these 7 GO processes, the most depleted were immune related functions that would be involved in responding to the presence of sarcopenic muscle cells, including leukocyte differentiation and monocyte chemotaxis. Other depleted functions linked to SEV also include those regulating protein degradation, cell responses to oxidative stress, muscle differentiation and exosome secretion.

In conjunction with the depleted GO processes, an additional 1312 were also found to be more enriched in SEV than NEV. Once again, the list of biological processes was filtered down to 5 biological functions related to this study being selected, which are presented as the green bars in figure 55. The GO processes chosen for presentation were not the most enriched, however, they are associated with sarcopenic myotube-derived secretome functional effects assessed in this chapter.

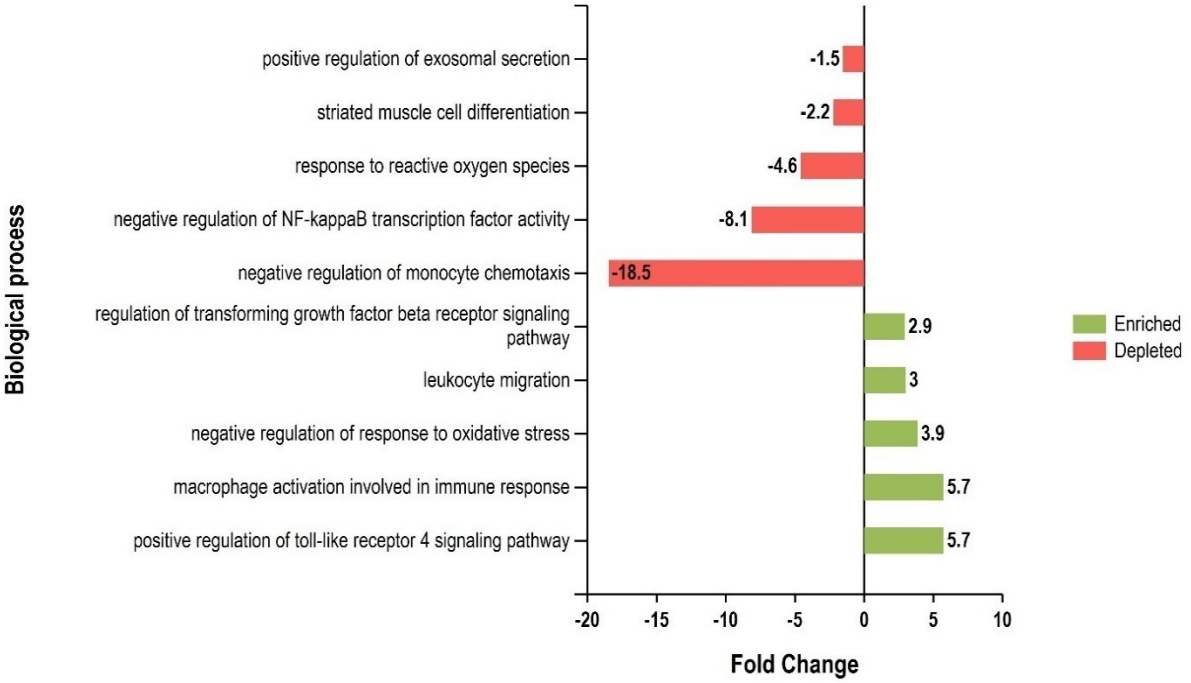

Figure 55. Functional enrichment analysis of proteins identified in sarcopenic myotube-derived EVs. Proteins of significantly different abundances (>95% significance, t-test) between sarcopenic EVs and normal EVs were subjected to bioinformatical analysis using the functional enrichment analysis tool, FunRich 3.1.3. Biological processes were allocated to all uploaded proteins and the degree of protein enrichment or depletion in sarcopenic EVs compared to normal EVs was quantified by fold change. Red bars correspond to biological processes that have been depleted, whilst green bars signify those that have been enriched.

The GO biological processes presented were further analysed by identifying the proteins that were associated with functions that were depleted or enriched. Table 1 contains a list of proteins that have been mapped to the 7 depleted functions shown in figure 55. Using UniProt IDs provided by FunRich 3.1.3 for these proteins, proteins were identified, and their functional information was also determined using the UniProt database. This allowed for the identification of the specific proteins that were responsible for the downregulated biological functions.

Biological function	Mapped proteins (UniProt ID)	Protein name
Positive regulation of exosomal secretion	Q61187	Tumour susceptibility gene 101
	Q9WU78	Programmed cell death 6interacting protein
	O08992	Syntenin-1
Striated muscle cell differentiation	Q07079	Insulin-like growth factorbinding protein 5
Response to reactive oxygen species	P35700	Peroxiredoxin-1
Negative regulation of NF-kappa B transcription factor activity	Q80TQ2	Ubiquitin carboxyl-terminal hydrolase CYLD
Negative regulation of monocyte chemotaxis	O70326	Gremlin-1

Table 1. Proteins mapped to downregulated biological functions of sarcopenic myotube-derived EVs versus normal myotube-derived EVs. Significantly downregulated protein abundancies were analysed using FunRich 3.1.3 software tool, which mapped these proteins to the 7 selected biological functions. Mapped proteins were searched for using the UniProt database for associated descriptions.

A similar approach was also taken for biological processes more enriched in SEV. Proteins mapped to the 5 chosen upregulated functions are displayed in Table 2. It is likely that the activity of the proteins listed in this table was increased such that their corresponding functions were enriched.

Biological function	Mapped proteins (UniProt ID)	Protein description
Regulation of TGF-β receptor signalling	P28301	Protein-lysine-6-oxidase
Leukocyte migration	P31230	Aminoacyl tRNA synthase complex-interacting multifunctional protein 1
Negative regulation of the response to oxidative stress	Q9QZQ8	Core histone macro-H2A.1
Macrophage activation involved in inflammatory response	Q61805	LPS-binding protein
Positive regulation of TLR4 signalling pathway	Q61805	LPS-binding protein

Table 2. Proteins mapped to upregulated biological functions of sarcopenic myotube-derived EVs versus normal myotube-derived EVs. Significantly upregulated proteins in sarcopenic myotube EVs were mapped against specific biological functions using FunRich 3.1.3 software tool. UniProt database was used to identify the mapped proteins and to determine their specific function.

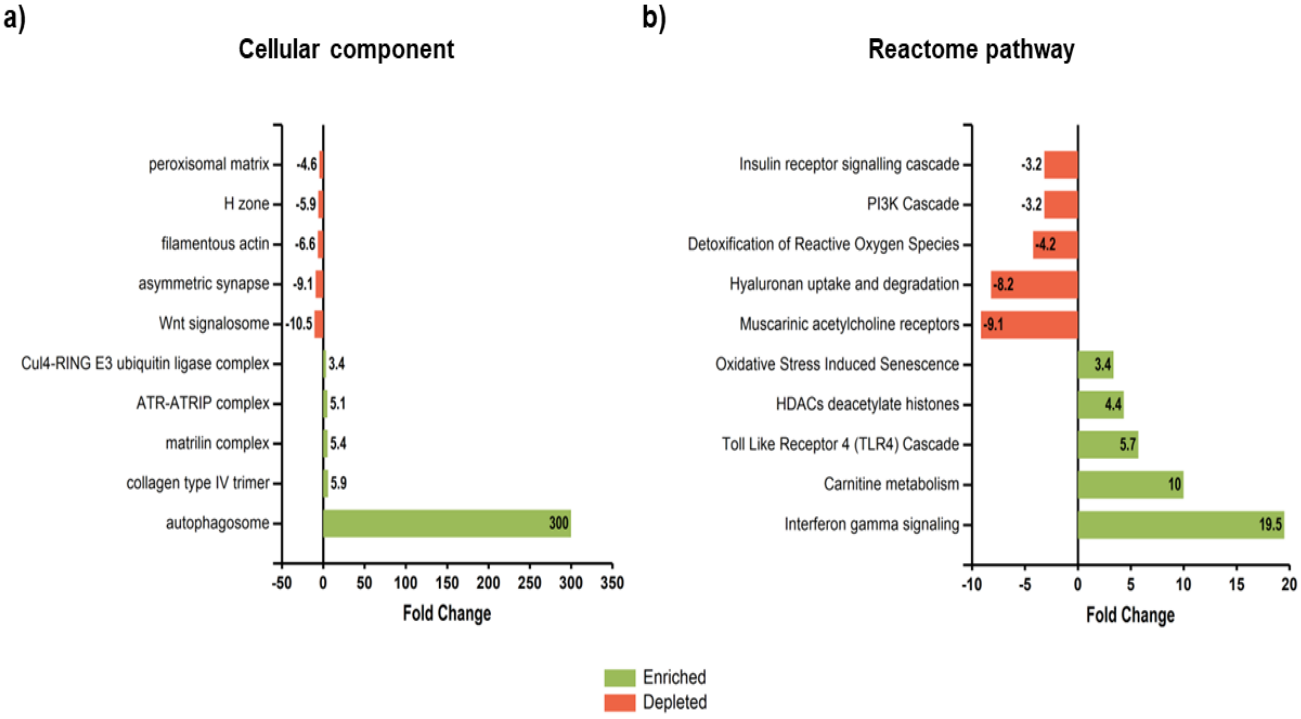

Figure 56. Gene ontology of differentially expressed proteins between SEV and NEV. FunRich 3.1.3 was used to assign all proteins to cellular components (a) and reactome pathways (b). The degree of gene enrichment or depletion was quantified by fold change.

In addition to biological processes, the cellular component and reactome pathways were also presented for SEV. The GO terms presented in figure 56 were selected based on their association with skeletal muscle ageing and muscle atrophy.

4.3 Discussion

4.3.1 Modelling sarcopenia

The successful development of a SF model of skeletal muscle in Chapter 3 provided scope for the establishment of a skeletal muscle disorder model associated with ageing. It has been shown that exposure to the glucocorticoid DEX induced characteristic myotube thinning connected to the muscle wasting condition sarcopenia, whilst retaining viability. This showcases the possibility of mimicking sarcopenia *in vitro* using C2C12 cells in a SF environment, which allows for the study of SEV in the absence of serum contaminating vesicles.

The sarcopenia model was validated by assessing changes in myotube diameter following DEX treatment. Diameter measurements showed DEX treatment reduced myotube diameter, and is a measure used to assess sarcopenia (Allen et al., 2021, Salvadori et al., 2020, Di Cesare Mannelli et al., 2020). Myotube diameter was the only method employed and alone it might not be sufficient to prove a sarcopenic phenotype was induced. For more robust validation of this model, additional assessment criteria should have been used to confirm sarcopenia induction. One such criterium is the measurement of the fusion index, which is the ratio of nuclei in myotubes compared to the total number of nuclei in the sample and can be assessed using immunocytochemistry (Bajaj et al., 2011). Furthermore, the absence or presence of skeletal muscle proteins could have been assessed. For example, the expression of myosin heavy chain and myogenin should be reduced whilst ubiquitin ligases atrogin-1 and MuRF1 upregulated (Kim et al., 2016, Nozaki et al., 2016). These validation methods are used to assess both sarcopenia and muscle atrophy, therefore it is difficult to soundly confirm sarcopenia was induced.

Glucocorticoid use is an inexpensive yet effective method of inducing sarcopenia in C2C12 myotubes and is often used to research this disorder. Many patients are commonly prescribed glucocorticoids to treat conditions such as arthritis and asthma, and muscle wasting is a common side effect of this medication (Sassoon et al., 2008). Despite this treatment causing atrophy, this effect would be observed in most individuals irrespective of age. Consequently, the use of DEX is not the most pathophysiologically relevant inducer of sarcopenia and in hindsight, it would be preferable to have used an alternative method to induce age associated muscle wasting.

Most alternative *in vitro* sarcopenia models use either murine C2C12 cells or rat L6 skeletal muscle cells, which are exposed to various substances, other than DEX to mimic the

conditions observed in sarcopenia. For example, an oxidatively stressed environment is associated with the onset of sarcopenia, therefore hydrogen peroxide (H_2O_2) treatment can be used to replicate this *in vitro* and induce sarcopenic characteristics via numerous mechanisms. (Fulle et al., 2004). Elevated oxidative stress in myotubes induces DNA damage which initiates the apoptotic programme, leading to a loss of muscle cells and mass (Siu et al., 2009). H_2O_2 has also been shown to increase ER stress, increase mitochondrial dysfunction and increase protein degradation via the activation of the UPS, all of which contribute to the development of a sarcopenic phenotype (Pierre et al., 2014, Fan et al., 2010, Kaur et al., 2019). Although H_2O_2 can replicate sarcopenia *in vitro*, this is to a certain extent as it only recreates the oxidative stress aspect of this condition and lacks others, such as the involvement of inflammaging and senescence on skeletal muscle (Mankhong et al., 2020).

Exposure of skeletal muscle cells to inflammatory cytokines is another sarcopenia model available for use *in vitro*. As older individuals experience age associated loss of muscle mass and function due to chronic low-grade inflammation, treatment with pro-inflammatory cytokines, such as TNF-α can model sarcopenia by incorporating inflammaging (Phillips and Leeuwenburgh, 2005). Like both glucocorticoids and H_2O_2, TNF-α treatment causes muscle atrophy by inducing protein degradation due to the upregulation of the activity of the ubiquitin ligases atrogin-1 and MuRF-1 (Li et al., 2005). High concentrations of this cytokine can also cause apoptosis of C2C12 myoblasts and L6 myotubes, another causative factor associated with sarcopenia (Sishi and Engelbrecht, 2011, Carotenuto et al., 2016, Marzetti and Leeuwenburgh, 2006). Though TNF-α treatment is an appropriate model due to high levels of this cytokine being linked to the development of sarcopenia, it does not feature other mechanisms of ageing associated with this condition, including mitochondrial dysfunction and senescence.

Furthermore, sphingolipid treatment, particularly the use of ceramides is also capable of inducing sarcopenia *in vitro*. Skeletal muscle tissue has been reported to accumulate ceramides with age and is an example of metabolic dysfunction during the ageing process (Al Saedi et al., 2022).. Ceramide treatment recreates muscle atrophy by increasing sarcoplasmic reticulum stress, autophagy, with ceramide C-2 specifically contributing to loss of muscle mass and strength by increasing oxidative stress, promoting mitochondrial fission and senescence (Russ et al., 2014, Smith et al., 2013, Jadhav et al., 2013). The ceramide model could be the most appropriate *in vitro* sarcopenia model as it combines multiple causative agents in one model compared to the models described above and is useful for the study of sarcopenic obesity, yet this model still lacks whole organism conditions, such as the influence of other tissues and the impact of inflammaging on skeletal muscle.

Despite the existence of numerous sarcopenia models, there are limitations associated with *in vitro* modelling when studying this muscle condition. *In vitro* models of sarcopenia often do not fully recreate the conditions of the cells in an individual suffering from sarcopenia. It is challenging to replicate the complex multifactorial nature of sarcopenia due to the difficulty of including all causative factors in one *in vitro* model. Results obtained from *in vitro* studies might not correlate to *in vivo* data, often a consequence of cultured skeletal muscle cells behaving differently to cells within an organism and will require confirmation using animal models and ultimately human studies.

h*In vivo* models are an improvement from *in vitro* systems, however these animal-based models also fall short of the real thing, with studies using human subjects with age-related sarcopenia being the most ideal method. Investigating this condition in sarcopenic individuals permits a whole organism approach, which recognises the effects of intrinsic and extrinsic factors, including the influence of other organs and tissues, the impact of diet and external environment on the development and progression of sarcopenia.

Whilst chemical inducers of muscle atrophy, including glucocorticoids and hydrogen peroxide can mimic sarcopenia *in vitro*, it is difficult to determine which stage of this condition cultured cells are in. Sarcopenia is categorised by three stages: presarcopenia, sarcopenia and severe sarcopenia, the clinical definitions of which are dependent on characterising muscle mass and physical performance (Santilli et al., 2014). An *in vitro* model such as is presented in this thesis cannot determine the extent of sarcopenia through the quantification of the aforementioned measures. Sarcopenia categorisation would instead be possible using *in vivo* models, such as senescence prone mice (SAMPs). Mice of the SAMP8 strain are in the presarcopenic stage at 8 months, whilst those aged 10 months are in the sarcopenic stage (Mankhong et al., 2020).

4.3.1.1 Modelling sarcopenia or muscle atrophy?

The sarcopenia model presented here might be cause for disagreement as it could be considered a model of skeletal muscle atrophy rather than sarcopenia. Both skeletal muscle conditions have similar characteristics, however sarcopenia is a form of muscle atrophy that is specifically associated with the ageing process, whilst muscle atrophy is the loss of muscle mass and strength which is not caused by ageing. This model of sarcopenia used DEX to induce muscle wasting and has also been employed by other studies to mimic sarcopenia *in vitro* and *in vivo* (Micheli et al., 2022, Di Cesare Mannelli et al., 2020, Felice et al., 2022, Kim et al., 2021, Baptista et al., 2013, Ouyang et al., 2022, Chiu et al., 2011). Furthermore, some molecular mechanisms are similar between muscle atrophy and sarcopenia, such as low

levels of the peroxisome proliferator-activated receptor γ coactivator *1a* and irisin (Cannavino et al., 2015, Qin et al., 2010, Yang et al., 2020, Chang and Kong, 2020).

A recent study evaluated whether the DEX induced muscle atrophy model can be used as an alternative to the aged animal sarcopenia models (Wang et al., 2023). Wang *et. al* compared 21-month-old naturally aged mice against DEX treated 3-month-old mice and discovered both groups shared comparable changes to their skeletal muscle, including decreased, fibre size, mass, and strength, as well the upregulation of genes associated with protein degradation and based on these findings the DEX model could be used as an alternative sarcopenia model, however when investigating sarcopenic molecular mechanisms caution is urged.

The use of glucocorticoids might not activate age-related processes that would constitute natural ageing and it is acknowledged that the model presented in this thesis might not be synonymous with sarcopenia but could be a model of muscle atrophy. This should be rectified in future investigations by substituting the DEX model for a more widely accepted sarcopenia model.

4.3.2 EV release by sarcopenic myotubes

Following development of a sarcopenia model, EVs produced by sarcopenic myotubes were characterised. Characterisation studies showed EV concentration did not differ when generated by normal or sarcopenic myotubes, however when concentrated and isolated via SEC, fewer SEV were measured compared to NEV. Following both the concentrating and SEC processes, the concentrations of both SEV and NEV were expected to be similar since this was observed in the unconcentrated secretomes. EVs could be lost during the SEC isolation process due to human error during the washing or fraction collection steps, for instance EVs might have been collected in the protein fraction, however it would be assumed this would influence NEV recovery in a similar manner. It is also possible that SEV might be more susceptible to aggregation during the concentration step, which can occur when using SEC, though this requires further investigation (van de Wakker et al., 2022). It is unknown why there is a clear difference between conditions following SEC but there is the possibility that there is no difference in the vesicle concentrations of concentrated normal and sarcopenic myotube secretomes, and further repetitions could confirm this hypothesis.

C2C12 numbers were controlled at the time of seeding, however it is difficult to comment on the number of cells present in the cultures following ITS differentiation and DEX treatment. During the differentiation process, multiple myoblasts fuse together to form a single myotube and this could alter the final cell concentration and consequently the EV count.

Both EV populations expressed the same EV markers, including tetraspanins, Alix and low levels of TSG101, suggesting the presence of exosome-like or small vesicles and was also evidenced in H_2O_2 treated myotube-derived EVs which were also isolated by ultracentrifugation (Guescini et al., 2017). Calnexin protein expression was low, suggesting high purity of the EV preparations. However, this contrasts with the Picca *et al.* study, which found CD63 and CD9 expression to be lower in individuals with sarcopenia and frailty, whilst CD81 expression was unvaried (Picca et al., 2020). Though this study also isolated EVs using ultracentrifugation for proteomic analysis, the difference in findings could be due to Picca *et al.* isolating circulating vesicles rather than those specifically produced by skeletal muscle.

There is conflicting evidence regarding EV release during sarcopenia. Hudson *et al*. showed DEX induced sarcopenia in C2C12 myotubes did not modify EV release compared to untreated myotubes (Hudson et al., 2014). This was also confirmed by Guescini *et al*. which found oxidative stress did not increase EV release or change vesicle size by C2C12 cells (Guescini et al., 2017). In contrast, Picca *et al.* have demonstrated increased levels of small EVs in the circulation of older sarcopenic and frail individuals (Picca et al., 2020). This investigation assessed EV release in elderly human adults, whilst the aforementioned studies were conducted *in vitro* using the murine C2C12 cell line in which sarcopenia was chemically induced and this could account for the disparity in the EV numbers reported. Overall, increased EV release by sarcopenic muscle is expected as a mechanism to expel damaged cellular components from the cell to minimise existing damage.

With regards to the current study, whilst EV release did not change under sarcopenic conditions, EV content was most likely modified. Sarcopenic myotubes might produce fewer or in the case of this study a similar number of EVs as normal myotubes but could preferentially package specific cargo into the EVs. Therefore, EV concentration might not be the crucial factor in the development and progression of sarcopenia, and rather vesicle content is of importance.

Despite particle concentration being similar between normal and sarcopenic myotubes (2000*xg* secretome), differences were observed in EV uptake by macrophages. Fewer SEV were internalised by J774 macrophages, whereas NEV were more readily incorporated into the immune cell. Skeletal muscle EVs have been shown to be taken up by other tissues, including the lungs, liver and heart (Aswad et al., 2014), however there is little information available regarding the mechanism of internalisation or EV uptake during muscle pathologies. Although fewer SEV were internalised in this study, it is possible that particle number is not the crucial factor but rather their contents. A high rate of SEV uptake by macrophages might

not be required as the selective packaging of cargo could be sufficient to elicit a response, however the role of particle dose must be considered when explaining differences in the uptake data in addition to other functional results discussed in subsequent sections.

A limitation of the work presented in this chapter is the lack of particle dosage measurements. The numbers of normal and sarcopenic particles used to treat both myotubes and macrophages were not identified prior to the commencement of functional experiments. Therefore, it is possible there were differences in the dose of normal and sarcopenic particles delivered to recipient cells, which could have impacted recipient cell behaviours and ultimately the end results. Despite there being no significant difference in concentration between the 2000*xg* secretomes, normal and sarcopenic particle numbers changed following the ultrafiltration concentrating step, which might have resulted in recipient cells being treated with more normal EVs than sarcopenic. As a result, it cannot be fully confirmed whether the effects observed when treating macrophages with either type of particle are true effects or a consequence of different EV doses.

The fluorescent labelling of EVs with BODIPY was used to assess the uptake ability of macrophages following co-culture with NEV or SEV. Uptake data show fluorescence values were reported for both sets of EVs at each time point, which is suggestive of the EVs being internalised by macrophages. However, the robustness of these data could be improved by measuring the MFI of macrophages in the absence of vesicles to determine the background fluorescence level and MFI values greater than this would prove EVs were phagocytosed by the macrophages. Furthermore, fluorescence labelling of the EVs does not indicate they were true EVs, since BODIPY as a lipophilic dye and will stain any particle with a lipid component (Marcu et al., 2020). Therefore, it is possible BODIPY labelled cell fragments or other non-EV lipid containing particles, which could have been internalised by the macrophages instead. Proteomic analyses of NEV and SEV show expression of the exosomal markers CD9, CD81, CD63, TSG101 and Alix, which would suggest the particles stained by BODIPY are EVs (Picca et al., 2020). The proteomic data showing the presence of EV proteins could have been supported with morphological evidence using cryo-EM to image the vesicles.

4.3.2.1 SEC-ultrafiltration EV isolation

Multiple methods can be combined to isolate and concentrate EVs derived from cell culture supernatants. Whilst SEC can increase the rate of EV recovery, a shortcoming of this method is that EV containing fractions are diluted when eluted from the column and necessitate an

additional step to re-concentrate the vesicles. For macrophage functional experiments, SEC isolation was combined with ultrafiltration to concentrate EVs. Following SEC, fractions 7 – 13 were pooled and concentrated using Amicon® 10 kDa centrifugal filter units with an Ultracel regenerated cellulose membrane. Concentrating EVs using ultrafiltration may result in loss of particles due to non-specific binding to the filter membrane, which can cause EVs to be trapped in the pores (Ramirez et al., 2018). The centrifugal filters used for concentration contain a membrane that is stated to limit non-specific protein binding and improved particle retention.

SEC isolation can maintain EV integrity; however it has been reported that this method can remove the protein corona surrounding the vesicles. SEC stripped human placental-derived stromal cell EVs of their protein corona, which prevented their angiogenic function. Upon re-establishing the corona, this EV function was restored (Wolf et al., 2022b). EV corona removal was also confirmed by Gomes *et al*., who ascertained protein recovery was lower in SEC isolated platelet-derived (Gomes et al., 2022). This finding implies the protein corona of NEV, SEV and later SenEV (results chapter 3) could have been removed by SEC prior to concentration, and this may have affected their ability to modulate macrophage function. Moreover, SEC can co-isolate unbound proteins with EVs and combining this method with ultrafiltration does not remove this material from the vesicle fraction (Kristensen et al., 2021). In contrast, plasma/serum EVs isolated by SEC and ultrafiltration have been shown to increase protein detection, were better at delivering packaged cargo but had a reduced signal during flow cytometric analyses (Tzaridis et al., 2021). Furthermore, comparison of SEC-ultrafiltration with ultracentrifugation has shown both methods isolated EVs the same proteomes, however SEC-ultrafiltration had a lower protein to vesicle ratio (Nordin et al., 2015). This study found ultracentrifugation isolated vesicles were prone to fusion and aggregation and this affected their *in vivo* distribution, an aspect that was not observed in SEC-ultrafiltration EVs.

These findings suggest that EV isolation and concentration methods should be considered depending on the aspect researchers wish to prioritise, for instance whether vesicle purity or integrity and functionality are more important.

4.3.3 The propagation of sarcopenia

Sarcopenia is a progressive disorder and in the absence of treatment skeletal muscle mass and function will steadily decline in affected adults. One explanation for the dissemination of this condition is the ability of sarcopenic muscle cells to confer a sarcopenic phenotype in healthy skeletal muscle tissue. Healthy myotubes exposed to sarcopenic myotube-derived

secretome exhibited signs of muscle atrophy, characterised by a reduced myotube diameter following treatment. This suggests the presence of a sarcopenic secretome in the vicinity of healthy skeletal muscle cells is sufficient to induce muscle wasting features in those cells. The bystander effect has already been implicated in the proliferation of senescence and it is also thought the presence of senescent cells in skeletal muscle tissue is responsible for the muscle atrophy associated with the development of sarcopenia. Section 5.2 assesses the senescence of myotubes by measuring $p16^{INK4a}$ expression, however expression of this cell cycle arrest protein was low. Despite this result, as discussed in the following chapter, senescent cells do not always express $p16^{INK4a}$ and so the sarcopenic myotubes could have a senescent phenotype; nonetheless other confirmation methods are needed to verify this.

The ability of existing sarcopenic cells to transfer sarcopenia to healthy tissue is likely a result of the components of the sarcopenic secretome. This secretome is complex and is comprised of many secretory components including myokines, EVs and microRNAs (miRNAs). Whist the current study did not investigate the role of miRNAs in sarcopenia, they are known to play a significant role in the regulation of skeletal muscle with many being involved in the myogenic process. This genetic material can be secreted alone or packaged into EVs to be delivered to recipient cells. Changes to secretion levels of miRNAs during ageing and pathophysiological skeletal muscle conditions can affect skeletal muscle mass. Rats with gastrocnemius muscle atrophy showed elevated levels of miR-29b and overexpression of this miRNA caused decreased myotube diameter in addition to reducing MyHC (Li et al., 2017). Furthermore, increased miR-29b has also been implicated in cachexia and ageing models (Li et al., 2017, Moraes et al., 2017). Whilst some skeletal muscle associated miRNAs are elevated during ageing and muscle atrophy, others are reduced. Although not investigated in the current study, research has shown DEX treatment of C2C12 myotubes can reduce their expression of miR23a (Hudson et al., 2014). miR-23a is associated with the regulation of the E3 ubiquitin ligases atrogin-1 and MuRF-1, which are involved in skeletal muscle protein degradation and ultimately muscle atrophy.

In addition to miRNAs, sarcopenic muscle can also secrete various proteins, including myostatin. Myostatin is a myokine and a member of the TGF-β super family which prevents myogenesis thereby limiting skeletal muscle hypertrophy (Chen et al., 2021a). However, during ageing expression of this protein can change. A cross sectional study comparing myostatin levels in healthy young and middle-aged adults with frail older adults found significant differences between the age groups. This comparison identified the elderly frail group as having the highest serum levels of myostatin and middle-aged adults had more than younger adults (Yarasheski et al., 2002). Furthermore, this team of researchers concluded

serum myostatin was inversely proportional to skeletal muscle mass. This is also supported by Bergen *et al*. who stated both healthy older women and older women with sarcopenia had higher circulating levels of myostatin than younger women (Bergen et al., 2015). However, this was only observed in women as older men displayed lower levels of myostatin than their younger counterparts. This suggests circulating levels of myostatin are likely to increase with age, yet this might be related to gender. Conflicting evidence has also been provided indicating there is no consensus regarding myostatin release during muscle wasting. Several studies found no difference in circulating myostatin levels between healthy older adults and those with sarcopenia (Tay et al., 2015, Hofmann et al., 2015). These contradictory findings suggest myostatin might not be the sole driving force for the development and progression of sarcopenia and that other factors are also involved. This theory is supported by myostatin inhibition experiments which report increased muscle mass, however myostatin blockade was not sufficient to restore muscle strength and function (Amthor et al., 2004, Rooks et al., 2020).

In addition to releasing soluble mediators, such as myostatin into their secretome, sarcopenic myotubes also produce EVs that can transport secreted components, which can affect myogenesis. Atrophic muscle in sarcopenia is likely to be under inflammatory conditions and will therefore secrete EVs carrying atrophy inducing factors to be delivered to healthy recipient muscle cells. This secretome facilitates the proliferation of sarcopenia within healthy skeletal muscle cells in a paracrine manner. For example, inflammatory myotubes have been shown to produce exosome-like vesicles containing myostatin, which upon uptake by healthy myoblasts were capable of inhibiting differentiation and promoted muscle atrophy (Kim et al., 2018). Unfortunately, myostatin was not detected in SEV by proteomic analysis, therefore it cannot be determined whether this protein was involved in inducing myotube atrophy.

ROS are also an important component of the skeletal muscle secretome with muscle cells generating high levels during normal function. However, this can be elevated in pathophysiological conditions as DEX treated C2C12 myotubes can significantly increase production of ROS (Chen et al., 2020). Raised levels of ROS in the secretome of sarcopenic myotubes is sufficient to induce atrophy in neighbouring healthy myotubes. Uptake of ROS by healthy myotubes causes changes to signalling pathways to stimulate the production inflammatory cytokines including TNF-α and IL-6, both of which promote muscle atrophy. Increased ROS production by sarcopenic myotubes can also reduce myotube diameter by enhancing muscle protein degradation by activation of MuRF-1 (Rodney et al., 2016, Qiu et al., 2018).

4.3.4 Sarcopenic secretome modulation of macrophage recruitment

Macrophages are involved in repair and regeneration during skeletal muscle damage and are essential for the maintenance of normal muscle function (Schilling, 2021). In addition to tissue resident macrophages, monocytes/macrophages must also be recruited from the circulation into the skeletal muscle tissue to support the reparative process. During ageing, the macrophage response is reportedly suppressed which promotes further damage and loss of muscle mass and strength.

Transwell migration data show whole unconcentrated sarcopenic secretome induced J774 macrophage migration to the same extent as the normal myotube secretome. Further investigation regarding the unconcentrated secretomes is required, as it is probable that there truly is a difference between normal and sarcopenic secretomes. In contrast, both SEV and SP were able to reduce total macrophage recruitment to a greater extent than normal secretome equivalents. In addition to the high error, the contrast between the unconcentrated sarcopenic secretome and the SEC fractions could be attributed to the presence of other mediators in the sarcopenic secretome, such as lipids that could counteract the anti-migratory effects of EVs and soluble proteins.

Surprisingly, the normal myotube secretome appeared to induce macrophage migration, which was an unexpected result, as under physiological conditions skeletal muscle does not have an immune presence except resident tissue macrophages. It might be suggested that the normal myotubes experienced injury, which caused increased macrophage recruitment, however these cells appeared undamaged and cell viability data show the myotubes to be metabolically active. Furthermore, it could also be concluded that in a high-density culture, as was the case with the normal myotubes, the presence of apoptotic cells induced macrophage migration. To eliminate the potential migratory effects of apoptotic cells, normal myotubes were washed to remove apoptotic cells from the culture prior to the generation and collection of a normal myotube derived secretome.

A horizontal migration platform was also employed to assess the ability of the sarcopenic myotube derived secretome to modulate macrophage migration. The horizontal Dunn chamber would have been the most ideal platform to investigate this, as it generates a true chemoattractant gradient, however, due to the limited mobility of the murine J774 macrophages this was not feasible. It is possible that the J774 cells were attempting to move from their point of origin but being firmly attached to the cover slip might have prevented any

noticeable migration. This “stickiness” could be alleviated in future by coating cover slips with fibronectin to help murine macrophage mobility (Digiacomo et al., 2017).

To counteract the stickiness of the J774 macrophages, THP-1-derived macrophage-like cells were utilised instead. THP/VD3 macrophage-like cells migrated further and faster in the presence of the unconcentrated sarcopenic secretome, however this was not directional migration. Similarly, the normal myotube secretome did not induce directional migration, which would be expected, as skeletal muscle in the absence of damage would not require a supplemented immune presence. It may be suggested that the use of cross species interaction in the horizontal migration platform could prevent recognition of murine bioactive molecules by human macrophage-like cells and therefore impair the results. However, recognition mechanisms are conserved across species, for example murine J774 macrophages recognise and tether human apoptotic Burkitt’s lymphoma cells for internalisation (Torr et al., 2012).

In both vertical and horizontal platforms, macrophage migration was not completely abrogated by the sarcopenic secretome, which is indicative of the involvement of multiple mechanisms in both macrophage recruitment and the inhibition of migration. The presence of certain myokines in the sarcopenic secretome might be responsible for the reduction of macrophage migration in the current study. The reduced macrophage migration observed with the SEC isolated sarcopenic components in the vertical assay and the unconcentrated sarcopenic secretome in the horizontal assay may be due to the presence of myokines. As mentioned previously, myostatin is a component of the sarcopenic secretome, which can prevent macrophage migration in addition to propagating the sarcopenia phenotype. Skeletal muscle potential to recruit reparative macrophages following injury in myostatin null mice is fully recovered to the levels observed in wild-type mice (McCroskery et al., 2005). However, the addition of recombinant myostatin to myostatin null mice negated this effect and reduced the chemotactic migration of macrophages into the muscle tissue (McCroskery et al., 2005). This is also corroborated with the use of a myostatin antagonist known as Mstn-ant1, which is a truncated form of myostatin. Siriett *et al*. inhibited myostatin activity in aged mice using Mstnant1, which rescued macrophage migration in treated mice (Siriett et al., 2007). Furthermore, macrophages isolated from Mstn-ant1 treated mice were observed to have better migratory potential than macrophages from control mice. It has been suggested myokines are transported in EVs and it is possible that myostatin could exert its inhibitory effects both in soluble form but also via vesicles.

Conversely, other mediators released into the secretome could be counteracting the effects elicited by myostatin. Mitochondrial dysfunction is implicated in ROS imbalance and is one of

the many causes of sarcopenia (Meng and Yu, 2010). The overproduction of ROS during sarcopenia can activate NF-κB signalling, which in turn activates the muscle inflammasome, which increases the release of pro-inflammatory cytokines, such as TNF-α, IL-6, IL-1 and IFNγ (Checa and Aran, 2020). These cytokines can encourage macrophage migration, but more importantly influence macrophage activation.

It is difficult to fully identify the factors that might be modulating macrophage migration towards normal and sarcopenic samples. The primary reason for this is that proteomic analysis was solely conducted on the EV fractions, therefore it cannot be determined which proteins present in the soluble protein fractions or the whole 2000*xg* were responsible for influencing migration. Regarding the proteomic data for NEV and SEV, calreticulin was identified in both samples, which could be functioning as a putative chemoattractant. Calreticulin is an “eat me” signal expressed on the surface of apoptotic cells and can mediate macrophage migration (Osman et al., 2017, Gold et al., 2010). Whilst cell viability of normal and sarcopenic myotubes was not reduced, it is possible that both cultures contained apoptotic cells that released small apoptotic bodies packaged with calreticulin, which acted as an inducer of migration. Though calreticulin in ageing conditions, calreticulin expression was higher in SEV compared to NEV (unpaired t-test, *$P< 0.05$), therefore increased macrophage migration towards SEV would be expected, though this was not the case. Furthermore, macrophage migration inhibitory factor (MIF) was also detected in both sets of EVs but had a greater level of expression in NEV (unpaired t-test, *$P< 0.05$). MIF can stimulate the migration of leukocytes and has been shown to promote macrophage chemotaxis in association with CD74 (Fan et al., 2010). This could be a possible explanation for the increased macrophage recruitment in response to NEV rather than SEV. However, in sarcopenic studies, MIF levels are higher in sarcopenic cohorts, which contradicts these data (Kwak et al., 2018).

Ideally, all components of the secretomes should be assessed for their protein content by MS and a supporting method, such as Western blot or ELISA. Furthermore, chemoattractants are not confined to the chemokine protein class but also consist of chemotactic lipids, including leukotriene B_4 (Iizuka et al., 2005). This lipid mediator can recruit multiple leukocytes, including and macrophage and has been found to be elevated in muscle atrophic conditions, however lipidomic profiling is required to confirm the production of leukotriene B_4 (Kim et al., 2022, Iizuka et al., 2005).

Ultimately, it is difficult to fully assess monocyte/macrophage infiltration of sarcopenic muscle in the present study as during ageing, skeletal muscle is influenced by systemic factors in addition to local intrinsic factors within the muscle tissue itself. Whilst skeletal muscle might

be attempting to repair myofiber damage during sarcopenia by recruiting reparative macrophages via its secretome, the age-associated chronic inflammation could be suppressing this attempt and further exacerbating the damage.

4.3.5 Sarcopenic regulation of macrophage respiratory burst

Due to the uncertainty surrounding macrophage recruitment to sarcopenic muscle, it is possible that the sarcopenic secretome specifically targets the effector functions of the pre-existing macrophages resident within the skeletal muscle instead. To ascertain this, the ability of sarcopenic myotube-derived secretome to modify respiratory burst function in macrophages was assessed. Immediate treatment with unconcentrated sarcopenic secretome had no effect on superoxide anion production and it was proposed that secretome mediators require time to exert their effects. In addition to this, it is likely that sarcopenic mediators do not operate on an all or nothing basis and rather elicit understated effects. To that end, the J774 macrophages were pre-treated with sarcopenic secretome prior to determining their respiratory burst activity in response to zymosan. Both normal and sarcopenic secretomes did not modify superoxide anion release compared to zymosan alone. It is possible that no effect was observed due to the secretomes not being sufficiently concentrated and potential results were masked. Subsequently, the separated EV and soluble protein components were individually tested, and differences were observed here. As expected, each normal secretome component reduced superoxide anion production, since in healthy undamaged, muscle inflammation is minimal and oxidative stress is tightly controlled. Conversely, SEV did not affect superoxide anion generation, however SP reduced respiratory burst activity. The cumulative effect of SEV and SP is incapable of minimising ROS release, possibly due to the presence of the EVs, yet when separated the reducing influence of the SP was finally observed. Despite the SP exhibiting an inhibitory effect on ROS production, this was not to the same extent as the normal secretome fractions, suggesting the sarcopenic secretome can contribute to local oxidative stress via macrophages.

The main source of macrophage-derived ROS is the NOX complex, which generates cytosolic superoxide anion during the oxidative burst. Following stimulation of macrophages, the various NOX subunits translocate to the plasma membrane and combine to form the complex (Jay Forman and Torres, 2001). The oxidative process can be triggered by numerous stimuli including pathogen associated LPS, damage associated molecular patterns such as DNA and nucleotides, cytokines (TNF-α and IFN-γ), ER stress, oxidised lipoproteins and the accumulation of unfolded proteins, which all promote the release of ROS in macrophages (Virág et al., 2019). Antioxidant enzymes are key to regulating the redox balance and protect

against oxidative stress. Superoxide dismutases are an important component of the antioxidant defence system and convert superoxide anion into H_2O_2, which itself can be broken down into either water and molecular oxygen by catalase or water or alcohols by glutathione peroxidase, both of which are also antioxidant enzymes (Birben et al., 2012, Shafiee et al., 2017). Non-enzymatic antioxidant molecules, such as glutathione and coenzyme 10 also contribute to the elimination of ROS by scavenging these species (Shafiee et al., 2017).

The complete sarcopenic secretome, specifically the vesicle portion may sustain the aged inflammatory muscle environment as it could contain pro-inflammatory cytokines. Consequently, it is likely that muscle derived cytokines are responsible for controlling macrophage respiratory burst. Elevated TNF-α levels in ageing skeletal muscle could promote its secretion in EVs and its release can activate macrophages to adopt a pro-inflammatory phenotype and generate ROS, including superoxide anion (GREIWE et al., 2001). It is difficult for superoxide anion to permeate cell membranes, but it and other exogenous ROS produced by macrophages can be internalised by adjacent muscle cells by transport through aquaporin channels (Bienert et al., 2007, Miller et al., 2010, Michaelson et al., 2013). Once inside the cell and combined with endogenous muscle ROS, macrophage-derived ROS can cause DNA damage, stimulate muscle protein degradation, oxidise amino acids and lipids, which prolongs sarcopenia (Lian et al., 2022). This macrophage response is also observed in the presence of IFN-γ. In addition to TNF-α, ageing skeletal muscle also has raised levels of IFN-γ, which could also be packaged into vesicles and secreted (Drummond et al., 2013). Like TNF-α, IFNγ also classically activates macrophages, which increases NADPH oxidase activity and stimulates oxidative burst to generate ROS (Hall et al., 2011).

The progression of sarcopenia appears to be associated with a concatenation of events, in which skeletal muscle inflammatory mediators released into the sarcopenic secretome induce ROS generation by macrophages, which perpetuates muscle damage and therefore maintains muscle wasting. Whilst this study has shown sarcopenic secretome is not efficient at recruiting macrophages, it has demonstrated that certain components of this secretome are capable of effecting other macrophage functions, such as their ROS producing ability. These data suggest that the sarcopenic secretome might exert its effects on the skeletal muscle resident macrophages rather than any infiltrating monocytes/macrophages.

4.3.6 Sarcopenia influenced macrophage polarisation

It is possible the secretome of sarcopenic myotubes can modulate macrophage function, such as migration and respiratory burst activity by influencing macrophage phenotype. This was tested both by determining the ability of the sarcopenic secretome to reduce the proinflammatory phenotype of M1 macrophages and by identifying secretome induced macrophage cytokines.

NF and both SR and SF were able to reduce NO_2^- production by LPS stimulated macrophages, whilst NR had no effect. The inability of the NR to minimise the M1 phenotype was unexpected, as a pro-inflammatory environment would not be found under physiological conditions, except in the case of acute muscle injury. Further investigation showed NEV and SEV limited macrophage NO_2^- release, whilst NP and SP did not. This highlights the individual effects of each component, as well as emphasising the different potencies of these fractions. For example, the strength of the NP is sufficient to nullify the anti-inflammatory effects of the NEV when both components are combined in the retentate.

Since inflammation has been linked to the development of sarcopenia, it was hypothesised that the sarcopenic secretome would induce the polarisation of M1 macrophages, however based on these data, it is implied that M1 phenotype dampening mediators are carried by both NEV and SEV. Despite both types of EV exerting a similar response on macrophage respiratory burst activity, there is a possibility that they elicit their effects in slightly different manners. By reducing NO_2^- release and therefore $^{\bullet}NO$ synthesis, the EV containing sarcopenic secretome could be supporting macrophages to adopt a more M2-like phenotype. A Taiwanese study comparing macrophage populations between young, middle-aged and older individuals reported those over the age of 65 (old) had a higher proportion of macrophages with an M2 signature in their skeletal muscle tissue than younger counterparts (Chen et al., 2021b). Furthermore, the older participants presenting with sarcopenia also displayed a higher level of TGF-β (Chen et al., 2021b). Therefore, it is possible that SEV might stimulate overproduction of M2 associated cytokines, including TGF-β. Unfortunately, the cytokine data in this chapter does not verify this, as macrophages treated with SEV or SP did not produce a detectable level of free active TGF-β.

Overall, very few cytokines were within the detectable range of this multi-plex cytokine assay and therefore it is likely that it was not of a sufficient sensitivity to measure low concentrations. Furthermore, the macrophage secretomes used in the multiplex cytokine assay were not concentrated prior to measurement. Consequently, the current study would benefit from

further investigation in which the macrophage secretomes are concentrated to increase the likelihood of cytokine detection, in addition to improving the sensitivity of the cytokine assay. It must also be noted that the measured cytokines were either undetected or at a very low level in the M2 control. The anti-inflammatory cytokines in particular were expected to be elevated in this sample, however their absence indicates the M2 control did not work and so these data must be interpreted with caution.

Despite most cytokines being below the detectable range, macrophage exposure to SEV and SP did stimulate the production of CCL22/MDC, although release of this cytokine was not a significant increase. Incubation with NP and SP induced the secretion of G-CSF, which is indicative of M2 macrophage polarisation and it has been suggested that there is a skewing of the macrophage population in aged skeletal muscle, with CD206+ M2 macrophages being the predominant phenotype in this tissue in older individuals, with their numbers increasing with age, whilst M1 macrophage numbers declined (Cui et al., 2019, Przybyla et al., 2006). Furthermore, M2 macrophages were also found to colocalise with intramuscular adipose tissue in ageing muscle. It is possible the accumulation of adipose tissue within skeletal muscle in the elderly facilitates the polarisation of M2 macrophages. Not all macrophage polarising signals are sourced from muscle cells but can originate from other cell types found within skeletal muscle. Adipocytes are also able to produce IL-4, IL-13, and adiponectin, all of which induce an M2 macrophage phenotype, which can contribute to the increased number of M2 macrophages in skeletal muscle (Kang et al., 2008, Mandal et al., 2011).

The notion of M2 macrophages being damaging and advocates of skeletal muscle atrophy can be considered as counterintuitive, as these macrophages are thought to minimise inflammation and promote muscle regeneration, however this M1 to M2 transition highlights macrophage dysfunction during ageing.

Macrophage G-CSF production could have been stimulated by the presence of factors in the SP component. For example, the cytokines IL-3, IL-17, IL-1 and TNF-α stimulate G-CSF release in immune and non-immune cells, and these could be present in the normal and sarcopenic protein components, yet this could not be confirmed using proteomic analysis as this was not conducted on the protein samples (Leizer et al., 1990). There is the possibility that G-CSF was already present within the protein fractions and was not macrophage derived. Skeletal muscle is a producer of G-CSF, with its release being triggered during tissue damage (Wright et al., 2015, Li et al., 2019). Again, G-CSF presence in the NP and SP samples could not be conducted, therefore it is unknown whether this cytokine was associated with these components and requires further investigation by undertaking MS analysis on all protein

fractions. Consequently, it cannot be completely established whether the G-CSF detected by LEGENDplex has originated from the muscle or macrophage secretomes.

In fact, there is little certainty that the cytokines within the detectable range were genuinely secreted by the macrophages rather than being introduced into the culture by the addition of the normal or sarcopenic EVs and proteins. With regards to the EV samples, the presence of these cytokines can be checked against the proteomic data. No pro- or anti-inflammatory cytokines were identified in the NEV or SEV proteomic analysis, which suggests they were of macrophage origin. It is possible that these cytokines might have been at too low a level to be detected by MS and this should be further verified by Western blot. The level of all cytokines tested should have been measured in the normal and sarcopenic secretomes prior to treating the macrophages. This would have allowed for background cytokine concentrations to be identified for the true macrophage-derived levels to be measured.

4.3.7 Ascertaining the sarcopenic EV proteome

4.3.7.1 Downregulated biological functions

Identifying the protein profile of SEV could provide an explanation for the functional effects elicited by this secretome component observed in earlier sections. For example, the secretion of exosomes was a biological function of interest, which was shown to be depleted. Downregulation of the exosomal secretion process is most likely responsible for the disparity in the number of vesicles released by sarcopenic myotubes and normal myotubes. SEV in this investigation were characterised as small EVs with a diameter less than 200 nm, therefore it is possible that most of the vesicles produced by sarcopenic myotubes are of endosomal origin. UniProt identified TSG101 as one of the proteins associated with the exosome production function. TSG101, a classical exosomal marker is involved in the ESCRT pathway and downregulation of this protein could prevent assembly of the ESCRT machinery required for exosome formation (Kowal et al., 2014, Théry et al., 2002). Consequently, it is possible that TSG101 expression in SEV is reduced, however this was not assessed in the current study. To confirm this, preferential loading of TSG101 into SEV could be measured by Western blot and compared to TSG101 expression in NEV. Similarly, programmed cell death 6interacting protein, alternatively known as Alix also participates in the ESCRT pathway and induces multivesicular body biogenesis in parent cells (Iavello et al., 2016). Syntenin-1 was the third protein connected to the exosomal secretion function and has been suggested as a putative universal exosomal marker (Kugeratski et al., 2021). Syntenin-1 mediated exosome generation requires interaction with Alix for intraluminal budding of the endosome membranes,

highlighting the importance of both proteins in this process (Baietti et al., 2012). Combined downregulation of all 3 proteins in sarcopenic myotubes would interfere with normal exosomal production and secretion, resulting in depletion of this function, as reflected in the SEV proteome.

The generation of new skeletal muscle tissue was another biological function found to be more depleted in SEV than in NEV. Skeletal muscle differentiation was downregulated and insulinlike growth factor-binding protein 5 (IGFBP-5) was mapped to this process. IGFBP-5 is a multifunctional protein that regulates the bioavailability of IGFs. In elderly women, serum levels of IGFBP-5 have been shown to decrease and this can limit the action of IGF-1 (Mohan et al., 1995). Human bone cells treated with DEX resulted in reduced IGFBP-5 protein levels, mimicking the ageing data (Mohan et al., 1995). A decrease in IGF-1 activates catabolic pathways and prevents skeletal muscle protein synthesis, thereby facilitating muscle atrophy (Yoshida and Delafontaine, 2020, Ahmad et al., 2020). The reduced release of sarcopenic EVs packaged with IGFBP-5 would explain the reduced myotube diameter of normal myotubes exposed to vesicle containing sarcopenic myotube-derived 2000*xg* whole secretome. However, normal myotube treatment with isolated SEV alone would confirm this hypothesis.

In addition to increased muscle atrophy with sarcopenia, sarcopenic muscle also loses its ability to protect itself from excessive oxidative stress associated with ageing process due to a decline in antioxidant enzymes (Cesare et al., 2020). MS data showed the response to ROS was more depleted in SEV and the protein associated with this downregulation was peroxiredoxin-1 (Prx-1). Prx-1 belongs to a family of antioxidant enzymes that are responsible for reducing hydrogen peroxide into water (Poole et al., 2011). Antioxidant enzymes, including Prx-1 can be loaded into EVs and be transported to recipient cells to scavenge ROS and RNS, however it is possible that sarcopenic myotubes do not have sufficient Prx-1 for use as EV cargo or they prevent the selective packaging of Prx-1 into vesicles for delivery (Bodega et al., 2019, Soleti et al., 2012). Since SEV do not minimise superoxide anion production by macrophages, as shown by the respiratory burst data, this free radical can be readily converted into hydrogen peroxide. With downregulation of Prx-1, as reflected by the SEV, excess hydrogen peroxide originating from either macrophages or sarcopenic muscle is not being neutralised due to the insufficient functioning of the antioxidant system. This would allow ROS to persist in the muscle microenvironment and promote tissue damage.

The negative regulation of the transcription factor NF-κB was also depleted in SEV and therefore reflects the processes occurring in the sarcopenic myotubes. Ubiquitin carboxylterminal hydrolase CYLD (CYLD) was mapped to this biological function and this protein is responsible for inhibiting the nuclear translocation of NF-κB and its subsequent

activation. Consequently, CYLD can modulate numerous NF-κB regulated processes, including inflammation and the innate immune response (Takami et al., 2007). Therefore, preventing the activity of CYLD can activate NF-κB and upregulate the expression of pro-inflammatory cytokines, including TNF-α, IL-6 and IL-1β (Zhang et al., 2018). By downregulating CYLD, sarcopenic myotubes could be promoting the prolonged release of pro-inflammatory mediators by both muscle cells and macrophages, causing damage and atrophy of muscle fibres, thereby maintaining sarcopenia.

Surprisingly, proteins linked to the negative regulation of monocyte chemotaxis were depleted in SEV. Due to reduced murine macrophage migration towards SEV, as observed in the transwell migration assay, SEV were expected to have increased expression of anti-migratory proteins. However, gremlin-1, a cytokine that prevents monocyte adhesion to endothelial cells, leukocyte recruitment and monocyte to macrophage differentiation was found to be downregulated, which does not correlate with the migration data presented in this chapter (Müller et al., 2014). Furthermore, gremlin-1 has been suggested as a candidate gene for lean body mass, which is a predictor of sarcopenia, yet the gremlin-1 protein was not shown to be highly expressed in SEV (Hai et al., 2012). Despite SEV reducing macrophage migration, it was not completely inhibited. This would suggest the depletion of gremlin-1 in sarcopenic myotubes promoted some macrophage recruitment.

There is a possibility that the depletion of gremlin-1 by sarcopenic myotubes is related to skeletal muscle regeneration following injury rather than monocyte migration. Gremlin-1 has been shown to be involved in the myogenic process as its expression is elevated during muscle repair and is localised to newly formed muscle fibres (Fabre et al., 2020). Gremlin-1 regulates skeletal muscle differentiation by facilitating satellite cell differentiation and limiting their renewal and return to a quiescent state (Fabre et al., 2020). Consequently, the downregulation of gremlin-1 diminishes the regenerative capacity of skeletal muscle, which prevents muscle repair and maintains tissue damage associated with sarcopenia.

4.3.7.2 Upregulated biological functions

Certain biological functions were also found to be more enriched in SEV than NEV. Regulation of TGF-β receptor signalling was upregulated in these vesicles and the protein mapped to this process being protein-lysine 6-oxidase, also referred to as lysyl oxidase (LOX). LOX regulates collagen deposition and ECM formation, therefore is actively involved in tissue remodelling during skeletal muscle regeneration following injury (Smith-Mungo and Kagan, 1998, Kagan and Li, 2003). This enzyme controls fibrogenesis through the modulation of TGF-β signalling, as LOX directly binds TGF-β and dampens its signalling (Atsawasuwan et al., 2008). However, during persistent inflammation such as the chronic form associated with ageing and sarcopenia, LOX expression remains elevated (Kagan, 1994, Cai et al., 2017). As a result,

this enzyme continuously activates fibroblasts to generate excessive amounts of matrix proteins, leading to tissue fibrosis (Mesarwi et al., 2015). Pathological upregulation of LOX allows this enzyme to maintain elevated TGF-β expression instead of limiting its secretion, as observed in atrophic muscle (Barry-Hamilton et al., 2010, Burks and Cohn, 2011). Selective packaging of LOX into SEV facilitates the replacement of healthy muscle with fibrotic tissue and could cause the propagation of sarcopenia, which reduces muscle function. Although, not detected in this study, elevated LOX could also induce macrophages to overproduce TGF-β, which could also contribute to a fibrotic muscle phenotype.

LOX activity is also associated with ROS release, as H_2O_2 is generated as a by-product during the reactions catalysed by this enzyme (Valls-Lacalle et al., 2022). Overexpression of this enzyme promotes ROS generation and is supported by the luminometry data which shows SEV treatment was unable to reduce superoxide anion production by LPS primed macrophages (Valls-Lacalle et al., 2022). Additionally, upregulation of LOX activity, as observed by proteomic data of SEV, increases collagen deposition, fibrosis and ultimately ECM stiffness (Desguerre et al., 2012). Intramuscular fibrosis is a characteristic of sarcopenia and a stiffened environment has been shown to promote the polarisation of macrophages into the M2 subset (Brack et al., 2007). This is supported by the NO_2^- data presented in this chapter, as SEV treatment with LPS stimulated macrophages reduced NO_2^- production by these phagocytes and thus their pro-inflammatory phenotype. Furthermore, M2 polarised macrophages exhibit increased expression of LOX, therefore it is possible that SEV associated LOX stimulates further LOX activity in macrophages which results in more ROS production and fibrosis (Takemoto et al., 2021).

Furthermore, LOX expression has been shown to induce macrophage migration. Glioblastoma cells upregulate LOX expression and preferentially secrete this enzyme which functions as a chemoattractant and recruiter of macrophages to the tumour site and is suppressed with LOX inhibition (Chen et al., 2019). Unfortunately, this was not observed in the migration data presented in this chapter. This effect may be confined to tumour associated macrophages only and might not translate to macrophages in the sarcopenic condition.

Leukocyte migration was another biological process upregulated in SEV, specifically the protein aminoacyl tRNA synthase complex-interacting multifunctional protein 1 (AIMP1). The role of this cytokine is to promote the expression of pro-inflammatory proteins in monocytes and macrophages, such as the chemokine MCP-1 (Ko et al., 2001). The expression of pro-inflammatory genes suggests AIMP1 induces the polarisation of M1 macrophages and has been observed in microglia. AIMP1 has been reported to activate microglia and increase the expression of M1 markers, including CD68, IL-1β, TNF-α and IL-6, whilst downregulating the expression of the M2 marker, CD206 in order to promote inflammation (Oh et al., 2022). Due

to its pro-inflammatory function, it would be assumed AIMP-1 would also promote ROS release as M1 macrophages are prolific producers of ROS, which would be supported by the luminometry data as SEV did not limit superoxide anion production of M1 polarised macrophages. The macrophage cytokine data in this chapter is inconclusive and does not confidently suggest the polarisation state of macrophages exposed to SEV to support the findings of the Oh *et. al*. AIMP1 also has a pathological role as lung cancer and renal disease patients also diagnosed with muscle wasting both exhibited upregulated levels of AIMP1, which was mapped to an increased inflammatory response, including regulation of the defence response and increased leukocyte infiltration (Aniort et al., 2019). Macrophage recruitment was stimulated in the presence of SEV in the transwell migration platform, though not equivalent to that of NP. This supports the finding of reduced gremlin-1 expression which is an inhibitor of monocyte migration, such that the elevation of one protein and depletion of the other possibly account for the macrophage recruitment observed in the presence of SEV. Physiologically, EVs are not secreted in isolation and are a component of a complex secretome which includes soluble mediators and other factors. The whole sarcopenic secretome did not induce significant macrophage migration, which suggests the soluble components could sufficiently override AIMP1 function in SEV.

Additionally, proteins associated with the negative regulation of the oxidative stress response were also upregulated. One such protein mapped to this process is core histone macro-H2A.1 (mH2A1). This protein is involved in transcriptional repression as it inhibits NF-κB binding (Angelov et al., 2003). The inactivation of NF-κB by mH2A1 can have an antioxidant effect through the prevention of NOX2 subunit gene transcription and the subsequent production of superoxide anion (Anrather et al., 2006, Lingappan, 2018). However, mH2A1 is not solely a repressor, it is also associated with the active transcription of some genes and so its function is deemed to be contradictory (Recoules et al., 2022). The contradictory role of mH2A1 is most likely a consequence of the existence of 2 isoforms which have opposing functions. Isoform 1 increases the expression of the extracellular antioxidant enzyme superoxide dismutase 3 (SOD3), which catalyses the conversion of superoxide anion free radical into hydrogen peroxide and water, whilst isoform 2 represses the activity of this enzyme (Dardenne et al., 2012). Consequently, mH2A1 can both promote and assuage oxidative stress. As the respiratory burst results suggest SEV are incapable of limiting superoxide anion production by pro-inflammatory macrophages, mH2A1.2 could be the upregulated isoform due to its SOD3 suppressing ability, thus contributing to persistent oxidative stress. Unfortunately, the FunRich 3.1.3 GO analysis does not provide mH2A1 isoforms, therefore the specific isoform detected in SEV can only be speculated.

Other immune response functions were also enriched in SEV, such as macrophage activation involved in inflammatory response and positive regulation of the TLR4 signalling pathway, arising from an upregulation of LPS-binding protein (LBP) expression. Due to endotoxemia, circulating levels of LPS are elevated in elderly individuals with muscle wasting and it is thought that LPS may be involved in the development of sarcopenia (Ghosh et al., 2015). LBP is required for LPS mediated activation and internalisation of the macrophage pattern recognition receptor, TLR-4 (Tsukamoto et al., 2018). Positive TLR-4 signalling induces macrophage activation, polarisation to the M1 subset and the production of pro-inflammatory cytokines, triggering the inflammatory response (Lu et al., 2008). LBP-LPS binding of TLR-4 also activates the NOX enzyme in M1 macrophages and stimulates the generation of ROS, leading to oxidative damage (Hsu and Wen, 2002). This LPS mediated activation of M1 macrophages also induces both migration and phagocytic processes in these immune cells, however this was not observed in the migration data presented in this chapter (Ostareck and Ostareck-Lederer, 2019). Whilst SEV did recruit macrophages in the transwell system, fewer migrated compared to the normal secretome components. LPS was absent from these *in vitro* cultures, which could account for the limited migration that would be seen in *in vivo* sarcopenia models. The continuous presence of LPS in the plasma combined with the selective release of LBP by sarcopenic myotubes via EVs contributes to the chronic low-grade inflammation observed in the elderly and possibly maintains the activation of pro-inflammatory macrophages in circulation (Minihane et al., 2015). Furthermore, SEV-derived LBP mediated LPS activation of skeletal muscle TLR-4 could promote muscle protein degradation by activation of the ubiquitin proteasome system (Doyle et al., 2011). Consequently, SEV could cause muscle atrophy, as shown by the reduced myotube diameter via the bystander effect when released as a component of the sarcopenic muscle secretome.

Of the depleted and enriched proteins discussed in this section, it was hypothesised that cytokines would also be mapped to certain biological processes, however these proteins were not detected by MS analyses. Several reasons could account for the absence of cytokines from the list of identified proteins. Firstly, massively represented proteins might prevent the ability to detect small soluble proteins, such as cytokines by MS. Furthermore, despite the absence of cytokines in EVs, as suggested by the proteomic data, it does not indicate that they were not secreted into the vesicles. Cytokines might be packaged into EVs by both normal and sarcopenic myotubes and exhibit biological activity yet remain undetected. For the detection of cytokines in the secretome of healthy and aged myotubes, more sensitive MS instrumentation is likely required. Additionally, cytokines could be associated with the EV protein corona, which is formed on the surface of vesicles (Nguyen and Lee, 2017). It is possible that the protein corona could be lost during the many processing steps involved in

the preparation of samples for MS analyses, resulting in the dissociation of cytokines from the EVs, which leads to their absence from the vesicle proteome.

A final comment must be made regarding the quality of GO annotations used to map up- or downregulated proteins to biological processes. GO annotations can be limiting as databases such as UniProt link proteins to generic and sometimes vague functions, which can make it difficult to identify exactly how a certain protein is involved in the process it has been mapped to.

4.3.7.3 Cellular compartments and reactome pathways

Several up- and down-regulated GO terms associated with cellular compartments and reactome pathways were selected due to their relevance to skeletal muscle function. For instance, “H zone”, “filamentous actin”, “asymmetric synapse” and “muscarinic acetylcholine receptors” are involved in muscle contraction and expression of proteins assigned to these categories was reduced in SEV. A consequence of sarcopenia is a loss of muscle strength and function that in part can be attributed to a reduction in structural proteins, such as actin and myosin (contained within the H zone), which are required to generate power for contraction (Kaasik et al., 2007, Lang et al., 2010). Muscle innervation is also essential for contraction and deterioration of the neuromuscular junction during ageing is a cause sarcopenia, which could be attributed to reduced expression of proteins associated with “asymmetric synapse”, “muscarinic acetylcholine receptors” and upregulation of “HDACS deacetylate histones” proteins, that are also elevated in the muscle of aged mice (Bao et al., 2020, Walsh et al., 2015).

Several signalling pathways were downregulated in SEV, including “Wnt signalosome”, “insulin receptor signalling cascade” and “PI3K cascade” and are involved in skeletal muscle repair and cell growth. Contrasting results were observed in a study of plasma EVs isolated from frail individuals, in which KEGG analysis identified the ageing related insulin signalling, PI3K-Akt and FoxO pathways to be elevated (Ipson et al., 2018). It should be noted that the Ipson study investigated frailty associated circulating EVs and used an alternative EV isolation method (ExoQuick) compared to this study, which might account for differences in findings. Protein synthesis is related to muscle growth and repair facilitated by the aforementioned signalling pathways. Downregulation of those pathways could have increased expression of proteins linked to the “Cul4-RING E3 ubiquitin ligase complex”, which is supported by Cul4 expression also being higher in older slow muscle fibres and UPS proteins being more abundant in an aged undernourished rat model of sarcopenia (Murgia et al., 2017, Barbé et al., 2022). Unlike the findings of Ipson *et al*., increased signalling of the IGF-1-PI3K-Akt pathway prevents the expression of atrophy inducing ubiquitin ligases thus inhibiting protein degradation (Sandri et al., 2013a).

The oxidative stress response was also found to be downregulated in SEV, as the "detoxification of ROS" and "peroxisomal matrix" categories were depleted. Proteomic analysis of sarcopenic rats has shown elevated expression of antioxidant enzymes to compensate for the increased oxidative stress, however it is unknown which enzymes were expressed (Chin et al., 2009). This contradicts a study using a mouse model of sarcopenia, which discovered that despite catalase and glutathione peroxidase gene expression being higher in sarcopenic animals, enzyme activity of these antioxidants was lower (Sullivan-Gunn and Lewandowski, 2013). Excess ROS release could have caused DNA damage, as "oxidative stress induced senescence" was upregulated in SEV, which links to the next results chapter. ROS induced DNA damage could have elevated the "ATR-ATRIP complex", which controls DNA repair mechanisms following damage. Though not a study involving proteomics, Muzembo *et al.* found oxidative DNA damage markers to be higher in elderly individuals with low grip strength (Muzembo et al., 2014).

ROS release can be stimulated by inflammatory cytokines, which is associated with the development of sarcopenia. Inflammatory pathways, "TLR4 cascade" and "IFN-γ signalling" were highly enriched in SEV compared to NEV, suggesting sarcopenic myotubes had adopted an inflammatory phenotype. Gene set enrichment analysis of different modes of skeletal muscle atrophy has shown IL-6 production, acute inflammatory response gene categories to be upregulated in DEX treated and aged mice, however it is unknown whether this was translated at the protein level (Hunt et al., 2021). This is supported by pro-inflammatory proteins that are responsible for activating NF-κB were elevated in ageing muscle contributing to chronic inflammation, however this study used elderly participants that did not present with sarcopenia (Ubaida-Mohien et al., 2019).

Intramuscular fibrosis is a component of sarcopenia, and several fibrotic categories were elevated in SEV. ECM related categories "matrilin complex" and "collagen type IV trimer" were enriched. Matrilin is known to induce collagen accumulation and collagen type IV deposition significantly increases in aged muscle as shown by murine proteomic analysis (Alonso et al., 2023, Lofaro et al., 2021). Coupled to the increase in fibrotic potential, SEV were depleted of proteins involved in "hyaluronan uptake and recycling". Hyaluronic acid supports skeletal muscle repair by promoting cell proliferation and protecting the tissue against oxidative stress thus reducing muscle atrophy, and this ability is limited as reflected by SEV (Stellavato et al., 2020).

Disrupted energy metabolism is another characteristic of muscle ageing, and supplementation with L-carnitine can increase muscle mass and limit atrophy. Unexpectedly, "carnitine metabolism" was upregulated in SEV, however this is contradicted by a study that found serum levels of this amino acid derivative to be lower in sarcopenic individuals (Takagi et al., 2022).

Increased release of proteins related to carnitine metabolism in SEV could have limited the transport of long-chain fatty acids to mitochondria for energy production in sarcopenic myotubes, however the sarcopenic myotube proteome would need to be analysed to confirm a difference between cell and EV expression.

Surprisingly, the “autophagosome” category was upregulated in SEV, which is unusual as the autophagy pathway is defective in sarcopenia leading to mitochondrial dysfunction, protein aggregation and eventually muscle atrophy (Carnio et al., 2014). It is unknown as to why sarcopenic myotubes would preferentially package autophagy related proteins into EVs, though it is possible that the excessive release of these proteins via vesicles reduces their abundance in cells, causing dysregulation of this pathway, though further work is required to confirm this hypothesis.

A cross sectional study of serum proteins from individuals with early sarcopenia showed enrichment of protein-lipid complexes and EVs in the cellular component category, whilst KEGG pathway analysis identified differentially expressed proteins were involved in growth hormone production and arachidonic acid metabolism, suggesting sarcopenia might be associated with dyslipidaemia (Wu et al., 2022). Unlike the current study, Wu *et al*. presented the top 20 significant results and used KEGG analysis, which comprises of broader terms compared to reactome pathways which uses more detailed entries. Furthermore, the Wu *et al*. study did not state whether serum proteins were in soluble form or EV associated.

It is difficult to make direct comparisons to other studies since very few have undertaken functional enrichment analysis of EVs specifically isolated from sarcopenic muscle tissue, with most if not all analysing EVs derived from plasma. Consequently, most comparisons were made against proteomic data of sarcopenic cells rather than EVs produced by these muscle cells. Whilst it is assumed that EVs reflect their parent cell it is difficult to ascertain this without having the corresponding sarcopenic myotube proteome to support this.

4.3.8 Future work

This investigation used DEX to model sarcopenia which could be considered as physiologically irrelevant. Despite being used by other researchers to mimic sarcopenia, DEX is thought to induce muscle atrophy instead. Future work concerning the molecular mechanisms governing the development of sarcopenia should use a model that is truly associated with the natural ageing process, such as aged mice models or the use of pro-inflammatory cytokines which are linked to the inflammaging process.

As mentioned in section 4.3.2, particle dosage measurements were not undertaken to ensure similar numbers of normal and sarcopenic EVs were delivered to recipient cells. This is a crucial step in the experimental process and should have been performed for robustness of

data. To prevent inconsistencies and potential differences in experimental results in future, TRPS analysis or other quantitative techniques, such as total protein via Western blot should be employed to confirm the particle amount delivered in a set volume and furthermore use these data to ensure the same dosage is applied when giving either normal or sarcopenic vesicles. This will also account for any differences in the total number of particles generated by either normal or sarcopenic myotubes between replicate experiments.

This study has only identified the SEV associated proteome whilst the remainder of the secretome also requires proteomic analyses. Although the skeletal muscle secretome has previously been elucidated, a comprehensive investigation of the sarcopenic secretome has not been conducted. A systematic review has identified a list of proteins that are differentially expressed in healthy and diseased skeletal muscle, some of which are associated with muscle atrophy (Florin et al., 2020). Despite the existence of this protein list, the secretome of sarcopenic myotubes generated using a SF system requires further investigation, as it is possible that this could be subtly different to the secretome obtained from a serum containing muscle model. Furthermore, the sarcopenic secretome consists of many factors, of which only the proteins have been explored. Consequently, the lipid mediators and genetic material, such as miRNAs produced as components of the secretome should also be considered.

Systemic chronic inflammation is associated with the development of sarcopenia and most studies regarding this muscle disorder determine the relationship between circulating levels of cytokines and other inflammatory mediators with loss of muscle mass and function (Dalle et al., 2017, Tuttle et al., 2020). Consequently, it is difficult to comment on specific elements of the sarcopenic secretome in mediating macrophage function specifically. Whilst blockade of pro-inflammatory cytokines, including TNF-α and IL-6 has shown to alleviate sarcopenia and prolong survival, it is not known whether this is targeting serum cytokines or those produced by sarcopenic skeletal muscle (Sciorati et al., 2020, Tsujinaka et al., 1996). Therefore, it is imperative to determine the sarcopenic secretome to better understand the role of atrophic muscle derived myokines in the development and progression of sarcopenia.

5. Results Chapter 3 – The effect of senescent skeletal muscle on macrophage function

5.1 Introduction

During both development and repair following injury, skeletal muscle undergoes myogenic differentiation to generate new muscle tissue either for growth or to replace damaged tissue (Rudnicki et al., 2008). The final stage of myogenesis is the morphological differentiation of single cell myoblasts into multinucleated myotubes, a process facilitated by cell fusion (Okazaki and Holtzer, 1966). These myotubes are terminally differentiated cells and are under cell cycle arrest, unresponsive to growth factors. It was previously thought that terminally differentiated cells were unable to experience cellular senescence due to their post-mitotic identity, however this school of thought is now being reconsidered. Despite being distinct from senescent cells, terminally differentiated cells, including neurons and adipocytes have been shown to develop senescent characteristics despite their inability to proliferate (Jurk et al., 2012, Minamino et al., 2009).

Cellular senescence is a biological process in which cells undergo cell cycle arrest triggered by intrinsic or extrinsic factors, such as oxidative stress, irradiation, telomere shortening and inflammation (McHugh and Gil, 2018). Once cells have committed to the senescent programme, they will adopt a senescent phenotype, which includes morphological and functional changes, such as a flattened spread shape and the release of pro-inflammatory cocktail of factors known as SASP (Kwon et al., 2019, Hernandez-Segura et al., 2018).

In healthy tissues, the short-term presence of senescent cells activates a beneficial senescent program, which promotes the recruitment of macrophages by SASP components to the site of cellular senescence, thus enabling interaction between senescent cells and the innate immune system. Macrophage infiltration allows for the identification and removal of senescent cells from affected tissue (Irvine et al., 2014). Studies suggest that once at the site of senescence, infiltrating macrophages clear senescent cells and drive tissue remodelling by facilitating the growth of skeletal muscle precursor cells to regenerate the injured tissue (Serrano, 2014). Conversely, in ageing tissue, senescent cell removal and subsequent repair processes may be impaired. Possible rationale for this outcome in aged skeletal muscle could be due to compromised macrophage recruitment and the persistence of senescent cells.

The key to furthering understanding concerning the driving force behind inadequate immune cell recruitment and insufficient senescent cell clearance is the senescent skeletal muscle secretome. A well-known product of senescent cells is the SASP, which is largely comprised of soluble mediators, however EVs are now thought to be another key component of the senescent secretome (Takahashi et al., 2017, Lehmann et al., 2008). EV content is

determined by the parent cell, however in a senescent environment, EVs secreted by senescent cells contain a modified cargo that can further exacerbate pathophysiological conditions. Due to phenotypic and functional changes in senescent cells, it is likely that their senescent EV cargo is also modified to reflect these alterations (Takasugi et al., 2017, Kavanagh et al., 2017). Senescent cell-derived EVs in conjunction with the soluble factors of the SASP may be involved in the propagation of senescence, the development of chronic inflammation and the failure of damage repair (Acosta et al., 2013, Weiner-Gorzel et al., 2015, Borghesan et al., 2019).

This chapter aims to investigate cellular senescence as another cause of skeletal muscle ageing, with a focus on the effects of senescence on muscle health. Firstly, this section will describe the development of an EV-free senescent murine skeletal muscle model using the healthy model established in chapter 3. As investigated in the sarcopenia chapter, this chapter will also determine the paracrine effects of the senescent muscle secretome and derived components, specifically on healthy skeletal muscle cells. Lastly, in addition to the local impact, the influence of senescent skeletal muscle on macrophage effector functions will also be explored to better understand the role this cellular interaction may play in the persistence of a damaged skeletal muscle phenotype in an aged setting.

5.2 Results

5.2.1 Development of a murine skeletal muscle model of senescence

Having established a healthy skeletal muscle model in chapter 3, this was used to develop a senescent model of skeletal muscle ageing in addition to the sarcopenia model. Senescence was induced in normal skeletal muscle myotubes by treatment with increasing concentrations of the chemotherapy agent etoposide. Etoposide induces senescence by creating breaks in double stranded DNA and by preventing topoisomerase II mediated DNA repair (te Poele et al., 2002). The accumulation of DNA damage causes cell cycle arrest and consequently cells become senescent. Senescent myotubes were identified by positive senescence-associated beta-galactosidase (SA-β-gal) activity, a known marker of cellular senescence. Positive SAβ-gal activity presented itself as a blue stain.

Figure 57 displays the levels of SA-β-gal activity in etoposide treated myotubes, with blue staining. In the absence of etoposide, minimal SA-β-gal activity was detected. The presence of positive blue staining was not concentrated in the normal myotubes but was confined to areas outside of the myotubes. This trend was also observed at a low etoposide concentration, as 5 μM etoposide treated myotubes showed SA-β-gal activity restricted to non-myotube areas. Increasing the etoposide concentration to 10 μM induced changes to the myotubes. This is the first concentration at which senescent myotubes were observed, as sections of the treated cells were shown to stain blue. Myotubes were also found to have a senescent phenotype with 20 μM etoposide, however an increase in drug concentration resulted in fewer myotubes in culture. Doubling the etoposide concentration to 40 μM exhibited some SA-β-gal activity, however this was confined to small thin myotubes. This high concentration was cytotoxic to some myotubes, as the remaining cells adopted a rounded morphology with many detaching from the growing surface. The highest etoposide concentration of 80 μM was toxic to all cells, as no myotubes were present and the culture largely consisted of cell corpses and debris.

As well as inducing sufficient myotube senescence, the chosen etoposide concentration had to be deemed non-toxic to the skeletal muscle cells. To determine the cytotoxicity of the various etoposide concentrations, the metabolic activity of treated myotubes was tested using MTT assay, to be used as an indirect measure of cell viability (figure 58). Lower concentrations of etoposide (5, 10 and 20 μM) maintained a similar cellular metabolic activity and therefore myotube viability as that observed in the absence of etoposide. However, etoposide concentrations greater than 20 μM, significantly reduced myotube metabolic activity compared to the untreated cells. 80 μM etoposide was the most cytotoxic concentration, due to its ability to reduce myotube metabolic activity by approximately half that of the non-senescent cells.

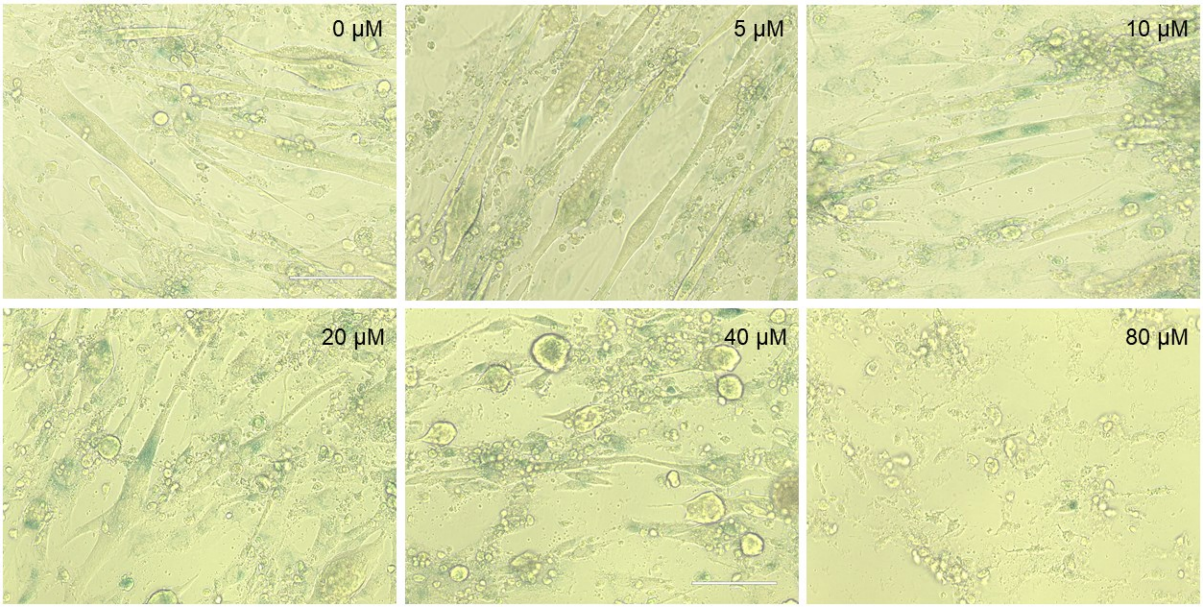

Figure 57. Senescence-associated beta-galactosidase activity of etoposide treated normal myotubes. Healthy myotubes were treated with increasing concentrations of etoposide (0, 5, 10, 20, 40 and 80 µM) for 24 hours. After treatment, cells were stained for SA-β-gal activity and imaged using bright field microscopy (40x magnification, scale bar = 100 µm) to identify an optimum etoposide concentration for senescence induction. Images shown are representative of the different etoposide concentrations used.

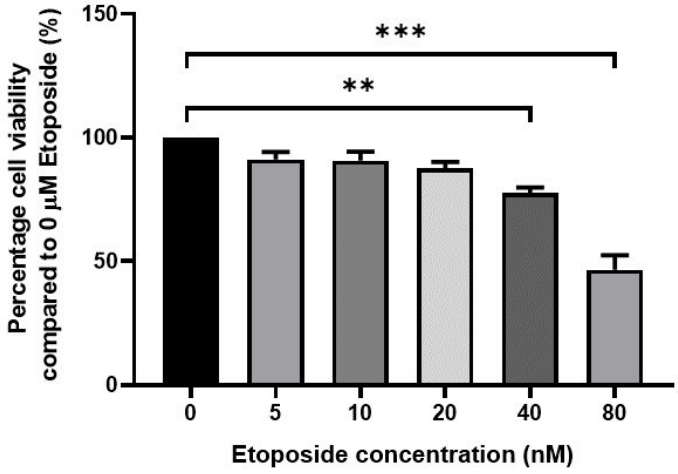

Figure 58. Myotube metabolic activity following treatment etoposide treatment. Normal C2C12 myotubes were treated with 0, 5, 10, 20, 40 and 80 µM etoposide for 24 hours. 24 hours post treatment, an MTT assay was conducted on the myotubes to indirectly determine cell viability and the minimum cytotoxic concentration of etoposide. 0 µM treated myotubes are shown to have 100% cell viability and all other etoposide concentrations compared to this. Data shown are mean ± SEM of 3 independent experiments, one-way ANOVA with Dunnett's *post-hoc* test, ***P<0.005* and ****P<0.0001*.

In addition to SA-β-gal activity and cell viability, the extent of senescence in etoposide treated myotubes was also determined by measuring $p16^{INK4a}$ protein expression, a known senescence marker. $p16^{INK4a}$ expression was also established in DEX treated myotubes to

elucidate whether sarcopenic myotubes also had a senescent phenotype (figure 59a). Whilst Western blot data show separation of various proteins, the protein bands for $p16^{INK4a}$ were very faint, suggesting low expression of this protein across all etoposide and DEX treated myotubes.

The band corresponding to the 10 μM etoposide treated myotubes appeared to be the most intense, whilst the 80 μM etoposide band was absent from the blot, indicating no expression, which was also mirrored in the sarcopenic myotubes (10 μM DEX). The amount of $p16^{INK4a}$ expression was quantified by performing densitometry analysis on the Western blots (figure 59b). Protein expression in the etoposide and DEX treated myotubes was compared to expression in the untreated control, which was given a density of 1.0. $p16^{INK4a}$ expression of myotubes treated with 5, 20, 40 μM etoposide and 10 μM DEX did not differ from the negative control, indicating minimal senescence induction. Conversely, the middling etoposide concentration of 10 μM displayed increased $p16^{INK4a}$ density, whilst expression for the highest concentration of 80 μM etoposide was significantly lower than the untreated myotubes.

The SA-β-gal activity, cell viability and $p16^{INK4a}$ expression results were used to identify an optimum etoposide concentration for myotube senescence induction and the development of a senescent skeletal muscle model. Taking both data into consideration, it was determined that 10 μM etoposide was the optimal concentration for the induction of cellular senescence, as it could stimulate SA-β-gal activity and induce $p16^{INK4a}$ expression to an extent whilst sustaining myotube viability. This concentration was used to produce senescent myotubes for all subsequent functional investigations.

Despite the interpretations made from both the Western blot and densitometry data, it must be noted that it is difficult to fully comment on $p16^{INK4a}$ expression for each concentration due to the absence of a loading control. In future, this Western blot would be repeated with the addition of an appropriate loading control such as β-actin.

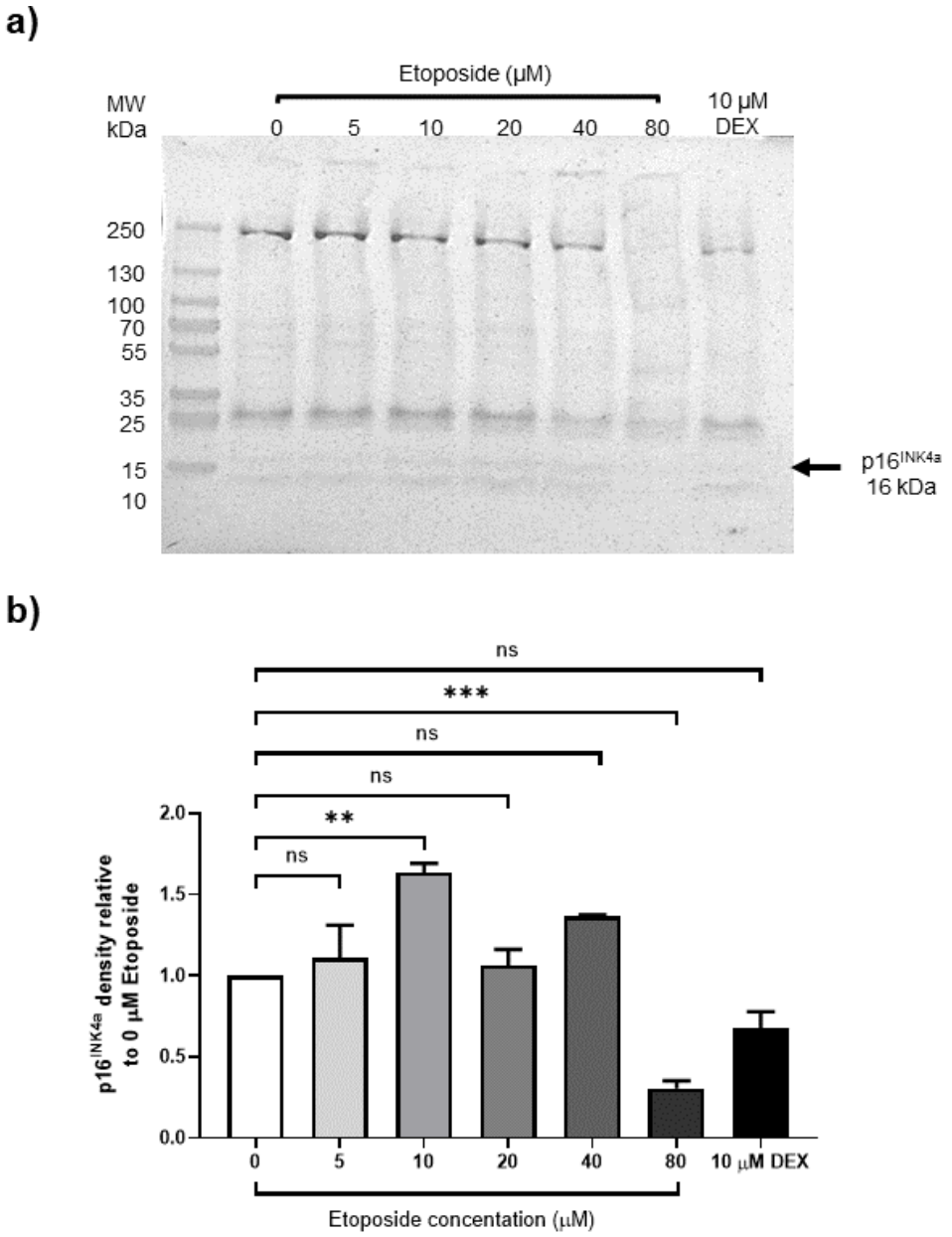

Figure 59. p16^{INK4a} expression of etoposide treated myotubes. C2C12 myotubes were treated with increasing concentrations of etoposide and the expression of senescent protein marker p16^{INK4a} was determined using SDS-PAGE. Western blot shown is representative of treatment conditions used (a). p16^{INK4a} protein quantification via densitometry analysis (b). Data shown are mean ± SEM of 3 independent experiments, one-way ANOVA with Dunnett's *post-hoc* test, ***P<0.005* and ****P<0.001*.

5.2.1.1 Characterising senescent myotube-derived EVs

As EVs are an element of the secretory profile of senescent cells, it was necessary to characterise the particles derived from the various forms of the senescent myotube secretome tested in subsequent functional assays. The whole 2000*xg* myotube secretomes were the first to have their EV populations defined, and this revealed the particle concentrations in both normal and senescent secretomes to be the same (figure 60a). Admittedly, there is a high

degree of error between experimental repeats and potential differences in the number of particles between the two secretomes could be made more evident with additional repeats. With regards to EV size, 2000*xg* normal and senescent myotube secretomes contain EVs of a similar size with both corresponding to the small EV class of particles (figure 60b).

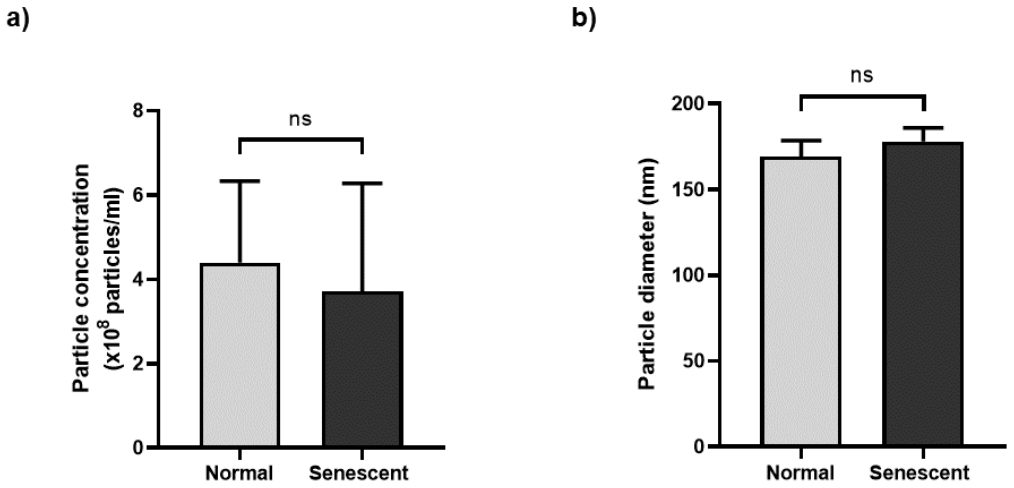

Figure 60. The characterisation of particles contained in whole senescent myotube secretome. TRPS analysis was used to count the number of particles in whole 2000*xg* normal and senescent myotube-derived secretomes (a) and to measure particle size (b). Data shown are mean ± SEM of 3 independent experiments, Welch's t-test. Particle concentration *P = 0.8516* and particle diameter *P = 0.5314*.

The EV containing retentates of the concentrated myotube secretomes were also analysed for EV concentration and size. Both concentrated normal and senescent secretomes produced a similar amount of EVs (figure 61a). It is most likely that there is a difference in the number of particles and further repeats are required to differentiate. The particle number indicates the spin filters were successful in concentrating the EVs from the 2000*xg* secretomes into the retentates, as the concentrations increased from hundreds of millions of particles/ml to billions of particles/ml. Regarding EV size, both NR and senescent myotube retentate (SenR) consisted of EVs of a similar diameter (figure 61b). The diameter of the two EV populations was less than 200 nm, which indicates these particles correspond to the small EV class and indicates the enrichment process did not affect their size.

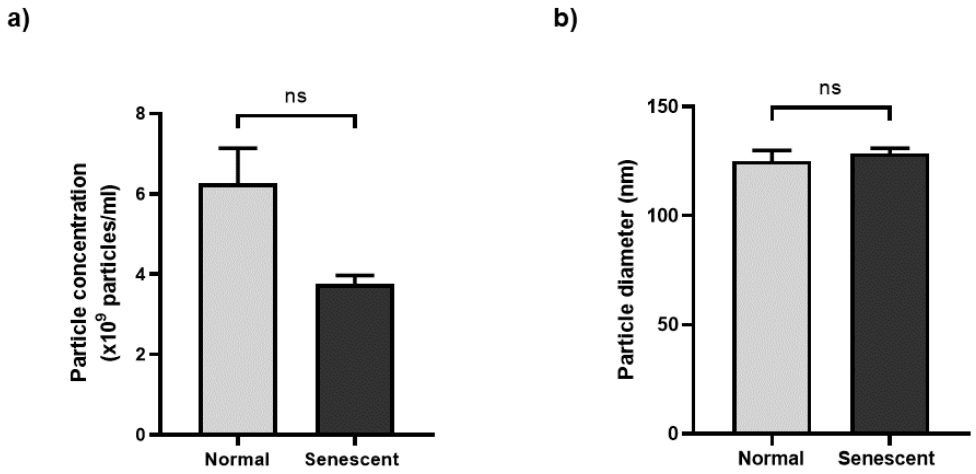

Figure 61. Particle characterisation of particles in concentrated senescent myotube secretome. Normal and senescent myotube 2000*xg* secretomes were concentrated using 30 kDa spin filters to produce retentate and filtrate fractions. The retentate fractions were measured for particle concentration (a) and size (b) using TRPS analysis. Data shown are mean ± SEM of 3 independent experiments, Welch's t-test. Particle concentration *P = 0.0982* and particle diameter *P = 0.5789*.

The 30 kDa retentates were used to extract the EV and soluble protein components of the secretome via SEC. The SEC isolated EV fractions derived from normal and senescent myotubes were further concentrated and characterised for concentration and size. However, due to difficulties arising with the operation of the TRPS qNano machine, only one repeat of EV measurement was undertaken. Assessing the data at face value suggest there are more senescent EVs (SenEV) than NEV in the SEC fractions, however it is difficult to comment on this with only a single experiment conducted (figure 62a). Though only a single repeat, these data show particle concentration remained in the billions of particles/ml region, like the 30 kDa concentrated retentates. EV diameter did not differ between the two EV populations, with their size being like the EVs in the 30 kDa retentate shown in figure 59b (figure 62b). Despite these initial interpretations of the data, further repetitions of this experiment are required to confirm these observations. Further characterisation was undertaken by assessing the abundance of EV marker proteins on ultracentrifuged vesicle samples (figure 62c). Both EV types expressed the exosomal markers CD81, CD63, CD9 and Alix, with CD81 expression being greater in SenEV than NEV. Neither showed high abundancy of TSG101 or calnexin.

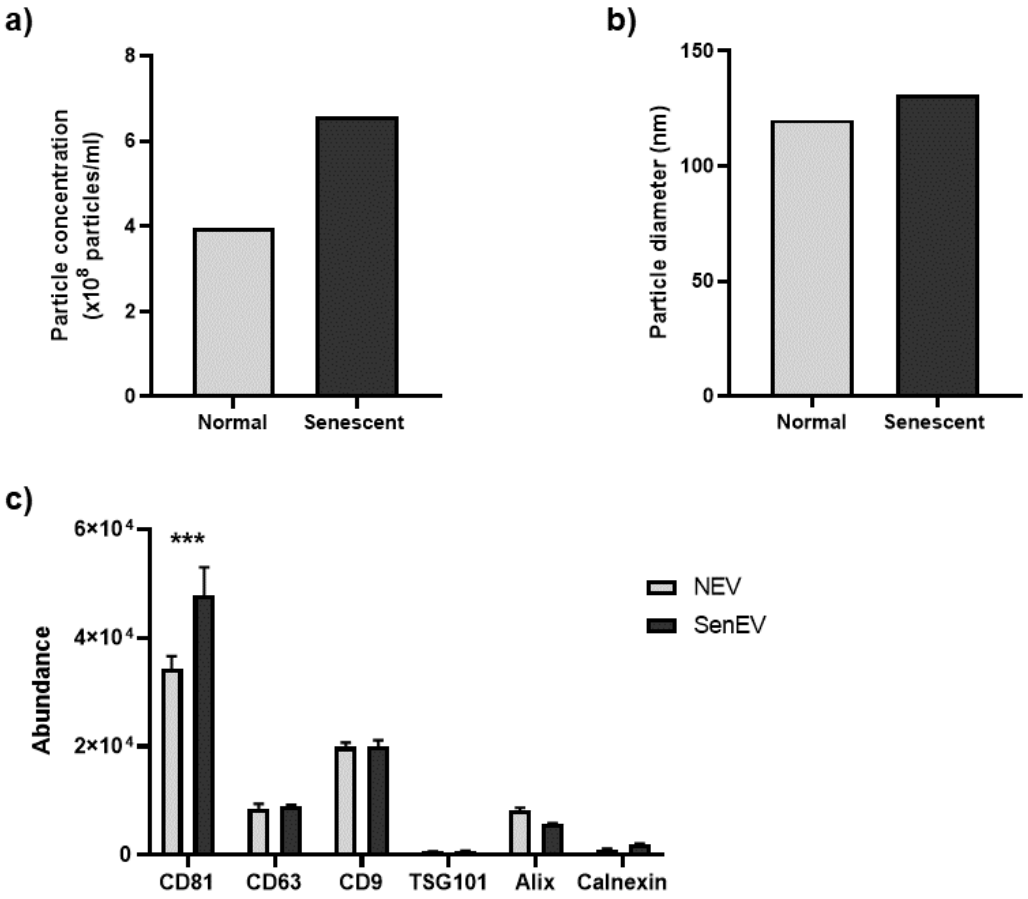

Figure 62. Characterisation of SEC isolated particles from senescent myotubes. Particles were separated from concentrated senescent myotube secretomes using SEC and particle concentration (a) and diameter (b) were measured using TRPS analysis, data shown are of 1 independent experiment. EV associated protein expression was also assessed on ultracentrifuged EVs (c), data shown are mean ± SEM of 3 independent experiments, two-way ANOVA with Sidak's *post hoc* test, ****P<0.0001*.

Having characterised SenEV based on their concentration and size, it was also necessary to determine the ability of recipient cells to internalise these particles. The functional effects of SenEV as a component of the skeletal muscle SASP can only be identified if they are successfully taken up by the cells they are intended to influence, such as macrophages. To ascertain this, NEV and SenEV were stained with the fluorescent dye BODIPY, after which the stained EVs were incubated with J774 macrophages for various time points. At the chosen time points, external fluorescence was quenched to only permit macrophage intracellular fluorescence and therefore internalised vesicles to be measured by flow cytometry. Fluorescence was reported as median fluorescence intensity as shown in figure 63.

J774 macrophages increasingly internalise NEV up to 40 minutes, after which the rate of uptake slows down and plateaus for the next 3 hours and 20 minutes. However, after 24 hours EV uptake increased to its highest point. A similar increase in vesicle incorporation was observed with SenEV, with maximum uptake observed after 24 hours of incubation with

macrophages. It is not known whether EV uptake would continue to rise for both samples after 24 hours as fluorescent measurement was halted at this point. For most time points, EV internalisation was the same for both NEV and SenEV, the exception being at the 20 to 40 minute time point during which fewer SenEV were internalised by macrophages than NEV.

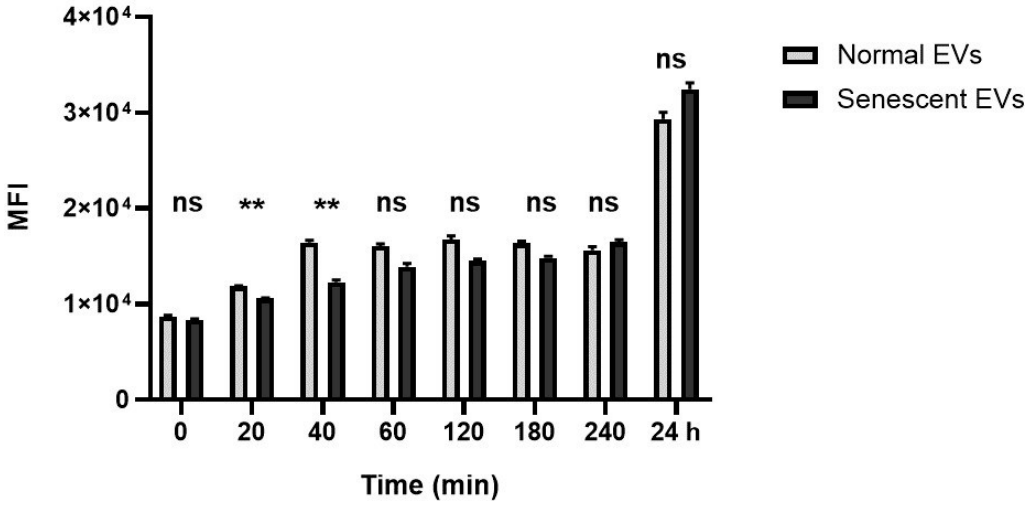

Figure 63. The uptake of senescent myotube-derived EVs by murine macrophages. BODIPY labelled normal and senescent EVs were incubated with J774 macrophages for 0, 20, 40, 60, 120, 180, 240 minutes and 24 hours. At each time point, extracellular fluorescence was quenched using trypan blue and internal fluorescence (MFI) measured by flow cytometry. Data shown are mean ± SEM of 3 independent experiments, two-way ANOVA with Sidak's *post hoc* test, ***P<0.005*.

5.2.2 The paracrine effects of whole senescent myotube secretome on healthy skeletal muscle cells

Studies have shown senescent cells to amass within numerous areas of the body and that this accumulation is responsible for the development of senescent tissue. The presence of senescent skeletal muscle cells facilitates the propagation of tissue senescence by stimulating healthy bystander cells to adopt a senescent phenotype (da Silva et al., 2019).

This part of the investigation aims to confirm the results of existing studies whilst using a SF model of skeletal muscle senescence. To this aim, normal myotubes were treated with the 2000*xg* secretome isolated from senescent myotubes and the development of senescent characteristics was identified. Exposing normal myotubes to the SASP containing secretome resulted in changes to cell morphology. These myotubes ceased to exist as long, thick branching cells, as seen on day 0 but instead exhibited increased thinning and shortening compared to untreated cells (figure 64). Furthermore, the overall health of the normal myotube

culture 24 hours post treatment appeared to be compromised, due to the rounded appearance and detachment of many cells.

To confirm the thinning effect of the senescent secretome, both the diameter and surface area of the normal myotubes were measured (figure 65). Figure 65a shows the myotube diameter of treated cells to be identical to that of the untreated myotubes on the day of treatment (day 0), whilst the diameter is significantly reduced following the addition of the senescent 2000*xg* secretome (day 1). This was also observed with surface area measurement, in which the senescent myotube secretome reduced the cell surface area of healthy myotubes 24 hours post incubation more than normal secretome (figure 65b).

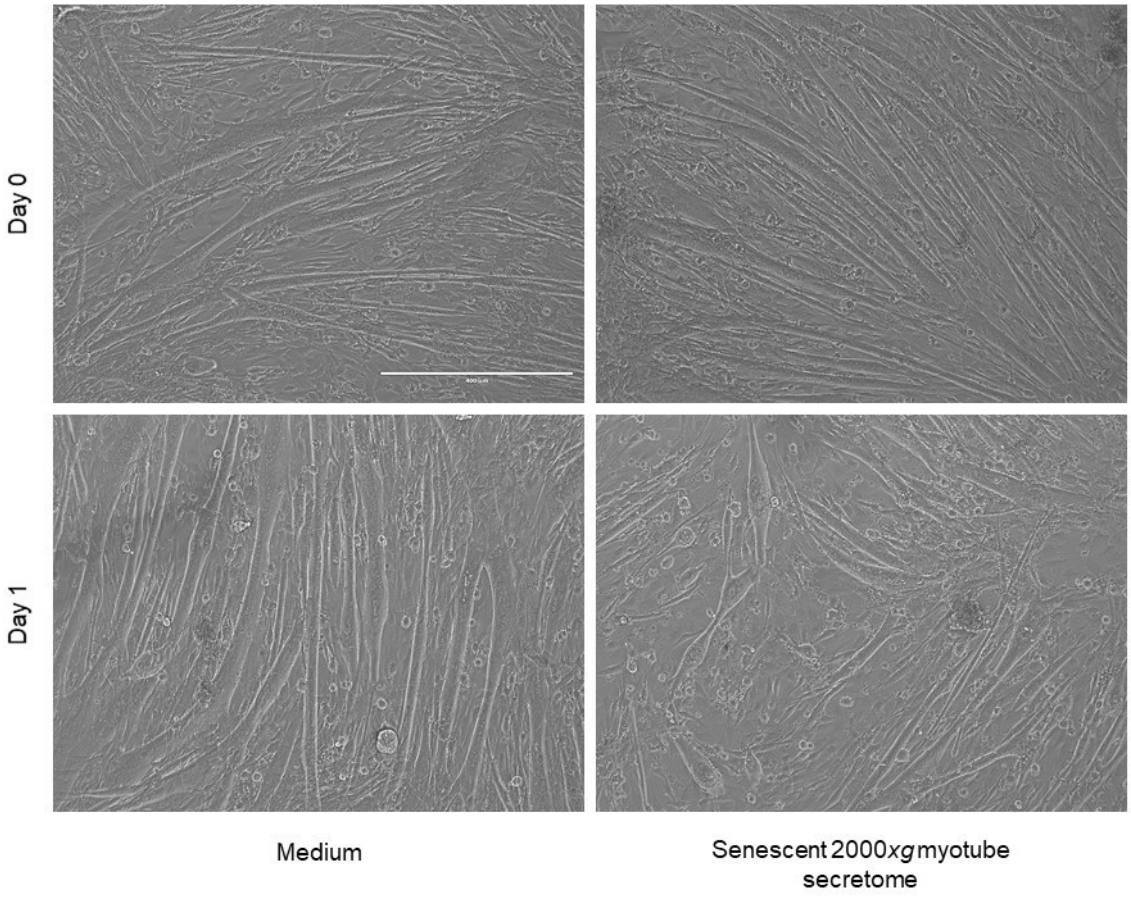

Figure 64. The bystander effect of senescent myotube-derived secretome. Representative phase contrast images (10x magnification, scale bar = 400 µm) of normal myotubes treated with the 2000*xg* secretome of senescent myotubes for 24 hours. Images were taken on the day of secretome exposure, designated day 0 and 24 hours post treatment, designated day 1.

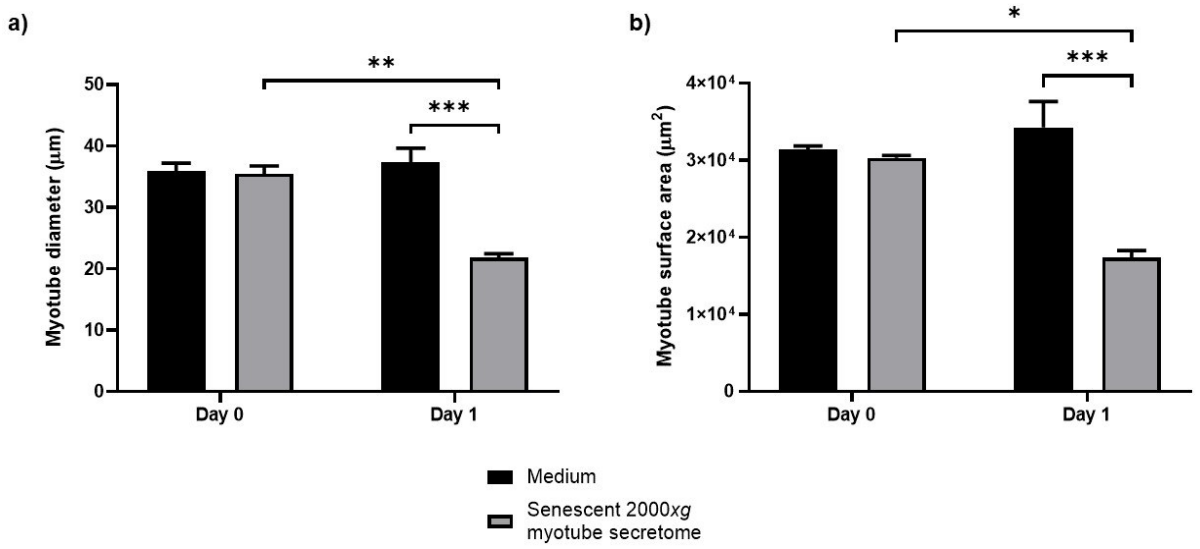

Figure 65. The ability of SASP containing 2000*xg* senescent secretome to induce myotube atrophy. Phase contrast images of myotubes treated with senescent myotube derived 2000*xg* secretome were measured for their diameter (a) and surface area (b) using ImageJ software. Data shown are mean ± SEM of 3 independent experiments, one-way ANOVA with Dunnett's *post-hoc* test, ***P<0.005* and ****P<0.0001*.

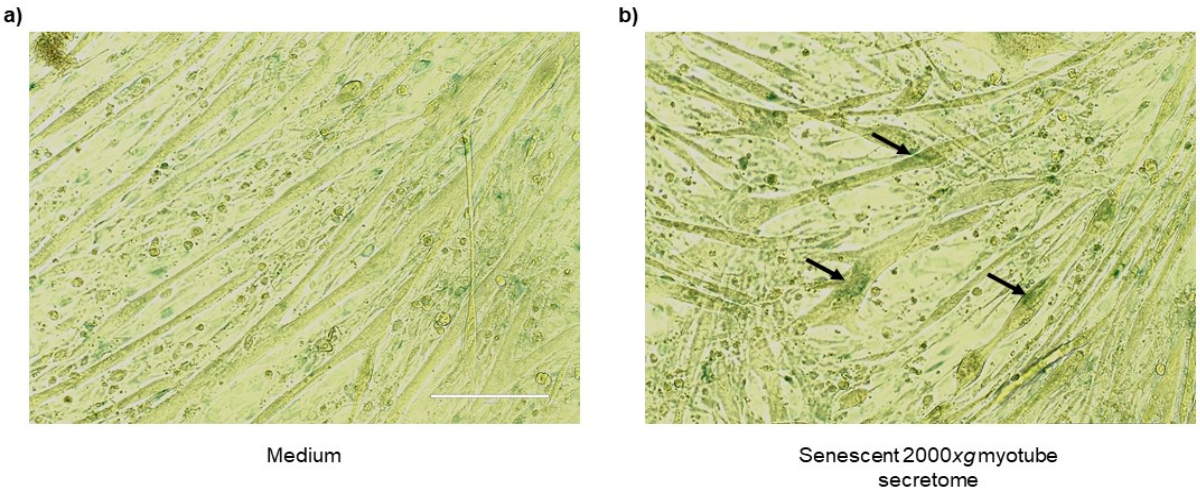

Figure 66. SA-β-gal activity of bystander myotubes treated with senescent myotube secretome. Following incubation with medium (a) or senescent 2000*xg* myotube secretome (b) for 24 hours, normal myotubes were stained SA-β-gal activity and imaged using bright field microscopy (10x magnification, scale bar = 400 µm). Images shown are representative of the treatment conditions used and black arrows signify areas of positive blue staining.

To further confirm the ability of the senescent myotube-derived 2000*xg* secretome to induce senescence in bystander myotubes, the SA-β-gal activity of treated cells was also determined. Figure 66 shows blue staining localised on myotubes exposed to the SASP containing senescent secretome. These data in conjunction with the diameter and surface area results suggest the healthy normal myotubes have adopted a senescent phenotype.

5.2.3 The migratory potential of senescent myotube-derived secretomes

5.2.3.1 Vertical migration – transwell assay

As discussed in section 4.2.4.1, vertical migration platforms are commonly used to assess the migratory potential of samples. The transwell system was also employed to determine the ability of senescent myotubes to induce the directional migration of J774 murine macrophages.

Senescent and normal myotube-derived 2000*xg* secretomes, which are complete secretomes containing both EVs and soluble mediators such as proteins, were the first to be tested. Both secretomes were added to the upper chamber of the transwell platform and the number of macrophages migrating to the underside of the permeable membrane and to the bottom of the transwell companion plate were counted.

Figure 67 displays the results for the underside of the transwell membrane. The images show Jenner-Giemsa stained macrophages adhered to the membrane in the presence of normal and senescent 2000*xg* secretomes (figure 67b and 67c), with an approximately similar number of cells recruited through the membrane pores. This was confirmed by the macrophage counts, which indicated the chemotactic potential of the two secretomes was identical (figure 67d).

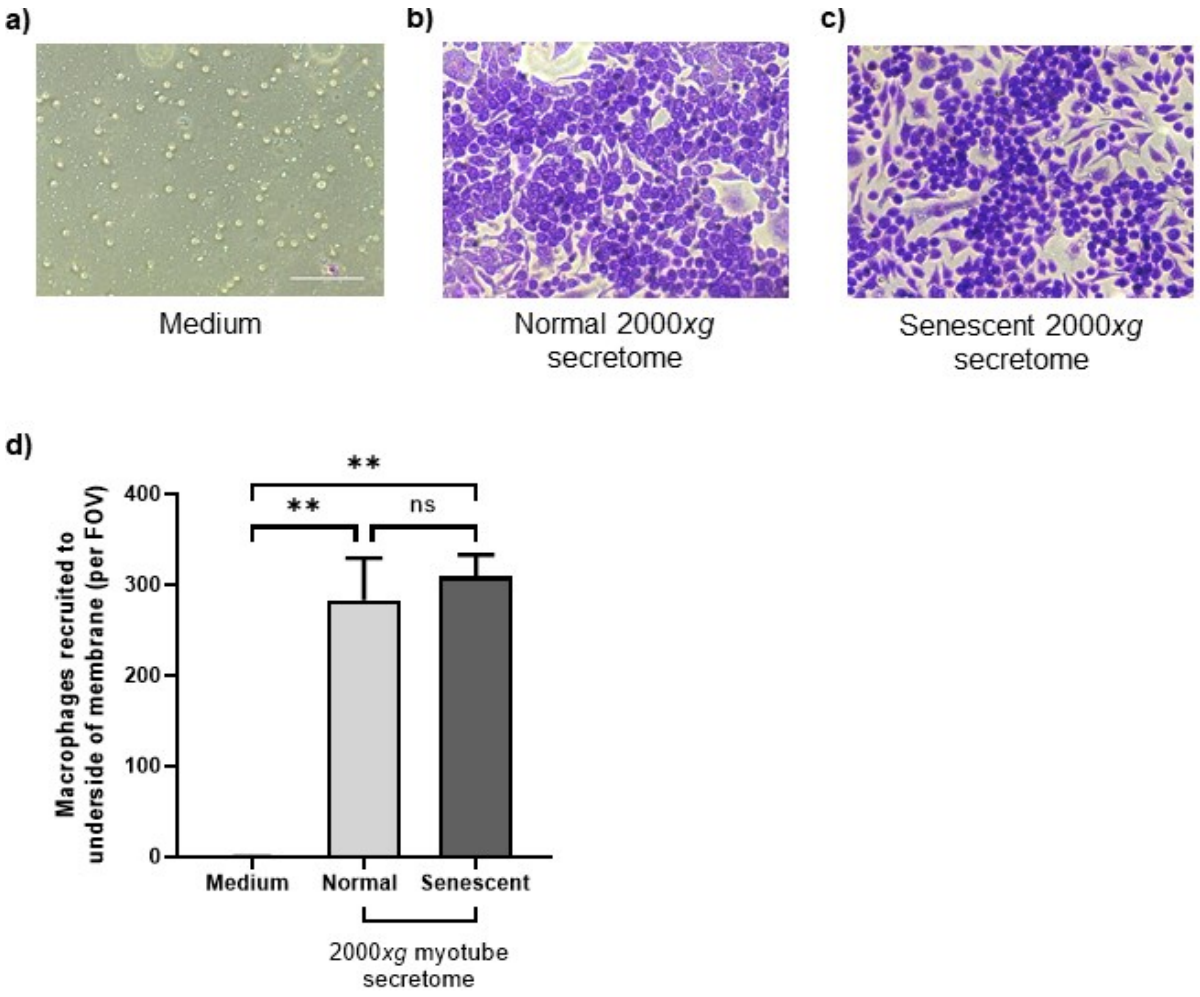

Figure 67. Transwell migration of J774 macrophages towards whole senescent myotube secretome. J774 macrophages were placed in the upper chamber of a transwell and their migration towards normal and senescent 2000*xg* myotube secretomes in the lower chamber was monitored for 24 hours. Following the incubation period, transwell inserts were stained with Jenner-Giemsa stains and images (40x magnification, scale bar = 100µm) taken of the underside of the permeable membrane (a – c). Macrophage number was determined via manual counting of cell in each image (d). Data shown are mean ± SEM of 3 independent experiments, one-way ANOVA with Dunnett's *post-hoc* test, ***P<0.005.* One-way ANOVA with Dunnett's *post-hoc* test comparing normal 2000*xg* secretome vs. senescent 2000*xg* secretome.

To further establish the migratory potential of the senescent 2000*xg* myotube secretome, the bottom of the well was also monitored for the presence of macrophages. The images of the well bottom show macrophages had detached from the underside of the transwell membrane and adhered to the bottom of the well, which contained the normal or senescent secretomes (figure 68b and 68c). There appears to be fewer cells migrating to bottom of the well than were found on the underside of the membrane, suggesting that the macrophages adhered to the membrane did not detach to migrate further towards the secretomes. Despite observing substantial macrophage migration towards normal and senescent 2000*xg* secretomes in the

images, quantitative analysis indicated that neither secretome was more potent than medium only or when compared to each other, which is due to the large variation (figure 68d).

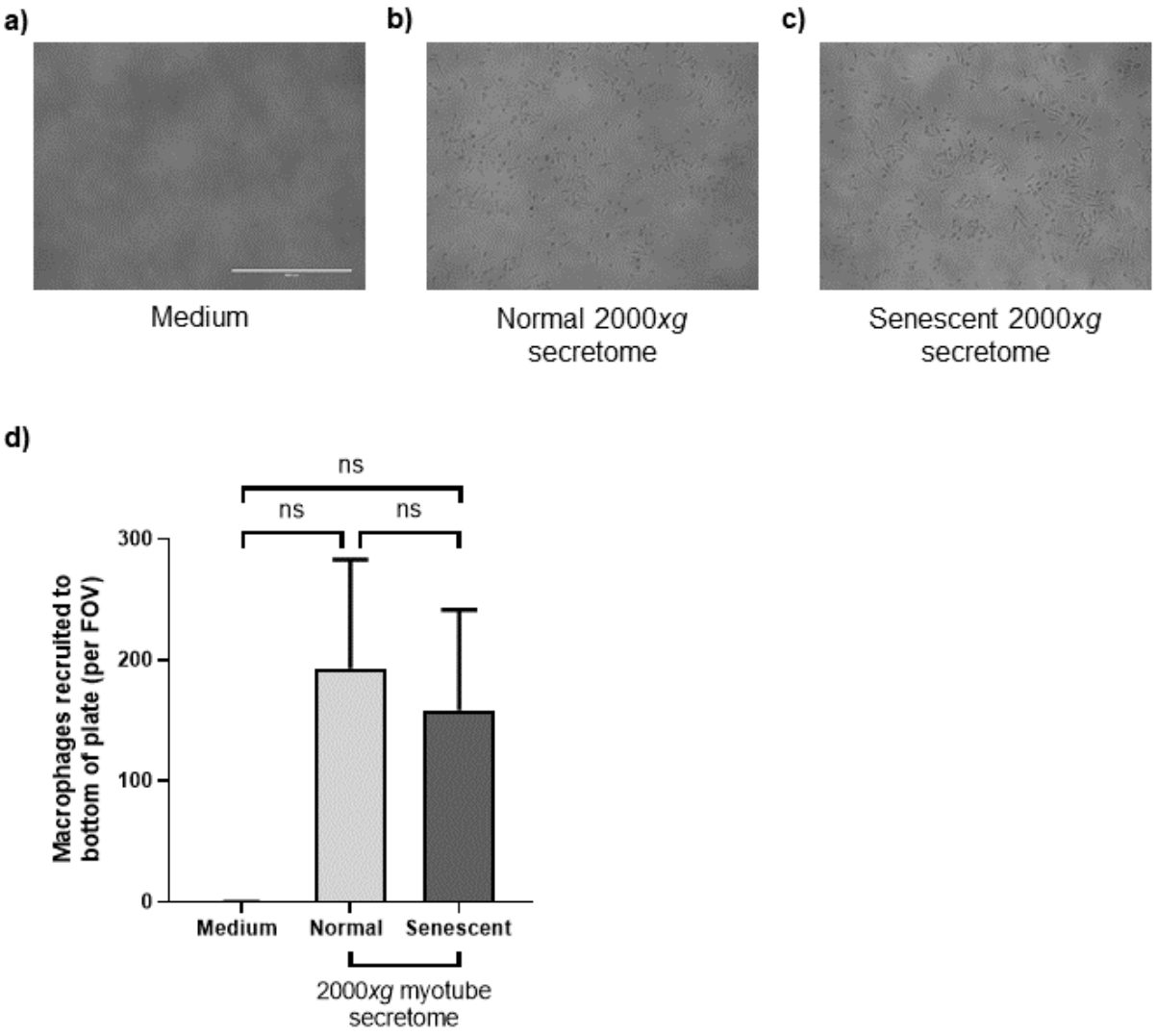

Figure 68. Murine macrophage migration through a transwell membrane towards whole senescent myotube secretome. Transwells containing J774 macrophages incubated with normal or senescent 2000*xg* myotube secretomes were imaged 24 hours post incubation. Macrophages migrating to the bottom of the transwell companion plate were imaged using phase contrast microscopy (10x magnification, scale bar = 400µm) and manual macrophage counts were performed (d). Data shown are mean ± SEM of 3 independent experiments, one-way ANOVA with Dunnett's *post-hoc* test, *ns*. One-way ANOVA with Dunnett's *post-hoc* test comparing normal 2000*xg* secretome vs. senescent 2000*xg* secretome.

Following the imaging of the membrane underside and the bottom of the well, the number of macrophages acquired from both positions were accumulated to provide a total cell count. This value shows the total number of macrophages migrating towards normal and senescent secretomes, by combining the initial and latter stages of chemotaxis to provide an overview of the recruiting potential of each secretome.

Irrespective of the data shown in figure 65 the total number of macrophages recruited by healthy and senescent secretomes is nevertheless greater than that of medium alone (figure 69). The combined value of cells indicates there was no difference in the migratory potential of either secretome, as both recruited a similar number of macrophages.

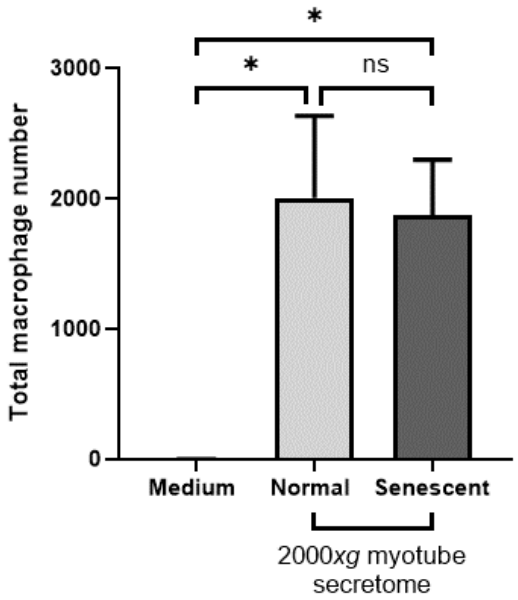

Figure 69. The total number of macrophages migrating towards whole senescent myotube derived secretome. The number of macrophages on the underside of the transwell membrane and the bottom of the well were combined to generate the total number of macrophages migrating towards either normal or senescent 2000*xg* myotube secretomes. Data shown are mean ± SEM of 3 independent experiments, one-way ANOVA with Dunnett's *post-hoc* test, **P<0.001*. One-way ANOVA with Dunnett's *post-hoc* test comparing normal 2000*xg* secretome vs. senescent 2000*xg* secretome.

To propose a secretome component responsible for the chemotactic behaviour of the macrophages in response to the 2000*xg* myotube secretomes, the secretomes were separated into EV and soluble protein fractions by SEC. The two fractions isolated from normal and senescent myotube secretomes were also tested in this vertical migration system. This investigation would provide insight into how each secretome component affects macrophage migration, as well as to establish whether they work in conjunction or act separately on these immune cells.

Firstly, the number of cells adhered to the underside of the transwell membrane were identified, providing a view of migration towards each secretome fraction in its early stages. The Jenner-Giemsa stained transwell membrane images show that in the presence of each fraction, the number of macrophages adhered to the underside changes. Both the NP and SenP were observed to have recruited the most J774 macrophages from the upper chamber to the underside of the membrane, as most of the membrane is covered in adhered cells

(figure 70c and 70e). In comparison, the NEV and SenEV appeared to induce fewer macrophages through the permeable membrane pores (figure 70b and 70d).

Quantitative analysis of the transwell membrane images show all fractions of both normal and senescent myotube origin were conducive to J774 macrophage migration (figure 70f), though the extent to which they were able to recruit macrophages was the same between all samples (figure 70g).

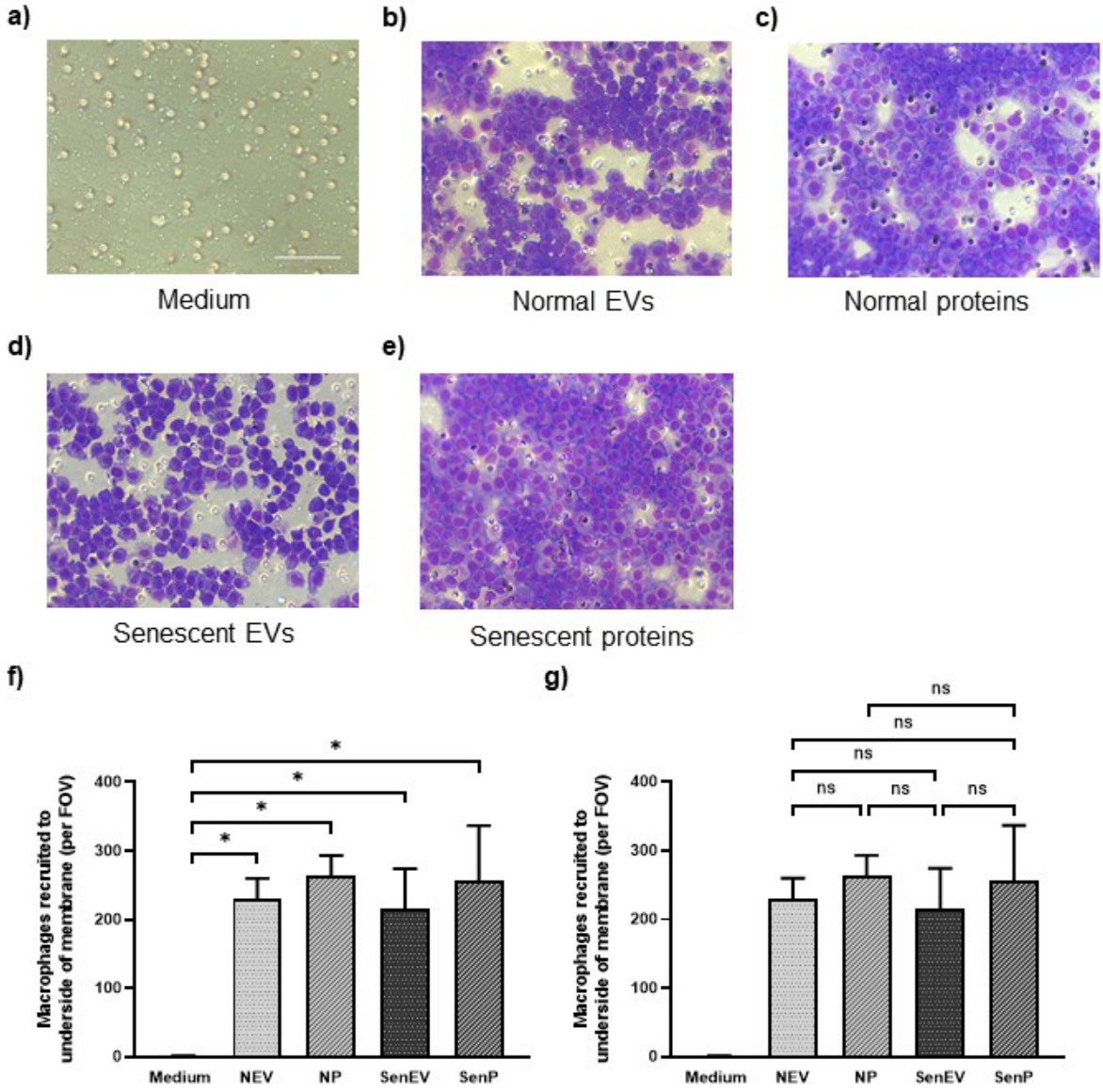

Figure 70. The ability of senescent EVs and soluble proteins to initiate macrophage migration. SEC isolated EVs and soluble proteins from normal (NEV and NP) and senescent myotubes (SenEV and SenP) were incubated with J774 macrophages in the vertical transwell system for 24 hours. End point images (40x magnification, scale bar = 100µm) were taken of the Jenner-Giemsa stained inserts to identify macrophages that had migrated to the underside of the permeable membrane on the transwell (a-e). All images shown are representative of the conditions used. Quantitative analysis was performed by manually counting the number of macrophages adhered to the membrane underside (f). Data shown are mean ± SEM of 3 independent experiments, one-way ANOVA with Dunnett's *post-hoc* test, **P<005*. One-way ANOVA with Tukey's *post-hoc* test also conducted (g).

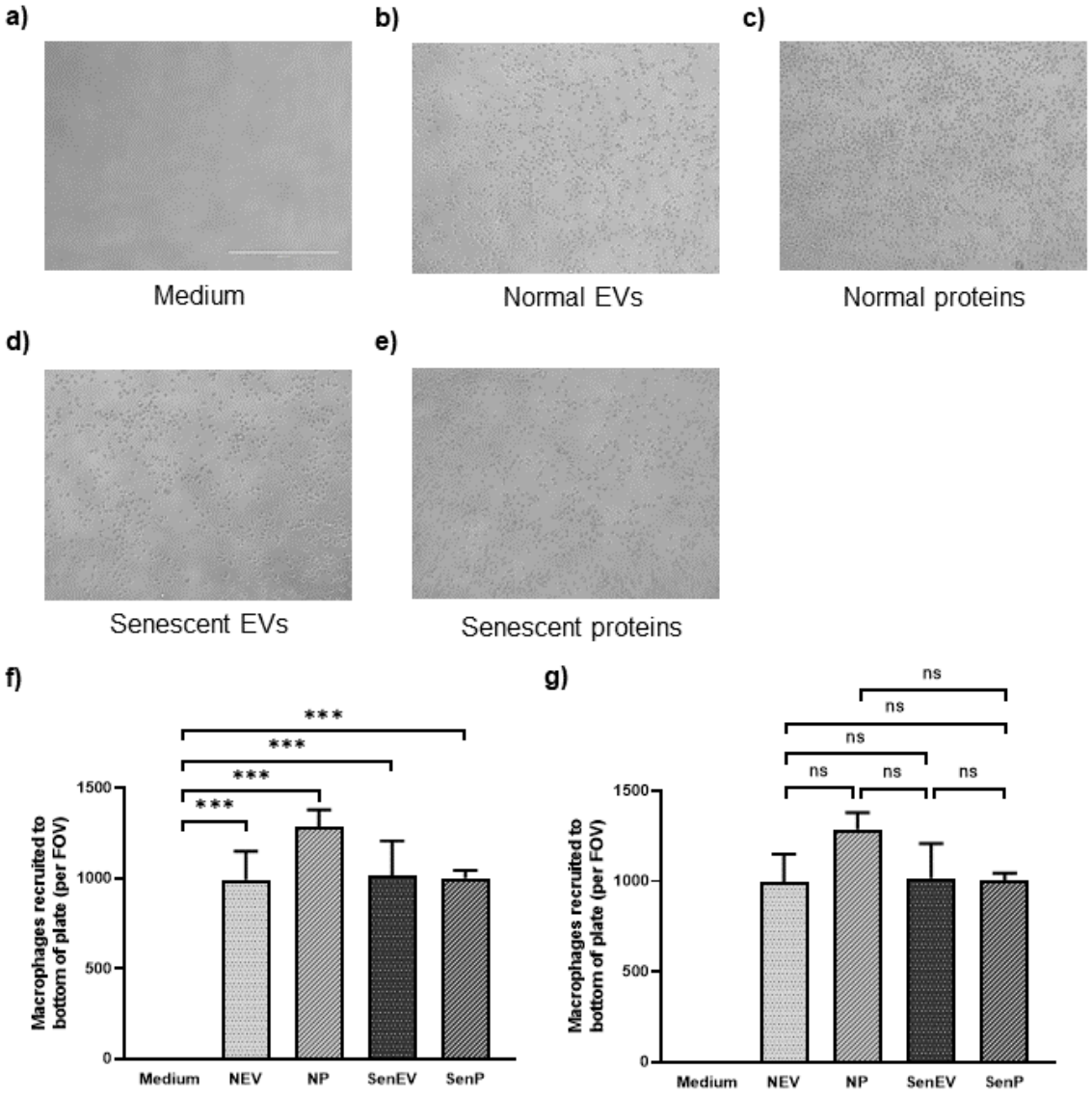

Figure 71. The recruitment of murine macrophages to senescent EVs and soluble proteins. Normal and senescent myotube derived EVs (NEV and SenEV) and soluble proteins (NP and SenP) were incubated with J774 macrophages in the vertical transwell system for 24 hours. Phase contrast images (10x magnification, scale bar = 400µm) of the bottom of the well were taken as end point images (a-e). All images shown are representative of the conditions used. The images were used to manually count the macrophages at the bottom of the wells (f). Data shown are mean ± SEM of 3 independent experiments, one-way ANOVA with Dunnett's *post-hoc* test, ****P<001*. One-way ANOVA with Tukey's *post-hoc* test also conducted (g).

Images of the well bottom suggest both normal and senescent fractions induced the migration of many macrophages from the upper chamber. NEV, SenEV and SenP (figure 71b, 71d, and 71e) all appeared to recruit a similar number of cells, whilst NP stimulated more macrophage migration than the other fractions (figure 71c). These initial observations were reflected by the quantitative data with NP alone appearing to be the most proficient macrophage recruiter, whilst the remaining fractions did not stimulate migration to the same extent but looked to be similar in their ability (figure 71f). However, comparing all fractions with one another showed

no difference in their macrophage recruiting potential (figure 71g). Comparison with the underside of the membrane indicates most macrophages were located at the bottom of well, suggesting these cells promptly detached to migrate towards each fraction.

As conducted with the 2000*xg* secretomes, the total number of macrophages recruited by the normal and senescent SEC fractions was calculated by combining cell numbers from the membrane and the bottom of the well (figure 72a). Initial suppositions suggested NP recruited the most macrophages however, this was not the case. EV and soluble protein fractions from normal and senescent myotubes were all shown to have the same macrophage recruiting ability (figure 72b).

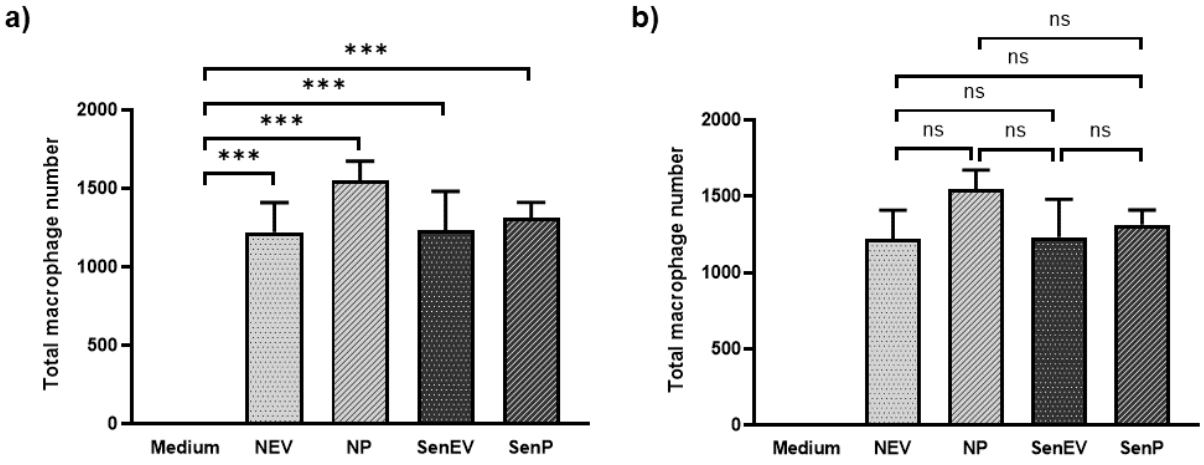

Figure 72. The total number of macrophages migrating towards senescent myotube secretome derived EVs and soluble proteins. The number of J774 macrophages on both the underside of the transwell membrane and at the bottom of the wells of the companion plate were combined to provide a total cell number migrating from the upper chamber transwell chamber to the lower chamber (a), where the normal and senescent myotube-derived EVs (NEV and SenEV) and soluble proteins (NP and SenP) were situated. Data shown are mean ± SEM of 3 independent experiments, one-way ANOVA with Dunnett's *post-hoc* test. A one-way ANOVA with Tukey's *post hoc* test was also conducted (b).

5.2.3.2 Horizontal migration – Dunn chamber

Figure 73 shows the migration tracks of macrophage-like cells migrating towards normal and senescent myotube 2000*xg* secretomes. Most cells exposed to normal 2000*xg* secretome appeared to move in the direction of the putative chemoattractant, with few straying from that line of migration (figure 73c). Despite the distance of macrophage-like cell migration towards the senescent 2000*xg* secretome being similar to that of the normal myotube secretome, migration appears to be less direct (figure 73d).

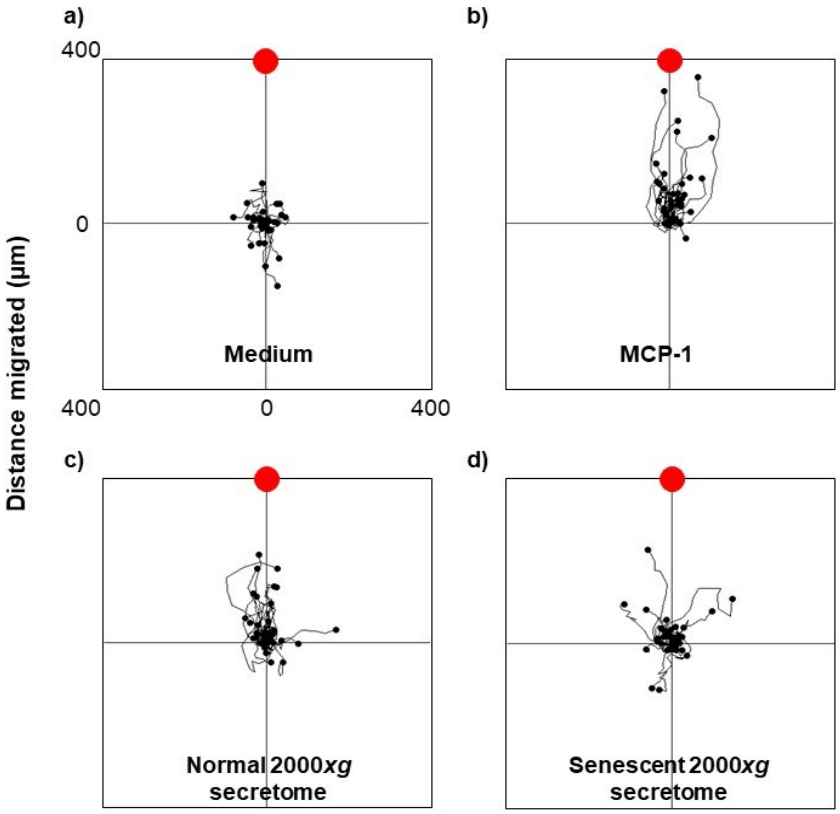

Figure 73. Migration plots of macrophage-like cells migrating towards putative senescent myotube-derived secretome. THP-1/VD3 macrophage-like cell coated cover slip was mounted onto a Dunn chamber containing macrophage medium, MCP-1, normal or senescent myotube 2000*xg* secretomes in the outer well, position represented by the red spot (a – d). Time-lapse microscopy was used to record cell migration for 2 hours. Macrophage-like cells were tracked using Chemotaxis and Migration Tool, to produce plots showing each cell as a black dot with a start point at the crosshairs. Plots shown are representative of the putative attractants used.

The migration of macrophage-like cells in response to the normal and senescent 2000*xg* secretomes was quantified using the same series of measures detailed in section 4.2.4.2. The first quantifiable measure was the distance migrated towards the potential chemoattractants. The Euclidean distance or the distance migrated from the starting point to the end point in a straight line in the presence of either secretome was not different to that of medium alone (figure 74a). This result was also observed with the accumulated distance migrated, with no difference between the two secretomes (figure 74b). Furthermore, macrophage-like cells did not migrate faster towards either the normal or senescent 2000*xg* secretomes (figure 74c). Regarding the directionality of movement, macrophage-like cells did not migrate directly towards the two secretomes (figure 74d and 74e).

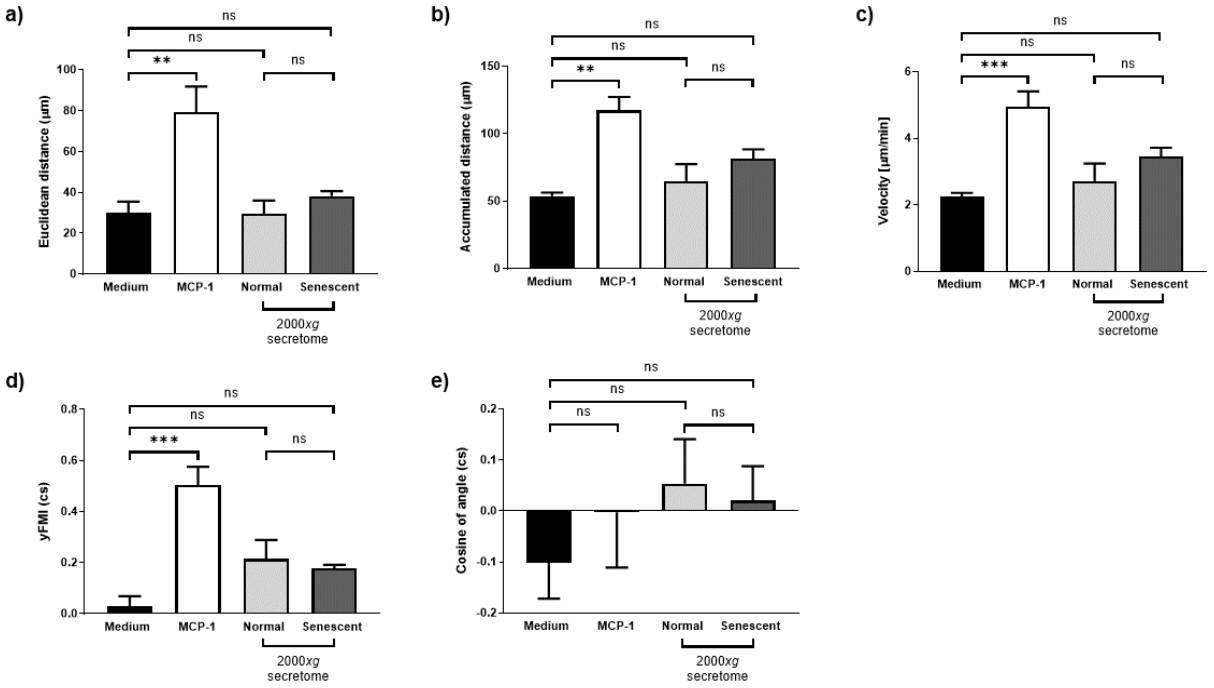

Figure 74. Migration measures used to assess the chemotactic potential of senescent myotube 2000*xg* secretome. Chemotaxis and Migration Tool software was used to quantitatively assess the extent of macrophage cell-like migration towards normal and senescent myotube 2000*xg* secretomes. The migratory measures investigated were Euclidean distance (a), accumulated distance (b), velocity (c) and two different assessors of directionality, yFMI (d) and cosine of angle (e). Data shown are mean ± SEM of 3 independent experiments, one-way ANOVA with Dunnett's *post-hoc* test vs. medium. A one-way ANOVA with Dunnett's *post-hoc* test vs. normal 2000*xg* secretome was also conducted.

It is possible that the 2000*xg* secretomes in their existing state were not sufficient to induce noticeable changes in the macrophage migratory response. The various components contained within the secretomes could be too dilute to elicit any effects. As conducted with the sarcopenic secretome in chapter 4, the senescent secretome was also concentrated using 30 kDa spin column filter units to produce a SenR consisting of EVs and large soluble mediators and a SenF containing low weight soluble mediators.

Both retentates and filtrates from normal and senescent secretomes were tested using the Dunn chamber to assess their chemotactic potential. Stark differences were observed in the migration tracks of macrophage-like cell moving towards NR and NF. NR induced migration appeared to be reduced compared to that of NF. Cells migrating towards NR did not travel far from their point of origin, whilst in the presence of NF, macrophage-like cells showed directional migration over a distance (figure 75c and 75d). Conversely, the concentrated senescent secretome fractions did not stimulate extensive migration. Migration towards SenR was greater than that towards SenF, with some macrophage-like cells exhibiting directional migration (figure 75e and 75f). However, macrophage-like cells exposed to the SenF showed

reduced migration. Most cells were clustered at the crosshairs, near to their starting points, with almost no cells entering the upper quadrants, suggesting limited migratory potential.

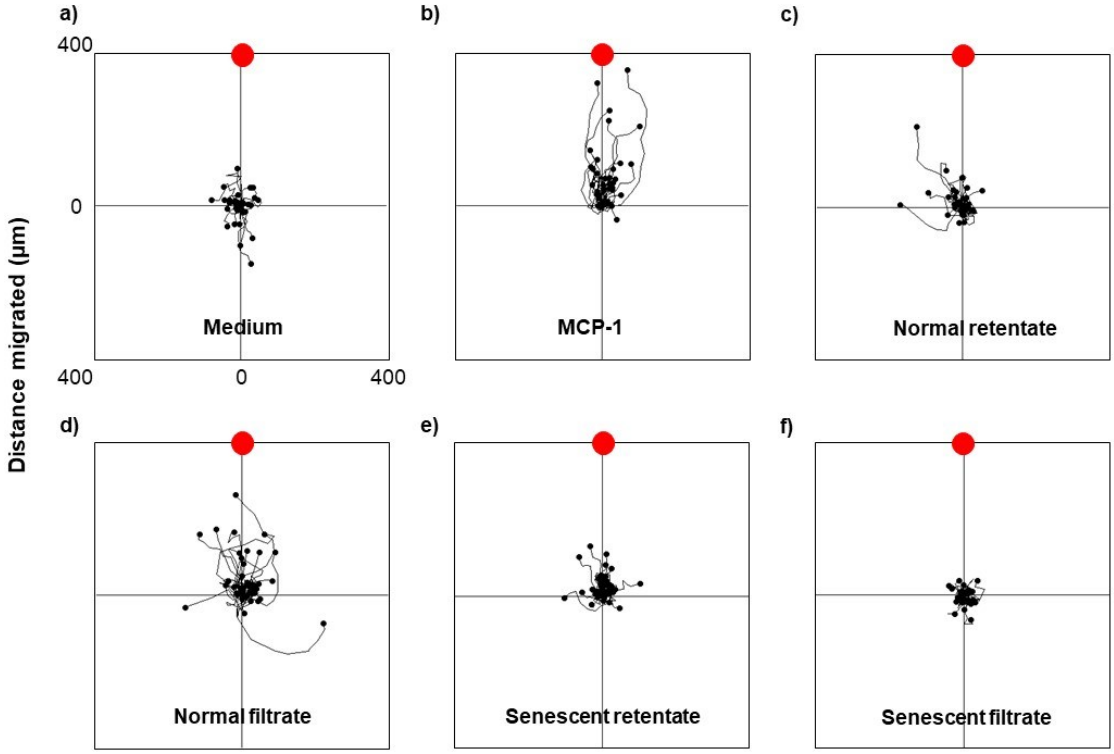

Figure 75. Paths of migration undertaken by macrophage-like cells exposed to concentrated senescent myotube-derived secretome fractions. Normal and senescent myotube-derived 2000*xg* secretomes were concentrated using 30 kDa spin filters to produce a retentate (c and e) and a filtrate (d and f). Both retentates and filtrates were added to the outer well of the Dunn chamber and THP1/VD3 macrophage-like cell migration was monitored using time-lapse microscopy for 2 hours. Following recording, migration plots were generated by tracking cells using Chemotaxis and Migration Tool. Cells migrated from the crosshairs towards the putative chemoattractants, the position signified by the red dot. Please note MCP-1 positive control (b) is identical to that shown in figure 71.

The retentate and filtrate migration plots displayed in figure 75 were also quantified to numerically determine the degree of migration (figure 76). The first quantified measure of migration was the distance migrated, stated as the Euclidean and accumulated distances. No normal or senescent secretome components (retentates and filtrates) induced significant migration in a straight line and there were no differences between samples (figure 76a and figure 76b), whilst only NF stimulated THP-D3 macrophage-like cells to migrate further and SenF significantly reduced the accumulated distance migrated by macrophages compared to NF (figure 76c and figure 76d). These cells also migrated faster in the presence of NF, with SenF induced migration being slower than NF (figure 76e and figure 76f); however this was

not directional movement (figure 77a and 77c). When comparing directional movement of all samples, no difference was observed (figure 77b and figure 77d).

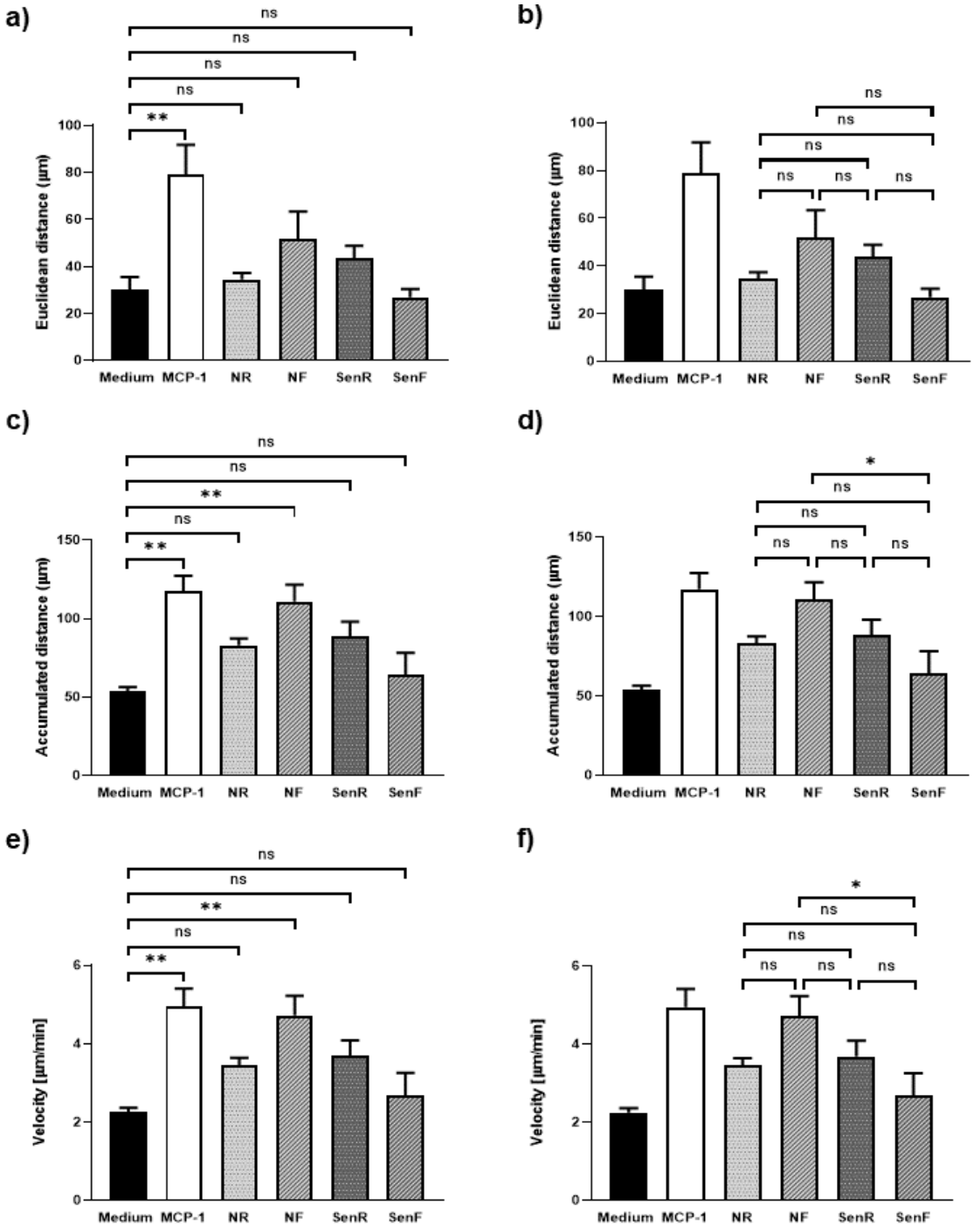

Figure 76. The migratory measures of macrophages migrating in response to concentrated senescent myotube secretomes. The migration of J774 macrophages to 30 kDa spin filter concentrated normal and senescent myotube-derived retentates (NR and SenR) and filtrates (NF and SenF) was quantitatively assessed using a series of measures including Euclidean distance (a), accumulated distance (c), velocity (d). Data shown are mean ± SEM of 3 or more independent experiments, one-way ANOVA with Dunnett's *post-hoc* test, ***P<0.01*. One-way ANOVA with Tukey's *post-hoc* test was also conducted (b, d and f), **P<0.05*.

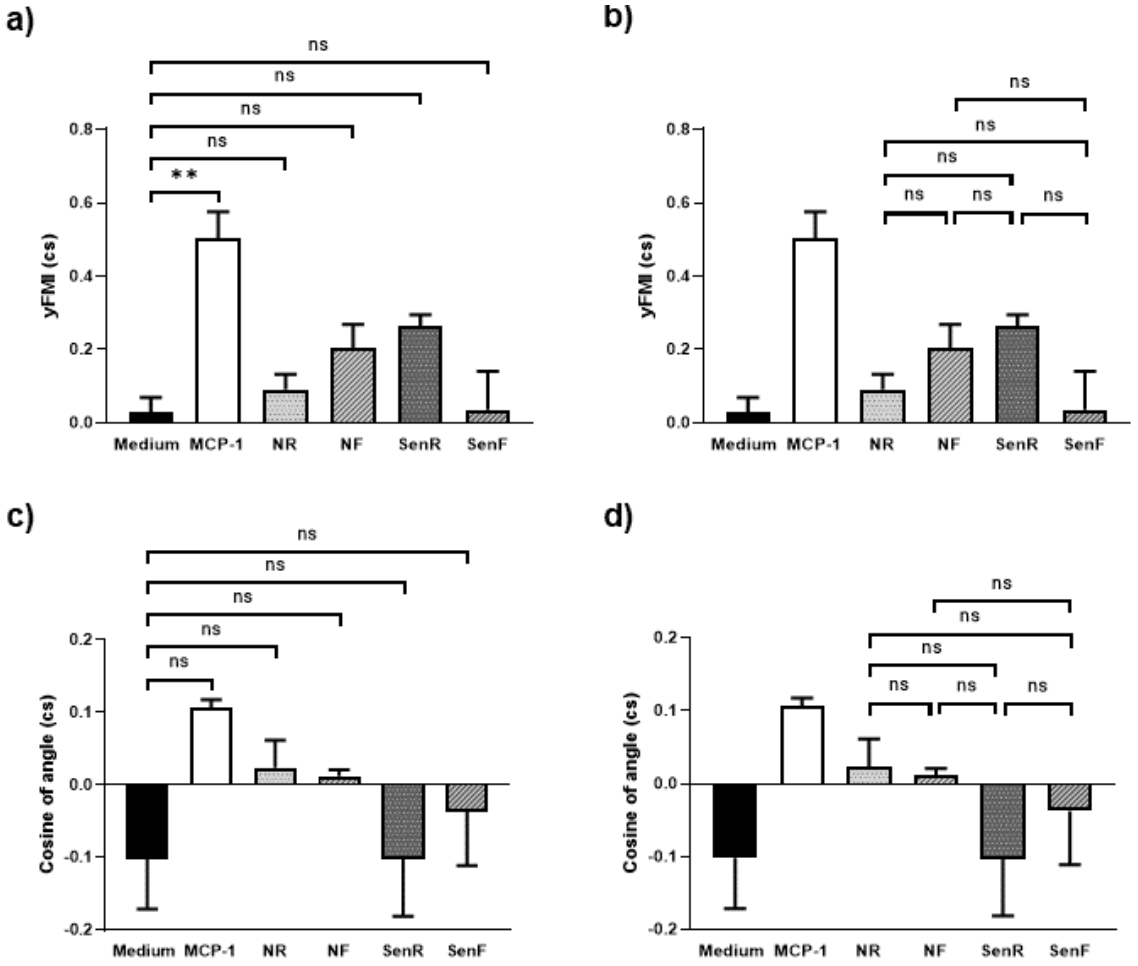

Figure 77. The migratory measures of macrophages migrating in response to concentrated senescent myotube secretomes. The directionality of migration of J774 macrophages to 30 kDa spin filter concentrated normal and senescent myotube-derived retentates (NR and SenR) and filtrates (NF and SenF) was quantitatively assessed via two measures, yFMI (a) and the cosine of angle (c). Data shown are mean ± SEM of 3 or more independent experiments, one-way ANOVA with Dunnett's *post-hoc* test, ***P<0.01*. One-way ANOVA with Tukey's *post-hoc* test was also conducted (b and d).

5.2.4 Senescent skeletal muscle regulation of macrophage respiratory burst

To determine the influence of senescent myotube secretome over macrophage ability to generate ROS, a luminometry assay, first stated in section 4.2.3 was conducted. Briefly, J774 macrophages were exposed to either normal or senescent myotube-derived 2000*xg* secretomes and superoxide anion release was measured over time via a chemiluminescent probe. After treatment, immediate measurement in the presence of normal and senescent myotube secretomes showed minimal superoxide anion production during the 1-hour measurement period (figure 78a). To confirm this finding, the total amount of superoxide anion was determined by calculating the area under the curve. This measure also mirrored the kinetic data, as normal or senescent secretome related total superoxide production did not

increase above that of the medium only control, with both secretomes having a similar effect (figure 78b). These data mirror the sarcopenic myotube 2000*xg* secretome results detailed in section 4.2.3, once again suggesting that the effect of normal and senescent secretomes could be exert a subtle effect and the format of this assay is not sufficiently sensitive to detect minor changes.

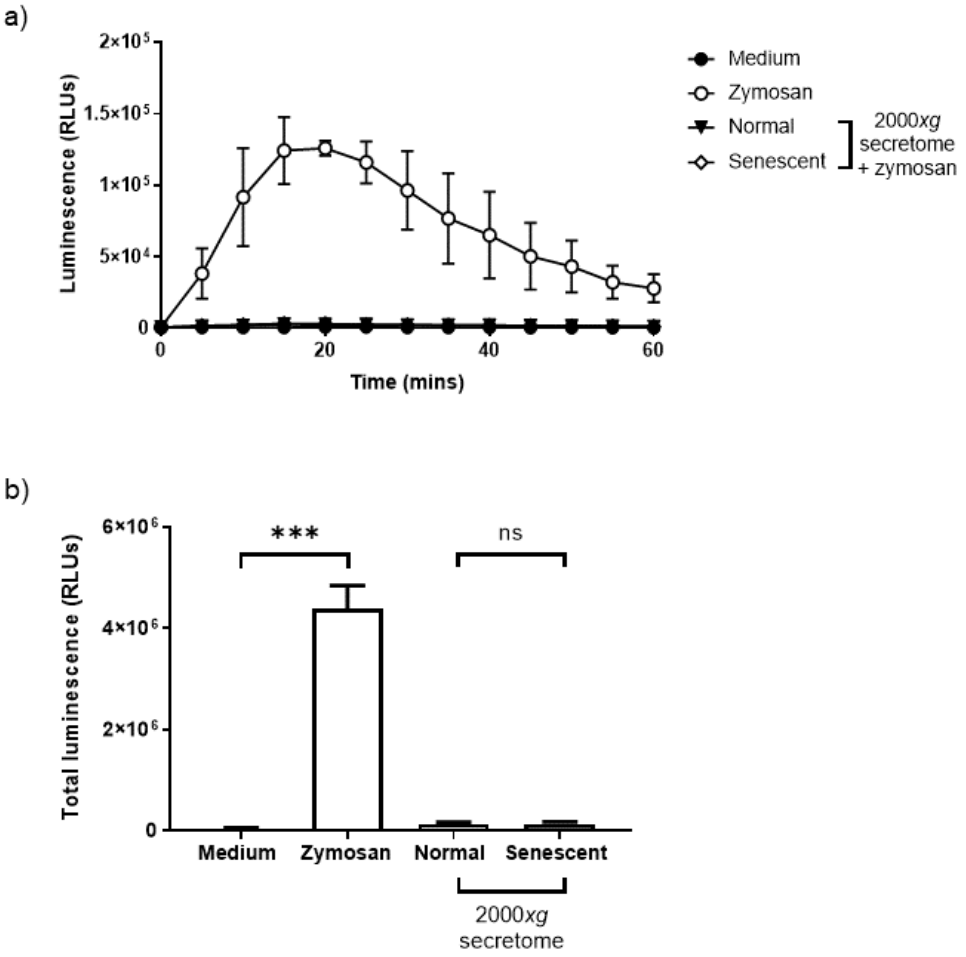

Figure 78. The effect of whole senescent myotube secretome on macrophage respiratory burst. Normal and senescent myotube-derived 2000*xg* secretomes were added to J774 macrophages in the presence of the chemiluminescent probe lucigenin. The relative amount of light released was measured every 5 minutes for 1 hour, with light produced corresponding to the amount of superoxide anion generated (a). The total amount of superoxide anion produced during the 1-hour measurement period was also determined (b). Data shown are mean ± SEM of 3 independent experiments, one-way ANOVA with Dunnett's *post-hoc* test, ****P<0.0001*. One-way ANOVA with Dunnett's *post-hoc* test vs. normal 2000*xg* also conducted.

As described in section 4.2.3, this chemiluminescent assay was modified by pre-incubating the normal and senescent myotube 2000*xg* secretomes with J774 macrophages for 4 hours prior to macrophage treatment with zymosan and eventual superoxide anion quantification. This permitted detection of small changes in superoxide anion generation above or below that

of the zymosan only positive control. Ultimately, this indicated whether the tested secretomes could improve an existing oxidatively stressed environment.

The kinetics of the macrophage respiratory burst indicate a rapid increase in superoxide anion production 5 minutes after exposure to zymosan for both normal and senescent secretomes (figure 79a). This rate increases until the 10-minute timepoint, with all conditions reaching maximum production at 20 minutes. The senescent 2000*xg* secretome treated macrophages mimic the superoxide anion generation profile of the macrophages exposed to zymosan alone, suggesting this secretome did not modify the respiratory burst function of macrophages. In contrast, the normal 2000*xg* secretome treated macrophages appear to release a lower amount of superoxide anion compared to the zymosan only and senescent secretome treated macrophages, despite following the same reaction kinetics. Using the kinetics of superoxide anion release, the total amount of superoxide anion produced was calculated for each secretome (figure 79b). Macrophages pre-treated with the senescent myotube secretome generated a similar amount of superoxide anion to the zymosan only and normal myotube secretome treated macrophages. It is possible that with repeated experimentation, the macrophages incubated with either the normal or senescent myotube 2000*xg* secretomes would show more distinction in the amount of superoxide anion they generate.

The potential differences observed with the 2000*xg* secretomes were further investigated by separation into their component parts, the EV and soluble protein fractions. This would identify whether one fraction was more potent than the other or whether both fractions were working in combination to elicit their effects. In the same manner as the whole secretomes, the EV and soluble proteins were pre-incubated with J774 macrophages for 4 hours and the cells exposed to zymosan immediately prior to superoxide anion measurement.

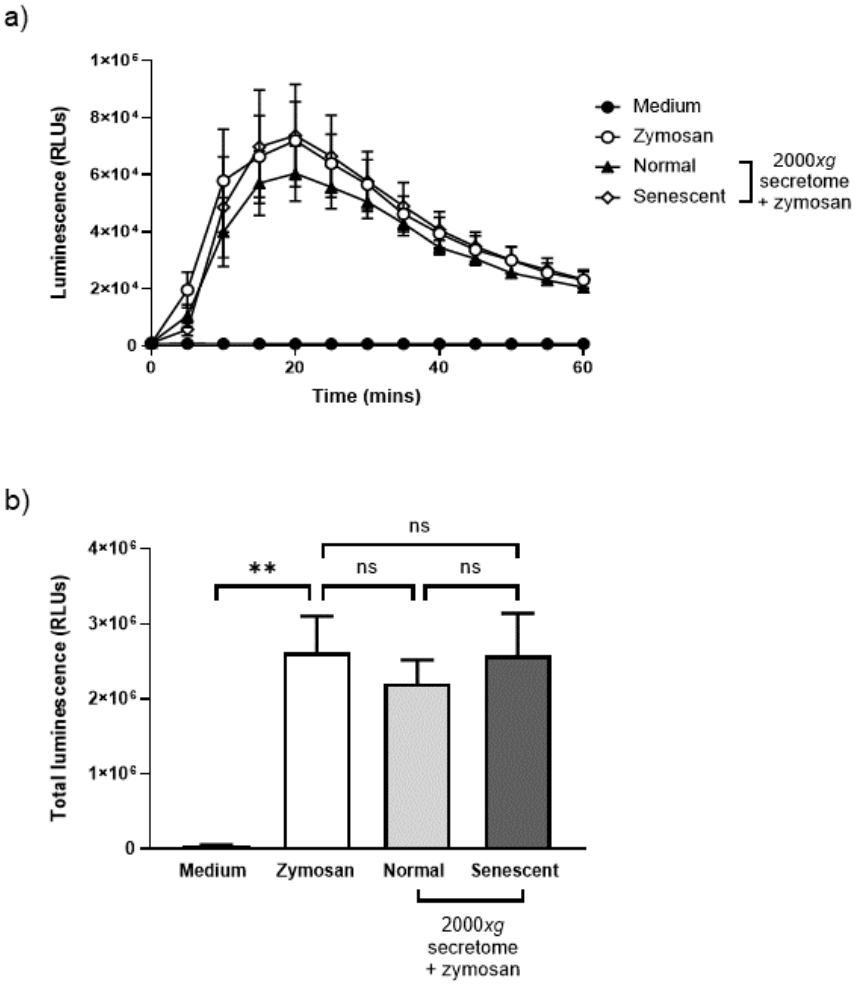

Figure 79. The ability of senescent myotube-derived secretome to reduce oxidative stress. Normal and senescent myotube-derived 2000*xg* secretomes were pre-incubated with J774 macrophages for 4 hours, after which the cells were exposed to zymosan. Immediately post zymosan addition, superoxide anion release was measured every 5 minutes for 1 hour (a). Using the kinetic reaction, the total amount of superoxide anion produced in 1 hour was calculated (b). Data shown are mean ± SEM of 3 independent experiments, one-way ANOVA with Dunnett's *post-hoc* test, ***P≤005*. One-way ANOVA with Dunnett's *post-hoc* test vs. normal 2000*xg* also conducted.

Figure 80a shows the SenEV and SenP followed the same superoxide anion release kinetics as the zymosan only macrophages, with all cells reaching peak production after 20 minutes. Compared to the 2000*xg* secretomes in figure 79, the maximum amount of superoxide anion produced by the isolated senescent fractions was less, which can be attributed to differences in zymosan batches used to initiate the respiratory burst response in the J774 macrophages. 20 minutes post zymosan exposure, the SenEV and SenP diverge from the zymosan only macrophages. Superoxide anion production by both SenEV and SenP declined at a faster rate compared to that of zymosan alone, with SenP being the more rapid of the two fractions. In contrast, NEV and NP muted the respiratory burst response. Maximal amount of superoxide anion release was achieved after 20 minutes by both fractions; however, the rate of production

was slower than their senescent counterparts. The two fractions did not appear to differ in their ability to stimulate superoxide anion release, as neither was distinguishable from the other.

To confirm the differences observed in the kinetic data, the total amount of superoxide anion generated during the 60-minute measurement period was quantified (figure 80b). The NEV and NP significantly reduced the amount of superoxide anion produced by J774 macrophages exposed to zymosan, however no discernible differences were observed between the two secretome components, which indicate both had a similar effect on macrophage respiratory burst. Whilst the normal secretome components were able to dampen oxidative stress, the two senescent fractions each induced different macrophage behaviour. The SenEV did not reduce superoxide anion production, as this component stimulated a similar release to that induced by zymosan alone. Conversely, macrophages pre-treated with SenP showed a decrease in the total amount of superoxide anion. Differences were also observed between the normal and senescent secretomes, as both NEV and NP were found to be more proficient at minimising superoxide anion release than either of the two senescent fractions (figure 80c).

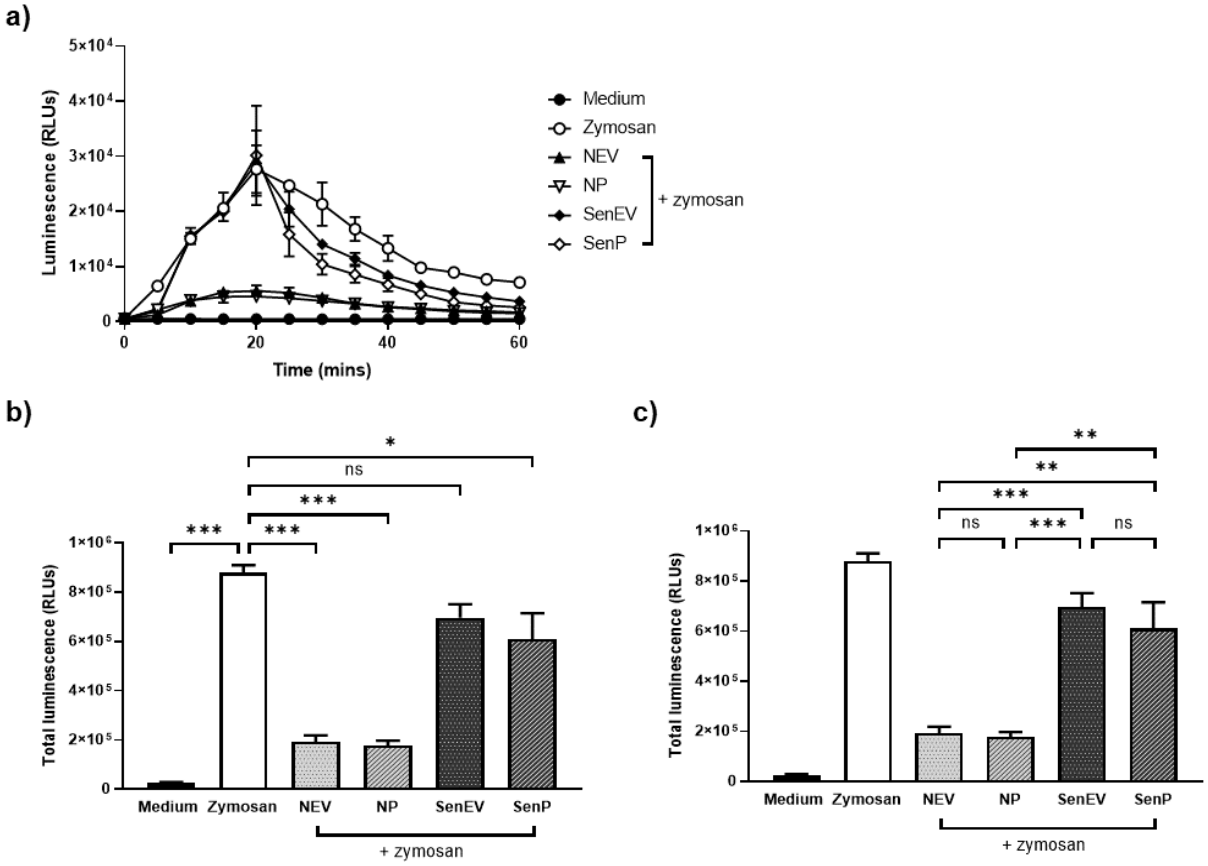

Figure 80. Macrophage respiratory burst response to senescent myotube-derived EVs and soluble proteins. J774 macrophages were pre-incubated with EVs and soluble proteins isolated from either normal (NEV and NP) or senescent myotubes (SenEV and SenP) for 4 hours. Following incubation, all macrophages were treated with zymosan, after which superoxide anion release was measured using a chemiluminescent probe every 5 minutes for a period of 60 minutes (a). The total amount of superoxide anion released by macrophages incubated with normal and senescent myotube secretome fractions during the 60 minutes was also calculated (b). Data shown are mean ± SEM of 3 independent experiments, one-way ANOVA with Dunnett's *post-hoc* test, ****P<0.0001*, **P<0.05*. One-way ANOVA with Tukey's *post-hoc* test also conducted (c), ****P<0.001* and ***P<0.005*.

5.2.5 Macrophage phenotype in the senescent skeletal muscle environment

As was conducted with the concentrated sarcopenic secretome, the concentrated senescent 2000*xg* was initially tested for its ability to stimulate NO_2^- production in J774 murine macrophages (figure 81a). Treatment with NR and NF did not produce a significant amount of NO_2^-, suggesting the M1 phenotype was not present in this population of macrophages. NO_2^- release was also undetectable in the presence of SenR and SenF. Due to this indiscernibility, J774 macrophages were polarised to a pro-inflammatory M1 phenotype using LPS prior to NO_2^- detection. This permitted the detection of small changes in macrophage NO_2^- release that were too slight to be revealed by the initial format of the Griess assay as shown in figure 81a. This modified version of the Griess reaction identified whether SenR and SenF facilitated

a pro-inflammatory environment by sustaining M1 polarisation or if they attempted to minimise this process.

The polarisation of J774 macrophages to an M1 subset highlighted differences in the concentrated myotube secretomes ability to influence NO_2^- release (figure 81b). The exposure of M1 J774 macrophages to NR did not alter NO_2^- production by LPS treated macrophages. In contrast, the addition of the NF showed a marked reduction in macrophage NO_2^- release. However, this effect was not observed with either of the senescent secretome components, suggesting that they do not alter macrophage polarisation capacity compared to the LPS only treated macrophages. On comparing all samples against each other, only NF reduced NO_2^- release to a greater extent than NR (figure 81c).

To further elucidate the cause of the concentrated myotube secretomes effects on NO_2^- production, the secretomes were separated into their EV and soluble protein components. Testing the isolated components in the Griess assay allowed for the determination of the influence each individual fraction elicited on M1 polarisation. Initially, the EV and soluble protein fractions were tested on resting M0 J774 macrophages in the absence of LPS to identify any changes they might induce alone on NO_2^- production (figure 82a). As expected, these components did not produce any noticeable impact on M1 polarisation, possibly due to the Griess assay in its current form not being suitably sensitive to detect small changes. Consequently, J774 macrophages were polarised to M1 macrophages using LPS besides the addition of the two SEC-isolated components, as was conducted with the concentrated myotube secretomes in figure 81b.

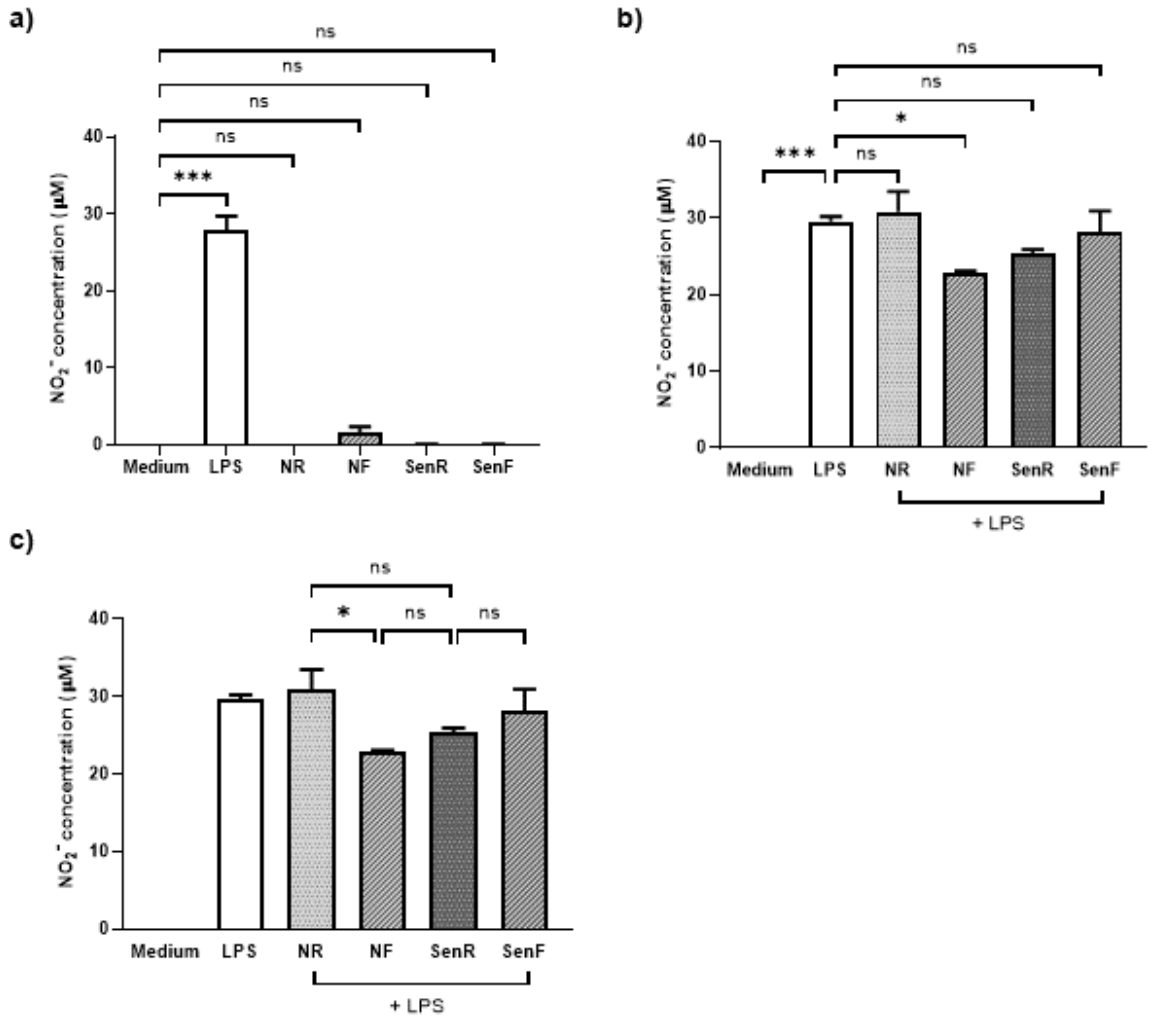

Figure 81. The ability of concentrated whole senescent secretome to minimise a proinflammatory macrophage polarisation. Normal and senescent myotube-derived 2000*xg* secretomes were concentrated using 30 kDa spin filters to create retentate (NR and SenR) and filtrate components (NF and SenF) and incubated with J774 macrophages for 48 hours. Post incubation, macrophage NO_2^- production was measured via the Griess reaction (a). J774 macrophages were initially polarised to M1 macrophages by exposure to LPS and then treated with normal and senescent retentates and filtrates, after which their ability to induce NO_2^- production was measured using Griess reaction (b). Data shown are ± SEM of 3 independent experiments, one-way ANOVA with Dunnett's *post-hoc* test, ****P<0.0001* and **P<0.05*. One-way ANOVA with Tukey's *post-hoc* test also conducted comparing retentates and filtrates against each other (c), **P<0.05*.

Polarisation to M1 macrophages revealed the subtle changes that the individual components elicited on NO_2^- production. Figure 82b shows that both EV and soluble protein containing fractions derived from normal and senescent myotube secretomes significantly reduced NO_2^- release from pre-existing M1 macrophages, therefore reducing the pro-inflammatory nature of this subset of macrophages. Comparison of all fractions with each other displayed no differences in their ability to minimise M1 polarisation, indicating equal capacity to reduce macrophage NO_2^- production. Comparing the SEC isolated fractions (figure 82b) with the spin filter concentrated secretome components (figure 81b) exhibits that when EVs and small

soluble mediators are combined, their M1 dampening ability is depleted, yet when separated it is reinstated. Despite all EVs and soluble proteins reducing NO_2^- compared to M1 polarised macrophages, all samples did this to a similar extent (figure 82c).

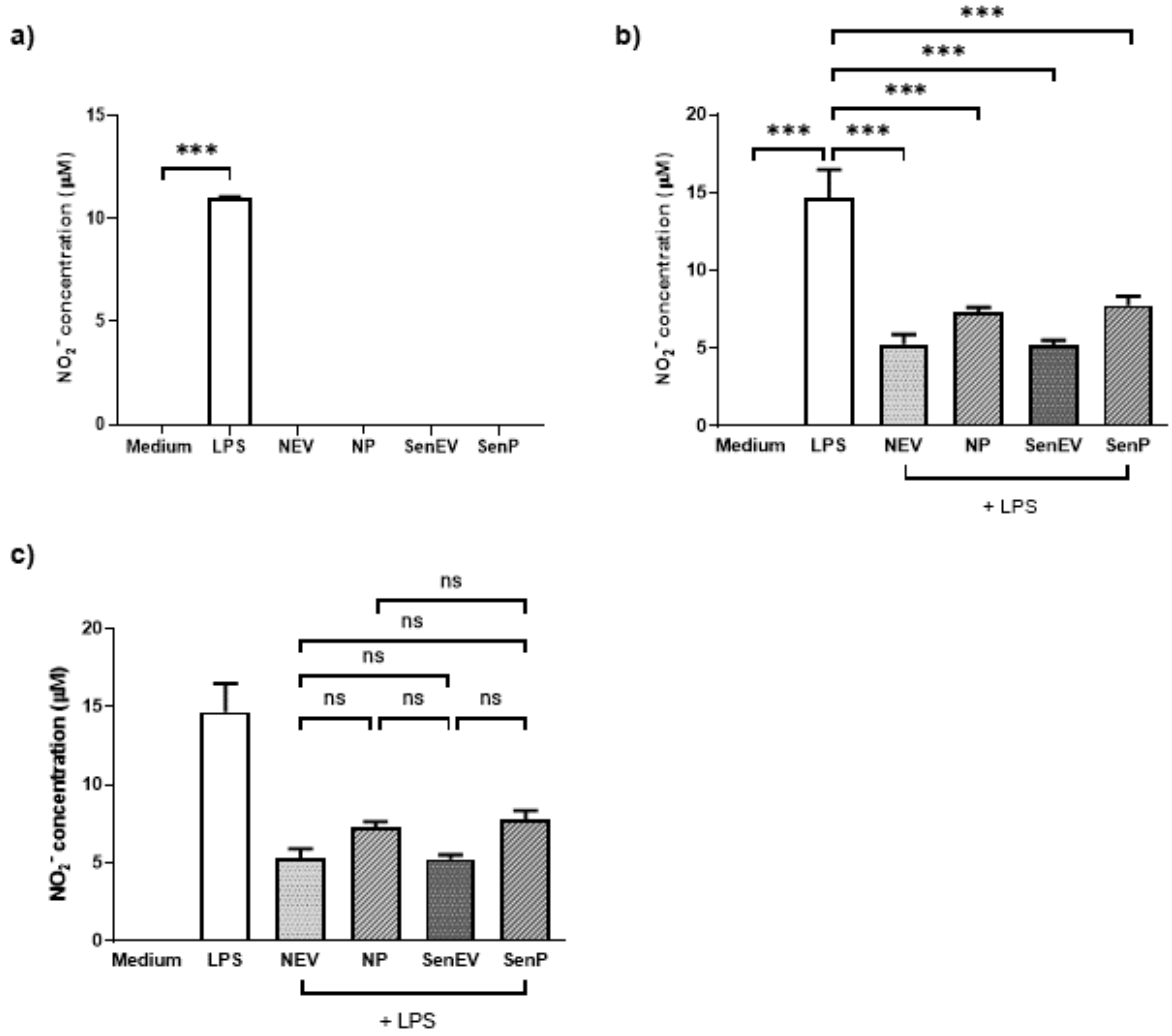

Figure 82. The ability of senescent EVs and soluble proteins to limit M1 macrophage polarisation. J774 macrophages incubated with EVs and soluble proteins isolated from both normal (NEV and NP) and senescent (SenEV and SenP) myotubes were measured for NO_2^- production using the Griess reaction (a). J774 macrophages were polarised to an M1 phenotype and incubated with normal or senescent myotube-derived EVs and soluble proteins for 48 hours. Following treatment, NO_2^- release was measured using Griess assay (b). Data shown are ± SEM of 3 independent experiments, one-way ANOVA with Dunnett's *post-hoc* test, ****P<0.0001*. One-way ANOVA with Tukey's *post-hoc* test conducted comparing all EV and soluble protein fractions (c).

5.2.5.1 Macrophage cytokine profiling

Figure 83 shows the concentration of numerous pro-inflammatory cytokines produced by J774 murine macrophages incubated with EVs and soluble proteins from both normal and senescent myotubes. The level of TNF-α produced by EV and soluble protein treated macrophages was detectable, however it was minimal and did not increase above that of

macrophages exposed to medium alone, nor did it equate to the concentration produced by M1 polarised macrophages (figure 83a). Measuring the pleiotropic cytokine IL-6 proved difficult, as with certain myotube treatments the concentration of this cytokine was below the level of detection (figure 83b). This was the case for macrophages incubated with SenEV. Despite the other treatment conditions generating detectable concentrations of IL-6, they did not reach considerable levels. The levels of IL-23, IL-18 and IL-1β were undetectable, suggesting the EV and soluble proteins isolated from both normal and senescent myotubes did not stimulate pro-inflammatory macrophage polarisation (figures 83c, 83d and 83e). The chemokine CXCL1/KC was also measured and has been shown to induce chemotaxis, particularly that of neutrophils. J774 macrophages treated with NP produced a significantly higher concentration of CXCL1/KC than both medium only and other secretome fraction treated counterparts (figure 83f). Whilst CXCL1/KC was detected in the presence of SenP, this was not a significant increase in concentration. The final two pro-inflammatory cytokines measured were IL-12p70 and IL12p40, both of which are members of the IL-12 cytokine family. Neither normal nor senescent myotube SEC isolated components induced detectable concentrations of IL-12p70 (figure 83g). The data show that very little IL-12p40 was released by treated J774 macrophages, with no conditions inducing the production of significantly different amounts of IL-12p40 to the medium only treated cells (figure 83h).

In addition to the measurement of pro-inflammatory cytokines, the level of anti-inflammatory and pro-resolving cytokines was also determined. The presence of these cytokines in the secretome of treated J774 macrophages would suggest these phagocytic cells have adopted an M2 phenotype, which are working to minimise the initial inflammatory response and to facilitate repair of damaged tissue. The multiplex panel used for assessing cytokine concentration also contained beads that detected 5 anti-inflammatory and pro-resolving cytokines: free active TGF-β1, IL-10, CCL17, CCL22 and G-CSF, which denote the M2 macrophage population. It must be noted that the M2 control did not work, as very few anti-inflammatory cytokines were at a detectable level in this sample.

With regards to this study, the concentration of TGF-β1 was mostly undetectable except in macrophages exposed to SenP (figure 84a). Despite being detected, due to the variability between samples, the concentration of TGF-β1 was not significantly different to that of macrophages treated with medium alone. The same trend was observed with IL-10, the level of which was too low to be detected by the multiplex bead assay (figure 84b). The concentration of CCL17/TARC was also found to be below the detectable range in all experimental samples except the LPS induced M1 control (figure 84c). CCL22/MDC was the sole cytokine of which quantifiable levels were measured, though no secretome components significantly increased its production by treated macrophages and there was no difference in

the amount released between each sample (figure 84d). The final M2 macrophage associated cytokine investigated was G-CSF, which was not detectable from macrophages treated with SenEV (figure 84e). Both NEV and SenP generated low levels of this cytokine, however this was not significantly different to the concentration produced by medium only treated J774 macrophages. Macrophage exposure to NP induced the release of a significantly higher amount of G-CSF than the other normal and senescent myotube components.

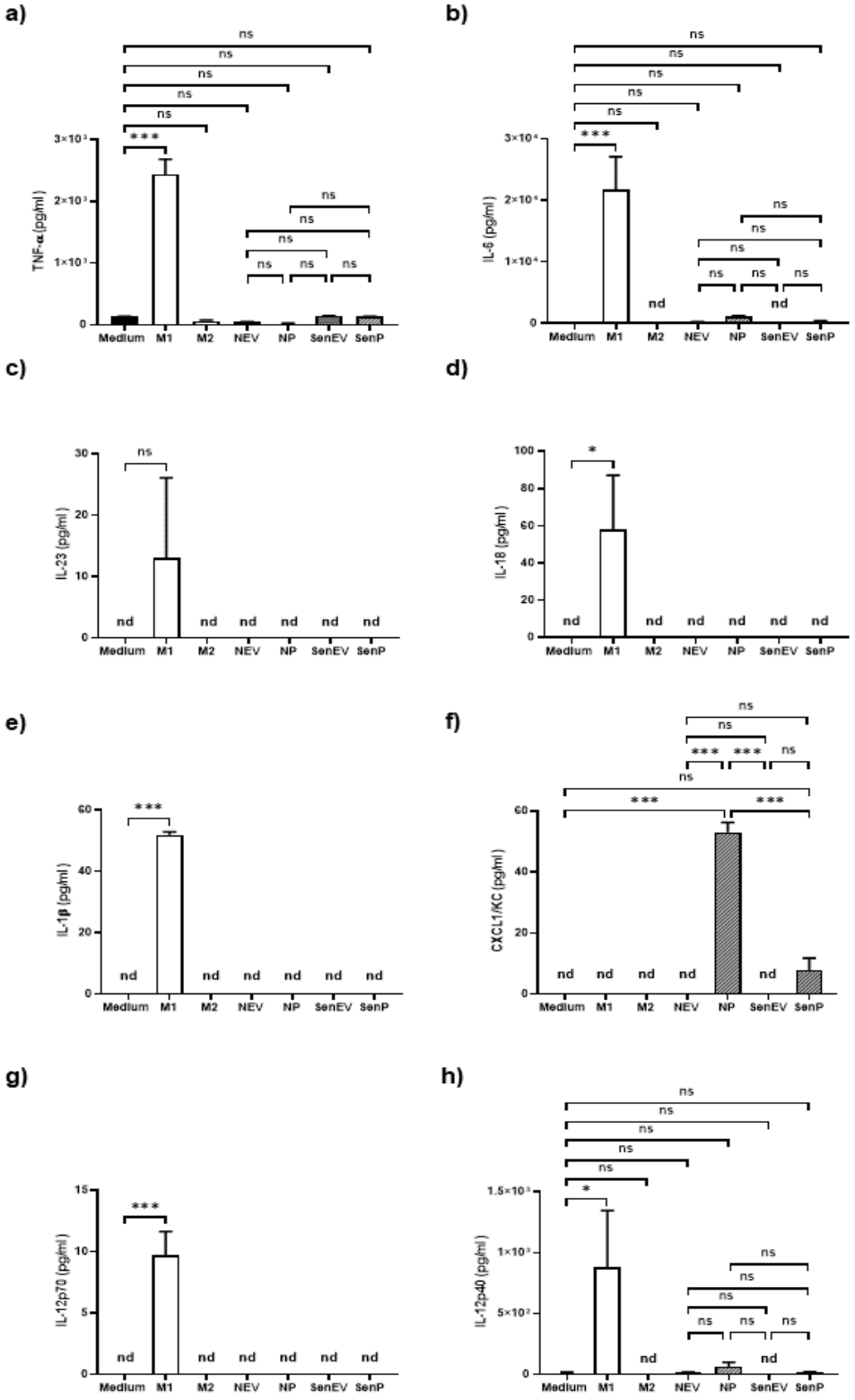

Figure 83. Pro-inflammatory cytokine profile of macrophages exposed to senescent myotube derived EVs and soluble proteins. J774 macrophages were treated with NEV and SenEV, and NP and SenP isolated from normal or senescent myotubes for 48 hours. Following treatment, the concentration of 8 pro-inflammatory macrophage cytokines was measured by a fluorescent multi-plex bead assay using flow cytometry. The cytokines measured were TNF-α (a), IL-6 (b), IL-23 (c), IL-18 (d), IL-1β (e), CXCL1/KC (f), IL-12p70 (g) and IL-12p40 (h). Data shown are ± SEM of 3 independent experiments, one-way ANOVA with Dunnett's *post-hoc* test, ****P<0.0001*, **P<0.05*. A one-way ANOVA with Tukey's *post hoc* test was also conducted: CXCL1/KC, ****P<0.0001*.

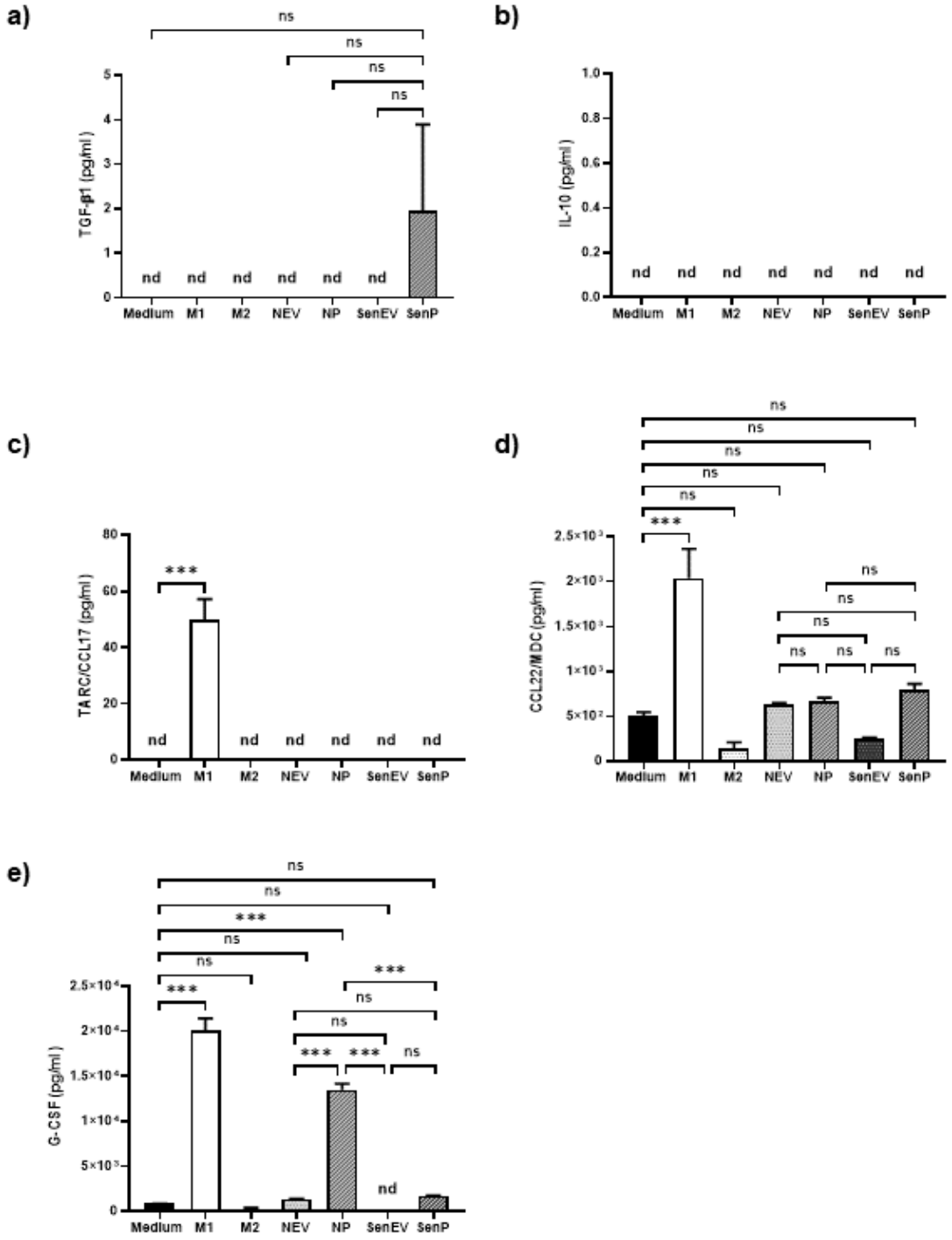

Figure 84. Macrophage anti-inflammatory cytokine release induced by senescent myotube derived EVs and soluble proteins. SEC isolated EVs and soluble proteins from normal and senescent myotubes were incubated with J774 murine macrophages. 48 hours post treatment, multiplex bead assay using flow cytometry was employed to measure the levels of free active TGF-β1 (a), IL-10 (b), TARC/CCL17 (c), CCL22/MDC (d) and G-CSF (e). Data shown are ± SEM of 3 independent experiments, one-way ANOVA with Dunnett's *post-hoc* test, ****P<0.0001*. A one-way ANOVA with Tukey's *post hoc* test for all measured cytokines.

5.2.6 Profiling the senescent myotube secretome

This chapter has highlighted the ability of the senescent myotube secretome to propagate a senescent phenotype to healthy cells, as well as modulating macrophage function. It is likely that these effects are controlled by specific factors contained within the SASP, such as EVs. As transporters of biological cargo, EVs can deliver selectively packaged proteins to recipient cells, such as myotubes and immune cells. During the development of skeletal muscle senescence as a hallmark of ageing, senescent myotubes may alter the profile of secreted proteins transported in EVs. The proteins contained within senescent vesicles may be responsible for the onset of muscle wasting and the progression of this age-related disorder. Consequently, this section aims to identify SenEV associated proteins using MS analyses, followed by GO analyses to assign functions to these proteins. It will also be determined whether EV proteins have been up- or downregulated and how this influences the biological processes they control. By ascertaining this information, it could help to explain some of the functional results presented earlier in this chapter.

NEV and SenEV were processed and analysed by MS, as previously described in section 4.2.5, with expert MS analyses provided by Dr Ivana Milic. 1152 proteins in total with unique peptide sequences were identified for both NEV and SenEV. Once again, these 1152 proteins were filtered to generate a list of proteins that when compared between NEV and SenEV, had significantly different abundances, for example proteins that were either significantly up- or downregulated in either sample. Proteins were filtered via a student's t-test, in which all proteins with a significance greater than 95% were retained and those below were excluded from the list. Following the filtering process, a total of 494 proteins were reported as having significantly different abundances.

The list of 494 proteins were further analysed using the functional enrichment tool FunRich 3.1.3, which quantified the degree of enrichment or depletion of the biological processes assigned to each protein. The degree of enrichment or depletion was reported as a fold change, which in this case is a measure that compares protein expression in SenEV against the expression of the same proteins in NEV. Therefore, biological functions stated as depleted were associated with proteins that were downregulated, whilst those that were enriched had upregulated proteins.

Of all GO biological processes identified, 1454 were more downregulated in SenEV than in their normal counterparts. Of the 1454, only 4 functions have been presented in figure 85 as these processes are related to the functional effects investigated in this chapter. The depleted functions were associated with immune responses, protein degradation and oxidative stress responses. Similarly, of the 1193 biological processes more upregulated in SenEV than in

NEV, only 5 have been included in figure 85 and are linked to cellular senescence, immune activation, protein catabolism, oxidative stress and angiotensin signalling.

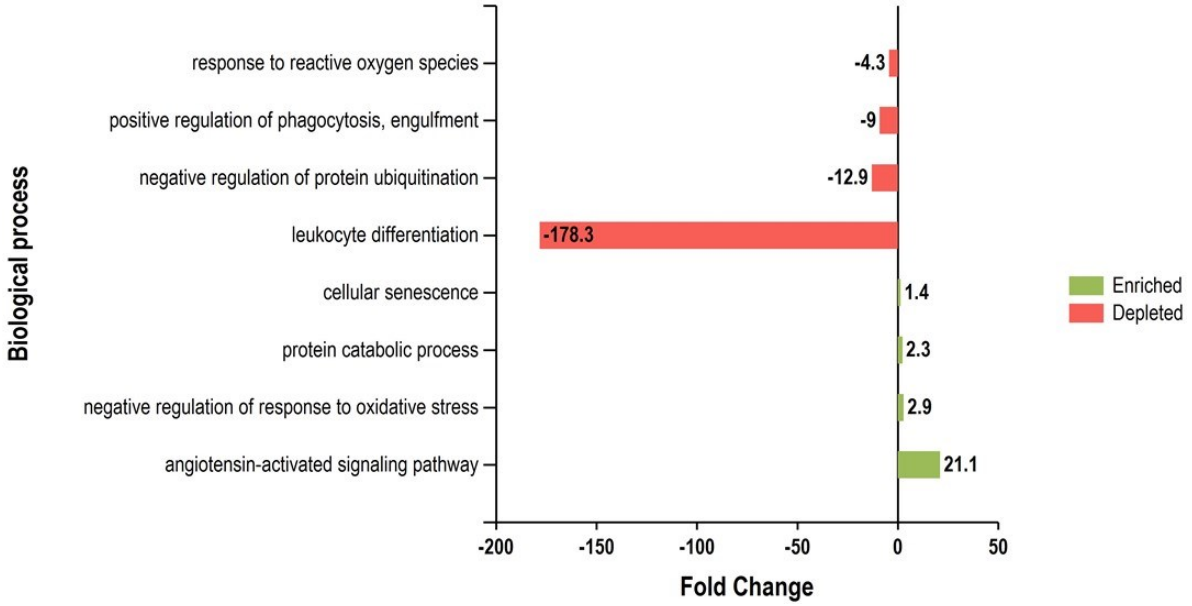

Figure 85. Functional enrichment or depletion of proteins in senescent myotube-derived EVs. Proteins of significantly different abundances between senescent and normal EVs, as decided by student's t-test were assigned GO biological functions. The degree of up- or downregulation of the proteins associated with each biological process was quantified and reported as a positive or negative fold change. Red bars correspond to proteins and their associated GO biological functions that have been depleted or downregulated and green bars correspond to those that were enriched or upregulated.

The proteins mapped to the biological processes in figure 83 were identified by the UniProt IDs provided by FunRich 3.1.3. The UniProt IDs via the UniProt database provided the full name of proteins and descriptions of the specific functions they are involved in. Table 3 contains a list of some of the proteins associated with the 4 downregulated GO biological functions as shown in figure 85. A similar list of proteins is shown in table 4, however these proteins have been mapped to the 4 enriched biological functions.

Biological function	Mapped proteins (UniProt ID)	Protein name
Response to reactive oxygen species	P35700	Peroxiredoxin-1
	P09671	Superoxide dismutase, mitochondrial
Positive regulation of phagocytosis, engulfment	P01027	Complement C3
Negative regulation of protein ubiquitination	Q9D1C8	Vacuolar protein sorting associated protein 28 homolog
	P63037	DnaJ homolog subfamily A member 1
Leukocyte differentiation	Q4JK59	Methylcytosine dioxygenase TET2

Table 3. GO biological functions downregulated in senescent EVs and their assigned proteins. Proteins significantly more downregulated in senescent EVs compared to normal EVs were mapped to 4 GO biological processes. Proteins were identified and details of their participation in various processes were ascertained using the UniProt database.

Biological function	Mapped proteins (UniProt ID)	Protein name
Cellular senescence	P14211	Calreticulin
Protein catabolic process	Q9JHR7	Insulin-degrading enzyme
Negative regulation of response to oxidative stress	Q9QZQ8	Core histone macro-H2A.1
Angiotensin-activated signalling pathway	P11798	Calcium/calmodulin dependent protein kinase type II subunit alpha

Table 4. Proteins mapped to upregulated senescent EV GO processes. Functional enrichment software was used to assign proteins which were significantly more enriched in senescent EVs compared to normal vesicles, to GO biological processes. UniProt database was used to identify protein names and to provide a description of the functions they modulate.

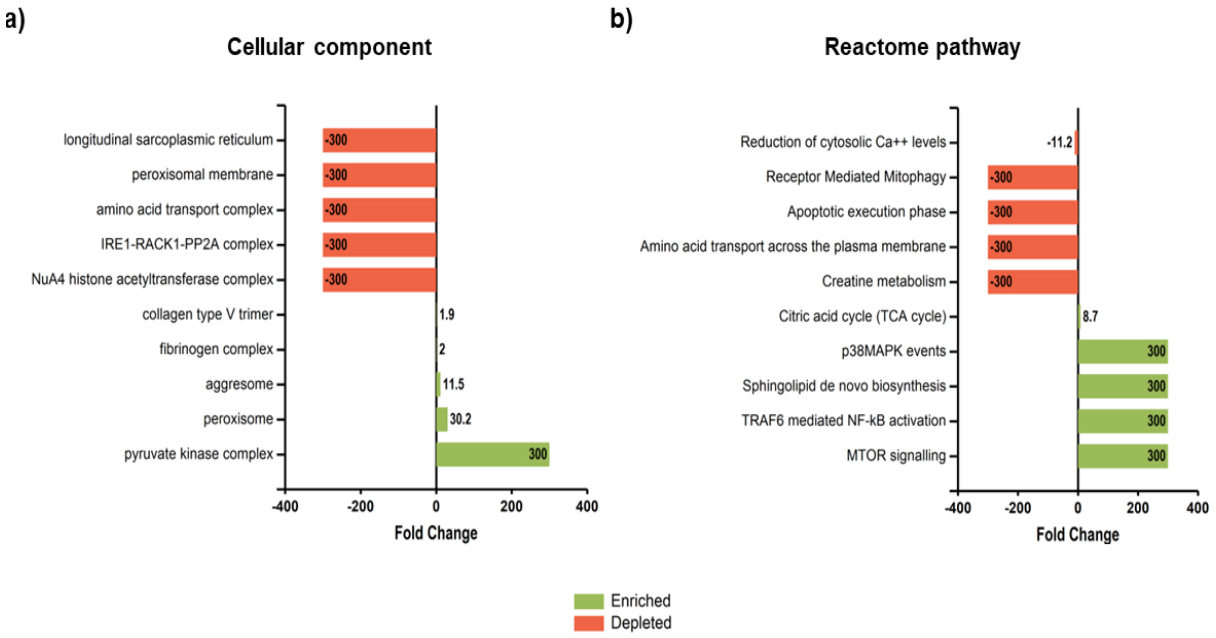

Figure 86. Functional enrichment analysis of differentially expressed proteins in SenEV. Proteins expressed by SenEV and NEV were assigned to GO terms associated with cellular component (a) and reactive pathways (b), which are presented as enriched in green or depleted in red.

Up- and down-regulated proteins associated with cellular component and reactome pathways have also been presented here. All pathways have not been presented and GO terms shown in figure 86 have been selected due their link to skeletal muscle function and senescence associated muscle atrophy.

5.3 Discussion

5.3.1 Modelling skeletal muscle senescence *in vitro*

Having established a viable SF model of skeletal muscle, it was necessary to determine whether this model could be successfully used to develop different SF models of muscle ageing, for the easy study of muscle-derived EVs. Chapter 4 has shown a sarcopenic model of ageing can be created using a SF system and the current chapter aimed to build on these findings by attempting to develop a senescent model of muscle ageing.

The adoption of a senescent phenotype by post-mitotic cells, such as myotubes and myofibers was previously thought to be impossible due to their entering irreversible cell cycle arrest. However, several studies have now shown that a variety of terminally differentiated cells can become senescent (Kang et al., 2011, Helman et al., 2016). This chapter supports these findings, as here it is shown that differentiated myotubes were successfully induced to senesce in the absence of animal serum and tested positive for SA-β-gal activity, a gold-standard marker in the identification of senescent cells (Dimri et al., 1995). This qualitatively evaluated senescence by the presence or absence of SA-β-gal, identified as blue staining, but ideally, SA-β-gal activity should be quantified for the numerical comparison of enzyme activity in putative senescent and non-senescent myotubes, for example by flow cytometry. Despite being a commonly used detector of cellular senescence, SA-β-gal activity is not a requirement for cells to become senescent and additional markers for senescence should be used to confirm this cell state.

In addition to the presence of SA-β-gal activity, cellular senescence in etoposide treated myotubes was also determined by probing for the protein $p16^{INK4a}$. Western blot analysis showed upregulated expression of this protein in senescent myotubes, suggesting these data coupled with the SA-β-gal activity were indicative of cellular senescence, however the bands corresponding to the presence of $p16^{INK4a}$ were faint in all experimental samples tested. $p16^{INK4a}$ is expressed in most senescent cell types but not all and low expression in the senescent myotubes could be explained by this. Some cells have shown positive senescence even in the absence of $p16^{INK4a}$ (Herbig et al., 2004, Freedman and Folkman, 2005, Renna et al., 2014). Senescent cells can also upregulate the expression of a different tumour suppressor protein, such as p53 or $p19^{ARF}$, the murine homolog of $p14^{ARF}$, which is an alternate reading frame protein product of the CDKN2A locus that also encodes for p16 (Lowe and Sherr, 2003). Furthermore, it has been suggested that human cells might favour the $p16^{INK4a}$ pathway, whilst murine cells as used in the current study, prefer the $p19^{ARF}$-p53 pathway.

Therefore, despite $p16^{INK4a}$ expression being another benchmark of senescence, in this study it might not have been the most suitable cell cycle arrest protein to search for. To investigate this, the expression of other cell cycle arrest related proteins in addition to $p16^{INK4a}$ could also be measured. This would provide more information regarding the molecular mechanisms regulating senescence induction in C2C12 skeletal myotubes.

To make senescence confirmation more robust, numerous tests should be performed to positively identify the presence of senescent cells in culture. This study employed two methods, yet both are not always expressed in senescent cells. Future work could also incorporate detection of IL-6 in the SASP to be used in combination with the other methods to fully confirm senescence induction.

5.3.2 EV release from senescent myotubes

Existing research has evidenced that with the onset of a senescent phenotype, the number of EVs secreted as part of the SASP increases to remove damaging genetic material from senescent cells (Misawa et al., 2020). Yet, this chapter has shown no difference in EV release between normal and senescent myotubes when whole and concentrated secretomes were measured. However, it is possible that SenEV concentration increased following SEC isolation, but further repeats are needed to confirm this. It is likely that this result is an anomaly and with repeated experimentation the difference between NEV and SenEV populations could be eliminated, since EVs were isolated from 2000*xg* secretomes, which showed no changes in the number of EVs produced. Failing to increase particle number, as reported by many other senescent studies could be attributed to the *in vitro* senescence inducing process. Myotubes were incubated with SF medium post etoposide exposure and senescence allowed to develop for 24 hours, after which secretomes were harvested. Senescence may have disseminated through the culture via secondary senescence, during which primary senescent cells induce senescence in healthy non-senescent cells in the vicinity (Admasu et al., 2021). Fáfian-Labora *et al*. have shown a decrease in EV secretion during secondary senescence compared to primary senescence (Fafián-Labora et al., 2020). This suggests that senescent myotubes could have entered secondary senescence and consequently, the senescent myotube-derived secretome contained fewer EVs at the time of collection. To confirm this theory, it would be necessary to differentiate between primary and secondary senescence to identify the precise stage the etoposide treated myotubes were in at the time of secretome collection.

Hettinger *et al*. reported an increase in EV secretion following oxidative stress induced senescence in human myoblasts compared to untreated cells (Hettinger et al., 2021). Despite most researchers reporting increased EV concentration by senescent cells, some studies

have demonstrated the opposite. In contrast to the Hettinger study, replicative senescence of murine myoblasts resulted in reduced EV release compared to differentiating myoblasts (Davies et al., 2021). It is likely that senescent cell-derived EV production is dependent on the method of senescence induction, with certain inducers stimulating elevated EV release whilst others cause a decrease. Furthermore, a longitudinal study of EVs circulating in peripheral blood found EV secretion declined with increasing age, as well as showing increased cellular uptake of ageing EVs (Eitan et al., 2017). Changes in EV release during senescence could be cell type specific, with many cells upregulating proteins to ensure more EVs are generated, whilst others might be actively minimising their release. Therefore, myotubes could belong to the group of cells that show reduced EV generation following senescence.

The exact mechanism responsible for increased EV secretion by senescent cells remains to be fully elucidated, however there is evidence of the involvement of p53 in the release of EVs during the cellular senescent programme. p53 responds to cellular stresses by upregulating the transcription of genes that are associated with numerous processes to ensure the affected cell maintains integrity and functions normally following stress management (Sheekey and Narita). This transcription factor can affect the endosomal pathway and influence the production and release of EVs (Yu et al., 2006, Feng, 2010). The increase of EV secretion by senescent cells can be attributed to a gene product regulated by p53, a multi-pass transmembrane protein known as tumour suppressor activated pathway-6 (TSAP6) (Wan et al., 2012). TSAP6 was originally identified as having a role in the regulation of the cell cycle and apoptosis, however it has also now been implicated in the non-classical exosomal secretion pathway (Passer et al., 2003, Lespagnol et al., 2008). TSAP6 deficient mice exhibit a nullified p53 dependent exosomal secretory pathway, resulting in reduced exosome release (Lespagnol et al., 2008), whilst deliberate overexpression of TSAP6 has shown to significantly increase the selective transport of proteins via exosome production.

In addition to inducing expression of TSAP6 to promote EV genesis, p53 can also modulate intracellular vesicle trafficking, ultimately influencing EV production. p53 can control whether cellular cargo will be targeted for lysosomal degradation or be packaged into EVs for release outside the senescent cell. p53 activity induces the transcription of CHMP4C, a subunit of the endosomal sorting complex required for transport III (ESCRT III) (Yu et al., 2009). ESCRT III is the most crucial component of the ESCRT machinery and is essential for late endosome membrane scission to form EVs (Bertin et al., 2020). As well as influencing ESCRT activity, p53 also increases the transcription of caveolin-1, which is a scaffolding protein associated with caveolae and is involved in the internalisation of membrane receptors into vesicles (Yu et al., 2009). By exerting its influence over numerous proteins involved in EV biogenesis, p53 can control the rate of EV release by senescent cells.

It can be hypothesised that the senescent myotubes had low p53 activity, with a different senescence associated protein such as $p19^{ARK}$ being predominant. Minimal p53 expression would reduce EV generation by the senescent myotubes due to a decline in TSAP6 and ESCRT III activity, which would be a rationale for the number of senescent myotube-derived EVs being similar to that produced by normal myotubes.

Besides discerning senescent and normal myotubes generated a similar number of EVs, this chapter has also shown that EV size did not change under ageing conditions. EV populations from both types of myotube were categorised as small EVs with a particle diameter <200 nm or exosome-like due to the expression of exosomal protein markers. In contrast, oxidative stress induced senescent C2C12 cells were found to release small EVs with increased expression of CD63 and TSG101, however these EVs were isolated using ExoQuick precipitating solution and analysed mRNA levels to determine EV protein expression levels (Hettinger et al., 2021). This result corresponds with the findings of other senescent cell-derived EVs, which have reported modal sizes between 100 nm to 200 nm (Han et al., 2020, Wallis et al., 2021, Jeon et al., 2019).

Although, EV concentrations between the two types of myotube were similar, the ability of recipient cells to take up these particles also had to be ascertained if the functional effects on recipient cells were to be investigated. J774 macrophage internalisation of SenEV was not significantly different to the uptake of NEV, implying these phagocytic cells had the same affinity for each vesicle. There is little information regarding macrophage uptake of EVs produced by senescent myotubes, though one study has shown senescent cell-derived EVs can be readily taken up by monocytes, which can affect their effector function (Freeman et al., 2018). It is possible that the differentiation and activation status of immune cells is linked to EV internalisation. Czernak *et al.* reported cancer cell-derived EVs were more efficiently internalised by macrophages and mature dendritic cells compared to monocytes and immature dendritic cells (Czernek et al., 2015). As this study was conducted using cancer EVs, it is difficult to determine whether a similar scenario occurs with SenEV.

5.3.3 Paracrine effects of myotube-derived SASP

The current study has shown whole senescent myotube-derived secretome or SASP to confer cellular senescence on normal myotubes. It is likely that a senescent bystander effect is responsible for reinforcing and maintaining senescence; a process in which exposure to senescent cells or their secreted products induces senescence in healthy proliferating neighbouring cells, similar to the traditional ionising radiation bystander effect (Prise and O'Sullivan, 2009). The senescence bystander effect is a phenomenon of interest that has also been investigated by Elbakrawy *et al.* who reported conditioned medium from irradiated cells

transferred senescence to healthy proliferating cultures (Elbakrawy et al., 2020). This team of researchers also showed irradiated cell-derived exosomes were capable of inducing senescence in healthy cells too, however this was not to the same extent as the irradiated cell conditioned medium, suggesting complete SASP is more effective at spreading senescence than individual SASP components alone (Elbakrawy et al., 2020). Another study has shown the transplantation of senescent cells into the skeletal muscle of immunodeficient mice caused myofibers surrounding the site of injection to exhibit an increase in markers associated with cellular senescence and were responsible for muscle fibre thinning (da Silva et al., 2019). The da Silva *et al*. study in conjunction with the findings of the paracrine effects of SASP in this chapter suggest a link between senescence in ageing and the development of the muscle wasting condition sarcopenia.

The secretome of senescent cells is complex, containing many bioactive molecules, which can have diverse downstream effects within the tissue microenvironment and systemically (Tchkonia et al., 2013). The SASP can be beneficial due to its ability to promote tissue regeneration when short term, whilst it exhibits detrimental properties and causes damage when it persists (Ritschka et al., 2017). The release of small EVs as a component of the SASP can have harmful effects within skeletal muscle. EVs isolated from senescent murine C2C12 myotubes *in vitro*, senescent primary human myotubes and ageing mice were all reported to contain significantly higher levels of the senescence associated microRNA, miRNA-34a-5p (Fulzele et al., 2019, Zheng et al., 2018). These miRNA-34a-5p carrying EVs can reduce the activity of the pro-survival deacetylase sirtuin-1 in many cell types with age and suppression of this protein has been linked to impaired skeletal muscle performance, suggesting ageing skeletal muscle EVs can damage this tissue (Owczarz et al., 2017, Mohamed et al., 2014). Release of this microRNA via EVs into the circulation can also have damaging effects further afield in other tissues. Exposure of young adult mice bone marrow stromal cells with miRNA34a-5p containing EVs both increased cellular senescence in these cells and reduced their viability (Fulzele et al., 2019).

Unfortunately, due to Covid-19 related time constraints further investigation of the role of SASP in inducing a senescent phenotype in normal myotubes could not be conducted. Consequently, future work would include a co-culture of senescent myotubes with normal myotubes to imitate physiological conditions in which senescent myotubes would be situated locally to normal myotubes within skeletal muscle tissue. This study does not show other forms of senescent signal transduction between senescent and normal myotubes, for example cargo delivery via EV, therefore the breakdown of the SASP into EV and soluble protein fractions would also be undertaken. Normal myotubes would subsequently be treated with each SASP

component to determine whether EVs, soluble proteins or both in tandem are responsible for the propagation of senescence in healthy cells.

Senescent cells are known to produce high levels of ROS, contained within the SASP and this is another aspect of the senescent myotube secretome that could be investigated. Following bystander effect experiments, the amount of internal ROS of SASP treated normal myotubes could be measured to confirm the senescent phenotype.

5.3.3.1 The influence of SASP on macrophage function

Senescent cells facilitate their own removal by the immune system by secreting immunomodulating factors via the SASP to maintain tissue homeostasis and prevent loss of function. However, during ageing senescent cells accumulate in tissues throughout the body, contributing to the ageing process and are associated with numerous age-related pathologies, including cardiovascular disease, neurodegenerative disorders, osteoporosis, frailty and sarcopenia (Campisi and Robert, 2014, McHugh and Gil, 2018). Their persistence in the elderly can be partly attributed to their ability to evade clearance by the immune system, suggesting the SASP signal is modified during chronic senescence.

This chapter tested the ability of senescent myotube-derived secretome to promote macrophage migration and the horizontal migration data suggested senescent myotube-derived secretome had no chemotactic potential. The horizontal platform utilised human THP1-derived macrophage-like cells against murine myotube-derived secretomes, which could account for the lack of migration. Murine J774 macrophage clearance of apoptotic human T cells has been previously shown, indicating some recognition mechanisms have been conserved between the two species, suggesting human phagocytes could respond to bioactive molecules within the murine myotube secretome (Torr et al., 2012). The horizontal migration data indicate THP-1/D3 macrophage-like cells covered a greater distance at a higher velocity only in the presence of the normal myotube filtrate, however this migration was nondirectional, which is indicative of chemokinesis. Chemokinesis can be induced even in the presence of a chemotactic gradient, which was the case in this study (Rumianek and Greaves, 2020, Gervais et al., 2001).

In contrast, the transwell migration data show J774 macrophages only migrated towards senescent secretomes under certain conditions. The vertical transwell assay showed murine macrophages migrated towards both normal and senescent secretomes (whole and concentrated). It was hypothesised that senescent myotubes in an aged setting would attempt to minimise macrophage recruitment via the SASP to evade clearance by the immune system thereby allowing for their accumulation, however the data do not reflect this theory. The use of a co-culture model could provide some explanation for these results, as well as highlighting

the involvement of the SASP in preventing senescent-immune cell interaction. For example, SASP components can promote ECM stiffening to prevent immune cell infiltration and clearance of senescent cells, thereby enabling senescent cell persistence (Mavrogonatou et al., 2019, Fane and Weeraratna, 2020). This senescent secretome feature was not demonstrated in the migration assays as senescent myotubes were not present to produce an ECM.

Another explanation for the migration data in this chapter could be that the senescent-derived myotube secretome can only affect immune cell function at the site of senescence. For example, senescent cells can prevent direct interaction with macrophages by upregulating CD47, a “don’t eat me” signal commonly expressed on normal cells (Lo et al., 2015). Increased expression of CD47 aids senescent cell immune evasion by inhibiting the macrophage effector function of phagocytosis and therefore impeding their clearance. Therefore, it is possible senescent cells, including the senescent myotubes in this chapter operate a “find me” but “don’t eat me” immune response. Another method of senescent cell secretome promoting senescent cell persistence was observed in senescent fibroblasts. The SASP of senescent fibroblasts impairs the ability of macrophages to induce apoptosis and reduces their phagocytic activity (Ogata et al., 2021). These macrophage functions were inhibited by SASP factors, including IL-1α and GM-CSF, which reduced TNF-α and PS receptor gene expressions of macrophages exposed to senescent fibroblasts (Ogata et al., 2021).

The effect of myotube SASP on other macrophage effector functions was also assessed. The ability of the senescent myotube secretome to modulate macrophage superoxide anion release was also investigated; the production of which is associated with pro-inflammatory M1 macrophages. Whilst pre-treating J774 macrophages with the whole senescent myotube secretome did not alter their superoxide anion producing ability, pre-treatment with SenP reduced its release. Separating the secretome into its constituent parts revealed certain components were better at influencing the respiratory burst function of the macrophages than others. By reducing superoxide anion production, SenP limited the inflammatory nature of J774 macrophages, making them less M1 in phenotype, which ultimately supports senescent myotube survival. Sufficient ROS production by macrophages is essential for their phagocytic function and for the effective clearance of senescent cells (Forrester et al., 2018). By reducing superoxide anion release, the SenP are inhibiting their internalisation by macrophages.

Furthermore, as SenEV did not affect superoxide anion production, it would suggest that they abrogated the effect of SenP in the whole senescent secretome. It is possible that due to an insufficient number of SenEV, they were unable to exert their full effect on macrophage

respiratory burst. To investigate this further, the respiratory burst assay should be repeated with a higher dose of SenEV to determine whether this is simply a dosing issue.

This interpretation is further supported by the macrophage phenotyping Griess assay data, which demonstrated that the concentrated senescent myotube secretome (retentate and filtrate) did not affect macrophage NO_2^- production, indicating the macrophages remained M1 polarised. Isolating SenEV and SenP from the SASP caused a significant reduction in NO_2release by LPS primed macrophages, which suggests the pro-inflammatory behaviour of these immune cells was being suppressed. The difference in response between the concentrated SASP and the separated SASP fractions could be attributed to the presence of other soluble factors within the concentrated secretome, which are removed during the SEC process used to isolate EVs and soluble proteins. The contemporaneous release of proimmunogenic soluble mediators could counteract the anti-inflammatory effects of both EVs and soluble proteins. Leukotrienes are one such factor, which are lipid mediators found at elevated levels within the SASP (Wiley et al., 2019, Lopes-Paciencia et al., 2019, Pils et al., 2021). Leukotriene C_4 promotes oxidative stress and the release of ROS by enabling the translocation of the ROS producing enzyme NADPH oxidase 4 (Dvash et al., 2015). As well as inducing ROS release, leukotriene C_4 also stimulates the production of $^{\bullet}NO$ by macrophages and polymorphonuclear leukocytes (Lärfars et al., 1999). Inhibiting phospholipase A2, the enzyme responsible for releasing arachidonic acid for the formation of pro-inflammatory leukotrienes, eicosanoids and prostaglandins promotes macrophage polarisation towards M2 macrophages (Ashley et al., 2016). This highlights the role of lipid mediators in facilitating the M1 pro-inflammatory phenotype. However, further MS analyses would be required for the detection of lipid mediators in the myotube SASP.

During ageing, chronic low-grade inflammation is accompanied by immunosuppressive responses, including an increase in the M2 macrophage population in both tissues and the systemic circulation (Wang et al., 2015, Costantini et al., 2018). Long-lived senescent cells can modify their SASP and increase secretion of anti-inflammatory components to recruit immunoregulatory cells and influence immune cell effector function within senescent tissue, which supports the respiratory burst and NO_2^- production data. These mediators released either in soluble form or carried by SenEV can preferentially polarise macrophages to an antiinflammatory M2 phenotype. For example, senescent thyrocyte secretome promotes an M2like phenotype in human monocytes and this is mediated by prostaglandin E2, which prevents immunosurveillance and clearance of senescent cells (Mazzoni et al., 2019). These ageassociated counteracting anti-inflammatory effects could account for the accumulation of senescent cells in skeletal muscle and the persistence of cellular senescence in this tissue.

Identification of the cytokine profile would have provided insight into the inflammatory status of J774 macrophages exposed to myotube SASP components. Unfortunately, the cytokine profiling data in this chapter show most cytokines were beyond the level of detection, indicating the multiplex fluorescence bead used to measure cytokine concentration was not sufficiently sensitive to detect low quantities. This was also the case for the M2 control, which should have exhibited high levels of all anti-inflammatory cytokines. An alternative method of M2 polarisation, other than IL-4 treatment is required to ensure this control sample works in future. Cytokine detection could be improved by concentrating the J774 macrophage secretomes prior to measurement. The only cytokines detected were the pro-inflammatory CXCL1/KC and the anti-inflammatory G-CSF, both of which were produced in response to macrophage treatment with NP and is discussed in section 4.3. CCL22/MDC release was observed by all myotube secretomes, however this was not significantly different to the untreated macrophages and could require additional repetitions to differentiate between secretome components. Irrespective of this result, the multiplex assay data suggest there was some macrophage production of free active TGF-β1 in the presence of SenP. Further experimentation is most likely required to confirm whether this myotube SASP component truly induces secretion of free active TGF-β1.

EVs can traffic a wide range of bioactive molecules, including cytokines and soluble receptors for uptake by recipient cells. Although not evidenced in this chapter, it is likely that both soluble factors and those packaged within EVs are involved in the propagation of senescence and the modification of macrophage function.

5.3.4 Mapping the senescent EV protein profile to senescent EV function

5.3.4.1 Downregulated biological functions

By deciphering the SenEV proteome, it is possible to explain some of the functional effects they elicit on both healthy myotubes and macrophages. Identification of downregulated proteins could provide insight into how senescent cells cause muscle wasting in aged individuals and could pinpoint potential protein targets for the treatment of skeletal muscle senescence.

One biological function more depleted in SenEV than in their normal counterparts was the response to ROS. Proteins associated with this process that were shown to be down regulated were Prx-1 and mitochondrial superoxide dismutase (SOD2), both of which are antioxidant enzymes. Prx-1 provides protection against oxidative stress by catalysing the conversion of hydrogen peroxide into water, whilst SOD2 converts superoxide anion into hydrogen peroxide and oxygen (Helman et al., 2016, Flynn and Melov, 2013). Depletion of these antioxidants by senescent myotubes, as reflected by their secreted EVs would make muscle cells more

susceptible to oxidative damage during cellular senescence. These data support the hypothesis that SASP helps maintain the oxidatively stressed environment in ageing muscle senescence, as senescent EVs were unable to reduce superoxide anion release by J774 macrophages. It is possible that as SenEV contain fewer SOD2 molecules, these vesicles are less able to clear macrophage-derived superoxide anion than NEV.

High oxidative stress environments, such as that found in senescent skeletal muscle, could result in macrophages releasing increased bursts of mitochondrial ROS, which could damage their mitochondria (Zorov et al., 2014). NEV with elevated expression of SOD2 could deliver this enzyme to macrophages to confer protection during muscle injury. In contrast, during ageing, SenEV may promote macrophage damage and induce senescence in these immune cells as they have fewer SOD2 enzymes to transport. In this scenario, the extension of the senescent phenotype to macrophages both within skeletal muscle tissue and further afield might sustain senescence, in addition to causing loss of muscle mass and function.

Furthermore, SOD2 deficiency may suggest another cause for the onset of myotube senescence and provide a better understanding of the events occurring within senescent myotubes. Reduced expression of SOD2 during the ageing process could lead to mitochondrial dysfunction, resulting in DNA damage and induction of cellular senescence (Velarde et al., 2012). Malfunctioning mitochondria in senescent myotubes could generate excess ROS as a component of the SASP and elevated ROS could be transferred to healthy myotubes, which supported by the reduced diameter of normal myotubes treated with whole senescent secretome. Similarly, Prx-1 can also protect against ROS induced cellular senescence, as Prx-1 knockout mice exhibit elevated $p16^{INK4a}$ expression and increased SAβ-gal activity (Park et al., 2017). With senescent myotubes downregulating their Prx-1 expression, such that very little is packaged into EVs, the cells are more susceptible to oxidative damage due to reduced hydrogen peroxide scavenging by Prx-1. The continued presence of hydrogen peroxide within the aged muscle environment maintains the senescent phenotype of existing senescent cells but also spreads senescence to healthy cells, including macrophages. It would have been beneficial to determine whether exposure to SenEV conferred senescence to J774 macrophages via the SASP bystander effect, as this would present a role for senescent macrophages in skeletal muscle senescence and associated muscle wasting.

With increased endotoxemia in elderly individuals and continuous exposure to LPS, mitochondrial ROS can facilitate LPS mediated pro-inflammatory cytokine production, potentially in both myotubes and macrophages (Ghosh et al., 2014, Bulua et al., 2011). The downregulation of SOD2 in SenEV might not efficiently eliminate mitochondrial generated

superoxide and therefore could actively encourage the release of tissue damaging proinflammatory cytokines that cause muscle atrophy.

SenEV were also found to have depleted negative regulation of protein ubiquitination to a greater extent than NEV. The onset of senescence is thought to activate the unfolded protein response (UPR), which is triggered in response to cellular stress (Pluquet et al., 2015). Senescent cells generate SASP, and the endoplasmic reticulum (ER) could be overwhelmed by having to produce the various overexpressed proteins comprising the secretome, causing proteotoxic stress and activating the UPR (Dörr et al., 2013). Under normal circumstances, the UPR coordinates with the UPS to alleviate protein misfolding and prevent their accumulation (Cybulsky, 2013). The UPR in conjunction with UPS could be activated during senescence to re-establish ER homeostasis, which would be detrimental to the production of SASP and the maintenance of senescence. However, DNAJA1, a protein associated with the UPR was also downregulated in SenEV, which would prevent appropriate UPR functioning (Gargalovic et al., 2006). This would allow for the continued production and secretion of SASP proteins, such as pro-inflammatory cytokines and other inflammatory mediators which in turn disseminate the senescent phenotype in skeletal muscle.

Another depleted immune function associated with SenEV was leukocyte differentiation, which was linked to downregulation of methylcytosine dioxygenase TET2, a protein responsible for DNA demethylation (Wu and Zhang, 2017). Reduced expression of this protein, for example during muscle senescence could increase the production of pro-inflammatory cytokines, i.e. IL-1β and IL-6, however, contradictorily it can also increase arginase expression, which is associated with M2 macrophages (Cull et al., 2017). TET2 is highly expressed during macrophage differentiation and downregulation of this protein demonstrates the EV-containing SASP can prevent the differentiation of macrophages in muscle tissue (Lio and Rao, 2019). The depletion of TET2 in SenEV could stimulate the generation and maintenance of M2 macrophages by preventing the polarisation of the M2 population into M1 cells which would be capable of clearing senescent associated tissue damage (Cull et al., 2015).

Another function for TET2 is the development of skeletal muscle, as this protein is highly expressed during myogenesis (Laker and Ryall, 2016). Therefore, in addition to limiting the immune response, downregulation of this protein during myotube senescence may affect the regenerative capacity of skeletal muscle and cause a loss of muscle mass (Zhang et al., 2022).

Senescent cells might persist in ageing individuals due to their ability to prevent clearance by evading the immune system (Pereira et al., 2019). One method of interfering with their removal

is to downregulate the expression of complement C3 to interfere with the positive regulation of phagocytosis, a process which was found to be more depleted in SenEV than in their normal counterparts. Complement C3 is a member of the complement pathway and this protein can be cleaved to produce the products, C3a and C3b (Zwarthoff et al., 2018). C3a is a chemoattractant and reduced C3a receptor signalling has been linked to impaired skeletal muscle regeneration due to a reduction in macrophage recruitment (Zhang et al., 2017). This is contradictory to the data presented in this chapter, as SenEV had the opposite effect and induced macrophage migration. Whilst a low level of C3a might prevent macrophage infiltration, it is likely that other proteins carried by SenEV could have a stronger influence and dampen any C3a mediated effects on migration.

C3b functions as an opsonin to label cells and target them for engulfment by macrophages (Walport, 2001, Merle et al., 2015). By downregulating the protein at the beginning of the pathway, senescent myotubes can escape immune clearance due to the absence of c3b mediated opsonisation. The permits senescent myotubes to persist within muscle tissue, thereby maintaining the senescent profile.

5.3.4.2 Upregulated biological functions

As expected, cellular senescence was more enriched in SenEV than in NEV. Increased expression of calreticulin was responsible for the upregulation of this function. Calreticulin is an “eat me” signal presented on the surface of apoptotic cells to target them for clearance by phagocytic cells (Park and Kim, 2017, Gardai et al., 2005). Upregulation of this protein in senescent myotubes could also encourage their removal by macrophages (Elder and Emmerson, 2020). However, as calreticulin abundancy was higher in SenEV a potential scenario could be that the senescent myotubes were increasing the secretion of calreticulin into vesicles to selectively remove it from the cells. Expelling calreticulin from senescent myotubes would prevent the exposure of this protein on their surface and possibly allow them to evade phagocytosis, facilitating senescent myotube persistence and the maintenance and propagation of a senescent muscle phenotype.

Elevated calreticulin expression can also increase immune cell migration, which could explain the increase in J774 macrophage recruitment by SenEV (Wang et al., 2012). However, an apoptotic cell study has shown that the early upregulation and secretion of calreticulin can disrupt macrophage phagocytosis (Osman et al., 2017). Pre-exposure of macrophages to soluble calreticulin stimulated the release of pro-inflammatory cytokines but surprisingly reduced the clearance of apoptotic cells and downregulated molecules involved in antigen presentation; inducing the activation of a macrophage that does not conform to the M1/M2 model (Osman et al., 2017). A similar scenario could have occurred in senescent myotubes,

such that the release of EV-associated calreticulin stimulated macrophage infiltration, however modified their ability to “eat” and remove the senescent cells. This would support the hypothesis that the EV containing senescent secretome creates an in-between hybrid macrophage, as SenEV were shown to reduce the M1 phenotype of J774 macrophages but could not reduce their ability to secrete ROS. The recruitment of hybrid macrophages by the myotube SASP could prevent their removal due to phagocytosis disruption and allow senescent myotubes to persist in ageing muscle tissue. It should be noted that this study was conducted using apoptotic human cells, therefore it is not known whether a similar outcome of the early secretion of calreticulin by murine senescent myotubes would induce the same effect on murine macrophages.

Age-related muscle wasting is linked to dysregulated proteostasis, with protein degradation occurring at a faster rate than protein synthesis. Therefore, it is not surprising that the protein catabolic process was more enriched in SenEV than in NEV. The protein mapped to this upregulated function was insulin-degrading enzyme (IDE), which is involved in the breakdown of insulin amongst other peptides (Duckworth et al., 1998). Insulin can prevent the degradation of skeletal muscle proteins by inhibiting the UPS, thereby alleviating muscle atrophy (Chen et al., 2011). Consequently, the increased expression of IDE in SenEV increases the breakdown of insulin, thus removing the inhibitor of the UPS to degrade more muscle proteins. The upregulated secretion of IDE in SenEV allows senescent myotubes to deliver this degradative enzyme to healthy non-senescent muscle cells and promote protein breakdown in them, as shown by the reduced diameter in normal cells upon exposure to the whole senescent myotube-derived secretome.

Senescent cells are reported to produces excess ROS, mostly a result of mitochondrial dysfunction (Victorelli and Passos, 2019), consequently the negative regulation of the response to oxidative stress was more enriched in SenEV. Increased expression of mH2A1 protein was mapped to this GO biological process. mH2A1 expression is elevated in human senescent fibroblasts and the ageing tissues of mice and primates, which supports the upregulation of this protein in SenEV (Kreiling et al., 2011). As stated in section 4.3.7.1, mh2A1 has contradictory functions as both a repressor and activator of transcription (Angelov et al., 2003, Recoules et al., 2022). For instance, different mH2A1 isoforms can have opposing effects, as isoform 1 increases SOD3 expression whilst isoform 2 downregulates the expression (Dardenne et al., 2012). Although the functional enrichment software did not state the isoform of this protein, it is likely that it could be isoform 2 since negative regulation of the oxidative stress response was enriched. Upregulated mH2A1 isoform 2 supresses SOD3 activity and therefore protection against oxidative stress is reduced. This provides some clarification of the respiratory burst data. SenEV did not reduce superoxide anion production

by zymosan stimulated macrophages; most likely a result of the reduced presence of SOD3 molecules in the vesicles.

Lastly, the angiotensin-activated signalling pathway was another GO biological process to be more enriched in SenEV, due to the upregulation of calcium/calmodulin-dependent protein kinase type II subunit alpha (CaMK2α). CaMK2α expression is increased during muscle atrophy and this possibly linked to its involvement in activating the angiotensin pathway (Chin, 2005). It is difficult to decipher the exact role of this protein in the angiotensin-activated signalling pathway, however angiotensin II levels are elevated in chronic kidney disease patients with muscle wasting (Yoshida et al., 2013). Muscle mass loss in these patients could be alleviated with angiotensin converting enzyme inhibitors, suggesting a role for angiotensin II in the onset of muscle atrophy (Yoshida et al., 2013).

Angiotensin II has also been implicated in kidney endothelial cell senescence and it is also possible for it to promote senescence in skeletal muscle. A possible explanation for this could be via angiotensin type I receptor (ATIR) binding, a receptor that is also expressed by macrophages (Yamamoto et al., 2011). Binding of this macrophage receptor can modulate the function of these immune cells. Positive signalling via this receptor can induce macrophage migration, the production of pro-inflammatory cytokines (Keidar et al., 2002) (Yamamoto et al., 2011). This corresponds to the ability of SenEV to increase recruitment of J774 macrophages. ATIR signalling can also activate NADPH oxidase and stimulate the release of ROS, which relates to the ability of SenEV to maintain superoxide anion production by zymosan treated J774 macrophages (Powers et al., 2018). By increasing oxidative stress through this pathway, SenEV can induce proteolysis, myotube senescence and subsequent atrophy of skeletal muscle.

5.3.4.3 Cellular component and reactome pathway

In addition to biological processes, differentially expressed SenEV proteins were assessed with regards to cellular component and reactome pathway, with a focus on GO terms related to senescence associated muscle atrophy.

Increased production and accumulation of sphingolipids during muscle ageing are linked to cellular senescence, as “sphingolipid *de novo* biosynthesis” was an elevated cellular component in SenEV (Laurila et al., 2022). Lipid uptake, transport and metabolism pathways were upregulated in senescent myocytes isolated from aged mice as shown by GSEA analysis, which all promote sphingolipid production (Moiseeva et al., 2023).

Cell protective mechanisms, such as “receptor mediated mitophagy” and “apoptosis execution phase” related proteins were also depleted in SenEV compared to NEV. The expression of

mitophagy inducing proteins was reduced in the muscles of ageing mice and inactive old women, which can cause mitochondrial dysfunction and sarcopenia (Joseph et al., 2013, García-Prat et al., 2016, Drummond et al., 2014). whilst preventing apoptosis ensures senescent myotubes persist.

Surprisingly energy metabolism related pathways were upregulated in SEV. Enrichment of the "TCA cycle" and "pyruvate kinase complex" highlights the increased metabolic activity of senescent myotubes, which could be due to extra energy required for SASP production (Sabbatinelli et al., 2019). GSEA reactome pathway analysis of RNA-seq data for senescent myoblasts shows upregulation of glycolytic pathways with the TCA cycle being enriched in these cells, therefore it is possible that cell-derived EVs could reflect this change (Shahini et al., 2021). Despite the similarity in results, this study investigated senescence in myoblasts rather than myotubes and their EVs so it is possible there could be some variation between cell types. Other energy metabolism systems are dysregulated with ageing, as "creatine metabolism" was also depleted in SenEV. MS based proteomic analysis of aged rat muscle showed downregulation of creatine kinase and creatine metabolism (Piec et al., 2005).

Alongside altered energy metabolism, SenEV also displayed changes to amino acid uptake as "amino acid transport complex" and "amino acid transport across plasma membrane" proteins were downregulated. These data are supported by mRNA and Western blot analyses of amino acid transporters which have shown reduced expression in elderly individuals compared to younger counterparts (Cuthbertson et al., 2005, Dickinson et al., 2013). Furthermore, depletion of the essential amino acid taurine has been reported to cause skeletal muscle senescence by inducing $p16^{INK4a}$ expression and limiting protein synthesis in aged mice (Ito et al., 2014).

SenEV proteins also reflect the negative impact of senescence on skeletal muscle function. These EVs were depleted of proteins relating to "longitudinal sarcoplasmic reticulum", also known as T-tubules. These structures regulate intracellular calcium (Ca^{2+}) levels required for generating action potentials to initial muscle contraction and reduced expression of proteins associated with this function could have resulted in downregulation of "reduction of cytosolic Ca^{2+} level" in SenEV (Al-Qusairi and Laporte, 2011). Senescent mice have shown increased concentration of intracellular Ca^{2+} though it has been

Another feature of skeletal muscle senescence is fibrosis and consequently, "collagen type V trimer" was enriched in SenEV. This is supported by histochemistry of muscle tissue from p21 expressing senescent mice, which showed increased accumulation of collagens compared to control mice (Englund et al., 2023). MS based proteomics of old mice similarly found collagen expression was elevated in the animal matrisome (Lofaro et al., 2021). The Lofaro *et al.* study

also established fibrinogen was upregulated in the muscles of aged mice, leading to a fibrotic phenotype and this was also observed in SenEV which showed enrichment of “fibrinogen complex” (Lofaro et al., 2021).

Protein aggregation increases with age and SenEV proteomics indicated enrichment of the “aggresome”, which is an aggregation of misfolded proteins (Kopito, 2000). Gel electrophoresis of protein aggregates isolated from skeletal muscle tissue of older individuals showed these structures contained more protein compared to younger muscle and were responsible for loss of muscle mass (Ayyadevara et al., 2016). Increased aggresome formation is likely linked to the “IRE1-RACK1-PP2A complex”, which was depleted in SenEV and suggests disrupted proteostasis. This complex detects mis-and unfolded protein induced ER stress and regulates the UPR (Liu et al., 2016). Gene ontology analysis has also identified upregulation of proteins associated with this complex in the skeletal muscle of older chickens (Zhang et al., 2021).

Surprisingly, proteins related to “peroxisome” structures were elevated in SenEV, as these cellular components are involved in ROS detoxification (Schrader and Fahimi, 2006). Conversely, peroxisomes can also generate ROS and contribute to oxidative stress, which is a feature of senescence, however it is unknown whether ROS production or scavenging functions are elevated in SenEV (Davalli et al., 2016). Peroxisomes also catabolise long chain fatty acids and increased peroxisome expression could be a consequence of upregulated sphingolipid synthesis and potential increase in lipid uptake (Wanders et al., 2016).

Signalling pathways were also differentially expressed, with mTOR signalling” upregulated in SenEV compared to NEV. This is corroborated by Tang *et al.* who used immunostaining to determine increased activation of mTOR complex in the muscles of aged mice and was found to be localised to atrophic fibres (Tang et al., 2019). Similar results were found in the muscles of sedentary elderly individuals, though this particular study used immunoblotting to ascertain increased expression of mTOR signalling proteins (Sandri et al., 2013b). In addition to mTOR signalling, “p38 MAPK events” associated proteins were also enriched in SenEV. Immunoblotting for proteins involved in this senescence associated signalling pathway showed they were overactivated in skeletal muscle biopsies isolated from elderly individuals (Yamaguchi et al., 2007). Furthermore, SenEV were also enriched in “TRAF6 mediated NF-κB activation”. This is corroborated by an increase in TRAF6 expression aged mice, as well as elevated NF-κB activation which induced ubiquitin ligase transcription, as shown by immunoblotting data (Li et al., 2020a).

Senescence invokes changes to gene transcription, as the “NuA4 histone acetyltransferase complex” was downregulated in SenEV. Little research has been conducted regarding this

histone acetyltransferase and its link to skeletal muscle senescence; consequently, comparative studies are lacking. Yoshihara *et al.* whilst not having identified NuA4 specifically, discovered the acetylation of numerous histones was significantly reduced in ageing mice and this was associated with muscle atrophy (Yoshihara et al., 2019).

A characteristic of cellular senescence is the ability of these cells to resist apoptosis and facilitate their own persistence (Hu et al., 2022). This is highlighted by SenEV, which exhibited reduced expression of "apoptotic execution phase" proteins. In comparison, senescent C2C12 myoblasts have a higher percentage of cells in early and late apoptosis and immunoblotting has shown these cells to increase expression of pro-apoptotic factors (Moustogiannis et al., 2021). The Moustogiannis *et al.* study investigated apoptosis in senescent myoblasts, whilst the data presented in this thesis used senescent myotubes. On the other hand, gene expression data has shown a decline in Bcl-2/BAX ratio in older mouse muscle, which resulted in a lower pro-apoptotic signal during ageing (Baker and Hepple, 2006). This suggests ageing skeletal muscle cells may or may not undergo apoptosis and this is influenced by the apoptotic signalling pathways involved.

Like the SEV proteome, research on senescent skeletal muscle derived EVs and their proteome is very limited. Many muscle EV based studies have investigated the presence of senescence inducing miRNA. SASP proteins, such as cytokines and adhesion molecules have been identified in senescence associated EVs, however functional enrichment analysis is severely lacking. Whilst this has made it difficult to draw comparisons between the results presented in this thesis and other studies, it highlights the need for extensive EV based research in this area to build upon existing knowledge of skeletal muscle SASP.

5.4 Future work

Indeed, it is difficult to make full conclusions from the evidence presented in this chapter, as skeletal muscle is a complex tissue that is comprised of different cell types and the current study only assesses myotube senescence. It is most likely that the accumulation of senescent cells in skeletal muscle during ageing predominantly arises from the progenitor satellite cell population rather than terminally differentiated myotubes. In addition to this, this study is simplified in that it does not consider the communication skeletal muscle undertakes with other tissues, such as adipose tissue and bone, both of which can influence the health and function of skeletal muscle particularly in an aged setting (Stanford and Goodyear, 2018, Novotny et al., 2015).

Furthermore, etoposide induced senescence may not be considered fully representative of the chronic senescence associated with ageing. To overcome this, a replicative senescence model would been more appropriate, in which myoblast cells are repeatedly passaged until a

high passage age is reached. The secretomes harvested from these truly aged cells would then be tested for their functional effects on other skeletal muscle cells and macrophages. With this method of senescence induction, it is likely that a different senescent phenotype will arise with a secretome that has a modified composition to that produced by the etoposide treated myotubes.

Communication between skeletal muscle and the immune system is bi-directional, with immune cells influencing skeletal muscle function and vice versa. This study chose to address the skeletal muscle side of this crosstalk only. Future work would include the assessment of the SASP primed macrophage secretome on normal and senescent skeletal muscle. This would complete the feedback loop between skeletal muscle and the innate immune system. This could again be furthered by incorporating other immune cells, such as NK cells and T cells which are also involved in the immunosurveillance of senescent cells.

6. Discussion

This project sought to better understand the possible mechanisms of crosstalk between skeletal muscle cells and the immune system and how this may change in conditions associated with muscle ageing, with EVs proposed as the putative method of communication. Extensive research has been conducted regarding the underlying mechanisms and characteristics associated with the onset of sarcopenia and skeletal muscle senescence, yet the role of macrophages in the development of these conditions is poorly understood and requires further investigation. Whilst it has been shown that the anti-inflammatory, pro-resolving M2 macrophage subtype comprise most of the macrophage population during age and are localised to ageing skeletal muscle, the effector function of these macrophages has not been assessed (Cui et al., 2019, Reidy et al., 2019). Research concerning the role of muscle secretomes in influencing macrophage responses is severely lacking. To date, only one very recently published study has investigated the impact of healthy myotube-derived EVs on macrophage function, however the specific effect of vesicles produced by ageing skeletal muscle associated conditions on macrophages is unknown (Yamaguchi et al., 2023). Whilst the present study has touched upon macrophage involvement in skeletal muscle ageing, there is scope for further research, which could propose macrophages as a putative therapeutic target in relation to sarcopenia and senescence.

6Polarisation states can provide insight into the effector functions of the different macrophage phenotypes and how they might respond to their microenvironment (Shapouri-Moghaddam et al., 2018). Macrophages are often discussed as pro-inflammatory M1 or anti-inflammatory and pro-resolving M2, which is the classic model of macrophage polarisation (Orecchioni et al., 2019). However, macrophage polarisation is far from an all or nothing system consisting of two different extremes, which has also been demonstrate in the present study (Mills et al., 2000). It is likely that there is a spectrum of mixed macrophage phenotypes in tissues, with macrophages having a combination of both M1 and M2 signatures (Joshi et al., 2010, Kosmac et al., 2018). For example, M2 macrophages known for their ability to resolve inflammation have also been shown to produce pro-inflammatory cytokines (Vogelpoel et al., 2014). Furthermore, whilst M2 macrophages can reduce their ability to phagocytose material, they also increase their release of pro-inflammatory cytokines in conjunction with this (Varin et al., 2010). The variety of macrophage phenotypes and their subsequent function is dependent on specific signals in the tissue in which they are found, as well as the presence of disease pathologies. This would provide an explanation for the contradictory macrophage effector function data presented in this study, in which some fractions of the sarcopenic and senescent secretomes promoted ROS release, whilst some suppressed NO_2^- production, in addition to both pro- and anti-inflammatory cytokine production by secretome component treated

macrophages. Exposure to the various pathological skeletal muscle secretomes could have induced polarisation of macrophages with a hybrid phenotype or macrophages of various polarisation states with small populations all responding differently, though further investigation is required to determine this.

6.1 *In vitro* skeletal muscle models – an oversimplification?

2D *in vitro* models will continue to provide a foundation for biological research, however their simplicity is often their limiting factor. This study has demonstrated that models of normal and pathophysiological skeletal muscle conditions can be recreated to an extent *in vitro*. The principal question regarding biological models is are they physiologically relevant? The skeletal muscle model presented in Chapter 3 did express some muscle specific proteins in the absence of serum-based differentiation. However, serum removal in a system that would normally be exposed to serum *in vivo* serves to make EV studies easier for the researcher but does not replicate the true environment. This raises the question as to whether EV research should be reviewed with regards to the use of SF cultures. MISEV 2018 states EVs should ideally be harvested from culture medium free from serum products, and cells requiring serum for growth or differentiation should be switched to a SF medium, yet this does not mimic *in vivo* conditions either (Théry et al., 2018). Despite the variability serum can introduce and the obvious ethical considerations regarding its use, it is perhaps more relevant to use serum in EV studies and use non-conditioned medium controls to determine the impact of the medium itself (Baker, 2016, van der Valk et al., 2004, Théry et al., 2018). It would be interesting to observe the results of this study were it to be repeated with serum containing differentiation medium, especially using *ex vivo* human serum or plasma which would increase the physiological relevance of the model (Allen et al., 2023).

Furthermore, the chemically induced sarcopenia model challenges the physiological significance of this culture. It has been established that sarcopenia is multifactorial in its underlying mechanisms but also that its outcome can be influenced by other aspects related to ageing, such as immunosenescence and inflammaging (Walston, 2012, Marcell, 2003, Nelke et al., 2019). Due to the complex nature of this muscle condition, it can be difficult to reproduce sarcopenia *in vitro*, which could explain why researchers attempt to model this condition using one or two causative factors, which ultimately simplifies the model (Sharples et al., 2012, Mankhong et al., 2020). Whilst *in vivo* models can overcome this by using aged animals, they too can be simplified to achieve faster results, such as using a high fat diet (Xie et al., 2021). Ultimately, this suggests all models can be simplified and can varying degrees of relevance. Despite the simplification of the models presented in this thesis, the pathological models did demonstrate aspects of the conditions they were attempting to represent. Overall,

the value of *in vitro* skeletal muscle modelling should not be lessened. Although using one causative agent to induce sarcopenia *in vitro* might not be representative of *in vivo* conditions, it allowed the effects of that cause to be fully understood, in this case the impact on macrophage function, which can be complicated by other endogenous and exogenous factors in whole organism studies.

6.2 To EV, or not to EV? That is the question

This study investigated the role of the EV component of the skeletal muscle secretome due to the putative role these particles could have in the development and propagation of age-related atrophic muscle conditions. The whole 2000*xg* sarcopenic and senescent secretomes reduced myotube diameter and it would be beneficial to ascertain which components (EVs, soluble proteins or other mediators) are specifically responsible for this effect. Regarding influence on macrophage function, in most cases the 2000*xg* secretomes had varied results, but further investigation of the individual fractions provided insight into the whole secretome effects. For instance, both whole sarcopenic and senescent 2000*xg* secretomes did not reduce superoxide anion release of M1 polarised macrophages, however assessing the EV and protein components of this secretome showed SEV and SenEV were responsible for these results and nullified the anti-inflammatory effects of the soluble proteins to do so. Consequently, this highlights the necessity of fractionating whole secretomes into the EV and protein components to determine whether they work together to modulate macrophage behaviour or in isolation, as well as assessing the power of their influence. In many of the functional experiments undertaken in this study, EVs had lesser effects when compared to the wider secretome. Whilst it could be concluded that very little is gained by researching the EV aspect of the secretomes, it is a useful endeavour as the EV data presented here can direct researchers to alternative secretome component(s), such as soluble proteins that are influencing macrophage behaviour. Furthermore, irrespective of the reduced impact of EVs in modulating macrophage function, undertaking proteomic analysis of SEV and SenEV was important, as this identified detrimental proteins. For example, SEV proteins associated with the oxidative stress response can explain the sarcopenic whole secretome results. Upregulated mH2A1 and downregulation of SOD3 in SEV contribute to the negative regulation of the response to oxidative stress and could be partly responsible for the inability of the sarcopenic secretome to minimise macrophage superoxide anion release, suggesting additional mechanisms as to why ROS production is elevated with this condition (Kadoguchi et al., 2020). Despite elucidating the EV proteomes, undertaking proteomic analysis of the soluble protein fraction would provide a more complete picture of the wider secretomes and provide insight into the beneficial effects the protein components may have.

Ultimately, all cell produced secretomes are comprised of multiple components and any effects a secretome may induce are due to the presence of these biologically active factors, and therefore could be potential therapeutic targets for the prevention and treatment of age associated skeletal muscle conditions.

6.3 Skeletal muscle senescence a cause of sarcopenia?

Although this study has considered sarcopenia and skeletal muscle senescence as separate entities independent of one another; it is likely that both are inextricably linked. Whilst being an effective measure against tumour progression, cellular senescence also has a dark side, as the accumulation of senescent cells during ageing has been implicated in the development of age associated disorders, including sarcopenia (Childs et al., 2015). Though this study did not show sarcopenic myotubes to have a senescent phenotype, senescent cells are present in ageing skeletal muscle tissue. Despite this thesis demonstrating myotube senescence is possible, skeletal muscle senescence has primarily been shown in the progenitor satellite cell population which leads to poor myotube formation and loss of regenerative capacity during ageing (He et al., 2021). It has been suggested that sarcopenia onset can be delayed by targeting muscle senescence, which is a feasible proposal as this study has shown myotube-derived SASP can detrimentally affect myotube mass, macrophage polarisation and ROS production, implying modulation of SASP production could be an efficacious therapeutic intervention (He et al., 2021, Freund et al., 2010, Wang et al., 2017).

6.4 Conclusions

This study has demonstrated that a murine skeletal muscle model can be successfully created in the absence of serum *in vitro*. This is a useful system for researchers interested in investigating skeletal muscle-derived EVs, without having to consider contaminating serum associated vesicles. This SF differentiation method can also be employed to study muscle EVs and their role in age-related skeletal muscle disorders, such as sarcopenia. Moreover, this SF model is not limited to the study of sarcopenia alone, it could be used for understanding the role of skeletal muscle EVs in both physiological and pathophysiological conditions. *In vivo* skeletal muscle research does negate the need for a SF muscle model; however, it is a useful tool for those who wish to conduct skeletal muscle EV experiments *in vitro*. This thesis has shown SF myogenesis is feasible in the murine C2C12 cell line, suggesting there is scope for this method in inducing differentiation in other species such as human myoblasts, however this would require further investigation.

The role of sarcopenic and senescent myotubes secretomes in the development and progression of age-related muscle atrophy is complex, with features both within skeletal muscle and the macrophage arm of the innate immune system being affected. Whilst both

secretomes employ the bystander effect to induce wasting of healthy muscle, their influence on macrophage function is not as straightforward, as at times sarcopenic and senescent myotube secretome components had varying effects. Figure 83 highlights the many factors, identified by this study and existing research, both within skeletal muscle and systemically, that contribute to the development and maintenance of age-associated muscle wasting. EV and soluble protein fractions from sarcopenic and senescent myotubes have individual effects and can modulate numerous macrophage functions, such as migration, ROS production and M1 phenotype, however it should be noted that physiologically, these components are not released in isolation but as components of a whole secretome. Consequently, it is likely that both secretomes stimulate the polarisation of macrophages that are of an in-between phenotype, neither completely M1 nor M2, which prevents the development of an appropriate inflammatory response to clear damaged cells and facilitate tissue repair. Furthermore, skeletal muscle ageing is not confined to events occurring within the tissue, other systemic age-related features, such as immunosenescence and low-grade chronic inflammation are contributing factors for the onset and progressive nature of sarcopenia. Therapeutics to prevent and delay the onset of sarcopenia could target any one of the causative agents shown in figure 87, however it is likely a multifactorial treatment strategy will have the greatest efficacy.

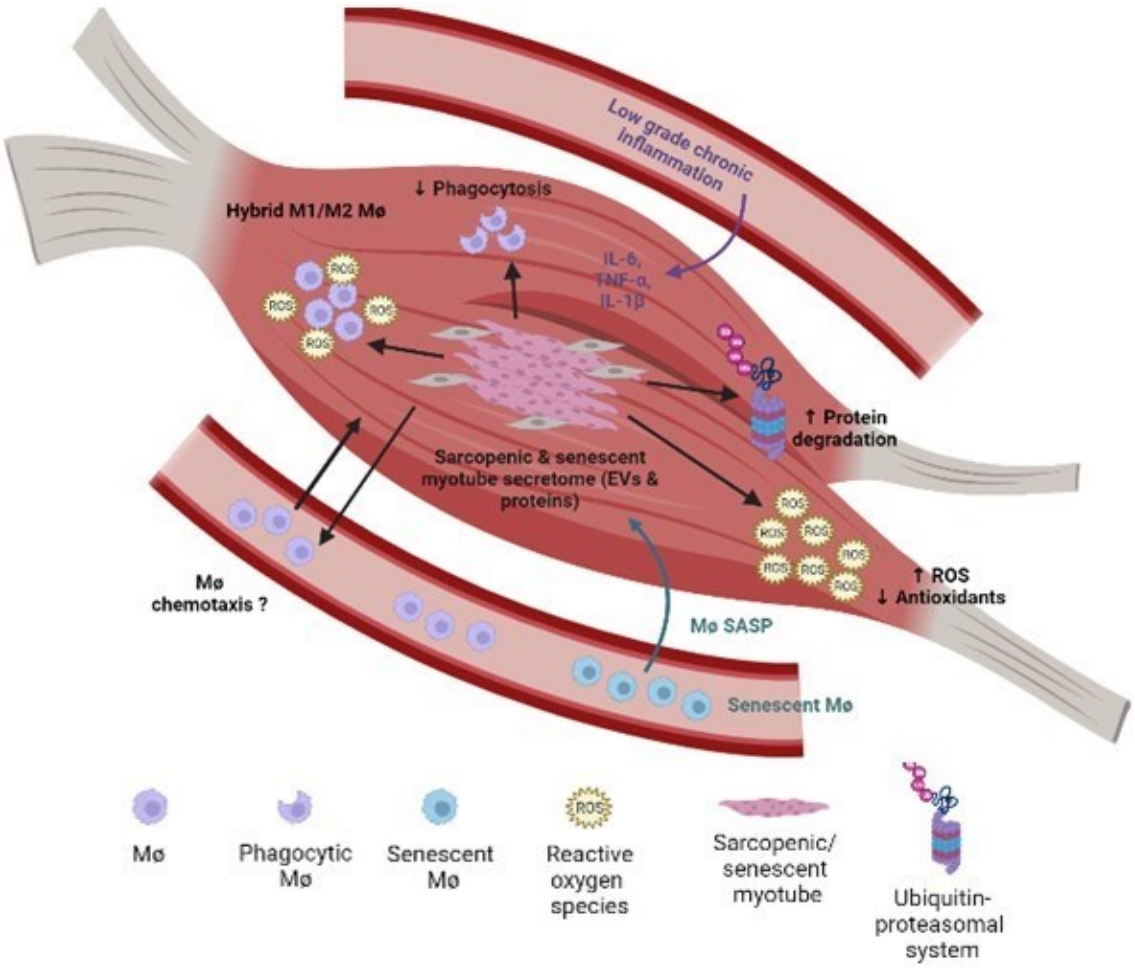

Figure 87. The convergence of skeletal muscle tissue endemic and systemic factors in the pathogenesis of age-related skeletal muscle wasting. Sarcopenic and senescent myotubes can maintain skeletal muscle damage and disseminate an atrophic phenotype through the tissue via their secretomes. These secretomes detrimentally affect muscle cells by inducing proteolysis, ROS production and limiting the response to oxidative stress, but can also modulate macrophage effector functions, including migration, respiratory burst, phagocytosis, and polarisation. Systemic factors elevated during the ageing process, such as immunosenescence and chronic low-grade inflammation also contribute to the development and progression of sarcopenia. (Figure created in BioRender.com).

6.5 Future Work

The murine C2C12 cell line is commonly used to model skeletal muscle and is fundamental for the study of muscle related disorders, however when investigating muscle pathologies affecting humans, it is essential this work is also performed using human cells. Accordingly, the work presented in this thesis would be repeated using a human muscle cell line, with the eventual aim of assessing the secretomes of primary skeletal muscle cells and macrophages both under physiological and aged atrophic conditions. This would remove any cross-species difficulties and would determine whether observations made using the murine models can be translated to a human muscle model or whether species differences exist.

As mentioned in section 6.2, ageing of the immune system is concurrent with skeletal muscle ageing. Due to the bidirectional nature of communication between skeletal muscle and the immune system, it is also necessary to investigate the influence of the aged monocyte/macrophage secretome on muscle cells. Macrophages isolated from young, healthy aged and aged individuals with sarcopenia would provide a complete picture of the macrophage response to ageing skeletal muscle. Healthy myoblasts and myotubes could be cultured in the secretome isolated from aged macrophages to determine the effect of both EVs and soluble factors on the ability of muscle cells to differentiate and regenerate. In relation to this, cross over studies could also be conducted in which macrophages from young and old individuals are incubated with sarcopenic and senescent myotube-derived secretomes and EVs to identify age related differences in the immune response.

Furthermore, it would be advantageous to identify the components comprising the aged macrophage secretome using MS. Elucidating these factors will further our understanding as to why the elderly experiencing healthy ageing do not develop sarcopenia and whether the aged macrophages in these individuals are different to those isolated from elderly individuals with sarcopenia. Moreover, identification of both macrophage and aged skeletal muscle components may suggest therapeutic targets for sarcopenia, including protein targets. The role of these proteins in age-related sarcopenia could be explained by knockdown experiments or antibody blockade, which would ultimately determine whether these proteins are viable therapeutic targets.

References

ACOSTA, J. C., BANITO, A., WUESTEFELD, T., GEORGILIS, A., JANICH, P., MORTON, J. P., ATHINEOS, D., KANG, T. W., LASITSCHKA, F., ANDRULIS, M., PASCUAL, G., MORRIS, K. J., KHAN, S., JIN, H., DHARMALINGAM, G., SNIJDERS, A. P., CARROLL, T., CAPPER, D., PRITCHARD, C., INMAN, G. J., LONGERICH, T., SANSOM, O. J., BENITAH, S. A., ZENDER, L. & GIL, J. 2013. A complex secretory program orchestrated by the inflammasome controls paracrine senescence. *Nat Cell Biol,* 15**,** 978-90.

ADMASU, T. D., RAE, M. & STOLZING, A. 2021. Dissecting primary and secondary senescence to enable new senotherapeutic strategies. *Ageing Res Rev,* 70**,** 101412.

AFSHAR BAKOOSHLI, M., LIPPMANN, E. S., MULCAHY, B., IYER, N., NGUYEN, C. T., TUNG, K., STEWART, B. A., VAN DEN DORPEL, H., FUEHRMANN, T., SHOICHET, M., BIGOT, A., PEGORARO, E., AHN, H., GINSBERG, H., ZHEN, M., ASHTON, R. S. & GILBERT, P. M. 2019. A 3D culture model of innervated human skeletal muscle enables studies of the adult neuromuscular junction. *Elife,* 8.

AFZALI, A. M., MÜNTEFERING, T., WIENDL, H., MEUTH, S. G. & RUCK, T. 2018. Skeletal muscle cells actively shape (auto)immune responses. *Autoimmun Rev,* 17**,** 518-529.

AHMAD, S. S., AHMAD, K., LEE, E. J., LEE, Y.-H. & CHOI, I. 2020. Implications of Insulin-Like Growth Factor-1 in Skeletal Muscle and Various Diseases. *Cells,* 9**,** 1773.

AIELLO, A., FARZANEH, F., CANDORE, G., CARUSO, C., DAVINELLI, S., GAMBINO, C. M., LIGOTTI, M. E., ZAREIAN, N. & ACCARDI, G. 2019. Immunosenescence and Its Hallmarks: How to Oppose Aging Strategically? A Review of Potential Options for Therapeutic Intervention. 10.

AKAZAWA, N., KISHI, M., HINO, T., TSUJI, R., TAMURA, K., HIOKA, A. & MORIYAMA, H. 2021. Relationship Between Aging and Intramuscular Adipose Tissue in Older Inpatients. *Journal of the American Medical Directors Association,* 22**,** 1287-1291.e1.

AKERS, J. C., RAMAKRISHNAN, V., NOLAN, J. P., DUGGAN, E., FU, C.-C., HOCHBERG, F. H., CHEN, C. C. & CARTER, B. S. 2016. Comparative Analysis of Technologies for Quantifying Extracellular Vesicles (EVs) in Clinical Cerebrospinal Fluids (CSF). *PLOS ONE,* 11**,** e0149866.

AL-QUSAIRI, L. & LAPORTE, J. 2011. T-tubule biogenesis and triad formation in skeletal muscle and implication in human diseases. *Skeletal Muscle,* 1**,** 26.

AL SAEDI, A., DEBRUIN, D. A., HAYES, A. & HAMRICK, M. 2022. Lipid metabolism in sarcopenia. *Bone,* 164**,** 116539.

ALEMÁN, H., ESPARZA, J., RAMIREZ, F. A., ASTIAZARAN, H. & PAYETTE, H. 2011. Longitudinal evidence on the association between interleukin-6 and C-reactive protein with the loss of total appendicular skeletal muscle in free-living older men and women. *Age and Ageing,* 40**,** 469475.

ALIBHAI, F. J., LIM, F., YEGANEH, A., DISTEFANO, P. V., BINESH-MARVASTI, T., BELFIORE, A., WLODAREK, L., GUSTAFSON, D., MILLAR, S., LI, S.-H., WEISEL, R. D., FISH, J. E. & LI, R.K. 2020. Cellular senescence contributes to age-dependent changes in circulating extracellular vesicle cargo and function. *Aging Cell,* 19**,** e13103.

ALLEN, S. L., ELLIOTT, B. T., CARSON, B. P. & BREEN, L. 2023. Improving physiological relevance of cell culture: the possibilities, considerations, and future directions of the ex vivo coculture model. *Am J Physiol Cell Physiol,* 324**,** C420-c427.

ALLEN, S. L., MARSHALL, R. N., EDWARDS, S. J., LORD, J. M., LAVERY, G. G. & BREEN, L. 2021. The effect of young and old ex vivo human serum on cellular protein synthesis and growth in an in vitro model of aging. 321**,** C26-C37.

ALONSO, N., MEINITZER, A., FRITZ-PETRIN, E., ENKO, D. & HERRMANN, M. 2023. Role of Vitamin K in Bone and Muscle Metabolism. *Calcified Tissue International,* 112**,** 178-196.

ALSUDAIS, H. & WIPER-BERGERON, N. 2019. Contaminating reactivity of a monoclonal CCAAT/Enhancer Binding Protein β antibody in differentiating myoblasts. *BMC Res Notes,* 12**,** 717.

AMTHOR, H., NICHOLAS, G., MCKINNELL, I., KEMP, C. F., SHARMA, M., KAMBADUR, R. & PATEL, K. 2004. Follistatin complexes Myostatin and antagonises Myostatin-mediated inhibition of myogenesis. *Developmental Biology,* 270**,** 19-30.

ANGELOV, D., MOLLA, A., PERCHE, P. Y., HANS, F., CÔTÉ, J., KHOCHBIN, S., BOUVET, P. & DIMITROV, S. 2003. The histone variant macroH2A interferes with transcription factor binding and SWI/SNF nucleosome remodeling. *Mol Cell,* 11**,** 1033-41.

ANGELOV, D., MOLLA, A., PERCHE, P.-Y., HANS, F., CÔTÉ, J., KHOCHBIN, S., BOUVET, P. & DIMITROV, S. 2003. The Histone Variant MacroH2A Interferes with Transcription Factor Binding and SWI/SNF Nucleosome Remodeling. *Molecular Cell,* 11**,** 1033-1041.
ANIORT, J., STELLA, A., PHILIPPONNET, C., POYET, A., POLGE, C., CLAUSTRE, A., COMBARET, L., BÉCHET, D., ATTAIX, D., BOISGARD, S., FILAIRE, M., ROSSET, E., BURLET-SCHILTZ, O., HENG, A.-E. & TAILLANDIER, D. 2019. Muscle wasting in patients with end-stage renal disease or early-stage lung cancer: common mechanisms at work. *Journal of cachexia, sarcopenia and muscle,* 10**,** 323-337.
ANRATHER, J., RACCHUMI, G. & IADECOLA, C. 2006. NF-kappaB regulates phagocytic NADPH oxidase by inducing the expression of gp91phox. *J Biol Chem,* 281**,** 5657-67.
APRAHAMIAN, T., TAKEMURA, Y., GOUKASSIAN, D. & WALSH, K. 2008. Ageing is associated with diminished apoptotic cell clearance in vivo. *Clinical and experimental immunology,* 152**,** 448455.
ARANGO DUQUE, G. & DESCOTEAUX, A. 2014. Macrophage cytokines: involvement in immunity and infectious diseases. *Frontiers in immunology,* 5**,** 491-491.
ARGILÉS, J. M., CAMPOS, N., LOPEZ-PEDROSA, J. M., RUEDA, R. & RODRIGUEZ-MAÑAS, L. 2016. Skeletal Muscle Regulates Metabolism via Interorgan Crosstalk: Roles in Health and Disease. *Journal of the American Medical Directors Association,* 17**,** 789-796.
ARNOLD, L., HENRY, A., PORON, F., BABA-AMER, Y., VAN ROOIJEN, N., PLONQUET, A., GHERARDI, R. K. & CHAZAUD, B. 2007. Inflammatory monocytes recruited after skeletal muscle injury switch into antiinflammatory macrophages to support myogenesis. *The Journal of experimental medicine,* 204**,** 1057-1069.
ASHLEY, J. W., HANCOCK, W. D., NELSON, A. J., BONE, R. N., TSE, H. M., WOHLTMANN, M., TURK, J. & RAMANADHAM, S. 2016. Polarization of Macrophages toward M2 Phenotype Is Favored by Reduction in iPLA2β (Group VIA Phospholipase A2). *The Journal of biological chemistry,* 291**,** 23268-23281.
ASWAD, H., FORTERRE, A., WIKLANDER, O. P. B., VIAL, G., DANTY-BERGER, E., JALABERT, A., LAMAZIÈRE, A., MEUGNIER, E., PESENTI, S., OTT, C., CHIKH, K., EL-ANDALOUSSI, S., VIDAL, H., LEFAI, E., RIEUSSET, J. & ROME, S. 2014. Exosomes participate in the alteration of muscle homeostasis during lipid-induced insulin resistance in mice. *Diabetologia,* 57**,** 21552164.
ASWAD, H., JALABERT, A. & ROME, S. 2016. Depleting extracellular vesicles from fetal bovine serum alters proliferation and differentiation of skeletal muscle cells in vitro. *BMC Biotechnology,* 16**,** 32.
ATSAWASUWAN, P., MOCHIDA, Y., KATAFUCHI, M., KAKU, M., FONG, K. S. K., CSISZAR, K. & YAMAUCHI, M. 2008. Lysyl oxidase binds transforming growth factor-beta and regulates its signaling via amine oxidase activity. *The Journal of biological chemistry,* 283**,** 34229-34240.
AYYADEVARA, S., BALASUBRAMANIAM, M., SURI, P., MACKINTOSH, S. G., TACKETT, A. J., SULLIVAN, D. H., SHMOOKLER REIS, R. J. & DENNIS, R. A. 2016. Proteins that accumulate with age in human skeletal-muscle aggregates contribute to declines in muscle mass and function in Caenorhabditis elegans. *Aging (Albany NY),* 8**,** 3486-3497.
BAAR, M. P., PERDIGUERO, E., MUÑOZ-CÁNOVES, P. & DE KEIZER, P. L. J. 2018. Musculoskeletal senescence: a moving target ready to be eliminated. *Current Opinion in Pharmacology,* 40**,** 147-155.
BACI, D., CHIRIVÌ, M., PACE, V., MAIULLARI, F., MILAN, M., RAMPIN, A., SOMMA, P., PRESUTTI, D., GARAVELLI, S., BRUNO, A., CANNATA, S., LANZUOLO, C., GARGIOLI, C., RIZZI, R. & BEARZI, C. 2020. Extracellular Vesicles from Skeletal Muscle Cells Efficiently Promote Myogenesis in Induced Pluripotent Stem Cells. *Cells,* 9.
BAIETTI, M. F., ZHANG, Z., MORTIER, E., MELCHIOR, A., DEGEEST, G., GEERAERTS, A., IVARSSON, Y., DEPOORTERE, F., COOMANS, C., VERMEIREN, E., ZIMMERMANN, P. & DAVID, G. 2012. Syndecan–syntenin–ALIX regulates the biogenesis of exosomes. *Nature Cell Biology,* 14**,** 677-685.
BAJAJ, P., REDDY, B., JR., MILLET, L., WEI, C., ZORLUTUNA, P., BAO, G. & BASHIR, R. 2011. Patterning the differentiation of C2C12 skeletal myoblasts. *Integr Biol (Camb),* 3**,** 897-909.
BAKER, D. J. & HEPPLE, R. T. 2006. Elevated caspase and AIF gene expression correlate with progression of sarcopenia during aging in male F344BN rats. *Experimental Gerontology,* 41**,** 1149-1156.
BAKER, D. J., WIJSHAKE, T., TCHKONIA, T., LEBRASSEUR, N. K., CHILDS, B. G., VAN DE SLUIS, B., KIRKLAND, J. L. & VAN DEURSEN, J. M. 2011. Clearance of p16Ink4a-positive senescent cells delays ageing-associated disorders. *Nature,* 479**,** 232-236.

BAKER, M. 2016. Reproducibility: Respect your cells! *Nature,* 537**,** 433-435.
BALBIS, A., BAQUIRAN, G., BERGERON, J. J. M. & POSNER, B. I. 2000. Compartmentalization and Insulin-Induced Translocations of Insulin Receptor Substrates, Phosphatidylinositol 3-Kinase, and Protein Kinase B in Rat Liver**This work was supported by grants from the Medical Research Council and from the National Cancer Institute of Canada, and by the Cleghorn Fund at McGill University and the M. Pollack Foundation of Montreal. *Endocrinology,* 141**,** 4041-4049.
BAO, Z., CUI, C., CHOW, S. K., QIN, L., WONG, R. M. Y. & CHEUNG, W. H. 2020. AChRs Degeneration at NMJ in Aging-Associated Sarcopenia-A Systematic Review. *Front Aging Neurosci,* 12**,** 597811.
BAPTISTA, I. L., SILVA, W. J., ARTIOLI, G. G., GUILHERME, J. P. L. F., LEAL, M. L., AOKI, M. S., MIYABARA, E. H. & MORISCOT, A. S. 2013. Leucine and HMB Differentially Modulate Proteasome System in Skeletal Muscle under Different Sarcopenic Conditions. *PLOS ONE,* 8**,** e76752.
BARBÉ, C., SALLES, J., CHAMBON, C., GIRAUDET, C., SANCHEZ, P., PATRAC, V., DENIS, P., BOIRIE, Y., WALRAND, S. & GUEUGNEAU, M. 2022. Characterization of the Skeletal Muscle Proteome in Undernourished Old Rats. *Int J Mol Sci,* 23.
BAREJA, A., HOLT, J. A., LUO, G., CHANG, C., LIN, J., HINKEN, A. C., FREUDENBERG, J. M., KRAUS, W. E., EVANS, W. J. & BILLIN, A. N. 2014. Human and mouse skeletal muscle stem cells: convergent and divergent mechanisms of myogenesis. *PLoS One,* 9**,** e90398.
BARRY-HAMILTON, V., SPANGLER, R., MARSHALL, D., MCCAULEY, S., RODRIGUEZ, H. M., OYASU, M., MIKELS, A., VAYSBERG, M., GHERMAZIEN, H., WAI, C., GARCIA, C. A., VELAYO, A. C., JORGENSEN, B., BIERMANN, D., TSAI, D., GREEN, J., ZAFFRYAR-EILOT, S., HOLZER, A., OGG, S., THAI, D., NEUFELD, G., VAN VLASSELAER, P. & SMITH, V. 2010. Allosteric inhibition of lysyl oxidase–like-2 impedes the development of a pathologic microenvironment. *Nature Medicine,* 16**,** 1009-1017.
BEAUDART, C., RIZZOLI, R., BRUYÈRE, O., REGINSTER, J.-Y. & BIVER, E. 2014. Sarcopenia: burden and challenges for public health. *Archives of public health = Archives belges de sante publique,* 72**,** 45-45.
BERGEN, H. R., FARR, J. N., VANDERBOOM, P. M., ATKINSON, E. J., WHITE, T. A., SINGH, R. J., KHOSLA, S. & LEBRASSEUR, N. K. 2015. Myostatin as a mediator of sarcopenia versus homeostatic regulator of muscle mass: insights using a new mass spectrometry-based assay. *Skeletal Muscle,* 5**,** 21.
BERNABEU-WITTEL, M., GONZÁLEZ-MOLINA, Á., FERNÁNDEZ-OJEDA, R., DÍEZ-MANGLANO, J., SALGADO, F., SOTO-MARTÍN, M., MUNIESA, M., OLLERO-BATURONE, M. & GÓMEZSALGADO, J. 2019. Impact of Sarcopenia and Frailty in a Multicenter Cohort of Polypathological Patients. 8**,** 535.
BERTIN, A., DE FRANCESCHI, N., DE LA MORA, E., MAITY, S., ALQABANDI, M., MIGUET, N., DI CICCO, A., ROOS, W. H., MANGENOT, S., WEISSENHORN, W. & BASSEREAU, P. 2020. Human ESCRT-III polymers assemble on positively curved membranes and induce helical membrane tube formation. *Nature Communications,* 11**,** 2663.
BERTOLDI, K., CECHINEL, L. R., SCHALLENBERGER, B., CORSSAC, G. B., DAVIES, S., GUERREIRO, I. C. K., BELLÓ-KLEIN, A., ARAUJO, A. S. R. & SIQUEIRA, I. R. 2018. Circulating extracellular vesicles in the aging process: impact of aerobic exercise. *Mol Cell Biochem,* 440**,** 115-125.
BHATNAGAR, S., PANGULURI, S. K., GUPTA, S. K., DAHIYA, S., LUNDY, R. F. & KUMAR, A. 2010. Tumor Necrosis Factor-α Regulates Distinct Molecular Pathways and Gene Networks in Cultured Skeletal Muscle Cells. *PLOS ONE,* 5**,** e13262.
BIENERT, G. P., MØLLER, A. L., KRISTIANSEN, K. A., SCHULZ, A., MØLLER, I. M., SCHJOERRING, J. K. & JAHN, T. P. 2007. Specific aquaporins facilitate the diffusion of hydrogen peroxide across membranes. *J Biol Chem,* 282**,** 1183-92.
BIKLE, D. D., TAHIMIC, C., CHANG, W., WANG, Y., PHILIPPOU, A. & BARTON, E. R. 2015. Role of IGF-I signaling in muscle bone interactions. *Bone,* 80**,** 79-88.
BILODEAU, P. A., COYNE, E. S. & WING, S. S. 2016. The ubiquitin proteasome system in atrophying skeletal muscle: roles and regulation. *American Journal of Physiology-Cell Physiology,* 311**,** C392-C403.
BIOLO, G., CEDERHOLM, T. & MUSCARITOLI, M. J. C. N. 2014. Muscle contractile and metabolic dysfunction is a common feature of sarcopenia of aging and chronic diseases: from sarcopenic obesity to cachexia. 33**,** 737-748.

BIRBEN, E., SAHINER, U. M., SACKESEN, C., ERZURUM, S. & KALAYCI, O. 2012. Oxidative stress and antioxidant defense. *World Allergy Organ J,* 5**,** 9-19.
BISCHOFF-FERRARI, H. A., ORAV, J. E., KANIS, J. A., RIZZOLI, R., SCHLÖGL, M., STAEHELIN, H. B., WILLETT, W. C. & DAWSON-HUGHES, B. 2015. Comparative performance of current definitions of sarcopenia against the prospective incidence of falls among community-dwelling seniors age 65 and older. *Osteoporosis International,* 26**,** 2793-2802.
BODEGA, G., ALIQUE, M., PUEBLA, L., CARRACEDO, J. & RAMÍREZ, R. M. 2019. Microvesicles: ROS scavengers and ROS producers. *Journal of Extracellular Vesicles,* 8**,** 1626654.
BODINE, S. C. & BAEHR, L. M. 2014. Skeletal muscle atrophy and the E3 ubiquitin ligases MuRF1 and MAFbx/atrogin-1. *Am J Physiol Endocrinol Metab,* 307**,** E469-84.
BODINE, S. C., LATRES, E., BAUMHUETER, S., LAI, V. K., NUNEZ, L., CLARKE, B. A., POUEYMIROU, W. T., PANARO, F. J., NA, E., DHARMARAJAN, K., PAN, Z. Q., VALENZUELA, D. M., DECHIARA, T. M., STITT, T. N., YANCOPOULOS, G. D. & GLASS, D. J. 2001. Identification of ubiquitin ligases required for skeletal muscle atrophy. *Science,* 294**,** 1704-8.
BORGES, F. T., REIS, L. A. & SCHOR, N. 2013. Extracellular vesicles: structure, function, and potential clinical uses in renal diseases. *Brazilian journal of medical and biological research = Revista brasileira de pesquisas medicas e biologicas,* 46**,** 824-830.
BORGHESAN, M., FAFIÁN-LABORA, J., ELEFTHERIADOU, O., CARPINTERO-FERNÁNDEZ, P., PAEZ-RIBES, M., VIZCAY-BARRENA, G., SWISA, A., KOLODKIN-GAL, D., XIMÉNEZEMBÚN, P., LOWE, R., MARTÍN-MARTÍN, B., PEINADO, H., MUÑOZ, J., FLECK, R. A., DOR, Y., BEN-PORATH, I., VOSSENKAMPER, A., MUÑOZ-ESPIN, D. & O'LOGHLEN, A. 2019. Small Extracellular Vesicles Are Key Regulators of Non-cell Autonomous Intercellular Communication in Senescence via the Interferon Protein IFITM3. *Cell Rep,* 27**,** 3956-3971.e6.
BOST, J. P., SAHER, O., HAGEY, D., MAMAND, D. R., LIANG, X., ZHENG, W., CORSO, G., GUSTAFSSON, O., GÖRGENS, A., SMITH, C. E., ZAIN, R., EL ANDALOUSSI, S. & GUPTA, D. 2022. Growth Media Conditions Influence the Secretion Route and Release Levels of Engineered Extracellular Vesicles. 11**,** 2101658.
BOSURGI, L., CORNA, G., VEZZOLI, M., TOUVIER, T., COSSU, G., MANFREDI, A. A., BRUNELLI, S. & ROVERE-QUERINI, P. 2012. Transplanted Mesoangioblasts Require Macrophage IL-10 for Survival in a Mouse Model of Muscle Injury. *The Journal of Immunology,* 188**,** 6267-6277.
BRACK, A. S., CONBOY, M. J., ROY, S., LEE, M., KUO, C. J., KELLER, C. & RANDO, T. A. J. S. 2007. Increased Wnt signaling during aging alters muscle stem cell fate and increases fibrosis. 317**,** 807-810.
BRAGA, M., SINHA HIKIM, A. P., DATTA, S., FERRINI, M. G., BROWN, D., KOVACHEVA, E. L., GONZALEZ-CADAVID, N. F. & SINHA-HIKIM, I. 2008. Involvement of oxidative stress and caspase 2-mediated intrinsic pathway signaling in age-related increase in muscle cell apoptosis in mice. *Apoptosis : an international journal on programmed cell death,* 13**,** 822-832.
BRIGITTE, M., SCHILTE, C., PLONQUET, A., BABA-AMER, Y., HENRI, A., CHARLIER, C., TAJBAKHSH, S., ALBERT, M., GHERARDI, R. K. & CHRÉTIEN, F. 2010. Muscle resident macrophages control the immune cell reaction in a mouse model of notexin-induced myoinjury. *Arthritis Rheum,* 62**,** 268-79.
BROUSSARD, S. R., MCCUSKER, R. H., NOVAKOFSKI, J. E., STRLE, K., SHEN, W. H., JOHNSON,
R. W., DANTZER, R. & KELLEY, K. W. 2004. IL-1β Impairs Insulin-Like Growth Factor IInduced Differentiation and Downstream Activation Signals of the Insulin-Like Growth Factor I Receptor in Myoblasts. *The Journal of Immunology,* 172**,** 7713-7720.
BRUNELLI, S. & ROVERE-QUERINI, P. 2008. The immune system and the repair of skeletal muscle. *Pharmacol Res,* 58**,** 117-21.
BUA, E., JOHNSON, J., HERBST, A., DELONG, B., MCKENZIE, D., SALAMAT, S. & AIKEN, J. M. 2006. Mitochondrial DNA-deletion mutations accumulate intracellularly to detrimental levels in aged human skeletal muscle fibers. *American journal of human genetics,* 79**,** 469-480.
BULUA, A. C., SIMON, A., MADDIPATI, R., PELLETIER, M., PARK, H., KIM, K.-Y., SACK, M. N., KASTNER, D. L. & SIEGEL, R. M. 2011. Mitochondrial reactive oxygen species promote production of proinflammatory cytokines and are elevated in TNFR1-associated periodic syndrome (TRAPS). *Journal of Experimental Medicine,* 208**,** 519-533.
BURKS, T. N. & COHN, R. D. 2011. Role of TGF-β signaling in inherited and acquired myopathies. *Skeletal muscle,* 1**,** 19-19.

BURZYN, D., KUSWANTO, W., KOLODIN, D., SHADRACH, J. L., CERLETTI, M., JANG, Y., SEFIK, E., TAN, T. G., WAGERS, A. J., BENOIST, C. & MATHIS, D. 2013. A special population of regulatory T cells potentiates muscle repair. *Cell,* 155**,** 1282-1295.
BUSATTO, S., YANG, Y., IANNOTTA, D., DAVIDOVICH, I., TALMON, Y. & WOLFRAM, J. 2022. Considerations for extracellular vesicle and lipoprotein interactions in cell culture assays. *J Extracell Vesicles,* 11**,** e12202.
BUTTERFIELD, T. A., BEST, T. M. & MERRICK, M. A. 2006. The dual roles of neutrophils and macrophages in inflammation: a critical balance between tissue damage and repair. *Journal of athletic training,* 41**,** 457-465.
BYDAK, B., PIERDONÁ, T. M., SEIF, S., SIDHOM, K., OBI, P. O., LABOUTA, H. I., GORDON, J. W. & SALEEM, A. 2022. Characterizing Extracellular Vesicles and Particles Derived from Skeletal Muscle Myoblasts and Myotubes and the Effect of Acute Contractile Activity. *Membranes,* 12**,** 464.
CAI, L., XIONG, X., KONG, X. & XIE, J. 2017. The Role of the Lysyl Oxidases in Tissue Repair and Remodeling: A Concise Review. *Tissue engineering and regenerative medicine,* 14**,** 15-30.
CAMPANARIO, S., RAMÍREZ-PARDO, I., HONG, X., ISERN, J. & MUÑOZ-CÁNOVES, P. 2021. Assessing Autophagy in Muscle Stem Cells. 8.
CAMPISI, J. & D'ADDA DI FAGAGNA, F. 2007. Cellular senescence: when bad things happen to good cells. *Nat Rev Mol Cell Biol,* 8**,** 729-40.
CAMPISI, J. & ROBERT, L. 2014. Cell senescence: role in aging and age-related diseases. *Interdiscip Top Gerontol,* 39**,** 45-61.
CANNAVINO, J., BROCCA, L., SANDRI, M., GRASSI, B., BOTTINELLI, R. & PELLEGRINO, M. A. 2015. The role of alterations in mitochondrial dynamics and PGC-1α over-expression in fast muscle atrophy following hindlimb unloading. *J Physiol,* 593**,** 1981-95.
CARMI, Y., VORONOV, E., DOTAN, S., LAHAT, N., RAHAT, M. A., FOGEL, M., HUSZAR, M., WHITE, M. R., DINARELLO, C. A. & APTE, R. N. 2009. The role of macrophage-derived IL-1 in induction and maintenance of angiogenesis. *J Immunol,* 183**,** 4705-14.
CARNIO, S., LOVERSO, F., BARAIBAR, M. A., LONGA, E., KHAN, M. M., MAFFEI, M., REISCHL, M., CANEPARI, M., LOEFLER, S. & KERN, H. J. C. R. 2014. Autophagy impairment in muscle induces neuromuscular junction degeneration and precocious aging. 8**,** 1509-1521.
CAROTENUTO, F., COLETTI, D., DI NARDO, P. & TEODORI, L. J. E. J. O. T. M. 2016. α-linolenic acid reduces TNF-induced apoptosis in C2C12 myoblasts by regulating expression of apoptotic proteins. 26.
CASTELL, J. V., GÓMEZ-LECHÓN, M. J., DAVID, M., ANDUS, T., GEIGER, T., TRULLENQUE, R., FABRA, R. & HEINRICH, P. C. 1989. Interleukin-6 is the major regulator of acute phase protein synthesis in adult human hepatocytes. *FEBS Lett,* 242**,** 237-9.
CASTIGLIONI, A., CORNA, G., RIGAMONTI, E., BASSO, V., VEZZOLI, M., MONNO, A., ALMADA, A. E., MONDINO, A., WAGERS, A. J., MANFREDI, A. A. & ROVERE-QUERINI, P. 2015. FOXP3+ T Cells Recruited to Sites of Sterile Skeletal Muscle Injury Regulate the Fate of Satellite Cells and Guide Effective Tissue Regeneration. *PloS one,* 10**,** e0128094-e0128094.
CESARE, M. M., FELICE, F., SANTINI, V. & DI STEFANO, R. 2020. Antioxidants in Sport Sarcopenia. *Nutrients,* 12**,** 2869.
CHANG, J. S. & KONG, I. D. 2020. Irisin prevents dexamethasone-induced atrophy in C2C12 myotubes. *Pflügers Archiv - European Journal of Physiology,* 472**,** 495-502.
CHARGÉ, S. B. P. & RUDNICKI, M. A. 2004. Cellular and Molecular Regulation of Muscle Regeneration. *Physiological Reviews,* 84**,** 209-238.
CHAWEEWANNAKORN, C., TSUCHIYA, M., KOIDE, M., HATAKEYAMA, H., TANAKA, Y., YOSHIDA, S., SUGAWARA, S., HAGIWARA, Y., SASAKI, K. & KANZAKI, M. 2018. Roles of IL-1α/β in regeneration of cardiotoxin-injured muscle and satellite cell function. *American Journal of Physiology-Regulatory, Integrative and Comparative Physiology,* 315**,** R90-R103.
CHAZAUD, B., BRIGITTE, M., YACOUB-YOUSSEF, H., ARNOLD, L., GHERARDI, R., SONNET, C., LAFUSTE, P. & CHRETIEN, F. 2009. Dual and beneficial roles of macrophages during skeletal muscle regeneration. *Exerc Sport Sci Rev,* 37**,** 18-22.
CHAZAUD, B., SONNET, C., LAFUSTE, P., BASSEZ, G., RIMANIOL, A. C., PORON, F., AUTHIER, F. J., DREYFUS, P. A. & GHERARDI, R. K. 2003. Satellite cells attract monocytes and use macrophages as a support to escape apoptosis and enhance muscle growth. *J Cell Biol,* 163**,** 1133-43.
CHECA, J. & ARAN, J. M. 2020. Reactive Oxygen Species: Drivers of Physiological and Pathological Processes. *J Inflamm Res,* 13**,** 1057-1073.

CHEN, C., YANG, J.-S., LU, C.-C., CHIU, Y.-J., CHEN, H.-C., CHUNG, M.-I., WU, Y.-T. & CHEN, F.A. 2020. Effect of Quercetin on Dexamethasone-Induced C2C12 Skeletal Muscle Cell Injury. *Molecules (Basel, Switzerland),* 25**,** 3267.
CHEN, H., MA, F., HU, X., JIN, T., XIONG, C. & TENG, X. 2013. Elevated COX2 expression and PGE2 production by downregulation of RXRα in senescent macrophages. *Biochemical and Biophysical Research Communications,* 440**,** 157-162.
CHEN, M.-M., ZHAO, Y.-P., ZHAO, Y., DENG, S.-L. & YU, K. 2021a. Regulation of Myostatin on the Growth and Development of Skeletal Muscle. 9.
CHEN, P., ZHAO, D., LI, J., LIANG, X., LI, J., CHANG, A., HENRY, V. K., LAN, Z., SPRING, D. J., RAO, G., WANG, Y. A. & DEPINHO, R. A. 2019. Symbiotic Macrophage-Glioma Cell Interactions Reveal Synthetic Lethality in PTEN-Null Glioma. *Cancer Cell,* 35**,** 868-884.e6.
CHEN, Q., LI, N., ZHU, W., LI, W., TANG, S., YU, W., GAO, T., ZHANG, J. & LI, J. 2011. Insulin alleviates degradation of skeletal muscle protein by inhibiting the ubiquitin-proteasome system in septic rats. *Journal of inflammation (London, England),* 8**,** 13-13.
CHEN, S.-E., JIN, B. & LI, Y.-P. 2007. TNF-alpha regulates myogenesis and muscle regeneration by activating p38 MAPK. *American journal of physiology. Cell physiology,* 292**,** C1660-C1671.
CHEN, Y.-Y., KAO, T.-W., CHIU, Y.-L., PENG, T.-C., YANG, H.-F. & CHEN, W.-L. 2021b. Association Between Interleukin-12 and Sarcopenia. *Journal of inflammation research,* 14**,** 2019-2029.
CHEN, Y. & YU, L. 2022. Extracellular vesicles: from bench to bedside. *Current Medicine,* 1**,** 3.
CHENG, M., NGUYEN, M.-H., FANTUZZI, G. & KOH, T. J. 2008. Endogenous interferon-γ is required for efficient skeletal muscle regeneration. *American Journal of Physiology-Cell Physiology,* 294**,** C1183-C1191.
CHENG, Q., ZHU, X., ZHANG, X., LI, H., DU, Y., HONG, W., XUE, S. & ZHU, H. 2014. A cross-sectional study of loss of muscle mass corresponding to sarcopenia in healthy Chinese men and women: reference values, prevalence, and association with bone mass. *J Bone Miner Metab,* 32**,** 7888.
CHILDS, B. G., DURIK, M., BAKER, D. J. & VAN DEURSEN, J. M. 2015. Cellular senescence in aging and age-related disease: from mechanisms to therapy. *Nature Medicine,* 21**,** 1424-1435.
CHIN, E. R. 2005. Role of Ca2+/calmodulin-dependent kinases in skeletal muscle plasticity. *J Appl Physiol (1985),* 99**,** 414-23.
CHIN, E. R., IBEBUNJO, C. & MCDOWELL, M. T. 2009. A proteomics-based approach to changes CHEN, Y. & YU, L. 2022. Extracellular vesicles: from bench to bedside. *Current Medicine,* 1**,** 3. in skeletal muscle gene expression with age-related sarcopenia. 23**,** 954.4-954.4.
CHIU, C.-S., WEBER, H., ADAMSKI, S., RAUCH, A., GENTILE, M. A., ALVES, S. E., KATH, G., FLORES, O. & WILKINSON, H. A. 2011. Non-invasive muscle contraction assay to study rodent models of sarcopenia. *BMC Musculoskeletal Disorders,* 12**,** 246.
CHOI, J. S., YOON, H. I., LEE, K. S., CHOI, Y. C., YANG, S. H., KIM, I. S. & CHO, Y. W. 2016. Exosomes from differentiating human skeletal muscle cells trigger myogenesis of stem cells and provide biochemical cues for skeletal muscle regeneration. *J Control Release,* 222**,** 10715
CHUNG, L., MAESTAS, D. R., JR., LEBID, A., MAGEAU, A., ROSSON, G. D., WU, X., WOLF, M. T., TAM, A. J., VANDERZEE, I., WANG, X., ANDORKO, J. I., ZHANG, H., NARAIN, R., SADTLER, K., FAN, H., ČIHÁKOVÁ, D., LE SAUX, C. J., HOUSSEAU, F., PARDOLL, D. M. & ELISSEEFF, J. H. 2020. Interleukin 17 and senescent cells regulate the foreign body response to synthetic material implants in mice and humans. *Sci Transl Med,* 12.
CIMORELLI, M., NIEUWLAND, R., VARGA, Z. & VAN DER POL, E. 2021. Standardized procedure to measure the size distribution of extracellular vesicles together with other particles in biofluids with microfluidic resistive pulse sensing. *PLoS One,* 16**,** e0249603.
CODATO, R., PERICHON, M., DIVOL, A., FUNG, E., SOTIROPOULOS, A., BIGOT, A., WEITZMAN, J. B. & MEDJKANE, S. 2019. The SMYD3 methyltransferase promotes myogenesis by activating the myogenin regulatory network. *Sci Rep,* 9**,** 17298.
COHN, R. D., VAN ERP, C., HABASHI, J. P., SOLEIMANI, A. A., KLEIN, E. C., LISI, M. T., GAMRADT, M., AP RHYS, C. M., HOLM, T. M., LOEYS, B. L., RAMIREZ, F., JUDGE, D. P., WARD, C. W. & DIETZ, H. C. 2007. Angiotensin II type 1 receptor blockade attenuates TGF-beta-induced failure of muscle regeneration in multiple myopathic states. *Nat Med,* 13**,** 204-10.
COLLADO, M. & SERRANO, M. 2010. Senescence in tumours: evidence from mice and humans. *Nat Rev Cancer,* 10**,** 51-7.

COLLINS, C. A., OLSEN, I., ZAMMIT, P. S., HESLOP, L., PETRIE, A., PARTRIDGE, T. A. & MORGAN, J. E. 2005. Stem Cell Function, Self-Renewal, and Behavioral Heterogeneity of Cells from the Adult Muscle Satellite Cell Niche. *Cell,* 122**,** 289-301.
COLLINS, C. J. & SEDIVY, J. M. 2003. Involvement of the INK4a/Arf gene locus in senescence. *Aging Cell,* 2**,** 145-50.
CONTRERAS, O., CÓRDOVA-CASANOVA, A. & BRANDAN, E. 2021. PDGF-PDGFR network differentially regulates the fate, migration, proliferation, and cell cycle progression of myogenic cells. *Cellular Signalling,* 84**,** 110036.
COOPER, R., HARDY, R., AIHIE SAYER, A., BEN-SHLOMO, Y., BIRNIE, K., COOPER, C., CRAIG, L., DEARY, I. J., DEMAKAKOS, P., GALLACHER, J., MCNEILL, G., MARTIN, R. M., STARR, J. M., STEPTOE, A. & KUH, D. 2011. Age and gender differences in physical capability levels from mid-life onwards: the harmonisation and meta-analysis of data from eight UK cohort studies. *PLoS One,* 6**,** e27899.
COPPÉ, J. P., KAUSER, K., CAMPISI, J. & BEAUSÉJOUR, C. M. 2006. Secretion of vascular endothelial growth factor by primary human fibroblasts at senescence. *J Biol Chem,* 281**,** 29568-74.
COPPÉ, J.-P., DESPREZ, P.-Y., KRTOLICA, A. & CAMPISI, J. 2010. The senescence-associated secretory phenotype: the dark side of tumor suppression. *Annual review of pathology,* 5**,** 99118.
COSTANTINI, A., VIOLA, N., BERRETTA, A., GALEAZZI, R., MATACCHIONE, G., SABBATINELLI, J., STORCI, G., DE MATTEIS, S., BUTINI, L., RIPPO, M. R., PROCOPIO, A. D., CARACENI, D., ANTONICELLI, R., OLIVIERI, F. & BONAFÈ, M. 2018. Age-related M1/M2 phenotype changes in circulating monocytes from healthy/unhealthy individuals. *Aging (Albany NY),* 10**,** 1268-1280.
CÔTE, C. H., TREMBLAY, M. H., DUCHESNE, E. & LAPOITE, B. M. 2008. Inflammation-induced leukocyte accumulation in injured skeletal muscle: role of mast cells. *Muscle Nerve,* 37**,** 75463.
COUPER, K. N., BLOUNT, D. G. & RILEY, E. M. 2008. IL-10: The Master Regulator of Immunity to Infection. 180**,** 5771-5777.
CRUZ-JENTOFT, A. J., BAEYENS, J. P., BAUER, J. M., BOIRIE, Y., CEDERHOLM, T., LANDI, F., MARTIN, F. C., MICHEL, J.-P., ROLLAND, Y., SCHNEIDER, S. M., TOPINKOVÁ, E., VANDEWOUDE, M., ZAMBONI, M. & EUROPEAN WORKING GROUP ON SARCOPENIA IN OLDER, P. 2010. Sarcopenia: European consensus on definition and diagnosis: Report of the European Working Group on Sarcopenia in Older People. *Age and ageing,* 39**,** 412-423.
CRUZ-JENTOFT, A. J., LANDI, F., SCHNEIDER, S. M., ZÚÑIGA, C., ARAI, H., BOIRIE, Y., CHEN, L.K., FIELDING, R. A., MARTIN, F. C., MICHEL, J.-P., SIEBER, C., STOUT, J. R., STUDENSKI,
S. A., VELLAS, B., WOO, J., ZAMBONI, M. & CEDERHOLM, T. 2014. Prevalence of and interventions for sarcopenia in ageing adults: a systematic review. Report of the International Sarcopenia Initiative (EWGSOP and IWGS). *Age and ageing,* 43**,** 748-759.
CSAPO, R., GUMPENBERGER, M. & WESSNER, B. 2020. Skeletal Muscle Extracellular Matrix – What Do We Know About Its Composition, Regulation, and Physiological Roles? A Narrative Review.
11.
CUI, C.-Y., DRISCOLL, R. K., PIAO, Y., CHIA, C. W., GOROSPE, M. & FERRUCCI, L. 2019. Skewed macrophage polarization in aging skeletal muscle. *Aging Cell,* 18**,** e13032.
CULL, A. H., SNETSINGER, B., BUCKSTEIN, R., WELLS, R. A. & RAUH, M. J. 2017. Tet2 restrains inflammatory gene expression in macrophages. *Experimental Hematology,* 55**,** 56-70.e13.
CULL, A., SNETSINGER, B. & RAUH, M. J. 2015. Tet2 Is a Novel Regulator of Murine Macrophage Differentiation and Polarization. *Blood,* 126**,** 646-646.
CUTHBERTSON, D., SMITH, K., BABRAJ, J., LEESE, G., WADDELL, T., ATHERTON, P., WACKERHAGE, H., TAYLOR, P. M. & RENNIE, M. J. 2005. Anabolic signaling deficits underlie amino acid resistance of wasting, aging muscle. *Faseb j,* 19**,** 422-4.
CYBULSKY, A. V. 2013. The intersecting roles of endoplasmic reticulum stress, ubiquitin–proteasome system, and autophagy in the pathogenesis of proteinuric kidney disease. *Kidney International,* 84**,** 25-33.
CZERNEK, L., CHWOROS, A. & DUECHLER, M. 2015. The Uptake of Extracellular Vesicles is Affected by the Differentiation Status of Myeloid Cells. *Scand J Immunol,* 82**,** 506-14.

DA SILVA, P. F. L., OGRODNIK, M., KUCHERYAVENKO, O., GLIBERT, J., MIWA, S., CAMERON, K.,
ISHAQ, A., SARETZKI, G., NAGARAJA-GRELLSCHEID, S., NELSON, G. & VON ZGLINICKI, T. 2019. The bystander effect contributes to the accumulation of senescent cells in vivo. *Aging cell,* 18**,** e12848-e12848.

DALLE, S., ROSSMEISLOVA, L. & KOPPO, K. 2017. The Role of Inflammation in Age-Related Sarcopenia. *Frontiers in physiology,* 8**,** 1045-1045.

DAMIANO, S., MUSCARIELLO, E., LA ROSA, G., DI MARO, M., MONDOLA, P. & SANTILLO, M. 2019. Dual Role of Reactive Oxygen Species in Muscle Function: Can Antioxidant Dietary Supplements Counteract Age-Related Sarcopenia? *International journal of molecular sciences,* 20**,** 3815.

DARDENNE, E., PIERREDON, S., DRIOUCH, K., GRATADOU, L., LACROIX-TRIKI, M., ESPINOZA, M. P., ZONTA, E., GERMANN, S., MORTADA, H., VILLEMIN, J. P., DUTERTRE, M., LIDEREAU, R., VAGNER, S. & AUBOEUF, D. 2012. Splicing switch of an epigenetic regulator by RNA helicases promotes tumor-cell invasiveness. *Nat Struct Mol Biol,* 19**,** 1139-46.

DAS, M., WILSON, K., MOLNAR, P. & HICKMAN, J. J. 2007. Differentiation of skeletal muscle and integration of myotubes with silicon microstructures using serum-free medium and a synthetic silane substrate. *Nature Protocols,* 2**,** 1795-1801.

DAVALLI, P., MITIC, T., CAPORALI, A., LAURIOLA, A. & D'ARCA, D. 2016. ROS, Cell Senescence, and Novel Molecular Mechanisms in Aging and Age-Related Diseases. *Oxid Med Cell Longev,* 2016**,** 3565127.

DAVIES, O. G., POWELL, S., RICKARD, J. J., CLANCY, M. & GOLDBERG OPPENHEIMER, P. 2021. Spectroscopic profiling variations in extracellular vesicle biochemistry in a model of myogenesis. 12**,** 20417314211022092.

DE KEIZER, P. L. J. 2017. The Fountain of Youth by Targeting Senescent Cells? *Trends in Molecular Medicine,* 23**,** 6-17.

DELANEY, K., KASPRZYCKA, P., CIEMERYCH, M. A. & ZIMOWSKA, M. 2017. The role of TGF-β1 during skeletal muscle regeneration. *Cell Biology International,* 41**,** 706-715.

DENG, B., WEHLING-HENRICKS, M., VILLALTA, S. A., WANG, Y. & TIDBALL, J. G. 2012. IL-10 triggers changes in macrophage phenotype that promote muscle growth and regeneration. *Journal of immunology (Baltimore, Md. : 1950),* 189**,** 3669-3680.

DESGUERRE, I., ARNOLD, L., VIGNAUD, A., CUVELLIER, S., YACOUB-YOUSSEF, H., GHERARDI, R. K., CHELLY, J., CHRETIEN, F., MOUNIER, R., FERRY, A. & CHAZAUD, B. 2012. A new model of experimental fibrosis in hindlimb skeletal muscle of adult mdx mouse mimicking muscular dystrophy. 45**,** 803-814.

DESHMUKH, A. S., MURGIA, M., NAGARAJ, N., TREEBAK, J. T., COX, J. & MANN, M. 2015. Deep proteomics of mouse skeletal muscle enables quantitation of protein isoforms, metabolic pathways, and transcription factors. *Mol Cell Proteomics,* 14**,** 841-53.

DHINDSA, S., GHANIM, H., GREEN, K., ABUAYSHEH, S., BATRA, M., MAKDISSI, A., CHAUDHURI, A., SANDHU, S. & DANDONA, P. 2019. Acute effects of insulin on skeletal muscle growth and differentiation genes in men with type 2 diabetes. *Eur J Endocrinol,* 181**,** K55-k59.

DI CESARE MANNELLI, L., MICHELI, L., LUCARINI, E., PARISIO, C., TOTI, A., TENCI, B., ZANARDELLI, M., BRANCA, J. J. V., PACINI, A. & GHELARDINI, C. 2020. Effects of the Combination of β-Hydroxy-β-Methyl Butyrate and R(+) Lipoic Acid in a Cellular Model of Sarcopenia. 25**,** 2117.

DI MARCO, S., MAZROUI, R., DALLAIRE, P., CHITTUR, S., TENENBAUM, S. A., RADZIOCH, D., MARETTE, A. & GALLOUZI, I.-E. 2005. NF-kappa B-mediated MyoD decay during muscle wasting requires nitric oxide synthase mRNA stabilization, HuR protein, and nitric oxide release. *Molecular and cellular biology,* 25**,** 6533-6545.

DICKINSON, J. M., DRUMMOND, M. J., COBEN, J. R., VOLPI, E. & RASMUSSEN, B. B. 2013. Aging differentially affects human skeletal muscle amino acid transporter expression when essential amino acids are ingested after exercise. *Clin Nutr,* 32**,** 273-80.

DIGIACOMO, G., TUSA, I., BACCI, M., CIPOLLESCHI, M. G., DELLO SBARBA, P. & ROVIDA, E. 2017. Fibronectin induces macrophage migration through a SFK-FAK/CSF-1R pathway. *Cell adhesion & migration,* 11**,** 327-337.

DIMRI, G. P., LEE, X., BASILE, G., ACOSTA, M., SCOTT, G., ROSKELLEY, C., MEDRANO, E. E., LINSKENS, M., RUBELJ, I., PEREIRA-SMITH, O. & ET AL. 1995. A biomarker that identifies senescent human cells in culture and in aging skin in vivo. *Proc Natl Acad Sci U S A,* 92**,** 93637.

DINARELLO, C., NOVICK, D., KIM, S. & KAPLANSKI, G. 2013. Interleukin-18 and IL-18 Binding Protein. 4.
DODDS, R. M., SYDDALL, H. E., COOPER, R., KUH, D., COOPER, C. & SAYER, A. A. 2016. Global variation in grip strength: a systematic review and meta-analysis of normative data. *Age and ageing,* 45**,** 209-216.
DÖRR, J. R., YU, Y., MILANOVIC, M., BEUSTER, G., ZASADA, C., DÄBRITZ, J. H., LISEC, J., LENZE, D., GERHARDT, A., SCHLEICHER, K., KRATZAT, S., PURFÜRST, B., WALENTA, S., MUELLER-KLIESER, W., GRÄLER, M., HUMMEL, M., KELLER, U., BUCK, A. K., DÖRKEN, B., WILLMITZER, L., REIMANN, M., KEMPA, S., LEE, S. & SCHMITT, C. A. 2013. Synthetic lethal metabolic targeting of cellular senescence in cancer therapy. *Nature,* 501**,** 421-5.
DOS SANTOS, L., CYRINO, E. S., ANTUNES, M., SANTOS, D. A. & SARDINHA, L. B. 2017. Sarcopenia and physical independence in older adults: the independent and synergic role of muscle mass and muscle function. *Journal of cachexia, sarcopenia and muscle,* 8**,** 245-250.
DOYLE, A., ZHANG, G., ABDEL FATTAH, E. A., EISSA, N. T. & LI, Y. P. 2011. Toll-like receptor 4 mediates lipopolysaccharide-induced muscle catabolism via coordinate activation of ubiquitinproteasome and autophagy-lysosome pathways. *Faseb j,* 25**,** 99-110.
DOYLE, L. M. & WANG, M. Z. 2019. Overview of Extracellular Vesicles, Their Origin, Composition, Purpose, and Methods for Exosome Isolation and Analysis. *Cells,* 8**,** 727.
DRUMMOND, M. J., ADDISON, O., BRUNKER, L., HOPKINS, P. N., MCCLAIN, D. A., LASTAYO, P. C. & MARCUS, R. L. 2014. Downregulation of E3 ubiquitin ligases and mitophagy-related genes in skeletal muscle of physically inactive, frail older women: a cross-sectional comparison. *J Gerontol A Biol Sci Med Sci,* 69**,** 1040-8.
DRUMMOND, M. J., TIMMERMAN, K. L., MARKOFSKI, M. M., WALKER, D. K., DICKINSON, J. M., JAMALUDDIN, M., BRASIER, A. R., RASMUSSEN, B. B. & VOLPI, E. 2013. Short-term bed rest increases TLR4 and IL-6 expression in skeletal muscle of older adults. *American journal of physiology. Regulatory, integrative and comparative physiology,* 305**,** R216-R223.
DUCKWORTH, W. C., BENNETT, R. G. & HAMEL, F. G. 1998. Insulin degradation: progress and potential. *Endocr Rev,* 19**,** 608-24.
DUNPHY, K., DOWLING, P., BAZOU, D. & O'GORMAN, P. 2021. Current Methods of Post-Translational Modification Analysis and Their Applications in Blood Cancers. *Cancers (Basel),* 13.
DVASH, E., HAR-TAL, M., BARAK, S., MEIR, O. & RUBINSTEIN, M. J. N. C. 2015. Leukotriene C4 is the major trigger of stress-induced oxidative DNA damage. 6**,** 1-15.
EITAN, E., GREEN, J., BODOGAI, M., MODE, N. A., BÆK, R., JØRGENSEN, M. M., FREEMAN, D. W., WITWER, K. W., ZONDERMAN, A. B., BIRAGYN, A., MATTSON, M. P., NOREN HOOTEN, N. & EVANS, M. K. 2017. Age-Related Changes in Plasma Extracellular Vesicle Characteristics and Internalization by Leukocytes. *Scientific Reports,* 7**,** 1342.
EITAN, E., ZHANG, S., WITWER, K. W. & MATTSON, M. P. 2015. Extracellular vesicle–depleted fetal bovine and human sera have reduced capacity to support cell growth. *Journal of Extracellular Vesicles,* 4**,** 26373.
ELBAKRAWY, E., KAUR BAINS, S., BRIGHT, S., AL-ABEDI, R., MAYAH, A., GOODWIN, E. & KADHIM, M. 2020. Radiation-Induced Senescence Bystander Effect: The Role of Exosomes. *Biology,* 9**,** 191.
ELDER, S. S. & EMMERSON, E. 2020. Senescent cells and macrophages: key players for regeneration? 10**,** 200309.
ENGLER , A. J., GRIFFIN , M. A., SEN , S., BÖNNEMANN , C. G., SWEENEY , H. L. & DISCHER , D. E. 2004. Myotubes differentiate optimally on substrates with tissue-like stiffness : pathological implications for soft or stiff microenvironments. *Journal of Cell Biology,* 166**,** 877-887.
ENGLUND, D. A., JOLLIFFE, A., AVERSA, Z., ZHANG, X., STURMLECHNER, I., SAKAMOTO, A. E., ZEIDLER, J. D., WARNER, G. M., MCNINCH, C., WHITE, T. A., CHINI, E. N., BAKER, D. J., VAN DEURSEN, J. M. & LEBRASSEUR, N. K. 2023. p21 induces a senescence program and skeletal muscle dysfunction. *Molecular Metabolism,* 67**,** 101652.
FABRE, O., GIORDANI, L., PARISI, A., PATTAMAPRAPANONT, P., AHWAZI, D., BRUN, C., CHAKROUN, I., TALEB, A., BLAIS, A., ANDERSEN, E., INGERSLEV, L. R., MAIRE, P., RUDNICKI, M., LAURENS, C., CITIRIKKAYA, K., GARDE, C., LUNDELL, L., DESHMUKH, A. S., MORO, C., BOURLIER, V., MOUNIER, R., GRAND, F. L. & BARRÈS, R. 2020. GREM1 is epigenetically reprogrammed in muscle cells after exercise training and controls myogenesis and metabolism. 2020.02.20.956300.

FAFIÁN-LABORA, J. A., RODRÍGUEZ-NAVARRO, J. A. & O'LOGHLEN, A. 2020. Small Extracellular Vesicles Have GST Activity and Ameliorate Senescence-Related Tissue Damage. *Cell Metabolism,* 32**,** 71-86.e5.
FAN, X., HUSSIEN, R., BROOKS, G. A. J. F. R. B. & MEDICINE 2010. H2O2-induced mitochondrial fragmentation in C2C12 myocytes. 49**,** 1646-1654.
FANE, M. & WEERARATNA, A. T. 2020. How the ageing microenvironment influences tumour progression. *Nat Rev Cancer,* 20**,** 89-106.
FELICE, F., CESARE, M. M., FREDIANELLI, L., DE LEO, M., CONTI, V., BRACA, A. & DI STEFANO, R. 2022. Effect of Tomato Peel Extract Grown under Drought Stress Condition in a Sarcopenia Model. 27**,** 2563.
FENG, Z. 2010. p53 regulation of the IGF-1/AKT/mTOR pathways and the endosomal compartment. *Cold Spring Harb Perspect Biol,* 2**,** a001057.
FERRANTE, C. J., PINHAL-ENFIELD, G., ELSON, G., CRONSTEIN, B. N., HASKO, G., OUTRAM, S. & LEIBOVICH, S. J. 2013. The adenosine-dependent angiogenic switch of macrophages to an M2-like phenotype is independent of interleukin-4 receptor alpha (IL-4Rα) signaling. *Inflammation,* 36**,** 921-931.
FERRINGTON, D. A., HUSOM, A. D. & THOMPSON, L. V. 2005. Altered proteasome structure, function, and oxidation in aged muscle. *Faseb j,* 19**,** 644-6.
FERRUCCI, L. & FABBRI, E. 2018. Inflammageing: chronic inflammation in ageing, cardiovascular disease, and frailty. *Nature Reviews Cardiology,* 15**,** 505-522.
FERRUZZA, S., ROSSI, C., SAMBUY, Y. & SCARINO, M. L. 2013. Serum-reduced and serum-free media for differentiation of Caco-2 cells. *Altex,* 30**,** 159-68.
FLORIN, A., LAMBERT, C., SANCHEZ, C., ZAPPIA, J., DURIEUX, N., TIEPPO, A. M., MOBASHERI, A. & HENROTIN, Y. 2020. The secretome of skeletal muscle cells: A systematic review. *Osteoarthritis and Cartilage Open,* 2**,** 100019.
FLYNN, J. M. & MELOV, S. 2013. SOD2 in mitochondrial dysfunction and neurodegeneration. *Free Radic Biol Med,* 62**,** 4-12.
FORRESTER, S. J., KIKUCHI, D. S., HERNANDES, M. S., XU, Q. & GRIENDLING, K. K. 2018. Reactive Oxygen Species in Metabolic and Inflammatory Signaling. 122**,** 877-902.
FORTERRE, A., JALABERT, A., BERGER, E., BAUDET, M., CHIKH, K., ERRAZURIZ, E., DE LARICHAUDY, J., CHANON, S., WEISS-GAYET, M., HESSE, A.-M., RECORD, M., GELOEN, A., LEFAI, E., VIDAL, H., COUTÉ, Y. & ROME, S. 2014. Proteomic Analysis of C2C12 Myoblast and Myotube Exosome-Like Vesicles: A New Paradigm for Myoblast-Myotube Cross Talk? *PLOS ONE,* 9**,** e84153.
FORTERRE, A., JALABERT, A., CHIKH, K., PESENTI, S., EUTHINE, V., GRANJON, A., ERRAZURIZ, E., LEFAI, E., VIDAL, H. & ROME, S. 2014b. Myotube-derived exosomal miRNAs downregulate Sirtuin1 in myoblasts during muscle cell differentiation. *Cell Cycle,* 13**,** 78-89.
FOSTER, W., LI, Y., USAS, A., SOMOGYI, G. & HUARD, J. 2003. Gamma interferon as an antifibrosis agent in skeletal muscle. *Journal of Orthopaedic Research,* 21**,** 798-804.
FRANCESCHI, C. & CAMPISI, J. 2014. Chronic inflammation (inflammaging) and its potential contribution to age-associated diseases. *J Gerontol A Biol Sci Med Sci,* 69 Suppl 1**,** S4-9.
FREEDMAN, D. A. & FOLKMAN, J. 2005. CDK2 translational down-regulation during endothelial senescence. *Exp Cell Res,* 307**,** 118-30.
FREEMAN, D. W., NOREN HOOTEN, N., EITAN, E., GREEN, J., MODE, N. A., BODOGAI, M., ZHANG, Y., LEHRMANN, E., ZONDERMAN, A. B. & BIRAGYN, A. J. D. 2018. Altered extracellular vesicle concentration, cargo, and function in diabetes. 67**,** 2377-2388.
FREUND, A., ORJALO, A. V., DESPREZ, P.-Y. & CAMPISI, J. 2010. Inflammatory networks during cellular senescence: causes and consequences. *Trends in molecular medicine,* 16**,** 238-246.
FRONTERA, W. R. & OCHALA, J. 2015. Skeletal Muscle: A Brief Review of Structure and Function. *Calcified Tissue International,* 96**,** 183-195.
FRÜHBEIS, C., HELMIG, S., TUG, S., SIMON, P. & KRÄMER-ALBERS, E. M. 2015. Physical exercise induces rapid release of small extracellular vesicles into the circulation. *J Extracell Vesicles,* 4**,** 28239.
FRY, C. S., KIRBY, T. J., KOSMAC, K., MCCARTHY, J. J. & PETERSON, C. A. 2017. Myogenic Progenitor Cells Control Extracellular Matrix Production by Fibroblasts during Skeletal Muscle Hypertrophy. *Cell Stem Cell,* 20**,** 56-69.
FRY, C. S., LEE, J. D., MULA, J., KIRBY, T. J., JACKSON, J. R., LIU, F., YANG, L., MENDIAS, C. L., DUPONT-VERSTEEGDEN, E. E., MCCARTHY, J. J. & PETERSON, C. A. 2015. Inducible

depletion of satellite cells in adult, sedentary mice impairs muscle regenerative capacity without affecting sarcopenia. *Nature Medicine,* 21**,** 76-80.
FU, X., XIAO, J., WEI, Y., LI, S., LIU, Y., YIN, J., SUN, K., SUN, H., WANG, H., ZHANG, Z., ZHANG, B.-T., SHENG, C., WANG, H. & HU, P. 2015. Combination of inflammation-related cytokines promotes long-term muscle stem cell expansion. *Cell research,* 25**,** 655-673.
FUJII, S., SAWA, T., IHARA, H., TONG, K. I., IDA, T., OKAMOTO, T., AHTESHAM, A. K., ISHIMA, Y., MOTOHASHI, H., YAMAMOTO, M. & AKAIKE, T. 2010. The critical role of nitric oxide signaling, via protein S-guanylation and nitrated cyclic GMP, in the antioxidant adaptive response. *The Journal of biological chemistry,* 285**,** 23970-23984.
FUJITA, H., ENDO, A., SHIMIZU, K. & NAGAMORI, E. 2010. Evaluation of serum-free differentiation conditions for C2C12 myoblast cells assessed as to active tension generation capability. *Biotechnol Bioeng,* 107**,** 894-901.
FULLE, S., PROTASI, F., DI TANO, G., PIETRANGELO, T., BELTRAMIN, A., BONCOMPAGNI, S., VECCHIET, L. & FANÒ, G. 2004. The contribution of reactive oxygen species to sarcopenia and muscle ageing. *Experimental Gerontology,* 39**,** 17-24.
FULZELE, S., MENDHE, B., KHAYRULLIN, A., JOHNSON, M., KAISER, H., LIU, Y., ISALES, C. M. & HAMRICK, M. W. 2019. Muscle-derived miR-34a increases with age in circulating extracellular vesicles and induces senescence of bone marrow stem cells. *Aging,* 11**,** 1791-1803.
FURMAN, D., CAMPISI, J., VERDIN, E., CARRERA-BASTOS, P., TARG, S., FRANCESCHI, C., FERRUCCI, L., GILROY, D. W., FASANO, A., MILLER, G. W., MILLER, A. H., MANTOVANI, A., WEYAND, C. M., BARZILAI, N., GORONZY, J. J., RANDO, T. A., EFFROS, R. B., LUCIA, A., KLEINSTREUER, N. & SLAVICH, G. M. 2019. Chronic inflammation in the etiology of disease across the life span. *Nature Medicine,* 25**,** 1822-1832.
GARCÍA-GARCÍA, V. A., ALAMEDA, J. P., PAGE, A. & CASANOVA, M. L. 2021. Role of NF-κB in Ageing and Age-Related Diseases: Lessons from Genetically Modified Mouse Models. *Cells,* 10.
GARCÍA-MARTÍNEZ, C., LÓPEZ-SORIANO, F. J. & ARGILÉS, J. M. 1993. Acute treatment with tumour necrosis factor-alpha induces changes in protein metabolism in rat skeletal muscle. *Mol Cell Biochem,* 125**,** 11-8.
GARCÍA-PRAT, L., MARTÍNEZ-VICENTE, M., PERDIGUERO, E., ORTET, L., RODRÍGUEZ-UBREVA, J., REBOLLO, E., RUIZ-BONILLA, V., GUTARRA, S., BALLESTAR, E., SERRANO, A. L., SANDRI, M. & MUÑOZ-CÁNOVES, P. 2016. Autophagy maintains stemness by preventing senescence. *Nature,* 529**,** 37-42.
GARDAI, S. J., MCPHILLIPS, K. A., FRASCH, S. C., JANSSEN, W. J., STAREFELDT, A., MURPHYULLRICH, J. E., BRATTON, D. L., OLDENBORG, P. A., MICHALAK, M. & HENSON, P. M. 2005. Cell-surface calreticulin initiates clearance of viable or apoptotic cells through transactivation of LRP on the phagocyte. *Cell,* 123**,** 321-34.
GARG, K., CORONA, B. T. & WALTERS, T. J. 2015. Therapeutic strategies for preventing skeletal muscle fibrosis after injury. *Front Pharmacol,* 6**,** 87.
GARGALOVIC, P. S., GHARAVI, N. M., CLARK, M. J., PAGNON, J., YANG, W.-P., HE, A., TRUONG, A., BARUCH-OREN, T., BERLINER, J. A., KIRCHGESSNER, T. G. & LUSIS, A. J. 2006. The Unfolded Protein Response Is an Important Regulator of Inflammatory Genes in Endothelial Cells. 26**,** 2490-2496.
GARIBALLA, S. & ALESSA, A. 2013. Sarcopenia: prevalence and prognostic significance in hospitalized patients. *Clin Nutr,* 32**,** 772-6.
GAWLITTA, D., BOONEN, K. J., OOMENS, C. W., BAAIJENS, F. P. & BOUTEN, C. V. 2008. The influence of serum-free culture conditions on skeletal muscle differentiation in a tissue-engineered model. *Tissue Eng Part A,* 14**,** 161-71.
GERVAIS, F. G., CRUZ, R. P. G., CHATEAUNEUF, A., GALE, S., SAWYER, N., NANTEL, F., METTERS, K. M. & O'NEILL, G. P. 2001. Selective modulation of chemokinesis, degranulation, and apoptosis in eosinophils through the PGD₂ receptors CRTH2 and DP. *Journal of Allergy and Clinical Immunology,* 108**,** 982-988.
GHOSH, S., LERTWATTANARAK, R., GARDUÑO JDE, J., GALEANA, J. J., LI, J., ZAMARRIPA, F., LANCASTER, J. L., MOHAN, S., HUSSEY, S. & MUSI, N. 2015. Elevated muscle TLR4 expression and metabolic endotoxemia in human aging. *J Gerontol A Biol Sci Med Sci,* 70**,** 23246.
GINGRICH, A., VOLKERT, D., KIESSWETTER, E., THOMANEK, M., BACH, S., SIEBER, C. C. & ZOPF, Y. 2019. Prevalence and overlap of sarcopenia, frailty, cachexia and malnutrition in older medical inpatients. *BMC Geriatrics,* 19**,** 120.

GIRARDI, F., TALEB, A., EBRAHIMI, M., DATYE, A., GAMAGE, D. G., PECCATE, C., GIORDANI, L., MILLAY, D. P., GILBERT, P. M., CADOT, B. & LE GRAND, F. 2021. TGFβ signaling curbs cell fusion and muscle regeneration. *Nature Communications,* 12**,** 750.
GOETSCH, S. C., HAWKE, T. J., GALLARDO, T. D., RICHARDSON, J. A. & GARRY, D. J. 2003. Transcriptional profiling and regulation of the extracellular matrix during muscle regeneration. *Physiological Genomics,* 14**,** 261-271.
GOLD, L. I., EGGLETON, P., SWEETWYNE, M. T., VAN DUYN, L. B., GREIVES, M. R., NAYLOR, S.-M., MICHALAK, M. & MURPHY-ULLRICH, J. E. 2010. Calreticulin: non-endoplasmic reticulum functions in physiology and disease. 24**,** 665-683.
GOMES, F. G., ANDRADE, A. C., WOLF, M., HOCHMANN, S., KRISCH, L., MAEDING, N., REGL, C., POUPARDIN, R., EBNER-PEKING, P., HUBER, C. G., MEISNER-KOBER, N., SCHALLMOSER, K. & STRUNK, D. 2022. Synergy of Human Platelet-Derived Extracellular Vesicles with Secretome Proteins Promotes Regenerative Functions. 10**,** 238.
GOMES, M. J., MARTINEZ, P. F., PAGAN, L. U., DAMATTO, R. L., CEZAR, M. D. M., LIMA, A. R. R., OKOSHI, K. & OKOSHI, M. P. 2017. Skeletal muscle aging: influence of oxidative stress and physical exercise. *Oncotarget,* 8**,** 20428-20440.
GOODMAN, C. A. 2019. Role of mTORC1 in mechanically induced increases in translation and skeletal muscle mass. *J Appl Physiol (1985),* 127**,** 581-590.
GOODMAN, M. N. 1991. Tumor necrosis factor induces skeletal muscle protein breakdown in rats. *Am J Physiol,* 260**,** E727-30.
GOODPASTER, B. H., PARK, S. W., HARRIS, T. B., KRITCHEVSKY, S. B., NEVITT, M., SCHWARTZ, A. V., SIMONSICK, E. M., TYLAVSKY, F. A., VISSER, M. & NEWMAN, A. B. 2006. The loss of skeletal muscle strength, mass, and quality in older adults: the health, aging and body composition study. *J Gerontol A Biol Sci Med Sci,* 61**,** 1059-64.
GORGOULIS, V., ADAMS, P. D., ALIMONTI, A., BENNETT, D. C., BISCHOF, O., BISHOP, C., CAMPISI, J., COLLADO, M., EVANGELOU, K., FERBEYRE, G., GIL, J., HARA, E., KRIZHANOVSKY, V., JURK, D., MAIER, A. B., NARITA, M., NIEDERNHOFER, L., PASSOS, J. F., ROBBINS, P. D., SCHMITT, C. A., SEDIVY, J., VOUGAS, K., VON ZGLINICKI, T., ZHOU, D., SERRANO, M. & DEMARIA, M. 2019. Cellular Senescence: Defining a Path Forward. *Cell,* 179**,** 813-827.
GOSWAMI, M. V., TAWALBEH, S. M., CANESSA, E. H. & HATHOUT, Y. 2021. Temporal Proteomic Profiling During Differentiation of Normal and Dystrophin-Deficient Human Muscle Cells. *J Neuromuscul Dis,* 8**,** S205-s222.
GOULDING, M., LUMSDEN, A. & PAQUETTE, A. J. 1994. Regulation of Pax-3 expression in the dermomyotome and its role in muscle development. *Development,* 120**,** 957-71.
GRANIC, A., MARTIN-RUIZ, C., DODDS, R. M., ROBINSON, L., SPYRIDOPOULOS, I., KIRKWOOD, T. B. L., VON ZGLINICKI, T. & SAYER, A. A. 2020. Immunosenescence profiles are not associated with muscle strength, physical performance and sarcopenia risk in very old adults: The Newcastle 85+ Study. *Mechanisms of Ageing and Development,* 190**,** 111321.
GREEN, T. D., PARK, J., YIN, Q., FANG, S., CREWS, A. L., JONES, S. L. & ADLER, K. B. 2012. Directed migration of mouse macrophages in vitro involves myristoylated alanine-rich C-kinase substrate (MARCKS) protein. *Journal of leukocyte biology,* 92**,** 633-639.
GREIWE, J. S., CHENG, B., RUBIN, D. C., YARASHESKI, K. E. & SEMENKOVICH, C. F. 2001. Resistance exercise decreases skeletal muscle tumor necrosis factor α in frail elderly humans. 15**,** 475-482.
GRIMBY, G. & SALTIN, B. 1983. The ageing muscle. *Clin Physiol,* 3**,** 209-18.
GUESCINI, M., CANONICO, B., LUCERTINI, F., MAGGIO, S., ANNIBALINI, G., BARBIERI, E., LUCHETTI, F., PAPA, S. & STOCCHI, V. 2015. Muscle Releases Alpha-Sarcoglycan Positive Extracellular Vesicles Carrying miRNAs in the Bloodstream. *PLoS One,* 10**,** e0125094.
GUESCINI, M., GUIDOLIN, D., VALLORANI, L., CASADEI, L., GIOACCHINI, A. M., TIBOLLO, P., BATTISTELLI, M., FALCIERI, E., BATTISTIN, L., AGNATI, L. F. & STOCCHI, V. 2010. C2C12 myoblasts release micro-vesicles containing mtDNA and proteins involved in signal transduction. *Experimental Cell Research,* 316**,** 1977-1984.
GUESCINI, M., MAGGIO, S., CECCAROLI, P., BATTISTELLI, M., ANNIBALINI, G., PICCOLI, G., SESTILI, P. & STOCCHI, V. 2017. Extracellular Vesicles Released by Oxidatively Injured or Intact C2C12 Myotubes Promote Distinct Responses Converging toward Myogenesis. *International journal of molecular sciences,* 18**,** 2488.

GUNNING, P. W., FERGUSON, V., BRENNAN, K. J. & HARDEMAN, E. C. 2001. Alpha-skeletal actin induces a subset of muscle genes independently of muscle differentiation and withdrawal from the cell cycle. *Journal of Cell Science,* 114**,** 513-524.
HADDAD, F., ZALDIVAR, F., COOPER, D. M. & ADAMS, G. R. 2005. IL-6-induced skeletal muscle atrophy. *Journal of Applied Physiology,* 98**,** 911-917.
HAI, R., PEI, Y. F., SHEN, H., ZHANG, L., LIU, X. G., LIN, Y., RAN, S., PAN, F., TAN, L. J., LEI, S. F., YANG, T. L., ZHANG, Y., ZHU, X. Z., ZHAO, L. J. & DENG, H. W. 2012. Genome-wide association study of copy number variation identified gremlin1 as a candidate gene for lean body mass. *J Hum Genet,* 57**,** 33-7.
HALL, B. M., BALAN, V., GLEIBERMAN, A. S., STROM, E., KRASNOV, P., VIRTUOSO, L. P., RYDKINA, E., VUJCIC, S., BALAN, K., GITLIN, I., LEONOVA, K., POLINSKY, A., CHERNOVA, O. B. & GUDKOV, A. V. 2016. Aging of mice is associated with p16(Ink4a)- and βgalactosidase-positive macrophage accumulation that can be induced in young mice by senescent cells. *Aging,* 8**,** 1294-1315.
HALL, D. T., MA, J. F., DI MARCO, S. & GALLOUZI, I.-E. 2011. Inducible nitric oxide synthase (iNOS) in muscle wasting syndrome, sarcopenia, and cachexia. 3**,** 702-715.
HAN, L., LONG, Q., LI, S., XU, Q., ZHANG, B., DOU, X., QIAN, M., JIRAMONGKOL, Y., GUO, J., CAO, L., CHIN, Y. E., LAM, E. W., JIANG, J. & SUN, Y. 2020. Senescent Stromal Cells Promote Cancer Resistance through SIRT1 Loss-Potentiated Overproduction of Small Extracellular Vesicles. *Cancer Res,* 80**,** 3383-3398.
HE, Y., XIE, W., LI, H., JIN, H., ZHANG, Y. & LI, Y. 2021. Cellular Senescence in Sarcopenia: Possible Mechanisms and Therapeutic Potential. *Front Cell Dev Biol,* 9**,** 793088.
HELMAN, A., KLOCHENDLER, A., AZAZMEH, N., GABAI, Y., HORWITZ, E., ANZI, S., SWISA, A., CONDIOTTI, R., GRANIT, R. Z., NEVO, Y., FIXLER, Y., SHREIBMAN, D., ZAMIR, A., TORNOVSKY-BABEAY, S., DAI, C., GLASER, B., POWERS, A. C., SHAPIRO, A. M. J., MAGNUSON, M. A., DOR, Y. & BEN-PORATH, I. 2016. p16Ink4a-induced senescence of pancreatic beta cells enhances insulin secretion. *Nature Medicine,* 22**,** 412-420.
HEPPLE, R. T., QIN, M., NAKAMOTO, H. & GOTO, S. 2008. Caloric restriction optimizes the proteasome pathway with aging in rat plantaris muscle: implications for sarcopenia. *American Journal of Physiology-Regulatory, Integrative and Comparative Physiology,* 295**,** R1231R1237.
HERBIG, U., JOBLING, W. A., CHEN, B. P., CHEN, D. J. & SEDIVY, J. M. 2004. Telomere shortening triggers senescence of human cells through a pathway involving ATM, p53, and p21(CIP1), but not p16(INK4a). *Mol Cell,* 14**,** 501-13.
HERNANDEZ-SEGURA, A., NEHME, J. & DEMARIA, M. 2018. Hallmarks of Cellular Senescence. *Trends Cell Biol,* 28**,** 436-453.
HERRANZ, N. & GIL, J. 2018. Mechanisms and functions of cellular senescence. *The Journal of Clinical Investigation,* 128**,** 1238-1246.
HESLOP, L., MORGAN, J. E. & PARTRIDGE, T. A. 2000. Evidence for a myogenic stem cell that is exhausted in dystrophic muscle. *Journal of Cell Science,* 113**,** 2299-2308.
HETTINGER, Z. R., KARGL, C. K., SHANNAHAN, J. H., KUANG, S. & GAVIN, T. P. 2021. Extracellular vesicles released from stress-induced prematurely senescent myoblasts impair endothelial function and proliferation. 106**,** 2083-2095.
HO, A. T. V., PALLA, A. R., BLAKE, M. R., YUCEL, N. D., WANG, Y. X., MAGNUSSON, K. E. G., HOLBROOK, C. A., KRAFT, P. E., DELP, S. L. & BLAU, H. M. 2017. Prostaglandin E2 is essential for efficacious skeletal muscle stem-cell function, augmenting regeneration and strength. *Proc Natl Acad Sci U S A,* 114**,** 6675-6684.
HOANG, D. H., NGUYEN, T. D., NGUYEN, H.-P., NGUYEN, X.-H., DO, P. T. X., DANG, V. D., DAM, P. T. M., BUI, H. T. H., TRINH, M. Q. & VU, D. M. J. F. I. M. B. 2020. Differential wound healing capacity of mesenchymal stem cell-derived exosomes originated from bone marrow, adipose tissue and umbilical cord under serum-and xeno-free condition. 7**,** 119.
HODGETTS, S., RADLEY, H., DAVIES, M. & GROUNDS, M. D. 2006. Reduced necrosis of dystrophic muscle by depletion of host neutrophils, or blocking TNFα function with Etanercept in mdx mice. *Neuromuscular Disorders,* 16**,** 591-602.
HOENE, M., RUNGE, H., HÄRING, H. U., SCHLEICHER, E. D. & WEIGERT, C. 2013. Interleukin-6 promotes myogenic differentiation of mouse skeletal muscle cells: role of the STAT3 pathway. *Am J Physiol Cell Physiol,* 304**,** C128-36.
HOFMANN, M., HALPER, B., OESEN, S., FRANZKE, B., STUPARITS, P., TSCHAN, H., BACHL, N., STRASSER, E.-M., QUITTAN, M., PLODER, M., WAGNER, K.-H. & WESSNER, B. 2015. Serum concentrations of insulin-like growth factor-1, members of the TGF-beta superfamily

and follistatin do not reflect different stages of dynapenia and sarcopenia in elderly women. *Experimental Gerontology,* 64**,** 35-45.
HSU, H. Y. & WEN, M. H. 2002. Lipopolysaccharide-mediated reactive oxygen species and signal transduction in the regulation of interleukin-1 gene expression. *J Biol Chem,* 277**,** 22131-9.
HU, L., LI, H., ZI, M., LI, W., LIU, J., YANG, Y., ZHOU, D., KONG, Q.-P., ZHANG, Y. & HE, Y. 2022. Why Senescent Cells Are Resistant to Apoptosis: An Insight for Senolytic Development. 10.
HUDSON, M. B., WOODWORTH-HOBBS, M. E., ZHENG, B., RAHNERT, J. A., BLOUNT, M. A., GOOCH, J. L., SEARLES, C. D. & PRICE, S. R. 2014. miR-23a is decreased during muscle atrophy by a mechanism that includes calcineurin signaling and exosome-mediated export. 306**,** C551-C558.
HUNT, L. C., GRACA, F. A., PAGALA, V., WANG, Y. D., LI, Y., YUAN, Z. F., FAN, Y., LABELLE, M., PENG, J. & DEMONTIS, F. 2021. Integrated genomic and proteomic analyses identify stimulus-dependent molecular changes associated with distinct modes of skeletal muscle atrophy. *Cell Rep,* 37**,** 109971.
HWANG, Y. C., CHO, I. J., JEONG, I. K., AHN, K. J. & CHUNG, H. Y. 2017. Differential association between sarcopenia and metabolic phenotype in Korean young and older adults with and without obesity. *Obesity (Silver Spring),* 25**,** 244-251.
IAVELLO, A., FRECH, V. S. L., GAI, C., DEREGIBUS, M. C., QUESENBERRY, P. J. & CAMUSSI, G. 2016. Role of Alix in miRNA packaging during extracellular vesicle biogenesis. *Int J Mol Med,* 37**,** 958-966.
IIZUKA, Y., YOKOMIZO, T., TERAWAKI, K., KOMINE, M., TAMAKI, K. & SHIMIZU, T. 2005. Characterization of a Mouse Second Leukotriene B4 Receptor, mBLT2: BLT2-DEPENDENT ERK ACTIVATION AND CELL MIGRATION OF PRIMARY MOUSE KERATINOCYTES*. *Journal of Biological Chemistry,* 280**,** 24816-24823.
IPSON, B. R., FLETCHER, M. B., ESPINOZA, S. E. & FISHER, A. L. 2018. Identifying Exosome-Derived MicroRNAs as Candidate Biomarkers of Frailty. *The Journal of Frailty & Aging,* 7**,** 100-103.
IRVINE, K. M., SKOIEN, R., BOKIL, N. J., MELINO, M., THOMAS, G. P., LOO, D., GABRIELLI, B., HILL, M. M., SWEET, M. J., CLOUSTON, A. D. & POWELL, E. E. 2014. Senescent human hepatocytes express a unique secretory phenotype and promote macrophage migration. *World J Gastroenterol,* 20**,** 17851-62.
ISMAEEL, A., VAN PELT, D. W., HETTINGER, Z. R., FU, X., RICHARDS, C. I., BUTTERFIELD, T. A., PETROCELLI, J. J., VECHETTI, I. J., CONFIDES, A. L., DRUMMOND, M. J. & DUPONT-VERSTEEGDEN, E. E. 2023. Extracellular vesicle distribution and localization in skeletal muscle at rest and following disuse atrophy. *Skelet Muscle,* 13**,** 6.
ITO, T., YOSHIKAWA, N., INUI, T., MIYAZAKI, N., SCHAFFER, S. W. & AZUMA, J. 2014. Tissue Depletion of Taurine Accelerates Skeletal Muscle Senescence and Leads to Early Death in Mice. *PLOS ONE,* 9**,** e107409.
JADHAV, K. S., DUNGAN, C. M., WILLIAMSON, D. L. J. M. O. A. & DEVELOPMENT 2013. Metformin limits ceramide-induced senescence in C2C12 myoblasts. 134**,** 548-559.
JANSSEN, I., HEYMSFIELD, S. B., WANG, Z. M. & ROSS, R. 2000. Skeletal muscle mass and distribution in 468 men and women aged 18-88 yr. *J Appl Physiol (1985),* 89**,** 81-8.
JANSSEN, I., SHEPARD, D. S., KATZMARZYK, P. T. & ROUBENOFF, R. 2004. The healthcare costs of sarcopenia in the United States. *J Am Geriatr Soc,* 52**,** 80-5.
JAY FORMAN, H. & TORRES, M. 2001. Redox signaling in macrophages. *Molecular Aspects of Medicine,* 22**,** 189-216.
JENSEN, S. M., BECHSHØFT, C. J. L., HEISTERBERG, M. F., SCHJERLING, P., ANDERSEN, J. L., KJAER, M. & MACKEY, A. L. 2020. Macrophage Subpopulations and the Acute Inflammatory Response of Elderly Human Skeletal Muscle to Physiological Resistance Exercise. *Frontiers in Physiology,* 11.
JEON, O. H., WILSON, D. R., CLEMENT, C. C., RATHOD, S., CHERRY, C., POWELL, B., LEE, Z., KHALIL, A. M., GREEN, J. J., CAMPISI, J., SANTAMBROGIO, L., WITWER, K. W. & ELISSEEFF, J. H. 2019. Senescence cell–associated extracellular vesicles serve as osteoarthritis disease and therapeutic markers. *JCI Insight,* 4.
JETHWA, N., CHUNG, G. H. C., LETE, M. G., ALONSO, A., BYRNE, R. D., CALLEJA, V. & LARIJANI, B. 2015. Endomembrane PtdIns(3,4,5)P3 activates the PI3K–Akt pathway. *Journal of Cell Science,* 128**,** 3456-3465.
JIMENEZ, L., YU, H., MCKENZIE, A. J., FRANKLIN, J. L., PATTON, J. G., LIU, Q. & WEAVER, A. M. 2019. Quantitative Proteomic Analysis of Small and Large Extracellular Vesicles (EVs) Reveals Enrichment of Adhesion Proteins in Small EVs. *Journal of Proteome Research,* 18**,** 947-959.

JOSEPH, A. M., ADHIHETTY, P. J., WAWRZYNIAK, N. R., WOHLGEMUTH, S. E., PICCA, A., KUJOTH, G. C., PROLLA, T. A. & LEEUWENBURGH, C. 2013. Dysregulation of mitochondrial quality control processes contribute to sarcopenia in a mouse model of premature aging. *PLoS One,* 8**,** e69327.

JOSHI, A. D., OAK, S. R., HARTIGAN, A. J., FINN, W. G., KUNKEL, S. L., DUFFY, K. E., DAS, A. & HOGABOAM, C. M. J. B. I. 2010. Interleukin-33 contributes to both M1 and M2 chemokine marker expression in human macrophages. 11**,** 1-10.

JURK, D., WANG, C., MIWA, S., MADDICK, M., KOROLCHUK, V., TSOLOU, A., GONOS, E. S., THRASIVOULOU, C., SAFFREY, M. J., CAMERON, K. & VON ZGLINICKI, T. 2012. Postmitotic neurons develop a p21-dependent senescence-like phenotype driven by a DNA damage response. *Aging cell,* 11**,** 996-1004.

KAASIK, P., UMNOVA, M., PEHME, A., ALEV, K., ARU, M., SELART, A. & SEENE, T. 2007. Ageing and dexamethasone associated sarcopenia: Peculiarities of regeneration. *The Journal of Steroid Biochemistry and Molecular Biology,* 105**,** 85-90.

KADOGUCHI, T., SHIMADA, K., MIYAZAKI, T., KITAMURA, K., KUNIMOTO, M., AIKAWA, T., SUGITA, Y., OUCHI, S., SHIOZAWA, T., YOKOYAMA-NISHITANI, M., FUKAO, K., MIYOSAWA, K., ISODA, K. & DAIDA, H. 2020. Promotion of oxidative stress is associated with mitochondrial dysfunction and muscle atrophy in aging mice. 20**,** 78-84.

KAGAN, H. M. & LI, W. 2003. Lysyl oxidase: properties, specificity, and biological roles inside and outside of the cell. *J Cell Biochem,* 88**,** 660-72.

KAKARLA, R., HUR, J., KIM, Y. J., KIM, J. & CHWAE, Y.-J. 2020. Apoptotic cell-derived exosomes: messages from dying cells. *Experimental & Molecular Medicine,* 52**,** 1-6.

KANG, J. S., HAN, M. H., KIM, G. Y., KIM, C. M., CHUNG, H. Y., HWANG, H. J., KIM, B. W. & CHOI, Y. H. 2015. Schisandrae semen essential oil attenuates oxidative stress-induced cell damage in C2C12 murine skeletal muscle cells through Nrf2-mediated upregulation of HO-1. *Int J Mol Med,* 35**,** 453-459.

KANG, K., REILLY, S. M., KARABACAK, V., GANGL, M. R., FITZGERALD, K., HATANO, B. & LEE, C.-H. 2008. Adipocyte-derived Th2 cytokines and myeloid PPARdelta regulate macrophage polarization and insulin sensitivity. *Cell metabolism,* 7**,** 485-495.

KANG, T.-W., YEVSA, T., WOLLER, N., HOENICKE, L., WUESTEFELD, T., DAUCH, D., HOHMEYER, A., GEREKE, M., RUDALSKA, R., POTAPOVA, A., IKEN, M., VUCUR, M., WEISS, S., HEIKENWALDER, M., KHAN, S., GIL, J., BRUDER, D., MANNS, M., SCHIRMACHER, P., TACKE, F., OTT, M., LUEDDE, T., LONGERICH, T., KUBICKA, S. & ZENDER, L. 2011. Senescence surveillance of pre-malignant hepatocytes limits liver cancer development. *Nature,* 479**,** 547-551.

KATO, T., SAEKI, H., TSUNEMI, Y., SHIBATA, S., TAMAKI, K. & SATO, S. 2011. Thymus and activation-regulated chemokine (TARC)/CC chemokine ligand (CCL) 17 accelerates wound healing by enhancing fibroblast migration. *Exp Dermatol,* 20**,** 669-74.

KAUR, N., GUPTA, P., SAINI, V., SHERAWAT, S., GUPTA, S., DUA, A., KUMAR, V., INJETI, E. & MITTAL, A. J. J. O. C. P. 2019. Cinnamaldehyde regulates H2O 2-induced skeletal muscle atrophy by ameliorating the proteolytic and antioxidant defense systems. 234**,** 6194-6208.

KAVANAGH, E. L., LINDSAY, S., HALASZ, M., GUBBINS, L. C., WEINER-GORZEL, K., GUANG, M. H. Z., MCGOLDRICK, A., COLLINS, E., HENRY, M., BLANCO-FERNÁNDEZ, A., P, O. G., FITZPATRICK, P., HIGGINS, M. J., DOWLING, P. & MCCANN, A. 2017. Protein and chemotherapy profiling of extracellular vesicles harvested from therapeutic induced senescent triple negative breast cancer cells. *Oncogenesis,* 6**,** e388.

KEEFE, A. C., LAWSON, J. A., FLYGARE, S. D., FOX, Z. D., COLASANTO, M. P., MATHEW, S. J., YANDELL, M. & KARDON, G. 2015. Muscle stem cells contribute to myofibres in sedentary adult mice. *Nature Communications,* 6**,** 7087.

KEIDAR, S., HEINRICH, R., KAPLAN, M. & AVIRAM, M. 2002. Oxidative stress increases the expression of the angiotensin-II receptor type 1 in mouse peritoneal macrophages. *J Renin Angiotensin Aldosterone Syst,* 3**,** 24-30.

KHAN, I. M., PERRARD, X. Y., BRUNNER, G., LUI, H., SPARKS, L. M., SMITH, S. R., WANG, X., SHI, Z. Z., LEWIS, D. E., WU, H. & BALLANTYNE, C. M. 2015. Intermuscular and perimuscular fat expansion in obesity correlates with skeletal muscle T cell and macrophage infiltration and insulin resistance. *International journal of obesity (2005),* 39**,** 1607-1618.

KHODABUKUS, A., PRABHU, N., WANG, J. & BURSAC, N. 2018. In Vitro Tissue-Engineered Skeletal Muscle Models for Studying Muscle Physiology and Disease. 7**,** 1701498.

KIM, H.-J., HIGASHIMORI, T., PARK, S.-Y., CHOI, H., DONG, J., KIM, Y.-J., NOH, H.-L., CHO, Y.-R., CLINE, G., KIM, Y.-B. & KIM, J. K. 2004. Differential Effects of Interleukin-6 and -10 on Skeletal Muscle and Liver Insulin Action In Vivo. *Diabetes,* 53**,** 1060-1067.
KIM, H.-J., KIM, S.-W., LEE, S.-H., JUNG, D.-W. & WILLIAMS, D. R. 2022. Inhibiting 5-lipoxygenase prevents skeletal muscle atrophy by targeting organogenesis signalling and insulin-like growth factor-1. 13**,** 3062-3077.
KIM, S., KIM, K., PARK, J. & JUN, W. 2021. Curcuma longa L. Water Extract Improves Dexamethasone-Induced Sarcopenia by Modulating the Muscle-Related Gene and Oxidative Stress in Mice. 10**,** 1000.
KIM, J. & LEE, J. 2016. Matrix metalloproteinase and tissue inhibitor of metalloproteinase responses to muscle damage after eccentric exercise. *Journal of exercise rehabilitation,* 12**,** 260-265.
KIM, S., LEE, M. J., CHOI, J. Y., PARK, D. H., KWAK, H. B., MOON, S., KOH, J. W., SHIN, H. K., RYU, J. K., PARK, C. S., PARK, J. H. & KANG, J. H. 2018. Roles of Exosome-Like Vesicles Released from Inflammatory C2C12 Myotubes: Regulation of Myocyte Differentiation and Myokine Expression. *Cellular Physiology and Biochemistry,* 48**,** 1829-1842.
KIM, J., PARK, M. Y., KIM, H. K., PARK, Y. & WHANG, K.-Y. 2016. Cortisone and dexamethasone inhibit myogenesis by modulating the AKT/mTOR signaling pathway in C2C12. *Bioscience, Biotechnology, and Biochemistry,* 80**,** 2093-2099.
KISLINGER, T., GRAMOLINI, A. O., PAN, Y., RAHMAN, K., MACLENNAN, D. H. & EMILI, A. 2005. Proteome Dynamics during C2C12 Myoblast Differentiation * S. *Molecular & Cellular Proteomics,* 4**,** 887-901.
KO, Y. G., PARK, H., KIM, T., LEE, J. W., PARK, S. G., SEOL, W., KIM, J. E., LEE, W. H., KIM, S. H., PARK, J. E. & KIM, S. 2001. A cofactor of tRNA synthetase, p43, is secreted to up-regulate proinflammatory genes. *J Biol Chem,* 276**,** 23028-33.
KOFFLER, J., KAUFMAN-FRANCIS, K., SHANDALOV, Y., EGOZI, D., AMIAD PAVLOV, D., LANDESBERG, A. & LEVENBERG, S. 2011. Improved vascular organization enhances functional integration of engineered skeletal muscle grafts. 108**,** 14789-14794.
KOPITO, R. R. J. T. I. C. B. 2000. Aggresomes, inclusion bodies and protein aggregation. 10**,** 524-530.
KORNILOV, R., PUHKA, M., MANNERSTRÖM, B., HIIDENMAA, H., PELTONIEMI, H., SILJANDER, P., SEPPÄNEN-KAIJANSINKKO, R. & KAUR, S. 2018. Efficient ultrafiltration-based protocol to deplete extracellular vesicles from fetal bovine serum. *J Extracell Vesicles,* 7**,** 1422674.
KOSMAC, K., PECK, B. D., WALTON, R. G., MULA, J., KERN, P. A., BAMMAN, M. M., DENNIS, R.A., JACOBS, C. A., LATTERMANN, C., JOHNSON, D. L. & PETERSON, C. A. 2018. Immunohistochemical Identification of Human Skeletal Muscle Macrophages. *Bio-protocol ,* 8**,** e2883.
KOWAL, J., TKACH, M. & THÉRY, C. 2014. Biogenesis and secretion of exosomes. *Current Opinion in Cell Biology,* 29**,** 116-125.
KREILING, J. A., TAMAMORI-ADACHI, M., SEXTON, A. N., JEYAPALAN, J. C., MUNOZ-NAJAR, U., PETERSON, A. L., MANIVANNAN, J., ROGERS, E. S., PCHELINTSEV, N. A., ADAMS, P. D. & SEDIVY, J. M. 2011. Age-associated increase in heterochromatic marks in murine and primate tissues. *Aging cell,* 10**,** 292-304.
KRISTENSEN, K., MÜNTER, R., KEMPEN, P. J., THOMSEN, M. E., STENSBALLE, A. & ANDRESEN, T. L. 2021. Isolation methods commonly used to study the liposomal protein corona suffer from contamination issues. *Acta Biomaterialia,* 130**,** 460-472.
KRYSTEL-WHITTEMORE, M., DILEEPAN, K. N. & WOOD, J. G. 2016. Mast Cell: A Multi-Functional Master Cell. 6.
KUGERATSKI, F. G., HODGE, K., LILLA, S., MCANDREWS, K. M., ZHOU, X., HWANG, R. F., ZANIVAN, S. & KALLURI, R. 2021. Quantitative proteomics identifies the core proteome of exosomes with syntenin-1 as the highest abundant protein and a putative universal biomarker. *Nat Cell Biol,* 23**,** 631-641.
KUMARI, R. & JAT, P. 2021. Mechanisms of Cellular Senescence: Cell Cycle Arrest and Senescence Associated Secretory Phenotype. 9.
KUSWANTO, W., BURZYN, D., PANDURO, M., WANG, K. K., JANG, Y. C., WAGERS, A. J., BENOIST, C. & MATHIS, D. 2016. Poor Repair of Skeletal Muscle in Aging Mice Reflects a Defect in Local, Interleukin-33-Dependent Accumulation of Regulatory T Cells. *Immunity,* 44**,** 355-367.
KWAK, J. Y., HWANG, H., KIM, S. K., CHOI, J. Y., LEE, S. M., BANG, H., KWON, E. S., LEE, K. P., CHUNG, S. G. & KWON, K. S. 2018. Prediction of sarcopenia using a combination of multiple serum biomarkers. *Sci Rep,* 8**,** 8574.

KWEE, B. J., BUDINA, E., NAJIBI, A. J. & MOONEY, D. J. 2018. CD4 T-cells regulate angiogenesis and myogenesis. *Biomaterials,* 178**,** 109-121.
KWON, S. M., HONG, S. M., LEE, Y.-K., MIN, S. & YOON, G. 2019. Metabolic features and regulation in cell senescence. *BMB reports,* 52**,** 5-12.
LAKER, R. C. & RYALL, J. G. 2016. DNA Methylation in Skeletal Muscle Stem Cell Specification, Proliferation, and Differentiation. *Stem Cells Int,* 2016**,** 5725927.
LANG, T., STREEPER, T., CAWTHON, P., BALDWIN, K., TAAFFE, D. R. & HARRIS, T. B. 2010. Sarcopenia: etiology, clinical consequences, intervention, and assessment. *Osteoporosis International,* 21**,** 543-559.
LANGECKER, M., ARNAUT, V., LIST, J. & SIMMEL, F. C. 2014. DNA nanostructures interacting with lipid bilayer membranes. *Acc Chem Res,* 47**,** 1807-15.
LANGEN, R. C., VAN DER VELDEN, J. L., SCHOLS, A. M., KELDERS, M. C., WOUTERS, E. F. & JANSSEN-HEININGER, Y. M. 2004. Tumor necrosis factor-alpha inhibits myogenic differentiation through MyoD protein destabilization. *Faseb j,* 18**,** 227-37.
LÄRFARS, G., LANTOINE, F. D. R., DEVYNCK, M.-A., PALMBLAD, J. & GYLLENHAMMAR, H. 1999. Activation of Nitric Oxide Release and Oxidative Metabolism by Leukotrienes B4, C4, and D4 in Human Polymorphonuclear Leukocytes. *Blood,* 93**,** 1399-1405.
LATERNSER, S., KELLER, H., LEUPIN, O., RAUSCH, M., GRAF-HAUSNER, U. & RIMANN, M. 2018. A Novel Microplate 3D Bioprinting Platform for the Engineering of Muscle and Tendon Tissues. *SLAS Technology,* 23**,** 599-613.
LAURILA, P.-P., WOHLWEND, M., LIMA, T., LUAN, P., HERZIG, S., ZANOU, N., CRISOL, B., BOU SLEIMAN, M., PORCU, E., GALLART-AYALA, H., HANDZLIK, M., WANG, Q., JAIN, S., D'AMICO, D., SALONEN, M., METALLO, C., KUTALIK, Z., EICHMANN, T., PLACE, N. & AUWERX, J. 2022. Sphingolipids accumulate in aged muscle, and their reduction counteracts sarcopenia. *Nature Aging,* 2**,** 1-17.
LAWSON, M. A. & PURSLOW, P. P. 2000. Differentiation of myoblasts in serum-free media: effects of modified media are cell line-specific. *Cells Tissues Organs,* 167**,** 130-7.
LE BIHAN, M. C., BARRIO-HERNANDEZ, I., MORTENSEN, T. P., HENNINGSEN, J., JENSEN, S. S., BIGOT, A., BLAGOEV, B., BUTLER-BROWNE, G. & KRATCHMAROVA, I. 2015. Cellular Proteome Dynamics during Differentiation of Human Primary Myoblasts. *J Proteome Res,* 14**,** 3348-61.
LE BIHAN, M.-C., BIGOT, A., JENSEN, S. S., DENNIS, J. L., ROGOWSKA-WRZESINSKA, A., LAINÉ, J., GACHE, V., FURLING, D., JENSEN, O. N., VOIT, T., MOULY, V., COULTON, G. R. & BUTLER-BROWNE, G. 2012. In-depth analysis of the secretome identifies three major independent secretory pathways in differentiating human myoblasts. *Journal of Proteomics,* 77**,** 344-356.
LEE, D. Y., LEE, S. Y., YUN, S. H., JEONG, J. W., KIM, J. H., KIM, H. W., CHOI, J. S., KIM, G. D., JOO, S. T., CHOI, I. & HUR, S. J. 2022. Review of the Current Research on Fetal Bovine Serum and the Development of Cultured Meat. *Food Sci Anim Resour,* 42**,** 775-799.
LEE, J. H. & JUN, H.-S. 2019. Role of Myokines in Regulating Skeletal Muscle Mass and Function. 10.
LEHMANN, B. D., PAINE, M. S., BROOKS, A. M., MCCUBREY, J. A., RENEGAR, R. H., WANG, R. & TERRIAN, D. M. 2008. Senescence-associated exosome release from human prostate cancer cells. *Cancer Res,* 68**,** 7864-71.
LEHRICH, B. M., LIANG, Y. & FIANDACA, M. S. 2021. Foetal bovine serum influence on in vitro extracellular vesicle analyses. *Journal of extracellular vesicles,* 10**,** e12061-e12061.
LEHRICH, B. M., LIANG, Y., KHOSRAVI, P., FEDEROFF, H. J. & FIANDACA, M. S. 2018. Fetal Bovine Serum-Derived Extracellular Vesicles Persist within Vesicle-Depleted Culture Media. *International journal of molecular sciences,* 19**,** 3538.
LEIZER, T., CEBON, J., LAYTON, J. E. & HAMILTON, J. A. 1990. Cytokine Regulation of Colony-Stimulating Factor Production in Cultured Human Synovial Fibroblasts: I. Induction of GM-CSF and G-CSF Production by Interleukin-1 and Tumor Necrosis Factor. *Blood,* 76**,** 1989-1996.
LESPAGNOL, A., DUFLAUT, D., BEEKMAN, C., BLANC, L., FIUCCI, G., MARINE, J. C., VIDAL, M., AMSON, R. & TELERMAN, A. 2008. Exosome secretion, including the DNA damage-induced p53-dependent secretory pathway, is severely compromised in TSAP6/Steap3-null mice. *Cell Death & Differentiation,* 15**,** 1723-1733.
LI, H., CHEN, Q., LI, C., ZHONG, R., ZHAO, Y., ZHANG, Q., TONG, W., ZHU, D. & ZHANG, Y. 2019. Muscle-secreted granulocyte colony-stimulating factor functions as metabolic niche factor ameliorating loss of muscle stem cells in aged mice. 38**,** e102154.

LI, J., CHAN, M. C., YU, Y., BEI, Y., CHEN, P., ZHOU, Q., CHENG, L., CHEN, L., ZIEGLER, O., ROWE, G. C., DAS, S. & XIAO, J. 2017. miR-29b contributes to multiple types of muscle atrophy. *Nat Commun,* 8**,** 15201.
LI, J., LEE, Y., JOHANSSON, H. J., MÄGER, I., VADER, P., NORDIN, J. Z., WIKLANDER, O. P. B., LEHTIÖ, J., WOOD, M. J. A. & ANDALOUSSI, S. E. 2015. Serum-free culture alters the quantity and protein composition of neuroblastoma-derived extracellular vesicles. *Journal of extracellular vesicles,* 4**,** 26883-26883.
LI, J., YI, X., YAO, Z., CHAKKALAKAL, J. V., XING, L. & BOYCE, B. F. 2020a. TNF Receptor-Associated Factor 6 Mediates TNFα-Induced Skeletal Muscle Atrophy in Mice During Aging. 35**,** 1535-1548.
LI, M., LIAO, L. & TIAN, W. 2020b. Extracellular Vesicles Derived From Apoptotic Cells: An Essential Link Between Death and Regeneration. 8.
LI, W. 2013. Phagocyte dysfunction, tissue aging and degeneration. *Ageing research reviews,* 12**,** 10051012.
LI, W., MOYLAN, J. S., CHAMBERS, M. A., SMITH, J. & REID, M. B. 2009. Interleukin-1 stimulates catabolism in C2C12 myotubes. *American Journal of Physiology-Cell Physiology,* 297**,** C706C714.
LI, Y. P. & REID, M. B. 2000. NF-kappaB mediates the protein loss induced by TNF-alpha in differentiated skeletal muscle myotubes. *Am J Physiol Regul Integr Comp Physiol,* 279**,** R116570.
LI, Y.-P. 2003. TNF-α is a mitogen in skeletal muscle. *American Journal of Physiology-Cell Physiology,* 285**,** C370-C376.
LI, Y.-P., CHEN, Y., JOHN, J., MOYLAN, J., JIN, B., MANN, D. L. & REID, M. B. J. T. F. J. 2005. TNF-α acts via p38 MAPK to stimulate expression of the ubiquitin ligase atrogin1/MAFbx in skeletal muscle. 19**,** 362-370.
LI, Y.-P., CHEN, Y., LI, A. S. & REID, M. B. 2003. Hydrogen peroxide stimulates ubiquitin-conjugating activity and expression of genes for specific E2 and E3 proteins in skeletal muscle myotubes. *American Journal of Physiology-Cell Physiology,* 285**,** C806-C812.
LIAN, D., CHEN, M. M., WU, H., DENG, S. & HU, X. 2022. The Role of Oxidative Stress in Skeletal Muscle Myogenesis and Muscle Disease. *Antioxidants (Basel),* 11.
LIEBER, R. L. & BODINE-FOWLER, S. C. 1993. Skeletal Muscle Mechanics: Implications for Rehabilitation. *Physical Therapy,* 73**,** 844-856.
LINGAPPAN, K. 2018. NF-κB in Oxidative Stress. *Current opinion in toxicology,* 7**,** 81-86.
LIO, C.-W. J. & RAO, A. 2019. TET Enzymes and 5hmC in Adaptive and Innate Immune Systems. 10.
LIU, D., LIU, X., ZHOU, T., YAO, W., ZHAO, J., ZHENG, Z., JIANG, W., WANG, F., AIKHIONBARE, F. O., HILL, D. L., EMMETT, N., GUO, Z., WANG, D., YAO, X. & CHEN, Y. 2016. IRE1-RACK1 axis orchestrates ER stress preconditioning-elicited cytoprotection from ischemia/reperfusion injury in liver. *J Mol Cell Biol,* 8**,** 144-56.
LIU, H., FERGUSSON, M. M., CASTILHO, R. M., LIU, J., CAO, L., CHEN, J., MALIDE, D., ROVIRA, II, SCHIMEL, D., KUO, C. J., GUTKIND, J. S., HWANG, P. M. & FINKEL, T. 2007. Augmented Wnt signaling in a mammalian model of accelerated aging. *Science,* 317**,** 803-6.
LIU, L., GE, D., MA, L., MEI, J., LIU, S., ZHANG, Q., REN, F., LIAO, H., PU, Q., WANG, T. & YOU, Z. 2012. Interleukin-17 and Prostaglandin E2 Are Involved in Formation of an M2 MacrophageDominant Microenvironment in Lung Cancer. *Journal of Thoracic Oncology,* 7**,** 1091-1100.
LO, J., LAU, E. Y., CHING, R. H., CHENG, B. Y., MA, M. K., NG, I. O. & LEE, T. K. 2015. Nuclear factor kappa B-mediated CD47 up-regulation promotes sorafenib resistance and its blockade synergizes the effect of sorafenib in hepatocellular carcinoma in mice. *Hepatology,* 62**,** 534-45. LONDHE, P. & DAVIE, J. K. 2011. Gamma Interferon Modulates Myogenesis through the Major Histocompatibility Complex Class II Transactivator, CIITA. *Molecular and Cellular Biology,* 31**,** 2854-2866.
LOFARO, F. D., CISTERNA, B., LACAVALLA, M. A., BOSCHI, F., MALATESTA, M., QUAGLINO, D., ZANCANARO, C. & BORALDI, F. 2021. Age-Related Changes in the Matrisome of the Mouse Skeletal Muscle. *Int J Mol Sci,* 22.
LOPATINA, T., BRUNO, S., TETTA, C., KALININA, N., PORTA, M. & CAMUSSI, G. 2014. Plateletderived growth factor regulates the secretion of extracellular vesicles by adipose mesenchymal stem cells and enhances their angiogenic potential. *Cell Communication and Signaling,* 12**,** 26.

LOPES-PACIENCIA, S., SAINT-GERMAIN, E., ROWELL, M.-C., RUIZ, A. F., KALEGARI, P. & FERBEYRE, G. 2019. The senescence-associated secretory phenotype and its regulation. *Cytokine,* 117**,** 15-22.
LOWE, S. W. & SHERR, C. J. 2003. Tumor suppression by Ink4a-Arf: progress and puzzles. *Curr Opin Genet Dev,* 13**,** 77-83.
LU, H., HUANG, D., RANSOHOFF, R. M. & ZHOU, L. 2011. Acute skeletal muscle injury: CCL2 expression by both monocytes and injured muscle is required for repair. *FASEB journal : official publication of the Federation of American Societies for Experimental Biology,* 25**,** 3344-3355.
LU, Y. C., YEH, W. C. & OHASHI, P. S. 2008. LPS/TLR4 signal transduction pathway. *Cytokine,* 42**,** 145-151.
LUAN, B., YOON, Y.-S., LAY, J. L., KAESTNER, K. H., HEDRICK, S. & MONTMINY, M. 2015. CREB pathway links PGE2 signaling with macrophage polarization. 112**,** 15642-15647.
MACALUSO, F. & MYBURGH, K. H. 2012. Current evidence that exercise can increase the number of adult stem cells. *J Muscle Res Cell Motil,* 33**,** 187-98.
MANDAL, P., PRATT, B. T., BARNES, M., MCMULLEN, M. R. & NAGY, L. E. 2011. Molecular mechanism for adiponectin-dependent M2 macrophage polarization: link between the metabolic and innate immune activity of full-length adiponectin. *J Biol Chem,* 286**,** 13460-9.
MANEA, M., MEZO, G., HUDECZ, F. & PRZYBYLSKI, M. 2007. Mass spectrometric identification of the trypsin cleavage pathway in lysyl-proline containing oligotuftsin peptides. *J Pept Sci,* 13**,** 227-36.
MANKHONG, S., KIM, S., MOON, S., KWAK, H. B., PARK, D. H. & KANG, J. H. 2020. Experimental Models of Sarcopenia: Bridging Molecular Mechanism and Therapeutic Strategy. *Cells,* 9.
MANN, C. J., PERDIGUERO, E., KHARRAZ, Y., AGUILAR, S., PESSINA, P., SERRANO, A. L. & MUÑOZ-CÁNOVES, P. 2011. Aberrant repair and fibrosis development in skeletal muscle. *Skeletal muscle,* 1**,** 21-21.
MANTOVANI, A., SICA, A., SOZZANI, S., ALLAVENA, P., VECCHI, A. & LOCATI, M. 2004. The chemokine system in diverse forms of macrophage activation and polarization. *Trends Immunol,* 25**,** 677-86.
MARCELL, T. J. 2003. Review Article: Sarcopenia: Causes, Consequences, and Preventions. *The Journals of Gerontology: Series A,* 58**,** M911-M916.
MARCU, I. C., EBERHARD, N., YERLY, A., BALMER, V., HEMPHILL, A., MOGEL, H., GASCHEN, V., STOFFEL, M. H. & BLUTEAU, J. 2020. Isolation of Human Small Extracellular Vesicles and Tracking of their Uptake by Retinal Pigment Epithelial Cells In Vitro. *Int J Mol Sci,* 21.
MARZETTI, E., CALVANI, R., CESARI, M., BUFORD, T. W., LORENZI, M., BEHNKE, B. J. & LEEUWENBURGH, C. 2013. Mitochondrial dysfunction and sarcopenia of aging: from signaling pathways to clinical trials. *The international journal of biochemistry & cell biology,* 45**,** 22882301.
MARZETTI, E., GUERRA, F., CALVANI, R., MARINI, F., BIANCOLILLO, A., GERVASONI, J., PRIMIANO, A., COELHO-JÚNIOR, H. J., LANDI, F., BERNABEI, R., BUCCI, C. & PICCA, A. 2020. Circulating Mitochondrial-Derived Vesicles, Inflammatory Biomarkers and Amino Acids in Older Adults With Physical Frailty and Sarcopenia: A Preliminary BIOSPHERE Multi-Marker Study Using Sequential and Orthogonalized Covariance Selection - Linear Discriminant Analysis. *Front Cell Dev Biol,* 8**,** 564417.
MARZETTI, E. & LEEUWENBURGH, C. 2006. Skeletal muscle apoptosis, sarcopenia and frailty at old age. *Experimental Gerontology,* 41**,** 1234-1238.
MATHIEU, M., MARTIN-JAULAR, L., LAVIEU, G. & THÉRY, C. 2019. Specificities of secretion and uptake of exosomes and other extracellular vesicles for cell-to-cell communication. *Nature Cell Biology,* 21**,** 9-17.
MAVROGONATOU, E., PRATSINIS, H., PAPADOPOULOU, A., KARAMANOS, N. K. & KLETSAS, D. 2019. Extracellular matrix alterations in senescent cells and their significance in tissue homeostasis. *Matrix Biol,* 75-76**,** 27-42.
MAZZONI, M., MAURO, G., ERRENI, M., ROMEO, P., MINNA, E., VIZIOLI, M. G., BELGIOVINE, C., RIZZETTI, M. G., PAGLIARDINI, S., AVIGNI, R., ANANIA, M. C., ALLAVENA, P., BORRELLO, M. G. & GRECO, A. 2019. Senescent thyrocytes and thyroid tumor cells induce M2-like macrophage polarization of human monocytes via a PGE2-dependent mechanism. *Journal of Experimental & Clinical Cancer Research,* 38**,** 208.
MCCROSKERY, S., THOMAS, M., PLATT, L., HENNEBRY, A., NISHIMURA, T., MCLEAY, L., SHARMA, M. & KAMBADUR, R. 2005. Improved muscle healing through enhanced

regeneration and reduced fibrosis in myostatin-null mice. *Journal of Cell Science,* 118**,** 35313541.
MCHUGH, D. & GIL, J. 2018. Senescence and aging: Causes, consequences, and therapeutic avenues. *The Journal of cell biology,* 217**,** 65-77.
MENG, S. J. & YU, L. J. 2010. Oxidative stress, molecular inflammation and sarcopenia. *Int J Mol Sci,* 11**,** 1509-26.
MERLE, N. S., NOE, R., HALBWACHS-MECARELLI, L., FREMEAUX-BACCHI, V. & ROUMENINA, L. T. 2015. Complement System Part II: Role in Immunity. 6.
MESARWI, O. A., SHIN, M. K., DRAGER, L. F., BEVANS-FONTI, S., JUN, J. C., PUTCHA, N., TORBENSON, M. S., PEDROSA, R. P., LORENZI-FILHO, G., STEELE, K. E., SCHWEITZER, M. A., MAGNUSON, T. H., LIDOR, A. O., SCHWARTZ, A. R. & POLOTSKY, V. Y. 2015. Lysyl Oxidase as a Serum Biomarker of Liver Fibrosis in Patients with Severe Obesity and Obstructive Sleep Apnea. *Sleep,* 38**,** 1583-91.
MICHAELSON, L. P., ILER, C. & WARD, C. W. 2013. ROS and RNS signaling in skeletal muscle: critical signals and therapeutic targets. *Annual review of nursing research,* 31**,** 367-387.
MICHELI, L., MITIDIERI, E., TURNATURI, C., VANACORE, D., CIAMPI, C., LUCARINI, E., CIRINO, G., GHELARDINI, C., SORRENTINO, R., DI CESARE MANNELLI, L. & D'EMMANUELE DI VILLA BIANCA, R. 2022. Beneficial Effect of H2S-Releasing Molecules in an In Vitro Model of Sarcopenia: Relevance of Glucoraphanin. 23**,** 5955.
MILJKOVIC, I., KUIPERS, A. L., CVEJKUS, R., BUNKER, C. H., PATRICK, A. L., GORDON, C. L. & ZMUDA, J. M. 2016. Myosteatosis increases with aging and is associated with incident diabetes in African ancestry men. *Obesity (Silver Spring, Md.),* 24**,** 476-482.
MILLER, E. W., DICKINSON, B. C. & CHANG, C. J. 2010. Aquaporin-3 mediates hydrogen peroxide uptake to regulate downstream intracellular signaling. 107**,** 15681-15686.
MILLS, C. D., KINCAID, K., ALT, J. M., HEILMAN, M. J. & HILL, A. M. 2000. M-1/M-2 Macrophages and the Th1/Th2 Paradigm. 164**,** 6166-6173.
MINAMINO, T. & KOMURO, I. 2007. Vascular cell senescence: contribution to atherosclerosis. *Circ Res,* 100**,** 15-26.
MINAMINO, T., ORIMO, M., SHIMIZU, I., KUNIEDA, T., YOKOYAMA, M., ITO, T., NOJIMA, A., NABETANI, A., OIKE, Y., MATSUBARA, H., ISHIKAWA, F. & KOMURO, I. 2009. A crucial role for adipose tissue p53 in the regulation of insulin resistance. *Nat Med,* 15**,** 1082-7.
MINIHANE, A. M., VINOY, S., RUSSELL, W. R., BAKA, A., ROCHE, H. M., TUOHY, K. M., TEELING, J. L., BLAAK, E. E., FENECH, M., VAUZOUR, D., MCARDLE, H. J., KREMER, B. H. A., STERKMAN, L., VAFEIADOU, K., BENEDETTI, M. M., WILLIAMS, C. M. & CALDER, P. C. 2015. Low-grade inflammation, diet composition and health: current research evidence and its translation. *The British journal of nutrition,* 114**,** 999-1012.
MISAWA, T., TANAKA, Y., OKADA, R. & TAKAHASHI, A. 2020. Biology of extracellular vesicles secreted from senescent cells as senescence-associated secretory phenotype factors. *Geriatr Gerontol Int,* 20**,** 539-546.
MO, C., ZHAO, R., VALLEJO, J., IGWE, O., BONEWALD, L., WETMORE, L. & BROTTO, M. 2015. Prostaglandin E2 promotes proliferation of skeletal muscle myoblasts via EP4 receptor activation. *Cell Cycle,* 14**,** 1507-16.
MOHAMED, J. S., WILSON, J. C., MYERS, M. J., SISSON, K. J. & ALWAY, S. E. 2014. Dysregulation of SIRT-1 in aging mice increases skeletal muscle fatigue by a PARP-1-dependent mechanism. *Aging (Albany NY),* 6**,** 820-34.
MOHAN, S., LIBANATI, C., DONY, C., LANG, K., SRINIVASAN, N. & BAYLINK, D. J. 1995. Development, validation, and application of a radioimmunoassay for insulin-like growth factor binding protein-5 in human serum and other biological fluids. *J Clin Endocrinol Metab,* 80**,** 263845.
MOISEEVA, V., CISNEROS, A., SICA, V., DERYAGIN, O., LAI, Y., JUNG, S., ANDRÉS, E., AN, J., SEGALÉS, J., ORTET, L., LUKESOVA, V., VOLPE, G., BENGURIA, A., DOPAZO, A., BENITAH, S. A., URANO, Y., DEL SOL, A., ESTEBAN, M. A., OHKAWA, Y., SERRANO, A. L., PERDIGUERO, E. & MUÑOZ-CÁNOVES, P. 2023. Senescence atlas reveals an aged-like inflamed niche that blunts muscle regeneration. *Nature,* 613**,** 169-178.
MONTGOMERY, R. R. & SHAW, A. C. 2015. Paradoxical changes in innate immunity in aging: recent progress and new directions. 98**,** 937-943.
MORAES, L. N., FERNANDEZ, G. J., VECHETTI-JÚNIOR, I. J., FREIRE, P. P., SOUZA, R. W. A., VILLACIS, R. A. R., ROGATTO, S. R., REIS, P. P., DAL-PAI-SILVA, M. & CARVALHO, R. F. 2017. Integration of miRNA and mRNA expression profiles reveals microRNA-regulated networks during muscle wasting in cardiac cachexia. *Sci Rep,* 7**,** 6998.

MOSSER, D. M. & EDWARDS, J. P. 2008. Exploring the full spectrum of macrophage activation. *Nat Rev Immunol,* 8**,** 958-69.
MOSTEIRO, L., PANTOJA, C., ALCAZAR, N., MARIÓN, R. M., CHONDRONASIOU, D., ROVIRA, M., FERNANDEZ-MARCOS, P. J., MUÑOZ-MARTIN, M., BLANCO-APARICIO, C., PASTOR, J.,
GÓMEZ-LÓPEZ, G., MARTINO, A. D., BLASCO, M. A., ABAD, M. & SERRANO, M. 2016. Tissue damage and senescence provide critical signals for cellular reprogramming in vivo. 354**,** aaf4445.
MOUSTOGIANNIS, A., PHILIPPOU, A., TASO, O., ZEVOLIS, E., PAPPA, M., CHATZIGEORGIOU, A. & KOUTSILIERIS, M. 2021. The Effects of Muscle Cell Aging on Myogenesis. *International journal of molecular sciences,* 22**,** 3721.
MUKUND, K. & SUBRAMANIAM, S. 2020. Skeletal muscle: A review of molecular structure and function, in health and disease. 12**,** e1462.
MÜLLER, I. I., CHATTERJEE, M., SCHNEIDER, M., BORST, O., SEIZER, P., SCHÖNBERGER, T., VOGEL, S., MÜLLER, K. A. L., GEISLER, T., LANG, F., LANGER, H. & GAWAZ, M. 2014. Gremlin-1 inhibits macrophage migration inhibitory factor-dependent monocyte function and survival. *International Journal of Cardiology,* 176**,** 923-929.
MURALIDHARAN-CHARI, V., CLANCY, J., PLOU, C., ROMAO, M., CHAVRIER, P., RAPOSO, G. & D'SOUZA-SCHOREY, C. 2009. ARF6-Regulated Shedding of Tumor Cell-Derived Plasma Membrane Microvesicles. *Current Biology,* 19**,** 1875-1885.
MURGIA, M., TONIOLO, L., NAGARAJ, N., CICILIOT, S., VINDIGNI, V., SCHIAFFINO, S., REGGIANI, C. & MANN, M. 2017. Single Muscle Fiber Proteomics Reveals Fiber-Type-Specific Features of Human Muscle Aging. *Cell Reports,* 19**,** 2396-2409.
MURPHY, M. M., LAWSON, J. A., MATHEW, S. J., HUTCHESON, D. A. & KARDON, G. 2011. Satellite cells, connective tissue fibroblasts and their interactions are crucial for muscle regeneration. *Development (Cambridge, England),* 138**,** 3625-3637.
MURRAY, P. J. & WYNN, T. A. 2011. Obstacles and opportunities for understanding macrophage polarization. *Journal of leukocyte biology,* 89**,** 557-563.
MURRAY, P. J., ALLEN, J. E., BISWAS, S. K., FISHER, E. A., GILROY, D. W., GOERDT, S., GORDON, S., HAMILTON, J. A., IVASHKIV, L. B., LAWRENCE, T., LOCATI, M., MANTOVANI, A., MARTINEZ, F. O., MEGE, J.-L., MOSSER, D. M., NATOLI, G., SAEIJ, J. P., SCHULTZE, J. L., SHIREY, K. A., SICA, A., SUTTLES, J., UDALOVA, I., VAN GINDERACHTER, J. A., VOGEL, S. N. & WYNN, T. A. 2014. Macrophage activation and polarization: nomenclature and experimental guidelines. *Immunity,* 41**,** 14-20.
MUZEMBO, B. A., NAGANO, Y., EITOKU, M., NGATU, N. R., MATSUI, T., BHATTI, S. A., HIROTA, R., ISHIDA, K. & SUGANUMA, N. 2014. A cross-sectional assessment of oxidative DNA damage and muscle strength among elderly people living in the community. *Environ Health Prev Med,* 19**,** 21-9.
MYTIDOU, C., KOUTSOULIDOU, A., KATSIOLOUDI, A., PROKOPI, M., KAPNISIS, K., MICHAILIDOU, K., ANAYIOTOS, A. & PHYLACTOU, L. A. J. T. F. J. 2021. Muscle-derived exosomes encapsulate myomiRs and are involved in local skeletal muscle tissue communication. 35**,** e21279.
NARDONE, O. M., DE SIRE, R., PETITO, V., TESTA, A., VILLANI, G., SCALDAFERRI, F. & CASTIGLIONE, F. 2021. Inflammatory Bowel Diseases and Sarcopenia: The Role of Inflammation and Gut Microbiota in the Development of Muscle Failure. 12.
NEELS, J. G. & OLEFSKY, J. M. 2006. Inflamed fat: what starts the fire? *J Clin Invest,* 116**,** 33-5.
NELKE, C., DZIEWAS, R., MINNERUP, J., MEUTH, S. G. & RUCK, T. 2019. Skeletal muscle as potential central link between sarcopenia and immune senescence. *eBioMedicine,* 49**,** 381-388.
NELSON, G., WORDSWORTH, J., WANG, C., JURK, D., LAWLESS, C., MARTIN-RUIZ, C. & VON ZGLINICKI, T. 2012. A senescent cell bystander effect: senescence-induced senescence. *Aging Cell,* 11**,** 345-9.
NGUYEN, V. H. & LEE, B. J. 2017. Protein corona: a new approach for nanomedicine design. *Int J Nanomedicine,* 12**,** 3137-3151.
NIE, M., LIU, J., YANG, Q., SEOK, H. Y., HU, X., DENG, Z. L. & WANG, D. Z. 2016. MicroRNA-155 facilitates skeletal muscle regeneration by balancing pro- and anti-inflammatory macrophages. *Cell Death & Disease,* 7**,** e2261-e2261.
NORDIN, J. Z., LEE, Y., VADER, P., MÄGER, I., JOHANSSON, H. J., HEUSERMANN, W., WIKLANDER, O. P. B., HÄLLBRINK, M., SEOW, Y., BULTEMA, J. J., GILTHORPE, J., DAVIES, T., FAIRCHILD, P. J., GABRIELSSON, S., MEISNER-KOBER, N. C., LEHTIÖ, J.,

SMITH, C. I. E., WOOD, M. J. A. & ANDALOUSSI, S. E. L. 2015. Ultrafiltration with size-exclusion liquid chromatography for high yield isolation of extracellular vesicles preserving intact biophysical and functional properties. *Nanomedicine: Nanotechnology, Biology and Medicine,* 11**,** 879-883.
NOVAK, M. L., WEINHEIMER-HAUS, E. M. & KOH, T. J. 2014. Macrophage activation and skeletal muscle healing following traumatic injury. *The Journal of pathology,* 232**,** 344-355.
NOVOTNY, S. A., WARREN, G. L. & HAMRICK, M. W. 2015. Aging and the muscle-bone relationship. *Physiology (Bethesda),* 30**,** 8-16.
NOZAKI, T., NIKAI, S., OKABE, R., NAGAHAMA, K. & ETO, N. 2016. A novel in vitro model of sarcopenia using BubR1 hypomorphic C2C12 myoblasts. *Cytotechnology,* 68**,** 1705-15.
O'BRIEN, K., BREYNE, K., UGHETTO, S., LAURENT, L. C. & BREAKEFIELD, X. O. 2020. RNA delivery by extracellular vesicles in mammalian cells and its applications. *Nature Reviews Molecular Cell Biology,* 21**,** 585-606.
OGATA, Y., YAMADA, T., HASEGAWA, S., SANADA, A., IWATA, Y., ARIMA, M., NAKATA, S., SUGIURA, K. & AKAMATSU, H. 2021. SASP-induced macrophage dysfunction may contribute to accelerated senescent fibroblast accumulation in the dermis. 30**,** 84-91.
OH, Y., JUNG, H.-J., HONG, S., CHO, Y., PARK, J., CHO, D. & KIM, T. S. 2022. Aminoacyl transfer ribonucleic acid synthetase complex-interacting multifunctional protein 1 induces microglial activation and M1 polarization via the mitogen-activated protein kinase/nuclear factor-kappa B signaling pathway. 16.
OKAZAKI, K. & HOLTZER, H. 1966. Myogenesis: fusion, myosin synthesis, and the mitotic cycle. *Proc Natl Acad Sci U S A,* 56**,** 1484-90.
ORECCHIONI, M., GHOSHEH, Y., PRAMOD, A. B. & LEY, K. 2019. Macrophage Polarization: Different Gene Signatures in M1(LPS+) vs. Classically and M2(LPS–) vs. Alternatively Activated Macrophages. 10.
ORTEGA, E., GARCÍA, J. J. & DE LA FUENTE, M. 2000. Modulation of adherence and chemotaxis of macrophages by norepinephrine. Influence of ageing. *Mol Cell Biochem,* 203**,** 113-7.
OSMAN, R., TACNET-DELORME, P., KLEMAN, J. P., MILLET, A. & FRACHET, P. 2017. Calreticulin Release at an Early Stage of Death Modulates the Clearance by Macrophages of Apoptotic Cells. *Front Immunol,* 8**,** 1034.
OSTARECK, D. H. & OSTARECK-LEDERER, A. 2019. RNA-Binding Proteins in the Control of LPS-Induced Macrophage Response. *Front Genet,* 10**,** 31.
O'SULLIVAN COYNE, G. & BUROTTO, M. 2017. MABp1 for the treatment of colorectal cancer. *Expert Opin Biol Ther,* 17**,** 1155-1161.
OUYANG, H., GAO, X. & ZHANG, J. 2022. Impaired expression of BCAT1 relates to muscle atrophy of mouse model of sarcopenia. *BMC Musculoskeletal Disorders,* 23**,** 450.
OVADYA, Y., LANDSBERGER, T., LEINS, H., VADAI, E., GAL, H., BIRAN, A., YOSEF, R., SAGIV, A., AGRAWAL, A., SHAPIRA, A., WINDHEIM, J., TSOORY, M., SCHIRMBECK, R., AMIT, I., GEIGER, H. & KRIZHANOVSKY, V. 2018. Impaired immune surveillance accelerates accumulation of senescent cells and aging. *Nature communications,* 9**,** 5435-5435.
OWCZARZ, M., BUDZINSKA, M., DOMASZEWSKA-SZOSTEK, A., BORKOWSKA, J., POLOSAK, J., GEWARTOWSKA, M., SLUSARCZYK, P. & PUZIANOWSKA-KUZNICKA, M. 2017. miR-34a and miR-9 are overexpressed and SIRT genes are downregulated in peripheral blood mononuclear cells of aging humans. *Exp Biol Med (Maywood),* 242**,** 1453-1461.
PANG, W. W., PRICE, E. A., SAHOO, D., BEERMAN, I., MALONEY, W. J., ROSSI, D. J., SCHRIER, S. L. & WEISSMAN, I. L. 2011. Human bone marrow hematopoietic stem cells are increased in frequency and myeloid-biased with age. 108**,** 20012-20017.
PARAMESWARAN, N. & PATIAL, S. 2010. Tumor necrosis factor-α signaling in macrophages. *Critical reviews in eukaryotic gene expression,* 20**,** 87-103.
PARK, S. J., KIM, J. M., KIM, J., HUR, J., PARK, S., KIM, K., SHIN, H. J. & CHWAE, Y. J. 2018. Molecular mechanisms of biogenesis of apoptotic exosome-like vesicles and their roles as damage-associated molecular patterns. *Proc Natl Acad Sci U S A,* 115**,** E11721-e11730.
PARK, S.-Y. & KIM, I.-S. 2017. Engulfment signals and the phagocytic machinery for apoptotic cell clearance. *Experimental & molecular medicine,* 49**,** e331-e331.
PARK, Y.-H., KIM, H.-S., LEE, J.-H., CHOI, S.-A., KIM, J.-M., OH, G. T., KANG, S. W., KIM, S.-U. & YU, D.-Y. 2017. Peroxiredoxin I participates in the protection of reactive oxygen speciesmediated cellular senescence. *BMB reports,* 50**,** 528-533.
PASSER, B. J., NANCY-PORTEBOIS, V., AMZALLAG, N., PRIEUR, S., CANS, C., ROBOREL DE CLIMENS, A., FIUCCI, G., BOUVARD, V., TUYNDER, M., SUSINI, L., MORCHOISNE, S., CRIBLE, V., LESPAGNOL, A., DAUSSET, J., OREN, M., AMSON, R. & TELERMAN, A.

2003. The p53-inducible TSAP6 gene product regulates apoptosis and the cell cycle and interacts with Nix and the Myt1 kinase. *Proc Natl Acad Sci U S A,* 100**,** 2284-9.
PEDERSEN, B. K. & FEBBRAIO, M. A. 2012. Muscles, exercise and obesity: skeletal muscle as a secretory organ. *Nature Reviews Endocrinology,* 8**,** 457-465.
PELT, D. W. V., JR., I. J. V., LAWRENCE, M. M., PELT, K. L. V., PATEL, P., MILLER, B. F., BUTTERFIELD, T. A. & DUPONT-VERSTEEGDEN, E. E. 2020. Serum extracellular vesicle miR-203a-3p content is associated with skeletal muscle mass and protein turnover during disuse atrophy and regrowth. *American Journal of Physiology-Cell Physiology,* 319**,** C419C431.
PERDIGUERO, E., SOUSA-VICTOR, P., RUIZ-BONILLA, V., JARDÍ, M., CAELLES, C., SERRANO, A. L. & MUÑOZ-CÁNOVES, P. 2011. p38/MKP-1-regulated AKT coordinates macrophage transitions and resolution of inflammation during tissue repair. *The Journal of cell biology,* 195**,** 307-322.
PEREIRA, B. I., DEVINE, O. P., VUKMANOVIC-STEJIC, M., CHAMBERS, E. S., SUBRAMANIAN, P., PATEL, N., VIRASAMI, A., SEBIRE, N. J., KINSLER, V., VALDOVINOS, A., LESAUX, C. J., PASSOS, J. F., ANTONIOU, A., RUSTIN, M. H. A., CAMPISI, J. & AKBAR, A. N. 2019. Senescent cells evade immune clearance via HLA-E-mediated NK and CD8(+) T cell inhibition. *Nat Commun,* 10**,** 2387.
PERRIER, P., MARTINEZ, F. O., LOCATI, M., BIANCHI, G., NEBULONI, M., VAGO, G., BAZZONI, F., SOZZANI, S., ALLAVENA, P. & MANTOVANI, A. 2004. Distinct Transcriptional Programs Activated by Interleukin-10 with or without Lipopolysaccharide in Dendritic Cells: Induction of the B Cell-Activating Chemokine, CXC Chemokine Ligand 13. *The Journal of Immunology,* 172**,** 7031-7042.
PETERSON, J. M., BAKKAR, N. & GUTTRIDGE, D. C. J. C. T. I. D. B. 2011. NF-κB signaling in skeletal muscle health and disease. 96**,** 85-119.
PHILLIPS, T. & LEEUWENBURGH, C. J. T. F. J. 2005. Muscle fiber-specific apoptosis and TNF-α signaling in sarcopenia are attenuated by life-long calorie restriction. 19**,** 1-33.
PICCA, A., BELI, R., CALVANI, R., COELHO-JÚNIOR, H. J., LANDI, F., BERNABEI, R., BUCCI, C., GUERRA, F. & MARZETTI, E. 2020. Older Adults with Physical Frailty and Sarcopenia Show Increased Levels of Circulating Small Extracellular Vesicles with a Specific Mitochondrial Signature. *Cells,* 9**,** 973.
PICCA, A., LEZZA, A. M. S., LEEUWENBURGH, C., PESCE, V., CALVANI, R., BOSSOLA, M., MANES-GRAVINA, E., LANDI, F., BERNABEI, R. & MARZETTI, E. 2018. Circulating Mitochondrial DNA at the Crossroads of Mitochondrial Dysfunction and Inflammation During Aging and Muscle Wasting Disorders. *Rejuvenation research,* 21**,** 350-359.
PIEC, I., LISTRAT, A., ALLIOT, J., CHAMBON, C., TAYLOR, R. G. & BECHET, D. 2005. Differential proteome analysis of aging in rat skeletal muscle. 19**,** 1143-1145.
PIERRE, N., BARBÉ, C., GILSON, H., DELDICQUE, L., RAYMACKERS, J.-M., FRANCAUX, M. J. B. & COMMUNICATIONS, B. R. 2014. Activation of ER stress by hydrogen peroxide in C2C12 myotubes. 450**,** 459-463.
PILLON, N. J., BILAN, P. J., FINK, L. N. & KLIP, A. 2013. Cross-talk between skeletal muscle and immune cells: muscle-derived mediators and metabolic implications. 304**,** E453-E465.
PILS, V., TERLECKI-ZANIEWICZ, L., SCHOSSERER, M., GRILLARI, J. & LÄMMERMANN, I. 2021. The role of lipid-based signalling in wound healing and senescence. *Mechanisms of Ageing and Development,* 198**,** 111527.
PINEDO-VILLANUEVA, R., WESTBURY, L. D., SYDDALL, H. E., SANCHEZ-SANTOS, M. T., DENNISON, E. M., ROBINSON, S. M. & COOPER, C. 2019. Health Care Costs Associated With Muscle Weakness: A UK Population-Based Estimate. *Calcif Tissue Int,* 104**,** 137-144.
PLUQUET, O., POURTIER, A. & ABBADIE, C. 2015. The unfolded protein response and cellular senescence. A Review in the Theme: Cellular Mechanisms of Endoplasmic Reticulum Stress Signaling in Health and Disease. 308**,** C415-C425.
POOLE, L. B., HALL, A. & NELSON, K. J. 2011. Overview of peroxiredoxins in oxidant defense and redox regulation. *Current protocols in toxicology,* Chapter 7**,** Unit7.9-Unit7.9.
POWERS, S. K., JI, L. L., KAVAZIS, A. N. & JACKSON, M. J. 2011. Reactive oxygen species: impact on skeletal muscle. *Comprehensive Physiology,* 1**,** 941-969.
POWERS, S. K., MORTON, A. B., HYATT, H. & HINKLEY, M. J. 2018. The Renin-Angiotensin System and Skeletal Muscle. *Exercise and sport sciences reviews,* 46**,** 205-214.
PRETTO, F., GHILARDI, C., MOSCHETTA, M., BASSI, A., ROVIDA, A., SCARLATO, V., TALAMINI, L., FIORDALISO, F., BISIGHINI, C., DAMIA, G., BANI, M. R., PICCIRILLO, R. & GIAVAZZI,

R. 2015. Sunitinib prevents cachexia and prolongs survival of mice bearing renal cancer by restraining STAT3 and MuRF-1 activation in muscle. *Oncotarget,* 6**,** 3043-3054.
PRISE, K. M. & O'SULLIVAN, J. M. 2009. Radiation-induced bystander signalling in cancer therapy. *Nat Rev Cancer,* 9**,** 351-60.
PRZYBYLA, B., GURLEY, C., HARVEY, J. F., BEARDEN, E., KORTEBEIN, P., EVANS, W. J., SULLIVAN, D. H., PETERSON, C. A. & DENNIS, R. A. 2006. Aging alters macrophage properties in human skeletal muscle both at rest and in response to acute resistance exercise. *Exp Gerontol,* 41**,** 320-7.
QIN, W., PAN, J., WU, Y., BAUMAN, W. A. & CARDOZO, C. 2010. Protection against dexamethasone-induced muscle atrophy is related to modulation by testosterone of FOXO1 and PGC-1α. *Biochem Biophys Res Commun,* 403**,** 473-8.
QIU, J., FANG, Q., XU, T., WU, C., XU, L., WANG, L., YANG, X., YU, S., ZHANG, Q., DING, F. & SUN, H. 2018. Mechanistic Role of Reactive Oxygen Species and Therapeutic Potential of Antioxidants in Denervation- or Fasting-Induced Skeletal Muscle Atrophy. 9.
RAMIREZ, M. I., AMORIM, M. G., GADELHA, C., MILIC, I., WELSH, J. A., FREITAS, V. M., NAWAZ, M., AKBAR, N., COUCH, Y. & MAKIN, L. J. N. 2018. Technical challenges of working with extracellular vesicles. 10**,** 881-906.
RAPOSO, G. & STOORVOGEL, W. 2013. Extracellular vesicles: exosomes, microvesicles, and friends. *The Journal of cell biology,* 200**,** 373-383.
RAYESS, H., WANG, M. B. & SRIVATSAN, E. S. 2012. Cellular senescence and tumor suppressor gene p16. *International journal of cancer,* 130**,** 1715-1725.
RECOULES, L., HEURTEAU, A., RAYNAL, F., KARASU, N., MOUTAHIR, F., BEJJANI, F., JARIELENCONTRE, I., CUVIER, O., SEXTON, T., LAVIGNE, A.-C. & BYSTRICKY, K. 2022. The histone variant macroH2A1.1 regulates RNA polymerase II-paused genes within defined chromatin interaction landscapes. *Journal of cell science,* 135**,** jcs259456.
REGULSKI, M. J. 2017. Cellular Senescence: What, Why, and How. *Wounds,* 29**,** 168-174.
REIDY, P. T., MCKENZIE, A. I., MAHMASSANI, Z. S., PETROCELLI, J. J., NELSON, D. B., LINDSAY,
C. C., GARDNER, J. E., MORROW, V. R., KEEFE, A. C., HUFFAKER, T. B., STODDARD, G. J., KARDON, G., O'CONNELL, R. M. & DRUMMOND, M. J. 2019. Aging impairs mouse skeletal muscle macrophage polarization and muscle-specific abundance during recovery from disuse. *American Journal of Physiology-Endocrinology and Metabolism,* 317**,** E85-E98.
RENNA, L. V., CARDANI, R., BOTTA, A., ROSSI, G., FOSSATI, B., COSTA, E. & MEOLA, G. 2014. Premature senescence in primary muscle cultures of myotonic dystrophy type 2 is not associated with p16 induction. *European journal of histochemistry : EJH,* 58**,** 2444-2444.
RITSCHKA, B., STORER, M., MAS, A., HEINZMANN, F., ORTELLS, M. C., MORTON, J. P., SANSOM, O. J., ZENDER, L. & KEYES, W. M. 2017. The senescence-associated secretory phenotype induces cellular plasticity and tissue regeneration. *Genes & development,* 31**,** 172-183.
ROCK, K. L., GRAMM, C., ROTHSTEIN, L., CLARK, K., STEIN, R., DICK, L., HWANG, D. & GOLDBERG, A. L. 1994. Inhibitors of the proteasome block the degradation of most cell proteins and the generation of peptides presented on MHC class I molecules. *Cell,* 78**,** 761-71. RODEN, M., PRICE, T. B., PERSEGHIN, G., PETERSEN, K. F., ROTHMAN, D. L., CLINE, G. W. & SHULMAN, G. I. 1996. Mechanism of free fatty acid-induced insulin resistance in humans. *The Journal of Clinical Investigation,* 97**,** 2859-2865.
RODNEY, G. G., PAL, R. & ABO-ZAHRAH, R. 2016. Redox regulation of autophagy in skeletal muscle. *Free Radical Biology and Medicine,* 98**,** 103-112.
ROMAGNOLI, C., IANTOMASI, T. & BRANDI, M. L. 2021. Available In Vitro Models for Human Satellite Cells from Skeletal Muscle. 22**,** 13221.
ROMANCINO, D. P., PATERNITI, G., CAMPOS, Y., DE LUCA, A., DI FELICE, V., D'AZZO, A. & BONGIOVANNI, A. 2013. Identification and characterization of the nano-sized vesicles released by muscle cells. *FEBS Letters,* 587**,** 1379-1384.
ROME, S., FORTERRE, A., MIZGIER, M. L. & BOUZAKRI, K. 2019. Skeletal Muscle-Released Extracellular Vesicles: State of the Art. *Frontiers in physiology,* 10**,** 929-929.
RONG, Y.-D., BIAN, A.-L., HU, H.-Y., MA, Y. & ZHOU, X.-Z. 2018. Study on relationship between elderly sarcopenia and inflammatory cytokine IL-6, anti-inflammatory cytokine IL-10. *BMC Geriatrics,* 18**,** 308.
ROOKS, D., SWAN, T., GOSWAMI, B., FILOSA, L. A., BUNTE, O., PANCHAUD, N., COLEMAN, L. A., MILLER, R. R., GARCIA GARAYOA, E., PRAESTGAARD, J., PERRY, R. G., RECKNOR,

C., FOGARTY, C. M., ARAI, H., CHEN, L.-K., HASHIMOTO, J., CHUNG, Y.-S., VISSING, J., LAURENT, D., PETRICOUL, O., HEMSLEY, S., LACH-TRIFILIEFF, E., PAPANICOLAOU, D. A. & ROUBENOFF, R. 2020. Bimagrumab vs Optimized Standard of Care for Treatment of Sarcopenia in Community-Dwelling Older Adults: A Randomized Clinical Trial. *JAMA Network Open,* 3**,** e2020836-e2020836.

ROSSI, D. J., BRYDER, D., ZAHN, J. M., AHLENIUS, H., SONU, R., WAGERS, A. J. & WEISSMAN, I. L. 2005. Cell intrinsic alterations underlie hematopoietic stem cell aging. 102**,** 9194-9199.

RUDNICKI, M. A., LE GRAND, F., MCKINNELL, I. & KUANG, S. 2008. The molecular regulation of muscle stem cell function. *Cold Spring Harb Symp Quant Biol,* 73**,** 323-31.

RUMIANEK, A. N. & GREAVES, D. R. 2020. How Have Leukocyte In Vitro Chemotaxis Assays Shaped Our Ideas about Macrophage Migration? 9**,** 439.

RUSS, D. W., WILLS, A. M., BOYD, I. M. & KRAUSE, J. J. E. G. 2014. Weakness, SR function and stress in gastrocnemius muscles of aged male rats. 50**,** 40-44.

RUSSO, L. & LUMENG, C. N. 2018. Properties and functions of adipose tissue macrophages in obesity. 155**,** 407-417.

RUYTINX, P., PROOST, P., VAN DAMME, J. & STRUYF, S. 2018. Chemokine-Induced Macrophage Polarization in Inflammatory Conditions. 9.

SABBATINELLI, J., PRATTICHIZZO, F., OLIVIERI, F., PROCOPIO, A. D., RIPPO, M. R. & GIULIANI, A. 2019. Where Metabolism Meets Senescence: Focus on Endothelial Cells. 10.

SACHS, S., ZARINI, S., KAHN, D. E., HARRISON, K. A., PERREAULT, L., PHANG, T., NEWSOM, S. A., STRAUSS, A., KEREGE, A., SCHOEN, J. A., BESSESEN, D. H., SCHWARZMAYR, T.,
GRAF, E., LUTTER, D., KRUMSIEK, J., HOFMANN, S. M. & BERGMAN, B. C. 2019. Intermuscular adipose tissue directly modulates skeletal muscle insulin sensitivity in humans. 316**,** E866-E879.

SADEGHI, H. M., SCHNELLE, J. F., THOMA, J. K., NISHANIAN, P. & FAHEY, J. L. 1999. Phenotypic and functional characteristics of circulating monocytes of elderly persons. *Exp Gerontol,* 34**,** 959-70.

SALVADORI, L., MANDRONE, M., MANENTI, T., ERCOLANI, C., CORNIOLI, L., LIANZA, M., TOMASI, P., CHIAPPALUPI, S., DI FILIPPO, E. S., FULLE, S., POLI, F., SORCI, G. & RIUZZI, F. 2020. Identification of Withania somnifera-Silybum marianum-Trigonella foenum-graecum Formulation as a Nutritional Supplement to Contrast Muscle Atrophy and Sarcopenia. *Nutrients,* 13.

SANDRI, M., BARBERI, L., BIJLSMA, A. Y., BLAAUW, B., DYAR, K. A., MILAN, G., MAMMUCARI, C., MESKERS, C. G., PALLAFACCHINA, G., PAOLI, A., PION, D., ROCERI, M., ROMANELLO, V., SERRANO, A. L., TONIOLO, L., LARSSON, L., MAIER, A. B., MUÑOZ-CÁNOVES, P., MUSARÒ, A., PENDE, M., REGGIANI, C., RIZZUTO, R. & SCHIAFFINO, S. 2013. Signalling pathways regulating muscle mass in ageing skeletal muscle: the role of the IGF1-Akt-mTORFoxO pathway. *Biogerontology,* 14**,** 303-23.

SANGER, J. W., WANG, J., FAN, Y., WHITE, J. & SANGER, J. M. 2010. Assembly and dynamics of myofibrils. *Journal of biomedicine & biotechnology,* 2010**,** 858606-858606.

SANJABI, S., OH, S. A. & LI, M. O. 2017. Regulation of the Immune Response by TGF-β: From Conception to Autoimmunity and Infection. *Cold Spring Harb Perspect Biol,* 9.

SANTILLI, V., BERNETTI, A., MANGONE, M. & PAOLONI, M. 2014. Clinical definition of sarcopenia. *Clinical cases in mineral and bone metabolism : the official journal of the Italian Society of Osteoporosis, Mineral Metabolism, and Skeletal Diseases,* 11**,** 177-180.

SASSOON, C. S., ZHU, E., PHAM, H. T., NELSON, R. S., FANG, L., BAKER, M. J. & CAIOZZO, V. J. 2008. Acute effects of high-dose methylprednisolone on diaphragm muscle function. *Muscle Nerve,* 38**,** 1161-72.

SAWANT, K. V., POLURI, K. M., DUTTA, A. K., SEPURU, K. M., TROSHKINA, A., GAROFALO, R. P. & RAJARATHNAM, K. 2016. Chemokine CXCL1 mediated neutrophil recruitment: Role of glycosaminoglycan interactions. *Scientific Reports,* 6**,** 33123.

SCHIAFFINO, S., PEREIRA, M. G., CICILIOT, S. & ROVERE-QUERINI, P. 2017. Regulatory T cells and skeletal muscle regeneration. *Febs j,* 284**,** 517-524.

SCHIAFFINO, S., ROSSI, A. C., SMERDU, V., LEINWAND, L. A. & REGGIANI, C. 2015. Developmental myosins: expression patterns and functional significance. *Skeletal Muscle,* 5**,** 22.

SCHILLING, J. D. 2021. Macrophages Fuel Skeletal Muscle Regeneration. *Immunometabolism,* 3.

SCHNEEMANN, M. & SCHOEDON, G. 2002. Species differences in macrophage NO production are important. *Nat Immunol,* 3**,** 102.

SCHRADER, M. & FAHIMI, H. D. 2006. Peroxisomes and oxidative stress. *Biochimica et Biophysica Acta (BBA) - Molecular Cell Research,* 1763**,** 1755-1766.
SCIORATI, C., GAMBERALE, R., MONNO, A., CITTERIO, L., LANZANI, C., DE LORENZO, R., RAMIREZ, G. A., ESPOSITO, A., MANUNTA, P., MANFREDI, A. A. & ROVERE-QUERINI, P. 2020. Pharmacological blockade of TNFα prevents sarcopenia and prolongs survival in aging mice. *Aging,* 12**,** 23497-23508.
SCIORATI, C., RIGAMONTI, E., MANFREDI, A. A. & ROVERE-QUERINI, P. 2016. Cell death, clearance and immunity in the skeletal muscle. *Cell death and differentiation,* 23**,** 927-937.
SERRANO, M. 2014. Senescence helps regeneration. *Dev Cell,* 31**,** 671-2.
SHAFIEE, G., KESHTKAR, A., SOLTANI, A., AHADI, Z., LARIJANI, B. & HESHMAT, R. 2017. Prevalence of sarcopenia in the world: a systematic review and meta- analysis of general population studies. *Journal of diabetes and metabolic disorders,* 16**,** 21-21.
SHAHINI, A., RAJABIAN, N., CHOUDHURY, D., SHAHINI, S., VYDIAM, K., NGUYEN, T., KULCZYK, J., SANTARELLI, T., IKHAPOH, I., ZHANG, Y., WANG, J., LIU, S., STABLEWSKI, A., THIYAGARAJAN, R., SELDEEN, K., TROEN, B. R., PEIRICK, J., LEI, P. & ANDREADIS, S. T. 2021. Ameliorating the hallmarks of cellular senescence in skeletal muscle myogenic progenitors in vitro and in vivo. 7**,** eabe5671.
SHAPOURI-MOGHADDAM, A., MOHAMMADIAN, S., VAZINI, H., TAGHADOSI, M., ESMAEILI, S.-A., MARDANI, F., SEIFI, B., MOHAMMADI, A., AFSHARI, J. T. & SAHEBKAR, A. 2018. Macrophage plasticity, polarization, and function in health and disease. 233**,** 6425-6440.
SHARPLES, A. P., PLAYER, D. J., MARTIN, N. R. W., MUDERA, V., STEWART, C. E. & LEWIS, M. P. 2012. Modelling in vivo skeletal muscle ageing in vitro using three-dimensional bioengineered constructs. 11**,** 986-995.
SHAW, A. C., GOLDSTEIN, D. R. & MONTGOMERY, R. R. 2013. Age-dependent dysregulation of innate immunity. *Nature reviews. Immunology,* 13**,** 875-887.
SHEEKEY, E. & NARITA, M. p53 in senescence – it's a marathon not a sprint. n/a.
SHELKE, G. V., LÄSSER, C., GHO, Y. S. & LÖTVALL, J. 2014. Importance of exosome depletion protocols to eliminate functional and RNA-containing extracellular vesicles from fetal bovine serum. *Journal of Extracellular Vesicles,* 3**,** 24783.
SHIMOZATO, O., UGAI, S.-I., CHIYO, M., TAKENOBU, H., NAGAKAWA, H., WADA, A., KAWAMURA, K., YAMAMOTO, H. & TAGAWA, M. 2006. The secreted form of the p40 subunit of interleukin (IL)-12 inhibits IL-23 functions and abrogates IL-23-mediated antitumour effects. 117**,** 22-28.
SHIOZUKA, M. & KIMURA, I. 2000. Improved Serum-free Defined Medium for Proliferation and Differentiation of Chick Primary Myogenic Cells. 17 %J Zoological Science**,** 201-207, 7.
SHIREMAN, P. K., CONTRERAS-SHANNON, V., OCHOA, O., KARIA, B. P., MICHALEK, J. E. & MCMANUS, L. M. 2007. MCP-1 deficiency causes altered inflammation with impaired skeletal muscle regeneration. *Journal of Leukocyte Biology,* 81**,** 775-785.
SICA, A. & MANTOVANI, A. 2012. Macrophage plasticity and polarization: in vivo veritas. *The Journal of Clinical Investigation,* 122**,** 787-795.
SILVA, A. M., SHEN, W., HEO, M., GALLAGHER, D., WANG, Z., SARDINHA, L. B. & HEYMSFIELD, S. B. 2010. Ethnicity-related skeletal muscle differences across the lifespan. *American journal of human biology : the official journal of the Human Biology Council,* 22**,** 76-82.
SIRIETT, V., SALERNO, M. S., BERRY, C., NICHOLAS, G., BOWER, R., KAMBADUR, R. & SHARMA, M. 2007. Antagonism of Myostatin Enhances Muscle Regeneration During Sarcopenia. *Molecular Therapy,* 15**,** 1463-1470.
SISHI, B. J. & ENGELBRECHT, A.-M. J. C. 2011. Tumor necrosis factor alpha (TNF-α) inactivates the PI3-kinase/PKB pathway and induces atrophy and apoptosis in L6 myotubes. 54**,** 173-184.
SIU, P. M., WANG, Y. & ALWAY, S. E. J. L. S. 2009. Apoptotic signaling induced by H2O2-mediated oxidative stress in differentiated C2C12 myotubes. 84**,** 468-481.
SMITH, M. E., TIPPETTS, T. S., BRASSFIELD, E. S., TUCKER, B. J., OCKEY, A., SWENSEN, A. C., ANTHONYMUTHU, T. S., WASHBURN, T. D., KANE, D. A. & PRINCE, J. T. J. B. J. 2013. Mitochondrial fission mediates ceramide-induced metabolic disruption in skeletal muscle. 456**,** 427-439.
SMITH-MUNGO, L. I. & KAGAN, H. M. 1998. Lysyl oxidase: properties, regulation and multiple functions in biology. *Matrix Biol,* 16**,** 387-98.
SNIJDERS, T., NEDERVEEN, J. P., MCKAY, B. R., JOANISSE, S., VERDIJK, L. B., VAN LOON, L. J. C. & PARISE, G. 2015. Satellite cells in human skeletal muscle plasticity. 6.

SOLETI, R., LAURET, E., ANDRIANTSITOHAINA, R. & CARMEN MARTÍNEZ, M. 2012. Internalization and induction of antioxidant messages by microvesicles contribute to the antiapoptotic effects on human endothelial cells. *Free Radic Biol Med,* 53**,** 2159-70.
SOUSA-VICTOR, P. & MUÑOZ-CÁNOVES, P. 2016. Regenerative decline of stem cells in sarcopenia. *Molecular Aspects of Medicine,* 50**,** 109-117.
SOUSA-VICTOR, P., GUTARRA, S., GARCÍA-PRAT, L., RODRIGUEZ-UBREVA, J., ORTET, L., RUIZBONILLA, V., JARDÍ, M., BALLESTAR, E., GONZÁLEZ, S., SERRANO, A. L., PERDIGUERO, E. & MUÑOZ-CÁNOVES, P. 2014. Geriatric muscle stem cells switch reversible quiescence into senescence. *Nature,* 506**,** 316-321.
SPENCER, N. F., NORTON, S. D., HARRISON, L. L., LI, G. Z. & DAYNES, R. A. 1996. Dysregulation of IL-10 production with aging: possible linkage to the age-associated decline in DHEA and its sulfated derivative. *Exp Gerontol,* 31**,** 393-408.
ST PIERRE, B. A. & TIDBALL, J. G. 1994. Differential response of macrophage subpopulations to soleus muscle reloading after rat hindlimb suspension. *J Appl Physiol (1985),* 77**,** 290-7.
STANFORD, K. I. & GOODYEAR, L. J. 2018. Muscle-Adipose Tissue Cross Talk. *Cold Spring Harb Perspect Med,* 8.
STEINSTRÄßER, L., JACOBSEN, F., HIRSCH, T., KESTING, M., CHOJNACKI, C., KRISP, C. & WOLTERS, D. 2010. Immunodepletion of high-abundant proteins from acute and chronic wound fluids to elucidate low-abundant regulators in wound healing. *BMC Research Notes,* 3**,** 335.
STELLAVATO, A., ABATE, L., VASSALLO, V., DONNIACUO, M., RINALDI, B. & SCHIRALDI, C. 2020. An in vitro study to assess the effect of hyaluronan-based gels on muscle-derived cells: Highlighting a new perspective in regenerative medicine. *PLoS One,* 15**,** e0236164.
STRLE, K., MCCUSKER, R. H., JOHNSON, R. W., ZUNICH, S. M., DANTZER, R. & KELLEY, K. W. 2008. Prototypical anti-inflammatory cytokine IL-10 prevents loss of IGF-I-induced myogenin protein expression caused by IL-1beta. *Am J Physiol Endocrinol Metab,* 294**,** E709-18.
SUGIMOTO, M. A., SOUSA, L. P., PINHO, V., PERRETTI, M. & TEIXEIRA, M. M. 2016. Resolution of Inflammation: What Controls Its Onset? *Front Immunol,* 7**,** 160.
SULLIVAN-GUNN, M. J. & LEWANDOWSKI, P. A. 2013. Elevated hydrogen peroxide and decreased catalase and glutathione peroxidase protection are associated with aging sarcopenia. *BMC geriatrics,* 13**,** 104-104.
SUNDARAM, P., PANG, Z., MIAO, M., YU, L. & WING, S. S. 2009. USP19-deubiquitinating enzyme regulates levels of major myofibrillar proteins in L6 muscle cells. *American Journal of Physiology-Endocrinology and Metabolism,* 297**,** E1283-E1290.
SWIFT, M. E., BURNS, A. L., GRAY, K. L. & DIPIETRO, L. A. 2001. Age-related alterations in the inflammatory response to dermal injury. *J Invest Dermatol,* 117**,** 1027-35.
SYVERUD, B. C., VANDUSEN, K. W. & LARKIN, L. M. 2016. Growth Factors for Skeletal Muscle Tissue Engineering. *Cells Tissues Organs,* 202**,** 169-179.
TAKAGI, A., HAWKE, P., TOKUDA, S., TODA, T., HIGASHIZONO, K., NAGAI, E., WATANABE, M., NAKATANI, E., KANEMOTO, H. & OBA, N. 2022. Serum carnitine as a biomarker of sarcopenia and nutritional status in preoperative gastrointestinal cancer patients. *J Cachexia Sarcopenia Muscle,* 13**,** 287-295.
TAKAHASHI, A., OKADA, R., NAGAO, K., KAWAMATA, Y., HANYU, A., YOSHIMOTO, S., TAKASUGI, M., WATANABE, S., KANEMAKI, M. T., OBUSE, C. & HARA, E. 2017. Exosomes maintain cellular homeostasis by excreting harmful DNA from cells. *Nat Commun,* 8**,** 15287.
TAKAMI, Y., NAKAGAMI, H., MORISHITA, R., KATSUYA, T., CUI, T.-X., ICHIKAWA, T., SAITO, Y., HAYASHI, H., KIKUCHI, Y., NISHIKAWA, T., BABA, Y., YASUDA, O., RAKUGI, H., OGIHARA, T. & KANEDA, Y. 2007. Ubiquitin Carboxyl-Terminal Hydrolase L1, a Novel Deubiquitinating Enzyme in the Vasculature, Attenuates NF-κB Activation. 27**,** 2184-2190.
TAKASUGI, M., OKADA, R., TAKAHASHI, A., VIRYA CHEN, D., WATANABE, S. & HARA, E. 2017. Small extracellular vesicles secreted from senescent cells promote cancer cell proliferation through EphA2. *Nat Commun,* 8**,** 15729.
TAKEMOTO, R., KAMIYA, T., ATOBE, T., HARA, H. & ADACHI, T. 2021. Regulation of lysyl oxidase expression in THP-1 cell-derived M2-like macrophages. 122**,** 777-786.
TAM, C. S., SPARKS, L. M., JOHANNSEN, D. L., COVINGTON, J. D., CHURCH, T. S. & RAVUSSIN, E. 2012. Low macrophage accumulation in skeletal muscle of obese type 2 diabetics and elderly subjects. *Obesity (Silver Spring, Md.),* 20**,** 1530-1533.

TANAKA, T., NARAZAKI, M. & KISHIMOTO, T. 2014. IL-6 in inflammation, immunity, and disease. *Cold Spring Harbor perspectives in biology,* 6**,** a016295-a016295.
TANG, H., INOKI, K., BROOKS, S. V., OKAZAWA, H., LEE, M., WANG, J., KIM, M., KENNEDY, C. L., MACPHERSON, P. C. D., JI, X., VAN ROEKEL, S., FRAGA, D. A., WANG, K., ZHU, J., WANG, Y., SHARP, Z. D., MILLER, R. A., RANDO, T. A., GOLDMAN, D., GUAN, K.-L. & SHRAGER, J. B. 2019. mTORC1 underlies age-related muscle fiber damage and loss by inducing oxidative stress and catabolism. 18**,** e12943.
TAPPARO, M., POMATTO, M. A. C., DEREGIBUS, M. C., PAPADIMITRIOU, E., CAVALLARI, C., D'ANTICO, S., COLLINO, F. & CAMUSSI, G. 2021. Serum Derived Extracellular Vesicles Mediated Delivery of Synthetic miRNAs in Human Endothelial Cells. 8.
TAY, L., DING, Y. Y., LEUNG, B. P., ISMAIL, N. H., YEO, A., YEW, S., TAY, K. S., TAN, C. H. & CHONG, M. S. 2015. Sex-specific differences in risk factors for sarcopenia amongst community-dwelling older adults. *AGE,* 37**,** 121.
TCHKONIA, T., MORBECK, D. E., VON ZGLINICKI, T., VAN DEURSEN, J., LUSTGARTEN, J., SCRABLE, H., KHOSLA, S., JENSEN, M. D. & KIRKLAND, J. L. 2010. Fat tissue, aging, and cellular senescence. *Aging Cell,* 9**,** 667-84.
TCHKONIA, T., ZHU, Y., VAN DEURSEN, J., CAMPISI, J. & KIRKLAND, J. L. 2013. Cellular senescence and the senescent secretory phenotype: therapeutic opportunities. *The Journal of clinical investigation,* 123**,** 966-972.
TE POELE, R. H., OKOROKOV, A. L., JARDINE, L., CUMMINGS, J. & JOEL, S. P. 2002. DNA Damage Is Able to Induce Senescence in Tumor Cells in Vitro and in Vivo1. *Cancer Research,* 62**,** 18761883.
TENG, M. W. L., BOWMAN, E. P., MCELWEE, J. J., SMYTH, M. J., CASANOVA, J.-L., COOPER, A. M. & CUA, D. J. 2015. IL-12 and IL-23 cytokines: from discovery to targeted therapies for immune-mediated inflammatory diseases. *Nature Medicine,* 21**,** 719-729.
THÉRY, C., AMIGORENA, S., RAPOSO, G. & CLAYTON, A. 2006. Isolation and characterization of exosomes from cell culture supernatants and biological fluids. *Current protocols in cell biology,* Chapter 3**,** Unit 3.22.
THÉRY, C., WITWER, K. W., AIKAWA, E., ALCARAZ, M. J., ANDERSON, J. D., ANDRIANTSITOHAINA, R., ANTONIOU, A., ARAB, T., ARCHER, F., ATKIN-SMITH, G. K., AYRE, D. C., BACH, J.-M., BACHURSKI, D., BAHARVAND, H., BALAJ, L., BALDACCHINO, S., BAUER, N. N., BAXTER, A. A., BEBAWY, M., BECKHAM, C., BEDINA ZAVEC, A., BENMOUSSA, A., BERARDI, A. C., BERGESE, P., BIELSKA, E., BLENKIRON, C., BOBISWOZOWICZ, S., BOILARD, E., BOIREAU, W., BONGIOVANNI, A., BORRÀS, F. E., BOSCH, S., BOULANGER, C. M., BREAKEFIELD, X., BREGLIO, A. M., BRENNAN, M. Á., BRIGSTOCK, D. R., BRISSON, A., BROEKMAN, M. L. D., BROMBERG, J. F., BRYLGÓRECKA, P., BUCH, S., BUCK, A. H., BURGER, D., BUSATTO, S., BUSCHMANN, D., BUSSOLATI, B., BUZÁS, E. I., BYRD, J. B., CAMUSSI, G., CARTER, D. R. F., CARUSO, S., CHAMLEY, L. W., CHANG, Y.-T., CHEN, C., CHEN, S., CHENG, L., CHIN, A. R., CLAYTON, A., CLERICI, S. P., COCKS, A., COCUCCI, E., COFFEY, R. J., CORDEIRO-DA-SILVA, A., COUCH, Y., COUMANS, F. A. W., COYLE, B., CRESCITELLI, R., CRIADO, M. F., D'SOUZASCHOREY, C., DAS, S., DATTA CHAUDHURI, A., DE CANDIA, P., DE SANTANA, E. F., DE WEVER, O., DEL PORTILLO, H. A., DEMARET, T., DEVILLE, S., DEVITT, A., DHONDT, B., DI VIZIO, D., DIETERICH, L. C., DOLO, V., DOMINGUEZ RUBIO, A. P., DOMINICI, M., DOURADO, M. R., DRIEDONKS, T. A. P., DUARTE, F. V., DUNCAN, H. M., EICHENBERGER, R. M., EKSTRÖM, K., EL ANDALOUSSI, S., ELIE-CAILLE, C., ERDBRÜGGER, U., FALCÓN-PÉREZ, J. M., FATIMA, F., FISH, J. E., FLORES-BELLVER, M., FÖRSÖNITS, A., FRELETBARRAND, A., et al. 2018. Minimal information for studies of extracellular vesicles 2018 (MISEV2018): a position statement of the International Society for Extracellular Vesicles and update of the MISEV2014 guidelines. *Journal of Extracellular Vesicles,* 7**,** 1535750.
THÉRY, C., ZITVOGEL, L. & AMIGORENA, S. 2002. Exosomes: composition, biogenesis and function. *Nature Reviews Immunology,* 2**,** 569-579.
TIDBALL, J. G. & WEHLING-HENRICKS, M. 2007. Macrophages promote muscle membrane repair and muscle fibre growth and regeneration during modified muscle loading in mice in vivo. *The Journal of physiology,* 578**,** 327-336.
TIDBALL, J. G. & WELC, S. S. 2015. Macrophage-Derived IGF-1 Is a Potent Coordinator of Myogenesis and Inflammation in Regenerating Muscle. *Molecular Therapy,* 23**,** 1134-1135.
TIDBALL, J. G. 2017. Regulation of muscle growth and regeneration by the immune system. *Nature reviews. Immunology,* 17**,** 165-178.

TONKIN, J., TEMMERMAN, L., SAMPSON, R. D., GALLEGO-COLON, E., BARBERI, L., BILBAO, D., SCHNEIDER, M. D., MUSARÒ, A. & ROSENTHAL, N. 2015. Monocyte/Macrophage-derived IGF-1 Orchestrates Murine Skeletal Muscle Regeneration and Modulates Autocrine Polarization. *Molecular Therapy,* 23**,** 1189-1200.

TORR, E. E., GARDNER, D. H., THOMAS, L., GOODALL, D. M., BIELEMEIER, A., WILLETTS, R., GRIFFITHS, H. R., MARSHALL, L. J. & DEVITT, A. 2012. Apoptotic cell-derived ICAM-3 promotes both macrophage chemoattraction to and tethering of apoptotic cells. *Cell death and differentiation,* 19**,** 671-679.

TSUJINAKA, T., FUJITA, J., EBISUI, C., YANO, M., KOMINAMI, E., SUZUKI, K., TANAKA, K., KATSUME, A., OHSUGI, Y., SHIOZAKI, H. & MONDEN, M. 1996. Interleukin 6 receptor antibody inhibits muscle atrophy and modulates proteolytic systems in interleukin 6 transgenic mice. *The Journal of Clinical Investigation,* 97**,** 244-249.

TSUKAMOTO, H., TAKEUCHI, S., KUBOTA, K., KOBAYASHI, Y., KOZAKAI, S., UKAI, I., SHICHIKU, A., OKUBO, M., NUMASAKI, M., KANEMITSU, Y., MATSUMOTO, Y., NOCHI, T., WATANABE, K., ASO, H. & TOMIOKA, Y. 2018. Lipopolysaccharide (LPS)-binding protein stimulates CD14-dependent Toll-like receptor 4 internalization and LPS-induced TBK1-IKKεIRF3 axis activation. *J Biol Chem,* 293**,** 10186-10201.

TUTTLE, C. S. L., THANG, L. A. N. & MAIER, A. B. 2020. Markers of inflammation and their association with muscle strength and mass: A systematic review and meta-analysis. *Ageing Research Reviews,* 64**,** 101185.

TZARIDIS, T., BACHURSKI, D., LIU, S., SURMANN, K., BABATZ, F., GESELL SALAZAR, M., VÖLKER, U., HALLEK, M., HERRLINGER, U., VORBERG, I., COCH, C., REINERS, K. S. & HARTMANN, G. 2021. Extracellular Vesicle Separation Techniques Impact Results from Human Blood Samples: Considerations for Diagnostic Applications. 22**,** 9211.

UBAIDA-MOHIEN, C., LYASHKOV, A., GONZALEZ-FREIRE, M., THARAKAN, R., SHARDELL, M., MOADDEL, R., SEMBA, R. D., CHIA, C. W., GOROSPE, M., SEN, R. & FERRUCCI, L. 2019. Discovery proteomics in aging human skeletal muscle finds change in spliceosome, immunity, proteostasis and mitochondria. *eLife,* 8**,** e49874.

UNITED NATIONS DEPARTMENT OF ECONOMIC AND SOCIAL AFFAIRS, P. D. 2020. World Population Ageing 2020 Highlights: Living arrangements of older persons (ST/ESA/SER.A/451).

UOZUMI, Y., ITO, T., HOSHINO, Y., MOHRI, T., MAEDA, M., TAKAHASHI, K., FUJIO, Y. & AZUMA, J. 2006. Myogenic differentiation induces taurine transporter in association with taurine mediated cytoprotection in skeletal muscles. *The Biochemical journal,* 394**,** 699-706.

VÄLIKANGAS, T., SUOMI, T. & ELO, L. L. 2016. A systematic evaluation of normalization methods in quantitative label-free proteomics. *Briefings in Bioinformatics,* 19**,** 1-11.

VALLS-LACALLE, L., PUERTAS-UMBERT, L., VARONA, S., MARTÍNEZ-GONZÁLEZ, J., RODRÍGUEZ, C. & RODRÍGUEZ-SINOVAS, A. 2022. Human Lysyl Oxidase Over-Expression Enhances Baseline Cardiac Oxidative Stress but Does Not Aggravate ROS Generation or Infarct Size Following Myocardial Ischemia-Reperfusion. 11**,** 75.

VAN DE WAKKER, S. I., VAN OUDHEUSDEN, J., MOL, E. A., ROEFS, M. T., ZHENG, W., GÖRGENS, A., EL ANDALOUSSI, S., SLUIJTER, J. P. G. & VADER, P. 2022. Influence of short term storage conditions, concentration methodsand excipients on extracellular vesicle recovery and function. *European Journal of Pharmaceutics and Biopharmaceutics,* 170**,** 59-69.

VAN DER VALK, J., MELLOR, D., BRANDS, R., FISCHER, R., GRUBER, F., GSTRAUNTHALER, G., HELLEBREKERS, L., HYLLNER, J., JONKER, F. H., PRIETO, P., THALEN, M. & BAUMANS, V. 2004. The humane collection of fetal bovine serum and possibilities for serum-free cell and tissue culture. *Toxicology in Vitro,* 18**,** 1-12.

VAN DEUN, J., MESTDAGH, P., SORMUNEN, R., COCQUYT, V., VERMAELEN, K., VANDESOMPELE, J., BRACKE, M., DE WEVER, O. & HENDRIX, A. 2014. The impact of disparate isolation methods for extracellular vesicles on downstream RNA profiling. *J Extracell Vesicles,* 3.

VAN DEURSEN, J. M. 2014. The role of senescent cells in ageing. *Nature,* 509**,** 439-446.

VARIN, A., MUKHOPADHYAY, S., HERBEIN, G. & GORDON, S. 2010. Alternative activation of macrophages by IL-4 impairs phagocytosis of pathogens but potentiates microbial-induced signalling and cytokine secretion. *Blood,* 115**,** 353-362.

VELARDE, M. C., FLYNN, J. M., DAY, N. U., MELOV, S. & CAMPISI, J. 2012. Mitochondrial oxidative stress caused by Sod2 deficiency promotes cellular senescence and aging phenotypes in the skin. *Aging,* 4**,** 3-12.

VELDHUIS-VLUG, A. G. & ROSEN, C. J. 2018. Clinical implications of bone marrow adiposity. 283**,** 121-139.
VERMA, N. D., HALL, B. M., PLAIN, K. M., ROBINSON, C. M., BOYD, R., TRAN, G. T., WANG, C., BISHOP, G. A. & HODGKINSON, S. J. 2014. Interleukin-12 (IL-12p70) Promotes Induction of Highly Potent Th1-Like CD4+CD25+ T Regulatory Cells That Inhibit Allograft Rejection in Unmodified Recipients. 5.
VICTORELLI, S. & PASSOS, J. F. 2019. Reactive Oxygen Species Detection in Senescent Cells. *Methods Mol Biol,* 1896**,** 21-29.
VILLALTA, S. A., NGUYEN, H. X., DENG, B., GOTOH, T. & TIDBALL, J. G. 2008. Shifts in macrophage phenotypes and macrophage competition for arginine metabolism affect the severity of muscle pathology in muscular dystrophy. *Human Molecular Genetics,* 18**,** 482-496.
VILLALTA, S. A., RINALDI, C., DENG, B., LIU, G., FEDOR, B. & TIDBALL, J. G. 2011. Interleukin-10 reduces the pathology of mdx muscular dystrophy by deactivating M1 macrophages and modulating macrophage phenotype. *Human molecular genetics,* 20**,** 790-805.
VIOLA, A., MUNARI, F., SÁNCHEZ-RODRÍGUEZ, R., SCOLARO, T. & CASTEGNA, A. 2019. The Metabolic Signature of Macrophage Responses. 10.
VIRÁG, L., JAÉN, R. I., REGDON, Z., BOSCÁ, L. & PRIETO, P. 2019. Self-defense of macrophages against oxidative injury: Fighting for their own survival. *Redox Biol,* 26**,** 101261.
VOGELPOEL, L. T. C., HANSEN, I. S., RISPENS, T., MULLER, F. J. M., VAN CAPEL, T. M. M., TURINA, M. C., VOS, J. B., BAETEN, D. L. P., KAPSENBERG, M. L., DE JONG, E. C. & DEN DUNNEN, J. 2014. Fc gamma receptor-TLR cross-talk elicits pro-inflammatory cytokine production by human M2 macrophages. *Nature communications,* 5**,** 5444-5444.
WALLIS, R., JOSIPOVIC, N., MIZEN, H., ROBLES-TENORIO, A., TYLER, E. J., PAPANTONIS, A. & BISHOP, C. L. 2021. Isolation methodology is essential to the evaluation of the extracellular vesicle component of the senescence-associated secretory phenotype. 10**,** e12041.
WALPORT, M. J. 2001. Complement. First of two parts. *N Engl J Med,* 344**,** 1058-66.
WALSH, M. E., BHATTACHARYA, A., SATARANATARAJAN, K., QAISAR, R., SLOANE, L., RAHMAN, M. M., KINTER, M. & VAN REMMEN, H. 2015. The histone deacetylase inhibitor butyrate improves metabolism and reduces muscle atrophy during aging. *Aging Cell,* 14**,** 957-70.
WALSTON, J. D. 2012. Sarcopenia in older adults. *Curr Opin Rheumatol,* 24**,** 623-7.
WALSTON, J., FEDARKO, N., YANG, H., LENG, S., BEAMER, B., ESPINOZA, S., LIPTON, A., ZHENG, H. & BECKER, K. 2008. The Physical and Biological Characterization of a Frail Mouse Model. *The Journals of Gerontology: Series A,* 63**,** 391-398.
WAN, C., FU, J., WANG, Y., MIAO, S., SONG, W. & WANG, L. 2012. Exosome-Related Multi-Pass Transmembrane Protein TSAP6 Is a Target of Rhomboid Protease RHBDD1-Induced Proteolysis. *PLOS ONE,* 7**,** e37452.
WANDERS, R. J. A., WATERHAM, H. R. & FERDINANDUSSE, S. 2016. Metabolic Interplay between Peroxisomes and Other Subcellular Organelles Including Mitochondria and the Endoplasmic Reticulum. 3.
WANG, B. Y., HSIAO, A. W., WONG, N., CHEN, Y. F., LEE, C. W. & LEE, W. Y. W. 2023. Is dexamethasone-induced muscle atrophy an alternative model for naturally aged sarcopenia model? *J Orthop Translat,* 39**,** 12-20.
WANG, E. 1995. Senescent human fibroblasts resist programmed cell death, and failure to suppress bcl2 is involved. *Cancer Res,* 55**,** 2284-92.
WANG, H. & WANG, B. 2016. Extracellular vesicle microRNAs mediate skeletal muscle myogenesis and disease (Review). *Biomed Rep,* 5**,** 296-300.
WANG, H. T., LEE, H. I., GUO, J. H., CHEN, S. H., LIAO, Z. K., HUANG, K. W., TORNG, P. L. & HWANG, L. H. 2012. Calreticulin promotes tumor lymphocyte infiltration and enhances the antitumor effects of immunotherapy by up-regulating the endothelial expression of adhesion molecules. *Int J Cancer,* 130**,** 2892-902.
WANG, L.-X., ZHANG, S.-X., WU, H.-J., RONG, X.-L. & GUO, J. 2019a. M2b macrophage polarization and its roles in diseases. *Journal of leukocyte biology,* 106**,** 345-358.
WANG, N., LIANG, H. & ZEN, K. 2014. Molecular Mechanisms That Influence the Macrophage M1–M2 Polarization Balance. 5.
WANG, R., YU, Z., SUNCHU, B., SHOAF, J., DANG, I., ZHAO, S., CAPLES, K., BRADLEY, L., BEAVER, L. M., HO, E., LÖHR, C. V. & PEREZ, V. I. 2017. Rapamycin inhibits the secretory phenotype of senescent cells by a Nrf2-independent mechanism. *Aging Cell,* 16**,** 564-574.

WANG, Y., WEHLING-HENRICKS, M., SAMENGO, G. & TIDBALL, J. G. 2015. Increases of M2a macrophages and fibrosis in aging muscle are influenced by bone marrow aging and negatively regulated by muscle-derived nitric oxide. *Aging cell,* 14**,** 678-688.

WANG, Y., WEHLING-HENRICKS, M., WELC, S. S., FISHER, A. L., ZUO, Q. & TIDBALL, J. G. 2019b. Aging of the immune system causes reductions in muscle stem cell populations, promotes their shift to a fibrogenic phenotype, and modulates sarcopenia. *FASEB journal : official publication of the Federation of American Societies for Experimental Biology,* 33**,** 1415-1427.

WANG, Y., WELC, S. S., WEHLING-HENRICKS, M. & TIDBALL, J. G. 2018. Myeloid cell-derived tumor necrosis factor-alpha promotes sarcopenia and regulates muscle cell fusion with aging muscle fibers. *Aging cell,* 17**,** e12828-e12828.

WATANABE, S., SUDO, Y., KIMURA, S., TOMITA, K., NOGUCHI, M., SAKURAI, H., SHIMIZU, M., TAKAHASHI, Y., SATO, R. & YAMAUCHI, Y. 2021. Skeletal muscle releases extracellular vesicles with distinct protein and miRNA signatures that accumulate and function within the muscle microenvironment. 2021.11.30.470551.

WEBBER, J. & CLAYTON, A. 2013. How pure are your vesicles? *J Extracell Vesicles,* 2.

WEIGERT, C., LEHMANN, R., HARTWIG, S. & LEHR, S. 2014. The secretome of the working human skeletal muscle—A promising opportunity to combat the metabolic disaster? *PROTEOMICS – Clinical Applications,* 8**,** 5-18.

WEINER-GORZEL, K., DEMPSEY, E., MILEWSKA, M., MCGOLDRICK, A., TOH, V., WALSH, A., LINDSAY, S., GUBBINS, L., CANNON, A., SHARPE, D., O'SULLIVAN, J., MURPHY, M., MADDEN, S. F., KELL, M., MCCANN, A. & FURLONG, F. 2015. Overexpression of the microRNA miR-433 promotes resistance to paclitaxel through the induction of cellular senescence in ovarian cancer cells. *Cancer Med,* 4**,** 745-58.

WHITMAN, S. A., WACKER, M. J., RICHMOND, S. R. & GODARD, M. P. 2005. Contributions of the ubiquitin–proteasome pathway and apoptosis to human skeletal muscle wasting with age. *Pflügers Archiv,* 450**,** 437-446.

WILEY, C. D., BRUMWELL, A. N., DAVIS, S. S., JACKSON, J. R., VALDOVINOS, A., CALHOUN, C., ALIMIRAH, F., CASTELLANOS, C. A., RUAN, R., WEI, Y., CHAPMAN, H. A., RAMANATHAN, A., CAMPISI, J. & JOURDAN LE SAUX, C. 2019. Secretion of leukotrienes by senescent lung fibroblasts promotes pulmonary fibrosis. *JCI insight,* 4**,** e130056.

WOLF, M., POUPARDIN, R. W., EBNER-PEKING, P., ANDRADE, A. C., BLÖCHL, C., OBERMAYER, A., GOMES, F. G., VARI, B., MAEDING, N., EMINGER, E., BINDER, H. M., RANINGER, A. M., HOCHMANN, S., BRACHTL, G., SPITTLER, A., HEUSER, T., OFIR, R., HUBER, C. G., ABERMAN, Z., SCHALLMOSER, K., VOLK, H. D. & STRUNK, D. 2022b. A functional corona around extracellular vesicles enhances angiogenesis, skin regeneration and immunomodulation. *J Extracell Vesicles,* 11**,** e12207.

WOLFE, R. R. 2006. The underappreciated role of muscle in health and disease. *The American Journal of Clinical Nutrition,* 84**,** 475-482.

WRAGG, N. M., MOSQUEIRA, D., BLOKPEOL-FERRERAS, L., CAPEL, A., PLAYER, D. J., MARTIN, N. R. W., LIU, Y. & LEWIS, M. P. 2020. Development of a 3D Tissue-Engineered Skeletal Muscle and Bone Co-culture System. 15**,** 1900106.

WRIGHT, C. R., BROWN, E. L., DELLA GATTA, P. A., FATOUROS, I. G., KARAGOUNIS, L. G., TERZIS, G., MASTORAKOS, G., MICHAILIDIS, Y., MANDALIDIS, D., SPENGOS, K., CHATZINIKOLAOU, A., METHENITIS, S., DRAGANIDIS, D., JAMURTAS, A. Z. & RUSSELL, A. P. 2015. Regulation of Granulocyte Colony-Stimulating Factor and Its Receptor in Skeletal Muscle is Dependent Upon the Type of Inflammatory Stimulus. *J Interferon Cytokine Res,* 35**,** 710-9.

WU, J., CAO, L., WANG, J., WANG, Y., HAO, H. & HUANG, L. 2022. Characterization of serum protein expression profiles in the early sarcopenia older adults with low grip strength: a cross-sectional study. *BMC Musculoskeletal Disorders,* 23**,** 894.

WU, X. & ZHANG, Y. 2017. TET-mediated active DNA demethylation: mechanism, function and beyond. *Nature Reviews Genetics,* 18**,** 517-534.

XIE, W. Q., HE, M., YU, D. J., WU, Y. X., WANG, X. H., LV, S., XIAO, W. F. & LI, Y. S. 2021. Mouse models of sarcopenia: classification and evaluation. *J Cachexia Sarcopenia Muscle,* 12**,** 538-554.

XU, Q., CUI, Y., LUAN, J., ZHOU, X., LI, H., HAN, J. J. B. & COMMUNICATIONS, B. R. 2018. Exosomes from C2C12 myoblasts enhance osteogenic differentiation of MC3T3-E1 pre-osteoblasts by delivering miR-27a-3p. 498**,** 32-37.

YAKABE, M., OGAWA, S., OTA, H., IIJIMA, K., ETO, M., OUCHI, Y. & AKISHITA, M. 2018. Inhibition of interleukin-6 decreases atrogene expression and ameliorates tail suspension-induced skeletal muscle atrophy. *PloS one,* 13**,** e0191318-e0191318.
YAMAGUCHI, A., MAESHIGE, N., YAN, J., MA, X., UEMURA, M., MATSUDA, M., NISHIMURA, Y., HASUNUMA, T., KONDO, H., FUJINO, H. & YUAN, Z.-M. 2023. Skeletal myotube-derived extracellular vesicles enhance itaconate production and attenuate inflammatory responses of macrophages. 14.
YAMAGUCHI, T., ARAI, H., KATAYAMA, N., ISHIKAWA, T., KIKUMOTO, K. & ATOMI, Y. 2007. Age-Related Increase of Insoluble, Phosphorylated Small Heat Shock Proteins in Human Skeletal Muscle. *The Journals of Gerontology: Series A,* 62**,** 481-489.
YAMAMOTO, S., YANCEY, P. G., ZUO, Y., MA, L.-J., KASEDA, R., FOGO, A. B., ICHIKAWA, I., LINTON, M. F., FAZIO, S. & KON, V. 2011. Macrophage polarization by angiotensin II-type 1 receptor aggravates renal injury-acceleration of atherosclerosis. *Arteriosclerosis, thrombosis, and vascular biology,* 31**,** 2856-2864.
YÁÑEZ-MÓ, M., SILJANDER, P. R. M., ANDREU, Z., ZAVEC, A. B., BORRÀS, F. E., BUZAS, E. I., BUZAS, K., CASAL, E., CAPPELLO, F., CARVALHO, J., COLÁS, E., CORDEIRO-DA SILVA, A., FAIS, S., FALCON-PEREZ, J. M., GHOBRIAL, I. M., GIEBEL, B., GIMONA, M., GRANER, M., GURSEL, I., GURSEL, M., HEEGAARD, N. H. H., HENDRIX, A., KIERULF, P., KOKUBUN, K., KOSANOVIC, M., KRALJ-IGLIC, V., KRÄMER-ALBERS, E.-M., LAITINEN, S., LÄSSER, C., LENER, T., LIGETI, E., LINĒ, A., LIPPS, G., LLORENTE, A., LÖTVALL, J., MANČEKKEBER, M., MARCILLA, A., MITTELBRUNN, M., NAZARENKO, I., NOLTE-'T HOEN, E. N. M., NYMAN, T. A., O'DRISCOLL, L., OLIVAN, M., OLIVEIRA, C., PÁLLINGER, É., DEL PORTILLO, H. A., REVENTÓS, J., RIGAU, M., ROHDE, E., SAMMAR, M., SÁNCHEZMADRID, F., SANTARÉM, N., SCHALLMOSER, K., OSTENFELD, M. S., STOORVOGEL, W., STUKELJ, R., VAN DER GREIN, S. G., VASCONCELOS, M. H., WAUBEN, M. H. M. & DE WEVER, O. 2015. Biological properties of extracellular vesicles and their physiological functions. *Journal of extracellular vesicles,* 4**,** 27066-27066.
YANG, S., LORO, E., WADA, S., KIM, B., TSENG, W.-J., LI, K., KHURANA, T. S. & ARANY, Z. 2020. Functional effects of muscle PGC-1alpha in aged animals. *Skeletal Muscle,* 10**,** 14.
YANG, W. & HU, P. 2018. Skeletal muscle regeneration is modulated by inflammation. *Journal of orthopaedic translation,* 13**,** 25-32.
YAO, Y., XU, X.-H. & JIN, L. 2019. Macrophage Polarization in Physiological and Pathological Pregnancy. *Frontiers in immunology,* 10**,** 792-792.
YARASHESKI, K. E., BHASIN, S., SINHA-HIKIM, I., PAK-LODUCA, J. & GONZALEZ-CADAVID, N. F. 2002. Serum myostatin-immunoreactive protein is increased in 60-92 year old women and men with muscle wasting. *J Nutr Health Aging,* 6**,** 343-8.
YE, F., MATHUR, S., LIU, M., BORST, S. E., WALTER, G. A., SWEENEY, H. L. & VANDENBORNE, K. 2013. Overexpression of insulin-like growth factor-1 attenuates skeletal muscle damage and accelerates muscle regeneration and functional recovery after disuse. *Experimental physiology,* 98**,** 1038-1052.
YIN, H., PRICE, F. & RUDNICKI, M. A. 2013. Satellite cells and the muscle stem cell niche. *Physiological reviews,* 93**,** 23-67.
YOON, P., KEYLOCK, K. T., HARTMAN, M. E., FREUND, G. G. & WOODS, J. A. 2004. Macrophage hypo-responsiveness to interferon-gamma in aged mice is associated with impaired signaling through Jak-STAT. *Mech Ageing Dev,* 125**,** 137-43.
YOSHIDA, T. & DELAFONTAINE, P. 2020. Mechanisms of IGF-1-Mediated Regulation of Skeletal Muscle Hypertrophy and Atrophy. *Cells,* 9.
YOSHIDA, T., TABONY, A. M., GALVEZ, S., MITCH, W. E., HIGASHI, Y., SUKHANOV, S. & DELAFONTAINE, P. 2013. Molecular mechanisms and signaling pathways of angiotensin IIinduced muscle wasting: potential therapeutic targets for cardiac cachexia. *The international journal of biochemistry & cell biology,* 45**,** 2322-2332.
YOSHIHARA, T., MACHIDA, S., TSUZUKI, T., KAKIGI, R., CHANG, S.-W., SUGIURA, T. & NAITO, H. 2019. Age-related changes in histone modification in rat gastrocnemius muscle. *Experimental Gerontology,* 125**,** 110658.
YOSHIOKA, Y., YAMAMURO, A. & MAEDA, S. J. B. J. O. P. 2003. Nitric oxide at a low concentration protects murine macrophage RAW264 cells against nitric oxide-induced death via cGMP signaling pathway. 139**,** 28.

YU, M., WANG, H., XU, Y., YU, D., LI, D., LIU, X. & DU, W. 2015. Insulin-like growth factor-1 (IGF-1) promotes myoblast proliferation and skeletal muscle growth of embryonic chickens via the PI3K/Akt signalling pathway. 39**,** 910-922.
YU, X., HARRIS, S. L. & LEVINE, A. J. 2006. The Regulation of Exosome Secretion: a Novel Function of the p53 Protein. *Cancer Research,* 66**,** 4795-4801.
YU, X., RILEY, T. & LEVINE, A. J. 2009. The regulation of the endosomal compartment by p53 the tumor suppressor gene. *Febs j,* 276**,** 2201-12.
ZHAN, M., JIN, B., CHEN, S.-E., REECY, J. M. & LI, Y.-P. 2007. TACE release of TNF-alpha mediates mechanotransduction-induced activation of p38 MAPK and myogenesis. *Journal of cell science,* 120**,** 692-701.
ZHANG, C., BARRIOS, M. P., ALANI, R. M., CABODI, M. & WONG, J. Y. 2016. A microfluidic Transwell to study chemotaxis. *Experimental Cell Research,* 342**,** 159-165.
ZHANG, C., WANG, C., LI, Y., MIWA, T., LIU, C., CUI, W., SONG, W.-C. & DU, J. 2017. Complement C3a signaling facilitates skeletal muscle regeneration by regulating monocyte function and trafficking. *Nature communications,* 8**,** 2078-2078.
ZHANG, H., WANG, S., ZHOU, Q., LIAO, Y., LUO, W., PENG, Z., REN, R. & WANG, H. 2022. Disturbance of calcium homeostasis and myogenesis caused by TET2 deletion in muscle stem cells. *Cell Death Discovery,* 8**,** 236.
ZHANG, J., CAO, J., GENG, A., WANG, H., CHU, Q., YANG, L., YAN, Z., ZHANG, X., ZHANG, Y., DAI, J. & LIU, H. 2021. Comprehensive Proteomic Characterization of the Pectoralis Major at Three Chronological Ages in Beijing-You Chicken. 12.
ZHANG, J., XIAO, Z., QU, C., CUI, W., WANG, X. & DU, J. 2014. CD8 T cells are involved in skeletal muscle regeneration through facilitating MCP-1 secretion and Gr1(high) macrophage infiltration. *J Immunol,* 193**,** 5149-60.
ZHANG, L.-M., ZHOU, J.-J. & LUO, C.-L. 2018. CYLD suppression enhances the pro-inflammatory effects and hyperproliferation of rheumatoid arthritis fibroblast-like synoviocytes by enhancing NF-κB activation. *Arthritis Research & Therapy,* 20**,** 219.
ZHANG, X., LI, H., HE, M., WANG, J., WU, Y. & LI, Y. 2022. Immune system and sarcopenia: Presented relationship and future perspective. *Experimental Gerontology,* 164**,** 111823.
ZHENG, Y., KONG, J., LI, Q., WANG, Y. & LI, J. 2018. Role of miRNAs in skeletal muscle aging. *Clinical interventions in aging,* 13**,** 2407-2419.
ZHU, J., LI, Y., SHEN, W., QIAO, C., AMBROSIO, F., LAVASANI, M., NOZAKI, M., BRANCA, M. F. & HUARD, J. 2007. Relationships between transforming growth factor-beta1, myostatin, and decorin: implications for skeletal muscle fibrosis. *J Biol Chem,* 282**,** 25852-63.
ZHU, Y., TCHKONIA, T., PIRTSKHALAVA, T., GOWER, A. C., DING, H., GIORGADZE, N., PALMER,
A. K., IKENO, Y., HUBBARD, G. B., LENBURG, M., O'HARA, S. P., LARUSSO, N. F., MILLER, J. D., ROOS, C. M., VERZOSA, G. C., LEBRASSEUR, N. K., WREN, J. D., FARR, J. N., KHOSLA, S., STOUT, M. B., MCGOWAN, S. J., FUHRMANN-STROISSNIGG, H., GURKAR, A. U., ZHAO, J., COLANGELO, D., DORRONSORO, A., LING, Y. Y., BARGHOUTHY, A. S., NAVARRO, D. C., SANO, T., ROBBINS, P. D., NIEDERNHOFER, L. J. & KIRKLAND, J. L. 2015. The Achilles' heel of senescent cells: from transcriptome to senolytic drugs. *Aging cell,* 14**,** 644-658.
ZOROV, D. B., JUHASZOVA, M. & SOLLOTT, S. J. 2014. Mitochondrial reactive oxygen species (ROS) and ROS-induced ROS release. *Physiological reviews,* 94**,** 909-950.
ZUBAREV, R. A. & MAKAROV, A. 2013. Orbitrap Mass Spectrometry. *Analytical Chemistry,* 85**,** 5288-5296.
ZWARTHOFF, S. A., BERENDS, E. T. M., MOL, S., RUYKEN, M., AERTS, P. C., JÓZSI, M., DE HAAS, C. J. C., ROOIJAKKERS, S. H. M. & GORHAM, R. D. 2018. Functional Characterization of Alternative and Classical Pathway C3/C5 Convertase Activity and Inhibition Using Purified Models. 9.

Appendices

Table 5. Cytokine profile of J774 macrophages treated with ageing skeletal muscle secretome derived EVs and soluble proteins. EV and soluble protein treated macrophage secretomes were measured using a LEGENDPlex multi-plex fluorescent bead assay on a flow cytometer. M1 and M2 samples correspond to J774 macrophages that have been polarised to an M1 or M2 macrophage phenotype. Data shown are of 3 biological replicates consisting of 2 technical replicates per sample.

Sample	Cytokines (pg/ml)												
	KC	TGFβ1 (Free Active)	IL-18	IL-23	MDC	IL-10	IL-12p70	IL-6	TNF-α	G-CSF	TARC	IL-12p40	IL-1β
Medium	<18.81	<40.50	<107.8	<198.35	437.85	<83.95	<9.63	69.24	129.68	836.04	<66.34	26.89	<42.82
	<18.81	<40.50	<107.8	<198.35	393.96	<83.95	<9.63	54.82	120.95	760.39	<66.34	19.84	<42.82
	<4.97	<11.62	<43.8	<76.94	537.09	<42.13	<3.59	92.19	135.55	889.76	<25.40	7.29	<24.11
	<4.97	<11.62	<43.8	<76.94	585.64	<42.13	<3.59	88.11	133.99	899.87	<25.40	7.36	<24.11
	<4.99	<11.88	<43.3	<76.75	548.71	<42.98	<3.39	101.7	144.02	887.93	<25.11	7.96	<23.40
	<4.99	<11.88	<43.3	<76.75	514.15	<42.98	<3.39	81.35	137.32	761.12	<25.11	6.74	<23.40
M1	<18.81	<40.50	<107.8	<198.35	1570.13	<83.95	11.67	11409.29	2200.26	19154.9	71.96	2010.48	56.79
	<18.81	<40.50	<107.8	<198.35	1246.42	<83.95	0	10981.03	1687.96	15360.58	0	1617.09	46.53
	<4.97	<11.62	91.4	<76.94	2445.24	<42.13	12.32	29645.82	2774.25	21848.92	60	436.05	53.6
	<4.97	<11.62	93	<76.94	2509.16	<42.13	12.08	26260.07	2667.13	20529.95	60.83	397.71	53.64
	<4.99	<11.88	75.1	0	1553.31	<42.98	9.79	21820.74	1971.27	18143.86	45.11	323.79	44.32
	<4.99	<11.88	88.4	78.2	2917.59	<42.98	12.21	30538.04	3426.75	25141.62	61.72	476.52	56.22
M2	<18.81	<40.50	<107.8	<198.35	296.91	<83.95	<9.63	45.61	97.96	638.4	<66.34	<12.56	<42.82
	<18.81	<40.50	<107.8	<198.35	262.09	<83.95	<9.63	0	80.73	511.33	<66.34	<12.56	<42.82
	<4.97	<11.62	<43.8	<76.94	76.44	<42.13	<3.59	<11.21	49.59	<40.98	<25.40	<0.86	<24.11
	<4.97	<11.62	<43.8	<76.94	81.67	<42.13	<3.59	<11.21	46.81	<40.98	<25.40	<0.86	<24.11
	<4.99	<11.88	<43.3	<76.75	84.5	<42.98	<3.39	<11.08	56.77	<41.88	<25.11	<0.91	<23.40

	<4.99	<11.88	<43.3	<76.75	59.67	<42.98	<3.39	<11.08	40.39	<41.88	<25.11	<0.91	<23.40
NEV	<18.81	<40.50	<107.8	<198.35	637.81	<83.95	<9.63	230.3	54.87	1457.78	<66.34	29.04	<42.82
	<18.81	<40.50	<107.8	<198.35	515.31	<83.95	<9.63	153.11	41.74	1174.66	<66.34	23.94	<42.82
	<4.97	<11.62	<43.8	<76.94	678.39	<42.13	<3.59	206.14	41.95	1272.39	<25.40	7.42	<24.11
	<4.97	<11.62	<43.8	<76.94	646.77	<42.13	<3.59	193.38	41.66	1228.92	<25.40	7.58	<24.11
	<4.99	<11.88	<43.3	<76.75	688.33	<42.98	<3.39	242.61	54.63	1461.58	<25.11	8.96	<23.40
	<4.99	<11.88	<43.3	<76.75	590.02	<42.98	<3.39	230.72	49.17	1370.24	<25.11	7.71	<23.40

NP	65.02	<40.50	<107.8	<198.35	656.21	<83.95	<9.63	1502.68	<41.25	13190.65	<66.34	162.85	<42.82
	53.72	<40.50	<107.8	<198.35	550.71	<83.95	<9.63	1161.05	<41.26	11006.85	<66.34	106.01	<42.82
	48.71	<11.62	<43.8	<76.94	682.64	<42.13	<3.59	1012.88	26.21	13679.98	<25.40	28.04	<24.11
	51.92	<11.62	<43.8	<76.94	725.38	<42.13	<3.59	1023.63	26.73	14485.33	<25.40	30.32	<24.11
	47.6	<11.88	<43.3	<76.75	711.13	<42.98	<3.39	962.93	25.57	14653.08	<25.11	26.36	<23.40
	51.11	<11.88	<43.3	<76.75	707.71	<42.98	<3.39	961.95	25.83	13850.72	<25.11	29.44	<23.40
SEV	<18.81	<40.50	<107.8	<198.35	563.3	<83.95	<9.63	152.12	222.69	926.27	<66.34	32.22	<42.82
	<18.81	<40.50	<107.8	<198.35	487.63	<83.95	<9.63	122	203.71	835.98	<66.34	27.23	<42.82
	<4.97	<11.62	<43.8	<76.94	807.96	<42.13	<3.59	166.62	264.23	998.25	<25.40	9.42	<24.11
	<4.97	<11.62	<43.8	<76.94	738.68	<42.13	<3.59	145.73	239.92	924.25	<25.40	9.46	<24.11
	<4.99	<11.88	<43.3	<76.75	688.62	<42.98	<3.39	148.34	232.03	881.67	<25.11	9.13	<23.40
	<4.99	<11.88	<43.3	<76.75	613.94	<42.98	<3.39	123.99	194.66	778.68	<25.11	6.69	<23.40
SP	31.72	<40.50	<107.8	<198.35	599.53	<83.95	<9.63	724.95	55.6	4851.76	<66.34	112.44	<42.82
	34.34	<40.50	<107.8	<198.35	698.18	<83.95	<9.63	875.94	62.57	5316.38	<66.34	135.33	<42.82
	24.92	<11.62	<43.8	<76.94	618.71	<42.13	<3.59	487.74	49.64	4857.98	<25.40	22.48	<24.11
	27.99	<11.62	<43.8	<76.94	856.58	<42.13	<3.59	585.22	52.74	5197.38	<25.40	26.9	<24.11
	17.72	<11.88	<43.3	<76.75	609.45	<42.98	<3.39	389.19	42.06	4281.69	<25.11	16.7	<23.40
	22.02	<11.88	<43.3	<76.75	707.72	<42.98	<3.39	479.86	53.62	4716.91	<25.11	21.15	<23.40

SenEV	<18.81	<40.50	<107.8	<198.35	242.05	<83.95	<9.63	<36.72	163.63	<112.37	<66.34	<12.56	<42.82
	<18.81	<40.50	<107.8	<198.35	202.47	<83.95	<9.63	<36.72	126.51	<112.37	<66.34	<12.56	<42.82
	<4.97	<11.62	<43.8	<76.94	275.31	<42.13	<3.59	23.12	142.95	<40.98	<25.40	<0.86	<24.11
	<4.97	<11.62	<43.8	<76.94	291.46	<42.13	<3.59	25.49	156.49	<40.98	<25.40	<0.86	<24.11
	<4.99	<11.88	<43.3	<76.75	251.43	<42.98	<3.39	28.72	144.69	45.49	<25.11	<0.91	<23.40
	<4.99	<11.88	<43.3	<76.75	221.51	<42.98	<3.39	24	126.88	0	<25.11	<0.91	<23.40
SenP	<18.81	<40.50	<107.8	<198.35	685.84	<83.95	<9.63	421.13	133.83	1582.63	<66.34	28.11	<42.82
	<18.81	<40.50	<107.8	<198.35	624.84	<83.95	<9.63	419.56	132.43	1560.65	<66.34	30.13	<42.82
	12	11.68	<43.8	<76.94	824.48	<42.13	<3.59	355.07	137.47	1930.58	<25.40	9.26	<24.11
	11.06	0	<43.8	<76.94	830.2	<42.13	<3.59	313.86	124.83	1561.15	<25.40	7.8	<24.11
	12.57	<11.88	<43.3	<76.75	955.48	<42.98	<3.39	393.41	139.11	1860.38	<25.11	8.18	<23.40
	11.45	<11.88	<43.3	<76.75	825.33	<42.98	<3.39	349.35	131.47	1595.99	<25.11	8.52	<23.40

Table 6. Proteins identified in differentiating C2C12 cells using bottom-up proteomic analysis. ITS differentiated C2C12 cells were collected on day 0, 1, 3 and 5 of the differentiation period and samples prepared for MS analysis. Proteins with 1 or more unique peptide sequence were considered to be identified when searched against the UniProt database. Proteins were quantified using Progenesis QI proteomics software. Data shown are of 3 biological repeats, which allowed for an ANOVA statistical test.

					Normalised abundance			
UniProt ID	**Peptide count**	**Unique peptides**	**Anova (p)**	**Protein name**	**Day 0**	**Day 1**	**Day 3**	**Day 5**
RAB6B_MOUSE	4	1	1.97E-12	Ras-related protein Rab-6B Rab6b	1143.620	987.947	0.000	0.000
BICL1_MOUSE	7	1	2.84E-12	BICD family-like cargo adapter 1 Bicdl1	62.938	136.165	0.000	0.134
NUCKS_MOUSE	3	1	4.49E-09	Nuclear ubiquitous casein and cyclin-dependent kinase substrate 1 Nucks1	268.430	1238.829	0.000	0.004

TPR_MOUSE	35	8	9.47E-09	Nucleoprotein TPR Tpr	2963.380	3562.042	1375.595	1101.775
HA13_MOUSE	2	1	2.26E-08	H-2 class I histocompatibility antigen, D-K alpha chain H2-D1	129.394	121.941	0.295	0.042
VW5B2_MOUSE	12	1	2.55E-08	von Willebrand factor A domain-containing protein 5B2 Vwa5b2	1063.103	2647.671	15504.728	14751.374
BIN1_MOUSE	18	8	2.73E-08	Myc box-dependent-interacting protein 1 Bin1	1021.859	1146.940	5338.381	6913.384
ATX2L_MOUSE	10	1	-08	Ataxin-2-like protein Atxn2l	353.092	139.193	0.672	0.504
ZWINT_MOUSE	3	1	3.24E -08 3.81E	ZW10 interactor Zwint	73.255	12.414	0.000	0.299
AP3B1_MOUSE	21	4	4.28E-08	AP-3 complex subunit beta-1 Ap3b1	38.808	0.090	46.773	59.794
CIP4_MOUSE	6	1	4.44E-08	Cdc42-interacting protein 4 Trip10	193.793	177.138	4.384	0.607
MYL1_MOUSE	10	5	1.16E-07	Myosin light chain 1/3, skeletal muscle isoform Myl1	464.574	760.577	7969.544	4560.495
IVD_MOUSE	10	1	1.92E-07	Isovaleryl-CoA dehydrogenase, mitochondrial Ivd	0.000	0.000	3.420	74.787
EIF3B_MOUSE	9	4	3.38E-07	Eukaryotic translation initiation factor 3 subunit B Eif3b	1304.943	1243.099	207.526	233.205
COMD2_MOUSE	3	1	4.20E-07	COMM domain-containing protein 2 Commd2	483.894	240.264	1.057	0.000

MYH10_MOUSE	52	4	-07	Myosin-10 Myh10	1456.221	523.389	19.231	20.528
CO3_MOUSE	18	2	-07 5.20E 6.27E	Complement C3 C3	27.289	0.000	2.804	155.614
IMDH2_MOUSE	12	6	6.39E-07	Inosine-5'-monophosphate dehydrogenase 2 Impdh2	1280.199	908.268	183.123	200.623
CND2_MOUSE	7	4	8.34E-07	Condensin complex subunit 2 Ncaph	263.936	480.781	70.902	25.553
ACTS_MOUSE	48	2	-07	Actin, alpha skeletal muscle Acta1	76.711	36.099	3313.450	2575.470
RBNS5_MOUSE	14	1	8.63E -06 1.11E	Rabenosyn-5 Rbsn	20.431	23.967	0.194	0.000

JHD2C_MOUSE	21	2	1.13E-06	Probable JmjC domain-containing histone demethylation protein 2C Jmjd1c	316.207	462.797	1685.854	1401.885
QKI_MOUSE	5	1	1.15E-06	Protein quaking Qki	879.353	2557.179	843.052	3.419
CY1_MOUSE	7	2	1.27E-06	Cytochrome c1, heme protein, mitochondrial Cyc1	927.056	2134.772	5486.648	4800.376
PPIA_MOUSE	20	8	1.43E-06	Peptidyl-prolyl cis-trans isomerase A Ppia	39615.884	60107.115	3252.857	9205.747
MIC19_MOUSE	3	2	1.49E-06	MICOS complex subunit Mic19 Chchd3	814.922	1530.458	3192.890	2687.748
LRMP_MOUSE	9	1	1.59E-06	Lymphoid-restricted membrane protein Lrmp	1897.889	127.083	380.404	626.260
CWC15_MOUSE	5	1	1.95E-06	Spliceosome-associated protein CWC15 homolog Cwc15	109.451	89.139	1.403	0.031
SERB_MOUSE	3	1	1.98E-06	Phosphoserine phosphatase Psph	2208.403	2605.633	9772.686	5779.040
RAB5C_MOUSE	11	3	2.00E-06	Ras-related protein Rab-5C Rab5c	568.306	884.996	2247.446	1205.892
LIMA1_MOUSE	10	2	2.10E-06	LIM domain and actin-binding protein 1 Lima1	455.484	550.418	15.763	25.187
ATAD1_MOUSE	5	1	2.22E-06	ATPase family AAA domaincontaining protein 1 Atad1	0.629	0.137	7.202	85.741
DPH2_MOUSE	4	1	2.52E-06	2-(3-amino-3-carboxypropyl)histidine synthase subunit 2 Dph2	0.022	0.000	1.725	118.816
RCC2_MOUSE	8	4	2.55E-06	Protein RCC2 Rcc2	1391.078	1548.314	516.633	169.047
RFA2_MOUSE	1	1	2.61E-06	Replication protein A 32 kDa subunit Rpa2	283.966	179.731	0.911	1.430
RL29_MOUSE	7	5	2.62E-06	60S ribosomal protein L29 Rpl29	1778.184	2452.423	157.930	55.779
TRA2B_MOUSE	2	1	2.90E-06	Transformer-2 protein homolog	222.943	56.614	0.390	1.077

				beta Tra2b				
PAIRB_MOUSE	18	8	2.90E-06	Plasminogen activator inhibitor 1 RNA-binding protein Serbp1	2254.740	975.046	463.576	257.754
NEUT_MOUSE	1	1	2.99E-06	Neurotensin/neuromedin N Nts	8.523	0.000	125.774	35.119
RHOC_MOUSE	6	1	3.07E-06	Rho-related GTP-binding protein RhoC Rhoc	165.510	0.000	12.449	157.325
ADHX_MOUSE	7	1	3.15E-06	Alcohol dehydrogenase class-3 Adh5	1888.230	2130.296	329.852	526.170
DHX15_MOUSE	18	3	3.16E-06	Pre-mRNA-splicing factor ATP-dependent RNA helicase DHX15 Dhx15	2376.900	2023.719	826.670	418.884
GELS_MOUSE	22	10	3.30E-06	Gelsolin Gsn	2439.982	4353.803	6419.346	6722.369
GRP78_MOUSE	46	13	3.42E-06	78 kDa glucose-regulated protein Hspa5	6938.074	9303.842	21797.063	17114.261
CALX_MOUSE	22	4	3.43E-06	Calnexin Canx	4081.997	5100.444	7279.612	6485.141
HP1B3_MOUSE	14	1	3.56E-06	Heterochromatin protein 1-binding protein 3 Hp1bp3	175.927	152.877	1.298	0.226
ZNF12_MOUSE	5	1	3.69E	Zinc finger protein 12 Znf12	26.971	103.843	1.451	1.050
EF1A2_MOUSE	15	1	-06 -06	3.70EElongation factor 1-alpha 2 Eef1a2				49.910
EF1A1_MOUSE	37	17	3.70E -06	Elongation factor 1-alpha 1 Eef1a1	128.868 43211.628	92.343 30964.369		16735.549
PRDX1_MOUSE	19	7	-06 -06	4.21E Peroxiredoxin-1 Prdx1	4152.538	5336.523	1659.651	1209.173
TNNC1_MOUSE	2	2	4.28E-06	Troponin C, slow skeletal and cardiac muscles Tnnc1	305.952	638.122	4967.634	3304.673

RBM3_MOUSE	7	5	4.30E-06	RNA-binding protein 3 Rbm3	2501.958	3778.502	423.570	95.964
AIFM1_MOUSE	11	4	4.55E-06	Apoptosis-inducing factor 1, mitochondrial Aifm1	457.484	850.040	2114.831	2059.106
VAMP3_MOUSE	2	1	4.60E-06	Vesicle-associated membrane protein 3 Vamp3	1278.495	1783.082	4733.031	3296.544
RAB32_MOUSE	4	1	4.60E	Ras-related protein Rab-32 Rab32	107.985	95.262	0.069	7.684
EPN4_MOUSE	3	2	4.82E	Clathrin interactor 1 Clint1	171.353	419.927	5.891	1.914
FLNA_MOUSE	133	28	-06	4.95E	Filamin-A Flna	7834.640	6203.411	2747.346
DESM_MOUSE	41	13	-06	9086.698			19048.903	19177.152
			-06	5.11E	Desmin Des	5946.800		
			-06 8147.777					
SYNC_MOUSE	24	4	5.17E-06	Asparagine--tRNA ligase, cytoplasmic Nars	577.510	901.896	4042.488	2182.642
EF2_MOUSE	84	30	5.43E-06	Elongation factor 2 Eef2	8517.034	7700.741	2155.743	3935.849

CCD47_MOUSE	8	2	5.50E-06	Coiled-coil domain-containing protein 47 Ccdc47	522.985	248.004	2678.315	1357.413
PRI1_MOUSE	7	1	5.65E-06	DNA primase small subunit Prim1	66.975	1.100	0.284	0.083
G3BP2_MOUSE	11	1	5.82E-06	Ras GTPase-activating proteinbinding protein 2 G3bp2	259.871	390.777	4.087	6.302
ACTBL_MOUSE	27	1	-06	Beta-actin-like protein 2 Actbl2	61.593	83.232	328.389	338.515
RL28_MOUSE	4	1	-06 5.85E 5.86E	60S ribosomal protein L28 Rpl28	5660.761	5438.728	2990.470	328.282
MLRS_MOUSE	5	2	6.00E-06	Myosin regulatory light chain 2, skeletal muscle isoform Mylpf	210.657	282.183	2516.279	728.518
MSI2H_MOUSE	3	2	6.49E-06	RNA-binding protein Musashi homolog 2 Msi2	76.426	225.054	917.485	561.004
PCBP2_MOUSE	14	5	7.21E-06	Poly(rC)-binding protein 2 Pcbp2	2719.792	3289.718	1286.018	2216.504

PARK7_MOUSE	13	7	7.41E-06	Protein/nucleic acid deglycase DJ-1 Park7	5219.524	6226.787	9039.021	2475.233
NNRE_MOUSE	6	3	7.58E-06	NAD(P)H-hydrate epimerase Naxe	820.304	1230.888	2708.139	2209.178
AP3D1_MOUSE	19	4	7.62E-06	AP-3 complex subunit delta-1 Ap3d1	2803.358	2429.824	1040.037	1321.116
CAND1_MOUSE	23	7	7.81E-06	Cullin-associated NEDD8dissociated protein 1 Cand1	1836.514	1976.638	1083.309	797.910
K22O_MOUSE	17	1	7.92E-06	Keratin, type II cytoskeletal 2 oral Krt76	21.555	377.284	9.437	1.428
DLGP5_MOUSE	13	1	8.06E-06	Disks large-associated protein 5 Dlgap5	36.498	1.780	0.367	0.032
COPG2_MOUSE	22	2	8.12E-06	Coatomer subunit gamma-2 Copg2	326.795	411.403	1152.845	119.798
TMOD1_MOUSE	7	1	8.28E-06	Tropomodulin-1 Tmod1	16.203	308.533	21.665	29.423
MA7D1_MOUSE	10	3	8.31E-06	MAP7 domain-containing protein 1 Map7d1	178.514	104.279	8.976	6.052
SEP11_MOUSE	10	5	8.48E-06	Septin-11 Sept11	2309.819	2713.600	3597.462	1728.236
SC22B_MOUSE	5	2	9.01E-06	Vesicle-trafficking protein SEC22b Sec22b	387.417	581.395	1707.706	837.152
KGUA_MOUSE	3	1	1.00E-05	Guanylate kinase Guk1	47.661	115.484	1.262	0.000
GFPT1_MOUSE	10	1	1.06E-05	Glutamine--fructose-6-phosphate aminotransferase [isomerizing] 1 Gfpt1	177.800	160.219	1.460	0.713
RAB25_MOUSE	4	1	1.11E-05	Ras-related protein Rab-25 Rab25	244.373	0.821	754.062	849.472
JUPI2_MOUSE	2	1	1.11E-05	Jupiter microtubule associated homolog 2 Jpt2	928.225	2402.257	1036.777	311.914
PSB4_MOUSE	8	6	1.13E-05	Proteasome subunit beta type-4 Psmb4	2425.518	4542.811	2369.382	882.740
F107B_MOUSE	2	1	1.14E-05	Protein FAM107B Fam107b	881.772	652.979	4.164	0.017

SYDC_MOUSE	12	4	1.15E-05	Aspartate--tRNA ligase, cytoplasmic Dars	1835.467	2704.695	3230.253	2895.821
CHD4_MOUSE	40	4	1.19E-05	Chromodomain-helicase-DNAbinding protein 4 Chd4	2108.546	1403.670	2494.832	1656.754
CAV1_MOUSE	4	2	-05	Caveolin-1 Cav1	1300.321	1545.253	106.547	23.021
PTGR1_MOUSE	10	4	-05 1.22E 1.24E	Prostaglandin reductase 1 Ptgr1	1880.693	2479.360	1705.595	676.087
AP5S1_MOUSE	4	1	1.26E-05	AP-5 complex subunit sigma-1 Ap5s1	132.769	1.764	438.446	222.088
GMPPA_MOUSE	2	1	1.28E-05	Mannose-1-phosphate guanyltransferase alpha Gmppa	44.405	1.008	0.895	0.002
DNPH1_MOUSE	6	1	1.28E-05	2'-deoxynucleoside 5'-phosphate N-hydrolase 1 Dnph1	1680.414	1752.191	26.457	99.405
IF4G2_MOUSE	32	2	1.29E-05	Eukaryotic translation initiation factor 4 gamma 2 Eif4g2	44.901	0.583	0.026	426.413
HNRPU_MOUSE	31	6	1.29E-05	Heterogeneous nuclear ribonucleoprotein U Hnrnpu	5753.645	4963.431	2089.180	1161.913
HNRPK_MOUSE	32	8	1.31E-05	Heterogeneous nuclear ribonucleoprotein K Hnrnpk	2041.679	2403.232	6761.198	3902.674
IMB1_MOUSE	24	7	1.32E-05	Importin subunit beta-1 Kpnb1	2976.972	2584.793	1162.046	812.064
RMXL1_MOUSE	7	1	1.32E-05	RNA binding motif protein, Xlinked-like-1 Rbmxl1	216.029	2.180	0.000	0.000
ADAT2_MOUSE	1	1	1.42E-05	tRNA-specific adenosine deaminase 2 Adat2	89.438	113.749	1.173	0.374
ECI1_MOUSE	11	5	1.43E-05	Enoyl-CoA delta isomerase 1, mitochondrial Eci1	1060.659	2006.909	5997.161	3798.208
NDKB_MOUSE	10	2	1.50E-05	Nucleoside diphosphate kinase B Nme2	5296.618	6893.640	2580.649	146.385
RAB44_MOUSE	3	1	1.64E-05	Ras-related protein Rab-44 Rab44	0.181	122.080	0.559	1.462
C1QT3_MOUSE	2	1	1.68E-05	Complement C1q tumor necrosis factor-related protein 3 C1qtnf3	546.740	2059.742	4005.137	5502.485

CLCA_MOUSE	5	1	1.69E-05	Clathrin light chain A Clta	244.392	1057.989	0.154	0.508
SGTA_MOUSE	2	1	1.86E-05	Small glutamine-rich tetratricopeptide repeat-containing protein alpha Sgta	62.151	87.339	12.817	0.966
CPIN1_MOUSE	4	2	1.94E	Anamorsin Ciapin1	18.503	94.646	0.071	0.005
1433T_MOUSE	22	10	1.95E	14-3-3 protein theta Ywhaq	8193.340	7565.542	2868.911	1496.895
VIGLN_MOUSE	34	3	-05	Vigilin Hdlbp	2510.517	3456.741	2333.432	1769.488
ANT3_MOUSE	9	2	-05 -05 -05	Antithrombin-III Serpinc1	4291.864	1493.766	236.687	181.024
			1.99E 2.02E					
TMED4_MOUSE	2	1	2.03E-05	Transmembrane emp24 domaincontaining protein 4 Tmed4	391.656	889.655	2663.789	1500.046
SYTC_MOUSE	21	3	2.04E-05	Threonine--tRNA ligase, cytoplasmic Tars	507.743	1096.399	2158.646	2077.305
PRPS1_MOUSE	7	1	2.05E-05	Ribose-phosphate pyrophosphokinase 1 Prps1	871.341	1041.231	186.953	2.622
PERI_MOUSE	21	1	2.05E-05	Peripherin Prph	60.404	153.201	65.606	26.157
PLPR4_MOUSE	6	2	2.16E-05	Phospholipid phosphatase-related protein type 4 Plppr4	337.962	43.286	2020.055	340.527
DPP2_MOUSE	4	1	2.16E-05	Dipeptidyl peptidase 2 Dpp7	0.000	0.000	1.767	159.116
SNP23_MOUSE	3	1	2.34E-05	Synaptosomal-associated protein 23 Snap23	325.437	166.628	8.528	2.366
OTU6B_MOUSE	3	2	2.40E-05	OTU domain-containing protein 6B Otud6b	2178.561	5092.464	8748.710	6858.364
TM109_MOUSE	1	1	2.42E-05	Transmembrane protein 109 Tmem109	2234.331	5291.939	12786.471	10656.399
IF4A1_MOUSE	46	15	2.51E-05	Eukaryotic initiation factor 4A-I Eif4a1	4820.036	4256.922	2841.793	1546.677
EIF3F_MOUSE	11	4	2.53E-05	Eukaryotic translation initiation factor 3 subunit F Eif3f	590.628	790.829	1211.380	818.908

UB2V1_MOUSE	9	2	2.57E-05	Ubiquitin-conjugating enzyme E2 variant 1 Ube2v1	2609.374	3674.396	7022.129	2366.192
CSDE1_MOUSE	15	1	2.59E-05	Cold shock domain-containing protein E1 Csde1	168.879	0.000	38.851	676.483
RL7A_MOUSE	17	5	2.63E-05	60S ribosomal protein L7a Rpl7a	1215.003	1027.625	15.109	13.058
COG1_MOUSE	13	1	2.63E-05	Conserved oligomeric Golgi complex subunit 1 Cog1	151.281	0.000	0.000	1.115
VAPA_MOUSE	11	4	2.63E-05	Vesicle-associated membrane protein-associated protein A Vapa	557.274	6158.948	380.333	228.904
TBB5_MOUSE	40	6	2.64E-05	Tubulin beta-5 chain Tubb5	509.686	942.707	1659.268	1580.858
RL13A_MOUSE	15	4	2.66E-05	60S ribosomal protein L13a Rpl13a	2614.984	2798.606	649.695	1563.632
DHX36_MOUSE	9	1	2.77E-05	ATP-dependent RNA helicase DHX36 Dhx36	0.000	28.546	0.000	0.000
G3P_MOUSE	49	23	3.00E-05	Glyceraldehyde-3-phosphate dehydrogenase Gapdh	12545.993	10855.729	18184.510	25675.842
NDUBA_MOUSE	5	3	3.11E-05	NADH dehydrogenase [ubiquinone] 1 beta subcomplex subunit 10 Ndufb10	602.600	1138.246	1894.029	2110.372
PSA1_MOUSE	11	9	3.14E-05	Proteasome subunit alpha type-1 Psma1	4102.597	4940.708	8144.089	4511.511
I2BPL_MOUSE	9	1	3.66E-05	Interferon regulatory factor 2binding protein-like Irf2bpl	131.854	67.196	924.710	239.215
OTUB1_MOUSE	4	2	3.79E-05	Ubiquitin thioesterase OTUB1 Otub1	841.245	1372.818	3292.246	1579.097
VAV3_MOUSE	8	1	3.80E-05	Guanine nucleotide exchange factor VAV3 Vav3	598.021	2739.974	3474.815	1451.349
LETM1_MOUSE	12	1	3.82E-05	Mitochondrial proton/calcium exchanger protein Letm1	666.596	834.114	1823.409	1468.708
NPM_MOUSE	22	9	3.85E-05	Nucleophosmin Npm1	7820.320	6654.771	1918.780	1993.771

UGPA_MOUSE	7	1	3.94E-05	UTP--glucose-1-phosphate uridylyltransferase Ugp2	53.583	535.444	770.736	878.753
JIP4_MOUSE	31	1	4.03E-05	C-Jun-amino-terminal kinaseinteracting protein 4 Spag9	678.436	1184.580	251.206	184.786
KCRM_MOUSE	12	3	-05	Creatine kinase M-type Ckm	929.335	1372.483	2710.296	3611.431
CDK4_MOUSE	4	1	-05 4.11E 4.13E	Cyclin-dependent kinase 4 Cdk4	123.765	24.095	1.281	0.123
ODPB_MOUSE	18	10	4.23E-05	Pyruvate dehydrogenase E1 component subunit beta, mitochondrial Pdhb	886.530	1879.645	6358.595	6382.492
ACADL_MOUSE	8	6	4.36E-05	Long-chain specific acyl-CoA dehydrogenase, mitochondrial Acadl	602.522	979.222	2429.880	2337.817
ETFB_MOUSE	10	3	4.37E-05	Electron transfer flavoprotein subunit beta Etfb	2437.389	3157.020	7252.859	5029.087
SPTB2_MOUSE	75	8	4.49E-05	Spectrin beta chain, nonerythrocytic 1 Sptbn1	693.287	2634.836	1209.348	917.162

RHOA_MOUSE	10	4	4.57E	Transforming protein RhoA Rhoa	536.369	35.267	11.233	2.527
NSF1C_MOUSE	4	1	-05				3.623	0.425
			-05	4.87ENSFL1 cofactor p47 Nsfl1c	274.735	404.093		
LYAR_MOUSE	8	2	4.88E-05	Cell growth-regulating nucleolar protein Lyar	74.121	13.802	2.652	0.065
MYBPH_MOUSE	6	1	5.00E	Myosin-binding protein H Mybph	3.491	0.000	452.375	886.481
CUX1_MOUSE	19	2	-05				305.708	2.596
			-05	5.06EHomeobox protein cut-like 1 Cux1	86.953	76.798		
LRIG2_MOUSE	14	1	5.15E-05	Leucine-rich repeats and immunoglobulin-like domains protein 2 Lrig2	1346.738	6411.856	630.402	284.468
NU155_MOUSE	10	1		Nuclear pore complex protein			5.858	0.953

			5.43E-05	Nup155 Nup155	40.391	0.000		
MRGBP_MOUSE	4	2	5.44E-05	MRG/MORF4L-binding protein Mrgbp	1309.813	893.717	6418.029	1558.185
CHRD1_MOUSE	4	1	5.53E-05	Cysteine and histidine-rich domain-containing protein 1 Chordc1	67.504	6.472	3.248	0.795
TXNL1_MOUSE	7	5	5.64E-05	Thioredoxin-like protein 1 Txnl1	2979.285	4092.136	6209.089	3685.225
TRI18_MOUSE	8	2	5.84E-05	E3 ubiquitin-protein ligase Midline-1 Mid1	19.977	192.910	558.850	374.857
TPM2_MOUSE	36	7	-05	5.92E Tropomyosin beta chain Tpm2			4031.104	1309.989
RN121_MOUSE	4	1	-05 760.907	1340.450 RING finger protein 121 Rnf121	5.93E 3666.716	8413.987	15609.002	11884.535
SDHA_MOUSE	15	6	5.99E-05	Succinate dehydrogenase [ubiquinone] flavoprotein subunit, 1022.555 mitochondrial Sdha	708.377		2119.552	1926.879
PGAM2_MOUSE	8	3	6.04E-05	Phosphoglycerate mutase 2 Pgam2	104.198	584.740	725.658	1688.125
CC127_MOUSE	3	1	6.10E-05	Coiled-coil domain-containing protein 127 Ccdc127	221.861	368.460	3.472	0.693
K2C5_MOUSE	37	5	6.13E-05	Keratin, type II cytoskeletal 5 Krt5	6259.745	1509.923	2013.975	2044.919
RL40_MOUSE	21	6	6.18E-05	Ubiquitin-60S ribosomal protein L40 Uba52	3180.370	7057.415	636.627	1158.841
FUMH_MOUSE	13	10	6.21E-05	Fumarate hydratase, mitochondrial Fh	1074.197	1502.813	2879.952	2919.659
KAPCA_MOUSE	5	1	6.23E-05	cAMP-dependent protein kinase catalytic subunit alpha Prkaca	175.226	521.849	721.049	769.544

MCAF1_MOUSE	3	1	6.27E-05	Activating transcription factor 7-interacting protein 1 Atf7ip	18.162	0.197	11.314	88.994

FHL2_MOUSE	5	1	6.45E-05	Four and a half LIM domains protein 2 Fhl2	205.597		348.090	0.150	5.900
PEA15_MOUSE	3	2	6.55E-05	Astrocytic phosphoprotein PEA-15 Pea15	769.978		717.839	4708.010	2027.322
UB2V2_MOUSE	8	2	6.56E-05	Ubiquitin-conjugating enzyme E2 variant 2 Ube2v2	321.876		346.715	1143.052	438.943
CLIC1_MOUSE	9	1	6.69E-05	Chloride intracellular channel protein 1 Clic1	10433.244		10710.118	7192.116	2107.397
MSH6_MOUSE	21	2	6.78E-05	DNA mismatch repair protein Msh6 Msh6	71.005		15.212	411.381	96.006
INF2_MOUSE	12	1	6.83E	Inverted formin-2 Inf2	712.754		493.502	79.309	124.872
1433F_MOUSE	17	5	-05		4111.257		3984.867	2657.695	1043.776
			-05	6.88E14-3-3 protein eta Ywhah					
RAB6A_MOUSE	13	3	7.07E-05	Ras-related protein Rab-6A Rab6a	1547.412		2049.448	4848.187	2446.828
MARE1_MOUSE	11	4	7.19E-05	Microtubule-associated protein RP/EB family member 1 Mapre1	2937.984		2713.874	1979.505	1014.211
ORN_MOUSE	10	2	7.27E-05	Oligoribonuclease, mitochondrial Rexo2	859.594		932.147	1954.405	855.417
ANXA1_MOUSE	31	10	7.28E-05	Annexin A1 Anxa1	13721.766		12659.196	6030.223	4897.718
IF4H_MOUSE	6	2	7.28E-05	Eukaryotic translation initiation factor 4H Eif4h	5963.457		3889.432	314.781	422.289
RL35_MOUSE	5	3	-05	7.65E 60S	1572.656	1649.449		28.100	83.345
MYH9_MOUSE	169	38	-05	ribosomal protein L35 Rpl35	12265.557	18045.464		9095.279	8494.059
			7.77E	Myosin-9 Myh9					
AP2B1_MOUSE	25	3	7.86E-05	AP-2 complex subunit beta Ap2b1	270.132		44.404	51.036	48.428

PK3CD_MOUSE	10	1	7.87E-05	Phosphatidylinositol 4,5-bisphosphate 3-kinase catalytic subunit delta isoform Pik3cd	174.020	0.000	9.945	15.159
RAB31_MOUSE	3	1	7.91E-05	Ras-related protein Rab-31 Rab31	216.924	221.548	5853.727	1530.663
RAB1B_MOUSE	11	4	7.96E-05	Ras-related protein Rab-1B Rab1b	1866.797	2086.860	239.990	92.291
HS90A_MOUSE	49	9	8.10E-05	Heat shock protein HSP 90-alpha Hsp90aa1	4614.780	4097.651	4303.682	1708.635
EF1D_MOUSE	14	7	8.21E-05	Elongation factor 1-delta Eef1d	5165.116	7197.017	8429.551	3834.104
ACTA_MOUSE	51	2	8.26E-05	Actin, aortic smooth muscle cta2	1063.144	1111.180	3157.031	4794.169
CO3A1_MOUSE	19	2	8.31E-05	Collagen alpha-1(III) chain Col3a1	133.005	1147.864	18.255	11.848
RTN2_MOUSE	3	1	8.75E-05	Reticulon-2 Rtn2	106.314	151.083	934.124	867.585

TIM23_MOUSE	4	2	8.87E-05	Mitochondrial import inner membrane translocase subunit Tim23 Timm23	3542.889	621.446	189.197	128.537
K1C13_MOUSE	17	3	8.90E-05	Keratin, type I cytoskeletal 13 Krt13	1107.778	627.033	182.190	153.394
ADT2_MOUSE	24	4	9.08E-05	ADP/ATP translocase 2 Slc25a5	2566.022	3466.958	1800.956	1108.384
RLA2_MOUSE	6	1	9.18E-05	60S acidic ribosomal protein P2 Rplp2	6640.920	9006.290	19803.151	7115.376
NUCL_MOUSE	32	9	9.41E-05	Nucleolin Ncl	1298.927	2814.640	4638.539	1862.689
ITB3_MOUSE	5	1	9.59E-05	Integrin beta-3 Itgb3	28.565	140.946	418.098	164.848
GORS2_MOUSE	5	2	9.78E-05	Golgi reassembly-stacking protein 2 Gorasp2	75.286	103.230	433.932	307.439
DNJC8_MOUSE	3	1	9.95E-05	DnaJ homolog subfamily C	98.136	0.121	0.000	0.000

				member 8 Dnajc8				
DHB12_MOUSE	13	3	1.00E-04	Very-long-chain 3-oxoacyl-CoA reductase Hsd17b12	4279.366	3680.002	1003.459	1217.091
HDGR2_MOUSE	10	3	1.07E-04	Hepatoma-derived growth factor-related protein 2 Hdgfl2	1985.333	1112.214	436.962	482.255
HMGN2_MOUSE	2	1	1.08E-04	Non-histone chromosomal protein HMG-17 Hmgn2	946.078	495.670	37.201	5.766
AATM_MOUSE	24	6	1.08E-04	Aspartate aminotransferase, mitochondrial Got2	3487.061	5570.523	6996.736	9452.681
MRT4_MOUSE	1	1	1.10E-04	mRNA turnover protein 4 homolog Mrto4	1024.024	616.231	3.817	8.937
KCC2D_MOUSE	9	1	1.11E-04	Calcium/calmodulin-dependent protein kinase type II subunit delta 5.564 Camk2d		157.653	43.430	0.000
ANXA5_MOUSE	31	11	-04	1.11E	Annexin A5 Anxa5	8308.068	14329.895	6747.971
VWC2_MOUSE	1	1	-04 8500.164	1.12E	Brorin Vwc2	10.657	1.677 0.007	70.093
AT2A1_MOUSE	26	3	1.14E-04	Sarcoplasmic/endoplasmic reticulum calcium ATPase 1 Atp2a1	1343.751	2119.665	2641.359	3965.271
GAPR1_MOUSE	3	1	1.16E-04	Golgi-associated plant pathogenesis-related protein 1 Glipr2	1990.124	2591.298	3393.219	1362.812
HMCS1_MOUSE	9	3	1.19E-04	Hydroxymethylglutaryl-CoA synthase, cytoplasmic Hmgcs1	518.585	1422.560	235.794	238.143

THIM_MOUSE	11	4	1.19E-04	3-ketoacyl-CoA thiolase, mitochondrial Acaa2	541.424	737.356	1359.100	2294.379
PCKGM_MOUSE	23	5	1.21E-04	Phosphoenolpyruvate carboxykinase [GTP], mitochondrial Pck2	972.112	1265.914	2978.698	2365.104
EIF2A_MOUSE	8	1	1.23E-04	Eukaryotic translation initiation factor 2A Eif2a	0.100	139.556	6.460	2.853
CSRP3_MOUSE	3	2	1.24E-04	Cysteine and glycine-rich protein 3 Csrp3	97.849	743.118	1236.109	1927.617
CSRP2_MOUSE	4	1	1.26E-04	Cysteine and glycine-rich protein 2 Csrp2	1616.833	2546.090	2892.190	1364.663
KI13A_MOUSE	12	3	1.27E-04	Kinesin-like protein KIF13A Kif13a	156.741	856.192	1044.893	704.383
CYFP1_MOUSE	13	3	1.28E-04	Cytoplasmic FMR1-interacting protein 1 Cyfip1	279.101	221.896	1114.455	904.427
SRS10_MOUSE	1	1	1.29E-04	Serine/arginine-rich splicing factor 10 Srsf10	4103.584	729.140	776.413	53.696
K1C10_MOUSE	17	4	1.32E-04	Keratin, type I cytoskeletal 10 Krt10	3475.436	5477.166	11653.392	4692.660
KAP0_MOUSE	13	4	1.34E-04	cAMP-dependent protein kinase type I-alpha regulatory subunit Prkar1a	805.512	1780.809	564.783	369.238
THIL_MOUSE	11	4	1.35E-04	Acetyl-CoA acetyltransferase, mitochondrial Acat1	234.032	435.432	823.714	812.941
ODO2_MOUSE	10	4	1.59E-04	Dihydrolipoyllysine-residue succinyltransferase component of 2-oxoglutarate dehydrogenase complex, mitochondrial Dlst	654.376	996.745	2702.893	2649.085
NASP_MOUSE	15	6	1.59E-04	Nuclear autoantigenic sperm protein Nasp	3138.483	2649.792	4452.346	1527.296
HXK2_MOUSE	19	1	-04	Hexokinase-2 Hk2	118.962	132.485	302.446	494.686
RL27_MOUSE	10	5	1.65E -04	60S ribosomal protein L27 Rpl27	1740.910	1706.163	222.719	1061.709

			1.66E					
CAH3_MOUSE	4	1	1.69E-04	Carbonic anhydrase 3 Ca3	358.983	1875.009	559.409	265.830
ACON_MOUSE	38	12	1.76E-04	Aconitate hydratase, mitochondrial Aco2	3530.220	4918.391	8691.959	10814.461
FUBP2_MOUSE	20	2	1.78E-04	Far upstream element-binding protein 2 Khsrp	1597.716	1562.233	1174.592	738.451
SHOT1_MOUSE	9	1	1.81E-04	Shootin-1 Shtn1	174.624	261.799	0.000	0.015
NEXN_MOUSE	14	4	1.85E-04	Nexilin Nexn	317.223	648.338	1892.236	1719.547
KAPCB_MOUSE	7	1	1.89E-04	cAMP-dependent protein kinase catalytic subunit beta Prkacb	36.760	88.832	152.221	136.425
GSTA4_MOUSE	8	6	1.90E-04	Glutathione S-transferase A4 Gsta4	5403.780	5851.699	866.190	1982.472
RU2A_MOUSE	11	7	1.94E-04	U2 small nuclear ribonucleoprotein A' Snrpa1	1802.923	2661.451	3614.640	1920.431
RBBP7_MOUSE	5	1	1.96E-04	Histone-binding protein RBBP7 Rbbp7	803.435	690.837	468.340	337.446
PYM1_MOUSE	2	1	1.97E-04	Partner of Y14 and mago Pym1	116.584	406.115	4.885	6.965
PURB_MOUSE	6	4	1.99E-04	Transcriptional activator protein Pur-beta Purb	435.393	647.488	1614.254	1277.875
FRIL2_MOUSE	4	1	-04	Ferritin light chain 2 Ftl2	2078.791	1692.881	22.100	122.533
BOLA1_MOUSE	3	1	2.00E-04 2.04E	BolA-like protein 1 Bola1	88.758	15.629	0.477	0.450
QCR7_MOUSE	4	3	2.04E-04	Cytochrome b-c1 complex subunit 7 Uqcrb	8075.819	10579.668	8975.738	1647.403
IFI4_MOUSE	6	1	2.09E-04	Interferon-activable protein 204 Ifi204	817.954	1.482	1.576	2.433
NCEH1_MOUSE	3	1	2.16E-04	Neutral cholesterol ester hydrolase 1 Nceh1	115.512	0.998	23.078	108.356

PSDE_MOUSE	9	3	2.19E-04	26S proteasome non-ATPase regulatory subunit 14 Psmd14	2071.431	2080.617	3912.935	2712.781
ABEC2_MOUSE	5	3	2.19E-04	C->U-editing enzyme APOBEC-2 Apobec2	107.772	258.496	392.484	1192.779
RRAGD_MOUSE	4	2	2.28E-04	Ras-related GTP-binding protein D Rragd	110.320	97.509	4.946	0.000
MFA1A_MOUSE	7	1	2.35E-04	Microfibrillar-associated protein 1A Mfap1a	72.536	11.920	1.890	0.350
ABCE1_MOUSE	27	7	2.46E-04	ATP-binding cassette sub-family E member 1 Abce1	1692.680	1985.964	2726.384	1809.793
QCR2_MOUSE	11	6	2.49E-04	Cytochrome b-c1 complex subunit 2, mitochondrial Uqcrc2	1185.934	1934.324	2905.757	3537.798
ACTN1_MOUSE	51	11	2.52E-04	Alpha-actinin-1 Actn1	1882.620	2479.767	3555.295	908.026
MP2K3_MOUSE	7	3	2.52E-04	Dual specificity mitogen-activated protein kinase kinase 3 Map2k3	4391.868	3488.695	2055.859	1026.650

GRP75_MOUSE	37	11	2.55E-04	Stress-70 protein, mitochondrial Hspa9	7882.962	8128.101	20931.733	18946.911
MYH7B_MOUSE	34	2	-04	Myosin-7B Myh7b	19.437	305.934	48.748	78.356
CNN3_MOUSE	21	6	-04 2.56E 2.57E	Calponin-3 Cnn3	2311.436	1573.641	4355.569	2745.573
DIC_MOUSE	6	2	2.57E-04	Mitochondrial dicarboxylate carrier Slc25a10	6.177	948.898	20.568	4.656
SMRC2_MOUSE	12	1	2.62E-04	SWI/SNF complex subunit SMARCC2 Smarcc2	103.093	187.986	884.221	394.000
AMACR_MOUSE	8	1	2.65E-04	Alpha-methylacyl-CoA racemase Amacr	353.327	922.087	1355.335	1590.352
EFHD2_MOUSE	7	1	2.67E-04	EF-hand domain-containing protein D2 Efhd2	434.790	440.187	15.394	5.333
CBR2_MOUSE	8	4	2.68E-04	Carbonyl reductase [NADPH] 2 Cbr2	493.158	1009.823	3119.669	2287.880

NCDN_MOUSE	4	1	-04	Neurochondrin Ncdn	113.264	24.679	0.513	3.451
ACTN3_MOUSE	31	3	2.72E-04 2.75E-04	Alpha-actinin-3 Actn3	1114.008	1764.169	2199.939	2067.172
ADDA_MOUSE	8	2	2.77E-04	Alpha-adducin Add1	43.122	227.431	1.257	5.412
RRP1_MOUSE	2	1	2.81E-04	Ribosomal RNA processing protein 1 homolog A Rrp1	41.103	0.194	3.344	1.559
AAK1_MOUSE	6	2	2.82E-04	AP2-associated protein kinase 1 Aak1	32.676	262.532	84.813	46.339
NOMO1_MOUSE	15	2	-04	Nodal modulator 1 Nomo1	134.447	156.771	2.704	1.825
DCTN1_MOUSE	30	4	2.87E-04 2.87E-04	Dynactin subunit 1 Dctn1	906.370	644.312	774.076	214.375
ENOB_MOUSE	42	11	2.90E-04	Beta-enolase Eno3	2361.785	3344.477	3974.970	4299.249
NIPS1_MOUSE	7	2	2.94E-04	Protein NipSnap homolog 1 Nipsnap1	254.124	645.951	942.282	1496.747
COMT_MOUSE	2	1	2.98E-04	Catechol O-methyltransferase Comt	194.385	576.359	973.283	810.320
MAOX_MOUSE	6	2	3.02E-04	NADP-dependent malic enzyme Me1	743.549	1236.969	1275.260	1587.306
LAMB1_MOUSE	16	3	-04	Laminin subunit beta-1 Lamb1	1035.605	892.929	1225.162	519.134
FERM2_MOUSE	11	2	3.05E-04 3.10E-04	Fermitin family homolog 2 Fermt2	82.387	0.363	66.826	52.509
XRCC6_MOUSE	7	1	3.13E-04	X-ray repair cross-complementing protein 6 Xrcc6	193.925	4.274	223.460	180.714

ODPA_MOUSE	6	3	3.20E-04	Pyruvate dehydrogenase E1 component subunit alpha, somatic form, mitochondrial Pdha1	947.464	969.279	3173.804	4068.344
MXRA7_MOUSE	2	1	3.24E-04	Matrix-remodeling-associated protein 7 Mxra7	209.171	241.634	1738.298	633.263

PPIC_MOUSE	7	4	3.28E-04	Peptidyl-prolyl cis-trans isomerase C Ppic	1204.600	2792.665	5104.926	4571.406
SMRD3_MOUSE	7	2	3.34E-04	SWI/SNF-related matrix-associated actin-dependent regulator of chromatin subfamily D member 3 Smarcd3	22.528	28.665	101.872	200.565
IPYR_MOUSE	10	4	3.39E-04	Inorganic pyrophosphatase Ppa1	537.640	959.471	2443.858	914.209
ABCA7_MOUSE	17	3	3.41E-04	ATP-binding cassette sub-family A member 7 Abca7	685.916	499.048	244.080	123.366
CNPY2_MOUSE	7	5	3.43E-04	Protein canopy homolog 2 Cnpy2	2110.098	2871.380	4621.459	2773.994
TCRG1_MOUSE	26	3	3.55E-04	Transcription elongation regulator 1 Tcerg1	540.310	1203.764	309.777	503.337
ALDH2_MOUSE	27	9	3.55E-04	Aldehyde dehydrogenase, mitochondrial Aldh2	3096.523	4521.802	7142.343	5147.590
PPIB_MOUSE	12	7	3.58E-04	Peptidyl-prolyl cis-trans isomerase B Ppib	6273.147	9901.322	14061.134	7436.204
PTPRG_MOUSE	7	2	3.59E-04	Receptor-type tyrosine-protein phosphatase gamma Ptprg	2676.193	3616.869	4424.021	5316.407
F207A_MOUSE	4	1	3.60E-04	Protein FAM207A Fam207a	367.861	367.901	8.898	2.179
CMC1_MOUSE	16	5	3.67E-04	Calcium-binding mitochondrial carrier protein Aralar1 Slc25a12	761.172	658.360	795.445	1372.309
CSK22_MOUSE	5	1	3.73E-04	Casein kinase II subunit alpha' Csnk2a2	11.140	50.762	2220.264	354.839
C1TC_MOUSE	28	8	3.74E-04	C-1-tetrahydrofolate synthase, cytoplasmic Mthfd1	1310.212	1018.604	1131.925	508.791
PRS7_MOUSE	18	8	3.75E-04	26S proteasome regulatory subunit 7 Psmc2	1946.369	2643.668	3160.242	3240.156
RS14_MOUSE	7	4	3.76E-04	40S ribosomal protein S14 Rps14	3301.381	3856.649	9622.580	4664.092
PDIA4_MOUSE	14	3	3.78E-04	Protein disulfide-isomerase A4 Pdia4	313.262	323.932	1710.928	863.276

DCAF6_MOUSE	11	2	3.79E-04	DDB1- and CUL4-associated factor 6 Dcaf6	1455.052	1163.914	3589.544	2715.946

RED_MOUSE	9	2	-04	Protein Red Ik	81.201	59.564	7.259	0.642
RAB8A_MOUSE	5	2	-04 3.95E 3.97E	Ras-related protein Rab-8A Rab8a	244.101	197.658	9.841	159.625
TAGL2_MOUSE	21	3	4.14E-04	Transgelin-2 Tagln2	2544.847	2635.744	860.659	397.496
NDUB5_MOUSE	3	1	4.34E-04	NADH dehydrogenase [ubiquinone] 1 beta subcomplex subunit 5, mitochondrial Ndufb5	0.000	24.587	552.790	562.772
TBB6_MOUSE	37	3	4.38E-04	Tubulin beta-6 chain Tubb6	942.071	796.250	2492.261	1214.700
ILF2_MOUSE	3	2	4.53E-04	Interleukin enhancer-binding factor 2 Ilf2	182.494	405.878	691.515	514.452
NUMA1_MOUSE	39	1	4.60E-04	Nuclear mitotic apparatus protein 1 Numa1	1103.323	1043.472	9.926	68.291
PRDX6_MOUSE	14	7	4.62E-04	Peroxiredoxin-6 Prdx6	2365.938	2169.602	4933.385	2181.058
PPIL1_MOUSE	3	1	4.63E-04	Peptidyl-prolyl cis-trans isomeraselike 1 Ppil1	318.397	376.713	7.729	6.041
FUBP1_MOUSE	13	1	4.67E-04	Far upstream element-binding protein 1 Fubp1	718.037	883.824	19.418	0.847
PSA_MOUSE	21	5	4.68E-04	Puromycin-sensitive aminopeptidase Npepps	2245.705	1799.356	5916.906	6142.085
RPN1_MOUSE	22	1	4.73E-04	Dolichyl-diphosphooligosaccharide--protein glycosyltransferase subunit 1 Rpn1	257.256	154.382	4.877	71.208
CELR3_MOUSE	27	3	4.75E-04	Cadherin EGF LAG seven-pass G-type receptor 3 Celsr3	1242.893	1127.378	2206.616	746.925
P5CR3_MOUSE	6	2	4.77E-04	Pyrroline-5-carboxylate reductase 3 Pycr3	541.110	933.121	1220.248	895.354
SERC_MOUSE	21	9	4.85E-04	Phosphoserine aminotransferase Psat1	2007.324	1327.868	3228.247	2968.143

RL19_MOUSE	5	2	4.91E-04	60S ribosomal protein L19 Rpl19	390.410	1211.928	2.441	80.426
FLIP1_MOUSE	9	1	4.98E-04	Filamin-A-interacting protein 1 Filip1	2653.779	24.181	9607.065	12919.233
FSCN1_MOUSE	14	8	5.10E-04	Fascin Fscn1	4208.111	4061.293	3069.249	1632.018
DHE3_MOUSE	18	5	5.32E-04	Glutamate dehydrogenase 1, mitochondrial Glud1	1819.914	2374.031	1607.548	949.988
PTMA_MOUSE	5	3	-04	Prothymosin alpha Ptma	95.085	2137.043	221.364	26.184
HXK1_MOUSE	26	4	-04 5.44E 5.46E	Hexokinase-1 Hk1	2292.931	2925.421	2976.241	1942.033
FAS_MOUSE	57	15	5.50E-04	Fatty acid synthase Fasn	1792.385	3865.694	1954.432	920.007

NDUS1_MOUSE	26	6	5.52E-04	NADH-ubiquinone oxidoreductase 75 kDa subunit, mitochondrial Ndufs1	1288.037	1588.743	2432.425	3296.323
PCNP_MOUSE	7	3	5.54E-04	PEST proteolytic signal-containing nuclear protein Pcnp	846.877	1219.613	550.541	318.480
CFA61_MOUSE	15	3	5.58E-04	Cilia- and flagella-associated protein 61 Cfap61	76.669	178.328	2.511	12.720
RLA0_MOUSE	20	8	5.59E-04	60S acidic ribosomal protein P0 Rplp0	12238.544	16674.779	18487.339	9177.154
1433E_MOUSE	31	15	-04	5.63E 14-3-3 protein epsilon Ywhae			15824.356	8419.894
PRDX4_MOUSE	8	3	-04 3690.080 5.63E	7043.606 Peroxiredoxin-4 Prdx4	945.531	1185.477	2565.401	1117.493
RL26_MOUSE	11	4	5.65E-04	60S ribosomal protein L26 Rpl26	945.983	967.482	100.701	596.005
VASP_MOUSE	12	3	5.66E-04	Vasodilator-stimulated phosphoprotein Vasp	9740.326	10265.558	4594.236	511.728
CPNS1_MOUSE	9	4	5.81E-04	Calpain small subunit 1 Capns1	3951.229	3760.086	2127.385	1128.797

HMGN3_MOUSE	1	1	5.85E-04	High mobility group nucleosome-binding domain-containing protein 108.468 3 Hmgn3	115.068	7.118	2.841	
PTMS_MOUSE	2	1	6.00E-04	Parathymosin Ptms	10.805	211.321	44.901	8.956
ALDR_MOUSE	17	6	6.00E-04	Aldose reductase Akr1b1	457.081	817.226	1613.969	1546.364
SRBS1_MOUSE	19	3	6.05E-04	Sorbin and SH3 domain-containing protein 1 Sorbs1	196.330	240.233	167.223	402.865
GSHR_MOUSE	8	3	6.10E-04	Glutathione reductase, mitochondrial Gsr	192.420	480.853	474.280	310.656
SPF45_MOUSE	4	1	6.20E-04	Splicing factor 45 Rbm17	406.343	307.575	324.810	2.591
K2C72_MOUSE	13	1	6.21E-04	Keratin, type II cytoskeletal 72 Krt72	141.578	188.207	1812.614	1740.630
SAP18_MOUSE	2	1	6.26E-04	Histone deacetylase complex subunit SAP18 Sap18	109.965	57.175	1.321	0.282
HMGA2_MOUSE	3	1	6.30E-04	High mobility group protein HMGI-C Hmga2	5576.107	1113.750	8.527	105.433
P4HA2_MOUSE	3	1	6.43E-04	Prolyl 4-hydroxylase subunit alpha-2 P4ha2	268.191	361.150	149.129	1.153
DYHC1_MOUSE	73	13	6.44E-04	Cytoplasmic dynein 1 heavy chain 1 Dync1h1	383.617	707.608	1527.321	560.891
KMT5B_MOUSE	4	1	6.73E-04	Histone-lysine N-methyltransferase KMT5B Kmt5b	7.611	1634.615	7.048	2.707
GLO2_MOUSE	1	1	6.79E-04	Hydroxyacylglutathione hydrolase, mitochondrial Hagh	53.522	46.779	10.461	2.159

EDF1_MOUSE	5	2	6.79E-04	Endothelial differentiation-related factor 1 Edf1	730.258	548.458	53.088	66.097
ALD1_MOUSE	8	1	6.83E-04	Aldose reductase-related protein 1 Akr1b7	419.254	1076.503	833.356	641.933
WDR11_MOUSE	16	1	7.13E-04	WD repeat-containing protein 11 Wdr11	66.891	44.448	1358.829	366.063
ZFY26_MOUSE	21	4	7.14E-04	Zinc finger FYVE domain-containing protein 26 Zfyve26	128.403	1410.167	1778.640	1468.370
PLXD1_MOUSE	9	1	7.17E-04	Plexin-D1 Plxnd1	86.355	6509.129	3.980	4.458
IF4A3_MOUSE	21	9	7.21E-04	Eukaryotic initiation factor 4A-III Eif4a3	3027.808	3081.462	3222.708	1781.498
YBOX1_MOUSE	12	5	7.22E-04	Nuclease-sensitive element-binding protein 1 Ybx1	3641.548	3211.375	764.102	557.202
ANXA2_MOUSE	56	23	-04		14026.440	28472.111	36602.174	22649.005
DNPEP_MOUSE	8	4	-04	7.23E Annexin A2 Anxa2	1157.262	3346.164	367.055	372.605
			7.30E	Aspartyl aminopeptidase Dnpep				
SRSF1_MOUSE	13	5	7.50E-04	Serine/arginine-rich splicing factor 1 Srsf1	1412.615	1491.092	2786.918	1300.586
ACADV_MOUSE	18	4	7.51E-04	Very long-chain specific acyl-CoA dehydrogenase, mitochondrial Acadvl	612.094	808.695	1461.234	1605.749
MDR1A_MOUSE	18	3	7.56E-04	Multidrug resistance protein 1A Abcb1a	851.108	186.437	307.698	317.383
KLC1_MOUSE	17	2	7.65E-04	Kinesin light chain 1 Klc1	308.738	294.153	956.963	1526.598
GBB1_MOUSE	7	1	7.65E-04	Guanine nucleotide-binding protein G(I)/G(S)/G(T) subunit beta-1 Gnb1	4.404	34.216	560.955	264.938

GSTO1_MOUSE	10	6	7.72E-04	Glutathione S-transferase omega-1 Gsto1	3258.025	2876.207	5132.806	3400.548
AL1L2_MOUSE	26	6	7.75E-04	Mitochondrial 10-formyltetrahydrofolate dehydrogenase Aldh1l2	1908.986	1953.852	3468.608	2099.695
TYB10_MOUSE	3	1	7.82E	Thymosin beta-10 Tmsb10	3255.652	1205.880	49.071	150.874
IMA5_MOUSE	5	2	-04		448.384	188.501	96.681	447.660
			-04	8.04EImportin subunit alpha-5 Kpna1				
STRAP_MOUSE	5	2	8.24E-04	Serine-threonine kinase receptor-associated protein Strap	685.162	363.505	20.370	41.548

WASF1_MOUSE	6	1	8.35E-04	Wiskott-Aldrich syndrome protein family member 1 Wasf1	69.274	700.308	2512.677	818.933
RL4_MOUSE	18	7	8.40E-04	60S ribosomal protein L4 Rpl4	4541.049	4821.169	1704.367	988.206
AP2A2_MOUSE	10	1	8.46E-04	AP-2 complex subunit alpha-2 Ap2a2	396.745	90.560	223.854	195.772
ZSC10_MOUSE	11	1	8.65E-04	Zinc finger and SCAN domaincontaining protein 10 Zscan10	831.005	843.910	12.761	19.934
IF4G1_MOUSE	21	2	8.66E-04	Eukaryotic translation initiation factor 4 gamma 1 Eif4g1	59.403	177.781	27.313	111.279
FKBP3_MOUSE	10	3	8.67E-04	Peptidyl-prolyl cis-trans isomerase FKBP3 Fkbp3	410.465	276.345	107.330	92.653
DX39A_MOUSE	14	3	8.71E-04	ATP-dependent RNA helicase DDX39A Ddx39a	1767.153	964.899	1095.604	691.610
TERA_MOUSE	49	15	8.73E-04	Transitional endoplasmic reticulum ATPase Vcp	3123.606	2947.128	6063.089	2684.465
PFKAM_MOUSE	10	1	8.85E-04	ATP-dependent 6-phosphofructokinase, muscle type Pfkm	182.759	351.561	326.587	1176.666
ANLN_MOUSE	11	3		Anillin Anln	5030.024	8980.681	3689.452	4505.289

CO4B_MOUSE	15	2	-04 -04 8.86E 8.91E	Complement C4-B C4b	1214.339	1375.649	1821.487	1230.925
ASH2L_MOUSE	4	1	8.94E-04	Set1/Ash2 histone methyltransferase complex subunit ASH2 Ash2l	182.992	11.466	3.651	1.214
TCPD_MOUSE	26	9	8.96E-04	T-complex protein 1 subunit delta Cct4	1912.388	3246.277	1662.090	707.315
GDIB_MOUSE	28	11	8.98E-04	Rab GDP dissociation inhibitor beta Gdi2	1264.885	2735.500	2607.862	1948.616
RS3_MOUSE	21	13	8.98E-04	40S ribosomal protein S3 Rps3	8750.127	13207.377	15751.608	7365.594
ANKE1_MOUSE	24	2	9.11E-04	Ankyrin repeat and EF-hand domain-containing protein 1 Ankef1	96.377	210.851	372.096	378.117
TNNC2_MOUSE	4	1	9.32E-04	Troponin C, skeletal muscle Tnnc2	15.279	76.887	216.236	1859.206
DHB8_MOUSE	7	2	9.44E-04	Estradiol 17-beta-dehydrogenase 8 Hsd17b8	728.584	120.817	258.365	473.521
CAN2_MOUSE	19	6	9.46E-04	Calpain-2 catalytic subunit Capn2	1941.710	1112.149	589.502	742.143
LASP1_MOUSE	5	3	9.76E-04	LIM and SH3 domain protein 1 Lasp1	1556.616	2485.596	1148.483	857.852
OAT_MOUSE	11	7	9.80E-04	Ornithine aminotransferase, mitochondrial Oat	832.007	1127.732	1619.896	1938.923
KIFA3_MOUSE	13	1	9.95E-04	Kinesin-associated protein 3 Kifap3	1.760	893.735	0.000	2.317
RSSA_MOUSE	13	5	9.99E-04	40S ribosomal protein SA Rpsa	6468.321	5341.097	3984.791	3194.670
NDUAA_MOUSE	5	3	1.01E-03	NADH dehydrogenase [ubiquinone] 1 alpha subcomplex subunit 10, mitochondrial Ndufa10	395.509	324.370	813.760	829.067
PZP_MOUSE	15	3	1.03E-03	Pregnancy zone protein Pzp	13919.343	1135.059	3753.677	1200.209

NLRP3_MOUSE	13	4	1.03E-03	NACHT, LRR and PYD domainscontaining protein 3 Nlrp3	5249.488	12892.442	11562.573	8539.909
HNRPM_MOUSE	37	14	1.04E-03	Heterogeneous nuclear ribonucleoprotein M Hnrnpm	3906.815	2630.572	3207.090	2171.000
ACL6A_MOUSE	5	1	-03	Actin-like protein 6A Actl6a	112.464	191.652	6.413	4.204
RAB7A_MOUSE	11	4	1.06E-03 1.06E	Ras-related protein Rab-7a Rab7a	4303.874	4031.741	5216.813	2690.275
COPE_MOUSE	4	2	1.10E-03	Coatomer subunit epsilon Cope	564.457	1040.580	2060.887	986.909
DC1L1_MOUSE	13	2	1.11E-03	Cytoplasmic dynein 1 light intermediate chain 1 Dync1li1	177.063	170.377	504.143	189.791
OPA1_MOUSE	9	2	1.11E-03	Dynamin-like 120 kDa protein, mitochondrial Opa1	277.816	734.098	79.546	7.315
ELAV1_MOUSE	10	4	-03	ELAV-like protein 1 Elavl1	7268.065	4615.925	2082.288	1509.258
PLST_MOUSE	22	7	1.11E-03 1.14E	Plastin-3 Pls3	851.202	999.298	1929.968	1335.760
SNX2_MOUSE	10	1	1.16E-03	Sorting nexin-2 Snx2	590.230	833.413	1608.999	1599.008
MED6_MOUSE	2	1	1.18E-03	Mediator of RNA polymerase II transcription subunit 6 Med6	0.614	165.077	6.803	0.034
KMT5A_MOUSE	5	1	1.18E-03	N-lysine methyltransferase KMT5A Kmt5a	243.379	448.822	3222.943	1521.689
MIRO1_MOUSE	8	3	1.20E-03	Mitochondrial Rho GTPase 1 Rhot1	1924.866	693.311	333.009	169.900
MAP1A_MOUSE	24	2	1.20E-03	Microtubule-associated protein 1A Map1a	130.160	51.968	162.298	1.136
TRI72_MOUSE	8	4	1.22E-03	Tripartite motif-containing protein 72 Trim72	352.975	514.805	562.231	1361.874
K2C1_MOUSE	23	1	1.23E-03	Keratin, type II cytoskeletal 1 Krt1	8466.778	8519.520	7015.818	3392.453
DDX1_MOUSE	13	3	1.29E-03	ATP-dependent RNA helicase DDX1 Ddx1	300.521	441.131	152.972	93.886

EZRI_MOUSE	43	6	1.30E-03	Ezrin Ezr	778.980	74.082	267.390	77.922
SUCB1_MOUSE	16	3	1.30E-03	Succinate--CoA ligase [ADP-forming] subunit beta, mitochondrial Sucla2	627.230	785.043	1280.090	1640.599
FXR2_MOUSE	5	1	1.33E-03	Fragile X mental retardation syndrome-related protein 2 Fxr2	257.228	28.579	15.119	0.113
CLIP2_MOUSE	13	2	1.35E-03	CAP-Gly domain-containing linker protein 2 Clip2	66.097	83.077	225.281	99.514
NDUS3_MOUSE	6	2	1.37E-03	NADH dehydrogenase [ubiquinone] iron-sulfur protein 3, mitochondrial 2694.753 Ndufs3		1400.863	7762.021	4562.925
RBM39_MOUSE	11	1	-03	1.40E RNA-binding protein 39 Rbm39			705.844	637.381
TPM1_MOUSE	35	3	-03 379.878	-03 554.387			13166.292	4568.735
			1.41E	Tropomyosin alpha-1 chain Tpm1	4913.741	4906.899		
EIF3M_MOUSE	9	2	1.42E-03	Eukaryotic translation initiation factor 3 subunit M Eif3m	258.501	1.191	0.402	25.270
SYVC_MOUSE	24	2	1.46E-03	Valine--tRNA ligase Vars	217.436	239.620	103.378	88.438
K2C6A_MOUSE	36	1	1.46E-03	Keratin, type II cytoskeletal 6A Krt6a	3113.887	4307.420	9689.859	6377.187
CBPQ_MOUSE	7	2	1.49E	Carboxypeptidase Q Cpq	0.000	126.701	351.017	328.513
TBB3_MOUSE	40	5	-03				6020.416	2449.939
			-03	1.50ETubulin beta-3 chain Tubb3	431.980	2323.934		
PRAF3_MOUSE	7	2	1.50E-03	PRA1 family protein 3 Arl6ip5	381.728	354.164	714.925	732.630
MACF1_MOUSE	81	4	1.51E-03	Microtubule-actin cross-linking factor 1 Macf1	522.142	625.266	1274.267	880.676
CNN2_MOUSE	16	2	1.52E-03	Calponin-2 Cnn2	112.521	300.079	327.274	187.170

ROA2_MOUSE	16	6	1.52E-03	Heterogeneous nuclear ribonucleoproteins A2/B1 Hnrnpa2b1	6275.077	6895.395	18058.256	5153.689
MCM2_MOUSE	11	1	1.52E-03	DNA replication licensing factor MCM2 Mcm2	266.615	20.598	60.512	24.925
PP2AB_MOUSE	8	4	1.54E-03	Serine/threonine-protein phosphatase 2A catalytic subunit 2156.874 beta isoform Ppp2cb	1373.900		4489.634	3004.947
CCND1_MOUSE	6	1	1.57E	G1/S-specific cyclin-D1 Ccnd1	33.658	8.298	0.465	0.667
PCBP1_MOUSE	13	5	-03 -03	1.61EPoly(rC)-binding protein 1 Pcbp1	2017.790	1628.418	1078.942	495.587
MYL9_MOUSE	7	2	1.62E-03	Myosin regulatory light polypeptide 9 Myl9	998.084	948.837	641.018	386.273

DX39B_MOUSE	15	3	1.63E-03	Spliceosome RNA helicase Ddx39b Ddx39b	1893.881	984.843	1431.347	1212.635
CO1A1_MOUSE	8	2	1.63E-03	Collagen alpha-1(I) chain Col1a1	13.875	62.952	99.007	132.685
EI2BA_MOUSE	7	2	1.63E-03	Translation initiation factor eIF-2B subunit alpha Eif2b1	470.311	828.054	10.140	90.591
TCPB_MOUSE	38	11	1.64E-03	T-complex protein 1 subunit beta Cct2	2099.790	1462.678	3365.906	2614.191
PSD12_MOUSE	13	5	1.65E-03	26S proteasome non-ATPase regulatory subunit 12 Psmd12	658.172	269.899	596.130	463.732
DIAP3_MOUSE	18	2	1.65E-03	Protein diaphanous homolog 3 Diaph3	49.676	168.848	1514.726	933.732
CYTB_MOUSE	4	1	1.67E-03	Cystatin-B Cstb	676.190	22.009	0.548	194.855
PKDRE_MOUSE	12	2	1.70E-03	Polycystic kidney disease and receptor for egg jelly-related protein Pkdrej	1529.590	1578.654	994.901	699.485
SPT6H_MOUSE	19	1	1.72E-03	Transcription elongation factor SPT6 Supt6h	407.586	596.964	182.979	100.030

PRC2C_MOUSE	29	1	1.72E-03	Protein PRRC2C Prrc2c	1473.109	2283.416	1539.352	933.460
PSA7_MOUSE	11	4	1.72E-03	Proteasome subunit alpha type-7 Psma7	2443.685	3353.486	5750.843	3018.804
RHG01_MOUSE	6	3	1.75E-03	Rho GTPase-activating protein 1 Arhgap1	199.558	50.328	99.395	233.875
PRAF2_MOUSE	3	2	-03	PRA1 family protein 2 Praf2	169.445	414.183	294.454	144.153
RTN4_MOUSE	34	13	1.76E -03 1.77E	Reticulon-4 Rtn4	986.419	1810.584	3296.488	2736.617
CLPP_MOUSE	7	3	1.78E-03	ATP-dependent Clp protease proteolytic subunit, mitochondrial Clpp	1165.820	9.129	2023.352	218.236
HCD2_MOUSE	8	4	1.79E-03	3-hydroxyacyl-CoA dehydrogenase type-2 Hsd17b10	742.362	835.124	2270.609	1718.425
ICAL_MOUSE	15	3	1.80E-03	Calpastatin Cast	76.460	70.825	8.798	0.621
RS17_MOUSE	12	7	1.82E-03	40S ribosomal protein S17 Rps17	6605.641	3672.589	254.516	450.090
SYRC_MOUSE	11	4	1.84E-03	Arginine--tRNA ligase, cytoplasmic Rars	356.816	196.102	449.472	1463.341
TXND5_MOUSE	8	5	1.88E-03	Thioredoxin domain-containing protein 5 Txndc5	1337.431	795.048	694.903	343.984
KHK_MOUSE	5	1	1.88E-03	Ketohexokinase Khk	2119.088	4088.532	2626.835	5645.319

ARL8B_MOUSE	5	2	1.89E-03	ADP-ribosylation factor-like protein 8B Arl8b	1790.818	2408.260	3367.038	2219.689
MATR3_MOUSE	18	6	1.90E-03	Matrin-3 Matr3	1321.194	1276.399	2303.295	1902.099
CCAR2_MOUSE	7	1	1.92E-03	Cell cycle and apoptosis regulator protein 2 Ccar2	425.766	1931.999	6013.818	2887.505
TMED9_MOUSE	6	4	1.93E-03	Transmembrane emp24 domaincontaining protein 9 Tmed9	1104.762	1806.007	3236.896	2567.849

RGS10_MOUSE	5	1	1.93E-03	Regulator of G-protein signaling 10 Rgs10	77.122	79.058		10.390	4.435
ECHA_MOUSE	36	9	1.94E-03	Trifunctional enzyme subunit alpha, mitochondrial Hadha	682.547	1212.818		1113.014	1384.205
VIME_MOUSE	84	37	1.95E-03	Vimentin Vim	34073.864	39836.762		42782.054	19836.992
GSTM1_MOUSE	11	3	1.99E-03	Glutathione S-transferase Mu 1 Gstm1	996.708	1814.249		2122.533	717.064
CAPZB_MOUSE	12	2	2.02E-03	F-actin-capping protein subunit beta Capzb	3503.360	2337.544		731.398	229.834
COPA_MOUSE	25	2	2.05E-03	Coatomer subunit alpha Copa	1822.642	1862.972		2160.343	1161.814
DPYL3_MOUSE	24	5	2.06E-03	Dihydropyrimidinase-related protein 3 Dpysl3	1557.527	1538.097		2555.972	2533.296
RL12_MOUSE	3	1	2.07E-03	60S ribosomal protein L12 Rpl12	29458.825	32925.959	35512.734		21049.691
RS12_MOUSE	3	2	2.16E-03	40S ribosomal protein S12 Rps12	2142.522	1425.433	6176.473		4437.744
DDX3L_MOUSE; DDX3Y_MOUSE	24	1	2.17E-03	Putative ATP-dependent RNA helicase Pl10 D1Pas1	169.954	371.087		961.652	563.282
GSTP1_MOUSE; GSTP2_MOUSE	14	10	2.17E-03	Glutathione S-transferase P 1 Gstp1	10114.902	19978.829		21182.624	13473.609
RS23_MOUSE	5	1	-03	40S ribosomal protein S23 Rps23	3790.849	4832.648		500.557	2720.919
HYAS1_MOUSE	5	1	2.21E-03	Hyaluronan synthase 1 Has1	4156.798	4909.222		499.100	88.894
MCTS1_MOUSE	3	2	2.22E-03	Malignant T-cell-amplified sequence 1 Mcts1	656.915	1179.176		2351.710	1774.089
GLCM_MOUSE	7	1	-03	Glucosylceramidase Gba	348.562	305.905		882.447	1080.805
ZO1_MOUSE	13	3	25E-03 2.23E 2.	Tight junction protein ZO-1 Tjp1	132.076	115.465		10.350	5.613

SLAI2_MOUSE	8	2	2.26E-03	SLAIN motif-containing protein 2 Slain2	190.822	62.924		40.527	17.266
DDX21_MOUSE	27	5	2.26E-03	Nucleolar RNA helicase 2 Ddx21	493.789	743.020		698.801	1631.718
LAGE3_MOUSE	5	2	2.26E-03	EKC/KEOPS complex subunit Lage3 Lage3	239.778	166.035		2446.760	930.090

IMA1_MOUSE	9	3	2.27E-03	Importin subunit alpha-1 Kpna2	599.844	231.753	30.247	118.071
COOA1_MOUSE	7	1	2.27E-03	Collagen alpha-1(XXIV) chain Col24a1	275.744	62.622	0.292	0.009
EWS_MOUSE	8	2	2.28E-03	RNA-binding protein EWS Ewsr1	885.127	985.366	2942.086	2266.733
FBRL_MOUSE	14	3	2.29E-03	rRNA 2'-O-methyltransferase fibrillarin Fbl	688.135	1155.539	1775.696	1134.860
CHIP_MOUSE	5	2	2.30E-03	STIP1 homology and U boxcontaining protein 1 Stub1	177.833	223.883	111.640	2.179
RS7_MOUSE	15	9	2.33E-03	40S ribosomal protein S7 Rps7	2986.089	4806.046	12737.175	6082.414
IQGA1_MOUSE	56	18	2.34E-03	Ras GTPase-activating-like protein IQGAP1 Iqgap1	2956.894	4073.254	3758.280	3379.170
RL34_MOUSE	5	1	2.34E-03	60S ribosomal protein L34 Rpl34	239.229	6.048	333.937	657.530
PSA3_MOUSE	4	3	2.34E-03	Proteasome subunit alpha type-3 Psma3	3132.164	3634.486	3051.521	2162.465
MTCH2_MOUSE	4	3	2.36E-03	Mitochondrial carrier homolog 2 Mtch2	641.507	819.550	1870.930	1259.512
PDLI4_MOUSE	11	3	2.40E-03	PDZ and LIM domain protein 4 Pdlim4	252.260	862.117	1096.061	370.868
PPM1G_MOUSE	4	2	-03	Protein phosphatase 1G Ppm1g	742.155	504.831	1648.732	1337.002
CALR_MOUSE	21	11	-03 2.40E 2.44E	Calreticulin Calr	2000.307	5647.139	2233.928	2068.327
SSRA_MOUSE	4	1	2.47E-03	Translocon-associated protein subunit alpha Ssr1	1243.538	800.447	44.464	173.708

FNTA_MOUSE	6	1	2.54E-03	Protein farnesyltransferase/geranylgeranyltransferase type-1 subunit alpha Fnta	4701.228	3623.805	19543.877	36908.204
MRCKB_MOUSE	14	1	2.55E-03	Serine/threonine-protein kinase MRCK beta Cdc42bpb	3016.740	221.004	21.209	192.163
PLEC_MOUSE	228	33	-03	Plectin Plec	4620.670	5964.974	3911.482	2370.316
LEG1_MOUSE	16	6	-03 2.55E 2.58E	Galectin-1 Lgals1	1385.519	863.163	5974.153	1424.073
NCOR2_MOUSE	15	2	2.61E-03	Nuclear receptor corepressor 2 Ncor2	123.886	270.877	14.972	11.117
P4HA1_MOUSE	15	2	2.62E-03	Prolyl 4-hydroxylase subunit alpha-1 P4ha1	332.848	396.282	178.854	1016.564
PP14B_MOUSE	2	1	2.64E-03	Protein phosphatase 1 regulatory subunit 14B Ppp1r14b	4073.596	4255.314	5.986	164.666
CENPE_MOUSE	43	1	2.66E-03	Centromere-associated protein E Cenpe	76.117	240.396	257.867	137.162
ATX2_MOUSE	12	1	2.66E-03	Ataxin-2 Atxn2	411.359	298.626	30.888	100.795
MYPT1_MOUSE	14	2	2.70E-03	Protein phosphatase 1 regulatory subunit 12A Ppp1r12a	231.457	163.980	1263.454	394.458
RS15_MOUSE	8	5	2.70E-03	40S ribosomal protein S15 Rps15	7711.166	7560.791	8685.095	4495.400
NDUB3_MOUSE	1	1	2.74E-03	NADH dehydrogenase [ubiquinone] 1 beta subcomplex subunit 3 Ndufb3	94.778	123.287	1684.680	1399.221
ARP2_MOUSE	14	7	2.75E-03	Actin-related protein 2 Actr2	1446.146	602.488	521.245	285.895
GNA11_MOUSE	7	1	2.76E-03	Guanine nucleotide-binding protein subunit alpha-11 Gna11	64.461	1.458	1.357	9.551
RTCA_MOUSE	7	3	2.77E-03	RNA 3'-terminal phosphate cyclase RtcA	3575.781	402.632	18.283	90.085
CISY_MOUSE	23	8		Citrate synthase, mitochondrial Cs	3312.885	4041.233	7352.439	7347.437

OTOAN_MOUSE	11	1	2.81E-03 2.82E-03	Otoancorin Otoa	13.746	0.001	218.485	81.473
DDAH2_MOUSE	5	2	2.85E-03	N(G),N(G)-dimethylarginine dimethylaminohydrolase 2 Ddah2	717.065	1024.605	1649.951	972.935
FKBP9_MOUSE	4	1	2.88E-03	Peptidyl-prolyl cis-trans isomerase FKBP9 Fkbp9	8440.077	518.436	480.682	774.109
STRBP_MOUSE	6	2	2.91E-03	Spermatid perinuclear RNA-binding protein Strbp	4428.375	1098.752	2589.342	5125.501
TOIP1_MOUSE	8	3	2.91E-03	Torsin-1A-interacting protein 1 Tor1aip1	248.783	223.811	134.991	0.122
6PGD_MOUSE	15	8	2.91E-03	6-phosphogluconate dehydrogenase, decarboxylating Pgd	1807.410	2891.057	1668.053	1243.085
SODC_MOUSE	8	5	2.92E-03	Superoxide dismutase [Cu-Zn] Sod1	414.146	1791.648	2094.775	3038.578
DLRB1_MOUSE	4	1	2.94E-03	Dynein light chain roadblock-type 1 Dynlrb1	580.941	1144.206	1035.857	2166.927
NUP37_MOUSE	3	1	2.96E-03	Nucleoporin Nup37 Nup37	296.047	231.834	8.557	38.173
SC23B_MOUSE	12	1	2.97E-03	Protein transport protein Sec23B Sec23b	72.983	94.381	192.651	134.848
ENOA_MOUSE	58	20	2.98E-03	Alpha-enolase Eno1	17577.316	14072.958	9247.410	10113.839

SPTN1_MOUSE	95	14	3.00E-03	Spectrin alpha chain, nonerythrocytic 1 Sptan1	1233.105	2378.910	3343.829	2283.736
PDLI1_MOUSE	9	4	3.01E-03	PDZ and LIM domain protein 1 Pdlim1	1011.091	1178.013	2182.570	992.814
MA1B1_MOUSE	5	2	3.01E-03	Endoplasmic reticulum mannosyloligosaccharide 1,2-alphamannosidase Man1b1	420.803	1472.971	10712.395	2157.419

USMG5_MOUSE	2	2	3.05E-03	Up-regulated during skeletal muscle growth protein 5 Usmg5	157.483		89.980	1454.527	1491.657
UBE2N_MOUSE	8	3	3.09E-03	Ubiquitin-conjugating enzyme E2 N Ube2n	2505.300		1058.949	5463.676	3831.320
IDHP_MOUSE	14	5	3.10E-03	Isocitrate dehydrogenase [NADP], mitochondrial Idh2	1464.204		1620.179	6737.908	2751.200
PIAS2_MOUSE	13	2	3.12E-03	E3 SUMO-protein ligase PIAS2 Pias2	271.801		227.753	485.695	415.459
IQGA2_MOUSE	16	3	3.12E-03	Ras GTPase-activating-like protein IQGAP2 Iqgap2	280.168		944.594	111.789	236.635
HEXI1_MOUSE	2	1	-03	Protein HEXIM1 Hexim1	202.603		10.293	3.728	0.528
MYH14_MOUSE	50	4	3.13E-03	Myosin-14 Myh14	357.055		342.369	940.931	962.153
UQCC2_MOUSE	2	1	3.27E-03	Ubiquinol-cytochrome-c reductase complex assembly factor 2 Uqcc2	154.808		186.552	910.450	692.251
ANM5_MOUSE	10	3	3.32E-03	Protein arginine Nmethyltransferase 5 Prmt5	275.065		370.587	665.569	519.954
GLOD4_MOUSE	9	6	3.33E-03	Glyoxalase domain-containing protein 4 Glod4	2164.837		1878.753	3001.305	2002.024
ACTN4_MOUSE	53	11	3.36E-03	Alpha-actinin-4 Actn4	3298.906		3068.458	3894.537	826.838
LAP4A_MOUSE	2	1	3.37E-03	Lysosomal-associated transmembrane protein 4A Laptm4a	846.749		17.027	0.789	9.745
RBM8A_MOUSE	4	1	3.39E-03	RNA-binding protein 8A Rbm8a	2138.829		1740.488	23.209	177.843
LDHA_MOUSE	33	13	3.39E-03	L-lactate dehydrogenase A chain Ldha	6029.500		6244.892	5749.602	2921.872
MYL6B_MOUSE	9	4	-03	Myosin light chain 6B Myl6b	397.705		607.458	2787.731	784.223
FUS_MOUSE	13	5	3.44E-03 3.52E-03	RNA-binding protein FUS Fus	1024.455 16861.585	852.575 14511.017		1698.313	1016.099
HEM3_MOUSE	9	3	3.53E-03	Porphobilinogen deaminase Hmbs				7952.181	9099.341

PTN22_MOUSE	14	4	3.54E-03	Tyrosine-protein phosphatase nonreceptor type 22 Ptpn22	429.882	52.506	270.826	304.516
PPCE_MOUSE	16	5	3.59E-03	Prolyl endopeptidase Prep	1477.114	1074.928	2142.913	1328.777
KANK2_MOUSE	8	1	3.60E-03	KN motif and ankyrin repeat domain-containing protein 2 Kank2	53.430	2.468	60.225	113.970
DYH3_MOUSE	33	2	3.61E-03	Dynein heavy chain 3, axonemal Dnah3	4.611	15.065	60.199	373.797
ANXA7_MOUSE	7	3	3.62E-03	Annexin A7 Anxa7	394.521	534.837	1023.910	780.006
CAP2_MOUSE	6	1	3.63E-03	Adenylyl cyclase-associated protein 2 Cap2	419.525	297.308	974.896	1544.197
P5CS_MOUSE	15	3	3.64E-03	Delta-1-pyrroline-5-carboxylate synthase Aldh18a1	376.580	499.729	1401.307	920.837
SEPT6_MOUSE	7	2	3.65E-03	Septin-6 Sept6	292.091	198.977	338.260	346.310
NSUN2_MOUSE	10	2	3.65E-03	tRNA (cytosine(34)-C(5))methyltransferase Nsun2	79.703	95.319	423.630	147.910
IPO5_MOUSE	22	8	-03	Importin-5 Ipo5	1306.964	2514.762	1521.007	1108.924
RYR3_MOUSE	41	6	-03 3.73E 3.73E	Ryanodine receptor 3 Ryr3	784.218	896.936	1801.559	1116.286
ATPB_MOUSE	42	25	3.74E-03	ATP synthase subunit beta, mitochondrial Atp5b	11321.558	17309.739	30065.861	27242.484
FLNC_MOUSE	82	18	3.77E-03	Filamin-C Flnc	1609.931	2723.404	4402.811	3789.825
PGH1_MOUSE	4	2	3.78E-03	Prostaglandin G/H synthase 1 Ptgs1	177.080	20.542	14.300	105.986
NB5R1_MOUSE	6	3	3.90E-03	NADH-cytochrome b5 reductase 1 Cyb5r1	478.197	544.431	2758.140	3016.211
PTGIS_MOUSE	11	4	3.90E-03	Prostacyclin synthase Ptgis	213.833	320.092	957.920	441.760
VDAC1_MOUSE	12	6	3.93E-03	Voltage-dependent anion-selective channel protein 1 Vdac1	5445.083	7197.830	15472.861	16708.504
ITA3_MOUSE	12	1		Integrin alpha-3 Itga3	561.912	584.815	116.708	154.479

ANXA3_MOUSE	20	7	-03 -03 3.93E 3.93E	Annexin A3 Anxa3	1811.571	3812.079	6928.235	2086.467
G6PD1_MOUSE	14	3	3.93E-03	Glucose-6-phosphate 1dehydrogenase X G6pdx	149.614	414.207	82.453	30.681
CAPR1_MOUSE	4	1	3.95E-03	Caprin-1 Caprin1	2321.795	2137.901	424.151	519.568
SRGP3_MOUSE	13	2	4.06E-03	SLIT-ROBO Rho GTPase-activating protein 3 Srgap3	2848.399	2084.020	11887.825	4922.945
PUR9_MOUSE	20	7	4.20E-03	Bifunctional purine biosynthesis protein PURH Atic	959.632	1275.328	784.502	595.555
NOP56_MOUSE	10	1	-03 4.21E		3066.711	2499.246	4666.167	5334.633
ACTB_MOUSE	56	4	22E-03 Nucleolar protein 56 Nop56 4. Actin, cytoplasmic 1 Actb		11125.286	12075.387	16246.995	10727.920
CBX3_MOUSE	9	4	4.25E-03	Chromobox protein homolog 3 Cbx3	2858.296	1720.745	1296.951	829.130
ZDBF2_MOUSE	19	2	4.28E-03	DBF4-type zinc finger-containing protein 2 homolog Zdbf2	518.193	1381.724	4607.616	3159.071
ODO1_MOUSE	19	6	4.28E-03	2-oxoglutarate dehydrogenase, mitochondrial Ogdh	125.529	359.944	377.528	540.608
NDUS2_MOUSE	3	1	4.29E-03	NADH dehydrogenase [ubiquinone] iron-sulfur protein 2, mitochondrial Ndufs2	378.065	962.773	564.685	1066.692
LRP1_MOUSE	34	3	4.32E-03	Prolow-density lipoprotein receptor-related protein 1 Lrp1	630.659	993.052	761.212	484.067
COPZ1_MOUSE	3	3	4.39E	Coatomer subunit zeta-1 Copz1	705.501	721.810	1145.680	256.892
ILK_MOUSE	14	4	-03 -03 4.43E ‹	Integrin-linked protein kinase	449.993	646.065	153.748	173.412
RS15A_MOUSE	7	1	4.43E-03	40S ribosomal protein S15a	2133.820	109.774	394.244	264.157

				Rps15a				
LMNA_MOUSE	65	14	4.46E-03	Prelamin-A/C Lmna	13059.062	13928.723	23035.252	24137.520
PA2G4_MOUSE	16	8	4.53E-03	Proliferation-associated protein 2G4 Pa2g4	2931.876	2594.114	2260.075	1698.674
RL17_MOUSE	6	4	4.58E-03	60S ribosomal protein L17 Rpl17	487.789	105.790	1.599	19.441
NQO1_MOUSE	6	2	4.60E-03	NAD(P)H dehydrogenase [quinone] 1 Nqo1	1991.231	2538.036	1794.994	641.942
UBXN4_MOUSE	4	2	4.64E-03	UBX domain-containing protein 4 Ubxn4	4266.851	3307.422	1664.710	2029.683
TPM4_MOUSE	24	5	4.69E-03	Tropomyosin alpha-4 chain Tpm4	1914.026	2964.044	875.406	549.625
TISD_MOUSE	3	1	4.70E-03	mRNA decay activator protein ZFP36L2 Zfp36l2	28.276	107.572	222.487	1261.639
RL38_MOUSE	4	2	4.72E-03	60S ribosomal protein L38 Rpl38	1173.021	1040.019	3638.560	2020.070
CSRP1_MOUSE	7	3	4.82E-03	Cysteine and glycine-rich protein 1 Csrp1	1959.284	2054.255	2086.548	985.557
PRP8_MOUSE	40	2	4.85E-03	Pre-mRNA-processing-splicing factor 8 Prpf8	2219.593	1636.264	2999.297	2131.124
LONM_MOUSE	32	10	4.85E-03	Lon protease homolog, mitochondrial Lonp1	1460.088	1721.184	2819.884	3092.220
NEMF_MOUSE	10	1	4.86E-03	Nuclear export mediator factor Nemf Nemf	4.270	124.827	33.467	1.629
UBE2K_MOUSE	6	2	4.89E-03	Ubiquitin-conjugating enzyme E2 K Ube2k	469.135	1182.689	2101.809	709.128
SYSC_MOUSE	13	9	4.93E-03	Serine--tRNA ligase, cytoplasmic Sars	1205.802	1355.263	2761.317	1810.738
FHL3_MOUSE	4	2	4.96E-03	Four and a half LIM domains protein 3 Fhl3	686.364	1098.506	1317.444	722.372

NDUB8_MOUSE	3	2	5.02E-03	NADH dehydrogenase [ubiquinone] 1 beta subcomplex subunit 8, mitochondrial Ndufb8	1916.153	698.781	269.966	688.754
SERPH_MOUSE	34	16	5.14E-03	Serpin H1 Serpinh1	6053.351	12898.582	14637.886	12965.432
NGBR_MOUSE	2	1	5.15E-03	Dehydrodolichyl diphosphate synthase complex subunit Nus1 Nus1	587.669	11.472	149.925	936.609
LRC59_MOUSE	12	4	5.23E-03	Leucine-rich repeat-containing protein 59 Lrrc59	2557.086	3377.156	2465.545	1524.396
SRP19_MOUSE	2	1	5.26E-03	Signal recognition particle 19 kDa protein Srp19	570.291	756.139	6805.491	2913.972
RSU1_MOUSE	7	4	5.29E-03	Ras suppressor protein 1 Rsu1	3569.460	4367.685	4210.114	2313.372
UBP42_MOUSE	12	2	5.36E-03	Ubiquitin carboxyl-terminal hydrolase 42 Usp42	82.049	681.080	151.912	6.531
ESYT1_MOUSE	24	7	5.40E-03	Extended synaptotagmin-1 Esyt1	1496.353	2192.691	1602.429	1568.324
SPCS3_MOUSE	3	1	5.53E-03	Signal peptidase complex subunit 3 Spcs3	465.539	1202.035	130.853	893.282
FABP5_MOUSE	3	2	5.54E-03	Fatty acid-binding protein, epidermal Fabp5	437.546	76.389	922.633	276.269
CIRBP_MOUSE	1	1	5.54E-03	Cold-inducible RNA-binding protein Cirbp	220.809	113.832	703.308	570.785
SCRN1_MOUSE	4	2	-03	Secernin-1 Scrn1	150.593	91.158	0.503	38.478
RL22_MOUSE	4	2	5.59E-03 5.60E	60S ribosomal protein L22 Rpl22	5088.008	3225.355	4608.915	2663.639
PSA6_MOUSE	7	4	5.60E-03	Proteasome subunit alpha type-6 Psma6	5294.920	4036.673	7795.658	4645.827
SERA_MOUSE	28	8	5.62E-03	D-3-phosphoglycerate dehydrogenase Phgdh	1549.564	1861.193	1037.669	1047.701
AATC_MOUSE	6	3	5.74E-03	Aspartate aminotransferase, cytoplasmic Got1	107.140	376.109	714.544	442.249

BLVRB_MOUSE	5	2	5.82E-03	Flavin reductase (NADPH) Blvrb	263.469	238.656		495.154	152.753
EIF3K_MOUSE	4	1	5.86E-03	Eukaryotic translation initiation factor 3 subunit K Eif3k	803.819	637.978		0.000	204.922
COPG1_MOUSE	18	2	5.87E-03	Coatomer subunit gamma-1 Copg1	143.548	53.678		16.852	11.735
YBOX3_MOUSE	8	3	5.90E-03	Y-box-binding protein 3 Ybx3	461.078	735.234		1571.222	751.610
ML12B_MOUSE	7	2	5.95E-03	Myosin regulatory light chain 12B Myl12b	13588.369	20093.566		23179.361	11804.252
BZW2_MOUSE	7	1	5.97E-03	Basic leucine zipper and W2 domain-containing protein 2 Bzw2	913.241	11.801		60.085	19.742
DDRGK_MOUSE	3	1	6.03E-03	DDRGK domain-containing protein 1 Ddrgk1	69.878	0.150		71.575	146.633
NMDE1_MOUSE	14	2	6.10E-03	Glutamate receptor ionotropic, NMDA 2A Grin2a	202.964	388.991		151.415	124.733
TNNT3_MOUSE	8	3	6.12E-03	Troponin T, fast skeletal muscle Tnnt3	734.110	2318.374		2067.401	1155.477
TPIS_MOUSE	17	5	6.17E-03	Triosephosphate isomerase Tpi1	870.566	689.147		57.525	238.129
DLDH_MOUSE	17	6	6.18E-03	Dihydrolipoyl dehydrogenase, mitochondrial Dld	1014.587	1136.963		3001.150	2401.820
DHX30_MOUSE	9	1	6.20E-03	Putative ATP-dependent RNA helicase DHX30 Dhx30	3070.884	1001.984		63.438	148.711
SYNJ2_MOUSE	18	3	-03	Synaptojanin-2 Synj2	4790.349	3681.680		9239.668	4093.491
BASI_MOUSE	2	1	-03 6.20E 6.32E	Basigin Bsg	366.650	56.376		24.366	66.283
SC61B_MOUSE	1	1	6.32E-03	Protein transport protein Sec61 subunit beta Sec61b	460.884	565.010		253.814	29.858
IL22_MOUSE	3	1	6.34E	Interleukin-22 Il22	117.256	0.246		437.226	1707.444
RINI_MOUSE	9	3	6.35E	Ribonuclease inhibitor Rnh1	2193.904	1661.529	3895.771		3657.794
ENPL_MOUSE	44	15		Endoplasmin Hsp90b1	7568.486	11201.528	12077.310		4750.787

RL30_MOUSE	5	2	6.38E-03 6.42E-03	60S ribosomal protein L30 Rpl30	2255.767	565.258		792.540	708.343
CG043_MOUSE	4	1	6.47E-03	Uncharacterized protein C7orf43 homolog	1065.445	2159.538		7681.379	3699.850
MRCKA_MOUSE	14	1	6.47E-03	Serine/threonine-protein kinase MRCK alpha Cdc42bpa	431.837	1798.033		2241.534	3044.202
RS19_MOUSE	9	4	6.48E-03 6.53E-03	40S ribosomal protein S19 Rps19	1849.977	432.565		364.642	1480.644
RBM25_MOUSE	9	4		RNA-binding protein 25 Rbm25	169.816	128.869		239.283	167.830

DOCK1_MOUSE	20	2	6.53E-03	Dedicator of cytokinesis protein 1 Dock1	704.566	1508.381	1002.761	716.689
RL23_MOUSE	6	3	6.53E-03	60S ribosomal protein L23 Rpl23	1193.189	2107.766	4818.303	2398.650
ERP29_MOUSE	7	4	6.55E-03	Endoplasmic reticulum resident protein 29 Erp29	975.116	1573.565	2752.842	1680.407
DHYS_MOUSE	4	1	6.57E-03	Deoxyhypusine synthase Dhps	117.669	4.535	2.095	73.589
RAGP1_MOUSE	15	2	6.58E-03	Ran GTPase-activating protein 1 Rangap1	2017.613	1568.984	1548.678	1305.820
RUXF_MOUSE	3	3	6.58E-03	Small nuclear ribonucleoprotein F Snrpf	513.054	40.881	532.313	195.967
PDIA3_MOUSE	34	20	6.63E-03	Protein disulfide-isomerase A3 Pdia3	1414.696	2396.175	5809.902	2316.428
CSN1_MOUSE	4	3	6.68E-03	COP9 signalosome complex subunit 1 Gps1	104.230	652.957	539.676	1897.086
SYWC_MOUSE	11	3	6.73E-03	Tryptophan--tRNA ligase, cytoplasmic Wars	243.469	289.484	677.652	610.594
CBR1_MOUSE	5	3	6.75E-03	Carbonyl reductase [NADPH] 1 Cbr1	611.573	698.287	500.340	316.258

SYYC_MOUSE	17	4	6.80E-03	Tyrosine--tRNA ligase, cytoplasmic Yars	1277.979	1487.988	2605.773	1924.514
K22E_MOUSE	33	9	6.86E-03	Keratin, type II cytoskeletal 2 epidermal Krt2	2788.286	3146.131	10185.718	4360.586
ACLY_MOUSE	26	5	6.88E-03	ATP-citrate synthase Acly	931.101	1290.325	701.452	427.936
RL22L_MOUSE	1	1	6.88E-03	60S ribosomal protein L22-like 1 Rpl22l1	709.511	286.569	10.796	111.029
UBA1_MOUSE	33	12	6.90E-03	Ubiquitin-like modifier-activating enzyme 1 Uba1	2458.755	3024.518	5001.008	2590.472
HMGB2_MOUSE	12	1	7.05E-03	High mobility group protein B2 Hmgb2	583.848	355.559	56.070	86.072
KTHY_MOUSE	4	1	-03	Thymidylate kinase Dtymk	77.571	118.474	5.780	0.000
RL10_MOUSE	8	2	7.10E -03 7.12E	60S ribosomal protein L10 Rpl10	2733.357	6148.982	6713.892	3374.482
ATPA_MOUSE	57	21	7.13E-03	ATP synthase subunit alpha, mitochondrial Atp5a1	3837.661	4367.053	11786.345	14441.721
DDX47_MOUSE	6	1	7.14E-03	Probable ATP-dependent RNA helicase DDX47 Ddx47	49.429	6.470	3.621	62.160
AP2A1_MOUSE	29	4	7.14E-03	AP-2 complex subunit alpha-1 Ap2a1	55.675	91.252	93.636	207.888

RALB_MOUSE	4	1	7.15E-03	Ras-related protein Ral-B Ralb	12.988	0.000	4.321	24.258
STML2_MOUSE	6	2	7.18E-03	Stomatin-like protein 2, mitochondrial Stoml2	4.528	1.872	15.146	215.527
RAN_MOUSE	9	2	7.19E-03	GTP-binding nuclear protein Ran Ran	3922.788	3362.499	7998.892	3096.969
THOC4_MOUSE	7	2	-03	THO complex subunit 4 Alyref	2084.942	2077.491	41.654	554.014
DPP9_MOUSE	8	2	7.20E -03 7.23E	Dipeptidyl peptidase 9 Dpp9	714.919	577.258	142.310	85.394

MCM4_MOUSE	15	3	7.30E-03	DNA replication licensing factor MCM4 Mcm4	1137.551	1025.383	642.806	516.871
GRIK4_MOUSE	7	1	7.34E-03	Glutamate receptor ionotropic, kainate 4 Grik4	48.224	0.000	23.619	335.723
BLM_MOUSE	14	2	7.52E-03	Bloom syndrome protein homolog Blm	1938.308	467.488	107.620	190.047
HNRLL_MOUSE	5	1	7.62E-03	Heterogeneous nuclear ribonucleoprotein L-like Hnrnpll	537.519	657.560	76.136	410.429
GLYC_MOUSE	5	1	7.63E-03	Serine hydroxymethyltransferase, cytosolic Shmt1	74.037	0.000	15.506	1.715
ACADS_MOUSE	7	2	7.78E-03	Short-chain specific acyl-CoA dehydrogenase, mitochondrial Acads	267.801	305.406	686.508	628.100
PRP4_MOUSE	6	1	7.78E-03	U4/U6 small nuclear ribonucleoprotein Prp4 Prpf4	26.080	87.371	832.616	581.113
DYN1_MOUSE	24	1	7.82E-03	Dynamin-1 Dnm1	877.908	126.125	276.445	280.479
TNNI2_MOUSE	7	5	7.90E-03	Troponin I, fast skeletal muscle Tnni2	3656.017	2026.280	3276.847	2319.439
SC23A_MOUSE	12	2	7.90E-03	Protein transport protein Sec23A Sec23a	478.122	572.136	1113.991	878.239
ZYX_MOUSE	10	4	7.91E-03	Zyxin Zyx	3555.233	3139.579	4452.607	2263.353
BIG1_MOUSE	14	3	7.94E-03	Brefeldin A-inhibited guanine nucleotide-exchange protein 1 Arfgef1	2144.397	143.961	615.117	973.887
GRPE1_MOUSE	6	1	8.00E-03	GrpE protein homolog 1, mitochondrial Grpel1	1.690	38.492	63.268	716.929
SDCB1_MOUSE	5	1	8.00E-03	Syntenin-1 Sdcbp	462.758	101.492	63.133	17.069
ITPR2_MOUSE	22	2	8.05E-03	Inositol 1,4,5-trisphosphate receptor type 2 Itpr2	1944.483	1915.301	3347.427	780.068

PPID_MOUSE	16	3	8.05E-03	Peptidyl-prolyl cis-trans isomerase D Ppid	507.537	241.969	506.083	461.934
LEG3_MOUSE	10	5	8.13E-03	Galectin-3 Lgals3	12534.887	11375.086	5412.228	4565.582
IFT52_MOUSE	6	1	8.13E-03	Intraflagellar transport protein 52 homolog Ift52	1150.775	3702.658	7674.258	5384.204
AN32A_MOUSE	8	3	8.13E-03	Acidic leucine-rich nuclear phosphoprotein 32 family member A Anp32a	538.485	810.499	1894.096	1198.252
AGRF2_MOUSE	17	1	8.13E-03	Adhesion G-protein coupled receptor F2 Adgrf2	2969.004	114.762	114.053	788.094
U5S1_MOUSE	22	3	8.14E-03	116 kDa U5 small nuclear ribonucleoprotein component Eftud2	450.462	690.808	441.594	504.192
CAH13_MOUSE	4	4	-03	Carbonic anhydrase 13 Ca13	1924.007	2162.801	2620.644	900.007
DYN2_MOUSE	36	5	8.19E -03 8.31E	Dynamin-2 Dnm2	445.747	1236.538	1413.947	1394.654
NLTP_MOUSE	4	1	8.31E-03	Non-specific lipid-transfer protein Scp2	270.000	607.882	989.481	1507.786
TSPO_MOUSE	1	1	8.34E-03	Translocator protein Tspo	0.000	0.000	145.914	0.276
MAP6_MOUSE	11	1	8.40E-03	Microtubule-associated protein 6 Map6	19028.160	1094.448	53.332	322.819
ACSL4_MOUSE	11	2	8.43E-03	Long-chain-fatty-acid--CoA ligase 4 Acsl4	1080.546	2405.721	2802.338	2520.977
ITA5_MOUSE	6	1	8.45E-03	Integrin alpha-5 Itga5	2570.527	429.000	536.241	41.598
WBP2_MOUSE	4	1	8.47E-03	WW domain-binding protein 2 Wbp2	172.717	15.047	2.518	118.229
COQ9_MOUSE	4	2	8.48E-03	Ubiquinone biosynthesis protein COQ9, mitochondrial Coq9	405.726	891.265	1153.846	1042.337
PALLD_MOUSE	12	1	8.51E-03	Palladin Palld	164.049	12.581	90.760	179.245
TTC17_MOUSE	14	2	8.55E-03	Tetratricopeptide repeat protein 17 Ttc17	1128.665	1206.735	2694.128	1112.244

HCDH_MOUSE	5	2	8.56E-03	Hydroxyacyl-coenzyme A dehydrogenase, mitochondrial Hadh	336.488	470.024	565.353	969.392
ARC1B_MOUSE	12	2	8.71E-03	Actin-related protein 2/3 complex subunit 1B Arpc1b	2641.471	5014.959	4533.985	2474.995
CH60_MOUSE	54	24	8.74E-03	60 kDa heat shock protein, mitochondrial Hspd1	6477.860	3824.077	5704.646	4834.828

NOP16_MOUSE	6	1	8.84E-03	Nucleolar protein 16 Nop16	205.656	60.192	7.329	5.194
DNJA1_MOUSE	9	5	8.86E-03	DnaJ homolog subfamily A member 1 Dnaja1	2957.629	5044.759	4151.054	2902.328
IF4E2_MOUSE	6	2	8.86E-03	Eukaryotic translation initiation factor 4E type 2 Eif4e2	1974.776	4262.323	5805.043	3505.352
IPO4_MOUSE	18	1	-03	8.87E Importin-	0.567	216.638	0.074	0.082
RS25_MOUSE	6	2	-03	4 Ipo4	14702.921	17686.307	19663.395	12790.477
			8.93E	40S ribosomal protein S25 Rps25				
EIF3E_MOUSE	13	4	8.96E-03	Eukaryotic translation initiation factor 3 subunit E Eif3e	189.471	47.881	341.290	227.107
TPPP3_MOUSE	6	2	9.00E-03	Tubulin polymerization-promoting protein family member 3 Tppp3	874.949	614.028	786.338	331.324
CCDC8_MOUSE	12	1	9.06E-03	Coiled-coil domain-containing protein 8 homolog Ccdc8	445.654	640.767	1709.653	808.333
ABCD2_MOUSE	14	1	9.17E-03	ATP-binding cassette sub-family D member 2 Abcd2	2648.852	3995.515	613.471	239.624
TRI23_MOUSE	4	1	9.20E-03	E3 ubiquitin-protein ligase TRIM23 Trim23	16.350	3.314	520.401	200.762
PSMD7_MOUSE	6	5	9.21E-03	26S proteasome non-ATPase regulatory subunit 7 Psmd7	886.985	853.964	595.599	483.542
SRCA_MOUSE	15	5	9.25E-03	Sarcalumenin Srl	248.329	421.629	960.951	1439.245
TCPW_MOUSE	8	2	9.33E-03	T-complex protein 1 subunit zeta-2	3.266	1.743	21.267	36.383

				Cct6b				
COMD3_MOUSE	4	1	9.36E-03	COMM domain-containing protein 3 Commd3	2928.806	3533.413	4488.323	2309.879
COF1_MOUSE	16	3	9.49E-03	Cofilin-1 Cfl1	9051.613	5370.348	2946.053	1371.924
LRFN1_MOUSE	5	1	9.61E-03	Leucine-rich repeat and fibronectin type III domain-containing protein 1 Lrfn1	808.853	150.541	14.495	46.094
ISY1_MOUSE	4	1	9.75E-03	Pre-mRNA-splicing factor ISY1 homolog Isy1	1143.600	1385.482	1127.614	173.631
PBDC1_MOUSE	5	1	9.77E	Protein PBDC1 Pbdc1	1098.865	1736.834	4023.436	1705.457
TPM3_MOUSE	31	3	-03 -03	9.78ETropomyosin alpha-3 chain pm3	3405.974	1923.228	2714.602	323.089
AN32B_MOUSE	10	1	9.80E-03	Acidic leucine-rich nuclear phosphoprotein 32 family member B Anp32b	17.303	84.963	1768.595	10.338

MD2L1_MOUSE	1	1	9.87E-03	Mitotic spindle assembly checkpoint protein MAD2A Mad2l1	2535.804	2389.206	788.205	763.698
LPPRC_MOUSE	46	9	1.01E-02	Leucine-rich PPR motif-containing protein, mitochondrial Lrpprc	4435.557	1690.837	667.450	674.403
BAG3_MOUSE	20	7	1.01E-02	BAG family molecular chaperone regulator 3 Bag3	778.571	944.436	442.012	556.072
LSM3_MOUSE	2	1	1.01E-02	U6 snRNA-associated Sm-like protein LSm3 Lsm3	312.955	27.498	112.127	489.464
DAB2_MOUSE	8	1	1.01E-02	Disabled homolog 2 Dab2	9280.490	3060.688	2752.519	832.454
G3ST3_MOUSE	13	2	1.02E-02	Galactose-3-O-sulfotransferase 3 Gal3st3	26.747	145.321	30.023	77.803
EF1G_MOUSE	16	8	1.02E-02	Elongation factor 1-gamma Eef1g	4706.909	2075.106	1180.880	1454.326

2AAA_MOUSE	24	9	1.03E-02	Serine/threonine-protein phosphatase 2A 65 kDa regulatory subunit A alpha isoform Ppp2r1a	2458.610	3326.657	4753.360	2739.341
RAB1A_MOUSE	11	3	1.03E-02	Ras-related protein Rab-1A Rab1A	388.996	241.166	304.948	41.840
DNJA2_MOUSE	12	5	1.04E-02	DnaJ homolog subfamily A member 2 Dnaja2	336.460	143.199	827.435	434.295
MCM5_MOUSE	20	4	1.05E-02	DNA replication licensing factor MCM5 Mcm5	613.021	835.530	2403.510	397.123
PGK2_MOUSE	14	1	1.06E-02	Phosphoglycerate kinase 2 Pgk2	107.196	111.995	57.205	70.735
MLP3A_MOUSE	2	2	1.06E-02	Microtubule-associated proteins 1A/1B light chain 3A Map1lc3a	460.488	488.067	867.458	1273.433
RM19_MOUSE	5	1	1.07E-02	39S ribosomal protein L19, mitochondrial Mrpl19	1790.356	2447.048	240.451	259.456
A2MG_MOUSE	10	3	1.07E-02	Alpha-2-macroglobulin-P A2m	2264.407	1591.579	650.382	1025.036
TADBP_MOUSE	6	5	1.09E-02	TAR DNA-binding protein 43 Tardbp	1639.444	1357.674	1247.068	846.142
SEPT9_MOUSE	16	7	09E-02	Septin-9 Sept9	1760.481	2529.184	2484.722	2172.274
YBOX2_MOUSE	5	1	1. 1.09E-02	Y-box-binding protein 2 Ybx2	200.282	60.804	32.581	41.762
P5CR2_MOUSE	8	4	1.11E-02	Pyrroline-5-carboxylate reductase 2 Pycr2	1020.883	1560.843	2480.368	1138.342
DFNA5_MOUSE	4	1	1.14E-02	Non-syndromic hearing impairment protein 5 homolog Dfna5	132.359	516.542	1134.329	295.551

OST48_MOUSE	11	1	1.15E-02	Dolichyl-diphosphooligosaccharide-protein glycosyltransferase 48 kDa subunit Ddost	508.018	31.882	151.301	5.932
TEBP_MOUSE	2	1	1.15E-02	Prostaglandin E synthase 3 Ptges3	4378.323	5538.633	9001.917	2997.311

FXR1_MOUSE	10	2	1.16E-02	Fragile X mental retardation syndrome-related protein 1 Fxr1	927.543	1479.168		1615.391	2498.527
TXLNA_MOUSE	8	3	-02	1.18E	Alpha-taxilin Txlna	88.479	13.301		15.849
1433Z_MOUSE	26	8	-02	142.187		10244.759	20645.459		8854.683
			-02						
			1.18E	14-3-3 protein zeta/delta Ywhaz	5867.384				
RS10_MOUSE	10	4	1.18E	40S ribosomal protein S10 Rps10	4640.187	2301.494		670.859	1080.266
AACS_MOUSE	10	2	1.20E	Acetoacetyl-CoA synthetase Aacs	106.476	229.246		171.502	157.043
MVP_MOUSE	28	7	-02			732.525		1031.471	822.941
			-02						
			-02	1.20E Major vault protein Mvp	525.185				
DYR_MOUSE	5	2	1.21E	Dihydrofolate reductase Dhfr	1936.154	1855.615		1856.544	797.574
WDR61_MOUSE	4	2	1.21E-02	WD repeat-containing protein 61 Wdr61	622.125	2116.620		2018.905	1544.010
F10A1_MOUSE	12	6	1.21E-02	Hsc70-interacting protein St13	1553.317	1880.990		1262.117	1124.121
SSBP_MOUSE	2	1	1.22E-02	Single-stranded DNA-binding protein, mitochondrial Ssbp1	5.052	1.915		191.995	82.672
BTF3_MOUSE	10	5	1.22E	Transcription factor BTF3 Btf3	4630.980	2670.552		74.612	307.810
CD2AP_MOUSE	10	1	-02			26.134		16.223	359.835
			-02	1.23ECD2-associated protein Cd2ap	272.731				
TCEA1_MOUSE	6	1	1.24E-02	Transcription elongation factor A protein 1 Tcea1	519.803	99.756		3.306	684.928
AHSA1_MOUSE	3	1	1.25E-02	Activator of 90 kDa heat shock protein ATPase homolog 1 Ahsa1	2.529	146.904		4.975	3.152
PUR8_MOUSE	10	4	1.25E	Adenylosuccinate lyase Adsl	545.436	569.308		338.432	26.209
CDV3_MOUSE	6	4	-02			1623.716		1266.310	495.788
			-02	1.25E Protein CDV3 Cdv3	2115.662				
ARPC2_MOUSE	11	5	1.27E-02	Actin-related protein 2/3 complex subunit 2 Arpc2	1614.503	2122.122		3640.295	1503.273

SMD3_MOUSE	4	2	1.27E-02	Small nuclear ribonucleoprotein Sm D3 Snrpd3	3502.187	2437.245	5628.203	4706.782
ACOC_MOUSE	19	8	1.27E-02	Cytoplasmic aconitate hydratase Aco1	1146.802	71.802	9507.730	1959.430
MTPN_MOUSE	3	2	1.28E-02	Myotrophin Mtpn	1574.953	581.050	1555.241	302.638
ACSL3_MOUSE	6	1	1.29E-02	Long-chain-fatty-acid--CoA ligase 3 Acsl3	135.766	476.337	873.446	1039.056
DECR_MOUSE	10	3	1.30E-02	2,4-dienoyl-CoA reductase, mitochondrial Decr1	1105.205	953.405	5696.175	2732.475
SYNP2_MOUSE	10	2	-02	Synaptopodin-2 Synpo2	73.546	356.438	94.192	497.748
MYH3_MOUSE	67	6	1.34E-02 1.34E	Myosin-3 Myh3	2110.229	2180.686	3427.516	1914.381
PRS6A_MOUSE	18	8	1.34E-02	26S proteasome regulatory subunit 6A Psmc3	2512.895	1581.900	2673.020	2702.388
LA_MOUSE	10	1	-02	Lupus La protein homolog Ssb	995.727	306.459	830.176	1357.255
NH2L1_MOUSE	5	2	-02 1.36E 1.36E	NHP2-like protein 1 Snu13	959.034	272.657	1910.573	1512.198
RAC1_MOUSE; RAC2_MOUSE; RAC3_MOUSE	5	2	1.36E-02	Ras-related C3 botulinum toxin substrate 1 Rac1	2770.333	3481.391	1282.920	1435.934
NWD2_MOUSE	26	1	1.36E-02	NACHT and WD repeat domaincontaining protein 2 Nwd2	2579.178	3108.030	426.200	1031.223
CATZ_MOUSE	4	2	-02	Cathepsin Z Ctsz	2927.345	2039.619	2026.313	1379.794
TPD54_MOUSE	5	1	-02 1.36E 1.37E	Tumor protein D54 Tpd52l2	2.501	18.034	156.909	109.125

FKBP4_MOUSE	15	7	1.38E-02	Peptidyl-prolyl cis-trans isomerase FKBP4 Fkbp4	1161.663	1007.359	1099.854	483.474
NMDZ1_MOUSE	16	4	1.38E-02	Glutamate receptor ionotropic, NMDA 1 Grin1	691.218	728.071	1553.193	1895.065
UBQL2_MOUSE	6	1	1.41E-02	Ubiquilin-2 Ubqln2	6.561	0.000	165.412	331.889
AMRP_MOUSE	7	2	1.41E-02	Alpha-2-macroglobulin receptorassociated protein Lrpap1	277.097	309.059	18.893	136.017
RANB3_MOUSE	3	1	1.41E-02	Ran-binding protein 3 Ranbp3	285.243	330.631	65.676	6.130
EIF3I_MOUSE	4	3	1.42E-02	Eukaryotic translation initiation factor 3 subunit I Eif3i	876.939	781.445	524.103	440.196
DPP3_MOUSE	4	1	-02	Dipeptidyl peptidase 3 Dpp3	668.306	799.317	1337.323	825.943
SNX3_MOUSE	5	4	-02 1.43E 1.46E	Sorting nexin-3 Snx3	3746.667	3511.437	3360.598	2148.448
CLH1_MOUSE	47	14	1.46E-02	Clathrin heavy chain 1 Cltc	2908.142	1523.599	744.155	933.724
CSN3_MOUSE	3	3	1.46E-02	COP9 signalosome complex subunit 3 Cops3	234.081	231.277	36.260	226.116
K0100_MOUSE	22	3	1.47E-02	Protein KIAA0100 Kiaa0100	12.944	142.570	138.371	55.199
EH1L1_MOUSE	23	2	1.47E-02	EH domain-binding protein 1-like protein 1 Ehbp1l1	2497.599	713.490	883.860	1697.803
PDCL3_MOUSE	5	1	-02	Phosducin-like protein 3 Pdcl3	624.710	25.466	106.749	8.806
MYL4_MOUSE	4	2	-02 1.48E 1.51E	Myosin light chain 4 Myl4	17.954	72.572	366.873	1005.558
PSD13_MOUSE	13	5	1.52E-02	26S proteasome non-ATPase regulatory subunit 13 Psmd13	824.960	331.944	176.926	212.171
RS28_MOUSE	3	3	1.53E-02	40S ribosomal protein S28 Rps28	2337.848	3143.316	5874.245	4366.016
TLL1_MOUSE	18	4	1.54E-02	Tolloid-like protein 1 Tll1	3103.147	2346.498	1842.916	1976.641
RS24_MOUSE	5	2	1.56E-02	40S ribosomal protein S24 Rps24	2004.644	1292.948	116.637	898.721

STIP1_MOUSE	26	6	1.56E-02	Stress-induced-phosphoprotein 1 Stip1	2393.931	2638.987	3713.287	2845.176
XRN2_MOUSE	13	1	1.58E-02	5'-3' exoribonuclease 2 Xrn2	18.473	12.988	190.355	117.608
TMM43_MOUSE	2	1	1.58E-02	Transmembrane protein 43 Tmem43	764.003	1203.543	970.736	543.425
K2C79_MOUSE	35	3	1.59E-02	Keratin, type II cytoskeletal 79 Krt79	396.480	98.937	1379.121	63.259
CYBP_MOUSE	11	2	1.60E-02	Calcyclin-binding protein Cacybp	78.974	407.870	678.695	584.539
ANM1_MOUSE	8	5	1.60E-02	Protein arginine Nmethyltransferase 1 Prmt1	1716.069	1660.073	1000.726	1066.009
VDAC3_MOUSE	12	1	1.61E-02	Voltage-dependent anion-selective channel protein 3 Vdac3	822.428	807.874	3836.861	1866.857
CAVN1_MOUSE	12	4	1.64E-02	Caveolae-associated protein 1 Cavin1	1660.347	2023.253	1544.120	725.943
ARF1_MOUSE; ARL11_MOUSE	10	1	1.65E-02	ADP-ribosylation factor 1 Arf1	1.763	3.430	76.882	4.016
HS90B_MOUSE	69	17	1.65E-02	Heat shock protein HSP 90-beta Hsp90ab1	29737.461	31041.371	21903.010	16427.569
SPIR2_MOUSE	9	3	1.65E-02	Protein spire homolog 2 Spire2	2515.401	2984.673	9166.410	4624.110
BTBDB_MOUSE	18	1	1.66E-02	Ankyrin repeat and BTB/POZ domain-containing protein BTBD11 Btbd11	73.276	6.723	56.688	306.112
IF4A2_MOUSE	29	1	1.67E-02	Eukaryotic initiation factor 4A-II Eif4a2	45.562	43.608	93.224	21.077
FPPS_MOUSE	14	6	1.68E-02	Farnesyl pyrophosphate synthase Fdps	114.226	1683.265	1151.723	318.156
CE170_MOUSE	21	3	1.68E-02	Centrosomal protein of 170 kDa Cep170	1320.666	2280.930	607.845	537.022
G6PI_MOUSE	24	12	1.76E-02	Glucose-6-phosphate isomerase Gpi	2398.953	1610.171	889.298	1492.938

MPRIP_MOUSE	20	3	1.76E-02	Myosin phosphatase Rho-interacting protein Mprip	1501.424	2018.268	767.929	1034.652
OXR1_MOUSE	8	1	1.78E-02	Oxidation resistance protein 1 Oxr1	41.560	3.717	0.962	0.894
MINK1_MOUSE	24	2	1.80E-02	Misshapen-like kinase 1 Mink1	472.514	824.169	663.828	522.840
PACN2_MOUSE	10	3	1.80E-02	Protein kinase C and casein kinase substrate in neurons protein 2 Pacsin2	1020.342	1065.342	1573.349	1265.179
RSMN_MOUSE	7	2	1.81E-02	Small nuclear ribonucleoproteinassociated protein N Snrpn	687.847	358.398	3.804	128.793
SF3B1_MOUSE	20	2	1.81E-02	Splicing factor 3B subunit 1 Sf3b1	286.696	202.604	24.314	65.612
SRSF2_MOUSE	6	2	1.82E-02	Serine/arginine-rich splicing factor 2 Srsf2	6251.348	6992.474	8690.480	6629.955
RS26_MOUSE	4	3	-02	40S ribosomal protein S26 Rps26	3548.555	1708.005	3757.659	2187.605
CYC_MOUSE	7	5	-02 1.83E 1.83E	Cytochrome c, somatic Cycs	226.824	225.995	1417.689	2148.434
VATH_MOUSE	6	1	1.83E-02	V-type proton ATPase subunit H Atp6v1h	48.875	9.934	0.825	0.007
HECD1_MOUSE	27	2	1.85E-02	E3 ubiquitin-protein ligase HECTD1 Hectd1	903.186	704.930	603.773	277.541
TRIPC_MOUSE	21	1	1.87E-02	E3 ubiquitin-protein ligase TRIP12 Trip12	120.012	136.032	220.337	263.232
SFXN3_MOUSE	8	4	1.88E-02	Sideroflexin-3 Sfxn3	587.505	632.053	2823.895	707.322
TCP4_MOUSE	7	2	1.89E-02	Activated RNA polymerase II transcriptional coactivator p15 Sub1	625.703	534.521	248.030	656.858
EIF3A_MOUSE	45	10	1.89E-02	Eukaryotic translation initiation factor 3 subunit A Eif3a	2357.705	2355.790	1663.631	1164.046
DC1L2_MOUSE	4	3	1.89E-02	Cytoplasmic dynein 1 light intermediate chain 2 Dync1li2	137.177	186.379	273.563	133.461

KCY_MOUSE	5	3	-02	UMP-CMP kinase Cmpk1	720.507	737.276	85.147	620.606
SOGA1_MOUSE	19	2	1.95E-02 1.95E	Protein SOGA1 Soga1	96.294	65.280	23.661	52.285
UGDH_MOUSE	16	7	1.96E-02	UDP-glucose 6-dehydrogenase Ugdh	2411.616	3665.840	1797.152	1128.542
PEX14_MOUSE	2	1	1.96E-02	Peroxisomal membrane protein PEX14 Pex14	61.803	1.566	0.764	121.599
LGUL_MOUSE	6	2	2.00E-02	Lactoylglutathione lyase Glo1	4121.263	3841.064	4635.600	3128.526
XRCC5_MOUSE	5	2	2.00E-02	X-ray repair cross-complementing protein 5 Xrcc5	331.986	166.359	194.852	54.198
HDGF_MOUSE	3	1	2.01E-02	Hepatoma-derived growth factor Hdgf	2.548	2.344	7.495	189.451
NUDC2_MOUSE	3	1	2.03E-02	NudC domain-containing protein 2 Nudcd2	2208.876	2611.405	3619.968	2167.051
ODP2_MOUSE	24	8	2.04E-02	Dihydrolipoyllysine-residue acetyltransferase component of pyruvate dehydrogenase complex, mitochondrial Dlat	5351.229	2842.151	1666.758	1822.897
RB11B_MOUSE; RB11A_MOUSE	10	5	2.06E-02	Ras-related protein Rab-11B Rab11b	2745.909	3118.908	5438.128	3335.857
TALDO_MOUSE	19	7	2.06E-02	Transaldolase Taldo1	4212.600	4192.294	14348.443	7868.714
HNRH1_MOUSE	8	1	2.07E-02	Heterogeneous nuclear ribonucleoprotein H Hnrnph1	403.507	425.652	517.384	229.191
DJC16_MOUSE	9	1	2.07E-02	DnaJ homolog subfamily C member 16 Dnajc16	2718.254	1608.466	1034.828	1048.399
RL21_MOUSE	10	4	2.09E-02	60S ribosomal protein L21 Rpl21	3907.706	2851.282	2253.240	733.513
GDIR1_MOUSE	11	5	2.11E-02	Rho GDP-dissociation inhibitor 1 Arhgdia	5850.867	4427.644	4169.875	1621.272
PRDX2_MOUSE	9	2	2.13E-02	Peroxiredoxin-2 Prdx2	2286.217	3621.279	3989.163	1953.089

PEBP1_MOUSE	5	3	2.17E-02	Phosphatidylethanolamine-binding protein 1 Pebp1	6304.175	10264.728	3268.818	5679.485
DENR_MOUSE	3	3	-02	Density-regulated protein Denr	308.270	431.764	1441.733	495.646
COF2_MOUSE	12	2	-02 2.17E 2.19E	Cofilin-2 Cfl2	1332.878	1459.394	253.799	995.033
UBP36_MOUSE	7	1	2.19E-02	Ubiquitin carboxyl-terminal hydrolase 36 Usp36	24.356	314.826	31.544	46.107
BZW1_MOUSE	11	4	2.20E-02	Basic leucine zipper and W2 domain-containing protein 1 Bzw1	569.107	296.648	306.994	244.573
SYEP_MOUSE	40	9	2.23E-02	Bifunctional glutamate/proline-tRNA ligase Eprs	1456.563	1768.170	1333.823	1064.450
CDC37_MOUSE	6	2	2.23E-02	Hsp90 co-chaperone Cdc37 Cdc37	1442.419	586.952	431.806	319.142
RAB2A_MOUSE	10	1	2.25E-02	Ras-related protein Rab-2A Rab2a	1782.490	1427.186	573.571	938.230
CLIC4_MOUSE	11	3	2.26E-02	Chloride intracellular channel protein 4 Clic4	1014.160	1316.108	2600.724	2055.398

PGES2_MOUSE	3	2	2.27E-02	Prostaglandin E synthase 2 Ptges2	212.425	115.040	377.694	668.430
4F2_MOUSE	11	3	2.27E-02	4F2 cell-surface antigen heavy chain Slc3a2	401.111	913.542	948.561	758.645
GDIA_MOUSE	10	2	2.28E-02	Rab GDP dissociation inhibitor alpha Gdi1	3590.969	840.148	4477.054	1045.942
COX41_MOUSE	2	1	2.33E-02	Cytochrome c oxidase subunit 4 isoform 1, mitochondrial Cox4i1	1106.003	384.409	79.984	313.336
AN32E_MOUSE	6	5	2.35E-02	Acidic leucine-rich nuclear phosphoprotein 32 family member E Anp32e	1927.814	1453.197	543.963	349.498
CYB5B_MOUSE	3	3	2.38E	Cytochrome b5 type B Cyb5b	787.256	640.988	256.584	177.713
PROF1_MOUSE	10	7	2.39E	Profilin-1 Pfn1	6643.123	2128.936	2040.605	1222.407
SQSTM_MOUSE	5	1		Sequestosome-1 Sqstm1	31.570	33.360	115.412	0.000

IPO9_MOUSE	12	3	-02 -02 -02 -02 -02 -02 2.39E 2.40E	Importin-9 Ipo9	285.680	146.629	185.134	158.165
RCN1_MOUSE	4	2	2.40E	Reticulocalbin-1 Rcn1	595.840	726.903	1394.743	815.090
DNM1L_MOUSE	15	2	2.40E	Dynamin-1-like protein Dnm1l	78.094	37.737	2.377	7.870
K1C14_MOUSE	29	2	2.41E-02	Keratin, type I cytoskeletal 14 Krt14	788.104	569.600	261.076	205.173
F120A_MOUSE	12	1	2.41E-02	Constitutive coactivator of PPARgamma-like protein 1 FAM120A	91.366	198.141	149.604	258.692
NAV3_MOUSE	16	2	-02	Neuron navigator 3 Nav3	1032.099	1732.433	343.463	592.744
DACH2_MOUSE	3	1	-02 2.46E 2.49E	Dachshund homolog 2 Dach2	3.571	0.000	115.130	15.309
SYLC_MOUSE	27	9	2.50E-02	Leucine--tRNA ligase, cytoplasmic Lars	1082.467	1052.917	1624.714	946.888
QCR1_MOUSE	7	1	2.50E-02	Cytochrome b-c1 complex subunit 1, mitochondrial Uqcrc1	347.850	46.136	431.646	383.322
ROAA_MOUSE	13	5	2.51E-02	Heterogeneous nuclear ribonucleoprotein A/B Hnrnpab	3564.262	3555.961	1460.044	1248.304
BOP1_MOUSE	11	2	2.58E-02	Ribosome biogenesis protein BOP1 Bop1	173.989	239.456	410.265	584.649
GLU2B_MOUSE	8	1	-02	Glucosidase 2 subunit beta Prkcsh	81.350	13.449	2.649	0.000
RL3_MOUSE	17	6	-02 2.58E 2.59E	60S ribosomal protein L3 Rpl3	1985.167	758.624	675.586	1569.101
EIF1B_MOUSE	3	1	2.60E-02	Eukaryotic translation initiation factor 1b Eif1b	116.311	230.220	1639.999	1560.283
RTTN_MOUSE	15	2	2.60E-02	Rotatin Rttn	3355.424	4547.740	6620.995	4983.084

USO1_MOUSE	17	2	2.60E-02	General vesicular transport factor p115 Uso1	223.657	133.857		49.768	263.476
BHMT1_MOUSE	13	2	2.62E-02	Betaine--homocysteine S-methyltransferase 1 Bhmt	910.064	972.619		4395.304	432.750
TENR_MOUSE	5	1	2.62E-02	Tenascin-R Tnr	368.538	81.045		148.250	1212.058
RACK1_MOUSE	13	3	2.62E-02	Receptor of activated protein C kinase 1 Rack1	6682.804	8229.345		10364.137	5842.608
SEP10_MOUSE	16	1	2.63E-02	Septin-10 Sept10	2.405	1.615		114.651	240.507
APT_MOUSE	6	2	2.63E-02	Adenine phosphoribosyltransferase Aprt	1619.672	50.281		25.715	308.914
LYZ1_MOUSE	3	1	2.64E	Lysozyme C-1 Lyz1	12.137	183.522		6.032	5.633
TLN2_MOUSE	37	6	-02 -02	2.64E Talin-2 Tln2	1000.893	821.253		692.055	437.881
GNL3_MOUSE	4	1	2.67E-02	Guanine nucleotide-binding protein-like 3 Gnl3	53.623	19.613		1.009	20.762
ANX11_MOUSE	8	1	-02		679.346	1162.766	1122.559		473.721
ACTG_MOUSE	54	2	-02 Anxa11 2.69E	2.68E Annexin A11 Actin, cytoplasmic 2 Actg1	50799.351	59000.148	65824.570		40070.397
UFC1_MOUSE	1	1	2.71E-02	Ubiquitin-fold modifier-conjugating enzyme 1 Ufc1	1796.133	3419.427		1694.593	1480.734
HAP28_MOUSE	4	1	2.72E-02	28 kDa heat- and acid-stable phosphoprotein Pdap1	1365.874	4217.655		4847.610	2491.206
RM53_MOUSE	4	1	2.72E-02	39S ribosomal protein L53, mitochondrial Mrpl53	47.641	25.041		6.836	1.494
SYMC_MOUSE	25	2	2.72E-02	Methionine--tRNA ligase,	514.287	555.064		478.439	332.742

				cytoplasmic Mars				
MYO1C_MOUSE	23	5	2.73E-02	Unconventional myosin-Ic Myo1c	719.503	896.697	1148.093	895.557
DEN4B_MOUSE	13	4	2.74E-02	DENN domain-containing protein 4B Dennd4b	1233.100	2236.150	3691.898	2477.997
RS9_MOUSE	10	1	-02	2.75E 40S ribosomal protein S9		10842.200	6393.132	2789.484
SAHH_MOUSE	23	6	-02 Rps9	7901.857		5072.852	4375.203	3055.419
			2.81E	Adenosylhomocysteinase Ahcy	4517.659			
SYCC_MOUSE	15	4	2.85E-02	Cysteine--tRNA ligase, cytoplasmic Cars	310.358	216.197	208.171	59.109
DOCK7_MOUSE	22	1	2.87E-02	Dedicator of cytokinesis protein 7 Dock7	31.968	0.742	9.748	6.325
PLIN3_MOUSE	9	7	2.87E-02	Perilipin-3 Plin3	1091.998	1663.063	928.259	1099.507
CSN2_MOUSE	4	2	2.88E-02	COP9 signalosome complex subunit 2 Cops2	284.497	31.459	7.500	59.342

LMNB1_MOUSE	27	6	-02	Lamin-B1 Lmnb1	1803.772	227.728	323.119	564.159
PRRC1_MOUSE	4	1	8E-02 2.88E 2.8	Protein PRRC1 Prrc1	1364.265	2122.615	375.615	2584.266
HNRH2_MOUSE	10	3	2.90E-02	Heterogeneous nuclear ribonucleoprotein H2 Hnrnph2	1364.025	1431.761	2011.671	995.662
KLH41_MOUSE	17	2	2.91E-02	Kelch-like protein 41 Klhl41	362.953	440.954	1302.244	2396.074
TNNI1_MOUSE	17	3	2.91E-02	Troponin I, slow skeletal muscle Tnni1	272.483	140.008	708.023	339.402
NBEA_MOUSE	18	3	2.95E-02	Neurobeachin Nbea	357.945	72.427	1001.263	300.414
GLSK_MOUSE	15	1	2.96E-02	Glutaminase kidney isoform, mitochondrial Gls	0.012	0.000	379.616	0.000

SEM5B_MOUSE	5	1	-02	Semaphorin-5B Sema5b	2.033	16.597	263.967	99.611
DMXL2_MOUSE	17	4	-02 2.96E 2.97E	DmX-like protein 2 Dmxl2	1810.522	854.257	2415.355	1230.924
TOP2A_MOUSE	30	2	2.97E-02	DNA topoisomerase 2-alpha Top2a	1636.370	1576.545	920.776	866.724
ESTD_MOUSE	8	2	2.98E-02	S-formylglutathione hydrolase Esd	4814.248	6559.501	7940.809	6183.115
CA198_MOUSE	3	1	2.98E-02	Uncharacterized protein C1orf198 homolog	29.662	151.937	143.871	160.955
S4A4_MOUSE	11	1	3.01E-02	Electrogenic sodium bicarbonate cotransporter 1 Slc4a4	2281.701	101.701	137.631	222.434
CLU_MOUSE	10	1	3.01E-02	Clustered mitochondria protein homolog Cluh	2.045	166.550	0.000	62.931
ECH1_MOUSE	7	2	3.03E-02	Delta(3,5)-Delta(2,4)-dienoyl-CoA isomerase, mitochondrial Ech1	9.713	283.317	36.646	43.155
SMD2_MOUSE	7	3	3.04E-02	Small nuclear ribonucleoprotein Sm D2 Snrpd2	451.498	397.812	2058.213	1031.754
ABHD8_MOUSE	2	2	-02	Protein ABHD8 Abhd8	2645.911	69.421	348.354	14.232
H2B1A_MOUSE	10	1	-02 3.04E 3.07E	Histone H2B type 1-A Hist1h2ba	342.509	237.410	737.353	470.004
PAPS1_MOUSE	11	1	3.15E-02	Bifunctional 3'-phosphoadenosine 5'-phosphosulfate synthase 1 Papss1	182.612	87.488	6.610	5.553
CCDC9_MOUSE	7	1	3.16E-02	Coiled-coil domain-containing protein 9 Ccdc9	935.743	231.040	1077.337	1281.587
PSB2_MOUSE	11	1	3.18E-02	Proteasome subunit beta type-2 Psmb2	772.922	227.330	6.969	94.103
FAF2_MOUSE	4	1	3.21E-02	FAS-associated factor 2 Faf2	285.660	18.525	2.709	29.216
PGAM1_MOUSE	14	8	3.21E-02	Phosphoglycerate mutase 1 Pgam1	9963.901	10578.946	14220.667	9558.682

SEPT7_MOUSE	9	5	-02	Septin-7 Sept7	763.315	960.087	1702.499	1409.648
FRIH_MOUSE	6	2	3.26E-02 3.27E-02	Ferritin heavy chain Fth1	710.874	388.323	83.615	27.659
SODM_MOUSE	5	2	3.30E-02	Superoxide dismutase [Mn], mitochondrial Sod2	470.617	261.713	885.035	606.692
M4K4_MOUSE	22	5	3.30E-02	Mitogen-activated protein kinase kinase kinase kinase 4 Map4k4	1658.046	2908.619	2539.172	2783.449
KI20B_MOUSE	17	2	3.32E-02	Kinesin-like protein KIF20B Kif20b	205.393	151.575	98.472	35.578
SCMC1_MOUSE	7	3	3.32E-02	Calcium-binding mitochondrial carrier protein SCaMC-1 Slc25a24	512.887	106.166	70.377	501.414
TBA1C_MOUSE	22	1	3.36E-02	Tubulin alpha-1C chain Tuba1c	10263.924	364.031	2735.970	2420.711
LRGUK_MOUSE	8	1	3.37E-02	Leucine-rich repeat and guanylate kinase domain-containing protein Lrguk	13.772	4.857	1.978	0.258
WRN_MOUSE	17	2	3.38E-02	Werner syndrome ATP-dependent helicase homolog Wrn	27.128	10.960	407.320	4.832
PLK1_MOUSE	7	2	3.38E-02	Serine/threonine-protein kinase PLK1 Plk1	7.123	15.747	107.652	41.516
MOB1A_MOUSE	5	1	3.39E-02	MOB kinase activator 1A Mob1a	3002.551	4980.036	6955.249	4412.117
CDC42_MOUSE	7	2	3.41E-02	Cell division control protein 42 homolog Cdc42	573.488	229.523	718.960	97.688
VINC_MOUSE	79	16	3.50E-02	Vinculin Vcl	4060.711	4149.612	6779.882	3613.719
CSN4_MOUSE	8	2	3.51E-02	COP9 signalosome complex subunit 4 Cops4	1098.566	1349.766	1028.792	685.858
EHD4_MOUSE	14	2	3.54E-02	EH domain-containing protein 4 Ehd4	285.245	368.878	145.963	99.937
SNX1_MOUSE	12	1	-02	Sorting nexin-1 Snx1	22.318	0.000	3.675	44.775
NXN_MOUSE	4	1	3.55E-02 3.56E-02	Nucleoredoxin Nxn	61.318	3.110	5.418	12.869
PYR1_MOUSE	27	2	3.57E-02	CAD protein Cad	4.361	33.706	28.895	248.535

CHCH2_MOUSE	1	1	3.61E-02	Coiled-coil-helix-coiled-coil-helix domain-containing protein 2 Chchd2	1710.297	1572.722	82.606	533.179
COPD_MOUSE	11	7	3.61E-02	Coatomer subunit delta Arcn1	1188.141	1493.109	1620.493	1474.503
HEM2_MOUSE	6	1	3.61E-02	Delta-aminolevulinic acid dehydratase Alad	506.722	21.653	44.464	144.381

PSB1_MOUSE	11	6	3.63E-02	Proteasome subunit beta type-1 Psmb1	2509.298	3288.309	1173.081	2019.588
PYGM_MOUSE	14	2	3.64E-02	Glycogen phosphorylase, muscle form Pygm	109.304	171.627	467.749	300.567
DLG2_MOUSE	29	2	3.67E-02	Disks large homolog 2 Dlg2	10.176	3.267	1555.043	79.021
PHP14_MOUSE	2	1	3.69E-02	14 kDa phosphohistidine phosphatase Phpt1	1256.521	161.840	750.003	581.382
DREB_MOUSE	7	2	-02	Drebrin Dbn1	1656.679	2568.950	1342.829	1393.830
IPO7_MOUSE	7	4	-02 3.69E 3.70E	Importin-7 Ipo7	607.535	414.434	376.824	277.992
TRADD_MOUSE	3	1	3.71E-02	Tumor necrosis factor receptor type 1-associated DEATH domain protein Tradd	171.223	0.000	23.834	37.598
SMC3_MOUSE	27	3	3.77E-02	Structural maintenance of chromosomes protein 3 Smc3	2525.756	1940.118	649.562	999.078
NACAM_MOUSE; NACA_MOUSE	86	24	3.86E-02	Nascent polypeptide-associated complex subunit alpha, muscle-specific form Naca	5629.590	7594.943	13659.432	7503.169
KIF2C_MOUSE	7	1	3.87E-02	Kinesin-like protein KIF2C Kif2c	560.358	775.804	551.247	1046.491
MTDC_MOUSE	6	2	3.90E-02	Bifunctional methylenetetrahydrofolate dehydrogenase/cyclohydrolase, mitochondrial Mthfd2	178.924	50.853	368.425	347.438
SIAS_MOUSE	3	2	3.92E-02	Sialic acid synthase Nans	459.807	711.916	1097.942	1104.645

ATPG_MOUSE	10	3	3.93E-02	ATP synthase subunit gamma, mitochondrial Atp5c1	1606.599	1569.783	2299.499	2612.072
CASP3_MOUSE	8	4	3.93E-02	Caspase-3 Casp3	1395.061	2155.774	1651.101	799.343
MED15_MOUSE	4	1	3.97E-02	Mediator of RNA polymerase II transcription subunit 15 Med15	998.631	2750.024	5313.618	1115.747
RFA1_MOUSE	10	1	3.99E-02	Replication protein A 70 kDa DNAbinding subunit Rpa1	749.280	530.545	244.343	381.495
CETN2_MOUSE	6	1	3.99E-02	Centrin-2 Cetn2	233.426	76.799	49.886	4.749
AIMP2_MOUSE	3	2	4.00E-02	Aminoacyl tRNA synthase complex-interacting multifunctional protein 2 Aimp2	117.777	63.799	12.669	24.749
BAF_MOUSE	2	1	4.05E-02	Barrier-to-autointegration factor Banf1	410.442	217.637	11.158	1441.883

NUCB2_MOUSE	4	1	4.05E-02	Nucleobindin-2 Nucb2	424.093	766.654	4.837	107.891
CPSF6_MOUSE	9	2	4.08E-02	Cleavage and polyadenylation specificity factor subunit 6 Cpsf6	141.960	144.841	343.847	534.900
CRTP1_MOUSE	2	1	-02	Cysteine-rich tail protein 1 Cysrt1	7.141	9.716	72.015	724.492
KLH40_MOUSE	4	1	-02 4.09E 4.09E	Kelch-like protein 40 Klhl40	1.587	0.000	21.745	30.756
MYO5A_MOUSE	30	1	4.13E-02	Unconventional myosin-Va Myo5a	39.787	9.379	4.083	0.000
ARPC4_MOUSE	4	2	4.18E-02	Actin-related protein 2/3 complex subunit 4 Arpc4	2727.129	6430.498	4538.123	4165.393
CDKAL_MOUSE	5	3	4.18E-02	Threonylcarbamoyladenosine tRNA methylthiotransferase Cdkal1	1185.855	1405.597	443.872	1111.213
THOP1_MOUSE	12	2	4.23E-02	Thimet oligopeptidase Thop1	2113.911	1325.602	2216.179	2330.043
ADPRH_MOUSE	3	2	4.26E-02	[Protein ADP-ribosylarginine] hydrolase Adprh	1740.172	2484.603	463.641	645.358
TES_MOUSE	4	1		Testin Tes	0.423	81.116	1.428	0.410

AQP5_MOUSE	4	2	-02 -02 4.27E 4.28E	Aquaporin-5 Aqp5	1979.884	1942.240	2477.546	1489.752
SPB6_MOUSE	16	9	4.29E-02	Serpin B6 Serpinb6	5090.812	4224.340	4139.156	3391.489
CAZA2_MOUSE	9	3	4.31E-02	F-actin-capping protein subunit alpha-2 Capza2	1083.738	1367.576	1902.688	1199.040
PABP2_MOUSE	2	1	4.32E-02	Polyadenylate-binding protein 2 Pabpn1	71.742	1397.909	1319.751	815.436
TRMB_MOUSE	4	1	4.34E-02	tRNA (guanine-N(7)-)methyltransferase Mettl1	333.256	326.298	42.705	24.996
STAM1_MOUSE	4	1	4.37E-02	Signal transducing adapter molecule 1 Stam	878.193	1169.942	2705.999	2077.888
EIF3C_MOUSE	14	3	4.37E-02	Eukaryotic translation initiation factor 3 subunit C Eif3c	779.745	559.373	243.587	261.683
AROS_MOUSE	4	2	4.38E-02	Active regulator of SIRT1 Rps19bp1	125.242	127.494	55.859	11.766
SND1_MOUSE	35	6	4.38E-02	Staphylococcal nuclease domaincontaining protein 1 Snd1	1985.756	1322.483	1270.756	2220.671
DHPR_MOUSE	4	1	4.41E-02	Dihydropteridine reductase Qdpr	1637.444	2063.537	3294.182	2245.259
M3K6_MOUSE	13	1	4.41E-02	Mitogen-activated protein kinase kinase kinase 6 Map3k6	243.544	571.699	42.868	38.790
SSH1_MOUSE	15	1	4.50E-02	Protein phosphatase Slingshot homolog 1 Ssh1	841.599	799.694	865.500	2243.453
SMC1A_MOUSE	52	4	4.50E-02	Structural maintenance of chromosomes protein 1A Smc1a	1961.146	2603.708	1703.014	2084.202
SPG17_MOUSE	39	5	4.53E-02	Sperm-associated antigen 17 Spag17	625.870	433.036	2479.370	4303.732
CATM_MOUSE	4	1		Cathepsin M Ctsm	213.946	190.321	24.023	27.129

COBL1_MOUSE	27	3	-02 -02 4.55E 4.58E	Cordon-bleu protein-like 1 Cobll1	58.366	65.470	31.971	20.201
SLD5_MOUSE	2	1	4.64E-02	DNA replication complex GINS protein SLD5 Gins4	221.763	33.180	10.781	31.418
MTA1_MOUSE	22	3	4.68E-02	Metastasis-associated protein MTA1 Mta1	59.284	53.845	228.738	30.230
A16A1_MOUSE	7	1	4.71E-02	Aldehyde dehydrogenase family 16 member A1 Aldh16a1	2.700	145.072	22.185	1.689
ARF4_MOUSE	10	2	4.71E-02	ADP-ribosylation factor 4 Arf4	4.334	0.354	129.710	2.733
HMGA1_MOUSE	2	1	4.71E-02	High mobility group protein HMGI/HMG-Y Hmga1	2088.227	1760.991	1020.548	439.330
DDX5_MOUSE	23	4	4.72E-02	Probable ATP-dependent RNA helicase DDX5 Ddx5	2590.479	1868.081	1302.839	1003.696
AP1B1_MOUSE	20	4	4.80E-02	AP-1 complex subunit beta-1 Ap1b1	1655.411	1000.730	795.495	1146.782
RAB18_MOUSE	7	1	4.82E-02	Ras-related protein Rab-18 Rab18	1040.120	1624.676	2144.564	1216.679
DRG1_MOUSE	4	2	4.85E-02	Developmentally-regulated GTPbinding protein 1 Drg1	52.269	0.305	23.750	0.882
RS6_MOUSE	12	7	4.85E-02	40S ribosomal protein S6 Rps6	2614.559	4734.556	1911.227	2023.421
ATPK_MOUSE	4	2	4.87E-02	ATP synthase subunit f, mitochondrial Atp5j2	483.790	926.190	1250.548	1326.241
TOM34_MOUSE	5	2	4.90E-02	Mitochondrial import receptor subunit TOM34 Tomm34	317.172	355.354	233.504	126.953
ACINU_MOUSE	20	2	4.92E-02	Apoptotic chromatin condensation inducer in the nucleus Acin1	79.681	85.679	72.281	21.277
6PGL_MOUSE	6	4	4.96E-02	6-phosphogluconolactonase Pgls	142.347	30.205	2427.441	191.909
CN166_MOUSE	9	4	5.02E-02	UPF0568 protein C14orf166 homolog	1704.965	869.005	1589.046	1341.419
E41L2_MOUSE	19	3		Band 4.1-like protein 2 Epb41l2	698.610	833.796	583.374	494.633

SURF4_MOUSE	2	1	5.03E-02 5.06E-02	Surfeit locus protein 4 Surf4	26.224	0.125	0.000	2.572
MY18A_MOUSE	12	4	5.08E-02	Unconventional myosin-XVIIIa Myo18a	675.848	955.917	2653.234	2062.329
APEX1_MOUSE	9	3	5.10E-02	DNA-(apurinic or apyrimidinic site) lyase Apex1	1285.015	1473.381	2117.868	934.542
IDI1_MOUSE	9	3	5.11E-02	Isopentenyl-diphosphate Deltaisomerase 1 Idi1	900.433	2148.973	1584.656	1548.610
EIF3G_MOUSE	4	1	5.12E-02	Eukaryotic translation initiation factor 3 subunit G Eif3g	295.765	338.451	1662.378	1092.087
TMC5_MOUSE	27	6	5.17E-02	Transmembrane channel-like protein 5 Tmc5	817.861	4632.540	2820.339	1731.361
DNJC9_MOUSE	8	2	5.18E-02	DnaJ homolog subfamily C member 9 Dnajc9	858.829	1316.823	1926.383	1031.571
CPSF5_MOUSE	7	1	5.19E-02	Cleavage and polyadenylation specificity factor subunit 5 Nudt21	2021.809	1434.887	5844.418	2132.013
SCPDL_MOUSE	1	1	5.19E-02	Saccharopine dehydrogenase-like oxidoreductase Sccpdh	40.626	0.000	0.000	0.000
NOLC1_MOUSE	9	1	5.26E-02	Nucleolar and coiled-body phosphoprotein 1 Nolc1	1702.332	1424.767	1310.971	1100.374
MESD_MOUSE	5	3	5.29E-02	LRP chaperone MESD Mesd	600.227	697.445	1252.564	1012.226
PFD2_MOUSE	6	2	5.32E-02	Prefoldin subunit 2 Pfdn2	908.789	1020.633	545.187	649.718
RPN2_MOUSE	10	4	5.32E-02	Dolichyl-diphosphooligosaccharide--protein glycosyltransferase subunit 2 Rpn2	257.653	380.557	570.312	425.244
RT29_MOUSE	7	2	5.35E-02	28S ribosomal protein S29, mitochondrial Dap3	728.484	718.084	627.343	264.849

TEX11_MOUSE	16	2	5.41E-02	Testis-expressed protein 11 Tex11	1568.641	427.911	714.679	950.177
ARL2_MOUSE	2	1	5.43E-02	ADP-ribosylation factor-like protein 2 Arl2	946.057	1584.846	457.301	2116.608
PP1A_MOUSE	5	1	5.45E-02	Serine/threonine-protein phosphatase PP1-alpha catalytic subunit Ppp1ca	4.210	31.882	25.610	16.862
ATP5L_MOUSE	2	2	5.49E-02	ATP synthase subunit g, mitochondrial Atp5l	907.885	800.732	3485.314	3945.156
RL9_MOUSE	13	3	-02	60S ribosomal protein L9 Rpl9	2350.926	3896.143	3108.190	3284.725
ANXA8_MOUSE	8	2	-02 5.52E 5.53E	Annexin A8 Anxa8	1093.779	541.970	2215.137	339.541
IGS10_MOUSE	21	1	5.56E-02	Immunoglobulin superfamily member 10 Igsf10	131.821	362.925	383.114	1227.948
PRS6B_MOUSE	11	5	5.57E-02	26S proteasome regulatory subunit 6B Psmc4	716.451	873.704	2569.079	1433.054

ARL1_MOUSE	2	1	5.60E-02	ADP-ribosylation factor-like protein 1 Arl1	516.838	821.497	106.430	540.905
PSA7L_MOUSE	7	1	5.61E-02	Proteasome subunit alpha type-7like Psma8	1353.805	2019.920	3169.976	1904.097
DHX9_MOUSE	25	5	5.61E-02	ATP-dependent RNA helicase A Dhx9	1225.552	564.957	999.993	1117.940
VPS35_MOUSE	11	2	5.64E-02	Vacuolar protein sorting-associated protein 35 Vps35	660.220	515.722	515.543	702.984
ANKR2_MOUSE	5	2	5.65E-02	Ankyrin repeat domain-containing protein 2 Ankrd2	10.888	20.281	100.810	277.697
S10AB_MOUSE	4	3	5.70E-02	Protein S100-A11 S100a11	248.615	288.038	44.947	270.995
PRS8_MOUSE	20	6	5.73E-02	26S proteasome regulatory subunit 8 Psmc5	449.816	535.809	681.758	706.677
IF2A_MOUSE	18	9	5.79E-02	Eukaryotic translation initiation factor 2 subunit 1 Eif2s1	1415.880	1376.203	2091.774	1403.314

ATP5H_MOUSE	11	8	5.82E-02	ATP synthase subunit d, mitochondrial Atp5h	1721.282	3651.337	159.920	2376.713
FLII_MOUSE	11	2	-02	Protein flightless-1 homolog Flii	418.889	740.066	474.658	460.346
TX1B3_MOUSE	3	1	-02 -02 5.85E 5.86E	Tax1-binding protein 3 Tax1bp3	252.036	5.103	893.361	394.284
1433B_MOUSE	22	3	5.87E	14-3-3 protein beta/alpha Ywhab	102.923	88.977	1528.226	178.565
CO1A2_MOUSE	18	1	5.90E-02	Collagen alpha-2(I) chain Col1a2	5.118	3.179	11.002	71.616
CSTFT_MOUSE	6	2	5.91E-02	Cleavage stimulation factor subunit 2 tau variant Cstf2t	393.882	668.825	245.052	159.373
AGAP2_MOUSE	6	1	5.91E-02	Arf-GAP with GTPase, ANK repeat and PH domain-containing protein 2 Agap2	1992.049	3700.537	3410.145	5052.532
CP2B9_MOUSE	4	1	5.92E-02	Cytochrome P450 2B9 Cyp2b9	22890.395	20690.748	28058.099	16808.378
SRSF9_MOUSE	2	1	5.93E-02	Serine/arginine-rich splicing factor 9 Srsf9	587.823	1832.205	4131.216	1589.109
GSTM3_MOUSE	4	1	5.98E-02	Glutathione S-transferase Mu 3 Gstm3	15.274	106.771	224.842	2.197
CKAP4_MOUSE	21	4	5.98E-02	Cytoskeleton-associated protein 4 Ckap4	261.706	188.996	1051.324	453.696
RRBP1_MOUSE	38	2	5.99E-02	Ribosome-binding protein 1 Rrbp1	877.590	1179.997	1143.898	496.540
NONO_MOUSE	18	6	5.99E-02	Non-POU domain-containing octamer-binding protein Nono	3442.506	1431.975	2473.308	1909.115
PP4R1_MOUSE	10	2	6.05E-02	Serine/threonine-protein phosphatase 4 regulatory subunit 1 Ppp4r1	2014.695	496.786	103.325	1153.052
DNLI1_MOUSE	21	3	6.07E-02	DNA ligase 1 Lig1	406.892	401.590	275.000	223.849
CE290_MOUSE	39	3	6.08E-02	Centrosomal protein of 290 kDa Cep290	50.463	143.881	73.910	69.533

UBQL4_MOUSE	4	2	6.08E-02	Ubiquilin-4 Ubqln4	45.830	2.615	20.884	16.099
PSMD5_MOUSE	7	3	6.11E-02	26S proteasome non-ATPase regulatory subunit 5 Psmd5	1486.076	75.786	132.785	48.399
EPN2_MOUSE	5	1	6.16E-02	Epsin-2 Epn2	36.669	12.498	2.587	64.102
PUF60_MOUSE	7	1	6.20E-02	Poly(U)-binding-splicing factor PUF60 Puf60	1252.943	1230.288	1818.177	1191.684
CO6A1_MOUSE	7	1	6.22E-02	Collagen alpha-1(VI) chain Col6a1	13.575	0.144	0.005	0.092
F120C_MOUSE	18	2	6.22E-02	Constitutive coactivator of PPARgamma-like protein 2 Fam120c	1669.318	3150.277	4138.014	3078.962
IMA3_MOUSE	4	1	6.30E-02	Importin subunit alpha-3 Kpna4	32.151	0.000	6.870	6.164
PCNA_MOUSE	12	5	6.35E-02	Proliferating cell nuclear antigen Pcna	2071.184	1357.467	1314.108	1103.452
UBAP2_MOUSE	6	1	6.36E-02	Ubiquitin-associated protein 2 Ubap2	1102.873	1180.868	307.046	589.314
RAVR1_MOUSE	6	2	6.37E-02	Ribonucleoprotein PTB-binding 1 Raver1	135.372	73.130	50.105	52.941
PR40A_MOUSE	6	1	6.40E-02	Pre-mRNA-processing factor 40 homolog A Prpf40a	529.477	904.772	627.399	586.571
NUFP2_MOUSE	3	1	6.41E-02	Nuclear fragile X mental retardation-interacting protein 2 Nufip2	73.401	21.327	532.985	212.674
ANXA4_MOUSE	19	5	-02	Annexin A4 Anxa4	2457.338	4320.429	4730.040	3777.543
RALY_MOUSE	6	2	-02 6.42E 6.43E	RNA-binding protein Raly Raly	984.444	777.094	696.617	744.609
HNRPC_MOUSE	15	7	6.44E-02	Heterogeneous nuclear ribonucleoproteins C1/C2 Hnrnpc	2125.450	1278.530	1958.010	862.763
RAD54_MOUSE	15	1	6.45E-02	DNA repair and recombination protein RAD54-like Rad54l	29.484	364.406	12.571	135.424
PDLI7_MOUSE	7	2	6.46E-02	PDZ and LIM domain protein 7 Pdlim7	204.558	88.315	252.490	265.593

ILEUA_MOUSE	8	5	6.50E-02	Leukocyte elastase inhibitor A Serpinb1a	685.331	1070.285	981.232	1086.921
CLCN5_MOUSE	14	1	6.50E-02	H(+)/Cl(-) exchange transporter 5 Clcn5	110.142	86.566	710.353	1112.084
HERP1_MOUSE	3	2	6.50E-02	Homocysteine-responsive endoplasmic reticulum-resident ubiquitin-like domain member 1 protein Herpud1	55.085	21.582	102.799	102.976
ETFA_MOUSE	13	6	6.54E-02	Electron transfer flavoprotein subunit alpha, mitochondrial Etfa	1893.134	1509.425	1173.718	534.985
SEN34_MOUSE	2	1	6.55E-02	tRNA-splicing endonuclease subunit Sen34 Tsen34	95.776	34.438	0.660	14.236
K2C1B_MOUSE	24	4	6.59E-02	Keratin, type II cytoskeletal 1b Krt77	1531.988	128.673	791.545	104.229
GET4_MOUSE	4	2	6.60E-02	Golgi to ER traffic protein 4 homolog Get4	527.736	773.834	115.845	197.085
CALU_MOUSE	11	4	6.60E-02	Calumenin Calu	331.479	528.761	371.701	277.597
GANAB_MOUSE	9	3	6.60E-02	Neutral alpha-glucosidase AB Ganab	330.300	188.137	619.029	283.796
NHRF1_MOUSE	5	2	6.67E-02	Na(+)/H(+) exchange regulatory cofactor NHE-RF1 Slc9a3r1	85.086	37.657	51.652	334.492
CDK1_MOUSE	17	10	6.74E-02	Cyclin-dependent kinase 1 Cdk1	4061.052	3771.174	4333.308	2693.852
ALDOC_MOUSE	8	1	6.76E-02	Fructose-bisphosphate aldolase C Aldoc	3668.536	4709.821	3645.781	3902.703
TIF1B_MOUSE	17	5	6.77E-02	Transcription intermediary factor 1beta Trim28	2547.868	2364.882	2320.872	1537.944
SH3L1_MOUSE	4	3	6.79E-02	SH3 domain-binding glutamic acidrich-like protein Sh3bgrl	302.765	52.070	163.707	208.235
UBP2L_MOUSE	8	3	6.81E-02	Ubiquitin-associated protein 2-like Ubap2l	735.895	612.698	535.328	280.148

HPS3_MOUSE	16	1	6.88E-02	Hermansky-Pudlak syndrome 3 protein homolog Hps3	6.004	15.292	15.705	155.304
SF3B6_MOUSE	2	1	-02	Splicing factor 3B subunit 6 Sf3b6	316.141	73.026	38.863	488.462
SGT1_MOUSE	7	3	6.88E-02 6.89E	Protein SGT1 homolog Sugt1	358.345	596.738	140.028	135.083
IL18_MOUSE	3	1	-02	Interleukin-18 Il18	497.820	0.896	597.744	16.877
BASP1_MOUSE	6	4	6.89E-02 6.92E	Brain acid soluble protein 1 Basp1	29.793	196.225	144.324	438.834

PA1B3_MOUSE	4	2	6.93E-02	Platelet-activating factor acetylhydrolase IB subunit gamma Pafah1b3	240.663	826.296	515.554	949.140
PSA4_MOUSE	8	1	6.96E-02	Proteasome subunit alpha type-4 Psma4	3550.194	3982.108	4207.259	3106.167
LTOR2_MOUSE	4	1	7.03E-02	Ragulator complex protein LAMTOR2 Lamtor2	84.971	0.581	0.978	138.897
THIC_MOUSE	13	8	7.06E-02	Acetyl-CoA acetyltransferase, cytosolic Acat2	4637.125	1008.509	843.037	477.735
ECHB_MOUSE	5	2	7.13E-02	Trifunctional enzyme subunit beta, mitochondrial Hadhb	212.421	30.364	10.338	192.699
MPCP_MOUSE	11	3	7.15E-02	Phosphate carrier protein, mitochondrial Slc25a3	718.707	749.677	1238.169	717.223
NAA20_MOUSE	1	1	7.19E-02	N-alpha-acetyltransferase 20 Naa20	1178.167	997.597	3767.771	4683.971
SF3A3_MOUSE	8	2	7.26E-02	Splicing factor 3A subunit 3 Sf3a3	334.124	437.401	615.489	487.708
PEX19_MOUSE	2	1	7.26E-02	Peroxisomal biogenesis factor 19 Pex19	4.443	44.492	192.927	118.736
SFXN1_MOUSE	6	2	7.27E-02	Sideroflexin-1 Sfxn1	172.974	25.625	387.585	107.779
DNJB6_MOUSE	3	1	7.29E-02	DnaJ homolog subfamily B member 6 Dnajb6	1434.597	1967.728	2288.011	1829.729

BICD2_MOUSE	25	1	7.41E-02	Protein bicaudal D homolog 2 Bicd2	369.049	911.555	668.006	731.031
YBEY_MOUSE	5	1	7.42E-02	Endoribonuclease YbeY Ybey	28.039	274.294	23.105	71.949
HSP72_MOUSE	25	2	7.45E-02	Heat shock-related 70 kDa protein 2 Hspa2	1871.127	1737.750	2825.094	2495.182
RS13_MOUSE	9	2	7.56E-02	40S ribosomal protein S13 Rps13	7574.532	7920.975	6669.566	5204.039
PDXD1_MOUSE	8	2	7.57E-02	Pyridoxal-dependent decarboxylase domain-containing protein 1 Pdxdc1	533.788	1066.237	1412.154	1556.280
CLIC5_MOUSE	4	1	7.64E-02	Chloride intracellular channel protein 5 Clic5	76.024	28.813	25.907	14.495
MIPT3_MOUSE	8	4	7.69E-02	TRAF3-interacting protein 1 Traf3ip1	3234.671	810.426	340.569	476.999
TIM50_MOUSE	2	1	7.76E-02	Mitochondrial import inner membrane translocase subunit TIM50 Timm50	106.683	0.435	26.732	59.984

RYR2_MOUSE	58	3	7.76E-02	Ryanodine receptor 2 Ryr2	401.820	283.695	743.834	307.381
TCPA_MOUSE	38	11	7.78E-02	T-complex protein 1 subunit alpha Tcp1	1826.600	2048.077	2347.790	1621.954
MARCS_MOUSE	4	3	7.78E-02	Myristoylated alanine-rich C-kinase substrate Marcks	371.612	1101.589	84.482	252.071
EPHA4_MOUSE	11	1	7.79E-02	Ephrin type-A receptor 4 Epha4	112.477	4.456	11.031	33.132
NDUB9_MOUSE	5	2	7.80E-02	NADH dehydrogenase [ubiquinone] 1 beta subcomplex subunit 9 Ndufb9	36.674	166.433	70.734	554.521
DYH17_MOUSE	35	7	7.82E-02	Dynein heavy chain 17, axonemal Dnah17	2332.322	2533.602	847.672	1273.328
SRSF3_MOUSE	6	1	7.82E-02	Serine/arginine-rich splicing factor 3 Srsf3	1273.258	1557.621	507.776	1003.777

UBE2O_MOUSE	13	3	7.83E-02	(E3-independent) E2 ubiquitinconjugating enzyme UBE2O Ube2o	84.540	99.454	76.186	20.470
CE152_MOUSE	22	5	7.84E-02	Centrosomal protein of 152 kDa Cep152	1297.970	1220.681	2363.239	733.615
ALAT2_MOUSE	11	3	7.85E-02	Alanine aminotransferase 2 Gpt2	709.977	571.243	2163.375	1619.288
NP1L1_MOUSE	8	4	7.89E-02	Nucleosome assembly protein 1like 1 Nap1l1	1544.898	2065.196	1838.773	989.471
DAPK1_MOUSE	6	1	7.89E-02	Death-associated protein kinase 1 Dapk1	124.150	57.070	1127.176	664.308
HKDC1_MOUSE	16	1	7.91E-02	Putative hexokinase HKDC1 Hkdc1	1.826	0.037	18.225	3.765
M2OM_MOUSE	11	3	7.96E-02	Mitochondrial 2-oxoglutarate/malate carrier protein Slc25a11	342.482	367.021	640.960	1051.674
PPP6_MOUSE	3	2	8.00E-02	Serine/threonine-protein phosphatase 6 catalytic subunit Ppp6c	287.153	215.150	247.318	111.217
FKBP2_MOUSE	1	1	8.03E-02	Peptidyl-prolyl cis-trans isomerase FKBP2 Fkbp2	1247.717	824.500	444.562	984.482
ROA3_MOUSE	22	7	8.04E-02	Heterogeneous nuclear ribonucleoprotein A3 Hnrnpa3	1520.174	631.749	1180.894	1212.135
IBP5_MOUSE	8	2	8.04E-02	Insulin-like growth factor-binding protein 5 Igfbp5	21.010	176.041	65.419	28.907

PREP_MOUSE	11	1	8.05E-02	Presequence protease, mitochondrial Pitrm1	5.089	50.894	157.428	3.763
DAZP1_MOUSE	2	1	-02	DAZ-associated protein 1 Dazap1	251.432	163.239	452.931	259.406
RL5_MOUSE	21	14	8.09E 8.14E -02	60S ribosomal protein L5 Rpl5	5200.197	6700.683	6252.947	3094.033

SCOT1_MOUSE	11	3	8.14E-02	Succinyl-CoA:3-ketoacid coenzyme A transferase 1, mitochondrial Oxct1	705.167	611.815	1245.183	804.063
VCIP1_MOUSE	18	2	8.18E-02	Deubiquitinating protein VCIP135 Vcpip1	1810.939	2720.791	2128.480	1528.461
RT27_MOUSE	9	1	8.18E-02	28S ribosomal protein S27, mitochondrial Mrps27	193.854	374.339	153.983	696.317
IF4B_MOUSE	18	5	8.18E-02	Eukaryotic translation initiation factor 4B Eif4b	2334.983	3844.485	3239.759	2683.969
PAK2_MOUSE	10	2	8.26E-02	Serine/threonine-protein kinase PAK 2 Pak2	564.116	535.340	754.867	530.639
BAG6_MOUSE	13	2	8.26E-02	Large proline-rich protein BAG6 Bag6	887.965	1353.938	686.525	560.210
UBR5_MOUSE	39	2	8.26E-02	E3 ubiquitin-protein ligase UBR5 Ubr5	252.840	457.905	618.801	472.631
COCA1_MOUSE	39	2	8.29E-02	Collagen alpha-1(XII) chain Col12a1	240.207	350.486	411.141	145.418
PRR12_MOUSE	13	1	-02	Proline-rich protein 12 Prr12	4753.753	6071.286	7017.718	1658.171
LARP1_MOUSE	21	2	8.36E-02 8.48E-02	La-related protein 1 Larp1	13.098	99.710	180.651	534.046
RL35A_MOUSE	8	5	8.49E-02	60S ribosomal protein L35a Rpl35a	1080.589	673.047	1590.725	1837.082
TANC2_MOUSE	14	2	8.52E-02	Protein TANC2 Tanc2	337.171	208.078	49.889	354.234
PPR21_MOUSE	15	3	8.55E-02	Protein phosphatase 1 regulatory subunit 21 Ppp1r21	1013.704	1092.055	989.426	1642.458
TCPH_MOUSE	33	13	8.58E-02	T-complex protein 1 subunit eta Cct7	2541.714	2509.591	3387.397	2221.867
WASC2_MOUSE	16	5	-02	WASH complex subunit 2 Washc2	279.691	482.145	366.037	569.206
CTNA1_MOUSE	29	7	8.62E-02 8.69E-02	Catenin alpha-1 Ctnna1	1388.783	1926.623	780.290	1056.476

PLAP_MOUSE	7	1	8.71E-02	Phospholipase A-2-activating protein Plaa	73.675	107.334	12.521	0.468
SEP15_MOUSE	1	1	8.82E-02	Selenoprotein F Selenof	261.935	58.762	17.818	826.131
IMPG1_MOUSE	6	1	8.85E-02	Interphotoreceptor matrix proteoglycan 1 Impg1	177.073	341.447	270.556	2.754
EST2A_MOUSE	1	1	8.99E-02	Pyrethroid hydrolase Ces2a Ces2a	180.188	194.526	4.174	7.109
PLP2_MOUSE	2	2	02E-02	Proteolipid protein 2 Plp2	1096.812	1564.429	258.457	259.212
SF3B5_MOUSE	1	1	-02 9. 9.08E	Splicing factor 3B subunit 5 Sf3b5	13.955	2.653	174.158	116.741
NSDHL_MOUSE	9	3	9.18E-02	Sterol-4-alpha-carboxylate 3dehydrogenase, decarboxylating Nsdhl	315.003	557.418	319.746	1422.322
GBB3_MOUSE	6	1	9.19E-02	Guanine nucleotide-binding protein G(I)/G(S)/G(T) subunit beta-3 Gnb3	313.483	796.580	2609.109	732.756
UBP14_MOUSE	13	3	9.20E-02	Ubiquitin carboxyl-terminal hydrolase 14 Usp14	1383.415	1636.614	1793.819	1405.528
ITB1_MOUSE	10	2	9.23E	Integrin beta-1 Itgb1	993.678	1260.694	1036.628	874.884
TOM1_MOUSE	3	1	9.26E	Target of Myb protein 1 Tom1	26.080	5.337	12.396	66.464
GBP4_MOUSE	5	1	-02	Guanylate-binding protein 4 Gbp4	226.002	923.511	20.969	148.927
CROCC_MOUSE	59	6	-02 -02 -02 9.32E 9.33E	Rootletin Crocc	1597.944	921.164	2604.819	795.001
ETFD_MOUSE	5	1	9.34E-02	Electron transfer flavoproteinubiquinone oxidoreductase, mitochondrial Etfdh	1.693	166.695	0.000	759.513
GPDM_MOUSE	15	5	9.37E-02	Glycerol-3-phosphate dehydrogenase, mitochondrial Gpd2	969.675	1505.976	1646.074	1044.358

1433G_MOUSE	17	2	9.40E-02	14-3-3 protein gamma Ywhag	482.674	1201.872	1655.918	343.625
IF2B_MOUSE	4	1	9.41E-02	Eukaryotic translation initiation factor 2 subunit 2 Eif2s2	673.712	576.528	1669.508	618.030
HNRDL_MOUSE	5	3	9.49E-02	Heterogeneous nuclear ribonucleoprotein D-like Hnrnpdl	525.334	297.297	193.208	290.204
RL36A_MOUSE	4	1	9.56E-02	60S ribosomal protein L36a Rpl36a	2818.654	915.050	543.165	913.059
NB5R2_MOUSE	1	1	9.57E-02	NADH-cytochrome b5 reductase 2 Cyb5r2	1618.274	143.018	957.821	352.245
HINT1_MOUSE	1	1	9.64E-02	Histidine triad nucleotide-binding protein 1 Hint1	6476.779	3147.497	12172.186	5516.820
VAT1_MOUSE	13	7	9.77E-02	Synaptic vesicle membrane protein VAT-1 homolog Vat1	3506.400	4067.651	5031.855	2520.064
CO7A1_MOUSE	24	7	9.84E-02	Collagen alpha-1(VII) chain Col7a1	647.420	1241.227	905.655	249.140
BIR1A_MOUSE	10	2	9.86E-02	Baculoviral IAP repeat-containing protein 1a Naip1	40.786	29.194	37.982	172.535
CNDG2_MOUSE	16	3	9.86E-02	Condensin-2 complex subunit G2 Ncapg2	770.329	1385.733	1893.643	1813.687
USP9X_MOUSE	27	3	1.01E-01	Probable ubiquitin carboxylterminal hydrolase FAF-X Usp9x	414.090	385.474	278.334	237.015
ASAH1_MOUSE	9	1	1.01E-01	Acid ceramidase Asah1	319.911	39.693	114.281	254.988
UAP1L_MOUSE	6	2	1.02E-01	UDP-N-acetylhexosamine pyrophosphorylase-like protein 1 Uap1l1	145.028	128.872	128.574	249.288
NUDC3_MOUSE	5	2	1.03E-01	NudC domain-containing protein 3 Nudcd3	7.057	32.363	55.901	263.405
FKB1A_MOUSE	1	1	1.03E-01	Peptidyl-prolyl cis-trans isomerase FKBP1A Fkbp1a	3883.290	1670.913	7006.077	3114.097
GDIR2_MOUSE	2	1	1.04E-01	Rho GDP-dissociation inhibitor 2 Arhgdib	2177.068	1951.038	2632.675	938.145

TRI16_MOUSE	3	1	1.04E-01	Tripartite motif-containing protein 16 Trim16	101.333	0.024	0.000	2.823
DKC1_MOUSE	7	1	1.04E-01	H/ACA ribonucleoprotein complex subunit 4 Dkc1	3.334	7.324	35.543	12.190
OLA1_MOUSE	5	1	-01	Obg-like ATPase 1 Ola1	681.657	271.562	6.896	550.287
FA49B_MOUSE	6	2	-01	Protein FAM49B Fam49b	317.818	223.803	163.675	141.031
			1.05E					
			1.06E					
DYSF_MOUSE	19	1	1.07E-01	Dysferlin Dysf	37.903	35.729	46.884	109.436
THIKA_MOUSE	6	1	1.08E-01	3-ketoacyl-CoA thiolase A, peroxisomal Acaa1a	2.266	0.080	49.754	20.194
TLN1_MOUSE	94	22	1.08E	Talin-1 Tln1	2432.767	2797.732	2801.351	1971.559
RASH_MOUSE	3	1	1.08E	GTPase HRas Hras	157.786	87.100	43.736	34.463
SEM6D_MOUSE	7	1	-01	Semaphorin-6D Sema6d	378.294	295.870	26.032	42.858
BUD31_MOUSE	1	1	-01	Protein BUD31 homolog Bud31	229.923	66.208	84.265	157.793
			-01					
			-01					
			1.09E					
			1.09E					
RT07_MOUSE	4	1	1.09E-01	28S ribosomal protein S7, mitochondrial Mrps7	46.004	141.917	149.282	409.279
HNRPQ_MOUSE	13	2	1.09E-01	Heterogeneous nuclear ribonucleoprotein Q Syncrip	650.576	876.338	1640.739	839.639

DISP2_MOUSE	6	1	1.10E-01	Protein dispatched homolog 2 Disp2	106.685	136.380	961.462	1435.552
TBD2B_MOUSE	9	2	1.10E-01	TBC1 domain family member 2B Tbc1d2b	99.459	54.328	43.800	136.876
KAD3_MOUSE	8	2	1.10E-01	GTP:AMP phosphotransferase AK3, mitochondrial Ak3	119.243	179.232	640.358	654.326
PP1R7_MOUSE	6	1	1.10E-01	Protein phosphatase 1 regulatory subunit 7 Ppp1r7	1.266	22.905	81.067	1.759
EIF3L_MOUSE	10	1	1.12E-01	Eukaryotic translation initiation factor 3 subunit L Eif3l	141.839	6.546	1.624	0.000

HNRPF_MOUSE	9	2	1.13E-01	Heterogeneous nuclear ribonucleoprotein F Hnrnpf	1497.814	1198.392	3161.903	1483.886
EFTU_MOUSE	14	7	1.13E-01	Elongation factor Tu, mitochondrial Tufm	400.897	786.162	1169.423	1470.111
WDR72_MOUSE	14	2	1.14E-01	WD repeat-containing protein 72 Wdr72	518.774	637.550	173.778	326.089
MYADM_MOUSE	3	2	1.14E-01	Myeloid-associated differentiation marker Myadm	1055.370	819.327	780.986	459.150
PHB_MOUSE	19	7	1.15E-01	Prohibitin Phb	3618.787	2948.280	5340.541	5110.728
SMUF1_MOUSE	22	5	1.15E-01	E3 ubiquitin-protein ligase SMURF1 Smurf1	1509.418	1888.920	1318.553	521.726
CPSF3_MOUSE	7	2	1.16E-01	Cleavage and polyadenylation specificity factor subunit 3 Cpsf3	77.637	20.884	253.907	40.247
KCMF1_MOUSE	2	1	1.16E-01	E3 ubiquitin-protein ligase KCMF1 Kcmf1	6.791	0.000	39.421	1.751
CAB39_MOUSE	7	2	1.16E-01	Calcium-binding protein 39 Cab39	5383.618	288.512	296.267	175.066
ACADM_MOUSE	6	1	1.16E-01	Medium-chain specific acyl-CoA dehydrogenase, mitochondrial Acadm	217.426	33.056	32.639	208.691
SETB1_MOUSE	11	1	1.17E-01	Histone-lysine N-methyltransferase SETDB1 Setdb1	9.499	66.638	191.065	0.604
ARPC3_MOUSE	10	7	1.17E-01	Actin-related protein 2/3 complex subunit 3 Arpc3	2604.854	2746.554	1026.547	1177.522
TCPZ_MOUSE	32	8	1.18E-01	T-complex protein 1 subunit zeta Cct6a	1877.031	1442.013	2216.977	1270.831
CSN6_MOUSE	4	2	1.18E-01	COP9 signalosome complex subunit 6 Cops6	726.241	814.262	708.014	986.304

KPYM_MOUSE	62	21	-01	1.19E	Pyruvate kinase PKM Pkm		2299.829	2853.317
PDIA1_MOUSE	36	17	-01				10835.560	7407.276
			723.396	2310.039				
			1.19E	Protein disulfide-isomerase P4hb	6529.241	8038.723		

PUR6_MOUSE	9	1	1.20E-01	Multifunctional protein ADE2 Paics	1076.856	304.318	59.399	472.792
SFPQ_MOUSE	21	7	1.20E-01	Splicing factor, proline- and glutamine-rich Sfpq	2603.405	2447.412	2580.514	4134.794
DEST_MOUSE	12	4	1.21E-01	Destrin Dstn	2192.574	2153.190	1206.646	1185.168
LAP2B_MOUSE	13	3	1.21E-01	Lamina-associated polypeptide 2, isoforms beta/delta/epsilon/gamma 1459.047 Tmpo	1047.212	4707.512	1120.636	
EI2BB_MOUSE	3	1	1.21E-01	Translation initiation factor eIF-2B subunit beta Eif2b2	657.977	779.326	2259.207	3212.419
PDIA6_MOUSE	17	9	1.21E-01	Protein disulfide-isomerase A6 Pdia6	2736.992	2852.153	5266.777	3067.472
HIBCH_MOUSE	9	2	1.22E-01	3-hydroxyisobutyryl-CoA hydrolase, mitochondrial Hibch	229.994	487.381	136.716	272.129
ACOT2_MOUSE	12	1	1.23E-01	Acyl-coenzyme A thioesterase 2, mitochondrial Acot2	66.611	88.606	353.776	346.727
ALBU_MOUSE	8	2	1.23E	Serum albumin Alb	1310.717	1157.981	1407.432	2536.865
WASH1_MOUSE	7	2	-01				180.041	122.390
			-01	1.23EWASH complex subunit 1 Washc1	896.192	56.441		
PIPNA_MOUSE	3	1	1.23E-01	Phosphatidylinositol transfer protein alpha isoform Pitpna	385.895	119.451	161.642	100.327
SRPRB_MOUSE	3	1	1.23E-01	Signal recognition particle receptor subunit beta Srprb	180.028	181.641	5.653	38.795
NUBP2_MOUSE	3	1	1.23E-01	Cytosolic Fe-S cluster assembly factor NUBP2 Nubp2	561.914	618.111	252.839	519.408
T2EB_MOUSE	6	2	1.24E-01	General transcription factor IIE subunit 2 Gtf2e2	215.125	98.811	242.831	167.936

HNRPD_MOUSE	5	2	1.24E-01	Heterogeneous nuclear ribonucleoprotein D0 Hnrnpd	818.508	204.238	253.018	547.366
RIR2_MOUSE; RIR2B_MOUSE	5	3	1.25E-01	Ribonucleoside-diphosphate reductase subunit M2 Rrm2	471.689	322.412	158.710	281.031
SNX6_MOUSE	10	3	1.25E-01	Sorting nexin-6 Snx6	116.186	221.912	42.637	12.293
NDUB4_MOUSE	1	1	1.25E-01	NADH dehydrogenase [ubiquinone] 1 beta subcomplex subunit 4 Ndufb4	4.617	112.616	20.386	1109.491

MAP4_MOUSE	36	10	1.26E-01	Microtubule-associated protein 4 Map4	852.769	1361.903	1924.575	1288.294
OBP1B_MOUSE	2	1	-01	Odorant-binding protein 1b Obp1b	15.309	39.054	1003.637	4.328
AMPL_MOUSE	9	3	-01 1.27E 1.28E	Cytosol aminopeptidase Lap3	667.532	468.675	306.252	146.783
RBP2_MOUSE	41	6	1.28E-01	E3 SUMO-protein ligase RanBP2 Ranbp2	2117.818	1960.503	1125.240	2428.377
RL27A_MOUSE	4	1	1.30E-01	60S ribosomal protein L27a Rpl27a	7878.403	9226.355	13005.934	7975.307
CH10_MOUSE	5	3	1.31E-01	10 kDa heat shock protein, mitochondrial Hspe1	3257.480	1322.125	1459.123	2283.880
COPB2_MOUSE	9	3	1.32E-01	Coatomer subunit beta' Copb2	221.155	82.090	95.575	51.273
IF5_MOUSE	6	1	1.33E-01	Eukaryotic translation initiation factor 5 Eif5	191.150	160.041	55.239	162.516
VATE1_MOUSE	11	3	1.33E-01	V-type proton ATPase subunit E 1 Atp6v1e1	1769.697	1883.878	1647.030	1452.191
NPL4_MOUSE	6	2	1.34E-01	Nuclear protein localization protein 4 homolog Nploc4	1902.821	1124.417	499.246	189.147
DUS3_MOUSE	5	3	1.34E-01	Dual specificity protein phosphatase 3 Dusp3	699.566	907.046	811.203	1972.180

CPSF7_MOUSE	6	1	1.34E-01	Cleavage and polyadenylation specificity factor subunit 7 Cpsf7	3.453	0.463	17.686	62.603
HNRPL_MOUSE	12	7	1.35E-01	Heterogeneous nuclear ribonucleoprotein L Hnrnpl	1747.158	2182.272	3102.110	2193.055
SRRT_MOUSE	15	1	1.35E-01	Serrate RNA effector molecule homolog Srrt	34.841	70.090	81.519	0.203
TM201_MOUSE	4	1	1.35E-01	Transmembrane protein 201 Tmem201	530.800	1166.268	921.056	319.832
SNRPA_MOUSE	5	1	1.35E-01	U1 small nuclear ribonucleoprotein A Snrpa	12.891	19.130	410.338	606.608
TYSY_MOUSE	7	1	1.36E-01	Thymidylate synthase Tyms	764.907	589.623	953.251	641.726
PDC6I_MOUSE	16	3	1.36E-01	Programmed cell death 6interacting protein Pdcd6ip	414.860	312.296	527.579	337.679
AK1CD_MOUSE	6	1	1.36E-01	Aldo-keto reductase family 1 member C13 Akr1c13	3.116	115.824	468.879	11.225
DDAH1_MOUSE	8	1	1.37E-01	N(G),N(G)-dimethylarginine dimethylaminohydrolase 1 Ddah1	6.929	0.280	0.185	0.080

SP16H_MOUSE	13	5	1.37E-01	FACT complex subunit SPT16 Supt16h	1071.694	975.981	1478.777	686.698
COMD5_MOUSE	4	1	1.37E-01	COMM domain-containing protein 5 Commd5	2628.104	1469.394	4005.613	2551.978
KRT82_MOUSE	19	4	-01	Keratin, type II cuticular Hb2 Krt82	986.004	1074.626	3438.586	1145.553
PLD2_MOUSE	21	3	-01 1.38E 1.38E	Phospholipase D2 Pld2	814.498	708.883	466.798	889.563
MRP_MOUSE	2	2	1.39E-01	MARCKS-related protein Marcksl1	1238.525	1524.569	1716.492	1678.722
TRPM4_MOUSE	10	1	1.40E-01	Transient receptor potential cation channel subfamily M member 4 Trpm4	743.204	804.048	1406.427	531.709
FAAA_MOUSE	3	1		Fumarylacetoacetase Fah	15.330	0.000	153.621	2.209

PFD5_MOUSE	3	1	-01 -01 1.40E 1.40E	Prefoldin subunit 5 Pfdn5	690.431	925.982	1994.849	1054.312
EIF3D_MOUSE	17	4	1.41E-01	Eukaryotic translation initiation factor 3 subunit D Eif3d	885.311	801.445	685.140	844.065
PGM5_MOUSE	10	4	1.41E-01	Phosphoglucomutase-like protein 5 Pgm5	50.809	34.616	1059.521	141.987
RT18B_MOUSE	11	3	1.42E-01	28S ribosomal protein S18b, mitochondrial Mrps18b	383.761	688.014	147.654	196.087
KCRB_MOUSE	5	2	1.43E-01	Creatine kinase B-type Ckb	171.641	44.558	156.757	624.934
CNOT7_MOUSE	2	1	1.43E-01	CCR4-NOT transcription complex subunit 7 Cnot7	117.625	41.669	14.587	131.233
K2C8_MOUSE	39	6	1.43E-01	Keratin, type II cytoskeletal 8 Krt8	2639.623	3574.522	5221.552	2964.308
RAB8B_MOUSE	4	1	1.44E-01	Ras-related protein Rab-8B Rab8b	58.166	137.111	3.958	36.578
PSMD1_MOUSE	13	1	1.44E-01	26S proteasome non-ATPase regulatory subunit 1 Psmd1	1407.517	1136.247	1102.017	640.148
SEPT2_MOUSE	10	7	1.45E-01	Septin-2 Sept2	1223.988	767.127	1399.922	889.708
SPTA1_MOUSE	16	1	1.46E-01	Spectrin alpha chain, erythrocytic 1 Spta1	1547.847	1710.359	2029.778	1227.808
FRIL1_MOUSE	2	1	1.46E-01	Ferritin light chain 1 Ftl1	556.357	85.605	106.581	22.864
RUXG_MOUSE	1	1	1.47E-01	Small nuclear ribonucleoprotein G Snrpg	43.704	11.330	113.599	327.997
TBCD7_MOUSE	3	1	1.47E-01	TBC1 domain family member 7 Tbc1d7	84.354	65.629	380.031	170.062
TPD52_MOUSE	5	1	1.47E-01	Tumor protein D52 Tpd52	315.605	129.381	108.064	128.335
EIF3H_MOUSE	7	4	1.49E-01	Eukaryotic translation initiation factor 3 subunit H Eif3h	768.699	354.554	369.690	138.182
RS20_MOUSE	6	3	1.50E-01	40S ribosomal protein S20 Rps20	29.915	129.588	1595.174	962.374

SNAA_MOUSE	6	3	1.50E-01	Alpha-soluble NSF attachment protein Napa	889.229	818.146	679.244	673.189
MYO9A_MOUSE	27	1	1.51E-01	Unconventional myosin-IXa Myo9a	33.820	76.970	48.923	246.274
PSD11_MOUSE	11	4	1.51E-01	26S proteasome non-ATPase regulatory subunit 11 Psmd11	419.417	1211.697	1258.242	212.825
MCM6_MOUSE	23	4	1.52E-01	DNA replication licensing factor MCM6 Mcm6	2332.291	1601.607	3793.506	1908.299
TRAP1_MOUSE	23	3	1.52E-01	Heat shock protein 75 kDa, mitochondrial Trap1	2382.595	2937.785	2362.320	2323.931
H2AV_MOUSE	7	2	1.53E	Histone H2A.V H2afv	7.649	18.501	231.766	357.995
MYO1D_MOUSE	18	3	1.53E	Unconventional myosin-Id Myo1d	961.564	4409.162	738.726	1878.815
OTOGL_MOUSE	10	1	-01	Otogelin-like protein Otogl	18.642	0.114	3.113	1179.957
DBNL_MOUSE	11	3	-01 -01 -01 -01 -01 -01 1.53E 1.53E	Drebrin-like protein Dbnl	429.279	488.982	255.607	294.495
ASNA_MOUSE	5	2	1.53E	ATPase Asna1 Asna1	415.092	682.366	859.831	262.151
BIEA_MOUSE	2	1	1.54E	Biliverdin reductase A Blvra	569.732	97.300	98.329	144.727
ZRAB2_MOUSE	22	4	1.55E-01	Zinc finger Ran-binding domaincontaining protein 2 Zranb2	831.794	1673.773	1300.155	762.830
NDUV2_MOUSE	5	1	1.56E-01	NADH dehydrogenase [ubiquinone] flavoprotein 2, mitochondrial Ndufv2	211.525	219.562	277.199	818.983
AIMP1_MOUSE	7	3	1.57E-01	Aminoacyl tRNA synthase complex-interacting multifunctional protein 1 Aimp1	460.994	348.502	472.937	1773.745
HEAT3_MOUSE	7	2	1.57E-01	HEAT repeat-containing protein 3 Heatr3	208.068	60.103	258.694	138.142
KPYR_MOUSE	18	1	1.58E-01	Pyruvate kinase PKLR Pklr	17.128	87.279	25.750	15.496
PRDX5_MOUSE	12	4	1.58E-01	Peroxiredoxin-5, mitochondrial	1284.030	1308.437	753.846	1816.642

				Prdx5				
S10A4_MOUSE	5	2	1.58E-01	Protein S100-A4 S100a4	866.885	735.472	1895.961	1707.749
DCUP_MOUSE	6	3	1.59E-01	Uroporphyrinogen decarboxylase Urod	231.434	96.473	84.860	167.908
NPVF_MOUSE	3	1	1.59E-01	Pro-FMRFamide-related neuropeptide VF Npvf	1805.091	1539.413	1147.961	811.212
VWA3A_MOUSE	23	1	1.59E-01	von Willebrand factor A domain-containing protein 3A Vwa3a	21.382	0.010	0.671	10.563
NEP1_MOUSE	11	2	1.60E-01	Ribosomal RNA small subunit methyltransferase NEP1 Emg1	126.211	31.658	70.270	134.712
RASN_MOUSE	2	1	-01	GTPase NRas Nras	1150.161	1455.570	628.143	1700.698
HYEP_MOUSE	9	4	-01 1.60E 1.61E	Epoxide hydrolase 1 Ephx1	844.893	1459.535	2668.549	1194.658
MIC60_MOUSE	21	9	1.61E-01	MICOS complex subunit Mic60 Immt	1618.561	1765.594	1562.521	2547.957
RAB14_MOUSE	10	1	1.62E-01	Ras-related protein Rab-14 Rab14	490.794	789.528	149.925	408.339
RPAB3_MOUSE	1	1	1.62E-01	DNA-directed RNA polymerases I, II, and III subunit RPABC3 Polr2h	584.628	179.087	198.227	236.637
RL23A_MOUSE	12	5	1.62E-01	60S ribosomal protein L23a Rpl23a	11857.181	11513.141	14263.662	8347.425
PSME1_MOUSE	5	2	1.63E-01	Proteasome activator complex subunit 1 Psme1	105.831	49.471	101.971	54.461
OTUD4_MOUSE	16	2	1.64E-01	OTU domain-containing protein 4 Otud4	83.138	10.480	22.844	22.927
GCP5_MOUSE	10	2	1.64E-01	Gamma-tubulin complex component 5 Tubgcp5	940.301	29.366	109.800	40.375
RL8_MOUSE	5	3	1.66E-01	60S ribosomal protein L8 Rpl8	1036.054	828.012	4374.138	683.400
SC31A_MOUSE	16	3	1.67E-01	Protein transport protein Sec31A Sec31a	92.536	334.017	304.613	370.421

GNAI2_MOUSE	5	2	1.68E-01	Guanine nucleotide-binding protein G(i) subunit alpha-2 Gnai2	1002.057	1305.725	786.754	910.633
NUP93_MOUSE	7	1	1.69E-01	Nuclear pore complex protein Nup93 Nup93	447.973	106.800	54.106	82.020
NTM1A_MOUSE	4	1	1.71E-01	N-terminal Xaa-Pro-Lys Nmethyltransferase 1 Ntmt1	55.804	10.213	0.000	1.009
CTNL1_MOUSE	14	1	1.72E-01	Alpha-catulin Ctnnal1	488.348	431.135	1531.350	591.366
UCRI_MOUSE	8	5	1.72E-01	Cytochrome b-c1 complex subunit Rieske, mitochondrial Uqcrfs1	489.546	752.066	729.341	1402.006
RGL3_MOUSE	8	1	1.73E-01	Ral guanine nucleotide dissociation stimulator-like 3 Rgl3	2.114	10.334	41.874	15.251
S10AA_MOUSE	4	3	1.74E-01	Protein S100-A10 S100a10	2592.774	1448.822	2393.741	3115.021
L1CAM_MOUSE	7	1	1.75E-01	Neural cell adhesion molecule L1 L1cam	160.645	257.176	91.809	230.406
UB2J2_MOUSE	4	1	1.75E-01	Ubiquitin-conjugating enzyme E2 J2 Ube2j2	5.129	0.483	82.648	1.047
PBIP1_MOUSE	10	4	1.76E-01	Pre-B-cell leukemia transcription factor-interacting protein 1 Pbxip1	298.400	441.073	632.149	859.642
KAD1_MOUSE	3	1	1.76E-01	Adenylate kinase isoenzyme 1 Ak1	25.117	27.931	134.867	601.940
PTH2_MOUSE	4	2	1.77E-01	Peptidyl-tRNA hydrolase 2, mitochondrial Ptrh2	185.443	61.605	174.773	328.963
CA087_MOUSE	8	2	1.78E-01	Uncharacterized protein C1orf87 homolog Gm12695	122.465	137.454	393.240	41.343
GALK1_MOUSE	5	2	1.78E-01	Galactokinase Galk1	644.080	576.392	819.359	902.916
ANR55_MOUSE	8	1	1.80E-01	Ankyrin repeat domain-containing protein 55 Ankrd55	103.397	86.552	175.704	432.984
MYOF_MOUSE	41	5	1.81E-01	Myoferlin Myof	1338.786	1956.689	1439.694	751.780
RD23B_MOUSE	7	2	1.81E-01	UV excision repair protein RAD23 homolog B Rad23b	156.833	5.643	166.425	5.212

ZCH18_MOUSE	8	1	1.82E-01	Zinc finger CCCH domaincontaining protein 18 Zc3h18	638.686	1224.154	398.505	371.347
PININ_MOUSE	9	1	1.82E-01	Pinin Pnn	213.127	6.140	29.859	8.408
AT2A2_MOUSE	36	8	1.82E-01	Sarcoplasmic/endoplasmic reticulum calcium ATPase 2 Atp2a2	908.913	1328.935	1104.336	1079.201
CO5A2_MOUSE	13	3	1.83E-01	Collagen alpha-2(V) chain Col5a2	99.186	114.624	222.142	365.667
C1QBP_MOUSE	4	2	1.84E-01	Complement component 1 Q subcomponent-binding protein, mitochondrial C1qbp	4216.441	2868.965	4503.350	3719.646
DCAKD_MOUSE	3	1	1.84E-01	Dephospho-CoA kinase domaincontaining protein Dcakd	0.000	153.573	405.856	235.297
TCTP_MOUSE	11	3	1.85E-01	Translationally-controlled tumor protein Tpt1	2180.118	2349.902	1305.957	1543.281
UACA_MOUSE	18	4	1.86E-01	Uveal autoantigen with coiled-coil domains and ankyrin repeats Uaca	962.101	881.658	295.840	2118.403
RTCB_MOUSE	25	3	1.87E-01	tRNA-splicing ligase RtcB homolog Rtcb	766.565	915.414	639.901	729.077
PI4KB_MOUSE	7	1	1.87E-01	Phosphatidylinositol 4-kinase beta Pi4kb	9.960	8.153	55.607	31.863
HS105_MOUSE	35	6	1.87E-01	Heat shock protein 105 kDa Hsph1	1253.683	894.120	551.355	682.254
ATLA3_MOUSE	5	1	-01	Atlastin-3 Atl3	3436.164	3218.893	4420.473	3541.032
TMOD3_MOUSE	8	2	-01 1.89E 1.89E	Tropomodulin-3 Tmod3	807.502	708.436	755.412	1488.266
RL18A_MOUSE	7	2	1.89E-01	60S ribosomal protein L18a Rpl18a	3762.281	4117.902	882.772	1436.004
DPOLM_MOUSE	7	1	1.89E-01	DNA-directed DNA/RNA polymerase mu Polm	115.363	577.212	339.400	56.902

RBMX_MOUSE	6	1	1.89E-01	RNA-binding motif protein, X chromosome Rbmx	0.058	4.580	24.716	0.010
OSBP2_MOUSE	11	2	1.89E-01	Oxysterol-binding protein 2 Osbp2	156.954	183.288	269.594	261.977
GRIP1_MOUSE	14	1	1.90E-01	Glutamate receptor-interacting protein 1 Grip1	44.454	1.008	6.021	162.423
DHB4_MOUSE	25	6	1.90E-01	Peroxisomal multifunctional enzyme type 2 Hsd17b4	974.879	2664.865	2254.889	1777.560
MPPA_MOUSE	5	1	1.91E-01	Mitochondrial-processing peptidase subunit alpha Pmpca	66.715	9.223	3.300	38.901
SRSF7_MOUSE	10	3	1.92E-01	Serine/arginine-rich splicing factor 7 Srsf7	643.178	532.717	251.877	288.910
DDB1_MOUSE	16	4	1.92E-01	DNA damage-binding protein 1 Ddb1	1321.520	1275.951	713.274	870.875
VSIG8_MOUSE	4	1	1.92E-01	V-set and immunoglobulin domaincontaining protein 8 Vsig8	141.855	88.566	164.032	194.744
TT21B_MOUSE	13	1	1.93E-01	Tetratricopeptide repeat protein 21B Ttc21b	2382.128	1580.691	1983.895	306.917
HYPK_MOUSE	8	1	1.94E-01	Huntingtin-interacting protein K Hypk	0.140	0.000	34.732	0.000
APCL_MOUSE	47	6	1.94E-01	Adenomatous polyposis coli protein 2 Apc2	517.360	729.542	971.007	863.497
INO1_MOUSE	3	2	1.94E-01	Inositol-3-phosphate synthase 1 Isyna1	464.268	398.427	303.718	367.169
PPIL3_MOUSE	2	1	1.94E-01	Peptidyl-prolyl cis-trans isomeraselike 3 Ppil3	145.063	39.473	0.000	12.026
MIF_MOUSE	3	2	1.96E-01	Macrophage migration inhibitory factor Mif	1494.135	1203.995	1962.387	2225.050
NAT10_MOUSE	12	1	1.97E-01	RNA cytidine acetyltransferase Nat10	107.643	72.658	100.358	28.299

NDUAD_MOUSE	3	1	1.97E-01	NADH dehydrogenase [ubiquinone] 1 alpha subcomplex subunit 13 Ndufa13	10.228	27.570	34.784	212.319
RS2_MOUSE	15	3	1.97E-01	40S ribosomal protein S2 Rps2	2714.587	1418.120	1599.457	636.530
IDH3A_MOUSE	15	6	1.98E-01	Isocitrate dehydrogenase [NAD] subunit alpha, mitochondrial Idh3a	1067.148	1004.381	2074.497	1959.745
IF1AX_MOUSE	4	4	2.01E-01	Eukaryotic translation initiation factor 1A, X-chromosomal Eif1ax	2515.382	1991.887	1789.510	531.615
NDUA6_MOUSE	4	2	2.01E-01	NADH dehydrogenase [ubiquinone] 1 alpha subcomplex subunit 6 Ndufa6	447.364	368.299	15018.037	5355.978
KAP3_MOUSE	9	4	2.02E-01	cAMP-dependent protein kinase type II-beta regulatory subunit Prkar2b	380.140	427.367	598.612	479.300
PDLI5_MOUSE	15	1	2.02E-01	PDZ and LIM domain protein 5 Pdlim5	786.559	627.220	442.205	131.155
TR112_MOUSE	6	1	2.02E-01	Multifunctional methyltransferase subunit TRM112-like protein Trmt112	689.644	300.580	46.311	378.456
TANC1_MOUSE	19	2	2.03E-01	Protein TANC1 Tanc1	1154.690	2926.086	1953.658	4447.763
GPSM2_MOUSE	12	1	2.03E-01	G-protein-signaling modulator 2 Gpsm2	0.000	1.965	141.474	0.061
AQP1_MOUSE	1	1	-01	Aquaporin-1 Aqp1	540.411	170.112	129.591	159.566
TAGL_MOUSE	10	2	-01 E-01 2.04E 2.04E	Transgelin Tagln	1749.117	950.648	1569.629	826.244
TEX15_MOUSE	17	1	2.04	Testis-expressed protein 15 Tex15	2.207	2.829	31.703	113.788
RS16_MOUSE	11	2	2.05E-01	40S ribosomal protein S16 Rps16	3084.975	2166.490	2060.878	4285.163
AK1A1_MOUSE	14	3	2.05E-01	Alcohol dehydrogenase [NADP(+)] Akr1a1	732.561	1178.811	1513.590	1303.910

ZFAN4_MOUSE	6	2	2.05E-01	AN1-type zinc finger protein 4 Zfand4	181.904	133.449	872.688	44.558
ERBIN_MOUSE	9	2	2.06E-01	Erbin Erbin	702.000	768.434	1212.653	966.480
SRSF5_MOUSE	7	1	2.06E-01	Serine/arginine-rich splicing factor 5 Srsf5	150.499	549.716	27.687	1549.661
SELB_MOUSE	7	1	2.08E-01	Selenocysteine-specific elongation factor Eefsec	39.058	5.677	92.614	18.743

IMPA1_MOUSE	6	3	2.09E-01	Inositol monophosphatase 1 Impa1	1317.976	1727.020	1689.386	1093.105
PLCL1_MOUSE	13	1	2.09E-01	Inactive phospholipase C-like protein 1 Plcl1	1971.821	2461.439	109.348	3800.066
ETS1_MOUSE	6	2	2.11E-01	Protein C-ets-1 Ets1	1499.992	2726.178	2386.728	1864.401
DNJB1_MOUSE	4	1	2.11E-01	DnaJ homolog subfamily B member 1 Dnajb1	2.007	110.461	140.256	5.545
RHG17_MOUSE	12	2	2.12E-01	Rho GTPase-activating protein 17 Arhgap17	91.232	64.760	109.448	22.429
CCD78_MOUSE	4	1	2.13E-01	Coiled-coil domain-containing protein 78 Ccdc78	60.097	318.122	2185.150	658.509
SARNP_MOUSE	12	3	2.13E-01	SAP domain-containing ribonucleoprotein Sarnp	181.998	124.970	793.985	21.335
NRDC_MOUSE	15	4	2.15E-01	Nardilysin Nrdc	534.288	1048.079	586.078	209.314
BACH_MOUSE	12	5	2.15E-01	Cytosolic acyl coenzyme A thioester hydrolase Acot7	1862.680	1208.080	941.848	1425.076
RL10L_MOUSE	10	2	2.16E-01	60S ribosomal protein L10-like Rpl10l	33.884	108.094	12.434	114.904
ZN431_MOUSE	4	1	2.17E-01	Zinc finger protein 431 Znf431	326.310	350.485	643.000	603.405
K1C15_MOUSE	20	2	2.17E-01	Keratin, type I cytoskeletal 15 Krt15	617.949	1139.338	3682.684	424.882
MA7D3_MOUSE	19	2	2.17E-01	MAP7 domain-containing protein 3 Map7d3	540.974	605.951	1176.563	309.125

MTAP_MOUSE	14	4	2.18E-01	S-methyl-5'-thioadenosine phosphorylase Mtap	3715.422	3564.101	3061.553	2093.448
SF3A1_MOUSE	17	1	2.18E-01	Splicing factor 3A subunit 1 Sf3a1	1274.348	1071.354	1033.774	1418.485
MP2K7_MOUSE	11	3	2.18E-01	Dual specificity mitogen-activated protein kinase kinase 7 Map2k7	53.548	67.397	86.070	126.610
BAX_MOUSE	2	1	2.19E-01	Apoptosis regulator BAX Bax	1537.008	2169.542	3622.317	1715.827
WDR82_MOUSE	4	1	2.19E-01	WD repeat-containing protein 82 Wdr82	769.268	478.436	321.401	566.071
DPY30_MOUSE	1	1	2.20E-01	Protein dpy-30 homolog Dpy30	339.567	29.576	14.877	0.016
HSH2D_MOUSE	4	1	2.20E-01	Hematopoietic SH2 domaincontaining protein Hsh2d	0.000	1.546	51.844	29.882
RL7_MOUSE	17	6	2.22E-01	60S ribosomal protein L7 Rpl7	3184.276	5335.912	4621.251	3219.368

COX17_MOUSE	2	1	2.23E-01	Cytochrome c oxidase copper chaperone Cox17	30.499	450.506	76.144	210.867
ACTY_MOUSE	6	2	2.25E-01	Beta-centractin Actr1b	1072.537	1023.103	933.967	773.138
MPPB_MOUSE	6	1	2.26E-01	Mitochondrial-processing peptidase subunit beta Pmpcb	398.679	425.248	227.417	308.485
SAE1_MOUSE	1	1	2.28E-01	SUMO-activating enzyme subunit 1 Sae1	348.023	87.689	235.300	144.981
CACP_MOUSE	7	1	2.28E-01	Carnitine O-acetyltransferase Crat	28.021	80.661	110.894	408.630
COX2_MOUSE	3	1	2.30E-01	Cytochrome c oxidase subunit 2 Mtco2	263.424	29.513	388.290	151.546
MTA2_MOUSE	16	1	2.30E-01	Metastasis-associated protein MTA2 Mta2	0.909	29.538	29.739	49.424
HMGB1_MOUSE	16	3	2.31E-01	High mobility group protein B1 Hmgb1	1353.522	836.809	1519.370	597.340
BPIB1_MOUSE	9	1	2.32E-01	BPI fold-containing family B member 1 Bpifb1	4725.514	8027.736	1654.861	2685.662

UBP5_MOUSE	19	4	2.33E-01	Ubiquitin carboxyl-terminal hydrolase 5 Usp5	318.292	368.649	593.829	501.208
TBA3_MOUSE	24	1	2.33E-01	Tubulin alpha-3 chain Tuba3a	70.340	92.845	397.479	88.205
K1C42_MOUSE	18	3	2.33E-01	Keratin, type I cytoskeletal 42 Krt42	202.959	203.979	127.337	709.660
MICU2_MOUSE	5	2	2.33E-01	Calcium uptake protein 2, mitochondrial Micu2	81.240	78.700	6.922	222.940
SNX9_MOUSE	9	2	2.33E-01	Sorting nexin-9 Snx9	231.100	60.676	159.442	117.909
TXND9_MOUSE	1	1	2.35E-01	Thioredoxin domain-containing protein 9 Txndc9	589.050	438.610	106.636	169.393
HSP74_MOUSE	31	7	2.35E-01	Heat shock 70 kDa protein 4 Hspa4	3377.316	3205.825	3519.148	2594.947
UBC12_MOUSE	5	2	2.36E-01	NEDD8-conjugating enzyme Ubc12 Ube2m	48.333	688.707	923.332	743.444
NIBL1_MOUSE	17	5	-01	Niban-like protein 1 Fam129b	182.152	77.386	631.579	107.869
RBM28_MOUSE	36	7	-01 2.37E 2.41E	RNA-binding protein 28 Rbm28	1724.279	2274.534	3099.791	2018.076
ACYP1_MOUSE	1	1	2.41E-01	Acylphosphatase-1 Acyp1	30.999	34.510	446.025	156.649
VMA5A_MOUSE	5	1	2.42E-01	von Willebrand factor A domain-containing protein 5A Vwa5a	128.173	159.783	84.543	254.799
SYAC_MOUSE	24	4	2.43E-01	Alanine--tRNA ligase, cytoplasmic Aars	756.684	556.799	857.018	536.390
VATA_MOUSE	18	2	2.43E-01	V-type proton ATPase catalytic subunit A Atp6v1a	68.268	14.045	197.863	14.136
DCTN2_MOUSE	6	2	2.43E-01	Dynactin subunit 2 Dctn2	272.199	747.810	1030.041	496.217
HS71A_MOUSE	18	1	2.45E-01	Heat shock 70 kDa protein 1A Hspa1a	56.897	347.651	95.560	45.360
THYG_MOUSE	18	2	2.45E-01	Thyroglobulin Tg	1153.716	990.849	813.731	931.257

CC110_MOUSE	7	1	2.46E-01	Coiled-coil domain-containing protein 110 Ccdc110	3637.802	3832.932	6054.115	2902.457
MCM3_MOUSE	22	6	2.46E-01	DNA replication licensing factor MCM3 Mcm3	655.483	564.886	565.285	436.715
IF6_MOUSE	7	2	2.47E-01	Eukaryotic translation initiation factor 6 Eif6	1175.287	1480.994	1100.584	715.073
GNA1_MOUSE	1	1	2.47E-01	Glucosamine 6-phosphate Nacetyltransferase Gnpnat1	42.004	0.514	0.000	119.238
PHLB1_MOUSE	24	2	2.51E-01	Pleckstrin homology-like domain family B member 1 Phldb1	191.307	605.733	441.902	489.037
DGKB_MOUSE	16	2	2.51E-01	Diacylglycerol kinase beta Dgkb	238.770	1001.041	221.920	74.566
TM121_MOUSE	6	1	2.52E-01	Transmembrane protein 121 Tmem121	364.896	253.690	25.782	205.065
LZIC_MOUSE	3	2	2.52E-01	Protein LZIC Lzic	636.470	1441.752	1762.336	774.364
MTA3_MOUSE	11	1	2.54E-01	Metastasis-associated protein MTA3 Mta3	0.038	119.361	1.759	0.486
PFD3_MOUSE	5	3	2.54E-01	Prefoldin subunit 3 Vbp1	1230.826	864.358	865.580	1215.214
RMP_MOUSE	7	1	2.55E-01	Unconventional prefoldin RPB5 interactor Uri1	1898.879	1240.503	3117.849	2038.856
3HIDH_MOUSE	7	1	2.56E-01	3-hydroxyisobutyrate dehydrogenase, mitochondrial Hibadh	51.176	16.755	122.979	257.575
DPYL2_MOUSE	25	6	2.57E-01	Dihydropyrimidinase-related protein 2 Dpysl2	1565.031	1606.999	2649.933	2155.188
FMR1_MOUSE	6	1	2.58E-01	Synaptic functional regulator FMR1 Fmr1	67.557	20.729	27.306	10.677
ASNS_MOUSE	10	5	2.60E-01	Asparagine synthetase [glutaminehydrolyzing] Asns	706.030	684.000	1214.160	813.472

NDUV1_MOUSE	4	1	2.63E-01	NADH dehydrogenase [ubiquinone] flavoprotein 1, mitochondrial Ndufv1	19.398	89.848	436.027	189.086
SKP1_MOUSE	7	1	2.63E-01	S-phase kinase-associated protein 1 Skp1	1231.731	890.425	192.234	630.657
CRIP2_MOUSE	4	2	2.65E-01	Cysteine-rich protein 2 Crip2	8429.531	10614.721	5225.266	7076.660
KHDR1_MOUSE	9	1	2.65E-01	KH domain-containing, RNAbinding, signal transductionassociated protein 1 Khdrbs1	10.955	40.903	338.437	0.085
TKT_MOUSE	10	3	2.65E	Transketolase Tkt	1028.678	778.932	390.665	497.898
RNBP6_MOUSE	7	1	2.65E	Ran-binding protein 6 Ranbp6	641.536	793.601	976.270	472.970
PARVA_MOUSE	3	1	-01	Alpha-parvin Parva	274.175	515.967	618.098	322.020
HYAS3_MOUSE	14	1	-01 -01 -01 2.66E 2.67E	Hyaluronan synthase 3 Has3	47.507	9.897	5.292	87.025
TMEDA_MOUSE	6	2	2.68E-01	Transmembrane emp24 domaincontaining protein 10 Tmed10	591.306	928.418	595.995	652.482
PGK1_MOUSE	35	7	2.69E-01	Phosphoglycerate kinase 1 Pgk1	3454.804	3637.309	3171.866	7251.027
PRDX3_MOUSE	4	1	2.71E-01	Thioredoxin-dependent peroxide reductase, mitochondrial Prdx3	241.917	145.677	1717.445	830.401
PSMD8_MOUSE	7	3	2.74E-01	26S proteasome non-ATPase regulatory subunit 8 Psmd8	784.012	1007.594	1358.740	1191.150
SCFD1_MOUSE	13	1	2.76E-01	Sec1 family domain-containing protein 1 Scfd1	781.409	549.754	842.656	320.882
XPP1_MOUSE	17	2	2.78E-01	Xaa-Pro aminopeptidase 1 Xpnpep1	224.869	220.970	350.783	392.859
PICAL_MOUSE	9	2	2.79E-01	Phosphatidylinositol-binding clathrin assembly protein Picalm	37.126	91.826	106.143	18.594
GCN1_MOUSE	46	4	2.79E-01	eIF-2-alpha kinase activator GCN1 Gcn1	59.747	22.115	25.455	38.413

CTND1_MOUSE	30	6	-01	Catenin delta-1 Ctnnd1	1157.698	1677.278	1721.389	957.544
CATA_MOUSE	8	3	-01 2.79E 2.80E	Catalase Cat	1006.223	1262.982	626.749	1460.395
WDR1_MOUSE	14	3	2.80E-01	WD repeat-containing protein 1 Wdr1	1883.175	1085.543	1470.978	1065.494
RS11_MOUSE	11	1	2.81E-01	40S ribosomal protein S11 Rps11	362.366	2680.950	3613.357	1432.743
U2AF2_MOUSE	3	1	2.82E-01	Splicing factor U2AF 65 kDa subunit U2af2	595.999	142.539	463.122	544.538

ITIH3_MOUSE	8	1	2.82E-01	Inter-alpha-trypsin inhibitor heavy chain H3 Itih3	1328.264	1322.229	357.044	889.012
SMC2_MOUSE	25	1	2.83E-01	Structural maintenance of chromosomes protein 2 Smc2	251.826	152.597	133.730	73.346
MYH11_MOUSE	41	1	2.83E	Myosin-11 Myh11	119.746	322.607	470.723	697.448
TENS3_MOUSE	12	2	2.83E	Tensin-3 Tns3	479.042	1538.018	1159.060	474.973
PEPD_MOUSE	13	2	-01	Xaa-Pro dipeptidase Pepd	315.894	335.449	642.694	350.194
KITH_MOUSE	3	1	-01 -01 -01 2.85E 2.87E	Thymidine kinase, cytosolic Tk1	41.398	8.099	4.872	2.161
PSB8_MOUSE	3	1	2.87E-01	Proteasome subunit beta type-8 Psmb8	1595.203	1782.756	2096.352	2027.406
AMOL2_MOUSE	18	1	-01	Angiomotin-like protein 2 Amotl2	0.530	0.001	17.454	12.831
H13_MOUSE	15	3	-01 2.88E 2.88E	Histone H1.3 Hist1h1d	55.898	81.765	279.800	338.392
POLK_MOUSE	14	2	2.88E-01	DNA polymerase kappa Polk	42.507	134.688	11.956	199.096
MSH2_MOUSE	9	1	2.91E-01	DNA mismatch repair protein Msh2 Msh2	63.087	16.851	7.535	27.759
NT5C_MOUSE	2	1	2.91E-01	5'(3')-deoxyribonucleotidase, cytosolic type Nt5c	0.279	6.523	108.085	81.863
TNPO1_MOUSE	7	2		Transportin-1 Tnpo1	387.897	9.324	60.867	23.417

TBB1_MOUSE	24	2	2.93E-01 2.94E-01	Tubulin beta-1 chain Tubb1	100.664	112.205	68.357	89.184
TBC15_MOUSE	7	1	2.95E-01	TBC1 domain family member 15 Tbc1d15	108.798	188.346	16.328	42.320
NEDD4_MOUSE	11	1	2.95E-01	E3 ubiquitin-protein ligase NEDD4 Nedd4	157.893	15.175	86.250	16.645
RUVB1_MOUSE	5	2	2.95E-01	RuvB-like 1 Ruvbl1	394.804	425.705	786.891	358.517
VATB2_MOUSE	14	3	2.97E-01	V-type proton ATPase subunit B, brain isoform Atp6v1b2	18.325	29.153	286.965	468.197
HSPB1_MOUSE	16	5	2.98E-01	Heat shock protein beta-1 Hspb1	5102.454	5158.826	3642.292	2673.822
ASSY_MOUSE	4	2	2.98E-01	Argininosuccinate synthase Ass1	1553.971	2010.572	914.637	1071.608
ARP3_MOUSE	13	2	2.99E-01	Actin-related protein 3 Actr3	1578.556	1758.708	1544.763	1074.877
MCA3_MOUSE	5	1	3.01E-01	Eukaryotic translation elongation factor 1 epsilon-1 Eef1e1	207.131	108.641	17.171	83.210
ARPC5_MOUSE	6	2	3.02E-01	Actin-related protein 2/3 complex subunit 5 Arpc5	792.908	627.296	597.327	391.711
LC7L3_MOUSE	3	1	3.02E-01	Luc7-like protein 3 Luc7l3	78.079	166.059	204.236	334.156
NUDC_MOUSE	6	4	3.02E-01	Nuclear migration protein nudC Nudc	388.877	291.844	311.778	84.849
PGAM5_MOUSE	7	3	3.03E-01	Serine/threonine-protein phosphatase PGAM5, mitochondrial Pgam5	708.589	691.209	904.621	936.832
ATPO_MOUSE	15	4	3.04E-01	ATP synthase subunit O, mitochondrial Atp5o	2055.664	3501.170	1065.256	4278.177
PSMG2_MOUSE	4	1	3.04E-01	Proteasome assembly chaperone 2 Psmg2	3.695	0.000	19.946	21.066
RFA3_MOUSE	4	1	3.05E-01	Replication protein A 14 kDa subunit Rpa3	52.957	1.454	9.826	0.693
CTBL1_MOUSE	14	3	3.07E-01	Beta-catenin-like protein 1 Ctnnbl1	62.490	44.337	29.424	121.443

IDHC_MOUSE	19	6	3.08E-01	Isocitrate dehydrogenase [NADP] cytoplasmic Idh1	341.163	605.707	582.954	334.718
CCD87_MOUSE	4	1	3.09E-01	Coiled-coil domain-containing protein 87 Ccdc87	420.968	375.186	12354.108	247.050
MDHM_MOUSE	32	7	3.09E-01	Malate dehydrogenase, mitochondrial Mdh2	7695.313	6969.196	6174.339	4757.281
LSM8_MOUSE	3	1	3.12E-01	U6 snRNA-associated Sm-like protein LSm8 Lsm8	72.124	0.000	0.000	0.588
RL10A_MOUSE	11	4	3.12E-01	60S ribosomal protein L10a Rpl10a	856.792	427.231	414.442	211.279
USH1C_MOUSE	11	1	3.12E-01	Harmonin Ush1c	501.708	444.346	637.013	457.142
DYHC2_MOUSE	27	4	3.14E-01	Cytoplasmic dynein 2 heavy chain 1 Dync2h1	82.795	203.516	567.747	136.637
ARHGG_MOUSE	25	2	3.15E-01	Rho guanine nucleotide exchange factor 16 Arhgef16	1296.222	1834.086	3697.510	1544.738
RS3A_MOUSE	17	3	3.15E-01	40S ribosomal protein S3a Rps3a	2272.613	1776.041	1814.440	2576.376
OSBL9_MOUSE	4	1	3.16E-01	Oxysterol-binding protein-related protein 9 Osbpl9	81.098	125.235	69.723	22.017
CCDB1_MOUSE	4	1	3.17E-01	Cyclin-D1-binding protein 1 Ccndbp1	32.670	268.252	605.634	23.902
TRXR1_MOUSE	10	2	3.18E-01	Thioredoxin reductase 1, cytoplasmic Txnrd1	188.951	108.468	64.580	63.387
CCAR1_MOUSE	20	2	3.20E-01	Cell division cycle and apoptosis regulator protein 1 Ccar1	432.526	198.696	279.227	150.998
F1142_MOUSE	5	1	3.22E-01	Protein FAM114A2 Fam114a2	0.000	19.526	66.458	0.000
KDM5B_MOUSE	16	4	3.25E-01	Lysine-specific demethylase 5B Kdm5b	406.057	164.769	293.788	443.387
XPO1_MOUSE	21	4	3.27E-01	Exportin-1 Xpo1	101.325	58.498	70.151	115.381
CS043_MOUSE	3	1	3.27E-01	Uncharacterized protein C19orf43 homolog	1736.743	1567.740	2162.708	1352.786

EMAL5_MOUSE	15	5	3.28E-01	Echinoderm microtubuleassociated protein-like 5 Eml5	776.447	923.590	1297.912	559.961
KBTB3_MOUSE	6	1	3.28E-01	Kelch repeat and BTB domaincontaining protein 3 Kbtbd3	7.868	5.209	73.350	238.443
TBAL3_MOUSE	18	1	3.30E-01	Tubulin alpha chain-like 3 Tubal3	0.101	0.000	218.327	0.024
TSNAX_MOUSE	8	1	3.30E-01	Translin-associated protein X Tsnax	49.588	0.131	6.873	6.369
HS71L_MOUSE	19	1	3.30E-01	Heat shock 70 kDa protein 1-like Hspa1l	861.395	1127.801	1329.140	951.101
COX5A_MOUSE	3	2	3.31E-01	Cytochrome c oxidase subunit 5A, mitochondrial Cox5a	1012.064	621.587	245.980	602.590
CNDP2_MOUSE	5	2	3.31E-01	Cytosolic non-specific dipeptidase Cndp2	274.011	104.822	140.570	177.438
MGDP1_MOUSE	2	2	3.33E-01	Magnesium-dependent phosphatase 1 Mdp1	61.878	325.873	823.782	164.165
TCPG_MOUSE	44	6	3.36E-01	T-complex protein 1 subunit gamma Cct3	4130.800	4779.851	3547.816	3975.281
DCTN3_MOUSE	5	1	-01	Dynactin subunit 3 Dctn3	973.324	1466.514	1631.978	1746.744
RL6_MOUSE	10	6	3.36E -01 3.37E	60S ribosomal protein L6 Rpl6	6030.735	9665.234	6599.397	5793.791
RM12_MOUSE	4	1	3.38E-01	39S ribosomal protein L12, mitochondrial Mrpl12	3281.334	3397.339	4350.849	6132.205
RS4X_MOUSE	18	8	3.39E-01	40S ribosomal protein S4, X isoform Rps4x	2878.127	6139.210	5464.365	5119.763
CFA52_MOUSE	11	5	3.40E-01	Cilia- and flagella-associated protein 52 Cfap52	2992.522	1546.799	2388.826	5048.413
PGM1_MOUSE	8	3	3.42E-01	Phosphoglucomutase-1 Pgm1	860.402	911.469	623.204	1091.603
CPSM_MOUSE	19	4	3.42E-01	Carbamoyl-phosphate synthase [ammonia], mitochondrial Cps1	593.924	208.052	58.459	178.520

CCD22_MOUSE	9	2	3.46E-01	Coiled-coil domain-containing protein 22 Ccdc22	39.010	14.654	8.023	28.123
TMM59_MOUSE	3	1	3.48E-01	Transmembrane protein 59 Tmem59	437.998	1359.391	70.735	138.470
PRP4B_MOUSE	15	1	3.48E-01	Serine/threonine-protein kinase PRP4 homolog Prpf4b	2.367	9.863	18.020	17.412
MOCS3_MOUSE	5	1	3.53E-01	Adenylyltransferase and sulfurtransferase MOCS3 Mocs3	4.262	2.798	240.584	11.152
ABLM1_MOUSE	11	3	3.54E-01	Actin-binding LIM protein 1 Ablim1	667.276	913.934	947.826	1163.532
ERF3A_MOUSE	15	3	3.55E-01	Eukaryotic peptide chain release factor GTP-binding subunit ERF3A Gspt1	585.529	634.297	424.754	436.161
MOCS1_MOUSE	5	1	3.56E-01	Molybdenum cofactor biosynthesis protein 1 Mocs1	1787.009	2168.289	918.498	1065.920
KBL_MOUSE	5	2	3.57E-01	2-amino-3-ketobutyrate coenzyme A ligase, mitochondrial Gcat	5975.858	4514.686	1765.989	2690.356
DCLK1_MOUSE	12	4	3.58E-01	Serine/threonine-protein kinase DCLK1 Dclk1	181.884	1308.370	320.374	667.863
IWS1_MOUSE	11	1	3.58E-01	Protein IWS1 homolog Iws1	51.294	60.442	8.221	1.131
NDEL1_MOUSE	7	2	3.59E-01	Nuclear distribution protein nudElike 1 Ndel1	109.473	59.979	463.196	115.172
CD97_MOUSE	6	2	3.61E-01	CD97 antigen Cd97	26.009	4.169	149.692	25.536
IF2G_MOUSE	11	1	3.62E-01	Eukaryotic translation initiation factor 2 subunit 3, X-linked Eif2s3x	729.933	798.388	509.403	515.902
PGRC2_MOUSE	4	1	3.62E-01	Membrane-associated progesterone receptor component 2 Pgrmc2	110.067	367.743	75.019	215.795
MAP1B_MOUSE	40	11	3.63E-01	Microtubule-associated protein 1B Map1b	1090.244	419.893	404.232	263.471

CHD6_MOUSE	34	2	3.64E-01	Chromodomain-helicase-DNAbinding protein 6 Chd6	1253.232	614.581	648.971	662.084
SYAP1_MOUSE	4	1	3.66E-01	Synapse-associated protein 1 Syap1	3139.486	3579.507	3947.659	3063.630
SYFA_MOUSE	5	1	3.68E-01	Phenylalanine--tRNA ligase alpha subunit Farsa	1.083	53.330	55.629	62.580
TWF1_MOUSE	4	1	3.71E-01	Twinfilin-1 Twf1	938.357	1287.696	1338.151	836.558
PYC_MOUSE	23	4	3.72E-01	Pyruvate carboxylase, mitochondrial Pc	572.925	215.495	692.689	405.403
TOPZ1_MOUSE	25	3	3.72E-01	Testis- and ovary-specific PAZ domain-containing protein 1 Topaz1	93.863	240.420	192.942	1570.861

AT1A1_MOUSE	19	1	3.73E-01	Sodium/potassium-transporting ATPase subunit alpha-1 Atp1a1	0.821	22.079	13.543	27.759
EF1B_MOUSE	8	3	3.75E-01	Elongation factor 1-beta Eef1b	8024.806	8116.927	9814.208	7275.914
RM11_MOUSE	6	1	3.81E-01	39S ribosomal protein L11, mitochondrial Mrpl11	6.907	20.918	15.640	270.190
EPDR1_MOUSE	2	2	3.81E-01	Mammalian ependymin-related protein 1 Epdr1	1699.029	1631.216	2525.249	1729.306
TNC18_MOUSE	29	2	3.84E-01	Trinucleotide repeat-containing gene 18 protein Tnrc18	170.951	237.624	276.316	177.677
SF3B3_MOUSE	19	3	3.85E-01	Splicing factor 3B subunit 3 Sf3b3	381.562	431.679	403.433	567.394
RL18_MOUSE	12	2	3.85E-01	60S ribosomal protein L18 Rpl18	2586.185	2941.262	3588.323	2187.473
TBA4A_MOUSE	23	2	-01	Tubulin alpha-4A chain Tuba4a	327.751	543.359	296.360	646.675
RS21_MOUSE	2	2	3.87E -01 3.88E	40S ribosomal protein S21 Rps21	2251.515	762.379	796.656	1120.878
MARC2_MOUSE	4	2	3.89E-01	Mitochondrial amidoxime reducing component 2 Marc2	479.459	704.714	621.556	645.436

SYFB_MOUSE	17	2	3.95E-01	Phenylalanine--tRNA ligase beta subunit Farsb	463.137	633.056	1005.382	772.376
CMYA5_MOUSE	26	2	3.95E-01	Cardiomyopathy-associated protein 5 Cmya5	367.022	417.820	269.591	233.301
PP1B_MOUSE	13	1	3.96E-01	Serine/threonine-protein phosphatase PP1-beta catalytic subunit Ppp1cb	0.000	0.033	136.768	0.059
MYG_MOUSE	5	2	3.97E-01	Myoglobin Mb	4.986	8.745	217.778	289.911
K2C73_MOUSE	27	2	3.98E-01	Keratin, type II cytoskeletal 73 Krt73	979.910	1013.446	945.645	1374.884
PNPH_MOUSE	5	2	3.99E-01	Purine nucleoside phosphorylase Pnp	358.353	438.277	543.762	628.464
DC1I2_MOUSE	10	3	4.02E-01	Cytoplasmic dynein 1 intermediate chain 2 Dync1i2	114.821	11.782	290.354	34.685
UMPS_MOUSE	7	2	4.03E-01	Uridine 5'-monophosphate synthase Umps	232.548	230.361	335.708	336.655
ALDOA_MOUSE	32	10	4.03E-01	Fructose-bisphosphate aldolase A Aldoa	3809.969	3443.792	4204.068	4728.356
SENP7_MOUSE	10	2	4.05E-01	Sentrin-specific protease 7 Senp7	17.920	11.968	1.670	140.754
AGM1_MOUSE	12	1	4.06E-01	Phosphoacetylglucosamine mutase Pgm3	248.739	856.515	694.604	685.125
S29A1_MOUSE	10	2	4.06E-01	Equilibrative nucleoside transporter 1 Slc29a1	1627.966	2404.469	3479.008	2189.060
CHTOP_MOUSE	9	1	4.06E-01	Chromatin target of PRMT1 protein Chtop	3629.218	3475.545	1683.355	2372.918
GOLI4_MOUSE	6	1	4.06E-01	Golgi integral membrane protein 4 Golim4	1043.272	1486.152	909.597	2243.913
MIC27_MOUSE	3	2	4.07E-01	MICOS complex subunit Mic27 Apool	164.822	207.061	132.428	128.345

CP110_MOUSE	15	2	4.07E-01	Centriolar coiled-coil protein of 110 kDa Ccp110	4289.711	3307.738	4587.782	2630.849
TCPQ_MOUSE	44	11	4.08E-01	T-complex protein 1 subunit theta Cct8	6220.019	5605.751	5934.387	5040.750
CKAP5_MOUSE	34	3	4.10E-01	Cytoskeleton-associated protein 5 Ckap5	151.641	75.871	85.407	73.506
GNA14_MOUSE	5	1	4.10E-01	Guanine nucleotide-binding protein subunit alpha-14 Gna14	152.210	93.889	107.400	57.835
ARF6_MOUSE	2	1	-01	ADP-ribosylation factor 6 Arf6	819.187	1802.087	2131.833	2223.410
RS8_MOUSE	10	2	4.11E -01 4.16E	40S ribosomal protein S8 Rps8	1680.511	2015.009	1433.662	1324.108
NEST_MOUSE	70	12	4.16E-01	Nestin Nes	4249.343	3192.862	4301.928	3756.270
KAD2_MOUSE	13	3	4.16E-01	Adenylate kinase 2, mitochondrial Ak2	1500.502	1155.506	1184.991	1060.130
TSN_MOUSE	4	2	4.18E-01	Translin Tsn	3753.576	5106.056	7073.404	3521.342
DDX6_MOUSE	8	1	4.18E-01	Probable ATP-dependent RNA helicase DDX6 Ddx6	28.069	78.919	296.390	232.679
COPB_MOUSE	15	3	-01	Coatomer subunit beta Copb1	147.849	281.840	281.481	229.568
KINH_MOUSE	27	4	4.19E -01 4.20E	Kinesin-1 heavy chain Kif5b	660.723	424.108	610.770	540.839
AT5F1_MOUSE	11	4	4.20E-01	ATP synthase F(0) complex subunit B1, mitochondrial Atp5f1	380.170	171.739	278.192	526.039
CSK2B_MOUSE	2	1	4.21E-01	Casein kinase II subunit beta Csnk2b	2528.511	3060.928	3173.054	4038.543
CRYAB_MOUSE	9	4	4.22E-01	Alpha-crystallin B chain Cryab	396.022	138.460	166.353	178.420
TTL12_MOUSE	11	1	4.22E-01	Tubulin--tyrosine ligase-like protein 12 Ttll12	470.842	363.845	258.723	348.829
RAP2B_MOUSE	1	1	4.22E-01	Ras-related protein Rap-2b Rap2b	172.888	106.944	258.890	85.391
SEC63_MOUSE	10	2	4.23E-01	Translocation protein SEC63 homolog Sec63	913.260	568.781	1268.166	199.068

SSRD_MOUSE	5	3	4.25E-01	Translocon-associated protein subunit delta Ssr4	1764.142	1515.843	1411.609	1359.897
NFU1_MOUSE	4	2	4.25E-01	NFU1 iron-sulfur cluster scaffold homolog, mitochondrial Nfu1	869.705	1128.463	1306.851	1156.562
CPNS2_MOUSE	3	1	-01	Calpain small subunit 2 Capns2	4.010	0.031	42.253	0.885
HOOK3_MOUSE	11	1	-01 4.25E 4.27E	Protein Hook homolog 3 Hook3	117.386	93.407	71.361	198.025
AT12A_MOUSE	15	2	4.30E-01	Potassium-transporting ATPase alpha chain 2 Atp12a	571.115	478.903	408.313	427.481
FLNB_MOUSE	88	17	-01	Filamin-B Flnb	3670.286	4883.681	4834.025	4190.400
IPO11_MOUSE	12	1	-01 4.33E 4.33E	Importin-11 Ipo11	36.371	0.689	0.150	0.007
ABCA4_MOUSE	27	2	4.34E-01	Retinal-specific ATP-binding cassette transporter Abca4	361.937	238.352	369.162	500.631
HUWE1_MOUSE	39	3	4.35E-01	E3 ubiquitin-protein ligase HUWE1 Huwe1	62.067	129.189	145.792	73.000
F210B_MOUSE	2	1	4.36E-01	Protein FAM210B, mitochondrial Fam210b	4.002	1.331	7.728	78.577
PRS4_MOUSE	21	6	4.38E-01	26S proteasome regulatory subunit 4 Psmc1	1256.626	601.572	1131.597	1090.604
ALPK3_MOUSE	14	2	4.39E-01	Alpha-protein kinase 3 Alpk3	58.033	100.326	521.337	186.609
GCP60_MOUSE	3	1	4.39E-01	Golgi resident protein GCP60 Acbd3	109.351	60.912	40.471	275.199
RL31_MOUSE	8	2	4.40E-01	60S ribosomal protein L31 Rpl31	888.702	296.692	67.751	772.927
RAB12_MOUSE	9	1	4.42E-01	Ras-related protein Rab-12 Rab12	870.037	1762.127	1327.292	1398.396
PHB2_MOUSE	17	4	4.43E-01	Prohibitin-2 Phb2	1822.714	2345.870	2530.104	2108.884
UB2L3_MOUSE	6	3	4.43E-01	Ubiquitin-conjugating enzyme E2 L3 Ube2l3	463.378	204.291	520.478	283.788

PSMD2_MOUSE	25	7	4.43E-01	26S proteasome non-ATPase regulatory subunit 2 Psmd2	1041.622	735.077	779.097	757.015
FBX21_MOUSE	5	2	-01	F-box only protein 21 Fbxo21	175.646	162.521	86.113	399.151
LKHA4_MOUSE	6	3	4.43E -01 4.44E	Leukotriene A-4 hydrolase Lta4h	1029.570	1058.718	1283.627	983.366
CND1_MOUSE	20	4	4.46E-01	Condensin complex subunit 1 Ncapd2	186.698	44.090	75.472	72.977
PTBP1_MOUSE	15	9	4.49E-01	Polypyrimidine tract-binding protein 1 Ptbp1	2731.885	2782.586	1791.508	1566.037
RU17_MOUSE	5	3	4.50E-01	U1 small nuclear ribonucleoprotein 70 kDa Snrnp70	1163.901	1557.531	1745.172	1100.311

HPRT_MOUSE	11	1	4.50E-01	Hypoxanthine-guanine phosphoribosyltransferase Hprt1	1602.172	1513.670	2671.827	1457.234
TFR1_MOUSE	22	5	-01	Transferrin receptor protein 1 Tfrc	361.536	625.830	416.652	733.889
TITIN_MOUSE	247	28	4.51E -01 4.52E	Titin Ttn	1459.609	1438.553	3199.224	1987.911
TOM70_MOUSE	8	1	4.55E-01	Mitochondrial import receptor subunit TOM70 Tomm70	170.917	433.506	184.114	63.031
RISC_MOUSE	7	5	4.56E-01	Retinoid-inducible serine carboxypeptidase Scpep1	1691.163	1409.252	1157.682	1580.083
PSA2_MOUSE	8	4	4.56E-01	Proteasome subunit alpha type-2 Psma2	1399.764	1004.840	972.935	934.872
MYH8_MOUSE	74	1	4.59E-01	Myosin-8 Myh8	389.558	377.509	665.301	392.269
RD23A_MOUSE	6	2	4.60E-01	UV excision repair protein RAD23 homolog A Rad23a	464.376	220.064	262.897	490.233
CAZA1_MOUSE	5	2	4.60E-01	F-actin-capping protein subunit alpha-1 Capza1	1234.599	1586.198	1719.011	1502.770
RM21_MOUSE	5	1	4.62E-01	39S ribosomal protein L21, mitochondrial Mrpl21	428.034	514.911	81.527	830.536

BIRC6_MOUSE	27	3	4.63E-01	Baculoviral IAP repeat-containing protein 6 Birc6	200.520	498.909	239.810	186.565
ISOC1_MOUSE	2	1	4.68E-01	Isochorismatase domain-containing protein 1 Isoc1	243.507	62.492	121.000	110.831
ERF1_MOUSE	8	2	4.69E-01	Eukaryotic peptide chain release factor subunit 1 Etf1	923.120	381.975	896.464	643.209
PSME3_MOUSE	9	5	4.70E-01	Proteasome activator complex subunit 3 Psme3	1336.923	1828.168	1486.132	1393.670
TMEM2_MOUSE	7	1	4.73E-01	Cell surface hyaluronidase Tmem2	296.921	405.403	813.569	111.121
REV3L_MOUSE	35	3	4.75E-01	DNA polymerase zeta catalytic subunit Rev3l	136.971	91.047	235.082	32.561
SAR1A_MOUSE; SAR1B_MOUSE	5	2	4.76E-01	GTP-binding protein SAR1a Sar1a	616.808	172.575	344.173	309.654
IF5A1_MOUSE; IF5A2_MOUSE	9	4	4.77E-01	Eukaryotic translation initiation factor 5A-1 Eif5a	1090.421	523.268	637.552	461.430
CO6A6_MOUSE	17	5	4.79E-01	Collagen alpha-6(VI) chain Col6a6	734.043	13681.944	42810.674	14570.999
SRRM1_MOUSE	13	1	4.80E-01	Serine/arginine repetitive matrix protein 1 Srrm1	3208.660	5257.907	6402.203	4507.093
RPGF2_MOUSE	18	2	4.81E-01	Rap guanine nucleotide exchange factor 2 Rapgef2	152.943	181.032	118.578	85.168
CSN8_MOUSE	4	2	4.83E-01	COP9 signalosome complex subunit 8 Cops8	1613.363	1928.857	1587.295	1435.717
HS74L_MOUSE	31	5	4.84E-01	Heat shock 70 kDa protein 4L Hspa4l	84.370	41.622	107.077	26.489
BROX_MOUSE	3	2	4.85E-01	BRO1 domain-containing protein BROX Brox	48.534	8.405	43.389	42.428

RANT_MOUSE	7	2	4.87E-01	GTP-binding nuclear protein Ran, testis-specific isoform Rasl2-9	392.137	545.126	651.101	395.400
WSCD1_MOUSE	6	1	4.87E-01	WSC domain-containing protein 1 Wscd1	51.346	51.036	77.904	76.466
GGA1_MOUSE	6	1	4.91E-01	ADP-ribosylation factor-binding protein GGA1 Gga1	105.789	64.771	189.170	172.198
XPO5_MOUSE	20	2	4.92E-01	Exportin-5 Xpo5	303.009	374.572	240.481	261.631
IMA4_MOUSE	3	2	4.93E-01	Importin subunit alpha-4 Kpna3	74.706	16.873	53.729	202.187
SACS_MOUSE	49	4	4.94E-01	Sacsin Sacs	809.470	806.601	1007.096	1050.679
CISD1_MOUSE	3	1	4.94E-01	CDGSH iron-sulfur domain-containing protein 1 Cisd1	13.449	26.588	3.979	387.780
SWT1_MOUSE	9	2	4.96E-01	Transcriptional protein SWT1 Swt1	507.542	1134.830	1454.269	1171.821
PEF1_MOUSE	3	1	4.98E-01	Peflin Pef1	8.480	0.315	0.000	0.000
ACBP_MOUSE	2	2	4.99E-01	Acyl-CoA-binding protein Dbi	1452.736	1101.386	414.464	1664.870
Z804A_MOUSE	7	1	4.99E-01	Zinc finger protein 804A Znf804a	132.729	163.952	377.031	176.604
ROA0_MOUSE	4	2	5.02E-01	Heterogeneous nuclear ribonucleoprotein A0 Hnrnpa0	1003.863	660.028	1320.175	751.197
NO40_MOUSE	6	1	5.04E-01	Nucleolar protein of 40 kDa Zcchc17	14.070	98.503	200.185	25.979
VDAC2_MOUSE	7	3	5.04E-01	Voltage-dependent anion-selective channel protein 2 Vdac2	1043.400	1044.043	1080.504	4571.068
CALM1_MOUSE	10	6	5.05E-01	Calmodulin-1 Calm1	12102.283	9245.348	6766.019	7743.132
SF01_MOUSE	3	3	5.08E-01	Splicing factor 1 Sf1	931.400	933.563	1166.787	832.407

GLRX3_MOUSE	7	2	5.08E-01	Glutaredoxin-3 Glrx3	14.755	229.818	20.986	1152.775
CSK21_MOUSE	2	1	5.10E-01	Casein kinase II subunit alpha Csnk2a1	225.373	363.768	276.740	179.629
SYK_MOUSE	9	1	5.12E	Lysine--tRNA ligase Kars	768.026	377.523	544.743	319.662
AIP_MOUSE	6	2	-01			832.185	954.301	989.530
			-01	5.14EAH receptor-interacting protein Aip	1412.240			

SMD1_MOUSE	2	1	5.16E-01	Small nuclear ribonucleoprotein Sm D1 Snrpd1	203.535	34.626	154.576	730.242
SET_MOUSE	6	2	5.17E-01	Protein SET Set	555.773	95.312	277.294	316.595
NCAM1_MOUSE	22	6	5.18E-01	Neural cell adhesion molecule 1 Ncam1	984.152	1659.438	1528.603	1679.983
GOLP3_MOUSE	3	1	5.22E-01	Golgi phosphoprotein 3 Golph3	46.303	0.000	6.036	1.487
PLCH1_MOUSE	17	2	5.22E-01	1-phosphatidylinositol 4,5bisphosphate phosphodiesterase eta-1 Plch1	258.807	652.867	274.540	153.944
MYL6_MOUSE	12	5	5.23E-01	Myosin light polypeptide 6 Myl6	4779.095	4746.270	6087.377	4000.827
LGI3_MOUSE	3	1	5.23E-01	Leucine-rich repeat LGI family member 3 Lgi3	3.316	38.981	11.213	6.582
CAN1_MOUSE	7	2	5.24E-01	Calpain-1 catalytic subunit Capn1	700.956	681.141	988.330	1534.783
CATD_MOUSE	7	3	5.27E-01	Cathepsin D Ctsd	969.541	1196.457	1162.447	1312.628
PRS10_MOUSE	8	4	5.28E-01	26S proteasome regulatory subunit 10B Psmc6	494.913	467.772	676.977	782.966
RAP1B_MOUSE	7	2	5.29E-01	Ras-related protein Rap-1b Rap1b	662.255	952.078	991.286	698.686
SMRC1_MOUSE	10	1	5.29E-01	SWI/SNF complex subunit SMARCC1 Smarcc1	27.922	85.196	72.172	1907.880
FTO_MOUSE	10	3	5.29E-01	Alpha-ketoglutarate-dependent dioxygenase FTO Fto	101.170	93.755	154.908	123.608
COR1C_MOUSE	7	2	5.29E-01	Coronin-1C Coro1c	1455.200	870.140	3948.588	1820.083

SSRP1_MOUSE	12	1	5.30E-01	FACT complex subunit SSRP1 Ssrp1	71.152	143.841	403.456	102.029
ALD2_MOUSE	12	2	5.33E-01	Aldose reductase-related protein 2 Akr1b8	339.572	457.796	336.403	430.801
COMD1_MOUSE	3	1	5.35E-01	COMM domain-containing protein 1 Commd1	148.187	109.915	73.392	90.609
PLPHP_MOUSE	8	5	5.36E-01	Pyridoxal phosphate homeostasis protein Prosc	637.432	687.689	494.405	456.867
RDH13_MOUSE	4	1	-01	Retinol dehydrogenase 13 Rdh13	119.770	51.014	9.241	82.512
PFD1_MOUSE	3	1	5.37E -01 5.39E	Prefoldin subunit 1 Pfdn1	361.734	441.797	111.703	505.356
PCBP3_MOUSE	3	1	5.43E-01	Poly(rC)-binding protein 3 Pcbp3	44.880	80.967	34.550	105.541
NDUS4_MOUSE	6	4	5.44E-01	NADH dehydrogenase [ubiquinone] iron-sulfur protein 4, mitochondrial Ndufs4	841.054	1018.084	816.865	1227.134
PSMD6_MOUSE	10	4	5.48E-01	26S proteasome non-ATPase regulatory subunit 6 Psmd6	290.057	392.285	204.200	343.621
CPNE3_MOUSE	9	3	5.52E-01	Copine-3 Cpne3	930.342	902.348	1204.833	1219.048
RIR1_MOUSE	12	3	5.56E-01	Ribonucleoside-diphosphate reductase large subunit Rrm1	195.805	114.645	123.584	164.959
LAMP2_MOUSE	4	1	5.56E-01	Lysosome-associated membrane glycoprotein 2 Lamp2	615.250	645.683	691.964	572.155
K1H1_MOUSE	10	1	5.61E-01	Keratin, type I cuticular Ha1 Krt31	405.513	48.447	94.210	10.311
ROA1_MOUSE	13	6	5.63E-01	Heterogeneous nuclear ribonucleoprotein A1 Hnrnpa1	1720.337	1871.718	2462.249	1022.201
RL13_MOUSE	10	3	5.63E-01	60S ribosomal protein L13 Rpl13	2782.819	3736.463	3547.925	3198.386
ACOT9_MOUSE	11	4	5.64E-01	Acyl-coenzyme A thioesterase 9, mitochondrial Acot9	306.727	450.343	647.724	375.866

SH3L3_MOUSE	2	1	5.64E-01	SH3 domain-binding glutamic acidrich-like protein 3 Sh3bgrl3	86.020	94.689	221.145	1245.487
ITA7_MOUSE	16	1	5.64E-01	Integrin alpha-7 Itga7	747.512	878.914	1549.103	1062.676
GATM_MOUSE	8	2	5.69E-01	Glycine amidinotransferase, mitochondrial Gatm	95.946	164.989	400.369	227.272
NB5R3_MOUSE	17	7	5.70E-01	NADH-cytochrome b5 reductase 3 Cyb5r3	5529.584	6950.722	7905.757	8289.203
SHLB1_MOUSE	9	2	5.71E-01	Endophilin-B1 Sh3glb1	120.500	100.935	424.303	166.008
LC7L2_MOUSE	7	1	5.71E-01	Putative RNA-binding protein Luc7like 2 Luc7l2	39.344	94.783	72.154	18.374
VAPB_MOUSE	5	2	5.73E-01	Vesicle-associated membrane protein-associated protein B Vapb	1715.289	1317.165	1252.355	1116.688
PCM1_MOUSE	20	2	5.74E-01	Pericentriolar material 1 protein Pcm1	193.878	160.579	198.526	286.312
NICN1_MOUSE	2	1	5.79E-01	Nicolin-1 Nicn1	219.202	396.748	426.041	303.639
CHMP5_MOUSE	6	3	5.80E-01	Charged multivesicular body protein 5 Chmp5	140.394	15.100	193.892	68.827
DDX3X_MOUSE	17	1	5.83E-01	ATP-dependent RNA helicase DDX3X Ddx3x	129.473	31.727	191.012	75.897
PABP1_MOUSE	24	9	5.84E-01	Polyadenylate-binding protein 1 Pabpc1	2404.804	2670.437	2300.850	2462.007
PTN23_MOUSE	18	2	5.84E-01	Tyrosine-protein phosphatase nonreceptor type 23 Ptpn23	38.584	22.229	29.294	6.327
PTPRE_MOUSE	5	1	5.86E-01	Receptor-type tyrosine-protein phosphatase epsilon Ptpre	21.321	34.658	185.246	256.363
WBP11_MOUSE	10	1	5.87E-01	WW domain-binding protein 11 Wbp11	469.440	476.170	722.524	539.170
AP180_MOUSE	11	2	5.92E-01	Clathrin coat assembly protein AP180 Snap91	98.808	1146.011	339.333	428.449

EHD1_MOUSE	15	2	5.92E-01	EH domain-containing protein 1 Ehd1	786.155	787.874	864.984	1017.419
ARHG2_MOUSE	22	2	5.94E-01	Rho guanine nucleotide exchange factor 2 Arhgef2	151.488	260.757	399.889	411.166
ATX10_MOUSE	7	1	5.94E-01	Ataxin-10 Atxn10	495.687	353.527	300.432	615.271
PASK_MOUSE	9	2	5.95E-01	PAS domain-containing serine/threonine-protein kinase Pask	803.660	964.984	3424.176	727.983
CRK_MOUSE	1	1	-01	Adapter molecule crk Crk	344.898	107.281	256.273	149.042
XPO2_MOUSE	28	10	-01 5.97E 5.99E	Exportin-2 Cse1l	1689.939	1674.971	1496.589	1426.221
SPRE_MOUSE	5	2	6.04E-01	Sepiapterin reductase Spr	1505.441	1687.469	2008.054	1831.260
DYLT1_MOUSE	1	1	6.10E-01	Dynein light chain Tctex-type 1 Dynlt1	209.773	140.538	120.228	176.876
PDCD6_MOUSE	4	1	6.10E-01	Programmed cell death protein 6 Pdcd6	792.410	493.643	391.846	453.290
CATB_MOUSE	7	2	6.12E-01	Cathepsin B Ctsb	134.173	71.737	28.812	65.994
HSP7C_MOUSE	50	10	6.14E-01	Heat shock cognate 71 kDa protein Hspa8	26816.475	25152.494	29947.916	24017.500
PIN1_MOUSE	6	1	6.17E-01	Peptidyl-prolyl cis-trans isomerase NIMA-interacting 1 Pin1	620.131	188.091	426.796	230.448
RL15_MOUSE	9	2	6.19E-01	60S ribosomal protein L15 Rpl15	1073.661	724.158	506.953	676.289
FANCI_MOUSE	16	4	6.20E-01	Fanconi anemia group I protein homolog Fanci	1085.032	1300.283	1472.720	1554.794
SUCA_MOUSE	6	2	6.22E-01	Succinate--CoA ligase [ADP/GDPforming] subunit alpha, mitochondrial Suclg1	223.757	132.303	318.383	220.311
NDUA8_MOUSE	6	3	6.23E-01	NADH dehydrogenase [ubiquinone] 1 alpha subcomplex subunit 8 Ndufa8	266.840	258.332	206.292	1393.229

NUP98_MOUSE	17	1	6.23E-01	Nuclear pore complex protein Nup98-Nup96 Nup98	29.152	16.667	18.965	4.207

STX16_MOUSE	6	1	-01	Syntaxin-16 Stx16	14.045	4.964	4.021	1.678
ANXA6_MOUSE	65	13	-01 6.24E 6.26E	Annexin A6 Anxa6	2081.865	2549.648	4603.836	3504.371
DDX17_MOUSE	24	2	6.27E-01	Probable ATP-dependent RNA helicase DDX17 Ddx17	512.856	572.329	896.674	889.305
RENT1_MOUSE	17	1	6.32E-01	Regulator of nonsense transcripts 1 Upf1	130.508	78.433	106.921	76.769
ENV2_MOUSE	2	1	6.33E-01	Retrovirus-related Env polyprotein from Fv-4 locus Fv4	55.961	5.069	4.348	47.949
TIM44_MOUSE	7	1	6.35E-01	Mitochondrial import inner membrane translocase subunit TIM44 Timm44	0.000	6.120	3.510	81.247
SYQ_MOUSE	11	2	6.35E-01	Glutamine--tRNA ligase Qars	126.921	60.847	69.678	78.395
WDR12_MOUSE	2	1	6.36E-01	Ribosome biogenesis protein WDR12 Wdr12	217.605	71.662	164.699	101.914
LUC7L_MOUSE	10	2	6.37E-01	Putative RNA-binding protein Luc7like 1 Luc7l	58.823	172.643	62.326	21.297
DJB11_MOUSE	4	1	6.38E-01	DnaJ homolog subfamily B member 11 Dnajb11	145.742	191.407	486.364	1099.342
SPEE_MOUSE	7	3	6.42E-01	Spermidine synthase Srm	202.442	346.704	212.013	282.849
ITPA_MOUSE	3	1	6.45E-01	Inosine triphosphate pyrophosphatase Itpa	247.874	856.833	378.488	808.612
ADT1_MOUSE	22	3	6.46E-01	ADP/ATP translocase 1 Slc25a4	169.756	801.373	4098.843	6787.522
MDHC_MOUSE	11	5	6.48E-01	Malate dehydrogenase, cytoplasmic Mdh1	1826.980	2497.086	2252.179	1798.933
NP1L4_MOUSE	8	1	6.49E-01	Nucleosome assembly protein 1like 4 Nap1l4	116.257	82.108	89.812	132.602

TECR_MOUSE	6	2	6.63E-01	Very-long-chain enoyl-CoA reductase Tecr	68.387	17.608	10.530	37.558
HYOU1_MOUSE	20	5	6.63E-01	Hypoxia up-regulated protein 1 Hyou1	610.801	1065.887	757.220	778.581
IF122_MOUSE	8	1	6.63E-01	Intraflagellar transport protein 122 homolog Ift122	2068.231	4087.432	4249.021	3133.226
TBG2_MOUSE	7	2	-01	Tubulin gamma-2 chain Tubg2	58.434	54.509	26.648	26.146
NDRG1_MOUSE	8	3	-01 6.65E 6.67E	Protein NDRG1 Ndrg1	139.235	94.147	131.544	244.867
RUVB2_MOUSE	15	4	6.67E-01	RuvB-like 2 Ruvbl2	902.959	891.963	1392.748	981.018

TRIM8_MOUSE	11	1	6.78E-01	Probable E3 ubiquitin-protein ligase TRIM8 Trim8	197.577	254.324	209.307	36.692
CC187_MOUSE	24	1	6.86E-01	Coiled-coil domain-containing protein 187 Ccdc187	1.835	3.265	65.225	8.537
FKB10_MOUSE	14	3	6.88E-01	Peptidyl-prolyl cis-trans isomerase FKBP10 Fkbp10	1166.600	896.265	957.461	1085.682
PIR_MOUSE	6	1	6.90E-01	Pirin Pir	28.617	11.382	27.413	19.304
NED4L_MOUSE	9	1	6.92E-01	E3 ubiquitin-protein ligase NEDD4like Nedd4l	180.951	219.902	111.177	101.922
CK071_MOUSE	3	1	6.94E-01	Uncharacterized protein C11orf71 homolog Gm5617	260.357	329.675	481.499	251.116
CAP1_MOUSE	12	5	6.95E-01	Adenylyl cyclase-associated protein 1 Cap1	1525.464	1393.648	1387.747	1118.723
MEMO1_MOUSE	1	1	6.95E-01	Protein MEMO1 Memo1	27.496	179.547	254.185	164.147
GUAA_MOUSE	11	2	7.05E-01	GMP synthase [glutaminehydrolyzing] Gmps	749.400	754.421	523.614	721.164
CD44_MOUSE	1	1	7.07E-01	CD44 antigen Cd44	3419.165	2468.946	4446.020	2091.056

RPR1B_MOUSE	3	1	7.12E-01	Regulation of nuclear pre-mRNA domain-containing protein 1B Rprd1b	90.398	48.599	29.595	54.513
RL14_MOUSE	14	4	7.19E-01	60S ribosomal protein L14 Rpl14	995.012	961.603	475.882	809.522
NDKA_MOUSE	11	3	7.20E-01	Nucleoside diphosphate kinase A Nme1	479.952	603.840	830.996	616.735
RAB10_MOUSE	10	2	-01	Ras-related protein Rab-10 Rab10	645.038	1100.345	818.729	825.394
EPIPL_MOUSE	31	3	7.21E-01 7.22E-01	Epiplakin Eppk1	2783.084	1784.574	1828.283	1850.782
EHD2_MOUSE	12	1	7.25E-01	EH domain-containing protein 2 Ehd2	79.903	27.023	83.456	33.439
E41L3_MOUSE	15	1	-01	Band 4.1-like protein 3 Epb41l3	81.124	105.146	56.978	50.416
ADT4_MOUSE	11	2	7.26E-01 7.26E-01	ADP/ATP translocase 4 Slc25a31	111.718	258.213	356.406	162.440
NPC2_MOUSE	7	4	7.31E-01	Epididymal secretory protein E1 Npc2	2937.860	2576.557	3622.098	2744.850
PSMD3_MOUSE	19	7	7.31E-01	26S proteasome non-ATPase regulatory subunit 3 Psmd3	1265.790	1369.475	1196.451	1098.299
TCPE_MOUSE	37	10	7.35E-01	T-complex protein 1 subunit epsilon Cct5	1921.788	2373.976	1871.113	2062.801

GT251_MOUSE	10	1	7.35E-01	Procollagen galactosyltransferase 1 Colgalt1	502.691	336.014	769.267	740.557
PAIP2_MOUSE	2	1	7.39E-01	Polyadenylate-binding proteininteracting protein 2 Paip2	142.122	0.000	9.367	4.196
TBB4B_MOUSE	39	1	-01	Tubulin beta-4B chain Tubb4b	900.697	1288.353	1502.945	2213.406
MOES_MOUSE	62	18	7.47E-01 7.48E-01	Moesin Msn	5963.077	5861.037	5357.048	6504.416

BIR1B_MOUSE	15	1	7.51E-01	Baculoviral IAP repeat-containing protein 1b Naip2	6.288	1.074	169.007	3.084
PRKDC_MOUSE	46	5	7.53E-01	DNA-dependent protein kinase catalytic subunit Prkdc	1362.683	1643.480	1090.401	931.004
RCC1_MOUSE	6	3	7.56E-01	Regulator of chromosome condensation Rcc1	607.415	670.925	538.477	581.771
PSB7_MOUSE	7	1	7.60E-01	Proteasome subunit beta type-7 Psmb7	1177.619	1262.039	2716.650	344.923
EMAL4_MOUSE	6	1	7.62E-01	Echinoderm microtubuleassociated protein-like 4 Eml4	766.326	893.026	720.659	650.602
ATP7B_MOUSE	5	1	7.71E-01	Copper-transporting ATPase 2 Atp7b	527.727	514.474	840.283	670.410
C1TM_MOUSE	37	6	7.73E-01	Monofunctional C1-tetrahydrofolate synthase, mitochondrial Mthfd1l	1176.453	971.074	1303.417	1021.187
U520_MOUSE	31	1	7.76E-01	U5 small nuclear ribonucleoprotein 200 kDa helicase Snrnp200	173.063	41.803	81.165	80.898
SGSM1_MOUSE	7	5	7.93E-01	Small G protein signaling modulator 1 Sgsm1	546.149	711.736	333.902	303.681
TAF1_MOUSE	24	5	8.02E-01	Transcription initiation factor TFIID subunit 1 Taf1	2003.725	2051.452	1979.064	1602.570
ATP5I_MOUSE	5	1	8.11E-01	ATP synthase subunit e, mitochondrial Atp5i	65.157	80.352	195.429	1108.369
H4_MOUSE	15	7	8.13E-01	Histone H4 Hist1h4a	1300.120	1803.478	1842.427	4013.419
PDCD5_MOUSE	4	1	8.15E-01	Programmed cell death protein 5 Pdcd5	595.761	606.231	385.408	659.182
RAI14_MOUSE	16	2	8.15E-01	Ankycorbin Rai14	48.861	89.301	82.603	39.466
RM01_MOUSE	6	1	8.15E-01	39S ribosomal protein L1, mitochondrial Mrpl1	1092.155	2064.738	1483.863	1265.006
TOM22_MOUSE	4	3	8.21E-01	Mitochondrial import receptor subunit TOM22 homolog Tomm22	632.023	927.256	784.248	822.296

NXP20_MOUSE	10	1	8.26E-01	Protein Noxp20 Fam114a1	81.656	515.215	151.131	87.409
GSTA3_MOUSE	7	1	8.26E-01	Glutathione S-transferase A3 Gsta3	23.194	34.612	7.546	11.507
TPP2_MOUSE	19	7	-01	Tripeptidyl-peptidase 2 Tpp2	464.991	365.885	519.998	505.931
API5_MOUSE	7	2	-01 8.35E 8.37E	Apoptosis inhibitor 5 Api5	60.617	28.253	149.121	56.172
ARMC8_MOUSE	10	1	8.40E-01	Armadillo repeat-containing protein 8 Armc8	2037.120	2345.477	2055.578	2656.246
RL24_MOUSE	8	1	8.41E-01	60S ribosomal protein L24 Rpl24	3778.538	6097.662	4400.599	4698.899
CLYBL_MOUSE	5	1	8.42E-01	Citrate lyase subunit beta-like protein, mitochondrial Clybl	89.525	399.007	333.866	837.342
TFIP8_MOUSE	1	1	8.45E-01	Tumor necrosis factor alpha induced protein 8 Tnfaip8	18.427	0.683	21.218	0.876
H2B1M_MOUSE; H2B1K_MOUSE; H2B3A_MOUSE	13	1	8.51E-01	Histone H2B type 1-M Hist1h2bm	24.514	24.131	17.496	50.777
CAPG_MOUSE	7	4	-01	Macrophage-capping protein Capg	4146.437	4303.186	4089.594	3873.452
FLOT1_MOUSE	4	1	-01 8.59E 8.62E	Flotillin-1 Flot1	8.379	322.676	81.543	44.523
H15_MOUSE	6	3	8.62E-01	Histone H1.5 Hist1h1b	779.244	702.493	387.000	478.020
PARP8_MOUSE	17	1	8.64E-01	Poly [ADP-ribose] polymerase 8 Parp8	770.693	823.958	637.105	799.996
MCM7_MOUSE	16	1	8.69E-01	DNA replication licensing factor MCM7 Mcm7	114.787	28.280	15.096	11.111
GYS1_MOUSE	5	1	8.71E-01	Glycogen [starch] synthase, muscle Gys1	841.891	668.053	785.907	849.526
HMGB3_MOUSE	2	1	8.71E-01	High mobility group protein B3 Hmgb3	37.307	23.982	33.340	37.551

G3BP1_MOUSE	13	3	8.74E-01	Ras GTPase-activating proteinbinding protein 1 G3bp1	1341.513	1245.247	1274.649	1472.908
MLEC_MOUSE	4	2	8.77E-01	Malectin Mlec	607.099	909.394	1025.313	629.427
PLOD3_MOUSE	7	1	8.82E-01	Procollagen-lysine,2-oxoglutarate 5-dioxygenase 3 Plod3	737.569	886.610	878.641	803.515
DCPS_MOUSE	7	5	8.83E-01	m7GpppX diphosphatase Dcps	1253.820	1002.504	1321.946	1556.737
ECHM_MOUSE	5	1	8.91E-01	Enoyl-CoA hydratase, mitochondrial Echs1	554.748	704.029	342.546	673.192
H2A1B_MOUSE	6	1	8.95E-01	Histone H2A type 1-B Hist1h2ab	1972.875	1704.501	1785.427	1826.749

K2C71_MOUSE	33	3	9.00E-01	Keratin, type II cytoskeletal 71 Krt71	387.909	418.755	367.376	328.035
HMGCL_MOUSE	2	1	9.01E-01	Hydroxymethylglutaryl-CoA lyase, mitochondrial Hmgcl	89.728	49.992	84.548	207.895
AKP13_MOUSE	24	2	9.06E-01	A-kinase anchor protein 13 Akap13	75.562	116.998	51.984	49.358
SYIC_MOUSE	27	6	9.09E-01	Isoleucine--tRNA ligase, cytoplasmic Iars	702.137	710.440	613.613	667.263
NAB2_MOUSE	9	3	9.10E-01	NGFI-A-binding protein 2 Nab2	87.145	58.869	132.020	88.935
PA1B2_MOUSE	2	1	9.11E-01	Platelet-activating factor acetylhydrolase IB subunit beta Pafah1b2	115.533	117.830	145.071	184.080
HSP7E_MOUSE	14	1	9.13E-01	Heat shock 70 kDa protein 14 Hspa14	38.583	3.217	101.401	36.466
GARS_MOUSE	29	6	9.13E-01	Glycine--tRNA ligase Gars	852.846	794.361	910.400	733.842
RT23_MOUSE	8	4	9.21E-01	28S ribosomal protein S23, mitochondrial Mrps23	316.358	271.217	472.566	411.507
LAP2A_MOUSE	13	3	9.22E-01	Lamina-associated polypeptide 2, isoforms alpha/zeta Tmpo	364.406	457.039	584.208	548.095
GGYF2_MOUSE	14	2	9.24E-01	GRB10-interacting GYF protein 2 Gigyf2	160.075	93.672	111.041	144.205

K2C4_MOUSE	15	1	9.27E-01	Keratin, type II cytoskeletal 4 Krt4	159.497	417.857	162.652	93.861
ZZEF1_MOUSE	18	2	9.33E-01	Zinc finger ZZ-type and EF-hand domain-containing protein 1 Zzef1	1149.820	1262.187	825.716	2171.631
H11_MOUSE	4	1	9.35E-01	Histone H1.1 Hist1h1a	517.423	601.499	611.262	818.096
RN213_MOUSE	43	5	9.37E-01	E3 ubiquitin-protein ligase RNF213 Rnf213	739.606	1514.683	1248.048	5796.989
CBX5_MOUSE	4	1	9.47E-01	Chromobox protein homolog 5 Cbx5	2131.106	3243.551	4154.228	2936.869
LARP4_MOUSE	11	3	9.48E-01	La-related protein 4 Larp4	83.698	219.618	283.149	408.775
AT2A3_MOUSE	33	4	9.49E-01	Sarcoplasmic/endoplasmic reticulum calcium ATPase 3 Atp2a3	1738.294	1869.019	1964.648	1905.603
PSB5_MOUSE	8	3	9.51E-01	Proteasome subunit beta type-5 Psmb5	3709.939	3920.312	5257.572	2869.165
IF2B1_MOUSE	10	2	9.53E-01	Insulin-like growth factor 2 mRNAbinding protein 1 Igf2bp1	37.942	276.923	26.103	58.308
PHOCN_MOUSE	3	1	9.55E-01	MOB-like protein phocein Mob4	142.196	262.371	420.721	354.656
LCAP_MOUSE	17	2	9.56E-01	Leucyl-cystinyl aminopeptidase Lnpep	48.810	95.972	24.131	25.272
PSMD4_MOUSE	4	2	9.61E-01	26S proteasome non-ATPase regulatory subunit 4 Psmd4	10911.249	12249.212	13418.270	10675.236
MBB1A_MOUSE	30	8	9.69E-01	Myb-binding protein 1A Mybbp1a	477.903	546.182	620.001	518.047
VPS29_MOUSE	4	1	9.80E-01	Vacuolar protein sorting-associated protein 29 Vps29	1858.031	2258.362	2942.482	1947.899
PLCB3_MOUSE	22	4	9.83E-01	1-phosphatidylinositol 4,5bisphosphate phosphodiesterase beta-3 Plcb3	550.833	587.619	992.809	812.572
H14_MOUSE	6	1	9.89E-01	Histone H1.4 Hist1h1e	2907.431	3367.973	2809.017	5714.937

PGP_MOUSE	5	2	9.97E-01	Glycerol-3-phosphate phosphatase Pgp	226.192	231.425	570.504	376.609

Table 7. Proteins identified in differentiating C2C12 derived EVs using bottom-up proteomic analysis. ITS differentiated C2C12 cell derived EVs were isolated on day 1, 3 and 5 of the differentiation period and samples prepared for MS analysis. Proteins with 1 or more unique peptide sequence were considered to be identified when searched against the UniProt database. Proteins were quantified using Progenesis QI proteomics software. Data shown are of 3 biological repeats, which allowed for an ANOVA statistical test.

					Normalised abundance		
UniProt ID	**Peptide count**	**Unique peptides**	**Anova (p)**	**Protein name**	**Day 1 EVs**	**Day 3 EVs**	**Day 5 EVs**
FMOD_MOUSE	5	1	2.20E-10	Fibromodulin Fmod	1291.782	0.000	0.000
HERC6_MOUSE	13	1	2.20E-10	E3 ISG15--protein ligase Herc6 Herc6	81.257	0.000	0.005
ZN583_MOUSE	5	1	2.20E-10 2.20E-10 2.69E-08 3.11E-08	Zinc finger protein 583 Znf583	0.000	1408.300	212.977
CHADL_MOUSE	9	1	6.96E-08	Chondroadherin-like protein Chadl	841.845	0.000	0.000
RHG01_MOUSE	6	1	2.79E-08	Rho GTPase-activating protein 1 Arhgap1	600.115	0.000	0.000
CRTC1_MOUSE	1	1	2.94E-08	CREB-regulated transcription coactivator 1 Crtc1	1820.758	0.000	0.000
KPTN_MOUSE	3	1	3.00E-08	KICSTOR complex protein kaptin Kptn	235.720	0.000	0.000
RRAGD_MOUSE	6	1	4.78E-08	Ras-related GTP-binding protein D Rragd	449.395	0.000	0.012
PLCB3_MOUSE	15	3	6.34E-08	1-phosphatidylinositol 4,5-bisphosphate phosphodiesterase beta-3 Plcb3	834.411	308.041	66.145
FHAD1_MOUSE	19	1	7.12E-08	Forkhead-associated domain-containing protein 1 Fhad1	105.903	0.000	0.205
ACTA_MOUSE	48	1	1.58E-07	Actin, aortic smooth muscle Acta2	628.666	3656.558	6512.775

ASIC3_MOUSE	4	1	2.16E	Acid-sensing ion channel 3 Asic3	223.727	0.000	0.000
NINL_MOUSE	19	1	2.41E	Ninein-like protein Ninl	114.668	0.000	0.000
KIRR1_MOUSE	4	1	3.45E	Kin of IRRE-like protein 1 Kirrel1	178.528	0.000	0.000
CLIC5_MOUSE	3	1	-07	Chloride intracellular channel protein 5 Clic5	851.426	0.000	0.000
MYH10_MOUSE	50	2	-07 -07 -07 -07 -07 -07 -07 3.83E 4.37E	Myosin-10 Myh10	1241.802	6985.717	12942.481
PGS1_MOUSE	8	2	5.34E	Biglycan Bgn	1243.460	4927.553	5868.885
TM117_MOUSE	3	1	7.63E	Transmembrane protein 117 Tmem117	33.745	0.000	0.000
SYQ_MOUSE	10	1	9.62E-07	Glutamine--tRNA ligase Qars	116.139	0.000	0.000
NMT1_MOUSE	10	2	1.15E-06	Glycylpeptide N-tetradecanoyltransferase 1 Nmt1	62.435	1053.528	2314.426
CUL4B_MOUSE	8	1	1.61E-06	Cullin-4B Cul4b	712.410	0.000	0.000

ACACA_MOUSE	28	5	1.81E	Acetyl-CoA carboxylase 1 Acaca	3688.847	9569.495	5351.935
NAR3_MOUSE	2	1	-06			4417.951	14835.738
			-06	2.19EEcto-ADP-ribosyltransferase 3 Art3	530.840		
AT2B2_MOUSE	14	1	3.13E-06	Plasma membrane calcium-transporting ATPase 2 Atp2b2	282.875	0.000	0.423
STEA2_MOUSE	8	2	3.33E-06	Metalloreductase STEAP2 Steap2	692.630	208.271	22.606
MIME_MOUSE	14	7	4.44E-06	Mimecan Ogn	2173.011	17261.281	26727.627
SYYC_MOUSE	10	1	5.71E-06	Tyrosine--tRNA ligase, cytoplasmic Yars	26.587	423.771	743.726
PDC6I_MOUSE	51	18	5.92E-06	Programmed cell death 6-interacting protein Pdcd6ip	126693.523	20545.141	26960.405

AR6P1_MOUSE	1	1	8.05E-06	ADP-ribosylation factor-like protein 6-interacting protein 1 Arl6ip1	43.855	0.000	0.000
ARL5B_MOUSE	1	1	-06	8.97E ADP-ribosylation factor-like protein		6257.595	6157.504
EF1G_MOUSE	13	5	-06 5B Arl5b 9.83E	2166.321 Elongation factor 1-gamma Eef1g	2730.544	19778.178	23673.342
U5S1_MOUSE	11	1	1.01E-05	116 kDa U5 small nuclear ribonucleoprotein component Eftud2	57.986	0.153	0.000
PLOD1_MOUSE	9	1	1.12E-05	Procollagen-lysine,2-oxoglutarate 5-dioxygenase 1 Plod1	1335.032	5014.194	5809.099
EPHA2_MOUSE	28	10	1.21E-05	Ephrin type-A receptor 2 Epha2	12880.177	4604.773	5329.698
ENPP3_MOUSE	7	1	1.44E-05	Ectonucleotide pyrophosphatase/phosphodiesterase family member 3 Enpp3	3.417	451.465	77.884
COCA1_MOUSE	97	28	1.44E	Collagen alpha-1(XII) chain Col12a1	45148.384	116132.584	57811.594
TBB2B_MOUSE	40	1	1.79E	Tubulin beta-2B chain Tubb2b	2741.573	6531.122	9352.386
PLSL_MOUSE	9	1	-05 -05 -05 -05 1.80E	Plastin-2 Lcp1	331.093	0.000	0.447
SYDC_MOUSE	11	1	2.14E	Aspartate--tRNA ligase, cytoplasmic Dars	692.251	2680.242	3599.881
GNAS1_MOUSE	32	6	2.28E-05	Guanine nucleotide-binding protein G(s) subunit alpha isoforms XLas Gnas	17567.262	4013.681	3970.199
MYO1C_MOUSE	48	13	-05 -05	2.78E Unconventional myosin-Ic Myo1c	21135.295	9041.887	11268.572
ACTS_MOUSE	44	2	2.78E	Actin, alpha skeletal muscle Acta1	720.042	3243.158	10220.726
PZP_MOUSE	20	4	2.79E-05	Pregnancy zone protein Pzp	32330.271	12046.515	8646.741
AEBP1_MOUSE	14	1	3.05E-05	Adipocyte enhancer-binding protein 1	48.161	0.000	0.482

				Aebp1			
BABA2_MOUSE	3	1	3.32E-05	BRISC and BRCA1-A complex member 2 Babam2	19.625	0.000	0.000
KPYM_MOUSE	57	26	3.35E-05	Pyruvate kinase PKM Pkm	77997.955	177832.814	186275.098
BASI_MOUSE	7	2	3.81E-05	Basigin Bsg	6882.120	1134.283	1255.084
DX39B_MOUSE	9	1	3.86E-05	Spliceosome RNA helicase Ddx39b Ddx39b	4.754	191.770	310.578
CE350_MOUSE	36	3	3.93E-05	Centrosome-associated protein 350 Cep350	162.365	1048.569	1420.366
NKG2D_MOUSE	2	1	3.98E-05	NKG2-D type II integral membrane protein Klrk1	0.466	335.721	33.107
PXDN_MOUSE	33	11	4.14E-05	Peroxidasin homolog Pxdn	11785.466	36295.381	21841.050
CO1A2_MOUSE	25	5	4.86E-05	Collagen alpha-2(I) chain Col1a2	2119.415	8606.730	4775.977
QCR2_MOUSE	4	1	4.93E-05	Cytochrome b-c1 complex subunit 2, mitochondrial Uqcrc2	1023.771	88.190	483.710
RU17_MOUSE	6	1	5.11E-05	U1 small nuclear ribonucleoprotein 70 kDa Snrnp70	23.773	1242.919	781.587
CO1A1_MOUSE	28	8	5.59E-05	Collagen alpha-1(I) chain Col1a1	1739.502	8027.682	3714.874
SVIL_MOUSE	20	4	5.72E-05	Supervillin Svil	1396.040	7049.194	13759.512
DDX17_MOUSE	10	1	5.74E-05	Probable ATP-dependent RNA helicase DDX17 Ddx17	45.831	0.000	0.580
CXA1_MOUSE	10	4	6.50E-05	Gap junction alpha-1 protein Gja1	7676.819	312.559	417.004
MVP_MOUSE	31	15	6.54E-05	Major vault protein Mvp	5655.912 15406.176	6035.081 29777.885	19930.722
FAS_MOUSE	103	19	6.94E-05	Fatty acid synthase Fasn			39774.247

CSN4_MOUSE	7	3	8.26E-05	COP9 signalosome complex subunit 4 Cops4	2275.854	8824.571	8466.378
ANXA1_MOUSE	33	17	-05	8.61E Annexin A1			10877.824
TCPA_MOUSE	40	14	-05 Anxa1		42760.559 10753.812		39268.916
			8.68E	T-complex protein 1 subunit alpha Tcp1	20354.109	48767.981	
EIF3C_MOUSE	16	2	9.60E-05	Eukaryotic translation initiation factor 3 subunit C Eif3c	791.569	2289.560	2846.338
FKBP4_MOUSE	8	3	9.76E-05	Peptidyl-prolyl cis-trans isomerase FKBP4 Fkbp4	763.930	1986.936	4198.130
MRO2B_MOUSE	20	1	9.88E-05	Maestro heat-like repeat-containing protein family member 2B Mroh2b	665.857	4515.314	4140.644
GPC1_MOUSE	14	5			15660.794 8476.751		6664.543
CD81_MOUSE	4	3	0.000104	Glypican-1 Gpc1	53196.749 10538.290		8659.436
			0.000114	CD81 antigen Cd81			
NOTC2_MOUSE	10	3	0.00012	Neurogenic locus notch homolog protein 2 Notch2	1681.165	49.519	176.164
AARD_MOUSE	5	2	0.000138	Alanine and arginine-rich domain-containing protein Aard	333.541	1396.823	674.300
SAHH_MOUSE	17	5	0.000157	Adenosylhomocysteinase Ahcy	4584.317	14640.016	15968.662

AT12A_MOUSE	11	2	0.000161	Potassium-transporting ATPase alpha chain 2 Atp12a	1163.437	7934.970	2769.362
HSP74_MOUSE	12	2	0.000165	Heat shock 70 kDa protein 4 Hspa4	10201.745	20266.860	22555.248
IGSF8_MOUSE	16	5	0.000175	Immunoglobulin superfamily member 8 Igsf8	10052.858	4218.499	2482.928
NMD3_MOUSE	5	1	0.000182	60S ribosomal export protein NMD3 Nmd3	32.640 0.000		0.067
RS3A_MOUSE	20	12			30985.212 11712.169		21717.279
			0.000202	40S ribosomal protein S3a Rps3a			

A2MG_MOUSE	8	1	0.000208	Alpha-2-macroglobulin-P A2m	655.538	2528.024	1209.618
NEST_MOUSE	23	3	0.000212	Nestin Nes	2109.322	4478.824	7367.457
BASP1_MOUSE	13	8	0.000212	Brain acid soluble protein 1 Basp1	8947.693	543.435	945.244
SAM9L_MOUSE	18	2	0.00022	Sterile alpha motif domain-containing protein 9-like Samd9l	529.146	22.180	63.549
CAD13_MOUSE	12	4	0.000228	Cadherin-13 Cdh13	3981.253	601.434	1475.705
RTCB_MOUSE	12	3	0.00023	tRNA-splicing ligase RtcB homolog Rtcb	4335.243	7627.287	10921.640
NOTC1_MOUSE	15	1	0.000236	Neurogenic locus notch homolog protein 1 Notch1	408.211	79.909	53.846
IPO4_MOUSE	9	2	0.000261	Importin-4 Ipo4	411.522	0.000	19.712
RGAP1_MOUSE	19	5	0.000262	Rac GTPase-activating protein 1 Racgap1	3384.725	233.959	292.286
PP1G_MOUSE	9	3	0.000273	Serine/threonine-protein phosphatase PP1-gamma catalytic subunit Ppp1cc	719.663	27.092	401.717
PDGFC_MOUSE	10	3	0.00029	Platelet-derived growth factor C Pdgfc	881.918	5795.524	5525.517
TOLIP_MOUSE	7	2	0.000304	Toll-interacting protein Tollip	2432.459	229.144	450.826
DC1L1_MOUSE	1	1	0.000304	Cytoplasmic dynein 1 light intermediate chain 1 Dync1li1	16.430	477.809	709.254
TCPZ_MOUSE	37	6	0.000313	T-complex protein 1 subunit zeta Cct6a	1713.396	6835.656	6684.358
ITA4_MOUSE	5	2	0.000317	Integrin alpha-4 Itga4	253.413	0.639	0.416
HNRPF_MOUSE	12	5	0.000329	Heterogeneous nuclear ribonucleoprotein F Hnrnpf	1616.704	542.778	229.210
HPRT_MOUSE	2	1	0.000332	Hypoxanthine-guanine phosphoribosyltransferase Hprt1	3330.703	1052.295	369.821
ANO6_MOUSE	10	3	0.000346	Anoctamin-6 Ano6	3678.680	456.656	958.126
TERA_MOUSE	53	21	0.000347	Transitional endoplasmic reticulum ATPase Vcp	13325.884	46294.577	18604.528

SYPL1_MOUSE	3	1			341.073		8.576	94.469
LAMA5_MOUSE	60	15	0.000356	Synaptophysin-like protein 1 Sypl1	16267.674		7051.849	6111.303
			0.000366	Laminin subunit alpha-5 Lama5				

ANM1_MOUSE	7	2	0.000367	Protein arginine N-methyltransferase 1 Prmt1	158.755		2253.228	1943.927
SNP23_MOUSE	10	8	0.000378	Synaptosomal-associated protein 23 Snap23	8276.618		2043.477	2609.581
SC5A2_MOUSE	7	2	0.000394	Sodium/glucose cotransporter 2 Slc5a2	491.365		1551.302	1208.617
COF1_MOUSE	8	1	0.000402	Cofilin-1 Cfl1	3144.889		40.205	129.563
GNAI2_MOUSE	15	7	0.000404	Guanine nucleotide-binding protein G(i) subunit alpha-2 Gnai2	20753.000		6125.123	6849.570
F10A1_MOUSE	9	6	0.000466	Hsc70-interacting protein St13	4842.732		736.541	1166.841
MATN2_MOUSE	16	3	0.000481	Matrilin-2 Matn2				2981.275
MYH9_MOUSE	131	32			2674.933	7030.265		94250.887
			0.000484	Myosin-9 Myh9	48414.321	69385.415		
TCPG_MOUSE	55	17	0.000509	T-complex protein 1 subunit gamma Cct3	39181.815	74886.472		62559.763
UBE2N_MOUSE	5	2	0.000529	Ubiquitin-conjugating enzyme E2 N Ube2n	3078.236		610.489	486.790
CAPG_MOUSE	6	3	0.000531	Macrophage-capping protein Capg	7748.735		4143.943	2781.089
SEPT7_MOUSE	9	2	0.000531	Septin-7 Sept7	541.421	3917.916		2081.169
PSA1_MOUSE	14	7	0.000547	Proteasome subunit alpha type-1 Psma1	11998.949	26019.461		15818.098
PSMD1_MOUSE	16	5	0.000585	26S proteasome non-ATPase regulatory subunit 1 Psmd1	4596.684		5766.488	8877.680
ISLR_MOUSE	6	2	0.000587	Immunoglobulin superfamily containing leucine-rich repeat protein Islr	1228.135		3967.252	6069.331
SODE_MOUSE	2	1	0.000603	Extracellular superoxide dismutase [Cu-Zn]	44.787		658.129	550.176

				Sod3			
SRC_MOUSE	12	1	0.000604	Neuronal proto-oncogene tyrosine-protein kinase Src Src	660.091	0.729	7.353
RL6_MOUSE	22	10	0.000606	60S ribosomal protein L6 Rpl6	27905.080	9990.218	7905.953
ABCG2_MOUSE	5	2	0.000619	ATP-binding cassette sub-family G member 2 Abcg2	328.672	11.120	60.332
NUCL_MOUSE	10	3	0.000621	Nucleolin Ncl	1193.192	4923.997	2700.960
SPEE_MOUSE	5	3	0.000628	Spermidine synthase Srm			7110.652
RS8_MOUSE	10	2					7668.814
TENA_MOUSE	66	15					35069.439
					3160.152	3523.627	
			0.00071	40S ribosomal protein S8 Rps8	21495.582	5647.186	
			0.000737	Tenascin Tnc	36157.875	71001.310	
					2024.054	1475.406	
FPPS_MOUSE	10	2	0.000747	Farnesyl pyrophosphate synthase Fdps			543.310
CO6A2_MOUSE	17	2	0.000762	Collagen alpha-2(VI) chain Col6a2	1522.842	4110.924	6953.807
RAB5B_MOUSE	6	2	0.000768	Ras-related protein Rab-5B Rab5b	1747.671	711.020	1657.421

PRAX_MOUSE	19	7	0.000834	Periaxin Prx	2379.146	5186.914	5686.071
SERC_MOUSE	11	3	0.000841	Phosphoserine aminotransferase ᵇsat1	5505.255	4941.169	11245.396
CLK4_MOUSE	10	1	0.000849	Dual specificity protein kinase CLK4 Clk4	215.589	0.000	0.000
VATB2_MOUSE	12	2	0.000893	V-type proton ATPase subunit B, brain isoform Atp6v1b2	1452.961	3989.807	5836.701
ANTR2_MOUSE	1	1	0.00091	Anthrax toxin receptor 2 Antxr2	375.611	16.277	2.435
KIF23_MOUSE	18	2	0.000949	Kinesin-like protein KIF23 Kif23	2298.727	84.898	98.752

TSP2_MOUSE	18	4	0.000956	Thrombospondin-2 Thbs2	1995.269	625.155	479.859
FMNL3_MOUSE	16	2	0.000978	Formin-like protein 3 Fmnl3	769.292	269.051	269.988
CTND1_MOUSE	19	3	0.000983	Catenin delta-1 Ctnnd1	1574.634	117.211	215.686
PCOC1_MOUSE	12	3	0.001015	Procollagen C-endopeptidase enhancer 1 Pcolce	3878.278	5972.340	1941.065
2AAB_MOUSE	12	1	0.001029	Serine/threonine-protein phosphatase 2A 65 kDa regulatory subunit A beta isoform Ppp2r1b	922.000	127.896	75.036
CH60_MOUSE	29	13	0.001033	60 kDa heat shock protein, mitochondrial Hspd1	18543.253	6005.253	5472.041
RL7_MOUSE	22	8	0.00106	60S ribosomal protein L7 Rpl7	33027.416	6018.414	8967.130
AT10D_MOUSE	12	3	0.001061	Probable phospholipid-transporting ATPase VD Atp10d	1669.758	6348.530	10888.550
TBB1_MOUSE	26	4	00107	0. Tubulin beta-1 chain Tubb1	20726.858	7617.019	6381.784
LAMB1_MOUSE	33	12	0.001084	Laminin subunit beta-1 Lamb1	13645.001	8087.596	6079.807
SMD1_MOUSE	2	1	0.001099	Small nuclear ribonucleoprotein Sm D1 Snrpd1	48.551	0.000	0.078
EF2_MOUSE	67	17	0.001106	Elongation factor 2 Eef2	21623.289	47342.110	56606.381
DYHC1_MOUSE	123	26	0.001116	Cytoplasmic dynein 1 heavy chain 1 Dync1h1	17600.584	21101.490	34909.793
TM86A_MOUSE	4	1	0.001145	Lysoplasmalogenase-like protein TMEM86A Tmem86a	4296.979	4353.261	1255.876
ERF_MOUSE	6	2	0.001238	ETS domain-containing transcription factor ERF Erf	1998.829	4893.169	3193.053

STK10_MOUSE	12	3	0.001352	Serine/threonine-protein kinase 10 Stk10	984.888	1712.242	2174.021
IF4E_MOUSE	3	1	0.00136	Eukaryotic translation initiation factor 4E Eif4e	317.406	948.831	1406.905
CLH1_MOUSE	47	10	0.001365	Clathrin heavy chain 1 Cltc	9013.890	8492.106	16642.927

ACTZ_MOUSE	8	3	0.001372	Alpha-centractin Actr1a	3169.565	5866.319	6903.469
AGRA3_MOUSE	6	1	0.001385	Adhesion G protein-coupled receptor A3 Adgra3	515.821	145.858	247.264
MMP2_MOUSE	8	5				13142.154	3476.849
COPG1_MOUSE	25	6	0.001394	72 kDa type IV collagenase Mmp2	3607.922	8049.061	4483.095
			0.001428	Coatomer subunit gamma-1 Copg1	2542.321		
ARC1B_MOUSE	5	2	0.001458	Actin-related protein 2/3 complex subunit 1B Arpc1b	1899.023	6054.582	9743.167
EZRI_MOUSE	23	3	0.001519	Ezrin Ezr	2426.713	418.522	343.077
IDHC_MOUSE	13	5	0.001559	Isocitrate dehydrogenase [NADP] cytoplasmic Idh1	38621.596	10443.624	10269.787
UXS1_MOUSE	8	3	0.001588	UDP-glucuronic acid decarboxylase 1 Uxs1	547.234	2911.802	2314.439
DPYL2_MOUSE	26	8	0.001638	Dihydropyrimidinase-related protein 2 Dpysl2	13699.213	24611.596	21693.083
VAT1_MOUSE	14	7	0.001639	Synaptic vesicle membrane protein VAT-1 homolog Vat1	27097.265	14630.479	15344.298
GELS_MOUSE	18	8	0.001691	Gelsolin Gsn	19831.895	9575.572	8809.984
ARK72_MOUSE	6	2	0.001692	Aflatoxin B1 aldehyde reductase member 2 Akr7a2	3368.788	663.085	937.264
ITB1_MOUSE	22	3		0.00171 Integrin beta-1 Itgb1	36172.836	21080.545	21074.673
NICA_MOUSE	9	2	0.001716	Nicastrin Ncstn	2170.392	924.316	1802.335
PABP1_MOUSE	10	5	0.001773	Polyadenylate-binding protein 1 Pabpc1	4292.987	2389.304	3530.095

YBOX1_MOUSE	8	5	0.001838	Nuclease-sensitive element-binding protein 1 Ybx1	4966.331	1529.503	856.890
SURF4_MOUSE	3	1	0.001849	Surfeit locus protein 4 Surf4	329.639	4.150	11.792
CHM2A_MOUSE	9	3	0.001871	Charged multivesicular body protein 2a Chmp2a	1959.329	4651.618	4508.761
TAOK1_MOUSE	12	2	0.001905	Serine/threonine-protein kinase TAO1 Taok1	4349.062	2137.664	2826.736
FSCN1_MOUSE	10	3	0.00191	Fascin Fscn1	994.517	5092.205	5475.009
ANXA7_MOUSE	14	4	0.00197	Annexin A7 Anxa7	7281.315	2420.679	2913.467
GAPR1_MOUSE	5	4	0.001995	Golgi-associated plant pathogenesis-related protein 1 Glipr2	35943.455	14548.091	9953.230
HS90A_MOUSE	46	6	0.002096	Heat shock protein HSP 90-alpha Hsp90aa1	9658.445	21031.876	25221.910
PLTP_MOUSE	14	2	0.002105	Phospholipid transfer protein Pltp	1186.349	8644.616	8411.816

EFCB3_MOUSE	5	1	0.002135	EF-hand calcium-binding domain-containing protein 3 Efcab3	3407.508		2176.692	1281.171
LEG1_MOUSE	3	3	0.002161	Galectin-1 Lgals1	4752.264		963.494	685.654
BAIP2_MOUSE	11	2	0.002204	Brain-specific angiogenesis inhibitor 1-associated protein 2 Baiap2	2069.070		738.002	767.973
ITAV_MOUSE	22	5	0.002332	Integrin alpha-V Itgav	3022.057		840.824	1991.089
BIR1A_MOUSE	22	3	0.002342	Baculoviral IAP repeat-containing protein 1a Naip1	3911.323		1426.055	755.603
FLOT2_MOUSE	5	1	0.002386	Flotillin-2 Flot2	230.052		677.976	606.665
HTRA1_MOUSE	16	6	0.002401	Serine protease HTRA1 Htra1	8312.031		7572.315	14098.744
VPS35_MOUSE	13	3	0.002434	Vacuolar protein sorting-associated protein 35 Vps35	2009.275		4305.082	5827.770
NID2_MOUSE	27	8			17781.516	33616.791		17700.517
TSP3_MOUSE	5	1	0.002459	Nidogen-2 Nid2	8559.215	6453.285		11062.444
			0.002495	Thrombospondin-3 Thbs3				
SYIC_MOUSE	15	4	0.002515	Isoleucine--tRNA ligase, cytoplasmic Iars	1642.030		2809.599	5238.973
CSPG4_MOUSE	13	2	0.002522	Chondroitin sulfate proteoglycan 4 Cspg4	593.234		435.533	79.028
VATA_MOUSE	9	3	0.002525	V-type proton ATPase catalytic subunit A Atp6v1a	3722.486		3348.500	1671.602
OLM2B_MOUSE	15	6						16366.073
DEND3_MOUSE	17	1	0.002538	Olfactomedin-like protein 2B Olfml2b	13388.954	23857.781		447.554
			0.002593	DENN domain-containing protein 3 Dennd3	50.208		362.501	
NDRG1_MOUSE	6	3	0.002627	Protein NDRG1 Ndrg1	1816.241		1016.765	550.363
MARCS_MOUSE	10	2	0.002627	Myristoylated alanine-rich C-kinase substrate Marcks	1268.830		8457.354	7220.714
KIF5A_MOUSE	20	3	0.002649	Kinesin heavy chain isoform 5A Kif5a	297.605		1522.565	882.696
CTNB1_MOUSE	18	1	0.00266	Catenin beta-1 Ctnnb1	387.938		1.451	3.506

RHEB_MOUSE	3	1	0.002684	GTP-binding protein Rheb Rheb	1518.369	94.616	31.495
GALK1_MOUSE	4	2	0.00276	Galactokinase Galk1	1459.042	3757.014	3461.357
CSN8_MOUSE	5	2	0.002785	COP9 signalosome complex subunit 8 Cops8	876.608	4369.465	3203.933
WDR81_MOUSE	12	1	0.002835	WD repeat-containing protein 81 Wdr81	8.154	129.017	544.835
SDCB1_MOUSE	25	9	0.002842	Syntenin-1 Sdcbp	64518.630	15002.797	24605.549
IF2G_MOUSE	11	3	0.002946	Eukaryotic translation initiation factor 2 subunit 3, X-linked Eif2s3x	1551.316	2242.073	6427.354
DLG1_MOUSE	7	1	0.00295	Disks large homolog 1 Dlg1	845.072	3006.154	931.731

PRS10_MOUSE	13	5	0.003005	26S proteasome regulatory subunit 10B Psmc6	10136.441	14997.545	18013.386
DNJB4_MOUSE	5	2	0.003017	DnaJ homolog subfamily B member 4 Dnajb4	3288.076	2098.672	324.658
GIT1_MOUSE	8	1	0.003094	ARF GTPase-activating protein GIT1 Git1	10354.968	5123.046	5533.631
DIP2A_MOUSE	22	3	0.003216	Disco-interacting protein 2 homolog A Dip2a	6372.230	2314.954	1574.499
TMEM2_MOUSE	8	1	0.003282	Cell surface hyaluronidase Tmem2	1276.826	51.897	384.648
CD166_MOUSE	10	2	0.003309	CD166 antigen Alcam	1657.528	206.306	329.657
ASM3B_MOUSE	4	2	0.00335	Acid sphingomyelinase-like phosphodiesterase 3b Smpdl3b	3040.550	748.616	696.432
GMPPA_MOUSE	5	2	0.003451	Mannose-1-phosphate guanyltransferase alpha Gmppa	25.917	288.669	183.505
ARRD1_MOUSE	4	3	0.003611	Arrestin domain-containing protein 1 Arrdc1	4548.109	331.274	563.753
RBBP7_MOUSE	6	3	0.003692	Histone-binding protein RBBP7 Rbbp7	1036.977	3531.953	3022.984
ABCA7_MOUSE	34	5	0.003707	ATP-binding cassette sub-family A member 7 Abca7	1506.359	2413.985	1127.390

RLA2_MOUSE	5	2	0.003727	60S acidic ribosomal protein P2 Rplp2				6399.138
PDIA1_MOUSE	18	8	0.00378	Protein disulfide-isomerase P4hb				8818.305
CTNA1_MOUSE	39	11	0.003815	Catenin alpha-1 Ctnna1	10694.772 13306.379	3298.840 9029.865		7719.047
IMB1_MOUSE	15	5	0.003862	Importin subunit beta-1 Kpnb1	12842.623 2326.347 26351.650	5922.049 3976.988 33599.257		4840.753
RL5_MOUSE	19	13	0.003986	60S ribosomal protein L5 Rpl5				44214.781
PSA2_MOUSE	8	5	0.004192	Proteasome subunit alpha type-2 Psma2	3057.448	15882.898		24982.475
ENOA_MOUSE	50	12	0.004208	Alpha-enolase Eno1	13809.661 12869.517	11482.547 10167.104		25775.790
1433E_MOUSE	21	12	0.004233	14-3-3 protein epsilon Ywhae	660.528	3757.638		4934.132
KLC1_MOUSE	6	3	0.004242	Kinesin light chain 1 Klc1				1292.216
IPO9_MOUSE	2	1	0.004336	Importin-9 Ipo9	370.711		12.034	1.341
LTBP1_MOUSE	19	1	0.004349	Latent-transforming growth factor beta-binding protein 1 Ltbp1	676.073		63.629	55.851
CO6A1_MOUSE	17	4	0.004485	Collagen alpha-1(VI) chain Col6a1	2993.035		5308.168	10102.426
ADA10_MOUSE	23	3	0.004493	Disintegrin and metalloproteinase domain-containing protein 10 Adam10	14554.416		6539.688	4921.241
S29A1_MOUSE	11	3	0.004563	Equilibrative nucleoside transporter 1 Slc29a1	1083.233		2637.245	3709.790
MINK1_MOUSE	15	1	0.004586	Misshapen-like kinase 1 Mink1	3.005		178.337	137.130

AT2B1_MOUSE	24	3	0.004612	Plasma membrane calcium-transporting ATPase 1 Atp2b1	5469.011		4892.009	7808.018
ITA7_MOUSE	51	20	0.004619	Integrin alpha-7 Itga7	75490.038	29672.029	49655.914	72903.115
RS6_MOUSE	15	7	0.004642	40S ribosomal protein S6 Rps6				29944.926
ODPB_MOUSE	4	2	0.004656	Pyruvate dehydrogenase E1 component subunit beta, mitochondrial Pdhb	1048.340		196.185	800.622
U520_MOUSE	38	6	0.004775	U5 small nuclear ribonucleoprotein 200 kDa helicase Snrnp200	2809.080		1356.851	1267.265
AN13B_MOUSE	9	1	0.004882	Ankyrin repeat domain-containing protein 13B Ankrd13b	24856.286		4942.099	4714.402
SYAC_MOUSE	14	2	0.005229	Alanine--tRNA ligase, cytoplasmic Aars	1668.384		2790.260	4226.003
S12A7_MOUSE	7	1	0.005232	Solute carrier family 12 member 7 Slc12a7	97.755		2.201	2.238
I17RA_MOUSE	10	3	0.005258	Interleukin-17 receptor A Il17ra	2158.733		10853.999	19752.326
PACN2_MOUSE	13	5	0.005263	Protein kinase C and casein kinase substrate in neurons protein 2 Pacsin2	9489.009		5917.282	5279.190
PRP19_MOUSE	7	2	0.005439	Pre-mRNA-processing factor 19 Prpf19	4276.876		11902.552	10514.791
ADPRH_MOUSE	6	1	0.005523	[Protein ADP-ribosylarginine] hydrolase Adprh	1355.913		2084.350	4715.339
NCAM1_MOUSE	20	3	0.005594	Neural cell adhesion molecule 1 Ncam1	5887.503		3309.898	2114.910
TM198_MOUSE	5	1	0.005612	Transmembrane protein 198 Tmem198	2460.518		512.181	59.580
PSMD7_MOUSE	6	3	0.005719	26S proteasome non-ATPase regulatory subunit 7 Psmd7	1408.187		2627.791	2254.727
SYNE2_MOUSE	61	5	0.005759	Nesprin-2 Syne2	1555.726		2303.335	244.992
S10AB_MOUSE	5	2	0.005777	Protein S100-A11 S100a11	915.767	130.197		122.602
NID1_MOUSE	38	11	0.005785	Nidogen-1 Nid1	50638.356	37445.678		22939.575
IMA7_MOUSE	3	1	0.005825	Importin subunit alpha-7 Kpna6	33.646	314.000		41.185
					56779.450	70404.956		

RSSA_MOUSE	13	8	0.00583	40S ribosomal protein SA Rpsa			98278.223
LCAP_MOUSE	16	4	0.005835	Leucyl-cystinyl aminopeptidase Lnpep	2740.958	4766.551	6894.955
PRAF3_MOUSE	6	3	0.005871	PRA1 family protein 3 Arl6ip5	578.443	178.883	1237.050
DHPR_MOUSE	4	1	0.005879	Dihydropteridine reductase Qdpr	927.542	1093.762	1898.950
RAB14_MOUSE	6	1	0.005891	Ras-related protein Rab-14 Rab14	1.571	0.003	199.636
MTUS1_MOUSE	11	1	0.005926	Microtubule-associated tumor suppressor 1 homolog Mtus1	57.839	7.793	0.103

Volume II

THIC_MOUSE	8	3	0.005933	Acetyl-CoA acetyltransferase, cytosolic Acat2	1201.628	2257.412	1839.260
CISY_MOUSE	8	3	0.005987	Citrate synthase, mitochondrial Cs	7577.530	9025.358	14646.291
AP2A2_MOUSE	21	2	0.006057	AP-2 complex subunit alpha-2 Ap2a2	308.509	1027.833	1274.795
EM55_MOUSE	9	2	0.006103	55 kDa erythrocyte membrane protein Mpp1	1834.624	439.550	902.318
CALU_MOUSE	4	1	0.006146	Calumenin Calu	894.309	1531.496	739.412
RRAS2_MOUSE	9	2	0.006186	Ras-related protein R-Ras2 Rras2	2390.752	636.834	179.544
CE290_MOUSE	64	9	0.006198	Centrosomal protein of 290 kDa Cep290	7378.454	17480.044	25224.397
ATPD_MOUSE	1	1	0.006249	ATP synthase subunit delta, mitochondrial Atp5d	228.533	1334.770	2205.221
RL9_MOUSE	10	5	0.006302	60S ribosomal protein L9 Rpl9	6133.030	478.456	254.969
DLG2_MOUSE	16	2	0.006377	Disks large homolog 2 Dlg2	260.223	2508.586	2005.010
LAPM5_MOUSE	4	1	0.006411	Lysosomal-associated transmembrane protein 5 Laptm5	907.122	2010.520	1272.187
COX41_MOUSE	5	2	0.006741	Cytochrome c oxidase subunit 4 isoform 1, mitochondrial Cox4i1	274.715	407.233	6018.842
ACTN2_MOUSE	12	2	0.006811	Alpha-actinin-2 Actn2	4981.315	1261.466	1470.668
ATPB_MOUSE	27	12	0.006845	ATP synthase subunit beta, mitochondrial Atp5b	26433.522	15051.600	25929.719
AGRL3_MOUSE	15	2	0.006992	Adhesion G protein-coupled receptor L3 Adgrl3	131.415	2.374	1.575
TECR_MOUSE	8	1					0.129

SYSC_MOUSE	20	8				0.074	10144.969
			0.007089	Very-long-chain enoyl-CoA reductase Tecr	18.998	10749.581	
			0.007108	Serine--tRNA ligase, cytoplasmic Sars	3433.537		
CSPG2_MOUSE	31	6	0.00712	Versican core protein Vcan	6378.463	12594.410	11499.717
AK1A1_MOUSE	2	1				161.655	317.867
			0.007217	Alcohol dehydrogenase [NADP(+)] Akr1a1	698.135		
INS1_MOUSE	2	1				4918.153	5510.467
			0.007237	Insulin-1 Ins1	2200.901		
HS71A_MOUSE	21	1	0.007318	Heat shock 70 kDa protein 1A Hspa1a	140.353	179.929	1625.769
TNIK_MOUSE	20	1	0.007449	Traf2 and NCK-interacting protein kinase Tnik	2423.349	44.055	1065.728
SAHH3_MOUSE	11	3	0.007526	Putative adenosylhomocysteinase 3 Ahcyl2	1889.247	581.941	230.657
S12A6_MOUSE	8	2	0.007555	Solute carrier family 12 member 6 Slc12a6	246.012	98.448	279.881
GNA11_MOUSE	10	2	0.007556	Guanine nucleotide-binding protein subunit alpha-11 Gna11	4903.823	1305.913	1069.912
GNAI3_MOUSE	5	2	0.007881	Guanine nucleotide-binding protein G(k) subunit alpha Gnai3	583.543	38.488	34.929

PGAM1_MOUSE	9	5	0.007918	Phosphoglycerate mutase 1 Pgam1	11300.488	4515.158	12526.829
PYR1_MOUSE	42	6	0.007986	CAD protein Cad	2528.512	6350.678	6748.309
PLAK_MOUSE	22	5				1513.255	2251.527
			0.008196	Junction plakoglobin Jup	4282.882		
EF1D_MOUSE	15	4	0.00841	Elongation factor 1-delta Eef1d	3329.589	6042.898	10198.876
IDHP_MOUSE	10	5	0.008412	Isocitrate dehydrogenase [NADP], mitochondrial Idh2	1665.183	4089.429	4109.404
LIPA2_MOUSE	29	4	0.008437	Liprin-alpha-2 Ppfia2	4862.373	9928.690	11517.754
CATD_MOUSE	5	2	0.008501	Cathepsin D Ctsd	2035.329	1273.875	1187.333
RACK1_MOUSE	15	3		Receptor of activated protein C kinase 1		8367.275	36210.504

			0.008545	Rack1	9036.861		
PSMD6_MOUSE	14	3	0.008702	26S proteasome non-ATPase regulatory subunit 6 Psmd6	1864.947	5186.102	5191.451
PLCD3_MOUSE	8	1	0.008827	1-phosphatidylinositol 4,5-bisphosphate phosphodiesterase delta-3 Plcd3	998.504	64.393	55.110
KCNA5_MOUSE	3	1	0.008838	Potassium voltage-gated channel subfamily A member 5 Kcna5	2345.050	22.121	7.331
DNPEP_MOUSE	12	1	0.008942	Aspartyl aminopeptidase Dnpep	338.230	635.776	54.866
CLAP1_MOUSE	11	2	0.009004	CLIP-associating protein 1 Clasp1	39932.482	70821.571	105043.040
CEP55_MOUSE	6	1	0.009009	Centrosomal protein of 55 kDa Cep55	337.487	15.923	57.467
CAN6_MOUSE	4	1	0.009014	Calpain-6 Capn6	382.338	857.158	1265.846
NUCB1_MOUSE	6	3	0.009041	Nucleobindin-1 Nucb1	734.076	296.969	310.146
EXT1_MOUSE	5	1	0.009061	Exostosin-1 Ext1	144.364	513.970	544.549
PFKAM_MOUSE	13	3	0.009149	ATP-dependent 6-phosphofructokinase, muscle type Pfkm	736.981	1670.088	5539.421
TFR1_MOUSE	21	5	0.009268	Transferrin receptor protein 1 Tfrc	5060.482	5328.257	9971.698
1433G_MOUSE	11	3	0.009339	14-3-3 protein gamma Ywhag	16294.904	6227.105	6067.843
EMIL1_MOUSE	11	1	0.009489	EMILIN-1 Emilin1	15259.350	364.047	121.685
PPIC_MOUSE	7	5	0.009509	Peptidyl-prolyl cis-trans isomerase C Ppic	6004.412	64.184	10256.941
CSTF3_MOUSE	11	1	0.009515	Cleavage stimulation factor 64 subunit 3 Cstf3	11803.875	79.268	19.431
FBLN2_MOUSE	20	5	0.009527	Fibulin-2 Fbln2	17610.393	858.725	9250.897
DDX3L_MOUSE	15	2		Putative ATP-dependent RNA helicase Pl10			489.366

			0.009617	D1Pas1	2531.557		
GNAO_MOUSE	16	4	0.009713	Guanine nucleotide-binding protein G(o) subunit alpha Gnao1	3639.996	8961.482	7871.363

MOT11_MOUSE	2	1	0.009815	Monocarboxylate transporter 11 Slc16a11	121.327	5.149	3.584
DHE3_MOUSE	7	5	0.00986	Glutamate dehydrogenase 1, mitochondrial Glud1	9115.425	3406.368	4724.193
EHD2_MOUSE	40	17	0.009982	EH domain-containing protein 2 Ehd2	28172.288	15724.936	12704.536
ACTG_MOUSE	50	3	0.010119	Actin, cytoplasmic 2 Actg1	26073.414 84808.030		47735.029
LOXL2_MOUSE	10	3	0.010564	Lysyl oxidase homolog 2 Loxl2	364.483	4448.611	1158.817
ACON_MOUSE	14	2	0.010606	Aconitate hydratase, mitochondrial Aco2	3616.065	3624.948	6310.189
PHB_MOUSE	7	4	0.011083	Prohibitin Phb	2375.727	612.489	1523.301
HS105_MOUSE	10	2	0.011259	Heat shock protein 105 kDa Hsph1	699.930	189.719	436.219
MYH6_MOUSE	18	1	0.011336	Myosin-6 Myh6	2552.830	7789.063	5960.218
RS19_MOUSE	11	5	0.011454	40S ribosomal protein S19 Rps19	5131.545	509.319	1134.769
NEDD4_MOUSE	13	3	0.011595	E3 ubiquitin-protein ligase NEDD4 Nedd4	4702.940	17424.346	19037.324
SYNC_MOUSE	11	2	0.011661	Asparagine--tRNA ligase, cytoplasmic Nars	3743.987	2403.001	4904.915
DAAM1_MOUSE	14	2	0.01175	Disheveled-associated activator of morphogenesis 1 Daam1	346.061	250.765	64.267
TTYH3_MOUSE	6	1	0.011798	Protein tweety homolog 3 Ttyh3	1650.006	785.717	400.892
NMT2_MOUSE	10	1	0.011969	Glycylpeptide N-tetradecanoyltransferase 2 Nmt2	57.609	230.873	527.536

FREM3_MOUSE	8	1	0.012043	FRAS1-related extracellular matrix protein 3 Frem3	15.337	0.634	244.360
RADI_MOUSE	24	3	0.012189	Radixin Rdx	676.510	961.000	2072.585
YBOX3_MOUSE	6	1	0.012268	Y-box-binding protein 3 Ybx3	174.705	678.614	962.492
RL28_MOUSE	6	1	0.012297	60S ribosomal protein L28 Rpl28	219.422	1777.774	1901.742
SRCRL_MOUSE	12	3	0.012557	Soluble scavenger receptor cysteine-rich domain-containing protein SSC5D Ssc5d	988.437	247.058	73.128
H3C_MOUSE	8	1	0.012673	Histone H3.3C H3f3c	9.530	1992.787	1047.021
UBA1_MOUSE	33	15	0.012794	Ubiquitin-like modifier-activating enzyme 1 Uba1	13986.522	21139.558	31038.510
DTNB_MOUSE	11	1	0.012816	Dystrobrevin beta Dtnb	461.463	2509.143	1400.379
RPN1_MOUSE	3	1	0.012989	Dolichyl-diphosphooligosaccharide--protein glycosyltransferase subunit 1 Rpn1	310.657	64.204	53.705
PSD12_MOUSE	22	4	0.013121	26S proteasome non-ATPase regulatory subunit 12 Psmd12	1705.772	514.557	1274.738
PCBP2_MOUSE	4	1	0.013265	Poly(rC)-binding protein 2 Pcbp2	317.211	0.000	12.790

PI4KA_MOUSE	23	5	0.013291	Phosphatidylinositol 4-kinase alpha Pi4ka	6019.898	8474.628	5704.402
RS7_MOUSE	11	6	0.013359	40S ribosomal protein S7 Rps7	6092.293	1492.819	4833.940
ARMX6_MOUSE	2	1	0.013518	Protein ARMCX6 Armcx6	0.274	190.289	119.408
TRXR1_MOUSE	4	1	0.013717	Thioredoxin reductase 1, cytoplasmic Txnrd1	146.962	3.852	17.042
MYO9A_MOUSE	36	7	0.013929	Unconventional myosin-IXa Myo9a	36659.739	15244.758	24100.565
RS15_MOUSE	9	6	0.013999	40S ribosomal protein S15 Rps15	10897.873	2534.098	1341.713
MB12B_MOUSE	6	2	0.014044	Multivesicular body subunit 12B Mvb12b	1532.054	434.096	145.275

YES_MOUSE	7	2	0.014104	Tyrosine-protein kinase Yes Yes1	195.428	8.195	20.840
PR2C3_MOUSE	3	2	0.014137	Prolactin-2C3 Prl2c3	458.707	60.341	9.953
SPIR2_MOUSE	14	1	0.014273	Protein spire homolog 2 Spire2	177.425	1037.542	398.213
ABRX2_MOUSE	2	2	0.014292	BRISC complex subunit Abraxas 2 Abraxas2	491.748	170.512	200.323
PGK1_MOUSE	42	12	0.014912	Phosphoglycerate kinase 1 Pgk1	27020.761	9796.105	19331.423
KCRB_MOUSE	2	2	0.015013	Creatine kinase B-type Ckb	930.133	124.961	158.393
PSMD2_MOUSE	25	8	0.015113	26S proteasome non-ATPase regulatory subunit 2 Psmd2	1511.793	2529.040	3781.030
DAAM2_MOUSE	14	1	0.015113	Disheveled-associated activator of morphogenesis 2 Daam2	694.431	99.260	0.000
TCPD_MOUSE	30	9	0.015127	T-complex protein 1 subunit delta Cct4	22331.731	16436.302	14807.753
PUR6_MOUSE	10	2	0.015185	Multifunctional protein ADE2 Paics	2781.003	976.368	970.345
RAB21_MOUSE	8	1	0.015249	Ras-related protein Rab-21 Rab21	431.544	101.279	429.709
ASNA_MOUSE	4	1	0.015513	ATPase Asna1 Asna1	73.385	128.295	11.551
PP2AA_MOUSE	2	1	0.015655	Serine/threonine-protein phosphatase 2A catalytic subunit alpha isoform Ppp2ca	713.812	2623.412	7278.953
CO3A1_MOUSE	47	9	0.015813	Collagen alpha-1(III) chain Col3a1	3308.810	7097.465	2357.810
1433Z_MOUSE	22	6	0.015896	14-3-3 protein zeta/delta Ywhaz	26730.178	6062.695	7632.689
PURB_MOUSE	6	4	0.016346	Transcriptional activator protein Pur-beta Purb	1848.418	4092.388	3399.798
SERPH_MOUSE	25	6	0.016579	Serpin H1 Serpinh1	7266.957	12004.795	9044.273
HCD2_MOUSE	3	2	0.016639	3-hydroxyacyl-CoA dehydrogenase type-2	902.065	702.185	316.138

				Hsd17b10			
DCTN1_MOUSE	28	3	0.016726	Dynactin subunit 1 Dctn1	797.985	838.211	1058.480

FARP1_MOUSE	19	8	0.016772	FERM, RhoGEF and pleckstrin domain-containing protein 1 Farp1	5236.591	2496.028	2796.857
APT_MOUSE	8	2	0.016879	Adenine phosphoribosyltransferase Aprt	1703.624	55.805	362.696
NB5R3_MOUSE	7	2	0.016911	NADH-cytochrome b5 reductase 3 Cyb5r3	4227.510	1295.760	2943.728
NSD1_MOUSE	45	5	0.01702	Histone-lysine N-methyltransferase, H3 lysine-36 and H4 lysine-20 specific Nsd1	2806.626	2161.055	753.063
DEN2A_MOUSE	14	1	0.017199	DENN domain-containing protein 2A Dennd2a	19.510	252.284	424.814
RN123_MOUSE	8	2	0.017338	E3 ubiquitin-protein ligase RNF123 Rnf123	202.466	967.724	2350.287
DC1I2_MOUSE	5	1	0.017458	Cytoplasmic dynein 1 intermediate chain 2 Dync1i2	91.728	69.609	337.530
FBX31_MOUSE	8	1	0.017468	F-box only protein 31 Fbxo31	29.159	74.747	130.990
IMA1_MOUSE	2	1	0.017786	Importin subunit alpha-1 Kpna2	1028.577	16.150	25.052
RLA0_MOUSE	20	6	0.01778	60S acidic ribosomal protein P0 Rplp0	10019.178	8678.086	21713.988
TBB2A_MOUSE	48	1	0.017837	Tubulin beta-2A chain Tubb2a	2571.957	4756.946	3352.836
LPPRC_MOUSE	11	5	0.018176	Leucine-rich PPR motif-containing protein, mitochondrial Lrpprc	1589.868	8393.140	7113.390
E41L3_MOUSE	18	4	0.018346	Band 4.1-like protein 3 Epb41l3	1027.513	208.350	105.408
ARPC3_MOUSE	6	3	0.018371	Actin-related protein 2/3 complex subunit 3 Arpc3	1211.312	9711.823	6535.773
ZFP92_MOUSE	11	3	0.018647	Zinc finger protein 92 Zfp92	9237.535	4895.538	5244.602
MOES_MOUSE	57	16	0.019017	Moesin Msn	35104.351	46918.719	31356.486

NCDN_MOUSE	7	3	0.019439	Neurochondrin Ncdn	18722.989	55171.580	53929.269
AACS_MOUSE	9	3	0.019531	Acetoacetyl-CoA synthetase Aacs	968.972	2725.294	2039.091
DHX9_MOUSE	13	4	0.019834	ATP-dependent RNA helicase A Dhx9	2464.568	3949.627	4301.340
MFGM_MOUSE	17	11	0.019851	Lactadherin Mfge8	107821.205	82215.953	64679.317
TPX2_MOUSE	20	6	0.019985	Targeting protein for Xklp2 Tpx2	8312.675	4140.052	2065.595
RL35_MOUSE	5	3	0.020157	60S ribosomal protein L35 Rpl35	4176.144	171.282	246.408
RL8_MOUSE	9	2	0.020413	60S ribosomal protein L8 Rpl8	542.602	60.709	160.264
RS9_MOUSE	13	3	0.020814	40S ribosomal protein S9 Rps9	1566.195	8062.725	8678.684
ALDR_MOUSE	12	6	0.02093	Aldose reductase Akr1b1	5334.274	10091.195	21346.373
LAMA2_MOUSE	28	2	0.021106	Laminin subunit alpha-2 Lama2	885.206	2092.107	2782.536
UGPA_MOUSE	10	3	0.02122	UTP--glucose-1-phosphate uridylyltransferase Ugp2	1402.902	2221.414	1178.486

IMA3_MOUSE	3	1	0.021729	Importin subunit alpha-3 Kpna4	80.969	23.880	3.268
ACTN4_MOUSE	30	6	0.021835	Alpha-actinin-4 Actn4	4708.014	1122.416	758.409
RTL9_MOUSE	14	2	0.021909	Retrotransposon Gag-like protein 9 Rtl9	1103.833	2487.828	2588.840
COPT1_MOUSE	4	2	0.022011	High affinity copper uptake protein 1 Slc31a1	804.175	303.562	298.084
TPP2_MOUSE	28	11	0.022104	Tripeptidyl-peptidase 2 Tpp2	14407.398	17843.286	22193.710
RAB1A_MOUSE	8	1			1037.126	319.626	166.422

			0.022186	Ras-related protein Rab-1A Rab1A			
PPCE_MOUSE	9	2	0.022265	Prolyl endopeptidase Prep	2321.808	2059.795	3065.973
ENPL_MOUSE	30	9	0.022317	Endoplasmin Hsp90b1	9402.255	5194.183	4918.889
H13_MOUSE	15	1	0.022684	Histone H1.3 Hist1h1d	117.851	0.000	29.654
ALDH2_MOUSE	12	7	0.022705	Aldehyde dehydrogenase, mitochondrial Aldh2	6002.218	3836.691	3536.270
HEXA_MOUSE	4	1	0.023066	Beta-hexosaminidase subunit alpha Hexa	382.931	1550.707	1377.903
G3P_MOUSE	37	20	0.023135	Glyceraldehyde-3-phosphate dehydrogenase Gapdh	67687.747	69725.749	129549.729
DDAH2_MOUSE	13	5	0.02359	N(G),N(G)-dimethylarginine dimethylaminohydrolase 2 Ddah2	15322.222	13281.445	10514.011
COPE_MOUSE	3	1	0.023664	Coatomer subunit epsilon Cope	172.928	0.000	0.000
KPYR_MOUSE	41	5	0.023901	Pyruvate kinase PKLR Pklr	1098.938	3358.283	4886.938
DNMT1_MOUSE	17	2	0.024051	DNA (cytosine-5)-methyltransferase 1 Dnmt1	4721.889	9393.475	7107.157
NCOA2_MOUSE	11	2	0.0246	Nuclear receptor coactivator 2 Ncoa2	1575.025	7601.061	3946.891
TNNC2_MOUSE	2	1	0.024748	Troponin C, skeletal muscle Tnnc2	150.952	4.689	0.000
EIF3I_MOUSE	5	3	0.024915	Eukaryotic translation initiation factor 3 subunit I Eif3i	2403.529	3760.193	8377.424
GDF15_MOUSE	7	4	0.024933	Growth/differentiation factor 15 Gdf15	2210.745	1646.534	1444.910
IMPA1_MOUSE	2	2	0.025102	Inositol monophosphatase 1 Impa1			189.530
PPM1F_MOUSE	4	2	0.025141	Protein phosphatase 1F Ppm1f	582.147	467.691	10574.766
GRP78_MOUSE	28	13	0.025252	78 kDa glucose-regulated protein Hspa5	3166.711 33341.254	13250.440	51051.359 34763.393
M4K4_MOUSE	13	2	0.025268	Mitogen-activated protein kinase kinase kinase 4 Map4k4	785.168	100.669	272.203
VDAC1_MOUSE	10	5	0.025413	Voltage-dependent anion-selective channel protein 1 Vdac1	9821.837	1452.295	4630.152

CD97_MOUSE	14	5			19813.061	13097.786		15128.542
JAM2_MOUSE	3	1	0.025503	CD97 antigen Cd97	1085.636	198.274		434.310
			0.026349	Junctional adhesion molecule B Jam2				

PLXA1_MOUSE	18	1	0.026759	Plexin-A1 Plxna1	632.909		53.115	543.887
PSDE_MOUSE	11	5	0.026935	26S proteasome non-ATPase regulatory subunit 14 Psmd14	5510.654		2145.237	3792.458
HNRH1_MOUSE	7	1	0.027496	Heterogeneous nuclear ribonucleoprotein H Hnrnph1	274.417		166.684	36.638
IFM3_MOUSE	5	3	0.028276	Interferon-induced transmembrane protein 3 Ifitm3	2580.908		3206.684	1724.032
HNRH2_MOUSE	11	2	0.02834	Heterogeneous nuclear ribonucleoprotein H2 Hnrnph2	378.340		973.190	775.254
MYO15_MOUSE	25	6	0.028436	Unconventional myosin-XV Myo15a	692.334		3494.270	2752.727
STRAP_MOUSE	6	1	0.028868	Serine-threonine kinase receptor-associated protein Strap	309.434		1190.666	1042.325
HS90B_MOUSE	61	15	0.029165	Heat shock protein HSP 90-beta Hsp90ab1	50869.879		74186.895	89251.511
KAP1_MOUSE	6	2	0.029496	cAMP-dependent protein kinase type I-beta regulatory subunit Prkar1b	11884.218		8654.268	7164.025
METK2_MOUSE	4	2	0.029694	S-adenosylmethionine synthase isoform type-2 Mat2a	2921.825		1310.248	1834.171
RL3_MOUSE	28	7	0.029705	60S ribosomal protein L3 Rpl3	8701.434		2109.070	3886.471
ANKH_MOUSE	8	3	0.029733	Progressive ankylosis protein Ankh	368.615		48.382	16.380
CYBP_MOUSE	4	2	0.029783	Calcyclin-binding protein Cacybp	518.339		890.902	175.976
CTNA2_MOUSE	22	2	0.029819	Catenin alpha-2 Ctnna2	1287.979 18716.533	177.792 22687.706		150.576
LAMC1_MOUSE	24	9	0.030006	Laminin subunit gamma-1 Lamc1				16447.662
RL4_MOUSE	23	10	0.030131	60S ribosomal protein L4 Rpl4				21728.791

RAN_MOUSE	7	1	0.030737	GTP-binding nuclear protein Ran Ran	51586.209 3720.555	28173.945 6502.601		8889.748
L2GL2_MOUSE	2	1	0.030748	Lethal(2) giant larvae protein homolog 2 Llgl2	690.749		3567.576	2404.502
RASK_MOUSE	5	1	0.031013	GTPase KRas Kras	280.357		807.274	274.047
EIF3E_MOUSE	12	4	0.031281	Eukaryotic translation initiation factor 3 subunit E Eif3e	1897.903		3114.857	4532.250
ITAL_MOUSE	8	2	0.031458	Integrin alpha-L Itgal	25381.247 40366.642	9713.405 20823.131		21923.385 25527.106
CLIC1_MOUSE	9	3	0.031481	Chloride intracellular channel protein 1 Clic1				
PEF1_MOUSE	4	2	0.031527	Peflin Pef1	979.047		398.785	1036.477
SNAA_MOUSE	4	2	0.03167	Alpha-soluble NSF attachment protein Napa	2418.728 34820.625	12299.984	1584.323	3625.062
RL7A_MOUSE	24	9	0.03178	60S ribosomal protein L7a Rpl7a				20569.143

KCNH5_MOUSE	13	3	0.031952	Potassium voltage-gated channel subfamily H member 5 Kcnh5	10004.940	1804.461	1678.673
SERA_MOUSE	13	3	0.032097	D-3-phosphoglycerate dehydrogenase Phgdh	2662.548	1290.105	1746.280
MDHM_MOUSE	16	3	0.032306	Malate dehydrogenase, mitochondrial Mdh2			4689.254
TTC17_MOUSE	11	3	0.032315	Tetratricopeptide repeat protein 17 Ttc17	6078.820 6465.186		12096.664
4F2_MOUSE	22	12	0.032405	4F2 cell-surface antigen heavy chain Slc3a2	35968.910	28729.000	35056.271
WDR1_MOUSE	8	2	0.032615	WD repeat-containing protein 1 Wdr1	3424.572	5820.063	8954.123
SKI_MOUSE	16	2	0.033172	Ski oncogene Ski	4336.294	521.449	1312.269
MCM2_MOUSE	6	3	0.033207	DNA replication licensing factor MCM2 Mcm2	4261.876	6885.406	6834.049
COIA1_MOUSE	16	3	0.033498	Collagen alpha-1(XVIII) chain Col18a1	7564.411	10942.806	8410.596

ARI1A_MOUSE	23	2	0.033522	AT-rich interactive domain-containing protein 1A Arid1a	4636.408	6552.269	2954.699
CALR_MOUSE	6	2	0.033572	Calreticulin Calr	4657.734	1953.799	1717.357
GRP75_MOUSE	26	7	0.033714	Stress-70 protein, mitochondrial Hspa9	11873.711	6755.072	7870.103
HYOU1_MOUSE	21	4	0.033864	Hypoxia up-regulated protein 1 Hyou1	89.260	265.408	955.449
OX2G_MOUSE	5	1	0.033931	OX-2 membrane glycoprotein Cd200	151.298	1092.560	70.084
IPO7_MOUSE	6	1	0.033943	Importin-7 Ipo7	0.000	2.986	64.316
DESM_MOUSE	24	10	0.034445	Desmin Des	11538.298	7442.790	9186.471
ZFP14_MOUSE	11	1	0.034498	Zinc finger protein 14 Zfp14	200.101	26.475	33.536
RALA_MOUSE	8	2	0.03473	Ras-related protein Ral-A Rala	3157.928	1630.202	1587.948
PREY_MOUSE	3	1	0.035055	Protein preY, mitochondrial Pyurf	0.000	0.054	216.341
EHD3_MOUSE	23	1	0.035149	EH domain-containing protein 3 Ehd3	289.011	7.552	17.075
CRYAB_MOUSE	8	5	0.035167	Alpha-crystallin B chain Cryab	5669.635	2071.707	14821.762
UBR2_MOUSE	8	2	0.035503	E3 ubiquitin-protein ligase UBR2 Ubr2	4330.000	21607.666	10671.289
WASF2_MOUSE	9	2	0.035858	Wiskott-Aldrich syndrome protein family member 2 Wasf2	1716.562	446.719	571.269
HNRPD_MOUSE	4	1	0.035884	Heterogeneous nuclear ribonucleoprotein D0 Hnrnpd	739.522	586.123	232.368
PEDF_MOUSE	8	2	0.036215	Pigment epithelium-derived factor	5005.209	3535.213	
FINC_MOUSE	113	28	Serpinf1	3415.250		104584.382	

			0.036736	Fibronectin Fn1	118264.656	198851.326	
AQP1_MOUSE	2	2	0.03686	Aquaporin-1 Aqp1	5669.535	6547.383	8116.829
M3K21_MOUSE	8	2	0.03704	Mitogen-activated protein kinase kinase kinase 21 Map3k21	3075.773	1064.219	1217.385
DDX21_MOUSE	16	4	0.037864	Nucleolar RNA helicase 2 Ddx21	2304.315	2787.738	3645.368
DEST_MOUSE	8	1	0.03883	Destrin Dstn	31.399	1321.915	728.913
RS2_MOUSE	19	9	0.03888	40S ribosomal protein S2 Rps2	7965.882	11229.729	22785.163
ZYX_MOUSE	4	3	0.038987	Zyxin Zyx	2220.216	1440.347	624.609
CELR3_MOUSE	66	6	0.03904	Cadherin EGF LAG seven-pass G-type receptor 3 Celsr3	4892.218	10371.044	6311.698
DDB1_MOUSE	11	1	0.03911	DNA damage-binding protein 1 Ddb1	408.865	3319.929	762.164
SYC1L_MOUSE	4	1	0.039154	Synaptonemal complex central element protein 1-like Syce1l	1110.188	6941.845	5253.878
AT2B4_MOUSE	15	1	0.039445	Plasma membrane calcium-transporting ATPase 4 Atp2b4	311.143	86.091	103.708
KAT6B_MOUSE	21	2	0.039505	Histone acetyltransferase KAT6B Kat6b	427.297	1365.583	890.148
DPP9_MOUSE	8	2	0.03961	Dipeptidyl peptidase 9 Dpp9	248.776	19.468	20.187
CYHR1_MOUSE	6	1	0.040122	Cysteine and histidine-rich protein 1 Cyhr1	770.431	76.975	221.205
CLIC4_MOUSE	5	2	0.041038	Chloride intracellular channel protein 4 Clic4	4259.482	3064.247	8621.884
EDIL3_MOUSE	7	3	0.041137	EGF-like repeat and discoidin I-like domain-containing protein 3 Edil3	3399.108	1549.528	2439.212
DOCK7_MOUSE	27	6	0.041293	Dedicator of cytokinesis protein 7 Dock7	9099.048	8643.122	14075.089
CHMP5_MOUSE	6	3	0.041372	Charged multivesicular body protein 5 Chmp5	2099.686	353.593	697.409
SNF8_MOUSE	2	1	0.041702	Vacuolar-sorting protein SNF8 Snf8	1152.192	576.018	495.832

ARHGH_MOUSE	36	5	0.041882	Rho guanine nucleotide exchange factor 17 Arhgef17	3077.940	9614.046	9384.770
IF6_MOUSE	4	1	76			154.085	136.114
MYO9B_MOUSE	36	2	0.042222	Eukaryotic translation initiation factor 6 Eif6	19.448	11746.573	5739.890
			0.0423	Unconventional myosin-IXb Myo9b	5469.946		
ACSL4_MOUSE	9	4	0.042615	Long-chain-fatty-acid--CoA ligase 4 Acsl4	2125.628	460.568	650.860
GIPC1_MOUSE	6	2	0.042936	PDZ domain-containing protein GIPC1 Gipc1	358.540	56.216	8.756
TBB6_MOUSE	44	4				6773.106	12034.232
SYLC_MOUSE	34	6	0.042937	Tubulin beta-6 chain Tubb6	6437.622	10376.210	10626.282
			0.043223	Leucine--tRNA ligase, cytoplasmic Lars	4492.486		
FKB10_MOUSE	7	1	0.043693	Peptidyl-prolyl cis-trans isomerase FKBP10 Fkbp10	4.248	280.039	114.492

CSKP_MOUSE	15	1	0.043705	Peripheral plasma membrane protein CASK Cask	796.998	245.628	434.830
TMC5_MOUSE	15	1	0.04474	Transmembrane channel-like protein 5 Tmc5	845.716	2061.476	126.414
DX39A_MOUSE	9	1	0.045215	ATP-dependent RNA helicase DDX39A Ddx39a	564.382	23.247	170.632
IGSF3_MOUSE	14	1	0.045531	Immunoglobulin superfamily member 3 Igsf3	297.490	91.196	152.943
LAMP1_MOUSE	4	2	0.045752	Lysosome-associated membrane glycoprotein 1 Lamp1	861.842	970.093	293.252
LIPB1_MOUSE	8	3					2035.546

NPTN_MOUSE	13	3	0.046425	Liprin-beta-1 Ppfibp1	11155.913	863.732	16410.794
			0.046654	Neuroplastin Nptn	12024.866	21658.340	
LY75_MOUSE	10	1	0.047276	Lymphocyte antigen 75 Ly75	140.623	61.430	37.745
KLH41_MOUSE	10	3	0.048028	Kelch-like protein 41 Klhl41	150.906	614.563	499.694
CTNA3_MOUSE	9	1	0.048229	Catenin alpha-3 Ctnna3	316.532	165.248	283.741
S4A7_MOUSE	11	2	0.048675	Sodium bicarbonate cotransporter 3 Slc4a7	261.398	111.888	47.366
SYTC_MOUSE	12	2	0.048679	Threonine--tRNA ligase, cytoplasmic Tars	1453.122	3200.926	3205.967
RPGF2_MOUSE	17	5	0.049021	Rap guanine nucleotide exchange factor 2 Rapgef2	3378.413	7364.307	4761.141
PRS7_MOUSE	24	7	0.049185	26S proteasome regulatory subunit 7 Psmc2	5335.250	7353.804	7810.194
C1QBP_MOUSE	5	1	0.049504	Complement component 1 Q subcomponent-binding protein, mitochondrial C1qbp	62.540	1126.569	876.673
STXB3_MOUSE	10	4	0.050221	Syntaxin-binding protein 3 Stxbp3	45166.366	11455.035	19188.286
TIF1B_MOUSE	9	1	0.050507	Transcription intermediary factor 1-beta Trim28	163.293	311.288	551.735
KAP3_MOUSE	6	3	0.050738	cAMP-dependent protein kinase type II-beta regulatory subunit Prkar2b	201.242	682.590	40.400
GSTM1_MOUSE	4	1	0.051107	Glutathione S-transferase Mu 1 Gstm1	1327.410	272.274	226.448
CHMP6_MOUSE	6	2	0.051509	Charged multivesicular body protein 6 Chmp6	1843.216	736.763	833.187
BIN1_MOUSE	10	4	0.051735	Myc box-dependent-interacting protein 1 Bin1	1661.817	1830.209	3288.021

GSTP1_MOUSE	11	4	0.05194			13882.159	11761.430
G6PI_MOUSE	22	7	0.052168	Glutathione S-transferase P 1 Gstp1 Glucose-6-phosphate isomerase Gpi	1479.461 5828.120	1459.463	1428.051

TTL12_MOUSE	5	2	0.052742	Tubulin--tyrosine ligase-like protein 12 Ttll12	360.273	1282.346	1930.376
WDR64_MOUSE	11	3	0.052829	WD repeat-containing protein 64 Wdr64	974.739	1095.716	3570.958
H14_MOUSE	8	1	0.0531	Histone H1.4 Hist1h1e	3768.936	1471.313	2005.989
EDC4_MOUSE	10	2	0.053606	Enhancer of mRNA-decapping protein 4 Edc4	412.635	103.713	528.334
MYL6_MOUSE	5	2	0.053882	Myosin light polypeptide 6 Myl6	1421.002	214.265	271.796
ARI3A_MOUSE	7	2	0.054228	AT-rich interactive domain-containing protein 3A Arid3a	370.184	110.526	171.265
PYGB_MOUSE	11	1	0.054461	Glycogen phosphorylase, brain form Pygb	1074.521	129.479	178.230
LAMP2_MOUSE	6	1	0.054513	Lysosome-associated membrane glycoprotein 2 Lamp2	4532.284	6988.657	6420.684
RL19_MOUSE	6	2			11018.602	4511.254	2476.798
SEPT9_MOUSE	12	4	0.055968 0.056244	60S ribosomal protein L19 Rpl19 Septin-9 Sept9	2679.633	1551.071	978.384
ADAM9_MOUSE	7	2	0.056394	Disintegrin and metalloproteinase domain-containing protein 9 Adam9	37.368	168.702	137.734
PARK7_MOUSE	5	2	0.056672	Protein/nucleic acid deglycase DJ-1 Park7	1319.939	746.545	192.617
CAD15_MOUSE	6	2	0.056997	Cadherin-15 Cdh15	667.128	48.311	81.828
LRC59_MOUSE	6	4	0.057677	Leucine-rich repeat-containing protein 59 Lrrc59	3661.748	287.081	509.475
CAZA2_MOUSE	6	2	0.057715	F-actin-capping protein subunit alpha-2 Capza2	799.181	560.374	2079.326
TBB3_MOUSE	41	1	0.058177	Tubulin beta-3 chain Tubb3	2482.341	2910.504	4347.361

RL30_MOUSE	4	1	0.058747	60S ribosomal protein L30 Rpl30	1780.548		175.782	47.573
RASL3_MOUSE	16	3	0.05897	RAS protein activator like-3 Rasal3	1284.920		5048.133	3743.600
PSA3_MOUSE	12	4	0.059148	Proteasome subunit alpha type-3 Psma3	1908.817		2561.493	4442.284
MRGB3_MOUSE	3	1	0.059457	Mas-related G-protein coupled receptor member B3 Mrgprb3	11.893		2.761	124.257
MYOF_MOUSE	62	18	0.059612	Myoferlin Myof	21552.249	37734.572		34929.551
RAB31_MOUSE	2	1	0.059874	Ras-related protein Rab-31 Rab31	103.069	0.323		1.256
TKT_MOUSE	7	1	0.059894	Transketolase Tkt	321.433		24.732	29.087
MRP7_MOUSE	14	1	0.059938	Multidrug resistance-associated protein 7 Abcc10	55.627		94.129	14.402
RS13_MOUSE	10	3	0.060048	40S ribosomal protein S13 Rps13	6709.812		750.216	540.687
ENOB_MOUSE	30	8	0.060121	Beta-enolase Eno3	11787.101		7229.592	6981.343

ABCA4_MOUSE	32	3	0.06111	Retinal-specific ATP-binding cassette transporter Abca4	422.103	287.355	1130.239
ATPG_MOUSE	4	2	0.061363	ATP synthase subunit gamma, mitochondrial Atp5c1	2025.639	936.798	2220.591
GPC5B_MOUSE	2	1	0.061373	G-protein coupled receptor family C group 5 member B Gprc5b	436.051	95.109	31.519
MET16_MOUSE	3	1	0.061552	U6 small nuclear RNA (adenine-(43)-N(6))-methyltransferase Mettl16	218.186	112.858	63.684
RCN1_MOUSE	2	1	0.06233	Reticulocalbin-1 Rcn1	146.967	39.861	3.000
MTF2_MOUSE	18	1	0.06235	Metal-response element-binding transcription factor 2 Mtf2	232.766	17.881	16.759
PLXB2_MOUSE	52	10				1632.070	36168.804

GSTO1_MOUSE	4	3	0.062403	Plexin-B2 Plxnb2	17473.631	27014.674	1631.271
			0.062408	Glutathione S-transferase omega-1 Gsto1	3745.518		
DICER_MOUSE	12	1	0.062692	Endoribonuclease Dicer Dicer1	393.441	164.438	95.477
CKAP4_MOUSE	13	3	0.062954	Cytoskeleton-associated protein 4 Ckap4	2060.314	876.576	1703.435
PRDX4_MOUSE	5	1	0.063715	Peroxiredoxin-4 Prdx4	64.167	147.975	40.203
DYST_MOUSE	58	8	064141	0.	Dystonin Dst	13620.093	13034.368
			4472.164				
VDAC3_MOUSE	4	1	0.064464	Voltage-dependent anion-selective channel protein 3 Vdac3	86.309	134.178	1132.711
PTPRA_MOUSE	5	2	0.064615	Receptor-type tyrosine-protein phosphatase alpha Ptpra	873.633	461.199	417.038
TM1L1_MOUSE	3	1	0.064626	TOM1-like protein 1 Tom1l1	87.502	3.701	4.704
IPYR_MOUSE	9	1	0.065024	Inorganic pyrophosphatase Ppa1	204.940	3.763	47.930
RL14_MOUSE	13	4	0.065336	60S ribosomal protein L14 Rpl14	7257.583	3300.718	2878.584
GARS_MOUSE	27	8	0.065785	Glycine--tRNA ligase Gars	7990.758	12137.477	11445.795
C1TC_MOUSE	22	6	0.066034	C-1-tetrahydrofolate synthase, cytoplasmic Mthfd1	981.173	2262.908	4280.216
PCBP1_MOUSE	7	2	0.066358	Poly(rC)-binding protein 1 Pcbp1	2453.550	515.235	457.278
EMIL2_MOUSE	13	2	0.066597	EMILIN-2 Emilin2	1322.143	450.241	719.692
DEN2C_MOUSE	20	7	0.068127	DENN domain-containing protein 2C Dennd2c	7968.240	4775.129	6263.990
TBA1C_MOUSE	24	1	0.06856	Tubulin alpha-1C chain Tuba1c	1028.273	6390.150	4808.340
SEP11_MOUSE	14	4	0.069433	Septin-11 Sept11			6361.353
VIME_MOUSE	48	21	0.069581	Vimentin Vim	1678.076 110871.445	7	51542.458

SAR1B_MOUSE	2	1	0.070372	GTP-binding protein SAR1b Sar1b	2.747	223.317	79.593
RL32_MOUSE	4	1	0.07080960S ribosomal protein L32 Rpl32		855.621	0.387	3.411
BLK_MOUSE	6	1	0.071114	Tyrosine-protein kinase Blk Blk	1482.786	6710.166	5068.343
APEX1_MOUSE	5	2	0.071339	DNA-(apurinic or apyrimidinic site) lyase Apex1	1057.201	366.682	1244.437
ATP5H_MOUSE	3	1	0.071707	ATP synthase subunit d, mitochondrial Atp5h	783.550	75.399	238.233
TCAF1_MOUSE	8	2	0.071944	TRPM8 channel-associated factor 1 Tcaf1	1425.501	235.433	474.059
HSP13_MOUSE	2	1	0.07237	Heat shock 70 kDa protein 13 Hspa13			520.075
HSPB1_MOUSE	13	9	0.072453	Heat shock protein beta-1 Hspb1			22886.353
AMPN_MOUSE	14	2	0.072454	Aminopeptidase N Anpep	61.109 65497.895 57.949 3209.525	632.589 19148.278 110.787 12140.539	246.241
TIMP2_MOUSE	5	4	0.072627	Metalloproteinase inhibitor 2 Timp2			4148.810
GGH_MOUSE	1	1	0.072851	Gamma-glutamyl hydrolase Ggh	67.300	1122.345	890.154
CPNE3_MOUSE	12	3	0.073172	Copine-3 Cpne3	1004.776	411.135	586.310
S16C6_MOUSE	3	1	0.073472	Short-chain dehydrogenase/reductase family 16C member 6 Sdr16c6	2809.103	6031.612	4283.720
IRAK4_MOUSE	11	1	0.074515	Interleukin-1 receptor-associated kinase 4 Irak4	43.550	247.892	92.542
IDH3A_MOUSE	8	2	0.074533	Isocitrate dehydrogenase [NAD] subunit alpha, mitochondrial Idh3a	828.040	1381.844	589.523
PP1A_MOUSE	3	2	0.074535	Serine/threonine-protein phosphatase PP1-alpha catalytic subunit Ppp1ca	3579.092	4303.271	5320.204
CUL5_MOUSE	7	1	0.074797	Cullin-5 Cul5	817.630	2797.857	2103.219
UGDH_MOUSE	6	1	0.075352	UDP-glucose 6-dehydrogenase Ugdh	817.285	1130.197	540.873

NOP2_MOUSE	4	1	0.075584	Probable 28S rRNA (cytosine-C(5))-methyltransferase Nop2	759.314	1823.015	2755.729
TBA8_MOUSE	23	1	0.075752	Tubulin alpha-8 chain Tuba8	252.688	1170.944	510.135
FLNC_MOUSE	44	8	0.07581	Filamin-C Flnc	11352.311	12661.175	17043.713
TBB5_MOUSE	41	3	0.075908	Tubulin beta-5 chain Tubb5	5649.538	3247.383	6580.825
DIP2B_MOUSE	31	6	0.076093	Disco-interacting protein 2 homolog B Dip2b	3320.248	1624.626	3718.522
EIF3K_MOUSE	2	1	0.076877	Eukaryotic translation initiation factor 3 subunit K Eif3k	170.738	1174.371	1179.895
LRP6_MOUSE	24	4	0.077823	Low-density lipoprotein receptor-related protein 6 Lrp6	7398.167	10634.428	6439.690

DYSF_MOUSE	19	2	0.078226	Dysferlin Dysf	2643.390	2169.409	3353.008
LSMD1_MOUSE	4	1	0.078564	N-alpha-acetyltransferase 38, NatC auxiliary subunit Naa38	1404.820	43.234	51.850
PSB7_MOUSE	11	6	0.078917	Proteasome subunit beta type-7 Psmb7	362.107	2134.271	1059.382
TPIS_MOUSE	12	6	0.078972	Triosephosphate isomerase Tpi1	7532.755	1302.544	6319.805
SYMC_MOUSE	12	1	0.07942	Methionine--tRNA ligase, cytoplasmic Mars	69.381	0.000	0.000
CAND1_MOUSE	20	5	0.079565	Cullin-associated NEDD8-dissociated protein 1 Cand1	898.826	282.366	1380.502
PP1B_MOUSE	7	1	0.079793	Serine/threonine-protein phosphatase PP1beta catalytic subunit Ppp1cb	429.612	190.650	914.064
PGRP3_MOUSE	8	1	0.080771	Peptidoglycan recognition protein 3 Pglyrp3	24.073	150.270	224.647
CK5P1_MOUSE	15	2	0.081146	CDK5 regulatory subunit-associated protein 1 Cdk5rap1	2804.979	8854.531	7410.854
CEGT_MOUSE	8	1	0.081258	Ceramide glucosyltransferase Ugcg	620.863	1864.489	929.084
NPM_MOUSE	12	3	0.081498	Nucleophosmin Npm1	1032.045	1377.911	315.362
JMY_MOUSE	11	3	0.081505	Junction-mediating and -regulatory protein Jmy	1183.415	5112.626	9613.335

RL23_MOUSE	6	3	0.081513	60S ribosomal protein L23 Rpl23	7674.779	3741.905	3500.075
CCD22_MOUSE	8	1	0.081894	Coiled-coil domain-containing protein 22 Ccdc22	82.137	11.524	17.564
ATX10_MOUSE	6	1	0.08225	Ataxin-10 Atxn10	137.774	0.000	0.000
ATPA_MOUSE	26	9	0.083524	ATP synthase subunit alpha, mitochondrial Atp5a1	21334.830	12392.017	18357.508
HYEP_MOUSE	5	2	0.08355	Epoxide hydrolase 1 Ephx1	1274.759	568.906	627.118
UBP2_MOUSE	6	2	0.083562	Ubiquitin carboxyl-terminal hydrolase 2 Usp2	2158.274	360.051	299.812
FUMH_MOUSE	5	3	0.084601	Fumarate hydratase, mitochondrial Fh	1946.606	1834.067	3701.282
PURA1_MOUSE	6	3	0.085317	Adenylosuccinate synthetase isozyme 1 Adssl1	710.886	531.085	1721.852
COPB2_MOUSE	11	1	0.085328	Coatomer subunit beta' Copb2	141.756	0.000	0.000
MRCKA_MOUSE	17	2	0.085873	Serine/threonine-protein kinase MRCK alpha Cdc42bpa	340.145	313.685	159.571
RL36_MOUSE	7	3	0.085883	60S ribosomal protein L36 Rpl36	8600.965	2567.979	3965.736
SYNJ2_MOUSE	13	1	0.086196	Synaptojanin-2 Synj2	0.104	16.205	424.948
CTL2_MOUSE	17	3	0.086289	Choline transporter-like protein 2 Slc44a2	5637.968	8239.862	7283.253

P4HA1_MOUSE	9	2	0.087197	Prolyl 4-hydroxylase subunit alpha-1 P4ha1	3854.118	6619.611	3861.035
ITA3_MOUSE	32	6	0.087232	Integrin alpha-3 Itga3	17222.563	10577.231	15988.020
CAP1_MOUSE	14	5	0.087526	Adenylyl cyclase-associated protein 1 Cap1	8448.432	9360.623	5691.668
RL13A_MOUSE	16	4	0.087762	60S ribosomal protein L13a Rpl13a	10914.418	5381.009	7966.302
MAST4_MOUSE	24	5	0.087915	Microtubule-associated serine/threonine-protein kinase 4 Mast4	2695.828	5869.869	7680.709
ITA5_MOUSE	25	5	0.088783	Integrin alpha-5 Itga5	12399.147	7292.258	7038.427
RL17_MOUSE	4	2	0.089387	60S ribosomal protein L17 Rpl17	4537.557	337.061	435.029
CP131_MOUSE	14	1	0.08958	Centrosomal protein of 131 kDa Cep131	626.336	377.791	393.104

ESTD_MOUSE	8	3	0.08985	S-formylglutathione hydrolase Esd	3477.258	3070.176	9015.274
RL22_MOUSE	4	1	0.090257	60S ribosomal protein L22 Rpl22	3256.597	323.444	696.507
FA49B_MOUSE	7	2	0.091287	Protein FAM49B Fam49b	246.470	131.455	30.260
AATC_MOUSE	6	3	0.091498	Aspartate aminotransferase, cytoplasmic Got1	2131.867	1182.177	959.368
RL40_MOUSE	24	7	0.091594	Ubiquitin-60S ribosomal protein L40 Uba52	14813.130	17988.510	23319.663
ABCF2_MOUSE	8	2	0.092661	ATP-binding cassette sub-family F member 2 Abcf2	1305.389	987.958	1544.921
KAD2_MOUSE	8	2	0.09	Adenylate kinase 2, mitochondrial Ak2	3002.068	6320.404	2579.708
COPB_MOUSE	28	2	2897	0.093045 Coatomer subunit beta Copb1	78.836	275.841	275.019
TBC8B_MOUSE	8	1	0.0946	TBC1 domain family member 8B Tbc1d8b	70.184	19.070	0.562
DHB12_MOUSE	9	3	0.094861	Very-long-chain 3-oxoacyl-CoA reductase Hsd17b12	1233.623	237.080	520.268
SF3B1_MOUSE	20	2	0.095818	Splicing factor 3B subunit 1 Sf3b1	21.288	237.184	22.385
ARP2_MOUSE	14	4	0.097164	Actin-related protein 2 Actr2	3692.290	7555.157	8886.471
CAZA1_MOUSE	7	4	0.097346	F-actin-capping protein subunit alpha-1 Capza1	3338.741	4086.059	5446.244
SODC_MOUSE	5	1	0.097575	Superoxide dismutase [Cu-Zn] Sod1	0.000	698.655	320.036
CTR1_MOUSE	4	1	0.098976	High affinity cationic amino acid transporter 1 Slc7a1	494.579	227.755	67.804
VP37B_MOUSE	7	2	0.099296	Vacuolar protein sorting-associated protein 37B Vps37b	765.033	58.384	30.666
ARPC2_MOUSE	11	3	0.099467	Actin-related protein 2/3 complex subunit 2	1855.010	1094.377	664.744

				Arpc2			
RS10_MOUSE	7	3	0.099536	40S ribosomal protein S10 Rps10	2880.327	3592.579	5332.579
RBL2_MOUSE	9	1	0.099657	Retinoblastoma-like protein 2 Rbl2	174.108	360.290	269.405

PSB1_MOUSE	13	7	0.099779	Proteasome subunit beta type-1 Psmb1	7402.930	17740.759	7574.773
ROA3_MOUSE	8	2	0.100189	Heterogeneous nuclear ribonucleoprotein A3 Hnrnpa3	764.364	372.753	36.438
DCTN5_MOUSE	2	1			596.732	801.822	284.789
HYDIN_MOUSE	78	16	0.101147	Dynactin subunit 5 Dctn5	35388.124	46814.957	54573.989
			0.101509	Hydrocephalus-inducing protein Hydin			
RS5_MOUSE	9	2	0.102668	40S ribosomal protein S5 Rps5	2308.590	637.483	493.114
SPEG_MOUSE	33	4	0.102733	Striated muscle-specific serine/threonine-protein kinase Speg	1837.594	2394.947	3070.273
STOM_MOUSE	11	3	0.102736	Erythrocyte band 7 integral membrane protein Stom	6320.299	2000.943	2515.357
MAP1B_MOUSE	21	3	0.103142	Microtubule-associated protein 1B Map1b	466.479	2727.876	2301.273
ERP29_MOUSE	2	1	0.103258	Endoplasmic reticulum resident protein 29 Erp29	344.453	114.985	442.271
PLD1_MOUSE	11	1	0.103269	Phospholipase D1 Pld1	864.107	1181.279	3682.183
TOM1_MOUSE	6	1	0.103683	Target of Myb protein 1 Tom1	261.866	22.112	18.280
CDV3_MOUSE	2	1	0.105388	Protein CDV3 Cdv3	3.409	110.980	36.732
NUP85_MOUSE	10	1	0.106442	Nuclear pore complex protein Nup85 Nup85	296.543	2648.107	1074.676
TRI47_MOUSE	15	2	0.107418	Tripartite motif-containing protein 47 Trim47	2346.621	1153.497	2148.585
IF2A_MOUSE	10	4	0.108088	Eukaryotic translation initiation factor 2 subunit 1 Eif2s1	3614.185	3945.822	5898.010
PFKAP_MOUSE	13	2	0.11088	ATP-dependent 6-phosphofructokinase, platelet type Pfkp	1183.085	847.465	1629.596
NU160_MOUSE	20	4	0.111578	Nuclear pore complex protein Nup160	1768.079	1120.959	2203.179

				Nup160			
ODFP2_MOUSE	15	3	0.112087	Outer dense fiber protein 2 Odf2	8640.141	3695.944	2505.011
MYADM_MOUSE	6	3	0.112362	Myeloid-associated differentiation marker Myadm	8045.770	6390.678	4817.316
PTPR2_MOUSE	2	1	0.112399	Receptor-type tyrosine-protein phosphatase N2 Ptprn2	957.050	1675.367	895.250
E41L2_MOUSE	32	9	0.112498	Band 4.1-like protein 2 Epb41l2	13017.653	17261.901	39043.692
EIF3H_MOUSE	4	1	0.113304	Eukaryotic translation initiation factor 3 subunit H Eif3h	319.088	1351.980	371.406
RL18_MOUSE	10	3	0.113427	60S ribosomal protein L18 Rpl18	19920.606	6284.264	8035.561
RD23B_MOUSE	2	1	0.113448	UV excision repair protein RAD23 homolog B Rad23b	153.482	0.090	18.023

SNX6_MOUSE	6	2	0.114455	Sorting nexin-6 Snx6	228.805	340.107	1140.578
NAA50_MOUSE	4	2	0.115419	N-alpha-acetyltransferase 50 Naa50	3.521	210.455	1911.070
FOG2_MOUSE	14	1	0.115601	Zinc finger protein ZFPM2 Zfpm2	3704.380	12983.495	6655.428
GRB2_MOUSE	2	1	0.115748	Growth factor receptor-bound protein 2 Grb2	578.145	247.001	230.805
RL21_MOUSE	8	4	0.116231	60S ribosomal protein L21 Rpl21	16754.232	6329.786	12558.417
MTL26_MOUSE	5	1	0.117421	Methyltransferase-like 26 Mettl26	1558.090	738.957	840.336
RECQ1_MOUSE	14	1	0.118062	ATP-dependent DNA helicase Q1 Recql	4017.613	4434.478	6133.839
OLA1_MOUSE	3	1	0.12053	Obg-like ATPase 1 Ola1	2.199		675.979
EHD4_MOUSE	34	9	0.122611	EH domain-containing protein 4 Ehd4	13680.998		23653.147
BMP4_MOUSE	2	1	0.123655	Bone morphogenetic protein 4 Bmp4	764.462	1894.623	1857.372

AT5F1_MOUSE	3	1	0.125063	ATP synthase F(0) complex subunit B1, mitochondrial Atp5f1	379.690	6213.796	11226.774
DPOE1_MOUSE	19	2	0.125566	DNA polymerase epsilon catalytic subunit A Pole	3826.081	378.073	593.286
PLOD3_MOUSE	6	1	0.126505	Procollagen-lysine,2-oxoglutarate 5-dioxygenase 3 Plod3	469.071	1297.926	1637.221
TCPW_MOUSE	13	1				199.247	94.216
CO5A2_MOUSE	10	3	0.127165	T-complex protein 1 subunit zeta-2 Cct6b	435.829	11029.202	29504.529
			0.127223	Collagen alpha-2(V) chain Col5a2	7050.318		
VP37C_MOUSE	6	2	0.127649	Vacuolar protein sorting-associated protein 37C Vps37c	3023.131	1619.615	2355.297
CD47_MOUSE	2	1	0.127776	Leukocyte surface antigen CD47 Cd47	1.238	11.247	94.295
DIAP3_MOUSE	23	1	0.128996	Protein diaphanous homolog 3 Diaph3	62.946	99.950	671.240
SPTA1_MOUSE	15	3	0.129464	Spectrin alpha chain, erythrocytic 1 Spta1	671.715	73.882	173.832
LRC40_MOUSE	10	1	0.12964	Leucine-rich repeat-containing protein 40 Lrrc40	20.409	0.000	0.109
CYFP1_MOUSE	24	4	0.130395	Cytoplasmic FMR1-interacting protein 1 Cyfip1	2016.436	2303.172	3301.503
MPRD_MOUSE	4	1	0.131261	Cation-dependent mannose-6-phosphate receptor M6pr	1199.369	699.505	807.908
HSH2D_MOUSE	2	1	0.131476	Hematopoietic SH2 domain-containing protein Hsh2d	2045.116	359.221	101.904
VINC_MOUSE	60	18	0.132379	Vinculin Vcl	22496.997	19774.951	17374.429
TMG4_MOUSE	5	2	0.132466	Transmembrane gamma-carboxyglutamic acid protein 4 Prrg4	2540.474	2364.579	7371.342

1433T_MOUSE	7	3	0.132923	14-3-3 protein theta Ywhaq	5349.898	2235.676	3213.094
ACADS_MOUSE	8	1	0.133128	Short-chain specific acyl-CoA dehydrogenase, mitochondrial Acads	81.148	0.000	3.704
PA1B3_MOUSE	1	1	0.134666	Platelet-activating factor acetylhydrolase IB subunit gamma Pafah1b3	67.354	0.000	0.000
S2542_MOUSE	6	1	0.135105	Mitochondrial coenzyme A transporter SLC25A42 Slc25a42	1878.909	4846.654	8488.205
TRAP1_MOUSE	22	4	0.136703	Heat shock protein 75 kDa, mitochondrial Trap1	3543.562	7483.418	5971.654
ACLY_MOUSE	33	7	0.137147	ATP-citrate synthase Acly	6130.602	6959.423	8179.887
ANGL2_MOUSE	10	2	0.137302	Angiopoietin-related protein 2 ngptl2	1758.062	2982.653	3835.807
PSMD3_MOUSE	18	6	0.139591	26S proteasome non-ATPase regulatory subunit 3 Psmd3	2340.354	2917.057	3891.690
PLEC_MOUSE	221	49			59581.531	46069.519	49607.553
H2AJ_MOUSE	6	2	0.139596 0.139596	Plectin Plec Histone H2A.J H2afj	2199.758	546.222	714.409
NRAP_MOUSE	28	3	0.140285	Nebulin-related-anchoring protein Nrap	571.425	6902.791	2344.048
GBB1_MOUSE	6	1	0.140408	Guanine nucleotide-binding protein G(I)/G(S)/G(T) subunit beta-1 Gnb1	5.661	106.791	43.529
KCY_MOUSE	1	1	0.14111	UMP-CMP kinase Cmpk1	283.685	37.803	444.826
AMFR_MOUSE	4	1	0.141468	E3 ubiquitin-protein ligase AMFR Amfr	301.647	2612.364	1826.127
STML3_MOUSE	4	1	0.141646	Stomatin-like protein 3 Stoml3	216.711	100.084	29.527
PRS23_MOUSE	14	5	0.141932	Serine protease 23 Prss23	2116.520	1743.058	3445.169
SAP_MOUSE	10	4					1309.442

COPA_MOUSE	34	5	0.143681	Prosaposin Psap	2373.669 15190.632	2067.369 21295.869		17753.942
			0.143975	Coatomer subunit alpha Copa				
RS26_MOUSE	3	1	0.144104	40S ribosomal protein S26 Rps26	401.650		148.036	34.480
ATG4A_MOUSE	3	1	0.144719	Cysteine protease ATG4A Atg4a	18.685		454.093	1454.254
FPRP_MOUSE	31	5	0.144974	Prostaglandin F2 receptor negative regulator Ptgfrn	1680.304		2319.887	944.675
H1T_MOUSE	5	1	0.14637	Histone H1t Hist1h1t	3752.826		3937.807	6255.634
INF2_MOUSE	8	4	0.147009	Inverted formin-2 Inf2	6229.946		7825.389	2517.967
DNJA1_MOUSE	12	4	0.147842	DnaJ homolog subfamily A member 1 Dnaja1	22643.022		5388.935	10074.614
CPNE1_MOUSE	3	1	0.149102	Copine-1 Cpne1	11.306		193.478	74.371
SH3G3_MOUSE	5	2	0.149702	Endophilin-A3 Sh3gl3	299.248		103.585	35.589

VATE1_MOUSE	3	1	0.150008	V-type proton ATPase subunit E 1 Atp6v1e1	452.855	110.343	819.970
EHMT1_MOUSE	11	2	0.152528	Histone-lysine N-methyltransferase EHMT1 Ehmt1	55.669	290.227	102.252
RL15_MOUSE	5	4	0.154315	60S ribosomal protein L15 Rpl15	3882.346	17506.145	13029.367
RHG29_MOUSE	14	2	0.155404	Rho GTPase-activating protein 29 Arhgap29	3285.637	1077.617	798.025
RS11_MOUSE	17	5	0.156235	40S ribosomal protein S11 Rps11	5154.820	1840.933	2524.465
IFM2_MOUSE	3	2	0.15712	Interferon-induced transmembrane protein 2 Ifitm2	1862.239	906.930	1586.436
LRP1_MOUSE	69	11	0.158116	Prolow-density lipoprotein receptor-related protein 1 Lrp1	7822.433	6310.240	5145.427
AOXD_MOUSE	17	1	0.158131	Aldehyde oxidase 4 Aox4	367.136	21.486	102.643
HNRPC_MOUSE	11	2	0.158441	Heterogeneous nuclear ribonucleoproteins C1/C2 Hnrnpc	589.727	126.978	39.291

SCRIB_MOUSE	10	4	0.158872	Protein scribble homolog Scrib	1736.908	2084.606	3318.609
DDX3X_MOUSE	22	2	0.159229	ATP-dependent RNA helicase DDX3X Ddx3x	84.005	2.580	229.284
IF4A1_MOUSE	29	4	0.161417	Eukaryotic initiation factor 4A-I Eif4a1	4255.834	2983.217	8613.023
PSMD8_MOUSE	5	1	0.162828	26S proteasome non-ATPase regulatory subunit 8 Psmd8	2303.663	3163.340	3804.277
MYH11_MOUSE	89	3	0.16	Myosin-11 Myh11	3814.874	4971.751	4776.844
RS12_MOUSE	3	1	0.16565	40S ribosomal protein S12 Rps12	1681.264	237.637	381.984
ESYT1_MOUSE	20	4	5599	Extended synaptotagmin-1 Esyt1	2725.085	1573.776	1822.909
SH3G1_MOUSE	9	1		Endophilin-A2 Sh3gl1	166.567	500.031	123.506
			0.165909				
			0.168705				
RL10_MOUSE	7	2	0.168929	60S ribosomal protein L10 Rpl10	8178.389	2905.694	1551.808
CDK1_MOUSE	12	4	0.168947	Cyclin-dependent kinase 1 Cdk1	3775.894	1831.722	1673.739
AP180_MOUSE	10	2	0.169152	Clathrin coat assembly protein AP180 Snap91	1164.503	703.942	1221.648
RS24_MOUSE	7	3	0.169706	40S ribosomal protein S24 Rps24	372.473	104.092	111.889
MYH1_MOUSE	30	5	0.169981	Myosin-1 Myh1	2056.619	5526.907	7601.975
ITPR3_MOUSE	24	7	0.170427	Inositol 1,4,5-trisphosphate receptor type 3 Itpr3	2218.535	4503.514	2166.890
VPS4A_MOUSE	9	1	0.170969	Vacuolar protein sorting-associated protein 4A Vps4a	1869.053	573.056	569.942

ANKE1_MOUSE	6	2	0.172664	Ankyrin repeat and EF-hand domain-containing protein 1 Ankef1	80.975	23.104	234.481
KMT2C_MOUSE	21	3	0.173111	Histone-lysine N-methyltransferase 2C Kmt2c	2950.972	4752.571	1402.022
BACH_MOUSE	14	3		Cytosolic acyl coenzyme A thioester		3291.757	2070.744

			0.173196	hydrolase Acot7	2597.617		
PSMD5_MOUSE	10	2	0.174302	26S proteasome non-ATPase regulatory subunit 5 Psmd5	540.729	169.166	132.457
M18BP_MOUSE	15	4	0.174304	Mis18-binding protein 1 Mis18bp1			5619.680
RAB13_MOUSE	5	2	0.176712	Ras-related protein Rab-13 Rab13			4982.279
1433B_MOUSE	19	4					5113.000
TCPQ_MOUSE	46	14					26651.391
					5547.562	14420.980	
					2817.952	4279.338	
			0.176887	14-3-3 protein beta/alpha Ywhab	3159.815	3760.381	
			0.177324	T-complex protein 1 subunit theta Cct8	24342.528	30781.286	
IMDH1_MOUSE	5	1	0.177411	Inosine-5'-monophosphate dehydrogenase 1 Impdh1	42.471	3.222	41.688
6PGD_MOUSE	13	5	0.179252	6-phosphogluconate dehydrogenase, decarboxylating Pgd	5600.971	5331.674	7833.266
ANXA4_MOUSE	23	9	0.181243	Annexin A4 Anxa4	13463.470	8001.649	13078.707
HINT1_MOUSE	2	1	0.181307	Histidine triad nucleotide-binding protein 1 Hint1	1586.532	368.379	1657.279
TSN7_MOUSE	3	2	0.182149	Tetraspanin-7 Tspan7	3243.848	1391.248	2374.883
MXRA7_MOUSE	1	1	0.1825	Matrix-remodeling-associated protein 7 Mxra7	108.314	7.756	22.020
PTBP1_MOUSE	3	1	0.182906	Polypyrimidine tract-binding protein 1 Ptbp1	20.746	494.458	779.750
CD109_MOUSE	13	1	0.183808	CD109 antigen Cd109	110.049	6.539	75.781
CUL4A_MOUSE	10	2	0.185485	Cullin-4A Cul4a	86.840	266.063	368.247
ASNS_MOUSE	23	5	0.187209	Asparagine synthetase [glutamine-hydrolyzing] Asns	5300.511	8933.637	8516.536

CB5D1_MOUSE	3	1	0.188008	Cytochrome b5 domain-containing protein 1 Cyb5d1	567.781		315.798	37.981
FKB1A_MOUSE	2	1	0.188131	Peptidyl-prolyl cis-trans isomerase FKBP1A Fkbp1a	953.654		248.743	253.821
ACTBL_MOUSE	30	1	0.188713	Beta-actin-like protein 2 Actbl2	0.000		41.841	0.041
RSU1_MOUSE	3	2	0.189401	Ras suppressor protein 1 Rsu1	1484.416		113.783	57.610
VASP_MOUSE	6	1	0.19158	Vasodilator-stimulated phosphoprotein Vasp	1628.730		33.892	0.000

KCNH3_MOUSE	12	2	0.191812	Potassium voltage-gated channel subfamily H member 3 Kcnh3	1281.946		2718.323	1899.282
CLCN5_MOUSE	12	4	0.191916	H(+)/Cl(-) exchange transporter 5 Clcn5	2316.028		871.592	734.456
GTR1_MOUSE	3	1	0.191984	Solute carrier family 2, facilitated glucose transporter member 1 Slc2a1	747.536		221.350	10.228
CE128_MOUSE	11	1	0.192454	Centrosomal protein of 128 kDa Cep128	88.283	1941.957		805.010
TCPE_MOUSE	45	16	0.192646	T-complex protein 1 subunit epsilon Cct5	17039.415	28839.176		18176.132
DRG1_MOUSE	2	1	0.19312	Developmentally-regulated GTP-binding protein 1 Drg1	151.300		14.290	13.301
RAI3_MOUSE	7	3	0.194364	Retinoic acid-induced protein 3 Gprc5a	5012.886		4611.264	3191.154
TNPO1_MOUSE	7	2	0.195506	Transportin-1 Tnpo1	8211.433		23110.037	38018.324
SMD3_MOUSE	10	2	0.196481	Small nuclear ribonucleoprotein Sm D3 Snrpd3	1630.121		5144.075	6431.149
PA2G4_MOUSE	10	3	0.197454	Proliferation-associated protein 2G4 Pa2g4	3693.596		3927.789	5252.352
TXNL1_MOUSE	5	1	0.198349	Thioredoxin-like protein 1 Txnl1	91.033		20.960	32.509
H15_MOUSE	5	3	0.19844	Histone H1.5 Hist1h1b				2836.795
PDIA3_MOUSE	19	10	0.199701	Protein disulfide-isomerase A3 Pdia3				7794.431

ML12B_MOUSE	6	1					2758.418
CBR1_MOUSE	6	1					8029.357
					3220.609	1853.862	
					12319.509	10694.937	
			0.200072	Myosin regulatory light chain 12B Myl12b	687.574	8544.193	
			0.202054	Carbonyl reductase [NADPH] 1 Cbr1	14797.057	10994.893	
6PGL_MOUSE	5	3	0.20272	6-phosphogluconolactonase Pgls	1055.343	458.249	1305.014
VDAC2_MOUSE	4	1	0.203586	Voltage-dependent anion-selective channel protein 2 Vdac2	1138.340	1106.869	1684.922
RUVB2_MOUSE	13	6	0.203845	RuvB-like 2 Ruvbl2	6501.044	7323.040	8858.504
CIP4_MOUSE	5	1	0.204458	Cdc42-interacting protein 4 Trip10	35.620	9.384	0.010
TBA1A_MOUSE	26	1				727.256	1449.146
			0.206434	Tubulin alpha-1A chain Tuba1a	31.714		
RAB5A_MOUSE	9	3	0.206971	Ras-related protein Rab-5A Rab5a	3482.692	3863.342	4597.111
GAR1_MOUSE	4	2	0.208328	H/ACA ribonucleoprotein complex subunit 1 Gar1	4624.259	3350.448	1338.453
F234A_MOUSE	6	2	0.209061	Protein FAM234A Fam234a	625.052	273.216	46.617
ARF4_MOUSE	5	1	0.2096	ADP-ribosylation factor 4 Arf4	317.157	327.332	1088.725
BPIFC_MOUSE	2	1				1320.473	1744.966
			0.21063	BPI fold-containing family C protein Bpifc	574.738		
CROCC_MOUSE	37	2	0.210851	Rootletin Crocc	468.147	88.909	94.575
PDE10_MOUSE	12	2	0.212809	cAMP and cAMP-inhibited cGMP 3',5'-cyclic phosphodiesterase 10A Pde10a	113.207	51.579	17.189

MDR1A_MOUSE	9	2	0.213377	Multidrug resistance protein 1A Abcb1a	241.040	43.799	1065.331
PSMD4_MOUSE	3	1	0.216674	26S proteasome non-ATPase regulatory subunit 4 Psmd4	706.819	1690.911	3646.282
CALM1_MOUSE	7	2	0.218205	Calmodulin-1 Calm1	594.297	4944.584	3005.299
TSN6_MOUSE	2	2	0.218297	Tetraspanin-6 Tspan6			3802.712

PSA5_MOUSE	9	4		Proteasome subunit alpha type-5 Psma5	2470.314 10774.730	1739.824 15228.863	11436.966
ANXA8_MOUSE	5	1	0.21838 0.220123	Annexin A8 Anxa8	191.938	333.654	13.860
MOB1A_MOUSE	6	3	0.22165	MOB kinase activator 1A Mob1a	6445.306	3065.382	3974.969
CTL1_MOUSE	12	2	0.222814	Choline transporter-like protein 1 Slc44a1	384.742	165.415	291.022
TNR6C_MOUSE	13	2	0.22684	Trinucleotide repeat-containing gene 6C protein Tnrc6c	7121.843	4557.520	3621.075
DAG1_MOUSE	8	1	0.227985	Dystroglycan Dag1	49.063	16.607	9.378
TPM4_MOUSE	14	3	0.230788	Tropomyosin alpha-4 chain Tpm4	3545.739	1041.327	1865.692
CSMD3_MOUSE	5	2	0.230795	CUB and sushi domain-containing protein 3 Csmd3	2144.242	986.844	1025.492
RLA1_MOUSE	3	2	0.233934	60S acidic ribosomal protein P1 Rplp1	3184.393	1195.716	4368.153
H4_MOUSE	4	3	0.23671	Histone H4 Hist1h4a	2120.849	7737.721	7410.118
S620A_MOUSE	3	1	0.238803	Sodium- and chloride-dependent transporter XTRP3A Slc6a20a	57.567	390.213	1529.435
TAGL2_MOUSE	15	8	0.239586	Transgelin-2 Tagln2	19408.487	11233.097	9882.165
AT1A1_MOUSE	27	8	0.240009	Sodium/potassium-transporting ATPase subunit alpha-1 Atp1a1	20280.937	16714.318	17849.811
RS15A_MOUSE	6	1	0.240013	40S ribosomal protein S15a Rps15a	1192.519	501.063	392.348
RS20_MOUSE	3	2	0.242311	40S ribosomal protein S20 Rps20	5862.655	353.013	389.561
ELAV1_MOUSE	8	1	0.244991	ELAV-like protein 1 Elavl1	667.474	368.610	274.274
EIF3D_MOUSE	8	3	0.245872	Eukaryotic translation initiation factor 3 subunit D Eif3d	1744.407	2230.100	3072.864
CD276_MOUSE	2	2	0.250792	CD276 antigen Cd276	2601.449	1867.846	1070.713
DDX5_MOUSE	18	5	0.252433	Probable ATP-dependent RNA helicase DDX5 Ddx5	5210.979	12958.574	16234.518

CTGF_MOUSE	5	1	0.257517	Connective tissue growth factor Ctgf	3659.912	955.719	1090.331
EIF3B_MOUSE	20	5	0.259563	Eukaryotic translation initiation factor 3 subunit B Eif3b	2895.037	1357.688	1403.012
TM109_MOUSE	2	1	0.26024	Transmembrane protein 109 Tmem109	1130.681	1588.875	484.385
NL1B5_MOUSE	11	1	0.261833	NACHT, LRR and PYD domains-containing protein 1b allele 5 Nlrp1b	1242.045	9771.219	22564.015
KINH_MOUSE	25	6	0.262867	Kinesin-1 heavy chain Kif5b	9523.629	13587.425	12209.887
RPAP3_MOUSE	10	1	0.263102	RNA polymerase II-associated protein 3 Rpap3	773.592	2568.383	2193.209
GDIA_MOUSE	6	1	0.266418	Rab GDP dissociation inhibitor alpha Gdi1	2431.003	1175.229	2232.549
TM9S1_MOUSE	3	1	0.267425	Transmembrane 9 superfamily member 1 Tm9sf1	62.771	984.345	161.897
ITA6_MOUSE	18	4	0.268347	Integrin alpha-6 Itga6	4041.806	5404.806	4081.480
COPD_MOUSE	8	1	0.268735	Coatomer subunit delta Arcn1	118.402	8.535	13.632
PYRG2_MOUSE	8	1	0.268935	CTP synthase 2 Ctps2	111.016	46.777	40.766
MYOC_MOUSE	8	1	0.271791	Myocilin Myoc	72.416	14.121	56.136
MDR1B_MOUSE	8	1	0.272228	Multidrug resistance protein 1B Abcb1b	213.406	65.966	119.317
LAP4A_MOUSE	3	2	0.272972	Lysosomal-associated transmembrane protein 4A Laptm4a	3386.486	1066.099	1417.992
ANPRC_MOUSE	6	2	0.27391	Atrial natriuretic peptide receptor 3 Npr3	321.701	1216.844	360.809
GSTA4_MOUSE	3	2	0.275191	Glutathione S-transferase A4 Gsta4	1697.907	1106.396	673.244
TSN9_MOUSE	2	2	0.275712	Tetraspanin-9 Tspan9	5988.980	4376.666	4905.246
OLFL3_MOUSE	5	1	0.276608	Olfactomedin-like protein 3 Olfml3	589.342	760.129	594.353
CP250_MOUSE	18	7	0.27772	Centrosome-associated protein CEP250	4191.287	4264.101	7048.944

				Cep250			
RAP1A_MOUSE	8	1	0.277722	Ras-related protein Rap-1A Rap1a	2139.388	1956.114	965.142
PRS8_MOUSE	19	3	0.277737	26S proteasome regulatory subunit 8 Psmc5	2932.381	4109.118	6740.185
NAA15_MOUSE	12	3	0.278309	N-alpha-acetyltransferase 15, NatA auxiliary subunit Naa15	651.874	408.419	221.720
RS14_MOUSE	8	1				505.468	520.962
RL34_MOUSE	6	1	0.279024	40S ribosomal protein S14 Rps14	1512.741	16233.979	16986.448
			0.282605	60S ribosomal protein L34 Rpl34	5777.446		
UB2L3_MOUSE	2	1	0.283981	Ubiquitin-conjugating enzyme E2 L3 Ube2l3	866.496	302.751	316.161
CHIP_MOUSE	8	1	0.290063	STIP1 homology and U box-containing protein 1 Stub1	1343.174	692.284	742.747
SPG17_MOUSE	41	4	0.29076	Sperm-associated antigen 17 Spag17	1966.863	1126.143	1275.458
EIF2A_MOUSE	9	2	0.291835	Eukaryotic translation initiation factor 2A Eif2a	1036.276	338.519	495.600

SMAP2_MOUSE	5	1	0.292185	Stromal membrane-associated protein 2 Smap2	3284.208	29.500	27.211
CALL3_MOUSE	6	4	0.294042	Calmodulin-like protein 3 Calml3	5597.568	6885.628	10920.349
MYL6B_MOUSE	4	1	0.294229	Myosin light chain 6B Myl6b	549.883	235.982	139.518
LG3BP_MOUSE	10	2	0.295661	Galectin-3-binding protein Lgals3bp	692.275	311.351	951.771
KLDC1_MOUSE	5	1	0.296167	Kelch domain-containing protein 1 Klhdc1	375.522	203.867	76.540
IBP5_MOUSE	9	5	0.297829	Insulin-like growth factor-binding protein 5 Igfbp5	5612.087	8360.360	5305.082
RS25_MOUSE	6	3					1243.651

PSB4_MOUSE	7	5				1311.785	5772.845
			0.298936	40S ribosomal protein S25 Rps25	2517.957	11256.932	
			0.299478	Proteasome subunit beta type-4 Psmb4	3439.184		
LIS1_MOUSE	5	1	0.301003	Platelet-activating factor acetylhydrolase IB subunit alpha Pafah1b1	600.813	824.176	1111.543
PRS6A_MOUSE	20	11	0.301103	26S proteasome regulatory subunit 6A Psmc3	8647.937	9045.990	11960.578
PRELP_MOUSE	7	1	0.301617	Prolargin Prelp	905.507	1053.758	177.600
FHL1_MOUSE	2	1	0.302472	Four and a half LIM domains protein 1 Fhl1	2248.384	1316.302	1327.048
TLN1_MOUSE	77	18					11144.922
			0.304934	Talin-1 Tln1	14357.418	11983.212	
RASA3_MOUSE	10	3	0.307414	Ras GTPase-activating protein 3 Rasa3	2961.189	2302.793	2604.834
G3BP2_MOUSE	5	3	0.310472	Ras GTPase-activating protein-binding protein 2 G3bp2	1706.451	6056.527	3852.086
MTAP_MOUSE	10	3	0.31142	S-methyl-5'-thioadenosine phosphorylase Mtap	2831.854	2434.428	3385.552
GREM1_MOUSE	2	1	0.312269	Gremlin-1 Grem1	317.056	14.143	39.105
P3H1_MOUSE	5	1	0.313576	Prolyl 3-hydroxylase 1 P3h1	71.345	298.134	651.447
GPDM_MOUSE	13	3	0.313652	Glycerol-3-phosphate dehydrogenase, mitochondrial Gpd2	5697.498	8406.870	7488.240
PDCD6_MOUSE	7	4	0.314052	Programmed cell death protein 6 Pdcd6	2887.048	3659.954	2264.800
VTI1A_MOUSE	2	1	0.314115	Vesicle transport through interaction with t-SNAREs homolog 1A Vti1a	490.319	591.975	109.116
PSA7_MOUSE	10	3	0.314957	Proteasome subunit alpha type-7 Psma7	3023.529	6582.623	6730.651
UBA6_MOUSE	9	1	0.315271	Ubiquitin-like modifier-activating enzyme 6 Uba6	343.675	1609.689	729.354
SFXN3_MOUSE	2	1	0.318411	Sideroflexin-3 Sfxn3	63.835	0.000	0.584

ARL3_MOUSE	1	1	0.320089	ADP-ribosylation factor-like protein 3 Arl3	498.905	232.556	307.785
ARF6_MOUSE	7	2	0.321235	ADP-ribosylation factor 6 Arf6	1589.005	142.593	92.752

ERBIN_MOUSE	13	1	0.321641	Erbin Erbin	786.337		374.785	768.061
EI2BB_MOUSE	3	1	0.322574	Translation initiation factor eIF-2B subunit beta Eif2b2	242.411		278.146	116.779
ADCY1_MOUSE	9	1	0.324633	Adenylate cyclase type 1 Adcy1	162.307		90.912	39.810
NIBL1_MOUSE	20	5	0.32483	Niban-like protein 1 Fam129b	8267.020		7062.000	8296.098
STK24_MOUSE	5	2	0.324884	Serine/threonine-protein kinase 24 Stk24	320.193		443.747	679.043
RL10A_MOUSE	7	5	0.325224	60S ribosomal protein L10a Rpl10a	6777.216		3171.643	5923.378
TS101_MOUSE	20	7	0.330001	Tumor susceptibility gene 101 protein Tsg101	6944.185		4813.724	7199.336
ANXA6_MOUSE	80	29	0.331377	Annexin A6 Anxa6	47987.189	64639.238		49898.014
CYS1_MOUSE	4	1	0.331548	Cystin-1 Cys1	2.297	3.509		76.941
CRY2_MOUSE	11	1	0.333804	Cryptochrome-2 Cry2	604.182		492.036	266.649
DRG2_MOUSE	6	1	0.337897	Developmentally-regulated GTP-binding protein 2 Drg2	358.581		230.419	98.121
RAC3_MOUSE	4	1	0.338251	Ras-related C3 botulinum toxin substrate 3 Rac3	1227.225		1818.121	1432.414
1433F_MOUSE	14	8	0.339182	14-3-3 protein eta Ywhah	12979.660		5864.080	8657.807
RL26_MOUSE	7	3	0.339821	60S ribosomal protein L26 Rpl26	5025.135		2351.888	3632.899
RYR1_MOUSE	44	5	0.341025	Ryanodine receptor 1 Ryr1	6543.347		5070.401	4772.572
PGBM_MOUSE	60	11	0.341584	Basement membrane-specific heparan sulfate proteoglycan core protein Hspg2	11325.514		7873.407	7983.944
RANG_MOUSE	4	1	0.342473	Ran-specific GTPase-activating protein Ranbp1	115.159		11.434	25.296

ATP4A_MOUSE	11	1	0.348164	Potassium-transporting ATPase alpha chain 1 Atp4a	30.874	230.482	438.302
CARL1_MOUSE	26	2	0.349339	F-actin-uncapping protein LRRC16A Carmil1	1155.536	4051.385	3293.182
RALB_MOUSE	7	1	0.349495	Ras-related protein Ral-B Ralb	1537.493	44.077	19.379
CAPZB_MOUSE	11	3	0.350637	F-actin-capping protein subunit beta Capzb	3064.686	5483.128	5337.050
ACOC_MOUSE	8	1	0.353513	Cytoplasmic aconitate hydratase Aco1	187.267	263.763	585.320
PRDX1_MOUSE	19	7	0.354791	Peroxiredoxin-1 Prdx1	6193.995	5934.381	3659.402
MCM4_MOUSE	9	1	0.35522	DNA replication licensing factor MCM4 Mcm4	155.031	92.572	66.109
RAP2B_MOUSE	5	1	0.355439	Ras-related protein Rap-2b Rap2b	160.359 14320.437	11.810 6923.729	22.062 6229.053
RL13_MOUSE	13	4	0.357032	60S ribosomal protein L13 Rpl13			
SEPT2_MOUSE	6	2	0.357221	Septin-2 Sept2	676.803	1104.409	1163.029
MYL1_MOUSE	5	3	0.357296	Myosin light chain 1/3, skeletal muscle isoform Myl1	1855.447	619.648	2287.357
VPS29_MOUSE	2	1	0.358398	Vacuolar protein sorting-associated protein 29 Vps29	388.289	2959.975	2619.102
SSPO_MOUSE	19	3	0.359941	SCO-spondin Sspo	24995.635	13563.033	20166.066
RAB8A_MOUSE	6	1	0.360648	Ras-related protein Rab-8A Rab8a	195.129	76.067	13.840
PDC10_MOUSE	4	1	0.36098	Programmed cell death protein 10 Pdcd10	4246.391	4591.550	7775.323
COMD2_MOUSE	6	3	0.362084	COMM domain-containing protein 2 Commd2	398.739	961.960	800.834
SYFB_MOUSE	10	4	0.363393	Phenylalanine--tRNA ligase beta subunit	3908.169	5365.862	5240.754

				Farsb			
FRIH_MOUSE	2	1			222.673	117.556	207.950
TITIN_MOUSE	552	57	0.363953	Ferritin heavy chain Fth1	60179.340	74346.232	76972.206
			0.364429	Titin Ttn			
EMAL5_MOUSE	15	3	0.364674	Echinoderm microtubule-associated protein-like 5 Eml5	3323.674	2961.920	4203.497
SPTN1_MOUSE	62	5	0.364758	Spectrin alpha chain, non-erythrocytic 1 Sptan1	9163.479	7390.882	4955.326
STX4_MOUSE	12	2	0.365378	Syntaxin-4 Stx4	2248.273	1994.009	3809.504
PSB2_MOUSE	9	2	0.365755	Proteasome subunit beta type-2 Psmb2	1443.905	7852.188	4050.793
DPYL3_MOUSE	20	4	0.367412	Dihydropyrimidinase-related protein 3 Dpysl3	42487.683	41364.318	29947.851
CRIP2_MOUSE	4	1	0.369953	Cysteine-rich protein 2 Crip2	1115.913	31.642	91.232
PGM1_MOUSE	8	2	0.372028	Phosphoglucomutase-1 Pgm1	47.728	31.730	47.065
RS27_MOUSE	3	2	0.372278	40S ribosomal protein S27 Rps27	991.183	1392.369	1365.782
IPO5_MOUSE	22	3	0.372506	Importin-5 Ipo5	945.085	1096.736	1199.756
PSB5_MOUSE	11	5	0.373071	Proteasome subunit beta type-5 Psmb5	2734.858	14982.534	9056.493
UB2V2_MOUSE	4	1	0.373514	Ubiquitin-conjugating enzyme E2 variant 2 Ube2v2	626.962	321.506	258.873
XPO1_MOUSE	12	2	0.373979	Exportin-1 Xpo1	589.655	285.126	249.440
LA_MOUSE	10	4	0.374831	Lupus La protein homolog Ssb	1277.999	1772.617	1878.732
PFKAL_MOUSE	12	4	0.375536	ATP-dependent 6-phosphofructokinase, liver type Pfkl	1508.225	763.842	932.456
CPNS1_MOUSE	4	3	0.378693	Calpain small subunit 1 Capns1	580.277	1168.422	1018.833
EIF3F_MOUSE	10	4	0.379466	Eukaryotic translation initiation factor 3 subunit F Eif3f	2524.401	1626.806	2913.810

YBEY_MOUSE	2	1	0.382398	Endoribonuclease YbeY Ybey	1.986	0.058	85.173
ZFY26_MOUSE	36	7	0.382639	Zinc finger FYVE domain-containing protein 26 Zfyve26	5128.974	9010.033	9375.502
LDHA_MOUSE	25	11	0.382672	L-lactate dehydrogenase A chain Ldha	14060.996	8099.654	7666.642
NPAS4_MOUSE	3	2	0.384482	Neuronal PAS domain-containing protein 4 Npas4	364.299	679.852	495.177
RAD50_MOUSE	20	2	0.385563	DNA repair protein RAD50 Rad50	1503.060	2735.846	2807.014
GCN1_MOUSE	42	5	3	0.38587eIF-2-alpha kinase activator GCN1 Gcn1	1741.746	1074.276	1978.887
CA109_MOUSE	2	1	0.386918	Uncharacterized protein C1orf109 homolog C1orf109	520.354	625.154	824.499
MCE1_MOUSE	6	1	0.392197	mRNA-capping enzyme Rngtt	1189.487	914.579	2842.353
PYRG1_MOUSE	9	1	0.393489	CTP synthase 1 Ctps1	40.836	0.381	6.972
GNA14_MOUSE	11	1	0.393922	Guanine nucleotide-binding protein subunit alpha-14 Gna14	35.693	258.543	289.666
RUVB1_MOUSE	12	2	0.396648	RuvB-like 1 Ruvbl1	2553.808	2971.803	2941.599
PRDX2_MOUSE	7	2	0.396656	Peroxiredoxin-2 Prdx2	6435.696	7586.849	4788.510
ABI1_MOUSE	5	2	0.396933	Abl interactor 1 Abi1	4165.480	3761.232	5278.661
SNAG_MOUSE	5	1	0.39852	Gamma-soluble NSF attachment protein Napg	143.100	0.077	1.917
SNX9_MOUSE	6	1	0.398722	Sorting nexin-9 Snx9	252.919	2431.868	1420.549
TCPH_MOUSE	36	15	0.399398	T-complex protein 1 subunit eta Cct7	22739.933	23230.905	20484.034
HMCS1_MOUSE	5	2	0.40272	Hydroxymethylglutaryl-CoA synthase, cytoplasmic Hmgcs1	3456.826	4864.894	3890.568
AQP5_MOUSE	8	3	0.407547	Aquaporin-5 Aqp5	11040.918	9522.750	10586.870
DCK_MOUSE	3	1	0.409504	Deoxycytidine kinase Dck	2565.301	3104.438	1788.724
RAB10_MOUSE	14	3	0.411917	Ras-related protein Rab-10 Rab10	977.247	474.152	403.914

VPS28_MOUSE	10	3	0.41236	Vacuolar protein sorting-associated protein 28 homolog Vps28	306.575	67.879	19.405
CA2D1_MOUSE	15	2	0.413658	Voltage-dependent calcium channel subunit alpha-2/delta-1 Cacna2d1	2683.157	2023.116	2846.835
RS17_MOUSE	12	7	5		14416.638	6893.141	8341.367
RHOA_MOUSE	6	1	0.41795	40S ribosomal protein S17 Rps17	364.443	0.000	0.000
			0.421875	Transforming protein RhoA Rhoa			

RB22A_MOUSE	4	1	0.425687	Ras-related protein Rab-22A Rab22a	2.465	93.998	31.238
AMPL_MOUSE	6	2	0.427328	Cytosol aminopeptidase Lap3	1584.410	1218.088	926.189
KI13A_MOUSE	13	3	0.428614	Kinesin-like protein KIF13A Kif13a	215.745	595.990	572.286
CA087_MOUSE	9	1	0.428631	Uncharacterized protein C1orf87 homolog Gm12695	1602.596	710.398	616.688
SHLB1_MOUSE	9	2	0.435905	Endophilin-B1 Sh3glb1	408.796	198.593	71.841
ADAD1_MOUSE	8	5	0.437056	Adenosine deaminase domain-containing protein 1 Adad1	3897.542	4354.888	5668.626
BZW1_MOUSE	6	1	0.437764	Basic leucine zipper and W2 domain-containing protein 1 Bzw1	738.061	512.811	759.088
KCIP1_MOUSE	6	2	0.439433	Kv channel-interacting protein 1 Kcnip1	3746.619	7543.983	3167.948
PRS4_MOUSE	23	3	0.440462	26S proteasome regulatory subunit 4 Psmc1	2390.785	4300.621	4560.451
CPT1B_MOUSE	9	3	0.442528	Carnitine O-palmitoyltransferase 1, muscle isoform Cpt1b	2851.301	4647.133	3695.842
TM1L2_MOUSE	3	1	0.445391	TOM1-like protein 2 Tom1l2	304.878	55.458	225.033
LASP1_MOUSE	4	3	0.44725	LIM and SH3 domain protein 1 Lasp1	853.742	835.426	514.362
ELOB_MOUSE	2	1	0.450625	Elongin-B Elob	376.341	555.284	2135.919
EIF3L_MOUSE	8	1	0.453939	Eukaryotic translation initiation factor 3 subunit L Eif3l	7.678	129.229	134.900
LUZP1_MOUSE	26	2	0.459748	Leucine zipper protein 1 Luzp1	8795.392	6337.715	7025.215

AT1A2_MOUSE	14	1	0.460332	Sodium/potassium-transporting ATPase subunit alpha-2 Atp1a2	500.276	406.931	475.535
ASPD_MOUSE	4	1			0.000	412.154	0.363
INSR_MOUSE	10	2	0.461821	Putative L-aspartate dehydrogenase Aspdh	11752.110	6914.572	7593.787
			0.466817	Insulin receptor Insr			
PHLB1_MOUSE	18	2	0.468883	Pleckstrin homology-like domain family B member 1 Phldb1	700.206	135.811	578.562
RAB25_MOUSE	5	1	0.47099	Ras-related protein Rab-25 Rab25	1664.100	5521.903	8723.728
PGFRB_MOUSE	6	1	0.471262	Platelet-derived growth factor receptor beta Pdgfrb	758.779	1087.277	834.181
TAF1_MOUSE	38	4	0.471534	Transcription initiation factor TFIID subunit 1 Taf1	7204.673	7301.558	8850.754
GDIR1_MOUSE	10	6	0.475402	Rho GDP-dissociation inhibitor 1 Arhgdia	21268.661	24250.368	27717.405
TWF1_MOUSE	3	1	0.476073	Twinfilin-1 Twf1	629.498	954.531	770.369

SYEP_MOUSE	32	7	0.480768	Bifunctional glutamate/proline--tRNA ligase Eprs	4324.408	5423.818	5670.522
CHP1_MOUSE	2	1		0.480818 Calcineurin B homologous protein	4468.607		4476.228
ANXA2_MOUSE	51	26	1 Chp1	3026.127			138287.797
			0.482696	Annexin A2 Anxa2	95165.281	116331.008	
CHM4B_MOUSE	6	2	0.485585	Charged multivesicular body protein 4b Chmp4b	3121.858	3996.396	3634.128
SRSF3_MOUSE	3	1	0.490583	Serine/arginine-rich splicing factor 3 Srsf3	23.684	326.153	215.099
PCNA_MOUSE	4	1	0.499772	Proliferating cell nuclear antigen Pcna	879.806	202.438	895.619
RASH_MOUSE	7	1				252.091	649.125
PSB3_MOUSE	5	3		0.5001 GTPase HRas Hras		14133.262	7934.274
				60.410			
			0.50213	Proteasome subunit beta type-3 Psmb3	5556.727		
PLCH1_MOUSE	14	4	0.504656	1-phosphatidylinositol 4,5-bisphosphate	5581.124	7924.255	5708.646

				phosphodiesterase eta-1 Plch1			
BLOM7_MOUSE	5	2	0.505024	Protein BLOM7 Kiaa0907	814.638	508.499	498.362
CHMP3_MOUSE	3	1	0.506707	Charged multivesicular body protein 3 Chmp3	236.515	25.096	130.041
ACADL_MOUSE	5	2	0.508028	Long-chain specific acyl-CoA dehydrogenase, mitochondrial Acadl	1137.420	898.626	781.212
ABCAH_MOUSE	12	2	0.508241	ATP-binding cassette sub-family A member 17 Abca17	434.179	346.270	264.035
SPB6_MOUSE	15	4	0.510345	Serpin B6 Serpinb6	786.906	967.000	1130.977
CPNE2_MOUSE	6	1	0.513383	Copine-2 Cpne2	106.517	537.688	550.241
RBM28_MOUSE	10	1	0.514538	RNA-binding protein 28 Rbm28	469.047	2581.645	1437.998
GLYC_MOUSE	7	2	0.515369	Serine hydroxymethyltransferase, cytosolic Shmt1	14542.158	10560.095	11239.736
ERBB2_MOUSE	10	1	0.516373	Receptor tyrosine-protein kinase erbB-2 Erbb2	97.498	1683.265	772.843
RRP1B_MOUSE	14	2	0.516379	Ribosomal RNA processing protein 1 homolog B Rrp1b	1391.616	2588.588	3210.354
OAT_MOUSE	6	4	0.517832	Ornithine aminotransferase, mitochondrial Oat	2965.137	4800.047	3677.543
LRC57_MOUSE	4	1	0.519551	Leucine-rich repeat-containing protein 57 Lrrc57	325.300	268.331	66.020
TSP1_MOUSE	18	3	0.519933	Thrombospondin-1 Thbs1	323.220	764.341	542.546
RL27_MOUSE	5	1	0.521812	60S ribosomal protein L27 Rpl27	776.775	1497.087	1563.800

ODP2_MOUSE	8	1	0.521855	Dihydrolipoyllysine-residue acetyltransferase component of pyruvate dehydrogenase complex, mitochondrial Dlat	535.093	390.470	406.849
YKT6_MOUSE	3	2	0.522358	Synaptobrevin homolog YKT6 Ykt6	648.762	2552.300	2996.169
NSDHL_MOUSE	4	2	0.526207	Sterol-4-alpha-carboxylate 3dehydrogenase, decarboxylating Nsdhl	2497.706	1872.489	1488.241
CD44_MOUSE	10	4	0.528803	CD44 antigen Cd44	3629.334	2498.783	2803.930
RASL2_MOUSE	10	1	0.529267	Ras GTPase-activating protein 4 Rasa4	1599.231	2353.623	1704.929
ENV1_MOUSE	12	3		MLV-related proviral Env polyprotein	3875.167	2392.800	1511.517
FRIL1_MOUSE	4	2	69 0.5295 0.535962	Ferritin light chain 1 Ftl1	5548.076	4919.520	5332.139
RS23_MOUSE	7	3	0.538608	40S ribosomal protein S23 Rps23	3402.123	2470.553	3449.228
RHOG_MOUSE	5	1	0.539804	Rho-related GTP-binding protein RhoG Rhog	910.095	1147.467	1093.280
XKR7_MOUSE	4	1	0.539955	XK-related protein 7 Xkr7	15.687	1.990	0.000
CTF8A_MOUSE	3	1	0.541255	Chromosome transmission fidelity protein 8 homolog isoform 2 Chtf8	988.620	640.602	522.437
2AAA_MOUSE	22	3	0.543061	Serine/threonine-protein phosphatase 2A 65 kDa regulatory subunit A alpha isoform Ppp2r1a	894.533	1112.546	1397.825
MMS19_MOUSE	6	2	0.543821	MMS19 nucleotide excision repair protein homolog Mms19	20.756	45.759	97.552
MBB1A_MOUSE	28	6	0.54498	Myb-binding protein 1A Mybbp1a	2230.905	3902.426	2827.650
ILEUA_MOUSE	3	2	0.545264	Leukocyte elastase inhibitor A Serpinb1a	890.985	3694.448	1574.254
RAB23_MOUSE	10	3		Ras-related protein Rab-23 Rab23	1232.977	1652.343	1639.338
RTN4_MOUSE	9	3	0.545694 0.545834	Reticulon-4 Rtn4	2425.744	2876.044	3678.380
PASK_MOUSE	8	4	0.54592	PAS domain-containing serine/threonineprotein kinase Pask	9611.692	13822.434	8800.360

SODM_MOUSE	4	1	0.546169	Superoxide dismutase [Mn], mitochondrial Sod2	881.818	445.572	1278.766
ARF1_MOUSE	9	1	0.547203	ADP-ribosylation factor 1 Arf1	52.446	238.357	114.896
STX2_MOUSE	2	1	0.548078	Syntaxin-2 Stx2	166.074	0.000	4.011
XPO2_MOUSE	30	9		Exportin-2 Cse1l	2052.112	3069.383	2890.206
RAP1B_MOUSE	8	2		Ras-related protein Rap-1b Rap1b	2110.721	1242.518	1010.947
			0.549331 0.55585				
H2A1B_MOUSE	2	1	0.560648	Histone H2A type 1-B Hist1h2ab	382.426	305.671	197.084

EFTU_MOUSE	7	1	0.56137 0.562376	Elongation factor Tu, mitochondrial Tufm	123.904	36.627	186.331
GMPR2_MOUSE	5	1		GMP reductase 2 Gmpr2	11.431	17.622	81.699
ANX11_MOUSE	12	5		Annexin A11 Anxa11	6453.015	6515.063	7881.064
CUX2_MOUSE	14	1	0.562397 0.563048	Homeobox protein cut-like 2 Cux2	653.916	64.365	275.535
CALX_MOUSE	7	3	0.565068	Calnexin Canx	1793.619	1533.362	1149.635
AT135_MOUSE	5	3	0.56542	Probable cation-transporting ATPase 13A5 Atp13a5	6978.726	10429.128	8008.925
LOXL3_MOUSE	8	1	0.56595	Lysyl oxidase homolog 3 Loxl3	597.406	550.149	856.093
RAB34_MOUSE	5	2	0.567368	Ras-related protein Rab-34 Rab34	905.066	558.708	578.288
TCPB_MOUSE	51	14		T-complex protein 1 subunit beta Cct2	21763.571	25510.847	25042.620
A1CF_MOUSE	6	1	0.567464 0.567846	APOBEC1 complementation factor A1cf	6614.613	9316.622	8211.632
DMRTA_MOUSE	12	2	0.569485	Doublesex- and mab-3-related transcription factor A1 Dmrta1	4241.335	7452.931	11670.566
AT1B3_MOUSE	6	3	0.571705	Sodium/potassium-transporting ATPase subunit beta-3 Atp1b3	3525.574	3144.301	2743.006

SYFA_MOUSE	7	2	0.57412	Phenylalanine--tRNA ligase alpha subunit Farsa	941.963	2621.182	1433.324
NEBL_MOUSE	4	1	0.575633	Nebulette Nebl	13.327	7.080	443.945
BMP1_MOUSE	9	1	0.579437	Bone morphogenetic protein 1 Bmp1	343.929	483.278	630.904
SDHA_MOUSE	10	1	0.579621	Succinate dehydrogenase [ubiquinone] flavoprotein subunit, mitochondrial Sdha	98.637	16.570	27.331
CDC42_MOUSE	8	5	0.580466	Cell division control protein 42 homolog Cdc42	1141.199	384.890	496.552
STIL_MOUSE	9	3	0.587651 0.597221	SCL-interrupting locus protein homolog Stil	1276.107	2178.514	3266.946
INT7_MOUSE	6	1		Integrator complex subunit 7 Ints7	2650.480	3546.034	2114.527
CLIP1_MOUSE	13	1	0.597916	CAP-Gly domain-containing linker protein 1 Clip1	243.477	2622.512	1729.666
SYRC_MOUSE	15	2	0.59864 0.600153	Arginine--tRNA ligase, cytoplasmic Rars	590.597	384.970	640.253
TADBP_MOUSE	6	4		TAR DNA-binding protein 43 Tardbp	1862.504	1644.940	1465.345
ARHGG_MOUSE	11	2	0.600304	Rho guanine nucleotide exchange factor 16 Arhgef16	7414.100	17310.469	12617.845
MB12A_MOUSE	6	3	0.60411 0.608471	Multivesicular body subunit 12A Mvb12a	823.150	568.316	883.890
PRAF2_MOUSE	3	2		PRA1 family protein 2 Praf2	1482.462	1257.060	1756.329
FLNB_MOUSE	57	10		Filamin-B Flnb	7559.652	6705.259	7283.580
RAB1B_MOUSE	12	3	0.608662 0.610489	Ras-related protein Rab-1B Rab1b	2988.773	1752.378	2047.573
RAB7A_MOUSE	10	3	0.614789	Ras-related protein Rab-7a Rab7a	6971.074	7925.621	7180.117
RL27A_MOUSE	2	1	0.615619	60S ribosomal protein L27a Rpl27a	8095.932	1716.566	1481.476
FLNA_MOUSE	108	32	0.618914	Filamin-A Flna	53394.487	58801.481	56306.211

UB2D3_MOUSE	2	1	0.622888	Ubiquitin-conjugating enzyme E2 D3 Ube2d3	1464.247	1046.976	1098.458
GFAP_MOUSE	4	1	0.625608	Glial fibrillary acidic protein Gfap	998.638	1119.560	1319.669
HXK1_MOUSE	16	4	0.625983	Hexokinase-1 Hk1	1779.842	1659.792	1869.374
E41L5_MOUSE	7	2		Band 4.1-like protein 5 Epb41l5	71.554	29.341	149.743
MYO10_MOUSE	19	5	0.628565 0.6361	Unconventional myosin-X Myo10	3068.628	6718.529	5034.831
ARP3_MOUSE	7	2	0.640159	Actin-related protein 3 Actr3	7953.051	7674.256	6581.533
PSA_MOUSE	8	3	0.644584	Puromycin-sensitive aminopeptidase Npepps	3917.978	2433.652	3474.312
PSD11_MOUSE	13	1	0.647027	26S proteasome non-ATPase regulatory subunit 11 Psmd11	1688.465	1327.560	1482.302
NACAM_MOUSE	26	6	0.650422	Nascent polypeptide-associated complex subunit alpha, muscle-specific form Naca	2982.628	2971.861	2473.184
GBB2_MOUSE	6	1	0.650736	Guanine nucleotide-binding protein G(I)/G(S)/G(T) subunit beta-2 Gnb2	5160.490	1398.438	2482.568
GNA13_MOUSE	6	2	0.654683	Guanine nucleotide-binding protein subunit alpha-13 Gna13	894.868	661.222	611.181
RS18_MOUSE	13	5	0.655497	40S ribosomal protein S18 Rps18	3833.668	4419.500	3127.681
ALBU_MOUSE	13	3	0.656824	Serum albumin Alb	142.032	184.352	386.749
CCM2_MOUSE	6	1	0.656879	Cerebral cavernous malformations protein 2 homolog Ccm2	78.832	18.814	25.577
KAD1_MOUSE	2	1	0.658846	Adenylate kinase isoenzyme 1 Ak1	2013.129	2825.868	2146.122
EF1B_MOUSE	3	1	0.661418	Elongation factor 1-beta Eef1b	1839.228	1815.261	1550.296
SNX3_MOUSE	1	1		Sorting nexin-3 Snx3	1738.353	779.975	841.649
ASAH1_MOUSE	5	1	0.663725 0.66459	Acid ceramidase Asah1	92.562	387.124	162.469
RAB5C_MOUSE	13	4	0.669467	Ras-related protein Rab-5C Rab5c	2484.607	3673.966	2553.730

SND1_MOUSE	12	1	0.670195	Staphylococcal nuclease domain-containing protein 1 Snd1	2646.424	3295.938	3528.560
PDLI4_MOUSE	3	1	0.670523	PDZ and LIM domain protein 4 Pdlim4	268.120	316.679	456.513
RB11A_MOUSE	9	4	0.678023	Ras-related protein Rab-11A Rab11a	4565.598	8552.342	7351.572
COF2_MOUSE	7	2	0.67855	Cofilin-2 Cfl2	3561.489	2606.024	4221.979

EF1A1_MOUSE	27	11	0.678596	Elongation factor 1-alpha 1 Eef1a1	54617.508	50387.789	56217.387
HNRPU_MOUSE	15	5	0.678716	Heterogeneous nuclear ribonucleoprotein U Hnrnpu	6820.366	9514.611	7841.463
RAB6B_MOUSE	6	2	0.678957	Ras-related protein Rab-6B Rab6b	956.199	1461.816	1010.038
SRSF2_MOUSE	4	3	0.684823	Serine/arginine-rich splicing factor 2 Srsf2	3174.192	2964.280	2596.743
PROF1_MOUSE	7	4		Profilin-1 Pfn1	3704.611	1114.587	1917.254
XRP2_MOUSE	5	1		Protein XRP2 Rp2	2334.965	2846.591	2193.793
			0.685978				
			0.686852				
PDIA6_MOUSE	10	1	0.688382	Protein disulfide-isomerase A6 Pdia6	1433.073	518.525	829.720
A16A1_MOUSE	8	1	0.6893	Aldehyde dehydrogenase family 16 member A1 Aldh16a1	401.965	357.465	256.933
HSP72_MOUSE	35	1	0.690328	Heat shock-related 70 kDa protein 2 Hspa2	1796.233	1187.512	1413.249
HNRPQ_MOUSE	9	4	0.690893	Heterogeneous nuclear ribonucleoprotein Q Syncrip	1861.409	1885.826	1459.029
LTOR1_MOUSE	3	1	0.691996	Ragulator complex protein LAMTOR1 Lamtor1	1684.208	1333.741	1396.066
RAB18_MOUSE	5	2	0.695766	Ras-related protein Rab-18 Rab18	1885.531	2772.688	2540.011
AP2B1_MOUSE	28	2	0.698	AP-2 complex subunit beta Ap2b1	746.010	863.989	617.915
RL31_MOUSE	5	1	0.702419	60S ribosomal protein L31 Rpl31	66.942	34.572	80.142
HBE_MOUSE	2	1	0.702711	Hemoglobin subunit epsilon-Y2 Hbb-y	702.117	413.555	745.182
CATB_MOUSE	1	1		Cathepsin B Ctsb	319.638	50.236	528.788

RL18A_MOUSE	6	1	0.703068 0.706121	60S ribosomal protein L18a Rpl18a				191.689
ANXA5_MOUSE	29	12	0.708031 0.709445	Annexin A5 Anxa5				10266.303
ACTN1_MOUSE	25	6		Alpha-actinin-1 Actn1	195.158	1427.850		2759.313
EHD1_MOUSE	35	7	0.710844	EH domain-containing protein 1 Ehd1	12165.091 3829.074 15222.729	9942.888 3696.395 17588.659		18634.262
ASPM_MOUSE	51	6	0.711759	Abnormal spindle-like microcephalyassociated protein homolog Aspm	3643.206		6643.297	5288.577
AAKG1_MOUSE	7	2	0.715462	5'-AMP-activated protein kinase subunit gamma-1 Prkag1	467.386		779.969	744.105
RB6I2_MOUSE	18	4	0.715993	ELKS/Rab6-interacting/CAST family member 1 Erc1	1927.428		2392.593	1740.924
RL24_MOUSE	7	3	0.719172	60S ribosomal protein L24 Rpl24	5565.211		3602.904	4700.701
RRAS_MOUSE	13	2	0.731834	Ras-related protein R-Ras Rras	877.852		850.982	634.833
RINI_MOUSE	13	4		Ribonuclease inhibitor Rnh1	750.304		1502.417	744.086
STIP1_MOUSE	15	3	0.732552 0.734685	Stress-induced-phosphoprotein 1 Stip1	1961.392		1444.001	1407.350

SIG10_MOUSE	3	1	0.73634	Sialic acid-binding Ig-like lectin 10 Siglec10	3354.553	3927.288	5098.834
CSN6_MOUSE	1	1	0.736777	COP9 signalosome complex subunit 6 Cops6	179.323	36.902	59.964
FBX4_MOUSE	2	1	0.737921	F-box only protein 4 Fbxo4	437.165	303.034	146.072

ABCE1_MOUSE	11	1	0.738459	ATP-binding cassette sub-family E member 1 Abce1	322.802	546.201	789.064
CK071_MOUSE	3	2	0.739913	Uncharacterized protein C11orf71 homolog Gm5617	1298.807	2134.951	1669.648
ALDOA_MOUSE	19	6	0.745373	Fructose-bisphosphate aldolase A Aldoa	9569.584	13309.739	9485.792
VPS16_MOUSE	9	3	0.747581	Vacuolar protein sorting-associated protein 16 homolog Vps16	2208.317	2135.020	1779.022
TBA4A_MOUSE	21	1	0.74822	Tubulin alpha-4A chain Tuba4a	1038.009	1418.523	1917.074
RS4X_MOUSE	14	5	0.748893	40S ribosomal protein S4, X isoform Rps4x	9984.353	6534.724	7241.934
RM28_MOUSE	4	1	0.753491	39S ribosomal protein L28, mitochondrial Mrpl28	1647.854	676.916	719.659
PAK1_MOUSE	8	2	0.754463	Serine/threonine-protein kinase PAK 1 Pak1	207.483	94.371	146.691
PLPP4_MOUSE	3	1	0.760186	Phospholipid phosphatase 4 Plpp4	159.920	428.884	877.665
CD82_MOUSE	14	4	0.761618	CD82 antigen Cd82	10784.298	8098.077	7937.260
UB2V1_MOUSE	6	2	0.762822	Ubiquitin-conjugating enzyme E2 variant 1 Ube2v1	4446.682	3435.638	4318.847
TSN14_MOUSE	4	2	0.770825	Tetraspanin-14 Tspan14	2141.224	798.636	699.291
LEG3_MOUSE	6	2	0.774453	Galectin-3 Lgals3	3051.375	2415.243	2401.529
MCA3_MOUSE	3	1	0.779928	Eukaryotic translation elongation factor 1 epsilon-1 Eef1e1	583.434	1240.691	1540.360
KMT2A_MOUSE	32	10	0.780551	Histone-lysine N-methyltransferase 2A Kmt2a	16414.173	20352.447	15057.117
FAT4_MOUSE	21	3	0.784168	Protocadherin Fat 4 Fat4	577.953	1287.716	1770.656
PRDX5_MOUSE	7	2	0.784356	Peroxiredoxin-5, mitochondrial Prdx5	1557.655	1144.439	1858.276
DNJA2_MOUSE	10	1	0.784818	DnaJ homolog subfamily A member 2 Dnaja2	102.142	146.628	198.933
ECM1_MOUSE	5	3	0.789232	Extracellular matrix protein 1 Ecm1	1931.546	1796.503	2057.876
CMTA1_MOUSE	15	4	0.791073	Calmodulin-binding transcription activator 1 Camta1	1313.432	728.657	1998.277

TCTP_MOUSE	6	4	0.791804	Translationally-controlled tumor protein Tpt1	2736.177	2299.700	2213.620

NHRF1_MOUSE	5	2	0.80038	Na(+)/H(+) exchange regulatory cofactor NHE-RF1 Slc9a3r1	349.520	339.173	236.274
PSD13_MOUSE	10	3	0.804013	26S proteasome non-ATPase regulatory subunit 13 Psmd13	3125.218	3337.686	3584.535
TRI59_MOUSE	2	1	0.805279	Tripartite motif-containing protein 59 Trim59	94.807	504.112	412.440
EIF3A_MOUSE	40	7	0.811328	Eukaryotic translation initiation factor 3 subunit A Eif3a	7344.383	8896.140	8985.515
ABCC9_MOUSE	8	2	0.812364	ATP-binding cassette sub-family C member 9 Abcc9	2404.148	1583.751	2801.573
LMNA_MOUSE	31	10	0.815976	Prelamin-A/C Lmna	24615.067	36896.838	32265.079
PACN3_MOUSE	8	2	0.818294	Protein kinase C and casein kinase II substrate protein 3 Pacsin3	1599.681	1801.550	1742.731
RIMS2_MOUSE	23	1	0.826587	Regulating synaptic membrane exocytosis protein 2 Rims2	313.297	228.151	155.046
TPM3_MOUSE	10	2	0.828244	Tropomyosin alpha-3 chain Tpm3	1075.922	1049.096	757.811
SYVC_MOUSE	58	16	0.830322	Valine--tRNA ligase Vars	28787.268	28821.905	32072.896
ARPC4_MOUSE	5	2	0.83129	Actin-related protein 2/3 complex subunit 4 Arpc4	607.247	1502.112	2767.773
TRI18_MOUSE	9	3	0.833104	E3 ubiquitin-protein ligase Midline-1 Mid1	1056.256	939.572	1000.017
RL23A_MOUSE	7	3	0.83469	60S ribosomal protein L23a Rpl23a	11491.391	12063.959	12198.189
RPAB3_MOUSE	2	1	0.836008	DNA-directed RNA polymerases I, II, and III subunit RPABC3 Polr2h	156.207	139.123	68.645
DCTN2_MOUSE	4	1	37476	Dynactin subunit 2 Dctn2	172.471	131.365	19.410
RS3_MOUSE	35	14	0.8		22729.763	16847.931	22392.860

			0.837817	40S ribosomal protein S3 Rps3			
TOM22_MOUSE	1	1	0.838515	Mitochondrial import receptor subunit TOM22 homolog Tomm22	448.891	392.321	585.754
NONO_MOUSE	10	1	0.840888	Non-POU domain-containing octamer-binding protein Nono	44.426	61.544	19.196
RS16_MOUSE	14	7	0.844145	40S ribosomal protein S16 Rps16	23465.638	17429.964	27412.390
RPN2_MOUSE	2	1	0.846282	Dolichyl-diphosphooligosaccharide--protein glycosyltransferase subunit 2 Rpn2	54.241	23.080	21.308
HMGA1_MOUSE	2	2	0.849029	High mobility group protein HMG-I/HMG-Y Hmga1	852.137	439.299	172.142
MY18A_MOUSE	26	4	0.851332	Unconventional myosin-XVIIIa Myo18a	6222.534	9559.170	8919.332

PUR2_MOUSE	5	1	0.851571	Trifunctional purine biosynthetic protein adenosine-3 Gart	5792.692	4988.985	4459.756
MAP1A_MOUSE	20	2	0.853139	Microtubule-associated protein 1A Map1a	459.021	1358.458	1045.923
ADT4_MOUSE	11	1	0.856783	ADP/ATP translocase 4 Slc25a31	686.879	603.283	744.293
SMAD1_MOUSE	4	2	0.857501	Mothers against decapentaplegic homolog 1 Smad1	1884.299	1773.630	1041.803
RHOB_MOUSE	4	1	0.858335	Rho-related GTP-binding protein RhoB Rhob	925.726	708.384	1180.282
AP2M1_MOUSE	12	1			254.314	234.083	240.161
ANXA3_MOUSE	29	15	0.859464 0.859928	AP-2 complex subunit mu Ap2m1 Annexin A3 Anxa3	44557.222	44038.158	39966.294
TPPC3_MOUSE	3	1	0.863409	Trafficking protein particle complex subunit 3 Trappc3	2331.374	2400.583	2307.687
ATPO_MOUSE	12	5	0.86844	ATP synthase subunit O, mitochondrial	1819.509	1954.307	2094.923

				Atp5o			
RT23_MOUSE	5	1	0.868573	28S ribosomal protein S23, mitochondrial Mrps23	78.464	79.247	108.154
PYGM_MOUSE	15	1	0.868814	Glycogen phosphorylase, muscle form Pygm	24.982	35.919	14.684
HBA_MOUSE	5	1	0.871307	Hemoglobin subunit alpha Hba	338.666	43.014	72.042
BIRC6_MOUSE	27	5	0.872305	Baculoviral IAP repeat-containing protein 6 Birc6	8961.082	9590.515	9190.769
SRSF7_MOUSE	5	2	0.878837	Serine/arginine-rich splicing factor 7 Srsf7	756.335	699.946	609.701
PPIB_MOUSE	5	1	0.881917	Peptidyl-prolyl cis-trans isomerase B Ppib	2112.683	2177.569	1968.821
FSIP2_MOUSE	52	7	0.882222	Fibrous sheath-interacting protein 2 Fsip2	10370.955	10002.336	8972.180
PFD2_MOUSE	2	1	0.883544	Prefoldin subunit 2 Pfdn2	1154.698	1154.634	1972.938
FANCM_MOUSE	14	3	0.884852	Fanconi anemia group M protein homolog Fancm	1322.949	1878.127	1369.772
LMX1B_MOUSE	1	1	0.885746	LIM homeobox transcription factor 1-beta Lmx1b	891.346	736.937	244.614
TLN2_MOUSE	49	6	0.892099	Talin-2 Tln2	1210.269	1114.350	1095.346
SORCN_MOUSE	5	1	0.895558	Sorcin Sri	2663.098	3039.778	2713.671
IF5A1_MOUSE	4	2	0.898665	Eukaryotic translation initiation factor 5A-1 Eif5a	779.324	820.514	499.471
RL12_MOUSE	6	3			16605.602	11311.987	17318.493
USH2A_MOUSE	26	2	0.900049 0.901797	60S ribosomal protein L12 Rpl12 Usherin Ush2A	7546.050	6261.555	3927.950
HMGA2_MOUSE	1	1	0.903431	High mobility group protein HMGI-C Hmga2	1126.389	1565.526	1073.485

DUS3_MOUSE	6	1	0.90403	Dual specificity protein phosphatase 3 Dusp3	580.301	161.245	169.238
PPIA_MOUSE	15	5	0.904593	Peptidyl-prolyl cis-trans isomerase A Ppia	9081.240	2722.617	2179.308
CAR19_MOUSE	8	1	0.906798	Caspase recruitment domain-containing protein 19 Card19	218.901	2861.699	350.905
NSMF_MOUSE	19	7	0.90693	NMDA receptor synaptonuclear signaling and neuronal migration factor Nsmf	8941.882	9852.664	9375.057
AATM_MOUSE	11	3	0.917414	Aspartate aminotransferase, mitochondrial Got2	1976.517	1712.960	2211.576
PUR9_MOUSE	13	4	0.921156	Bifunctional purine biosynthesis protein PURH Atic	1873.609	1281.519	1330.420
AAAT_MOUSE	7	2	0.922282	Neutral amino acid transporter B(0) Slc1a5	1842.901	2249.539	2460.594
IDI1_MOUSE	5	1	0.932926	Isopentenyl-diphosphate Delta-isomerase 1 Idi1	140.536	32.153	11.450
H2A2A_MOUSE	5	1	0.935052	Histone H2A type 2-A Hist2h2aa1	890.176	1068.667	893.352
LIN7C_MOUSE	6	1	0.937473	Protein lin-7 homolog C Lin7c	1977.952	699.446	774.210
FYCO1_MOUSE	7	2	0.939478	FYVE and coiled-coil domain-containing protein 1 Fyco1	909.370	1071.813	840.293
UBR4_MOUSE	81	18	0.939709	E3 ubiquitin-protein ligase UBR4 Ubr4	10624.850	10337.883	11346.372
PEBP1_MOUSE	4	2	0.939913	Phosphatidylethanolamine-binding protein 1 Pebp1	2821.705	2753.897	1719.000
GLPC_MOUSE	2	2	0.943096	Glycophorin-C Gypc	831.877	410.970	234.684
PRS6B_MOUSE	15	6	0.94361	26S proteasome regulatory subunit 6B Psmc4	1867.196	1893.421	1807.891
UNC80_MOUSE	28	5	6	Protein unc-80 homolog Unc80	4202.613	4138.320	5887.994
H2B1P_MOUSE	10	1	0.94777 0.950145	Histone H2B type 1-P Hist1h2bp	2815.686	1622.384	1750.400
TRIPC_MOUSE	19	3	0.951466	E3 ubiquitin-protein ligase TRIP12 Trip12	4518.988	6084.415	10186.027

G3BP1_MOUSE	2	1	0.951802	Ras GTPase-activating protein-binding protein 1 G3bp1	327.576		680.535	773.526
ECHA_MOUSE	10	3	0.955238	Trifunctional enzyme subunit alpha, mitochondrial Hadha	647.082		360.306	299.400
ARHG2_MOUSE	13	1	0.955431	Rho guanine nucleotide exchange factor 2 Arhgef2	2484.658		1546.550	1513.342
GLT14_MOUSE	5	2	0.956893	Polypeptide Nacetylgalactosaminyltransferase 14 Galnt14	43.979		47.182	109.865
NIPA_MOUSE	2	1	0.961474	Nuclear-interacting partner of ALK Zc3hc1				2313.684
HSP7C_MOUSE	62	15	0.963594	Heat shock cognate 71 kDa protein Hspa8	1916.430 86924.541	4264.281	80724.687	84143.192
CB078_MOUSE	6	2	0.963682	Uncharacterized protein C2orf78 homolog Gm5592	383.668		571.021	516.434
IQGA1_MOUSE	48	21	0.96595	Ras GTPase-activating-like protein IQGAP1 Iqgap1	23263.171		22578.579	23050.794
ILK_MOUSE	12	4	0.967561	Integrin-linked protein kinase Ilk	314.821		253.747	274.002
DCTN3_MOUSE	6	2	0.971328	Dynactin subunit 3 Dctn3	3654.148		4111.484	4743.610
S12A1_MOUSE	10	2		Solute carrier family 12 member 1 Slc12a1	3829.444		3662.602	3759.093
STEA3_MOUSE	5	2	0.972003 0.973357	Metalloreductase STEAP3 Steap3	667.914		684.047	745.371
GLT13_MOUSE	7	2	0.976815	Polypeptide Nacetylgalactosaminyltransferase 13 Galnt13	1109.603		581.952	542.538
TMOD3_MOUSE	5	3	0.977801	Tropomodulin-3 Tmod3	796.245		716.507	766.249
PRDX6_MOUSE	7	4	0.978474	Peroxiredoxin-6 Prdx6	2198.944		2260.675	2221.398
CSK21_MOUSE	3	1		Casein kinase II subunit alpha Csnk2a1	525.221		70.334	92.395
ECD_MOUSE	6	2	0.978843 0.980471	Protein ecdysoneless homolog Ecd	4158.478		3815.630	4672.913

CSKI2_MOUSE	7	1	0.983042	Caskin-2 Caskin2	1640.330	932.063	2177.087
LRGUK_MOUSE	8	1	0.985195	Leucine-rich repeat and guanylate kinase domain-containing protein Lrguk	5625.786	7603.925	5985.756
GDIB_MOUSE	21	6	0.997897	Rab GDP dissociation inhibitor beta Gdi2	3139.613	3043.806	3799.609

Table 8. Proteins identified in normal, sarcopenic and senescent myotube derived EVs using bottom-up proteomics. Proteins with 1 or more unique peptide sequence were considered to be identified when searched against the UniProt database. Proteins were quantified using Progenesis QI proteomics software. Data shown are of 3 biological repeats, which allowed for an ANOVA statistical test.

					Normalised abundance		
UniProt ID	**Peptide count**	**Unique peptides**	**Anova (p)**	**Protein name**	**Normal EVs**	**Sarcopenic EVs**	**Senescent EVs**
TAF7_MOUSE	1	1	6.32E-09	Transcription initiation factor TFIID subunit 7 Taf7	9559.740	2244.233	1804.695
EST1F_MOUSE	1	1	1.10E-08	Carboxylesterase 1F Ces1f	16767.519	2536.414	2714.484
DPYL3_MOUSE	10	7	1.18E-08	Dihydropyrimidinase-related protein 3 Dpysl3	136710.918	21515.861	20298.152
CFAH_MOUSE	11	11	2.09E	Complement factor H Cfh	4318.747	11806.529	3671.935
LBP_MOUSE	8	8	-08			12128.296	1812.813
			-08	2.57ELipopolysaccharide-binding protein Lbp	2044.087		
FBLN1_MOUSE	10	9	2.88E-08	Fibulin-1 Fbln1	5314.769	27531.402	5067.844
ATPA_MOUSE	12	10	3.93E-08	ATP synthase subunit alpha, mitochondrial Atp5f1a	1099.902	3607.646	4475.866
XKR6_MOUSE	1	1	-08	6.63EXK-related protein 6 Xkr6			133.151
GPC1_MOUSE	15	14	-08		1755.232	123.818	139714.264
					37361.252	121722.943	
					224692.009	18834.390	

			7.54E	Glypican-1	Gpc1			
OTOG_MOUSE	1	1	7.74E	Otogelin	Otog			18004.139
TRFE_MOUSE	4	3	-08				6724.181	8057.829
			-08 7.88E	Serotransferrin	Tf			
PZP_MOUSE	6	4				30060.260	15088.586	14350.743
			8.24E	Pregnancy zone protein	Pzp	113085.790		
TLN1_MOUSE	34	32	-08				9860.558	8204.969
			-08 8.33E	Talin-1	Tln1	20448.021		
ACM4_MOUSE	1	1	1.08E-07	Muscarinic acetylcholine receptor M4	Chrm4	40815.098	4621.833	3830.144
CYHR1_MOUSE	1	1	1.42E-07	Cysteine and histidine-rich protein 1	Cyhr1	67062.270	6498.852	7168.200
CO4A1_MOUSE	5	5	1.57E-07	Collagen alpha-1(IV) chain	Col4a1	810.380	4581.518	813.318
CBPN_MOUSE	1	1	2.19E-07	Carboxypeptidase N catalytic chain	Cpn1	154.610	0.014	0.824
CHP1_MOUSE	2	2	2.25E-07	Calcineurin B homologous protein 1	Chp1	111741.858	9527.712	10053.216
ACTS_MOUSE	39	8	2.29E-07	Actin, alpha skeletal muscle	Acta1	11644.940	42397.309	19145.783

AT2A1_MOUSE	2	2	2.39E-07	Sarcoplasmic/endoplasmic reticulum calcium ATPase 1	Atp2a1	4180.070	737.329	481.668
FINC_MOUSE	93	88	-07					
COCA1_MOUSE	81	76	-07					
			Fn1					
			2.89E	Collagen alpha-1(XII) chain	Col12a1			
CO4B_MOUSE	3	3	3.12E	Complement C4-B	C4b	3026.330	456.511	288.552
PRG4_MOUSE	8	8	-07					
			-07 3.84E	Proteoglycan 4	Prg4			

						1219568.044	1571411.075	3169367.842
						37446.372	100768.121	41891.546

ERI1_MOUSE	1	1	4.66E-07	3'-5' exoribonuclease 1 Eri1	3101.070	229.290	213.987
FLIP1_MOUSE	2	1	4.74E-07	Filamin-A-interacting protein 1 Dlip1	0.000	39.979	20.722
KLH41_MOUSE	8	7	5.04E-07	Kelch-like protein 41 Klhl41	6942.195	9993.489	6571.143
PSMD3_MOUSE	11	9	5.95E-07	26S proteasome non-ATPase regulatory subunit 3 Psmd3	170071.243	25156.157	25239.522
ISLR_MOUSE	5	5	6.65E-07	Immunoglobulin superfamily containing leucine-rich repeat protein Islr	2151.197	1424.128	768.346
TFR1_MOUSE	9	8	6.88E-07	Transferrin receptor protein 1 Tfrc	10965.814	2715.177	2749.533
NID1_MOUSE	19	15	7.49E-07	Nidogen-1 Nid1	196370.311	28773.183	30018.848
THRB_MOUSE	2	2	8.93E-07	Prothrombin F2	2215.036	322.978	146.315
TRXR1_MOUSE	8	7	9.09E-07	Thioredoxin reductase 1, cytoplasmic Txnrd1	2324.774	1146.641	1078.718
PGS2_MOUSE	13	12	9.67E-07	Decorin Dcn	35020.298	13840.352	27966.335
UBP44_MOUSE	1	1	1.01E-06	Ubiquitin carboxyl-terminal hydrolase 44 Usp44	4644.367	537.707	607.609
ODO2_MOUSE	2	2	1.03E-06	Dihydrolipoyllysine-residue succinyltransferase component of 2-oxoglutarate dehydrogenase complex, mitochondrial Dlst	35.001	166.712	218.867
MYH3_MOUSE	37	16	1.05E-06	Myosin-3 Myh3	2669.929	6011.958	3256.706
CO4A2_MOUSE	15	15	1.06E-06	Collagen alpha-2(IV) chain Col4a2	2544.755	15971.129	3932.573
SPA3N_MOUSE	14	9	1.58E-06	Serine protease inhibitor A3N Serpina3n	1187.530	21776.414	2564.590
TTL12_MOUSE	1	1	1.80E-06	Tubulin--tyrosine ligase-like protein 12	0.000	53.689	22.804

				Ttll12			
PEDF_MOUSE	19	17	2.04E-06	Pigment epithelium-derived factor Serpinf1	139703.720	62268.265	87461.382

TMC5_MOUSE	1	1	2.31E-06	Transmembrane channel-like protein 5 Tmc5	95874.606	7660.023	6670.896
RTN4_MOUSE	12	12	-06	Reticulon-4 Rtn4	10989.021	20970.994	13215.989
PRDX1_MOUSE	13	10	2.39E-06	Peroxiredoxin-1 Prdx1	96434.562	21858.731	26664.566
			2.60E				
CO5A1_MOUSE	10	8	-06	Collagen alpha-1(V) chain Col5a1	761.948	1603.740	1736.933
HPT_MOUSE	2	1	3.03E-06	Haptoglobin Hp	4599.598	590.201	701.581
			3.03E				
AATM_MOUSE	5	5	3.59E-06	Aspartate aminotransferase, mitochondrial Got2	1065.265	1337.085	2255.336
MYBPH_MOUSE	3	3	-06	Myosin-binding protein H Mybph	2092.096	5185.415	2607.143
A2MG_MOUSE	6	4	4.12E-06	Alpha-2-macroglobulin-P A2m	25160.902	2799.563	3256.461
			4.36E				
RS20_MOUSE	2	2	-06	40S ribosomal protein S20 Rps20	898.664	1932.195	1523.450
VINC_MOUSE	32	26	4.39E-06	Vinculin Vcl	42336.992	19561.283	20799.178
			4.60E				
SYLC_MOUSE	11	11	4.74E-06	Leucine--tRNA ligase, cytoplasmic Lars1	2042.096	2957.347	1550.983
DVL1_MOUSE	1	1	4.94E-06	Segment polarity protein dishevelled homolog DVL-1 Dvl1	1128.691	111.817	85.429
PUR2_MOUSE	1	1	5.71E-06	Trifunctional purine biosynthetic protein adenosine-3 Gart	287.461	68.768	43.266
CBPQ_MOUSE	7	6		Carboxypeptidase Q Cpq	3830.775	1767.548	2374.064

SPON2_MOUSE	5	4	5.77E-06	Spondin-2 Spon2	3573.047	644.818	1451.450
TIMP3_MOUSE	1	1	7.22E-06	Metalloproteinase inhibitor 3 Timp3	195.215	108.690	406.373
SODE_MOUSE	4	4	8.09E-06	Extracellular superoxide dismutase [Cu-Zn] Sod3	3211.648	923.696	2979.494
RS27L_MOUSE	1	1	8.11E-06	40S ribosomal protein S27-like Rps27l	1058.599	770.598	384.295
CASQ1_MOUSE	10	10	8.35E-06	Calsequestrin-1 Casq1	5103.020	30112.312	15502.939
EHD1_MOUSE	22	14	8.83E-06	EH domain-containing protein 1 Ehd1	11547.479	7196.979	12904.996
VTNC_MOUSE	1	1	9.45E-06	Vitronectin Vtn	13071.273	3860.567	2250.758
DESM_MOUSE	36	29	9.52E-06	Desmin Des	41995.696	75431.435	63329.648
IBP5_MOUSE	9	9	1.12E-05	Insulin-like growth factor-binding protein 5 Igfbp5	22458.291	10498.112	17635.506
GSLG1_MOUSE	1	1	1.14E-05	Golgi apparatus protein 1 Glg1	240.342	40.472	27.385
CO6A2_MOUSE	6	6	1.21E-05	Collagen alpha-2(VI) chain Col6a2	1151.429	2091.005	947.341

APOE_MOUSE	1	1	1.23E-05	Apolipoprotein E Apoe	238.161	104.184	74.528
PXDN_MOUSE	21	17	1.25E-05	Peroxidasin homolog Pxdn	6979.596	5989.246	9380.991
SPTN1_MOUSE	9	7	1.44E-05	Spectrin alpha chain, non-erythrocytic 1 Sptan1	245.709	689.424	432.044
CAVN4_MOUSE	2	2	1.49E-05	Caveolae-associated protein 4 Cavin4	180.707	396.054	189.577
TBB6_MOUSE	31	9		Tubulin beta-6 chain Tubb6	14258.765	19398.332	10932.856

			1.61E				
EST1E_MOUSE	1	1	-05	Carboxylesterase 1E Ces1e	2174.213	247.409	165.217
ANT3_MOUSE	10	9	1.76E -05 1.81E	Antithrombin-III Serpinc1	8668.040	2032.677	1642.732
CYLD_MOUSE	1	1	1.88E-05	Ubiquitin carboxyl-terminal hydrolase CYLD Cyld	4702.992	406.590	531.682
MAOX_MOUSE	3	3	-05	NADP-dependent malic enzyme Me1	2771.839	878.946	1111.189
TRIO_MOUSE	1	1	1.91E -05 1.99E	Triple functional domain protein Trio	1993.704	528.305	529.983
IMDH2_MOUSE	4	4	2.10E-05	Inosine-5'-monophosphate dehydrogenase 2 Impdh2	1364.941	2298.819	4092.278
FLNC_MOUSE	68	55	3E-05	Filamin-C Flnc	49630.208	73331.339	60176.658
TIMP1_MOUSE	2	2	-05 2.1 2.21E	Metalloproteinase inhibitor 1 Timp1	1661.296	1675.715	4837.349
LMNA_MOUSE	32	31	2.37E-05	Prelamin-A/C Lmna	94998.186	57077.383	53625.765
SYEP_MOUSE	12	11	2.44E-05	Bifunctional glutamate/proline--tRNA ligase Eprs1	2321.556	3066.218	2079.447
DNPEP_MOUSE	13	12	-05	Aspartyl aminopeptidase Dnpep	9342.199	5031.522	4032.160
RTN2_MOUSE	3	3	2.53E -05 2.71E	Reticulon-2 Rtn2	247.639	1013.713	636.478
USO1_MOUSE	2	2	2.84E-05	General vesicular transport factor p115 Uso1	1193.626	411.385	310.448
MVP_MOUSE	33	30	-05	Major vault protein Mvp	30934.056	49899.506	53302.591
RSSA_MOUSE	7	7	2.91E -05 3.19E	40S ribosomal protein SA Rpsa	20310.331	31567.662	19334.783
TBB2A_MOUSE	31	4	3.40E-05	Tubulin beta-2A chain Tubb2a	1058.004	2484.532	1055.230
PGM5_MOUSE	7	5	3.42E-05	Phosphoglucomutase-like protein 5 Pgm5	1195.030	2903.708	1991.131

PHB2_MOUSE	5	4	-05	Prohibitin-2 Phb2	198.680	548.505	841.933
LOXL1_MOUSE	10	8	3.57E-05 3.60E	Lysyl oxidase homolog 1 Loxl1	6091.460	6544.685	21615.309
ATPB_MOUSE	16	15	3.62E-05	ATP synthase subunit beta, mitochondrial Atp5f1b	6970.424	12561.951	15295.788

H3C_MOUSE	6	6	3.80E-05	Histone H3.3C H3-5	128680.606	377697.065	466299.995
PRS8_MOUSE	11	9	3.81E-05	26S proteasome regulatory subunit 8 Psmc5	6000.376	8102.524	6152.020
CNO10_MOUSE	1	1	3.87E-05	CCR4-NOT transcription complex subunit 10 Cnot10	2280.706	453.382	411.554
KCC2A_MOUSE	1	1	3.89E-05	Calcium/calmodulin-dependent protein kinase type II subunit alpha Camk2a	6.983	141.328	178.888
CTL2A_MOUSE	4	3	3.97E-05	Protein CTLA-2-alpha Ctla2a	6340.028	3235.621	1406.861
PRS6B_MOUSE	14	14	4.07E-05	26S proteasome regulatory subunit 6B Psmc4	4552.990	8530.629	4693.481
H14_MOUSE	9	2	-05	Histone H1.4 H1-4	5439.149	23261.973	27399.934
S10AB_MOUSE	1	1	4.21E-05 4.26E	Protein S100-A11 S100a11	18822.670	3896.670	4093.252
RAB5A_MOUSE	2	1	-05	Ras-related protein Rab-5A Rab5a	368.976	152.345	206.610
RS25_MOUSE	3	3	4.36E-05 4.63E	40S ribosomal protein S25 Rps25	34920.385	9162.536	7062.278
IMB1_MOUSE	10	10	4.68E-05	Importin subunit beta-1 Kpnb1	4899.333	3399.737	2833.882
TXND5_MOUSE	4	4	4.74E-05	Thioredoxin domain-containing protein 5 Txndc5	1533.535	764.453	958.058
ISPD_MOUSE	1	1	4.91E-05	D-ribitol-5-phosphate cytidylyltransferase Crppa	5795.244	1422.567	1398.162
EF1B_MOUSE	3	3		Elongation factor 1-beta Eef1b	2518.197	1431.987	1625.607

RL5_MOUSE	9	9	5.10E-05	60S ribosomal protein L5 Rpl5	10765.911	6958.075	7249.759
POSTN_MOUSE	20	17	5.32E-05	Periostin Postn	12392.214	56482.220	9367.977
GPX3_MOUSE	4	3	5.41E-05	Glutathione peroxidase 3 Gpx3	241.057	1002.699	75.938
H11_MOUSE	6	4	5.66E-05	Histone H1.1 H1-1	2569.275	5627.923	6639.771
SYSC_MOUSE	11	11	5.83E-05	Serine--tRNA ligase, cytoplasmic Sars1	6383.242	6482.473	4258.987
SRCA_MOUSE	5	4	5.83E-05	Sarcalumenin Srl	396.511	944.737	569.437
RAN_MOUSE	6	3	6.14E-05	GTP-binding nuclear protein Ran Ran	10896.827	11103.181	7625.878
RS15A_MOUSE	5	5	8.27E-05	40S ribosomal protein S15a Rps15a	5833.217	8618.466	6871.866
ITIH2_MOUSE	3	3	8.36E-05	Inter-alpha-trypsin inhibitor heavy chain H2 Itih2	2501.052	316.061	453.404
LRC17_MOUSE	3	3	8.37E-05	Leucine-rich repeat-containing protein 17 Lrrc17	571.897	835.452	351.943

RS3A_MOUSE	10	10	8.42E-05	40S ribosomal protein S3a Rps3a	19264.184	14219.916	
CASQ2_MOUSE	18	17	8.43E-05	Calsequestrin-2 Casq2	13056.017	85231.995	189786.283	167432.297
FBLN3_MOUSE	1	1	8.50E-05	EGF-containing fibulin-like extracellular matrix protein 1 Efemp1	125.228	22.186	18.556
PROF1_MOUSE	8	7	8.53E-05	Profilin-1 Pfn1	5895.216	3746.140	2920.870
SYMC_MOUSE	3	3	8.60E-05	Methionine--tRNA ligase, cytoplasmic Mars1	88.359	418.854	214.885

SYIC_MOUSE	14	11	8.71E-05	Isoleucine--tRNA ligase, cytoplasmic Iars1	3291.322	4034.871	2741.546
TRAF6_MOUSE	1	1	8.76E-05	TNF receptor-associated factor 6 Traf6	10630.550	1910.521	1725.700
PGP_MOUSE	1	1	8.80E-05	Glycerol-3-phosphate phosphatase Pgp	79.440	177.886	149.358
RS27A_MOUSE	8	8	9.00E-05	Ubiquitin-40S ribosomal protein S27a Rps27a	37942.778	64374.662	60852.549
HSP72_MOUSE	10	1	9.74E-05	Heat shock-related 70 kDa protein 2 Hspa2	18.225	65.269	77.416
H10_MOUSE	4	3	0.000102	Histone H1.0 H1-0	1677.875	5801.079	5561.187
PSD12_MOUSE	15	15	0.000106	26S proteasome non-ATPase regulatory subunit 12 Psmd12	7188.870	5087.527	4137.797
GLNA_MOUSE	2	2	0.000113	Glutamine synthetase Glul	528.272	845.671	309.046
FLNA_MOUSE	27	18	0.000114	Filamin-A Flna	18772.506	9394.679	10832.201
SERC_MOUSE	15	15	0.000116	Phosphoserine aminotransferase Psat1	10447.628	5963.841	5623.488
ANXA5_MOUSE	17	16	0.000117	Annexin A5 Anxa5	13170.417	12606.139	19360.238
HEXA_MOUSE	8	7	0.000119	Beta-hexosaminidase subunit alpha Hexa	3108.621	4967.299	4877.495
DCTN1_MOUSE	4	3	0.00012	Dynactin subunit 1 Dctn1	154.272	299.239	221.463
PRS7_MOUSE	19	19	0.000122	26S proteasome regulatory subunit 7 Psmc2	12628.840	15081.903	11021.363
GREM1_MOUSE	1	1	0.000125	Gremlin-1 Grem1	125.795	7.047	162.336
DLDH_MOUSE	2	2	0.000128	Dihydrolipoyl dehydrogenase, mitochondrial Dld	263.774	442.160	534.009
CO1A1_MOUSE	36	33	0.000131	Collagen alpha-1(I) chain Col1a1	22670.105	20708.971	48585.393
RS6_MOUSE	7	5	0.00013	40S ribosomal protein S6 Rps6	5477.858	10091.223	9507.079

DCAF8_MOUSE	1	1	0.000131	DDB1- and CUL4-associated factor 8 Dcaf8	58.191	207.680	205.401
CATD_MOUSE	15	14	0.000132	Cathepsin D Ctsd	11322.305	18860.051	26136.257
NID2_MOUSE	28	24	0.000134	Nidogen-2 Nid2	18499.578	31006.673	34213.828
PURA1_MOUSE	3	3	0.000136	Adenylosuccinate synthetase isozyme 1 Adss1	914.593	1490.783	1023.132
GYS1_MOUSE	6	5	0.000138	Glycogen [starch] synthase, muscle Gys1	363.590	976.485	474.568
KINH_MOUSE	17	14	0.000139	Kinesin-1 heavy chain Kif5b	3437.519	4862.331	3928.167
HEP2_MOUSE	1	1	0.000142	Heparin cofactor 2 Serpind1	545.886	105.559	109.831
ITIH1_MOUSE	5	4	0.000144	Inter-alpha-trypsin inhibitor heavy chain H1 Itih1	1862.396	655.836	496.991
CSPG4_MOUSE	1	1	0.000145	Chondroitin sulfate proteoglycan 4 Cspg4	457.408	275.991	269.655
FPRP_MOUSE	22	18	0.000148	Prostaglandin F2 receptor negative regulator Ptgfrn	25282.595	21037.872	35361.969
ACTB_MOUSE	34	8	0.00015	Actin, cytoplasmic 1 Actb	103233.061	144318.180	107694.540
PYGM_MOUSE	17	13	0.000153	Glycogen phosphorylase, muscle form Pygm	5560.915	10521.975	7179.938
ITA7_MOUSE	15	12	0.000163	Integrin alpha-7 Itga7	5547.792	4961.941	9490.708
CERU_MOUSE	5	5	0.000165	Ceruloplasmin Cp	4464.603	1615.556	1162.744
TCPZ_MOUSE	21	17	0.000168	T-complex protein 1 subunit zeta Cct6a	42600.382	34499.673	29707.620
FRIH_MOUSE	2	2	0.00017	Ferritin heavy chain Fth1	883.538	587.702	752.839
PCOC1_MOUSE	10	10	0.000171	Procollagen C-endopeptidase enhancer 1 Pcolce	25675.742	42905.090	48222.917
SDC4_MOUSE	3	3	0.000173	Syndecan-4 Sdc4	983.583	1230.497	2424.906
MARCS_MOUSE	6	6	0.000182	Myristoylated alanine-rich C-kinase substrate Marcks	1621.563	1460.293	2089.302
ITB1_MOUSE	7	6		Integrin beta-1 Itgb1	3849.890	3493.091	6616.395

FUMH_MOUSE	3	3	0.000186 0.00019	Fumarate hydratase, mitochondrial Fh	392.317	611.593	909.142
H13_MOUSE	10	1	0.000204	Histone H1.3 H1-3	42.060	457.625	378.467
AEBP1_MOUSE	21	19	0.000207	Adipocyte enhancer-binding protein 1 Aebp1	16467.858	22957.749	34341.620
YBOX1_MOUSE	8	7	0.000207	Y-box-binding protein 1 Ybx1	1984.813	824.347	1658.069

RS14_MOUSE	4	4	0.000212	40S ribosomal protein S14 Rps14	3259.904	2547.069	1753.288
AMPL_MOUSE	6	5	0.000216	Cytosol aminopeptidase Lap3	3204.952	1073.120 164033.877	1232.216 92743.663
MMP2_MOUSE	22	19	0.00022	72 kDa type IV collagenase Mmp2	87954.583		
NP1L4_MOUSE	4	3	0.000224	Nucleosome assembly protein 1-like 4 Nap1l4	1435.629	870.285	911.396
COPG1_MOUSE	5	4	0.000229	Coatomer subunit gamma-1 Copg1	1295.683	2618.933	3703.586
A2AP_MOUSE	1	1	0.000239	Alpha-2-antiplasmin Serpinf2	497.181	66.017	64.503
SAP_MOUSE	7	6	0.00024	Prosaposin Psap	9483.389	16613.238	16435.092
H15_MOUSE	10	9	0.00025	Histone H1.5 H1-5	12682.881	36037.337	43762.680
OAF_MOUSE	2	2	0.000251	Out at first protein homolog Oaf	1123.493	560.435	756.371
NP1L1_MOUSE	4	3	0.000253	Nucleosome assembly protein 1-like 1 Nap1l1	4113.583	2726.810	2706.161
AT1A1_MOUSE	2	1	0.00026	Sodium/potassium-transporting ATPase subunit alpha-1 Atp1a1	328.197	78.912	138.897
ASNS_MOUSE	10	10	0.000279	Asparagine synthetase [glutaminehydrolyzing] Asns	5595.513	5614.319	3988.763
MIME_MOUSE	17	16	0.00029	Mimecan Ogn	84114.274	69302.422	37013.133
CH60_MOUSE	8	7	0.000293	60 kDa heat shock protein, mitochondrial Hspd1	1305.084	1576.771	2816.761
LYOX_MOUSE	5	4	0.000295	Protein-lysine 6-oxidase Lox	5183.454	15812.656	10935.926
SERPH_MOUSE	12	12	0.000297	Serpin H1 Serpinh1	6647.047	10756.721	9433.423

SYWC_MOUSE	3	3	0.000297	Tryptophan--tRNA ligase, cytoplasmic Wars1	1312.169	921.581	653.833
QPCT_MOUSE	1	1	0.000305	Glutaminyl-peptide cyclotransferase Qpct	108.765	32.238	95.249
PGK1_MOUSE	20	14	0.000306	Phosphoglycerate kinase 1 Pgk1	30301.801	36780.275	23565.129
PFKAL_MOUSE	4	2	0.000309	ATP-dependent 6-phosphofructokinase, liver type Pfkl	47.642	210.026	94.997
TCPE_MOUSE	20	19	0.000317	T-complex protein 1 subunit epsilon Cct5	27339.188	23304.679	16550.046
PHB_MOUSE	3	3	0.000323	Prohibitin Phb	179.238	300.296	556.483
TPM4_MOUSE	3	3	0.000326	Tropomyosin alpha-4 chain Tpm4	518.571	664.027	1137.883

PP2AA_MOUSE	4	3	0.000331	Serine/threonine-protein phosphatase 2A catalytic subunit alpha isoform Ppp2ca	4457.189	2635.702	2054.846
KAP0_MOUSE	9	5	0.000338	cAMP-dependent protein kinase type Ialpha regulatory subunit Prkar1a	3568.180	3784.765	2693.132
TCPG_MOUSE	22	20	0.000341	T-complex protein 1 subunit gamma Cct3	45968.825	36087.887	28705.535
MRP7_MOUSE	1	1	0.000349	ATP-binding cassette sub-family C member 10 Abcc10	447.201	602.997	408.697
C1QT3_MOUSE	4	4	0.000354	Complement C1q tumor necrosis factorrelated protein 3 C1qtnf3	12716.005	19979.031	10175.873
1433F_MOUSE	8	2	0.000358	14-3-3 protein eta Ywhah	726.441	257.570	321.432
TBB5_MOUSE	25	3	0.000368	Tubulin beta-5 chain Tubb5	10858.474	16157.340	11336.831
ACTN2_MOUSE	9	1	0.000372	Alpha-actinin-2 Actn2	305.552	364.538	186.070
SHLB1_MOUSE	2	2	0.00038	Endophilin-B1 Sh3glb1	102.742	50.540	67.460
GREB1_MOUSE	1	1	0.000385	Protein GREB1 Greb1	284.856	491.307	670.731
MYH1_MOUSE	32	7	0.000389	Myosin-1 Myh1	270.734	1642.061	611.895

A1AT6_MOUSE	1	1	0.000396	Alpha-1-antitrypsin 1-6 Serpina1f	11792.004	5370.714	4911.779
ENOB_MOUSE	22	15	0.000397	Beta-enolase Eno3	34672.979	31921.673	28091.075
GDIB_MOUSE	14	9	0.000397	Rab GDP dissociation inhibitor beta Gdi2	6781.262	4855.710	4347.969
TET2_MOUSE	1	1	0.000408	Methylcytosine dioxygenase TET2 Tet2	334.469	15.293	2.264
EXT2_MOUSE	4	4	0.000411	Exostosin-2 Ext2	2137.444	1339.037	1789.630
ANXA8_MOUSE	8	7	0.000418	Annexin A8 Anxa8	1172.770	1037.863	1937.061
PRELP_MOUSE	6	6	0.00042	Prolargin Prelp	3044.213	4330.224	4490.535
CO3A1_MOUSE	45	42	0.000442	Collagen alpha-1(III) chain Col3a1	65148.733	56133.928	104153.810
FBLN2_MOUSE	13	12	0.000452	Fibulin-2 Fbln2	11315.505	24806.092	17204.793
CISY_MOUSE	2	2	0.000459	Citrate synthase, mitochondrial Cs	695.311	1088.029	1389.230
SEM7A_MOUSE	3	3	0.000463	Semaphorin-7A Sema7a	539.848	206.500	578.880
FLNB_MOUSE	14	7	0.000487	Filamin-B Flnb	1732.648	1193.703	1469.225
STIP1_MOUSE	3	2	0.000499	Stress-induced-phosphoprotein 1 Stip1	482.186	224.168	259.562
G6PI_MOUSE	14	13	0.000521	Glucose-6-phosphate isomerase Gpi	13613.748	7345.790	8401.247
VDAC1_MOUSE	5	4	0.000536	Voltage-dependent anion-selective channel protein 1 Vdac1	1086.061	1585.581	2353.330
REEP5_MOUSE	1	1	0.000537	Receptor expression-enhancing protein 5 Reep5	21.337	362.805	249.657
CYFP1_MOUSE	3	1	0.000542	Cytoplasmic FMR1-interacting protein 1 Cyfip1	117.335	50.394	66.274
ENOA_MOUSE	34	27	0.000547	Alpha-enolase Eno1	118769.883	87143.960	84041.426
TS101_MOUSE	3	3	0.000551	Tumor susceptibility gene 101 protein Tsg101	610.617	420.327	703.443
MATN2_MOUSE	6	4	0.000553	Matrilin-2 Matn2	417.838	2325.013	859.307
FRPD1_MOUSE	2	1	0.000557	FERM and PDZ domain-containing protein 1 Frmpd1	398.847	1083.971	204.002

CR1L_MOUSE	1	1	0.000561	Complement component receptor 1-like protein Cr1l	50.830	96.154	183.771
GELS_MOUSE	26	25	0.000566	Gelsolin Gsn	83403.331	88683.536	60025.439
PRS6A_MOUSE	14	14	0.000576	26S proteasome regulatory subunit 6A Psmc3	9356.278	12752.388	8663.482
H2AY_MOUSE	3	1	0.000581	Core histone macro-H2A.1 Macroh2a1	160.397	643.121	566.671
ITA3_MOUSE	4	4	0.000586	Integrin alpha-3 Itga3	142.108	200.092	509.425
MIF_MOUSE	2	2	0.000595	Macrophage migration inhibitory factor Mif	5341.016	3253.434	2520.414
MYL1_MOUSE	9	7	0.00061	Myosin light chain 1/3, skeletal muscle isoform Myl1	1664.324	2720.827	2417.048
MYH4_MOUSE	25	2	0.000613	Myosin-4 Myh4	20.581	112.275	38.057
CATB_MOUSE	9	8	0.000638	Cathepsin B Ctsb	16382.075	22125.442	27195.993
TBA4A_MOUSE	16	2	0.000649	Tubulin alpha-4A chain Tuba4a	1188.122	1608.793	746.800
TBB4B_MOUSE	27	1	0.000652	Tubulin beta-4B chain Tubb4b	1042.272	1917.433	1166.567
FSTL1_MOUSE	5	4	0.000667	Follistatin-related protein 1 Fstl1	3966.738	2600.551	5440.209
DNJA1_MOUSE	2	2	0.00067	DnaJ homolog subfamily A member 1 Dnaja1	91.564	466.552	202.187
B4GA1_MOUSE	1	1	0.000698	Beta-1,4-glucuronyltransferase 1 B4gat1	57.707	142.594	167.620
MDHM_MOUSE	12	10	0.000703	Malate dehydrogenase, mitochondrial Mdh2	8467.024	8814.867	13795.362
MYL6_MOUSE	5	4	0.000711	Myosin light polypeptide 6 Myl6	2489.795	1563.660	1432.741

RS12_MOUSE	1	1	0.000711	40S ribosomal protein S12 Rps12	85.732	75.920	22.873
XPO1_MOUSE	9	9	0.000713	Exportin-1 Xpo1	1311.602	1383.117	987.507
CCD80_MOUSE	21	20	0.000741	Coiled-coil domain-containing protein 80 Ccdc80	12047.300	18476.798	11965.684
RS4X_MOUSE	12	11	0.000743	40S ribosomal protein S4, X isoform	7835.985	13054.716	9132.865

				Rps4x			
NSF1C_MOUSE	5	5	0.000756	NSFL1 cofactor p47 Nsfl1c	772.226	1257.041	1135.111
NUCKS_MOUSE	1	1	0.000791	Nuclear ubiquitous casein and cyclindependent kinase substrate 1 Nucks1	47.236	114.766	164.083
ACON_MOUSE	2	2	0.000807	Aconitate hydratase, mitochondrial Aco2	195.885	855.711	794.798
GLYM_MOUSE	1	1	0.000815	Serine hydroxymethyltransferase, mitochondrial Shmt2	62.963	198.636	195.421
CS1A_MOUSE	1	1	0.000832	Complement C1s-A subcomponent C1sa	482.808	209.414	356.441
CO1A2_MOUSE	31	28	0.000849	Collagen alpha-2(I) chain Col1a2	28404.846	20700.123	33836.973
PRDX3_MOUSE	1	1	0.000856	Thioredoxin-dependent peroxide reductase, mitochondrial Prdx3	48.981	86.154	146.340
CTBL1_MOUSE	2	2	0.000863	Beta-catenin-like protein 1 Ctnnbl1	91.781	253.896	74.231
FHL1_MOUSE	2	2	0.000865	Four and a half LIM domains protein 1 Fhl1	937.366	586.960	687.200
CALX_MOUSE	6	6	0.000876	Calnexin Canx	1034.163	2158.485	2026.232
TCPB_MOUSE	25	25	0.000906	T-complex protein 1 subunit beta Cct2	44354.476	44353.926	32299.657
DX39A_MOUSE	4	3	0.000911	ATP-dependent RNA helicase DDX39A Ddx39a	1913.601	2473.354	1802.959
G3BP2_MOUSE	1	1	0.000917	Ras GTPase-activating protein-binding protein 2 G3bp2	17.047	46.587	42.450
CAP1_MOUSE	8	7	0.000917	Adenylyl cyclase-associated protein 1 Cap1	6638.917	4967.314	4588.921
LAMP1_MOUSE	4	1	0.000924	Lysosome-associated membrane glycoprotein 1 Lamp1	64.246	166.508	240.460
GALK1_MOUSE	2	2	0.000985	Galactokinase Galk1	671.705	457.377	438.330
EPB41_MOUSE	1	1	0.000995	Protein 4.1 Epb41	42.828	122.089	250.282

PFKAM_MOUSE	10	7	0.000998	ATP-dependent 6-phosphofructokinase, muscle type Pfkm	2913.249	5268.279	3205.359
LG3BP_MOUSE	9	8	0.001022	Galectin-3-binding protein Lgals3bp	13140.696	5301.303	8745.358
FBN1_MOUSE	8	6	0.001036	Fibrillin-1 Fbn1	5819.921	1519.385	4288.963
G3P_MOUSE	24	20	0.001037	Glyceraldehyde-3-phosphate dehydrogenase Gapdh	68928.053	69878.087	44824.719
MY18A_MOUSE	7	6	0.001042	Unconventional myosin-XVIIIa Myo18a	540.596	1004.284	450.432
DDX6_MOUSE	2	2	0.001044	Probable ATP-dependent RNA helicase DDX6 Ddx6	250.180	485.274	373.250
RTTN_MOUSE	2	1	0.001067	Rotatin Rttn	497.009	911.168	829.247
SND1_MOUSE	4	3	0.001083	Staphylococcal nuclease domaincontaining protein 1 Snd1	361.088	345.232	189.949
GPC5C_MOUSE	1	1	0.001089	G-protein coupled receptor family C group 5 member C Gprc5c	238.769	595.357	658.432
UBP5_MOUSE	5	5	0.001126	Ubiquitin carboxyl-terminal hydrolase 5 Usp5	2725.483	3366.359	3893.092
MYADM_MOUSE	1	1	0.001135	Myeloid-associated differentiation marker Myadm	582.197	845.133	1243.660
TGFB3_MOUSE	1	1	0.001172	Transforming growth factor beta-3 proprotein tarb3	30.465	14.976	25.564
SEPT7_MOUSE	5	5	0.00123	Septin-7 Septin7	2273.121	2060.815	1757.649
EHD2_MOUSE	5	3	0.001251	EH domain-containing protein 2 Ehd2	151.021	119.885	263.870
RTN1_MOUSE	1	1	0.001273	Reticulon-1 Rtn1	433.854	759.631	676.887
TENA_MOUSE	6	6	0.001281	Tenascin Tnc	281.519	598.258	459.716
LDHA_MOUSE	19	17	0.001286	L-lactate dehydrogenase A chain Ldha	51379.109	35183.341	35437.326
PSME1_MOUSE	1	1	0.00129	Proteasome activator complex subunit 1 Psme1	30.793	10.037	29.537

CALR_MOUSE	9	9	0.001301	Calreticulin Calr	5294.763	7469.219	8910.715
PGS1_MOUSE	14	12	0.001316	Biglycan Bgn	73984.325	55711.118	97156.647
CO5A2_MOUSE	13	10	0.001322	Collagen alpha-2(V) chain Col5a2	2185.038	4486.510	5358.876
ACTN3_MOUSE	14	8	0.001335	Alpha-actinin-3 Actn3	1702.577	2846.365	2511.939
TRI72_MOUSE	8	7	0.001367	Tripartite motif-containing protein 72 Trim72	1707.067	2582.549	2545.904

RL30_MOUSE	4	4	0.00137	60S ribosomal protein L30 Rpl30	2557.190	4080.906	3005.262
CO3_MOUSE	4	4	0.001398	Complement C3 C3	27295.813	6754.729	3667.337
RS16_MOUSE	8	8	0.001445	40S ribosomal protein S16 Rps16	16911.854	23275.602	17092.697
IGSF8_MOUSE	7	6	0.001471	Immunoglobulin superfamily member 8 Igsf8	2834.170	2710.156	4234.768
SVEP1_MOUSE	1	1	0.001478	Sushi, von Willebrand factor type A, EGF and pentraxin domain-containing protein 1 Svep1	55.777	141.292	44.453
HSPB1_MOUSE	11	11	0.00149	Heat shock protein beta-1 Hspb1	32055.262	25466.970	18270.101
NEST_MOUSE	10	9	0.001494	Nestin Nes	5161.688	6908.925	6296.316
CO6A1_MOUSE	12	12	0.0015	Collagen alpha-1(VI) chain Col6a1	3892.544	6715.826	3198.981
STRAP_MOUSE	5	5	0.001533	Serine-threonine kinase receptor-associated protein Strap	793.150	656.380	404.943
EF2_MOUSE	34	32	0.001533	Elongation factor 2 Eef2	101342.054	105382.110	123835.235
TCPD_MOUSE	15	14	0.001546	T-complex protein 1 subunit delta Cct4	18738.501	21709.003	17399.259
CHMP5_MOUSE	2	2	0.001555	Charged multivesicular body protein 5 Chmp5	2059.131	1664.267	2484.469
ANXA2_MOUSE	31	29	0.001557	Annexin A2 Anxa2	96097.530	110319.506	145195.398
EDIL3_MOUSE	3	3	0.001564	EGF-like repeat and discoidin I-like domain-containing protein 3 Edil3	511.205	252.869	448.357

AIMP2_MOUSE	1	1	0.001564	Aminoacyl tRNA synthase complex-interacting multifunctional protein 2 Aimp2	40.571		127.536	28.607
CTRB1_MOUSE	7	6	0.001596	Chymotrypsinogen B Ctrb1	3928.080		10193.637	3230.023
NUCB2_MOUSE	1	1	0.001609	Nucleobindin-2 Nucb2	102.603		59.471	65.882
AMPN_MOUSE	8	8	0.001613	Aminopeptidase N Anpep	1591.310		1610.369	2300.588
APT_MOUSE	3	3	0.001651	Adenine phosphoribosyltransferase Aprt	1349.865		1305.070	609.126
BACH_MOUSE	2	2	0.001667	Cytosolic acyl coenzyme A thioester hydrolase Acot7	641.677		401.297	257.864
FSCN1_MOUSE	6	6	0.001679	Fascin Fscn1	2795.305		2377.753	1700.174
ATRN_MOUSE	1	1	0.001686	Attractin Atrn	61.550		3.612	0.093
SYVC_MOUSE	12	11	0.00172	Valine--tRNA ligase Vars1	2720.275		2929.047	2102.459

ANX11_MOUSE	9	8	0.00173	Annexin A11 Anxa11	5068.582		6667.064	8771.985
VAT1_MOUSE	6	6	0.001765	Synaptic vesicle membrane protein VAT-1 homolog Vat1	4051.190		4703.642	6380.151
PLST_MOUSE	3	1	0.001774	Plastin-3 Pls3	405.369		234.634	195.240
LGMN_MOUSE	4	3	0.001835	Legumain Lgmn	1082.205	1522.053		1617.685
KPYM_MOUSE	33	29	0.001842	Pyruvate kinase PKM Pkm	158127.033	138686.400		119802.845
SDCB1_MOUSE	7	6	0.001861	Syntenin-1 Sdcbp	8847.942		5999.769	10576.972
CSN7B_MOUSE	1	1	0.001921	COP9 signalosome complex subunit 7b Cops7b	127.153		71.733	88.327
TCPA_MOUSE	22	22	0.001957	T-complex protein 1 subunit alpha Tcp1	45230.035		42186.610	33899.324
TERA_MOUSE	48	44	0.001971	Transitional endoplasmic reticulum ATPase Vcp	98784.630		146667.605	146861.970

ZC3H4_MOUSE	1	1	0.001974	Zinc finger CCCH domain-containing protein 4 Zc3h4	185.927	64.194	28.652
SYYC_MOUSE	11	9	0.001994	Tyrosine--tRNA ligase, cytoplasmic Yars1	1144.825	1492.292	1452.584
CYTC_MOUSE	5	5	0.001996	Cystatin-C Cst3	2505.641	5518.991	2438.483
DCLK1_MOUSE	3	3	0.002042	Serine/threonine-protein kinase DCLK1 Dclk1	533.570	983.560	561.839
PUR8_MOUSE	4	4	0.002054	Adenylosuccinate lyase Adsl	884.861	1270.911	1169.633
PABP1_MOUSE	8	8	0.002083	Polyadenylate-binding protein 1 Pabpc1	3074.386	4133.183	3436.305
PRAF3_MOUSE	6	6	0.002097	PRA1 family protein 3 Arl6ip5	1973.450	6739.366	2739.248
UBA1_MOUSE	20	14	0.002106	Ubiquitin-like modifier-activating enzyme 1 Uba1	9654.465	12310.949	8967.245
UROK_MOUSE	1	1	0.002148	Urokinase-type plasminogen activator Plau	52.917	145.045	194.089
SHIP2_MOUSE	3	2	0.002155	Phosphatidylinositol 3,4,5-trisphosphate 5-phosphatase 2 Inppl1	271.357	160.711	68.504
VATD_MOUSE	2	2	0.002218	V-type proton ATPase subunit D Atp6v1d	857.687	637.595	454.458
DPYL2_MOUSE	8	5	0.00225	Dihydropyrimidinase-related protein 2 Dpysl2	2907.414	3713.118	3408.112
MTMR9_MOUSE	1	1	0.002266	Myotubularin-related protein 9 Mtmr9	4738.486	1942.200	2228.770
HP1B3_MOUSE	4	4	0.002283	Heterochromatin protein 1-binding protein 3 Hp1bp3	1357.921	2206.961	2911.458

PDCL3_MOUSE	1	1	0.002308	Phosducin-like protein 3 Pdcl3	119.229	36.855	23.612
SC31A_MOUSE	4	3	0.002326	Protein transport protein Sec31A Sec31a	206.013	447.245	244.983
HNRPC_MOUSE	1	1	0.002359	Heterogeneous nuclear ribonucleoproteins C1/C2 Hnrnpc	232.609	363.725	357.623
RL15_MOUSE	4	4	0.002372	60S ribosomal protein L15 Rpl15	1964.292	3517.346	3917.911
IF1AX_MOUSE	3	3	0.002435	Eukaryotic translation initiation factor 1A, X-chromosomal Eif1ax	1501.881	788.415	844.603
PSA_MOUSE	8	6	0.002458	Puromycin-sensitive aminopeptidase Npepps	1581.951	2488.725	2174.559
KV2A7_MOUSE	1	1	0.002474	Ig kappa chain V-II region 26-10	254.429	12.669	9.573
RL4_MOUSE	11	10	0.00248	60S ribosomal protein L4 Rpl4	4440.129	6123.448	7311.898
TXNL1_MOUSE	6	5	0.002494	Thioredoxin-like protein 1 Txnl1	1292.877	985.607	920.345
HEM2_MOUSE	9	9	0.002549	Delta-aminolevulinic acid dehydratase Alad	5259.694	3345.516	3967.189
ANXA4_MOUSE	15	13	0.00257	Annexin A4 Anxa4	8100.825	5974.301	7701.972
PLTP_MOUSE	10	10	0.002581	Phospholipid transfer protein Pltp	6880.236	6609.912	11524.329
ENPL_MOUSE	11	9	0.002592	Endoplasmin Hsp90b1	6949.009	5093.365	7146.913
SYDC_MOUSE	16	14	0.00269	Aspartate--tRNA ligase, cytoplasmic Dars1	8864.217	12847.605	9930.371
ST32B_MOUSE	1	1	0.002709	Serine/threonine-protein kinase 32B Stk32b	303.642	563.276	469.329
RS24_MOUSE	3	3	0.00272	40S ribosomal protein S24 Rps24	1494.438	4881.334	3205.791
FBLN5_MOUSE	6	6	0.002724	Fibulin-5 Fbln5	6945.159	10324.356	9522.350
SYAC_MOUSE	4	4	0.002724	Alanine--tRNA ligase, cytoplasmic Aars1	560.589	363.578	280.597
ZN654_MOUSE	1	1	0.00273	Zinc finger protein 654 Znf654	149.575	92.216	203.313
S39A8_MOUSE	1	1	0.002764	Metal cation symporter ZIP8 Slc39a8	1282.232	726.549	1025.269
FGF21_MOUSE	2	2	0.002796	Fibroblast growth factor 21 Fgf21	701.174	319.083	342.090

IFI2_MOUSE	2	2	0.002898	Interferon-activable protein 202 Ifi202	233.556	516.009	578.076
PLA1A_MOUSE	1	1	0.002974	Phospholipase A1 member A Pla1a	218.222	559.024	558.464
H2A1B_MOUSE	5	2	0.003005	Histone H2A type 1-B H2ac4	3410.485	11569.201	12211.559
ADA10_MOUSE	1	1	0.003007	Disintegrin and metalloproteinase domain containing protein 10 Adam10	35.395	9.894	29.989
SFRP2_MOUSE	4	4	0.003017	Secreted frizzled-related protein 2 Sfrp2	1387.855	763.954	1417.052
ERF1_MOUSE	5	4	0.003021	Eukaryotic peptide chain release factor subunit 1 Etf1	1291.448	945.552	903.881
SPA3B_MOUSE	1	1	0.003028	Serine protease inhibitor A3B Serpina3b	291.055	60.437	56.222
SUMO2_MOUSE	1	1	0.003041	Small ubiquitin-related modifier 2 Sumo2	100.919	78.606	170.460
CD34_MOUSE	3	3	0.003049	Hematopoietic progenitor cell antigen CD34 Cd34	1359.154	1715.140	2241.244
PDGFC_MOUSE	2	2	0.003097	Platelet-derived growth factor C Pdgfc	392.830	390.180	237.523
NAA16_MOUSE	1	1	0.003158	N-alpha-acetyltransferase 16, NatA auxiliary subunit Naa16	167.733	269.959	405.194
EI2BA_MOUSE	1	1	0.003161	Translation initiation factor eIF-2B subunit alpha Eif2b1	40.066	149.669	170.920
PIPNA_MOUSE	1	1	0.003201	Phosphatidylinositol transfer protein alpha isoform Pitpna	643.609	282.862	339.832
PCNA_MOUSE	1	1	0.003208	Proliferating cell nuclear antigen Pcna	404.484	122.957	218.757
EF1A1_MOUSE	19	13	0.003278	Elongation factor 1-alpha 1 Eef1a1	54620.832	67733.643	43875.428
ROA2_MOUSE	5	5	0.00328	Heterogeneous nuclear ribonucleoproteins A2/B1 Hnrnpa2b1	804.373	986.854	1336.106
COPB_MOUSE	7	6	0.003319	Coatomer subunit beta Copb1	1106.684	1066.274	890.892
UBE2Z_MOUSE	1	1	0.003356	Ubiquitin-conjugating enzyme E2 Z Ube2z	346.774	463.029	446.804

RL8_MOUSE	4	4	0.003378	60S ribosomal protein L8 Rpl8	1390.933	2734.168	2531.090
SYHM_MOUSE	1	1	0.003389	Histidine--tRNA ligase, mitochondrial Hars2	55.461	275.101	319.174
C1QT1_MOUSE	1	1	0.003417	Complement C1q tumor necrosis factor related protein 1 C1qtnf1	72.645	123.504	99.438
H12_MOUSE	10	1	0.003459	Histone H1.2 H1-2	146.972	1622.945	1315.332
ACTBL_MOUSE	18	1	0.003476	Beta-actin-like protein 2 Actbl2	0.249	47.051	1.587
NEDD8_MOUSE	1	1	0.003492	NEDD8 Nedd8	1155.365	337.145	732.030

EIF3L_MOUSE	9	9	0.003526	Eukaryotic translation initiation factor 3 subunit L Eif3l	2802.113	2785.622	2353.066
SYNC_MOUSE	8	8	0.003623	Asparagine--tRNA ligase, cytoplasmic NARS1	4505.156	5045.415	3943.260
SEPT9_MOUSE	7	6	0.003626	Septin-9 Septin9	2084.352	2737.019	2215.682
IF2B_MOUSE	1	1	0.003635	Eukaryotic translation initiation factor 2 subunit 2 Eif2s2	43.386	120.392	142.088
RASH_MOUSE	1	1	0.003667	GTPase HRas Hras	29.244	18.570	121.387
IF2A_MOUSE	6	6	0.003697	Eukaryotic translation initiation factor 2 subunit 1 Eif2s1	4903.115	4370.227	3556.657
TXD12_MOUSE	1	1	0.003718	Thioredoxin domain-containing protein 12 Txndc12	143.985	47.215	43.094
RLA0_MOUSE	10	10	0.003718	60S acidic ribosomal protein P0 Rplp0	19550.740	15982.295	15726.197
DCPS_MOUSE	3	3	0.003819	m7GpppX diphosphatase Dcps	576.682	393.120	375.317
NONO_MOUSE	4	1	0.003845	Non-POU domain-containing octamerbinding protein Nono	212.653	279.488	5.004
RAP1A_MOUSE	2	2	0.003883	Ras-related protein Rap-1A Rap1a	1679.292	1202.210	1825.674
TSP1_MOUSE	2	2	0.003901	Thrombospondin-1 Thbs1	1053.524	749.796	1085.629

TOP1_MOUSE	5	5	0.00393	DNA topoisomerase 1 Top1	531.070	963.180	1001.269
ORC1_MOUSE	1	1	0.003956	Origin recognition complex subunit 1 Orc1	338.432	215.227	283.411
ECM29_MOUSE	1	1	0.004013	Proteasome adapter and scaffold protein ECM29 Ecpas	117.193	64.702	45.112
ENPP1_MOUSE	2	2	0.004101	Ectonucleotide pyrophosphatase/phosphodiesterase family member 1 Enpp1	121.749	50.876	348.603
IMA3_MOUSE	1	1	0.004117	Importin subunit alpha-3 Kpna4	445.304	77.605	27.179
PRS10_MOUSE	4	4	0.004157	26S proteasome regulatory subunit 10B Psmc6	2349.020	2816.220	1842.414
CAV1_MOUSE	3	2	0.004177	Caveolin-1 Cav1	477.503	989.218	496.176
RL3_MOUSE	7	6	0.004208	60S ribosomal protein L3 Rpl3	1983.456	3081.964	2940.053

TCP4_MOUSE	3	3	0.004228	Activated RNA polymerase II transcriptional coactivator p15 Sub1	2098.556	1152.457	1541.412
IL1AP_MOUSE	1	1	0.004263	granuloctcsfcc-1 receptor accessory protein Il1rap	137.369	31.493	36.891
RACK1_MOUSE	11	11	0.004282	Receptor of activated protein C kinase 1 Rack1	26221.764	33305.186	23650.205
ACACA_MOUSE	1	1	0.004286	Acetyl-CoA carboxylase 1 Acaca	4.669	48.379	19.566
CATZ_MOUSE	4	4	0.004293	Cathepsin Z Ctsz	2438.995	1521.208	1655.337
BIN1_MOUSE	14	12	0.004296	Myc box-dependent-interacting protein 1 Bin1	12030.306	13380.984	9576.081
EF1G_MOUSE	11	10	0.004297	Elongation factor 1-gamma Eef1g	6147.047	7466.281	4716.143
NUCB1_MOUSE	11	9	0.004364	Nucleobindin-1 Nucb1	2484.257	2252.215	2953.990

ROAA_MOUSE	6	6	0.004372	Heterogeneous nuclear ribonucleoprotein A/B Hnrnpab	3049.623	1816.912	2124.473
DHE3_MOUSE	6	6	0.004421	Glutamate dehydrogenase 1, mitochondrial Glud1	1775.369	1718.515	2711.770
EHD4_MOUSE	28	23	0.004451	EH domain-containing protein 4 Ehd4	22277.947	19936.253	29948.362
CPNE1_MOUSE	1	1	0.004526	Copine-1 Cpne1	22.812	25.818	76.265
FXR1_MOUSE	2	2	0.004609	Fragile X mental retardation syndrome-related protein 1 Fxr1	122.714	355.146	311.423
DDX3L_MOUSE	2	2	0.004619	Putative ATP-dependent RNA helicase Pl10 D1Pas1	172.072	427.637	273.749
TTC23_MOUSE	1	1	0.004669	Tetratricopeptide repeat protein 23 Ttc23	601.916	99.334	68.679
DYHC1_MOUSE	26	24	0.004786	Cytoplasmic dynein 1 heavy chain 1 Dync1h1	1935.585	3311.894	2953.130
TMEDA_MOUSE	3	1	0.004818	Transmembrane emp24 domain-containing protein 10 Tmed10	473.470	1033.664	791.404
SERA_MOUSE	9	7	0.004834	D-3-phosphoglycerate dehydrogenase Phgdh	6626.900	5368.197	4303.287
VPS28_MOUSE	2	2	0.004878	Vacuolar protein sorting-associated protein 28 homolog Vps28	134.832	117.512	237.290
FAAA_MOUSE	1	1	0.004989	Fumarylacetoacetase Fah	235.973	260.974	10.328
ALBU_MOUSE	4	4	0.005059	Albumin Alb	232693.122	35101.346	33501.630

2AAA_MOUSE	11	10	0.005164	Serine/threonine-protein phosphatase 2A 65 kDa regulatory subunit A alpha isoform Ppp2r1a	6503.207	5341.920	5208.490
RL10_MOUSE	2	1	0.005189	60S ribosomal protein L10 Rpl10	322.427	525.436	464.589
H2A2A_MOUSE	6	1	0.00521	Histone H2A type 2-A Hist2h2aa1	1616.095	4568.676	4324.471

NCKP1_MOUSE	2	1	0.005243	Nck-associated protein 1 Nckap1	59.593	86.537	38.177
EIF3E_MOUSE	13	13	0.005418	Eukaryotic translation initiation factor 3 subunit E Eif3e	5437.450	6964.269	5670.304
COPG2_MOUSE	2	2	0.005524	Coatomer subunit gamma-2 Copg2	50.053	151.934	136.694
APEH_MOUSE	3	3	0.005563	Acylamino-acid-releasing enzyme Apeh	685.822	469.037	689.783
MP2K1_MOUSE	1	1	0.005677	Dual specificity mitogen-activated protein kinase kinase 1 Map2k1	48.014	110.510	67.342
SPSY_MOUSE	2	2	0.005852	Spermine synthase Sms	262.429	139.511	161.563
ARPC5_MOUSE	1	1	0.005916	Actin-related protein 2/3 complex subunit 5 Arpc5	480.064	584.097	787.149
ATR_MOUSE	1	1	0.006042	Serine/threonine-protein kinase ATR Atr	71.726	376.138	294.609
TMED9_MOUSE	2	1	0.006044	Transmembrane emp24 domaincontaining protein 9 Tmed9	758.701	1488.410	1405.682
RB11B_MOUSE	9	1	0.006103	Ras-related protein Rab-11B Rab11b	444.189	553.685	370.977
1433E_MOUSE	19	14	0.006206	14-3-3 protein epsilon Ywhae	17832.677	12947.658	16876.827
PDC6I_MOUSE	14	12	0.00621	Programmed cell death 6-interacting protein Pdcd6ip	8147.732	5576.182	5790.835
RSU1_MOUSE	6	6	0.006222	Ras suppressor protein 1 Rsu1	2965.635	2038.525	2943.133
CALU_MOUSE	10	9	0.006376	Calumenin Calu	7298.945	6112.972	3712.653
RPAB1_MOUSE	1	1	0.006448	DNA-directed RNA polymerases I, II, and III subunit RPABC1 Polr2e	54.842	45.964	25.338
CD9_MOUSE	2	2	0.006683	CD9 antigen Cd9	19910.435	14812.604	19931.429
ANXA7_MOUSE	7	7	0.006836	Annexin A7 Anxa7	3008.067	3318.357	5090.366
RL22_MOUSE	2	2	0.006903	60S ribosomal protein L22 Rpl22	1646.107	2413.605	1829.348
GDIA_MOUSE	6	2	0.006972	Rab GDP dissociation inhibitor alpha Gdi1	255.586	171.263	257.553

ALD1_MOUSE	4	1	0.00699	Aldo-keto reductase family 1 member B7 Akr1b7	31.764	117.108	50.577
MOES_MOUSE	40	28	0.007008	Moesin Msn	38060.296	29609.893	40246.618
MACF1_MOUSE	7	6	0.007024	Microtubule-actin cross-linking factor 1 Macf1	451.905	800.481	298.839
RL23_MOUSE	3	3	0.007055	60S ribosomal protein L23 Rpl23	1813.336	1463.003	1175.862
TADBP_MOUSE	2	1	0.007167	TAR DNA-binding protein 43 Tardbp	15.570	60.463	42.911
EIF3B_MOUSE	3	3	0.007243	Eukaryotic translation initiation factor 3 subunit B Eif3b	591.328	658.873	533.444
TPR_MOUSE	1	1	0.007274	Nucleoprotein TPR Tpr	143.210	62.805	81.224
CD47_MOUSE	5	5	0.007283	Leukocyte surface antigen CD47 Cd47	912.592	1165.764	1736.046
RU17_MOUSE	1	1	0.007293	U1 small nuclear ribonucleoprotein 70 kDa Snrnp70	347.012	558.073	476.389
PCSK9_MOUSE	1	1	0.007295	Proprotein convertase subtilisin/kexin type 9 Pcsk9	291.076	101.090	130.975
PSMD6_MOUSE	9	8	0.007307	26S proteasome non-ATPase regulatory subunit 6 Psmd6	5808.735	4058.764	3557.942
AIMP1_MOUSE	1	1	0.007354	Aminoacyl tRNA synthase complex-interacting multifunctional protein 1 Aimp1	36.417	113.314	101.451
TEKT3_MOUSE	1	1	0.007372	Tektin-3 Tekt3	304.124	197.355	383.415
RS23_MOUSE	1	1	0.007375	40S ribosomal protein S23 Rps23	1576.866	2707.443	2051.213
PSA6_MOUSE	10	10	0.007409	Proteasome subunit alpha type-6 Psma6	28962.794	24046.510	21316.617
AASD1_MOUSE	1	1	0.007476	Alanyl-tRNA editing protein Aarsd1 Aarsd1	536.570	93.657	42.578
GBB1_MOUSE	2	1	0.007524	Guanine nucleotide-binding protein G(I)/G(S)/G(T) subunit beta-1 Gnb1	812.134	678.987	1502.914
TPM1_MOUSE	8	4	0.007543	Tropomyosin alpha-1 chain Tpm1	1443.133	1882.513	1770.457

ADPRH_MOUSE	4	4	0.007549	[Protein ADP-ribosylarginine] hydrolase Adprh	1920.478	2275.850	1440.602
CAD13_MOUSE	5	4	0.007667	Cadherin-13 Cdh13	1035.703	2350.287	2205.823
TWF1_MOUSE	2	1	0.007677	Twinfilin-1 Twf1	206.750	89.915	150.948

IDHC_MOUSE	12	10	0.00773	Isocitrate dehydrogenase [NADP] cytoplasmic Idh1	5754.235	4846.307	4136.787
ANXA6_MOUSE	29	26	0.007738	Annexin A6 Anxa6	37293.143	26753.963	39461.875
MOT1_MOUSE	3	3	0.007761	Monocarboxylate transporter 1 Slc16a1	935.411	749.760	1134.971
LGUL_MOUSE	5	5	0.007856	Lactoylglutathione lyase Glo1	1760.436	1646.107	2105.730
PDIA3_MOUSE	17	16	0.008058	Protein disulfide-isomerase A3 Pdia3	11361.417	8488.087	10772.222
WDR1_MOUSE	6	6	0.008063	WD repeat-containing protein 1 Wdr1	4070.470	5958.469	5681.145
OLFL3_MOUSE	5	4	0.008337	Olfactomedin-like protein 3 Olfml3	5627.482	4430.201	4026.524
RS9_MOUSE	8	8	0.008338	40S ribosomal protein S9 Rps9	18327.539	29415.896	23472.186
MA7D3_MOUSE	1	1	0.008367	MAP7 domain-containing protein 3 Map7d3	2.236	18.585	228.489
HCD2_MOUSE	1	1	0.00856	3-hydroxyacyl-CoA dehydrogenase type-2 Hsd17b10	30.451	106.522	401.930
CRP_MOUSE	1	1	0.008808	C-reactive protein Crp	238.464	124.809	118.686
RL27A_MOUSE	2	2	0.008856	60S ribosomal protein L27a Rpl27a	862.398	1236.744	1099.846
IBP3_MOUSE	1	1	0.00889	Insulin-like growth factor-binding protein 3 Igfbp3	7343.158	10801.680	9920.463
CPNE2_MOUSE	4	3	0.008975	Copine-2 Cpne2	1649.425	1181.671	1886.883
EIF3I_MOUSE	2	2	0.009011	Eukaryotic translation initiation factor 3 subunit I Eif3i	581.254	766.014	651.990
MUG1_MOUSE	1	1	0.009091	Murinoglobulin-1 Mug1	783.950	16.823	14.138
STRN3_MOUSE	4	3	0.009306	Striatin-3 Strn3	625.360	987.714	763.893

GGH_MOUSE	1	1	0.009668	Gamma-glutamyl hydrolase Ggh	442.095	389.173	207.695
HYEP_MOUSE	2	2	0.009723	Epoxide hydrolase 1 Ephx1	328.474	255.171	325.052
UGPA_MOUSE	11	11	0.00973	UTP--glucose-1-phosphate uridylyltransferase Ugp2	8619.585	9066.719	7370.284
CHM4B_MOUSE	3	3	0.00973	Charged multivesicular body protein 4b Chmp4b	912.072	637.466	1365.079
PACN3_MOUSE	2	2	0.009855	Protein kinase C and casein kinase II substrate protein 3 Pacsin3	404.587	523.201	878.182
ESYT1_MOUSE	1	1	0.00989	Extended synaptotagmin-1 Esyt1	11.926	1.972	4.639
YBOX3_MOUSE	2	1	0.010279	Y-box-binding protein 3 Ybx3	39.578	12.746	12.017
CSN4_MOUSE	11	11	0.010346	COP9 signalosome complex subunit 4 Cops4	5229.000	5567.574	5737.191
CTL1_MOUSE	2	2	0.010419	Choline transporter-like protein 1 Slc44a1	58.957	122.121	197.025
FA5_MOUSE	2	2	0.010481	Coagulation factor V F5	612.393	411.028	336.021
RUVB1_MOUSE	10	10	0.010651	RuvB-like 1 Ruvbl1	6028.941	6728.104	5105.535
ADRM1_MOUSE	3	3	0.010654	Proteasomal ubiquitin receptor ADRM1 Adrm1	220.669	354.346	256.973
SNAA_MOUSE	4	4	0.010676	Alpha-soluble NSF attachment protein Napa	883.138	585.575	855.788
CRYAB_MOUSE	9	9	0.010694	Alpha-crystallin B chain Cryab	24172.491	48747.630	23481.332
S29A1_MOUSE	2	2	0.011014	Equilibrative nucleoside transporter 1 Slc29a1	765.008	849.475	491.639
RL18A_MOUSE	2	2	0.011104	60S ribosomal protein L18a Rpl18a	130.914	260.990	197.152
AP2B1_MOUSE	4	2	0.01111	AP-2 complex subunit beta Ap2b1	577.004	374.670	316.310
PURB_MOUSE	13	10	0.011199	Transcriptional activator protein Pur-beta Purb	10244.057	8733.565	10896.155

SSRA_MOUSE	1	1	0.011201	Translocon-associated protein subunit alpha Ssr1	69.062	249.576	314.089
DDAH2_MOUSE	1	1	0.011242	N(G),N(G)-dimethylarginine dimethylaminohydrolase 2 Ddah2	90.673	41.678	75.755
HA10_MOUSE	2	1	0.011376	H-2 class I histocompatibility antigen, Q10 alpha chain H2-Q10	199.105	11.485	6.616
PAIRB_MOUSE	1	1	0.011427	Plasminogen activator inhibitor 1 RNAbinding protein Serbp1	213.561	204.001	130.642
U520_MOUSE	1	1	0.011455	U5 small nuclear ribonucleoprotein 200 kDa helicase Snrnp200	3.199	37.075	34.837
MYL4_MOUSE	3	2	0.011561	Myosin light chain 4 Myl4	461.878	331.531	411.825
TCPH_MOUSE	22	20	0.011822	T-complex protein 1 subunit eta Cct7	22690.102	21671.178	19404.982
RANG_MOUSE	1	1	0.012051	Ran-specific GTPase-activating protein Ranbp1	116.143	90.038	164.421
AATC_MOUSE	10	9	0.012106	Aspartate aminotransferase, cytoplasmic Got1	3531.725	2771.870	3039.967

CRSPL_MOUSE	2	1	0.0122	Peptidase inhibitor R3HDML R3hdml	97.268	164.476	161.378
AP2D_MOUSE	1	1	0.012308	Transcription factor AP-2-delta Tfap2d	267.546	120.957	150.445
ITAV_MOUSE	1	1	0.012373	Integrin alpha-V Itgav	20.554	26.031	87.287
HS90A_MOUSE	29	16	0.012412	Heat shock protein HSP 90-alpha Hsp90aa1	24635.060	18228.140	21591.642
HTRA1_MOUSE	15	13	0.012546	Serine protease HTRA1 Htra1	24505.492	19219.125	14560.487
OSTP_MOUSE	2	2	0.012719	Osteopontin Spp1	1661.047	1576.804	3193.269
LIS1_MOUSE	2	1	0.012775	Platelet-activating factor acetylhydrolase IB subunit beta Pafah1b1	315.791	121.934	106.653
SPB6_MOUSE	15	14	0.012956	Serpin B6 Serpinb6	13957.478	15150.313	12304.520

CAP2_MOUSE	6	6	0.013051	Adenylyl cyclase-associated protein 2 Cap2	1963.896	2431.591	1532.562
ARP2_MOUSE	6	5	0.013077	Actin-related protein 2 Actr2	1893.357	1582.979	1178.118
RS11_MOUSE	6	5	0.013105	40S ribosomal protein S11 Rps11	8975.824	12232.493	9656.336
SORCN_MOUSE	3	2	0.013171	Sorcin Sri	470.518	297.105	606.453
FAS_MOUSE	27	26	0.013189	Fatty acid synthase Fasn	9386.049	9632.301	8345.782
CDC37_MOUSE	1	1	0.013355	Hsp90 co-chaperone Cdc37 Cdc37	344.385	175.394	226.174
VAPA_MOUSE	1	1	0.013364	Vesicle-associated membrane proteinassociated protein A Vapa	198.500	249.870	132.316
NB5R3_MOUSE	2	2	0.013392	NADH-cytochrome b5 reductase 3 Cyb5r3	632.047	457.068	374.713
IPYR_MOUSE	1	1	0.013449	Inorganic pyrophosphatase Ppa1	389.460	251.977	231.570
EIF3F_MOUSE	8	8	0.013501	Eukaryotic translation initiation factor 3 subunit F Eif3f	6211.935	5734.816	4185.072
PPGB_MOUSE	5	5	0.013573	Lysosomal protective protein Ctsa	900.258	1376.828	1849.518
SRPX2_MOUSE	3	3	0.013582	Sushi repeat-containing protein SRPX2 Srpx2	378.096	404.237	657.798
CAZA1_MOUSE	2	2	0.013702	F-actin-capping protein subunit alpha-1 Capza1	1115.374	844.887	743.094
BLMH_MOUSE	2	2	0.013726	Bleomycin hydrolase Blmh	1460.412	945.946	1075.118
TCO2_MOUSE	3	3	0.013828	Transcobalamin-2 Tcn2	3127.155	2343.225	2580.165
NSDHL_MOUSE	1	1	0.014117	Sterol-4-alpha-carboxylate 3dehydrogenase, decarboxylating Nsdhl	50.416	115.939	69.834
CAND2_MOUSE	1	1	0.014231	Cullin-associated NEDD8-dissociated protein 2 Cand2	12.329	42.072	6.654
RL19_MOUSE	3	3	0.014527	60S ribosomal protein L19 Rpl19	2283.176	3394.555	2818.575
RS26_MOUSE	2	2	0.014536	40S ribosomal protein S26 Rps26	7446.389	11836.798	9794.149

AP2M1_MOUSE	4	4	0.014547	AP-2 complex subunit mu Ap2m1	741.219	816.778	675.789
RL28_MOUSE	5	5	0.014649	60S ribosomal protein L28 Rpl28	3125.949	4417.301	3575.632
PPP5_MOUSE	1	1	0.015005	Serine/threonine-protein phosphatase 5 Ppp5c	88.815	45.539	41.316
TICN2_MOUSE	1	1	0.015069	Testican-2 Spock2	393.967	1821.593	1822.474
GSHB_MOUSE	7	4	0.015735	Glutathione synthetase Gss	970.024	1115.904	681.772
THIM_MOUSE	1	1	0.015802	3-ketoacyl-CoA thiolase, mitochondrial Acaa2	39.164	53.500	90.097
LAMP2_MOUSE	2	2	0.015861	Lysosome-associated membrane glycoprotein 2 Lamp2	2464.987	2573.365	3473.290
KLC1_MOUSE	2	2	0.015897	Kinesin light chain 1 Klc1	215.583	382.648	232.286
EIF3A_MOUSE	14	12	0.015963	Eukaryotic translation initiation factor 3 subunit A Eif3a	4364.860	5700.238	4807.051
UBC12_MOUSE	3	3	0.016041	NEDD8-conjugating enzyme Ubc12 Ube2m	403.649	469.119	284.157
LEG1_MOUSE	2	2	0.01647	Galectin-1 Lgals1	7031.448	4848.177	4482.261
DC1L1_MOUSE	3	3	0.016665	Cytoplasmic dynein 1 light intermediate chain 1 Dync1li1	348.258	590.937	510.665
MYH9_MOUSE	82	59	6877	Myosin-9 Myh9	60481.351	64833.009	56443.880
MYH10_MOUSE	16	2	0.01 0.01696	Myosin-10 Myh10	24.116	114.773	73.612
ILEUA_MOUSE	4	4	0.017195	Leukocyte elastase inhibitor A Serpinb1a	1271.002	1664.703	1738.692
RET_MOUSE	1	1	0.01731	Proto-oncogene tyrosine-protein kinase receptor Ret Ret	600.688	803.237	592.951
XPO2_MOUSE	6	5	0.017325	Exportin-2 Cse1l	707.274	934.484	601.493
CCG1_MOUSE	1	1	0.017489	Voltage-dependent calcium channel gamma-1 subunit Cacng1	12.810	82.949	355.950

PSD11_MOUSE	13	11	0.017586	26S proteasome non-ATPase regulatory subunit 11 Psmd11	8185.481	9121.391	7535.937
RL27_MOUSE	3	3	0.017736	60S ribosomal protein L27 Rpl27	3587.984	6472.225	5573.985
MYO1C_MOUSE	1	1	0.017799	Unconventional myosin-Ic Myo1c	1.843	17.994	2.317
ADHX_MOUSE	5	4	0.017847	Alcohol dehydrogenase class-3 Adh5	1382.316	767.121	785.488
4F2_MOUSE	3	2	0.018634	4F2 cell-surface antigen heavy chain Slc3a2	1222.222	677.491	1158.676
COIA1_MOUSE	4	3	0.018847	Collagen alpha-1(XVIII) chain Col18a1	603.897	619.585	781.495
BASI_MOUSE	6	5	0.018943	Basigin Bsg	3026.204	2801.827	3884.238
RL24_MOUSE	4	4	0.019164	60S ribosomal protein L24 Rpl24	4990.522	7979.889	7369.643
BASP1_MOUSE	3	3	0.019184	Brain acid soluble protein 1 Basp1	424.308	495.873	734.392
EXT1_MOUSE	4	4	0.01968	Exostosin-1 Ext1	782.414	389.092	738.539
IBP7_MOUSE	3	3	0.019695	Insulin-like growth factor-binding protein 7 Igfbp7	646.335	362.708	871.834
CACB1_MOUSE	2	1	0.019929	Voltage-dependent L-type calcium channel subunit beta-1 Cacnb1	51.372	84.591	107.873
PLPP1_MOUSE	2	2	0.020174	Phospholipid phosphatase 1 Plpp1	280.695	446.043	533.342
RFOX3_MOUSE	1	1	0.020471	RNA binding protein fox-1 homolog 3 Rbfox3	141.375	97.407	93.098
PDIA6_MOUSE	11	11	0.020584	Protein disulfide-isomerase A6 Pdia6	7102.382	5804.936	6153.894
DDX1_MOUSE	1	1	0.020612	ATP-dependent RNA helicase DDX1 Ddx1	21.451	75.010	39.938
IF4A1_MOUSE	23	13	0.020669	Eukaryotic initiation factor 4A-I Eif4a1	12872.339	16633.687	10069.406
ATPO_MOUSE	2	1	0.020738	ATP synthase subunit O, mitochondrial Atp5po	52.966	121.020	129.955
SC23A_MOUSE	5	4	0.020764	Protein transport protein Sec23A Sec23a	1341.414	2327.777	2264.983
HSP13_MOUSE	1	1	0.020938	Heat shock 70 kDa protein 13 Hspa13	86.515	107.883	167.806
TSN6_MOUSE	2	1		Tetraspanin-6 Tspan6	864.914	2034.912	1827.149

DPP2_MOUSE	3	2	0.021033 0.021209	Dipeptidyl peptidase 2 Dpp7	314.722	313.385	433.342
TSP2_MOUSE	1	1	0.021345	Thrombospondin-2 Thbs2	2.782	37.066	7.697

JSPR1_MOUSE	1	1	0.021456	Junctional sarcoplasmic reticulum protein 1 Jsrp1	178.077	329.805	215.317
CLCB_MOUSE	1	1	0.021531	Clathrin light chain B Cltb	289.893	298.782	370.341
RAB5C_MOUSE	4	3	0.021737	Ras-related protein Rab-5C Rab5c	725.011	562.122	419.247
CPNS1_MOUSE	7	6	0.022049	Calpain small subunit 1 Capns1	1407.958	802.127	1191.035
RL35_MOUSE	1	1	0.022272	60S ribosomal protein L35 Rpl35	460.344	1100.863	997.739
RS5_MOUSE	3	2	0.022285	40S ribosomal protein S5 Rps5	889.635	1051.526	905.410
THOP1_MOUSE	10	9	0.022557	Thimet oligopeptidase Thop1	2454.922	3378.073	3356.401
PSMD5_MOUSE	3	2	0.02287	26S proteasome non-ATPase regulatory subunit 5 Psmd5	425.535	273.617	351.673
NIBA2_MOUSE	4	3	92	Protein Niban 2 Niban2	380.896	601.058	556.674
TITIN_MOUSE	4	3	0.0228 0.023234	Titin Ttn	362.739	454.798	284.453
SET_MOUSE	3	3	0.023394	Protein SET Set	3658.709	2088.497	3007.192
ACTN1_MOUSE	24	11	0.023406	Alpha-actinin-1 Actn1	5733.044	5189.764	4940.744
RNT2A_MOUSE	2	2	0.023417	Ribonuclease T2-A Rnaset2a	822.222	493.918	631.602
RS17_MOUSE	5	5	0.023491	40S ribosomal protein S17 Rps17	1535.239	2955.277	1866.238
BIR1A_MOUSE	1	1	0.023706	Baculoviral IAP repeat-containing protein 1a Naip1	24660.403	19797.374	30236.048
RL13A_MOUSE	6	5	0.023816	60S ribosomal protein L13a Rpl13a	4461.214	6588.647	4908.441
PPP6_MOUSE	2	1	0.024053	Serine/threonine-protein phosphatase 6 catalytic subunit Ppp6c	92.894	49.052	50.219

KNDC1_MOUSE	1	1	0.024419	Kinase non-catalytic C-lobe domaincontaining protein 1 Kndc1	92.614	668.678	429.190
ACLY_MOUSE	8	8	0.024469	ATP-citrate synthase Acly	1496.970	2007.558	1856.039
NIF3L_MOUSE	1	1	0.024839	NIF3-like protein 1 Nif3l1	95.028	99.811	139.244
ECI1_MOUSE	1	1	0.025201	Enoyl-CoA delta isomerase 1, mitochondrial Eci1	42.965	79.046	99.828
H2AV_MOUSE	3	1	0.025325	Histone H2A.V H2az2	756.081	3001.000	1942.099
ACOT1_MOUSE	1	1	0.025465	Acyl-coenzyme A thioesterase 1 Acot1	54.489	33.594	49.755
MLP3A_MOUSE	1	1	0.025952	Microtubule-associated proteins 1A/1B light chain 3A Map1lc3a	0.000	86.527	49.948

H4_MOUSE	12	11	0.026007	Histone H4 H4c1	48279.401	238710.585	218173.732
SYCC_MOUSE	2	2	0.02626	Cysteine--tRNA ligase, cytoplasmic Cars1	351.636	519.192	610.914
2ABA_MOUSE	2	1	0.026297	Serine/threonine-protein phosphatase 2A 55 kDa regulatory subunit B alpha isoform Ppp2r2a	88.116	176.821	89.454
PRS23_MOUSE	3	3	0.026544	Serine protease 23 Prss23	1392.542	1654.882	2167.645
HNRPK_MOUSE	4	4	0.026959	Heterogeneous nuclear ribonucleoprotein K Hnrnpk	2114.072	2269.904	1731.265
UN45B_MOUSE	2	2	0.027436	Protein unc-45 homolog B Unc45b	613.226	379.616	350.685
PDIA4_MOUSE	5	5	0.02746	Protein disulfide-isomerase A4 Pdia4	1885.818	971.978	1677.961
CRLF1_MOUSE	1	1	0.027503	Cytokine receptor-like factor 1 Crlf1	183.369	175.916	103.109
TKT_MOUSE	7	7	0.02779	Transketolase Tkt	1342.072	1501.947	1822.865
CYBP_MOUSE	1	1	0.028152	Calcyclin-binding protein Cacybp	153.834	99.331	138.758
AT2A2_MOUSE	1	1	0.028233	Sarcoplasmic/endoplasmic reticulum calcium ATPase 2 Atp2a2	5.291	54.569	21.033

TM9S1_MOUSE	1	1	0.028323	Transmembrane 9 superfamily member 1 Tm9sf1	4398.127	4816.147	3869.734
KAP2_MOUSE	2	2	0.028755	cAMP-dependent protein kinase type IIalpha regulatory subunit Prkar2a	270.577	369.069	314.827
LAP2A_MOUSE	1	1	0.029034	Lamina-associated polypeptide 2, isoforms alpha/zeta Tmpo	155.490	268.915	205.418
RS18_MOUSE	8	7	0.029165	40S ribosomal protein S18 Rps18	10336.841	20875.485	12542.518
AMRP_MOUSE	1	1	0.029382	Alpha-2-macroglobulin receptorassociated protein Lrpap1	79.831	122.551	101.644
SMD3_MOUSE	1	1	0.029854	Small nuclear ribonucleoprotein Sm D3 Snrpd3	109.142	260.075	172.501
H2B1A_MOUSE	2	1	0.030283	Histone H2B type 1-A H2bc1	48.814	59.612	100.441
TNNC1_MOUSE	1	1	0.030468	Troponin C, slow skeletal and cardiac muscles Tnnc1	367.958	419.134	661.659
PIGR_MOUSE	1	1	0.030517	Polymeric immunoglobulin receptor Pigr	451.084	703.237	614.218
NACAM_MOUSE	2	1	0.031003	Nascent polypeptide-associated complex subunit alpha, muscle-specific form Naca	66.020	152.238	145.758
SPTB2_MOUSE	7	5	0.031211	Spectrin beta chain, non-erythrocytic 1 Sptbn1	471.198	749.057	642.353
VATB2_MOUSE	7	5	0.032053	V-type proton ATPase subunit B, brain isoform Atp6v1b2	7818.434	5115.221	6617.940
PUR9_MOUSE	3	2	0.032058	Bifunctional purine biosynthesis protein ATIC Atic	566.397	567.677	398.047
PLOD1_MOUSE	15	11	0.03224	Procollagen-lysine,2-oxoglutarate 5dioxygenase 1 Plod1	10967.221	13301.623	8593.564
MFGM_MOUSE	12	12	0.032252	Lactadherin Mfge8	7547.104	8710.688	9626.203
KLH40_MOUSE	4	3	0.033104	Kelch-like protein 40 Klhl40	298.331	699.153	464.278

KCRM_MOUSE	12	12	033818	Creatine kinase M-type Ckm	8513.177	9779.331	8376.790
OLA1_MOUSE	3	3	0. 0.034658	Obg-like ATPase 1 Ola1	1086.580	1208.733	938.052
VAMP5_MOUSE	3	1	0.034867	Vesicle-associated membrane protein 5 Vamp5	72.364	2.563	69.830
OBSCN_MOUSE	1	1	0.034933	Obscurin Obscn	39.390	178.394	119.460
CSN3_MOUSE	4	3	0.035454	COP9 signalosome complex subunit 3 Cops3	876.625	733.006	822.060
AT1B3_MOUSE	2	2	0.036055	Sodium/potassium-transporting ATPase subunit beta-3 Atp1b3	774.273	873.070	1197.404
COMD2_MOUSE	1	1	0.03661	COMM domain-containing protein 2 Commd2	48.260	111.931	102.461
AQP1_MOUSE	1	1	0.036929	Aquaporin-1 Aqp1	146.097	195.853	231.125
PSMD7_MOUSE	10	10	0.037121	26S proteasome non-ATPase regulatory subunit 7 Psmd7	3964.467	5157.344	4060.837
SYQ_MOUSE	2	2	0.0374	Glutamine--tRNA ligase Qars1	159.596	216.456	146.933
PPIB_MOUSE	9	8	0.03774	Peptidyl-prolyl cis-trans isomerase B Ppib	6901.033	8444.117	10086.993
RL21_MOUSE	6	6	0.037912	60S ribosomal protein L21 Rpl21	3324.979	4999.606	3354.476
TKTL1_MOUSE	1	1	0.03793	Transketolase-like protein 1 Tktl1	514.275	681.863	731.549
DHYS_MOUSE	1	1	0.037933	Deoxyhypusine synthase Dhps	47.892	50.456	3.441

HDGF_MOUSE	4	4	0.038273	Hepatoma-derived growth factor Hdgf	1056.396	893.468	1194.376
6PGD_MOUSE	11	11	0.038649	6-phosphogluconate dehydrogenase, decarboxylating Pgd	4958.202	4205.656	4257.504
HS105_MOUSE	1	1	0.03873	Heat shock protein 105 kDa Hsph1	303.877	445.470	398.343
ECM1_MOUSE	6	5	0.038759	Extracellular matrix protein 1 Ecm1	4946.841	4258.966	5153.018
RINI_MOUSE	2	2		Ribonuclease inhibitor Rnh1	526.956	297.109	348.580

BAG6_MOUSE	1	1	0.038791 0.03885	Large proline-rich protein BAG6 Bag6	42.684	95.452	63.804
CD63_MOUSE	3	3	0.038904	CD63 antigen Cd63	8485.216	6077.444	9068.651
AGRE5_MOUSE	5	5	0.039048	Adhesion G protein-coupled receptor E5 Adgre5	1169.379	1431.921	1989.351
COPD_MOUSE	3	3	0.039104	Coatomer subunit delta Arcn1	446.047	467.614	521.767
MOB1A_MOUSE	2	2	0.0402	MOB kinase activator 1A Mob1a	248.851	324.377	348.410
TSK_MOUSE	1	1	0.040244	Tsukushi Tsku	307.936	424.805	372.409
UAP1L_MOUSE	5	3	0.040775	UDP-N-acetylhexosamine pyrophosphorylase-like protein 1 Uap1l1	808.281	939.682	1106.340
H2B1B_MOUSE	8	2	0.040833	Histone H2B type 1-B H2bc3	13484.653	46190.640	54546.794
NPNT_MOUSE	3	2	0.040868	Nephronectin Npnt	518.336	1064.198	694.812
NCAM1_MOUSE	10	10	0.041031	Neural cell adhesion molecule 1 Ncam1	4155.736	4927.108	5414.188
GAS6_MOUSE	1	1	0.041041	Growth arrest-specific protein 6 Gas6	186.815	369.236	125.432
PSB2_MOUSE	9	8	0.041532	Proteasome subunit beta type-2 Psmb2	11269.363	8484.261	9128.302
ABEC2_MOUSE	4	3	0.041911	C->U-editing enzyme APOBEC-2 Apobec2	369.659	568.736	154.827
RSMB_MOUSE	2	2	0.041994	Small nuclear ribonucleoproteinassociated protein B Snrpb	105.522	217.451	182.438
SRSF1_MOUSE	3	2	0.042353	Serine/arginine-rich splicing factor 1 Srsf1	534.755	510.316	606.961
CA2D1_MOUSE	5	4	0.042588	Voltage-dependent calcium channel subunit alpha-2/delta-1 Cacna2d1	645.102	425.466	619.989
RL11_MOUSE	2	2	0.042696	60S ribosomal protein L11 Rpl11	3900.437	4687.407	3399.780
USP9X_MOUSE	2	1	0.042732	Probable ubiquitin carboxyl-terminal hydrolase FAF-X Usp9x	16.076	95.437	49.362

ANGL2_MOUSE	3	2	0.043582	Angiopoietin-related protein 2 Angptl2	383.089	398.699	585.693
HA1D_MOUSE	1	1	0.044166	H-2 class I histocompatibility antigen, K-D alpha chain H2-K1	348.142	122.110	139.299
DAG1_MOUSE	13	12	0.044839	Dystroglycan Dag1	11079.701	9316.941	7903.189
RPAC1_MOUSE	1	1	0.045009	DNA-directed RNA polymerases I and III subunit RPAC1 Polr1c	64.681	71.199	32.986
PGAM2_MOUSE	3	1	0.045587	Phosphoglycerate mutase 2 Pgam2	267.620	314.535	151.368
BIP_MOUSE	19	17	0.046312	Endoplasmic reticulum chaperone BiP Hspa5	22686.749	14985.419	20084.930
HIPL1_MOUSE	1	1	0.046334	HHIP-like protein 1 Hhipl1	4.322	11.502	8.788
TLL2_MOUSE	5	1	0.046402	Tolloid-like protein 2 Tll2	1021.782	610.934	600.910
TBB2B_MOUSE	31	2	0.046448	Tubulin beta-2B chain Tubb2b	1178.243	1628.149	1048.039
PSA3_MOUSE	12	11	0.046696	Proteasome subunit alpha type-3 Psma3	20493.232	16724.606	17248.681
RENT1_MOUSE	1	1	0.046799	Regulator of nonsense transcripts 1 Upf1	4.709	36.030	29.925
UBP14_MOUSE	3	3	0.047227	Ubiquitin carboxyl-terminal hydrolase 14 Usp14	366.888	262.878	254.036
NMT1_MOUSE	3	3	0.047334	Glycylpeptide N-tetradecanoyltransferase 1 Nmt1	307.733	449.869	367.158
CAVN1_MOUSE	6	5	0.04753	Caveolae-associated protein 1 Cavin1	1536.042	2215.879	1385.103
MED23_MOUSE	1	1	0.047644	Mediator of RNA polymerase II transcription subunit 23 Med23	134.090	107.563	172.716
HNRLL_MOUSE	1	1	0.048297	Heterogeneous nuclear ribonucleoprotein L-like Hnrnpll	11.681	16.143	8.560
CTL2_MOUSE	9	6	0.048434	Choline transporter-like protein 2 Slc44a2	2654.775	2909.133	3885.348
SODM_MOUSE	1	1	0.048597	Superoxide dismutase [Mn], mitochondrial Sod2	146.472	217.448	345.156
SAHH_MOUSE	12	11		Adenosylhomocysteinase Ahcy	5498.306	6243.257	4836.099

SLIT2_MOUSE	2	2	0.048671 0.049738	Slit homolog 2 protein Slit2	43.714	74.573	82.852
PLBL2_MOUSE	1	1	0.054023	Putative phospholipase B-like 2 Plbd2	74.827	136.665	69.495
ERP44_MOUSE	2	1	0.054208	Endoplasmic reticulum resident protein 44 Erp44	316.745	343.356	264.369
HSDL2_MOUSE	1	1	0.05422	Hydroxysteroid dehydrogenase-like protein 2 Hsdl2	157.219	269.715	214.737
RAC1_MOUSE	3	3	0.054942	Ras-related C3 botulinum toxin substrate 1 Rac1	1675.119	1151.480	1425.026
HEXB_MOUSE	4	4	0.055592	Beta-hexosaminidase subunit beta Hexb	6320.117	6492.492	14355.546
ACTZ_MOUSE	6	2	0.05691	Alpha-centractin Actr1a	2477.402	2643.104	1935.524
PTGIS_MOUSE	2	2	0.057738	Prostacyclin synthase Ptgis	85.032	128.023	75.449
ROA3_MOUSE	1	1	0.058004	Heterogeneous nuclear ribonucleoprotein A3 Hnrnpa3	276.483	417.751	566.837
TMOD3_MOUSE	1	1	0.058202	Tropomodulin-3 Tmod3	24.132	36.073	101.210
PLS3_MOUSE	4	4	0.058423	Phospholipid scramblase 3 Plscr3	862.031	897.875	1415.345
RWDD1_MOUSE	1	1	0.059044	RWD domain-containing protein 1 Rwdd1	495.858	419.465	336.899
GLU2B_MOUSE	3	1	0.059267	Glucosidase 2 subunit beta Prkcsh	45.268	22.960	38.205
VATE1_MOUSE	2	2	0.059684	V-type proton ATPase subunit E 1 Atp6v1e1	410.703	340.405	430.292
PSA4_MOUSE	8	8	0.060434	Proteasome subunit alpha type-4 Psma4	26047.635	21994.203	21401.720
PPIA_MOUSE	9	9	0.061135	Peptidyl-prolyl cis-trans isomerase A Ppia	20312.335	16165.952	13221.505
CGL_MOUSE	3	2	0.061945	Cystathionine gamma-lyase Cth	137.784	66.206	52.512
SYTC_MOUSE	6	6	0.062174	Threonine--tRNA ligase 1, cytoplasmic Tars1	4223.537	3239.475	2904.744

BAP31_MOUSE	1	1	0.062973	B-cell receptor-associated protein 31 Bcap31	326.361	545.344	355.615
EI2BB_MOUSE	4	2	0.063597	Translation initiation factor eIF-2B subunit beta Eif2b2	235.038	274.832	135.417
COPA_MOUSE	12	9	0.064982	Coatomer subunit alpha Copa	1799.997	2128.201	2072.868
EIF3C_MOUSE	8	6	0.06544	Eukaryotic translation initiation factor 3 subunit C Eif3c	1088.165	1480.639	1349.683
VPS29_MOUSE	2	2	0.06567	Vacuolar protein sorting-associated protein 29 Vps29	598.933	432.710	630.912
RL17_MOUSE	1	1	0.066204	60S ribosomal protein L17 Rpl17	1106.724	1419.699	1331.560
RUVB2_MOUSE	9	9	0.066701	RuvB-like 2 Ruvbl2	3022.667	3684.312	2783.151
SEP11_MOUSE	5	2	0.067535	Septin-11 Septin11	477.882	602.341	535.876
INO1_MOUSE	1	1	0.067552	Inositol-3-phosphate synthase 1 Isyna1	43.903	14.661	46.927
SBDS_MOUSE	2	1	0.06796	Ribosome maturation protein SBDS Sbds	102.582	82.702	41.237
EXOS2_MOUSE	1	1	0.068604	Exosome complex component RRP4 Exosc2	212.170	351.502	306.363
IPO7_MOUSE	6	6	0.069375	Importin-7 Ipo7	1216.893	1380.264	1230.901
ANXA1_MOUSE	20	18	.069158	Annexin A1 Anxa1	27912.444	27367.373	33769.537
GANAB_MOUSE	2	1	0.071688	Neutral alpha-glucosidase AB Ganab	65.534	174.290	148.889
P5CR3_MOUSE	1	1	0.071776	Pyrroline-5-carboxylate reductase 3 Pycr3	290.990	213.036	243.160
ITA5_MOUSE	1	1	0.073115	Integrin alpha-5 Itga5	40.074	65.270	78.887
TALDO_MOUSE	8	7	0.073655	Transaldolase Taldo1	1777.140	2078.768	2054.872
TPM2_MOUSE	11	5	0.074015	Tropomyosin beta chain Tpm2	2422.192	2481.646	3220.966
TIF1B_MOUSE	1	1	0.075363	Transcription intermediary factor 1-beta Trim28	20.457	63.640	13.912

CD81_MOUSE	3	3	0.07579	CD81 antigen Cd81	34300.257	36531.980	47811.208
METK2_MOUSE	3	2	0.075796	S-adenosylmethionine synthase isoform type-2 Mat2a	216.176	396.218	198.841
MYG_MOUSE	1	1	0.076152	Myoglobin Mb	13.554	72.109	34.076
TSN9_MOUSE	1	1	0.076336	Tetraspanin-9 Tspan9	298.543	366.343	204.178
PRS4_MOUSE	10	9	0.077069	26S proteasome regulatory subunit 4 Psmc1	2660.374	3561.312	2268.649
THIC_MOUSE	3	2	0.077653	Acetyl-CoA acetyltransferase, cytosolic Acat2	926.803	1173.192	1311.019
1433Z_MOUSE	15	11	0.077993	14-3-3 protein zeta/delta Ywhaz	27209.888	20098.737	25725.053
IQGA1_MOUSE	6	5	0.078446	Ras GTPase-activating-like protein IQGAP1 Iqgap1	669.959	438.839	586.999
RAB10_MOUSE	5	2	0.078493	Ras-related protein Rab-10 Rab10	729.540	580.005	710.138
HNRPF_MOUSE	4	2	0.078676	Heterogeneous nuclear ribonucleoprotein F Hnrnpf	651.919	841.741	758.828
OLM2B_MOUSE	2	2	0.079145	Olfactomedin-like protein 2B Olfml2b	933.129	820.211	699.130
CSN5_MOUSE	9	8	0.079161	COP9 signalosome complex subunit 5 Cops5	3643.542	3255.673	2435.647
RPAP1_MOUSE	1	1	0.080248	RNA polymerase II-associated protein 1 Rpap1	494.200	480.685	834.728
MTAP_MOUSE	2	1	0.080801	S-methyl-5'-thioadenosine phosphorylase Mtap	380.511	565.257	361.202
DNJA2_MOUSE	7	7	0.080919	DnaJ homolog subfamily A member 2 Dnaja2	4498.022	3975.331	3410.703
OTU7B_MOUSE	1	1	0.081275	OTU domain-containing protein 7B Otud7b	462.070	199.330	377.896
OSTF1_MOUSE	1	1	0.082059	Osteoclast-stimulating factor 1 Ostf1	82.110	22.293	111.153

GRHPR_MOUSE	1	1	0.082441	Glyoxylate reductase/hydroxypyruvate reductase Grhpr	95.234	67.294	83.646
RL7A_MOUSE	10	8	0.08262	60S ribosomal protein L7a Rpl7a	16389.040	19709.231	20145.067
6PGL_MOUSE	2	2	0.082802	6-phosphogluconolactonase Pgls	420.217	368.873	631.646
RL23A_MOUSE	3	2	0.085024	60S ribosomal protein L23a Rpl23a	836.600	620.409	857.083
PSA1_MOUSE	15	15	0.085788	Proteasome subunit alpha type-1 Psma1	28492.289	24452.411	23397.868
MTNA_MOUSE	1	1	0.086205	Methylthioribose-1-phosphate isomerase Mri1	149.699	192.400	209.399
CD82_MOUSE	7	6	0.08646	CD82 antigen Cd82	13167.720	10978.845	13156.234
RUXE_MOUSE	2	2	0.08832	Small nuclear ribonucleoprotein E Snrpe	100.589	179.602	185.396
ROA1_MOUSE	3	3	0.089139	Heterogeneous nuclear ribonucleoprotein A1 Hnrnpa1	1134.200	1158.998	1458.759
RL32_MOUSE	3	2	0.089268	60S ribosomal protein L32 Rpl32	962.516	1570.035	1398.334
GSTA4_MOUSE	2	1	0.089751	Glutathione S-transferase A4 Gsta4	347.122	254.372	217.658
GLOD4_MOUSE	4	3	0.089764	Glyoxalase domain-containing protein 4 Glod4	1444.983	852.204	1324.200
FRIL1_MOUSE	1	1	0.09009	Ferritin light chain 1 Ftl1	144.627	0.000	0.000
IDI1_MOUSE	1	1	0.090576	Isopentenyl-diphosphate Delta-isomerase 1 Idi1	90.226	100.897	50.169
GSTM1_MOUSE	9	5	0.090609	Glutathione S-transferase Mu 1 Gstm1	947.636	870.289	1202.210
DHX15_MOUSE	2	2	0.090963	Pre-mRNA-splicing factor ATP-dependent RNA helicase DHX15 Dhx15	232.987	287.820	151.136
GRB2_MOUSE	1	1	0.091277	Growth factor receptor-bound protein 2 Grb2	193.480	63.121	176.867
ANM1_MOUSE	6	6	0.09142	Protein arginine N-methyltransferase 1 Prmt1	2899.662	2670.507	2183.933
RS13_MOUSE	8	8		40S ribosomal protein S13 Rps13	9210.650	12353.107	9127.138

GFAP_MOUSE	1	1	0.092799 0.093084	Glial fibrillary acidic protein Gfap	1798.164	1671.880	441.661
1433B_MOUSE	17	8	0.093378	14-3-3 protein beta/alpha Ywhab	6619.352	6633.438	3809.901
CLU_MOUSE	2	2	0.093872	Clustered mitochondria protein homolog Cluh	334.632	398.731	395.786
SRSF3_MOUSE	1	1	0.094395	Serine/arginine-rich splicing factor 3 Srsf3	410.628	549.365	508.767
BAG3_MOUSE	1	1	0.094808	BAG family molecular chaperone regulator 3 Bag3	391.438	293.732	261.959
RS10_MOUSE	2	2	0.095923	40S ribosomal protein S10 Rps10	728.188	686.333	369.371
ANGP1_MOUSE	3	3	0.096322	Angiopoietin-1 Angpt1	1467.768	1144.995	913.526
RCN1_MOUSE	2	2	0.09683	Reticulocalbin-1 Rcn1	4705.031	3791.664	6187.532
GSTO1_MOUSE	3	3	0.096949	Glutathione S-transferase omega-1 Gsto1	446.359	329.359	325.894
PSA7_MOUSE	12	8	951	Proteasome subunit alpha type-7 Psma7	11878.233	14876.366	11320.220
IDE_MOUSE	1	1	0.096992 0.098	Insulin-degrading enzyme Ide	32.649	72.155	91.566
UGDH_MOUSE	2	2	0.099132	UDP-glucose 6-dehydrogenase Ugdh	617.314	797.064	686.749
ENV1_MOUSE	2	2	0.101338	MLV-related proviral Env polyprotein	247.796	397.176	304.911
PHOCN_MOUSE	1	1	413	MOB-like protein phocein Mob4	339.112	202.369	348.428
CLH1_MOUSE	36	31	0.101 0.101678	Clathrin heavy chain 1 Cltc	13977.359	12350.252	14179.583
CSPG2_MOUSE	3	1	0.10174	Versican core protein Vcan	75.604	531.616	224.142
CAPZB_MOUSE	3	3	0.101878	F-actin-capping protein subunit beta Capzb	2144.827	1718.011	1930.734
PDIA1_MOUSE	15	13	0.102153	Protein disulfide-isomerase P4hb	8430.961	10319.896	10900.791
STOM_MOUSE	10	8	0.103366	Stomatin Stom	2424.351	2453.052	1827.326
OTUB1_MOUSE	2	1	0.104613	Ubiquitin thioesterase OTUB1 Otub1	215.095	248.689	121.033

ASPD_MOUSE	1	1	0.105124	Putative L-aspartate dehydrogenase Aspdh	617.217	796.283	734.746
RAB14_MOUSE	7	4	0.105365	Ras-related protein Rab-14 Rab14	1247.836	1919.200	1292.079

U2AF2_MOUSE	1	1	0.106763	Splicing factor U2AF 65 kDa subunit U2af2	38.855	4.252	5.730
EPDR1_MOUSE	2	2	0.1069	Mammalian ependymin-related protein 1 Epdr1	842.463	578.092	820.618
PPID_MOUSE	3	3	0.107387	Peptidyl-prolyl cis-trans isomerase D Ppid	774.894	395.533	568.811
S10A4_MOUSE	2	2	0.108724	Protein S100-A4 S100a4	3095.834	3386.253	3395.076
PPIC_MOUSE	5	5	0.109022	Peptidyl-prolyl cis-trans isomerase C Ppic	3776.204	3508.983	5211.150
MLRS_MOUSE	1	1	0.109985	Myosin regulatory light chain 2, skeletal muscle isoform Mylpf	151.740	365.965	318.762
RAB5B_MOUSE	5	4	0.110126	Ras-related protein Rab-5B Rab5b	613.080	466.277	472.319
TIMP2_MOUSE	8	6	0.110314	Metalloproteinase inhibitor 2 timp2	15813.072	19255.677	19852.109
RENR_MOUSE	12	12	0.111628	Renin receptor Atp6ap2	5373.370	6147.797	4566.682
PSME3_MOUSE	1	1	0.112424	Proteasome activator complex subunit 3 Psme3	117.881	170.062	155.882
APOH_MOUSE	1	1	0.112888	Beta-2-glycoprotein 1 Apoh	228.373	20.815	9.739
CALM1_MOUSE	1	1	0.112968	Calmodulin-1 Calm1	21.178	62.497	214.471
SNX1_MOUSE	1	1	0.113006	Sorting nexin-1 Snx1	619.850	307.659	330.342
SEPT4_MOUSE	1	1	0.113342	Septin-4 Septin4	88.086	107.990	86.650
EF1D_MOUSE	9	8	0.113601	Elongation factor 1-delta Eef1d	5249.369	4644.359	3987.774

HSP74_MOUSE	7	7	0.115484	Heat shock 70 kDa protein 4 Hspa4	2376.722	2445.709	2261.132
UB2V1_MOUSE	3	3	0.115821	Ubiquitin-conjugating enzyme E2 variant 1 Ube2v1	425.976	721.770	665.156
PRP19_MOUSE	4	4	0.116	Pre-mRNA-processing factor 19 Prpf19	2069.823	2662.315	2377.998
SF3A1_MOUSE	1	1	0.118228	Splicing factor 3A subunit 1 Sf3a1	170.355	205.013	359.635
NFIA_MOUSE	1	1	0.118901	Nuclear factor 1 A-type Nfia	113.983	135.791	159.451
AK1A1_MOUSE	4	3	0.119609	Aldo-keto reductase family 1 member A1 Akr1a1	902.979	643.495	724.051
IF2G_MOUSE	8	3	0.120727	Eukaryotic translation initiation factor 2 subunit 3, X-linked Eif2s3x	1228.833	1567.411	1500.926
ALDOA_MOUSE	25	24	0.121736	Fructose-bisphosphate aldolase A Aldoa	155517.140	165616.835	146001.738
1433G_MOUSE	16	6	0.122187	14-3-3 protein gamma Ywhag	4466.957	3391.864	5400.021

ACTN4_MOUSE	24	13	0.122626	Alpha-actinin-4 Actn4	6960.057	5872.910	6484.204
1433T_MOUSE	8	3	0.122932	14-3-3 protein theta Ywhaq	1113.524	772.744	944.272
CATL1_MOUSE	7	5	0.124374	Procathepsin L Ctsl	8201.926	6649.862	7577.534
THTM_MOUSE	1	1	0.124487	3-mercaptopyruvate sulfurtransferase Mpst	153.679	94.164	93.249
UXT_MOUSE	1	1	0.12587	Protein UXT Uxt	13622.302	3486.314	3337.608
UEVLD_MOUSE	1	1	0.126626	Ubiquitin-conjugating enzyme E2 variant 3 Uevld	139.398	69.941	39.438
UBP47_MOUSE	1	1	0.127298	Ubiquitin carboxyl-terminal hydrolase 47 Usp47	8.840	21.205	17.594
A4_MOUSE	8	6	0.1276	Amyloid-beta A4 protein App	2165.214	1980.869	3252.560
RS3_MOUSE	16	16	0.127726	40S ribosomal protein S3 Rps3	33620.563	41317.936	29760.537

PSA2_MOUSE	11	11	0.128353	Proteasome subunit alpha type-2 Psma2	18881.592	15299.833	14111.617
TNNI1_MOUSE	3	2	0.128607	Troponin I, slow skeletal muscle Tnni1	228.063	359.734	342.318
MSLN_MOUSE	9	7	0.128772	Mesothelin Msln	5582.677	6828.721	5556.458
BMP1_MOUSE	7	3	0.129069	Bone morphogenetic protein 1 Bmp1	2437.167	1834.513	2687.028
TCEA3_MOUSE	1	1	0.129855	Transcription elongation factor A protein 3 Tcea3	11156.582	13136.688	12270.941
PSA5_MOUSE	8	7	0.130316	Proteasome subunit alpha type-5 Psma5	24006.942	19899.636	18887.048
GID8_MOUSE	1	1	0.13203	Glucose-induced degradation protein 8 homolog Gid8	113.862	226.730	159.325
CSK21_MOUSE	1	1	0.133339	Casein kinase II subunit alpha Csnk2a1	163.694	273.214	192.357
DACT1_MOUSE	1	1	0.134151	Dapper homolog 1 Dact1	75.954	75.532	164.203
PEPD_MOUSE	1	1	0.134172	Xaa-Pro dipeptidase Pepd	43.757	20.250	32.061
SRBS2_MOUSE	1	1	0.134218	Sorbin and SH3 domain-containing protein 2 Sorbs2	399.794	395.797	290.726
CRIP2_MOUSE	3	3	0.135259	Cysteine-rich protein 2 Crip2	1273.393	1803.001	1993.051
CHM2A_MOUSE	2	1	0.13583	Charged multivesicular body protein 2a Chmp2a	1501.443	1378.336	1672.459
ARC1A_MOUSE	1	1	0.136427	Actin-related protein 2/3 complex subunit 1A Arpc1a	104.580	56.539	185.095
DCNL1_MOUSE	1	1	0.136522	DCN1-like protein 1 Dcun1d1	25.552	6.611	16.862
SC5A2_MOUSE	1	1	0.137384	Sodium/glucose cotransporter 2 Slc5a2	21.923	108.299	34.631
HA1B_MOUSE	1	1	0.138225	H-2 class I histocompatibility antigen, K-B alpha chain H2-K1	117.105	178.110	100.145
CKAP5_MOUSE	1	1	0.139315	Cytoskeleton-associated protein 5 Ckap5	1541.025	981.907	1345.504
PGAM1_MOUSE	8	6	0.139415	Phosphoglycerate mutase 1 Pgam1	7022.674	6057.344	4039.133

MRS2_MOUSE	1	1	0.140178	Magnesium transporter MRS2 homolog, mitochondrial Mrs2	1162.459	433.089	489.152
GRP1_MOUSE	1	1	0.140425	RAS guanyl-releasing protein 1 Rasgrp1	407.895	463.047	509.657
IF4A2_MOUSE	12	1	0.141448	Eukaryotic initiation factor 4A-II Eif4a2	893.041	1433.295	1002.175
CILP1_MOUSE	31	29	0.141976	Cartilage intermediate layer protein 1 Cilp	66292.455	55777.315	60062.345
OBSL1_MOUSE	2	2	0.143083	Obscurin-like protein 1 Obsl1	239.478	287.072	142.995
SEPT2_MOUSE	9	9	0.148178	Septin-2 Septin2	5158.898	4921.103	3920.778
PURA_MOUSE	4	2	0.148695	Transcriptional activator protein Pur-alpha Pura	254.466	390.822	420.641
GSTP1_MOUSE	5	4	0.149782	Glutathione S-transferase P 1 Gstp1	1864.498	1801.044	1445.014
ATX10_MOUSE	1	1	0.149857	Ataxin-10 Atxn10	158.990	93.214	108.023
RAB7A_MOUSE	4	4	0.150066	Ras-related protein Rab-7a Rab7a	2257.049	2663.198	2867.701
IF4E_MOUSE	1	1	0.153707	Eukaryotic translation initiation factor 4E Eif4e	69.937	156.649	85.413
PSMD4_MOUSE	2	1	0.153972	26S proteasome non-ATPase regulatory subunit 4 Psmd4	582.435	629.169	429.248
HINT1_MOUSE	1	1	0.156734	Histidine triad nucleotide-binding protein 1 Hint1	71.465	116.933	150.058
RAB6A_MOUSE	12	3	0.157527	Ras-related protein Rab-6A Rab6a	1210.701	459.098	660.794
BMAL2_MOUSE	1	1	0.159244	Aryl hydrocarbon receptor nuclear translocator-like protein 2 Arntl2	47.742	90.925	86.602
CAZA2_MOUSE	3	2	0.159253	F-actin-capping protein subunit alpha-2 Capza2	1974.394	2238.936	1834.128
SGCD_MOUSE	1	1	0.159527	Delta-sarcoglycan Sgcd	45.600	57.846	101.151
ACTY_MOUSE	5	2	0.15993	Beta-centractin Actr1b	432.466	375.867	320.898
KCY_MOUSE	1	1		UMP-CMP kinase Cmpk1	795.181	524.768	737.622

AMACR_MOUSE	1	1	0.160878 0.160908	Alpha-methylacyl-CoA racemase Amacr	659.093	540.812	732.607
RL10A_MOUSE	4	4	0.161323	60S ribosomal protein L10a Rpl10a	4211.280	3901.498	4715.844
CREG1_MOUSE	1	1	0.162577	Protein CREG1 Creg1	57.800	90.224	27.596
PLEC_MOUSE	81	68	0.163771	Plectin Plec	24464.954	27418.381	24738.096
RL9_MOUSE	5	4	0.164692	60S ribosomal protein L9 Rpl9	2485.965	3429.318	2283.879
PSMD2_MOUSE	19	18	0.165475	26S proteasome non-ATPase regulatory subunit 2 Psmd2	9492.941	10667.058	9747.126
CLIC4_MOUSE	6	5	0.165751	Chloride intracellular channel protein 4 Clic4	3471.245	3384.504	2800.359
CAD15_MOUSE	14	13	0.165853	Cadherin-15 Cdh15	12946.483	10353.529	14894.253
SYFA_MOUSE	2	2	0.166265	Phenylalanine--tRNA ligase alpha subunit Farsa	685.882	920.538	693.397
GALNS_MOUSE	1	1	0.166277	N-acetylgalactosamine-6-sulfatase Galns	105.340	25.577	53.189
PSB7_MOUSE	6	6	0.166849	Proteasome subunit beta type-7 Psmb7	9379.304	8304.516	9557.276
GARS_MOUSE	9	9	0.167568	Glycine--tRNA ligase Gars1	7600.807	8199.670	7390.647
RL29_MOUSE	1	1	0.170939	60S ribosomal protein L29 Rpl29	213.718	263.075	309.982
ARP3_MOUSE	10	8	0.171703	Actin-related protein 3 Actr3	8347.092	7140.521	6663.066
PSD13_MOUSE	11	11	0.173641	26S proteasome non-ATPase regulatory subunit 13 Psmd13	6107.622	6294.680	5573.016
DYH17_MOUSE	1	1	0.174206	Dynein axonemal heavy chain 17 Dnah17	4485.273	3259.505	5971.185
AKAP4_MOUSE	1	1	0.175153	A-kinase anchor protein 4 Akap4	100806.143	11348.618	12024.216
IF6_MOUSE	1	1	0.176255	Eukaryotic translation initiation factor 6 Eif6	229.126	117.399	258.674
ALDR_MOUSE	12	11	0.177158	Aldo-keto reductase family 1 member B1 Akr1b1	26009.125	25529.726	22981.123

PTN23_MOUSE	1	1	0.178621	Tyrosine-protein phosphatase nonreceptor type 23 Ptpn23	159.430	209.892	167.241
CDC42_MOUSE	1	1	0.178739	Cell division control protein 42 homolog Cdc42	1194.433	899.009	1184.054
PRDX2_MOUSE	8	8	0.178758	Peroxiredoxin-2 Prdx2	20765.397	18885.650	20976.069
RSPRY_MOUSE	1	1	0.179036	RING finger and SPRY domain-containing protein 1 Rspry1	16.704	42.036	0.877
SERB_MOUSE	1	1	0.179106	Phosphoserine phosphatase Psph	62.449	51.842	99.752
ANTR1_MOUSE	1	1	0.182731	Anthrax toxin receptor 1 Antxr1	6660.173	529.741	480.895
PP1B_MOUSE	2	2	0.183173	Serine/threonine-protein phosphatase PP1-beta catalytic subunit Ppp1cb	361.858	411.161	354.169
HCDH_MOUSE	2	1	0.183206	Hydroxyacyl-coenzyme A dehydrogenase, mitochondrial Hadh	56.799	51.580	90.401
RPB3_MOUSE	1	1	0.183224	DNA-directed RNA polymerase II subunit RPB3 Polr2c	108.627	112.200	72.579
RS8_MOUSE	7	7	0.184021	40S ribosomal protein S8 Rps8	17856.794	20502.339	21096.752
NDKA_MOUSE	5	2	0.184446	Nucleoside diphosphate kinase A Nme1	484.760	290.383	335.095
RHEB_MOUSE	1	1	0.184512	GTP-binding protein Rheb Rheb	65.510	150.438	128.542
DHX9_MOUSE	4	4	0.185311	ATP-dependent RNA helicase A Dhx9	434.342	620.373	511.922
CADH2_MOUSE	2	2	0.185481	Cadherin-2 Cdh2	946.184	570.750	588.809
RISC_MOUSE	1	1	0.186735	Retinoid-inducible serine carboxypeptidase Scpep1	513.386	389.090	272.691
GDIR1_MOUSE	4	3	0.187307	Rho GDP-dissociation inhibitor 1 Arhgdia	4756.452	4315.752	5664.224
FBLN4_MOUSE	3	3	0.189538	EGF-containing fibulin-like extracellular matrix protein 2 Efemp2	949.170	969.807	1139.507
CAND1_MOUSE	15	12	0.190588	Cullin-associated NEDD8-dissociated protein 1 Cand1	2701.925	2418.051	2269.183

TCTP_MOUSE	6	6	0.193889	Translationally-controlled tumor protein Tpt1	5550.016	4655.322	4325.608
KAPCA_MOUSE	2	1	0.194868	cAMP-dependent protein kinase catalytic subunit alpha Prkaca	539.254	724.692	892.556
MTA70_MOUSE	1	1	0.195156	N6-adenosine-methyltransferase subunit METTL3 Mettl3	2616.800	2071.190	2885.698
MDHC_MOUSE	7	7	0.196544	Malate dehydrogenase, cytoplasmic Mdh1	5709.523	4974.776	5391.327
PCBP2_MOUSE	3	1	0.196741	Poly(rC)-binding protein 2 Pcbp2	1010.323	903.958	592.199
RL26_MOUSE	5	5	0.198622	60S ribosomal protein L26 Rpl26	9681.726	11413.956	6834.860

RBBP4_MOUSE	2	2	0.198905	Histone-binding protein RBBP4 Rbbp4	554.914	520.665	493.508
SYFB_MOUSE	2	2	0.200353	Phenylalanine--tRNA ligase beta subunit Farsb	104.056	135.777	134.675
LEG3_MOUSE	7	5	0.20114	Galectin-3 Lgals3	8864.395	10493.290	12221.241
MALD1_MOUSE	1	1	0.201895	MARVEL domain-containing protein 1 Marveld1	145.723	126.046	156.794
PPCE_MOUSE	6	6	0.202548	Prolyl endopeptidase Prep	3516.687	3955.898	3082.828
DDB1_MOUSE	15	13	0.203888	DNA damage-binding protein 1 Ddb1	4513.590	4244.296	4140.497
PSB1_MOUSE	15	15	0.203949	Proteasome subunit beta type-1 Psmb1	26851.098	19203.668	23407.175
RL18_MOUSE	7	6	0.207004	60S ribosomal protein L18 Rpl18	11117.133	14278.465	11940.278
EIF3M_MOUSE	7	7	0.207926	Eukaryotic translation initiation factor 3 subunit M Eif3m	2685.392	2284.838	3243.363
RS7_MOUSE	5	4	0.209691	40S ribosomal protein S7 Rps7	1700.036	2160.338	1285.170
ANXA3_MOUSE	13	12	0.210417	Annexin A3 Anxa3	5329.354	6560.238	6694.373
CH1B1_MOUSE	1	1	0.211204	Charged multivesicular body protein 1b-1 Chmp1b1	143.477	105.431	165.939

VATA_MOUSE	7	6	0.21279	V-type proton ATPase catalytic subunit A Atp6v1a	1897.400	1394.190	1694.093
RRAS2_MOUSE	2	1	0.216215	Ras-related protein R-Ras2 Rras2	90.239	83.436	106.698
NUD16_MOUSE	1	1	0.217461	U8 snoRNA-decapping enzyme Nudt16	78.149	85.989	102.124
VMA5A_MOUSE	1	1	0.221384	von Willebrand factor A domain-containing protein 5A Vwa5a	47.080	29.027	81.980
SF3B3_MOUSE	4	2	0.221949	Splicing factor 3B subunit 3 Sf3b3	222.141	195.943	263.495
FKBP3_MOUSE	1	1	0.223947	Peptidyl-prolyl cis-trans isomerase FKBP3 Fkbp3	16116.190	1392.730	1951.222
ASAH1_MOUSE	5	5	0.227877	Acid ceramidase Asah1	1341.942	1102.964	1150.622
HMGA1_MOUSE	1	1	0.228991	High mobility group protein HMG-I/HMG-Y Hmga1	128.548	39.619	51.338
TPP2_MOUSE	3	3	0.231087	Tripeptidyl-peptidase 2 Tpp2	267.120	301.008	234.141
VA0D1_MOUSE	1	1	0.23168	V-type proton ATPase subunit d 1 Atp6v0d1	20.510	12.624	24.222
ACOC_MOUSE	2	2	0.232172	Cytoplasmic aconitate hydratase Aco1	291.534	300.060	387.431
PSB6_MOUSE	5	5	0.232628	Proteasome subunit beta type-6 Psmb6	19165.564	15478.753	16329.715

ESTD_MOUSE	4	4	0.234233	S-formylglutathione hydrolase Esd	1341.224	1117.493	1064.722
RS2_MOUSE	8	8	0.237107	40S ribosomal protein S2 Rps2	42554.561	31227.122	26033.507
EIF2A_MOUSE	1	1	0.237293	Eukaryotic translation initiation factor 2A Eif2a	42.539	44.391	33.238
TR150_MOUSE	1	1	0.237648	Thyroid hormone receptor-associated protein 3 Thrap3	406.639	264.212	378.362
BCAM_MOUSE	3	2	0.239109	Basal cell adhesion molecule Bcam	126.939	162.842	201.062
ADH7_MOUSE	2	1	0.240627	All-trans-retinol dehydrogenase [NAD(+)] ADH7 Adh7	180.840	156.699	213.476

HNRPQ_MOUSE	4	3	0.240744	Heterogeneous nuclear ribonucleoprotein Q Syncrip	948.387	1027.596	1121.935
SPEE_MOUSE	3	2	0.241962	Spermidine synthase Srm	241.457	314.401	244.069
PLMN_MOUSE	2	1	0.243237	Plasminogen Plg	485.544	11.402	31.338
TMED1_MOUSE	1	1	0.243576	Transmembrane emp24 domaincontaining protein 1 Tmed1	36.823	74.826	38.992
RADI_MOUSE	12	1	0.245112	Radixin Rdx	461.854	395.843	470.005
PDC10_MOUSE	2	2	0.247295	Programmed cell death protein 10 Pdcd10	320.709	383.351	267.671
HSP7C_MOUSE	35	24	0.248054	Heat shock cognate 71 kDa protein Hspa8	85434.160	83738.669	92201.902
DYN2_MOUSE	10	4	0.248376	Dynamin-2 Dnm2	2038.191	2064.216	2347.419
ARPC2_MOUSE	10	9	0.250954	Actin-related protein 2/3 complex subunit 2 Arpc2	3080.296	2907.219	3446.102
MPRD_MOUSE	1	1	0.25174	Cation-dependent mannose-6-phosphate receptor M6pr	169.592	104.639	127.105
XPP1_MOUSE	5	4	2242	Xaa-Pro aminopeptidase 1 Xpnpep1	945.105	736.785	563.612
NUDC_MOUSE	2	2	0.25 0.255688	Nuclear migration protein nudC Nudc	249.476	244.284	276.428
RS15_MOUSE	4	4	0.255812	40S ribosomal protein S15 Rps15	1352.971	2031.667	1869.952
CSN8_MOUSE	5	4	0.258368	COP9 signalosome complex subunit 8 Cops8	2061.552	2736.208	2361.728
CAN1_MOUSE	1	1	0.260246	Calpain-1 catalytic subunit Capn1	64.139	140.035	189.857
TNNT2_MOUSE	1	1	0.26141	Troponin T, cardiac muscle Tnnt2	11.616	29.243	34.847
CD80_MOUSE	1	1	0.26152	T-lymphocyte activation antigen CD80 Cd80	217.753	133.027	240.423
FPPS_MOUSE	4	4	0.263298	Farnesyl pyrophosphate synthase Fdps	2716.477	2165.776	2430.636
TOLIP_MOUSE	3	3	0.264838	Toll-interacting protein Tollip	688.397	798.481	700.974

COF2_MOUSE	3	2	0.264865	Cofilin-2 Cfl2	2044.407	2602.184	3000.370
TRI33_MOUSE	1	1	0.266	E3 ubiquitin-protein ligase TRIM33 Trim33	889.983	709.195	1110.526
ARHG2_MOUSE	1	1	0.270129	Rho guanine nucleotide exchange factor 2 Arhgef2	31.131	34.393	15.687
FKB10_MOUSE	2	2	0.272367	Peptidyl-prolyl cis-trans isomerase FKBP10 Fkbp10	370.427	444.056	359.850
SPRC_MOUSE	5	3	0.272459	SPARC Sparc	7837.583	9393.468	11079.415
RL36_MOUSE	2	1	0.275768	60S ribosomal protein L36 Rpl36	1267.903	1698.961	1556.910
FST_MOUSE	2	1	0.276243	Follistatin Fst	3579.356	4342.459	3063.413
QCR2_MOUSE	1	1	0.277411	Cytochrome b-c1 complex subunit 2, mitochondrial Uqcrc2	120.471	184.183	161.211
TRIP4_MOUSE	1	1	0.278564	Activating signal cointegrator 1 Trip4	589.703	1605.563	454.112
KPYR_MOUSE	3	1	0.282325	Pyruvate kinase PKLR Pklr	820.228	888.178	633.642
TPIS_MOUSE	11	10	0.28248	Triosephosphate isomerase Tpi1	19867.952	17283.220	16108.142
CC182_MOUSE	1	1	0.282686	Coiled-coil domain-containing protein 182 Ccdc182	147.354	194.145	254.066
SYRC_MOUSE	6	5	0.286274	Arginine--tRNA ligase, cytoplasmic Rars1	5381.822	3953.432	4061.497
SAE1_MOUSE	2	2	0.288156	SUMO-activating enzyme subunit 1 Sae1	193.864	152.784	178.448
ERP29_MOUSE	2	2	0.288452	Endoplasmic reticulum resident protein 29 Erp29	522.557	350.128	425.441
ARPC4_MOUSE	4	4	0.289646	Actin-related protein 2/3 complex subunit 4 Arpc4	3463.790	2866.805	2744.330
GEMI5_MOUSE	1	1	0.289974	Gem-associated protein 5 Gemin5	2506.249	1405.260	1712.656
CLCA_MOUSE	2	2	0.29066	Clathrin light chain A Clta	699.743	621.156	587.892
PFD5_MOUSE	2	2	0.29373	Prefoldin subunit 5 Pfdn5	140.302	70.139	87.179
RS19_MOUSE	1	1	0.295916	40S ribosomal protein S19 Rps19	37.907	37.925	9.529

TSNAX_MOUSE	6	6	0.302089	Translin-associated protein X Tsnax	110079.231	4933.679	6054.481
ENOG_MOUSE	5	1	0.30343	Gamma-enolase Eno2	137.950	158.544	186.245
MASP1_MOUSE	1	1	0.305071	Mannan-binding lectin serine protease 1 Masp1	376.005	230.157	203.508
PBDC1_MOUSE	1	1	0.305148	Protein PBDC1 Pbdc1	119.794	252.800	146.182
PEBB_MOUSE	1	1	0.306238	Core-binding factor subunit beta Cbfb	626.002	344.277	519.850
PRIO_MOUSE	1	1	0.306437	Major prion protein Prnp	290.777	181.017	248.930
MINP1_MOUSE	1	1	0.307855	Multiple inositol polyphosphate phosphatase 1 Minpp1	97.259	82.707	77.732
NACA_MOUSE	3	3	0.314099	Nascent polypeptide-associated complex subunit alpha Naca	761.408	988.768	1007.483
BABA2_MOUSE	1	1	0.318936	BRISC and BRCA1-A complex member 2 Babam2	31.784	43.943	32.141
CUL3_MOUSE	1	1	0.3232	Cullin-3 Cul3	29.982	25.036	61.283
AUTS2_MOUSE	1	1	0.326404	Autism susceptibility gene 2 protein homolog Auts2	2575.979	5848.576	2546.286
GORS2_MOUSE	1	1	0.329744	Golgi reassembly-stacking protein 2 Gorasp2	27.498	70.871	30.673
COPB2_MOUSE	8	6	0.334589	Coatomer subunit beta' Copb2	2010.210	2260.590	1997.450
EIF3H_MOUSE	7	7	0.336176	Eukaryotic translation initiation factor 3 subunit H Eif3h	2654.022	2367.321	2564.915
IMA4_MOUSE	1	1	0.338135	Importin subunit alpha-4 Kpna3	44.648	56.338	61.894
PFD2_MOUSE	1	1	0.341787	Prefoldin subunit 2 Pfdn2	301.166	301.033	414.275
RL6_MOUSE	10	10	0.347051	60S ribosomal protein L6 Rpl6	18951.879	21651.158	19084.954
RAB2A_MOUSE	4	2	0.349167	Ras-related protein Rab-2A Rab2a	520.350	421.325	439.310

AP1B1_MOUSE	4	2	0.351604	AP-1 complex subunit beta-1 Ap1b1	222.176	248.441	280.509
AP2A2_MOUSE	6	3	0.352722	AP-2 complex subunit alpha-2 Ap2a2	604.495	518.402	628.603
CAB39_MOUSE	1	1	0.353549	Calcium-binding protein 39 Cab39	40.901	63.045	80.510
MA2A1_MOUSE	1	1	0.355673	Alpha-mannosidase 2 Man2a1	63.002	84.880	109.538
PACN2_MOUSE	4	3	0.356019	Protein kinase C and casein kinase substrate in neurons protein 2 Pacsin2	1055.024	1341.189	1392.903
PPT1_MOUSE	2	2	0.356276	Palmitoyl-protein thioesterase 1 Ppt1	424.910	464.630	722.749
ABHD8_MOUSE	1	1	0.356364	Protein ABHD8 Abhd8	33427.848	3041.225	3160.031
RL7_MOUSE	11	10	93	60S ribosomal protein L7 Rpl7	14786.432	14525.221	12507.232
FCL_MOUSE	1	1	0.3563 0.356416	GDP-L-fucose synthase Gfus	89.160	73.807	84.925
IF2H_MOUSE	5	4	0.356549	Eukaryotic translation initiation factor 2 subunit 3, Y-linked Eif2s3y	1332.210	1583.603	1540.055
HNRH1_MOUSE	5	1	0.358941	Heterogeneous nuclear ribonucleoprotein H Hnrnph1	40.598	81.816	62.205
CSN2_MOUSE	4	4	0.359898	COP9 signalosome complex subunit 2 Cops2	413.308	464.071	390.488
CTBP1_MOUSE	1	1	0.360551	C-terminal-binding protein 1 Ctbp1	44.066	62.468	85.602
PGM1_MOUSE	7	6	0.361084	Phosphoglucomutase-1 Pgm1	1547.867	1347.055	1411.656
PTGR1_MOUSE	2	2	0.361845	Prostaglandin reductase 1 Ptgr1	170.430	107.043	134.620
DCTN2_MOUSE	2	2	0.366425	Dynactin subunit 2 Dctn2	416.184	308.747	315.149
ARPC3_MOUSE	8	8	0.367371	Actin-related protein 2/3 complex subunit 3 Arpc3	3819.668	3505.472	3970.054
VP37C_MOUSE	2	2	0.367753	Vacuolar protein sorting-associated protein 37C Vps37c	405.253	328.137	406.357

GNAI2_MOUSE	2	1	0.368985	Guanine nucleotide-binding protein G(i) subunit alpha-2 Gnai2	3.203	6.989	10.964
DCTN3_MOUSE	2	1	0.370704	Dynactin subunit 3 Dctn3	375.724	338.978	299.664
FHL3_MOUSE	1	1	0.372397	Four and a half LIM domains protein 3 Fhl3	109.025	89.042	90.092
HXK1_MOUSE	3	3	0.374793	Hexokinase-1 Hk1	403.397	480.916	503.094
GPD1L_MOUSE	3	2	0.375531	Glycerol-3-phosphate dehydrogenase 1like protein Gpd1l	121.762	153.704	162.226
OX2G_MOUSE	2	2	0.375784	OX-2 membrane glycoprotein Cd200	451.236	403.502	487.607
TNPO1_MOUSE	1	1	0.376964	Transportin-1 Tnpo1	51.648	37.842	35.906
DJB11_MOUSE	4	4	0.381004	DnaJ homolog subfamily B member 11 Dnajb11	3537.836	3533.274	2809.356
NAGK_MOUSE	1	1	0.381838	N-acetyl-D-glucosamine kinase Nagk	32.825	58.072	50.776
NAA20_MOUSE	1	1	0.389475	N-alpha-acetyltransferase 20 Naa20	232.747	343.596	331.562
CBPE_MOUSE	2	2	0.392224	Carboxypeptidase E Cpe	1259.198	1085.044	1193.557
LRP1_MOUSE	14	13	0.392827	Prolow-density lipoprotein receptorrelated protein 1 Lrp1	1796.989	1760.469	1639.904
PGTA_MOUSE	1	1	0.401147	Geranylgeranyl transferase type-2 subunit alpha Rabggta	40.044	58.438	64.763
EPCAM_MOUSE	1	1	0.405813	Epithelial cell adhesion molecule Epcam	48.965	55.131	66.383
ENKD1_MOUSE	1	1	0.407206	Enkurin domain-containing protein 1 Enkd1	534.163	578.066	482.039
COF1_MOUSE	4	4	0.410792	Cofilin-1 Cfl1	5051.384	3886.268	4331.494
PEBP1_MOUSE	5	4	0.424609	Phosphatidylethanolamine-binding protein 1 Pebp1	4514.847	2439.237	2915.242
PA2G4_MOUSE	9	9	0.427073	Proliferation-associated protein 2G4 Pa2g4	2832.204	2927.915	2634.660

PGBM_MOUSE	47	44	0.427355	Basement membrane-specific heparan sulfate proteoglycan core protein Hspg2	37247.330	38489.535	39716.035
HDHD2_MOUSE	1	1	0.434484	Haloacid dehalogenase-like hydrolase domain-containing protein 2 Hdhd2	15.908	7.613	1.680
CSTN1_MOUSE	2	1	0.434709	Calsyntenin-1 Clstn1	96.391	119.567	156.922
ABCE1_MOUSE	3	2	0.434902	ATP-binding cassette sub-family E member 1 Abce1	7480.734	4222.925	5376.648
EZRI_MOUSE	10	2	0.435033	Ezrin Ezr	276.188	220.474	283.613
PA1B2_MOUSE	1	1	0.435976	Platelet-activating factor acetylhydrolase IB subunit alpha2 Pafah1b2	170.948	165.284	100.033
TETN_MOUSE	1	1	0.441234	Tetranectin Clec3b	252.034	234.046	145.615
ADPRS_MOUSE	1	1	0.44203	ADP-ribose glycohydrolase ARH3 Adprs	94.261	127.368	138.956
CD151_MOUSE	1	1	0.443231	CD151 antigen Cd151	113.198	144.385	176.856
STAC3_MOUSE	1	1	0.445141	SH3 and cysteine-rich domain-containing protein 3 Stac3	38.136	74.750	30.152
SFPQ_MOUSE	2	1	0.446526	Splicing factor, proline- and glutamine-rich Sfpq	243.685	344.919	166.527
PSB4_MOUSE	14	12	0.447057	Proteasome subunit beta type-4 Psmb4	29308.621	32207.808	26573.950
HS90B_MOUSE	39	25	0.44997	Heat shock protein HSP 90-beta Hsp90ab1	82885.623	75898.024	75854.101
HPRT_MOUSE	1	1	0.457494	Hypoxanthine-guanine phosphoribosyltransferase Hprt1	132.018	86.821	116.527
PLOD2_MOUSE	1	1	0.458164	Procollagen-lysine,2-oxoglutarate 5dioxygenase 2 Plod2	96.037	119.362	152.988
PGFRL_MOUSE	4	4	0.459595	Platelet-derived growth factor receptorlike protein Pdgfrl	1368.473	1163.368	1133.127

PLPHP_MOUSE	1	1	0.460016	Pyridoxal phosphate homeostasis protein Plpbp	137.116	108.369	144.883
NGBR_MOUSE	1	1	0.46343	Dehydrodolichyl diphosphate synthase complex subunit Nus1 Nus1	348.927	407.658	391.674
CSN7A_MOUSE	3	2	0.468954	COP9 signalosome complex subunit 7a Cops7a	1097.323	993.988	1316.503
PUR4_MOUSE	1	1	0.469079	Phosphoribosylformylglycinamidine synthase Pfas	241.975	263.004	232.973
KCRB_MOUSE	8	6	0.473276	Creatine kinase B-type Ckb	11432.816	17970.488	12924.920
NRDC_MOUSE	1	1	0.479226	Nardilysin Nrdc	34.432	38.242	53.345
IPO5_MOUSE	7	5	7	Importin-5 Ipo5	928.773	1015.550	1045.689
RAB1A_MOUSE	6	2	0.48344 0.483751	Ras-related protein Rab-1A Rab1A	944.064	829.268	797.660
SEM3B_MOUSE	2	1	0.48623	Semaphorin-3B Sema3b	30.626	35.442	51.766
ASAP2_MOUSE	1	1	0.48737	Arf-GAP with SH3 domain, ANK repeat and PH domain-containing protein 2 Asap2	5168.474	11313.927	4765.058
PEPL1_MOUSE	2	1	0.488286	Probable aminopeptidase NPEPL1 Npepl1	127.915	147.627	161.770
RL12_MOUSE	3	3	0.488599	60S ribosomal protein L12 Rpl12	6105.137	6383.942	5963.649
PAI1_MOUSE	4	4	0.496928	Plasminogen activator inhibitor 1 Serpine1	1395.563	1557.609	1351.160
RTRAF_MOUSE	1	1	0.498339	RNA transcription, translation and transport factor protein RTRAF	31.510	2.354	4.907
CSN6_MOUSE	6	6	0.498367	COP9 signalosome complex subunit 6 Cops6	3743.864	3999.330	3200.632

LOXL3_MOUSE	4	2	0.503337	Lysyl oxidase homolog 3 Loxl3	873.036	1044.428	1285.975
GNPI1_MOUSE	1	1	0.507136	Glucosamine-6-phosphate isomerase 1 Gnpda1	156.329	141.741	180.860

EIF3K_MOUSE	3	3	0.508312	Eukaryotic translation initiation factor 3 subunit K Eif3k	1199.302	1295.013	1123.187
PSB5_MOUSE	13	13	0.508353	Proteasome subunit beta type-5 Psmb5	17895.977	15998.164	17161.065
CD44_MOUSE	3	3	0.508817	CD44 antigen Cd44	2147.711	1655.939	2003.860
COMD3_MOUSE	1	1	0.510866	COMM domain-containing protein 3 Commd3	243.975	228.347	261.524
TOM1_MOUSE	7	7	0.511011	Target of Myb protein 1 Tom1	1255.050	1277.838	1184.483
ANM5_MOUSE	1	1	0.513559	Protein arginine N-methyltransferase 5 Prmt5	79.201	71.574	100.126
PLAP_MOUSE	2	2	0.517938	Phospholipase A-2-activating protein Plaa	336.215	303.653	286.669
FRPD4_MOUSE	1	1	0.518361	FERM and PDZ domain-containing protein 4 Frmpd4	0.008	31.885	0.956
VPS35_MOUSE	11	10	0.521758	Vacuolar protein sorting-associated protein 35 Vps35	3981.612	4281.384	4010.553
DUS3_MOUSE	1	1	0.527229	Dual specificity protein phosphatase 3 Dusp3	90.095	132.057	54.552
PSB3_MOUSE	8	8	0.544565	Proteasome subunit beta type-3 Psmb3	20217.830	19004.903	17419.243
SYK_MOUSE	4	4	0.549397	Lysine--tRNA ligase Kars1	2012.854	2022.661	1874.609
ARL2_MOUSE	1	1	0.559961	ADP-ribosylation factor-like protein 2 Arl2	180.201	196.717	191.953
GDIR2_MOUSE	1	1	0.562999	Rho GDP-dissociation inhibitor 2 Arhgdib	125.754	141.136	196.165
GET3_MOUSE	3	2	0.563711	ATPase GET3 Get3	840.574	688.898	669.486
VP26A_MOUSE	1	1	0.565323	Vacuolar protein sorting-associated protein 26A Vps26a	197.448	185.303	191.801
PLP2_MOUSE	1	1	0.568509	Proteolipid protein 2 Plp2	814.749	726.780	839.958
TCPQ_MOUSE	23	23	0.577269	T-complex protein 1 subunit theta Cct8	35465.289	33081.784	34040.952
IGF2_MOUSE	2	2	0.584087	Insulin-like growth factor II Igf2	271.696	320.534	348.845

PSDE_MOUSE	9	9	0.586752	26S proteasome non-ATPase regulatory subunit 14 Psmd14	8923.668	9219.231	8215.762

ITM2B_MOUSE	3	3	0.587341	Integral membrane protein 2B Itm2b	664.570	607.817	550.931
PP1R7_MOUSE	3	3	0.595786	Protein phosphatase 1 regulatory subunit 7 Ppp1r7	886.467	884.345	748.387
ITPA_MOUSE	2	2	0.597078	Inosine triphosphate pyrophosphatase Itpa	483.338	371.513	486.406
BUB3_MOUSE	2	2	0.599538	Mitotic checkpoint protein BUB3 Bub3	164.435	175.853	191.686
CTNA1_MOUSE	2	1	0.601972	Catenin alpha-1 Ctnna1	858.124	722.268	711.994
RL35A_MOUSE	4	4	0.603875	60S ribosomal protein L35a Rpl35a	26141.646	23449.238	21341.672
PLAK_MOUSE	1	1	0.604017	Junction plakoglobin Jup	8.096	51.805	2.916
HNRPD_MOUSE	3	2	0.606396	Heterogeneous nuclear ribonucleoprotein D0 Hnrnpd	713.023	755.190	613.213
KLC2_MOUSE	2	1	0.609632	Kinesin light chain 2 Klc2	454.701	494.376	418.453
BIEA_MOUSE	1	1	0.609892	Biliverdin reductase A Blvra	123.687	108.692	109.726
S10A6_MOUSE	3	3	0.613181	Protein S100-A6 S100a6	8525.355	8305.919	8341.434
SPRE_MOUSE	2	2	0.615342	Sepiapterin reductase Spr	319.462	329.801	370.860
RLA1_MOUSE	1	1	0.615839	60S acidic ribosomal protein P1 Rplp1	1686.539	2678.090	2480.975
MYL6B_MOUSE	4	3	0.616524	Myosin light chain 6B Myl6b	537.889	545.657	595.367
CAN2_MOUSE	1	1	0.62468	Calpain-2 catalytic subunit Capn2	42.836	50.962	46.696
ARC1B_MOUSE	5	5	0.627789	Actin-related protein 2/3 complex subunit 1B Arpc1b	2485.991	2368.626	2191.311
DEST_MOUSE	1	1	0.632782	Destrin Dstn	18.809	3.266	9.393
MAP1A_MOUSE	1	1	0.632852	Microtubule-associated protein 1A Map1a	72.939	73.605	55.128

ACADL_MOUSE	1	1	0.633349	Long-chain specific acyl-CoA dehydrogenase, mitochondrial Acadl	732.012	722.404	586.307
PSMD1_MOUSE	11	10	0.636671	26S proteasome non-ATPase regulatory subunit 1 Psmd1	3468.030	3610.748	3479.549
ARMC8_MOUSE	1	1	0.640685	Armadillo repeat-containing protein 8 Armc8	263.476	257.382	175.577
RAB1B_MOUSE	7	1	0.641153	Ras-related protein Rab-1B Rab1b	311.725	366.017	315.225
AACS_MOUSE	1	1	0.648521	Acetoacetyl-CoA synthetase Aacs	19.895	23.697	27.283
EXTL2_MOUSE	2	1	0.65283	Exostosin-like 2 Extl2	236.181	190.545	189.849

UBE2N_MOUSE	2	1	0.664546	Ubiquitin-conjugating enzyme E2 N Ube2n	174.916	220.628	219.744
C1RA_MOUSE	1	1	0.665455	Complement C1r-A subcomponent C1ra	296.529	520.994	254.341
PSMD8_MOUSE	4	3	0.665731	26S proteasome non-ATPase regulatory subunit 8 Psmd8	1587.086	1492.802	1503.188
VIME_MOUSE	37	30	0.668945	Vimentin Vim	45746.463	45418.411	42404.371
LYZ1_MOUSE	1	1	0.672448	Lysozyme C-1 Lyz1	1997.315	1773.666	1899.696
KAT2B_MOUSE	1	1	0.673595	Histone acetyltransferase KAT2B Kat2b	567.231	601.973	630.964
WDR61_MOUSE	1	1	0.676279	WD repeat-containing protein 61 Wdr61	168.012	163.077	140.889
DPP3_MOUSE	4	3	0.676365	Dipeptidyl peptidase 3 Dpp3	1472.780	1245.390	1434.252
COX5A_MOUSE	1	1	0.684604	Cytochrome c oxidase subunit 5A, mitochondrial Cox5a	155.425	98.106	145.766
LKHA4_MOUSE	2	2	0.691676	Leukotriene A-4 hydrolase Lta4h	906.332	844.178	792.021
AIF1L_MOUSE	1	1	0.694205	Allograft inflammatory factor 1-like Aif1l	28.507	25.185	15.754
ML12B_MOUSE	8	2	0.721139	Myosin regulatory light chain 12B Myl12b	2900.123	3284.432	2868.565

HTSF1_MOUSE	1	1	0.721503	HIV Tat-specific factor 1 homolog Htatsf1	14722.501	12432.792	9786.455
NDKB_MOUSE	6	2	0.722351	Nucleoside diphosphate kinase B Nme2	3170.208	2840.128	2474.877
PRDX5_MOUSE	2	2	0.729158	Peroxiredoxin-5, mitochondrial Prdx5	382.416	335.863	321.304
MK01_MOUSE	2	2	0.730265	Mitogen-activated protein kinase 1 Mapk1	362.371	339.379	368.460
PROS_MOUSE	1	1	0.732885	Vitamin K-dependent protein S Pros1	7381.649	5269.311	5908.641
RHOA_MOUSE	3	1	0.734985	Transforming protein RhoA Rhoa	398.188	351.870	337.173
PNPH_MOUSE	1	1	0.735037	Purine nucleoside phosphorylase Pnp	91.387	65.698	84.643
PTTG_MOUSE	1	1	0.739269	Pituitary tumor-transforming gene 1 protein-interacting protein Pttg1ip	141.015	160.236	133.953
NAA25_MOUSE	2	2	0.748418	N-alpha-acetyltransferase 25, NatB auxiliary subunit Naa25	36.717	55.282	61.262
IGSF3_MOUSE	1	1	0.752963	Immunoglobulin superfamily member 3 Igsf3	1521.104	1118.094	1196.492
DCUP_MOUSE	1	1	0.756896	Uroporphyrinogen decarboxylase Urod	72.433	73.682	57.775
DPOLB_MOUSE	1	1	0.760533	DNA polymerase beta Polb	263.230	335.214	273.808
MCA3_MOUSE	5	5	0.762908	Eukaryotic translation elongation factor 1 epsilon-1 Eef1e1	988.637	1107.592	916.707
SGTA_MOUSE	3	3	0.765585	Small glutamine-rich tetratricopeptide repeat-containing protein alpha Sgta	571.652	436.469	565.296
PDCD6_MOUSE	3	2	0.768333	Programmed cell death protein 6 Pdcd6	1077.273	1009.138	1219.464
ARGL1_MOUSE	1	1	0.774862	Arginine and glutamate-rich protein 1 Arglu1	243.120	240.928	320.778
MEP50_MOUSE	2	2	0.775325	Methylosome protein 50 Wdr77	244.438	164.038	210.006
F10A1_MOUSE	5	5	0.780433	Hsc70-interacting protein St13	3154.530	3171.938	3291.064

TMF1_MOUSE	1	1	0.785056	TATA element modulatory factor Tmf1	40.348	51.639	49.457
FKBP4_MOUSE	4	3	0.790644	Peptidyl-prolyl cis-trans isomerase FKBP4 Fkbp4	538.167	597.906	535.867
PTPRK_MOUSE	1	1	0.794749	Receptor-type tyrosine-protein phosphatase kappa Ptprk	153.086	182.360	141.778
RL10L_MOUSE	2	1	0.794949	60S ribosomal protein L10-like Rpl10l	119.607	128.659	120.577
FA43A_MOUSE	1	1	0.798495	Protein FAM43A Fam43a	1180.703	1106.981	1206.843
ASPG_MOUSE	1	1	0.802849	N(4)-(beta-N-acetylglucosaminyl)-Lasparaginase Aga	81.232	93.032	84.937
SRSF2_MOUSE	1	1	0.809338	Serine/arginine-rich splicing factor 2 Srsf2	564.055	597.857	558.072
NPM_MOUSE	8	7	0.815342	Nucleophosmin Npm1	5124.449	5333.986	4994.396
CAN10_MOUSE	1	1	0.826685	Calpain-10 Capn10	685.222	721.758	789.082
IF5_MOUSE	2	2	0.830687	Eukaryotic translation initiation factor 5 Eif5	145.785	132.354	136.943
RL14_MOUSE	4	4	0.834073	60S ribosomal protein L14 Rpl14	5967.003	5985.628	6215.379
ARK72_MOUSE	1	1	0.85279	Aflatoxin B1 aldehyde reductase member 2 Akr7a2	82.920	64.890	48.119
PRDX6_MOUSE	8	8	0.855159	Peroxiredoxin-6 Prdx6	4159.738	3868.009	3969.510
AQP5_MOUSE	2	2	0.856731	Aquaporin-5 Aqp5	1099.773	1030.540	1100.281
CSN1_MOUSE	8	8	0.857168	COP9 signalosome complex subunit 1 Gps1	2080.824	1806.911	1896.637
VAS1_MOUSE	2	2	0.867729	V-type proton ATPase subunit S1 Atp6ap1	531.353	470.053	467.487
CAPG_MOUSE	6	6	0.872964	Macrophage-capping protein Capg	2250.199	2140.623	2135.885
COPE_MOUSE	5	4	0.873716	Coatomer subunit epsilon Cope	1303.440	1249.945	1394.711
PARK7_MOUSE	5	5	0.874255	Parkinson disease protein 7 homolog Park7	1788.036	1577.694	1742.390

BROX_MOUSE	2	2	0.880517	BRO1 domain-containing protein BROX Brox	246.298	289.568	262.104
BTF3_MOUSE	2	2	0.883849	Transcription factor BTF3 Btf3	343.990	440.395	399.888
KAD1_MOUSE	6	6	0.885221	Adenylate kinase isoenzyme 1 Ak1	1393.679	1342.782	1265.008
PCBP1_MOUSE	4	2	0.898741	Poly(rC)-binding protein 1 Pcbp1	1490.258	1506.360	1361.393
OMD_MOUSE	2	1	0.900236	Osteomodulin Omd	4365.565	2362.881	3107.264
DHPR_MOUSE	1	1	0.906954	Dihydropteridine reductase Qdpr	80.197	85.996	84.309
NUCL_MOUSE	10	10	0.910812	Nucleolin Ncl	10868.761	11091.244	11088.187
MYMK_MOUSE	1	1	0.913563	Protein myomaker Mymk	102.807	115.738	113.063
CLIC1_MOUSE	7	6	0.91622	Chloride intracellular channel protein 1 Clic1	5245.197	5505.611	5377.038
APEX1_MOUSE	1	1	0.923706	DNA-(apurinic or apyrimidinic site) endonuclease Apex1	260.752	204.433	211.046
ALD2_MOUSE	6	2	0.928412	Aldose reductase-related protein 2 Akr1b8	696.855	642.480	631.158
QSOX1_MOUSE	18	16	0.932005	Sulfhydryl oxidase 1 Qsox1	17174.332	16939.208	17128.503
LDLR_MOUSE	2	2	0.936728	Low-density lipoprotein receptor	570.255	558.899	586.652
ZYX_MOUSE	1	1	0.937039	Zyxin	538.705	128.632	172.310
ARP5L_MOUSE	2	2	0.93768	Actin-related protein 2/3 complex subunit 5-like protein Arpc5l	532.934	511.594	530.547
GRP75_MOUSE	1	1	0.946139	Stress-70 protein, mitochondrial Hspa9	43.704	40.047	45.203
RL13_MOUSE	9	9	0.956785	60S ribosomal protein L13 Rpl13	21675.388	20790.054	21163.784
GAMT_MOUSE	1	1	0.960294	Guanidinoacetate N-methyltransferase Gamt	283.249	296.773	290.841
TAGL2_MOUSE	9	8	0.963894	Transgelin-2 Tagln2	4258.382	4045.524	4195.580
BAG2_MOUSE	1	1	0.968846	BAG family molecular chaperone regulator 2 Bag2	199.617	186.805	214.594

IFM2_MOUSE	2	1	0.982571	Interferon-induced transmembrane protein 2 Ifitm2	338.685	332.488	347.015
GNAQ_MOUSE	1	1	0.986949	Guanine nucleotide-binding protein G(q) subunit alpha Gnaq	789.686	707.796	706.070
ARF1_MOUSE	7	6	0.993424	ADP-ribosylation factor 1 Arf1	1217.290	1185.325	1214.491